

**COMPUTATIONAL FLUID DYNAMICS MODELING WITH EXPERIMENTAL
VALIDATION OF THE COMPLEX SPATIO-TEMPORAL PHENOMENA IN SLURRY
BUBBLE COLUMN REACTORS FOR FISCHER-TROPSCH SYNTHESIS**

by

Omar M. Basha

B.S. Chemical Engineering, Texas A&M University at Qatar, 2010

M.S. Chemical Engineering, Texas A&M University at Qatar, 2012

Submitted to the Graduate Faculty of
The Swanson School of Engineering in partial fulfillment
of the requirements for the degree of
Doctor of Philosophy in Chemical Engineering

University of Pittsburgh

2016

UNIVERSITY OF PITTSBURGH
SWANSON SCHOOL OF ENGINEERING

This dissertation was presented

by

Omar M. Basha

It was defended on

November 4th, 2016

and approved by

Shiao-Hung Chiang, Ph.D., Professor Emeritus, Department of Chemical and Petroleum Engineering

George Klinzing, Ph.D., Professor, Department of Chemical and Petroleum Engineering

Ipsita Banerjee, Ph.D., Associate Professor, Department of Chemical and Petroleum Engineering

Patrick Smolinski, Ph.D., Associate Professor, Department of Mechanical Engineering and Materials Science

Isaac K. Gamwo, Ph.D., Senior Research Chemical Engineer, U.S. Department of Energy

Dissertation Director: Badie I. Morsi, Ph.D., Professor, Department of Chemical and Petroleum Engineering

Copyright © by Omar M. Basha

2016

**CFD MODELING WITH EXPERIMENTAL VALIDATION OF THE COMPLEX
SPATIO-TEMPORAL PHENOMENA IN SLURRY BUBBLE COLUMN REACTORS
FOR FISCHER-TROPSCH SYNTHESIS**

Omar M. Basha, Ph.D.

University of Pittsburgh, 2016

A multiphase Eulerian, three-dimensional, computational fluid dynamics (CFD) model was developed and implemented in ANSYS, Fluent v14.5 to predict the local hydrodynamics and the overall performance of Slurry Bubble Column Reactors (SBCRs) for Fischer Tropsch (F-T) synthesis [1, 2]. The CFD model predictions were validated against the experimental gas holdup profiles obtained under ambient conditions by Yu and Kim [3] for air-water-glass beads system and by Chen et al. [4] for N₂-Drakeol-glass beads system. The model predictions were also validated against the overall gas holdup data for He/N₂ mixtures, as surrogates for H₂/CO, measured in a molten F-T reactor wax containing iron catalyst, under operating conditions typical to those of F-T synthesis in our pilot-scale SBCR, available in the Reactor and Process Engineering Laboratory (RAPEL) at the University of Pittsburgh. These validations, carried out in the absence of F-T reactions, showed that the inclusion of the RNG k - ϵ turbulence model, coupled with the gas-liquid drag model by Wen-Yu [5], the liquid-solid drag model by Schiller -Naumann [6] and the lift coefficient by Tomiyama et al. [7], along with our empirical mass transfer coefficients correlation into the CFD model, led to the most accurate predictions of the experimental data mentioned above.

The validated CFD model was then used to predict the effects of internals and spargers design on the local hydrodynamics in our pilot-scale (0.3-m ID, 3-m height) SBCR and the effects of internals on the local hydrodynamics in a larger-scale conceptual SBCR (1-m ID, 10-m height), in

the absence of F-T reactions. Moreover, the kinetic expressions for F-T and WGS reactions measured for iron catalyst provided by the National Institute for Clean-and-Low-Carbon Energy (NICE), China were incorporated into the validated CFD model and the subsequent model was then used to predict the local hydrodynamics and the overall performance of our pilot-scale SBCR and those of the commercial-scale (5.8-m ID, 30-height) SBCR by NICE. The simulation results are described in the following:

- In the absence of F-T reactions, the effect of parallel internals on the local hydrodynamics (gas holdup, liquid and gas velocity vectors, and mixing intensities) were predicted in the pilot-scale SBCR reactor, provided with a 6-arms spider gas sparger, using the CFD model. The simulation results showed that the presence of internals increased the gas holdup, the gas and liquid velocities and the turbulence intensities, and led to more even gas holdup radial distribution in the reactor. Also, larger liquid recirculation cells were present in the upper part of the reactor around the internals after 40 s, while smaller and faster liquid recirculation cells were present in the vicinity of the sparger.
- In the absence of F-T reactions, the effects of the gas sparger types and orifice orientations on the gas holdup, Sauter mean bubble diameter, axial concentration profiles, mean axial velocity profiles and flow structure were predicted in the pilot-scale SBCR, including no internals, using the CFD model. Three spargers (a 6-arms spider and a concentric ring sparger, both with upward- and downward-facing orifices, and a perforated plate) were used. The simulation results showed that the spargers with downward-facing orifices were more effective in solids dispersion and exhibited larger Sauter bubble diameters when compared with those of upward-facing orifices. The 6-arms spider spargers resulted in smaller Sauter bubble diameters when compared with those of the concentric ring spargers. For the spider spargers, faster and smaller

liquid recirculation cells appeared in the vicinity of the spargers, whereas, larger and slower liquid recirculation cells appeared after about 0.36-m measured from the bottom flange. For the concentric ring and perforated plate spargers, however, slower and larger liquid recirculation cells were present throughout the reactor starting at the top of the distributor.

- In the absence of F-T reactions, the effects of internals configuration (3 parallel and 4 bundled) on the gas holdup and liquid axial velocity were predicted in the large-scale conceptual SBCR using the CFD model. A concentric-ring sparger, consisting of 3 concentric-rings with 333, 167 and 111 identical (7-mm ID) orifices was used. The simulation results showed that using parallel internals led to faster and larger liquid recirculations at a much earlier time when compared with those using bundled internals. Liquid recirculations were stronger when using 1-bundled or 3-bundled internals than those when using a 4-bundled or 5-bundled internals; and the liquid backmixing profiles were governed by the clearance between the internals and the reactor's wall. Also, using bundled internals exhibited smoother radial gas holdup profiles, with lower local gas holdup values, when compared with those using parallel internals.
- In the presence of F-T and WGS reaction kinetics with iron catalyst, the gas holdup, the Sauter mean bubble diameter and the performance (CO and H₂ conversions, and C₅⁺ products yield) of the pilot-scale SBCR, provided with one-bundled internals (one, 2.5-inch pipe at the center surrounded by six, 1.75-inch pipes in a hexagonal pattern) and a 6-arms spider sparger, were predicted using the CFD model. The simulations were carried out using catalyst concentrations of 5, 10 and 15 vol.% and H₂/CO ratios of 1, 1.5 and 2, at a pressure of 20.5 bar, a temperature of 443 K, and a superficial gas velocity of 0.24 m/s. The simulation results showed that the gas holdup and Sauter mean bubble diameter axial profiles in the presence of F-T reactions were different from those predicted in the absence of F-T chemical reactions. Also, the CO and H₂

conversions increased with increasing catalyst concentration; and our pilot-scale SBCR can produce a maximum yield of 1.87 tons/day of C_5^+ products using a H_2/CO ratio of 2/1 and a catalyst concentration of 15 vol%.

- In the presence of F-T and WGS reaction kinetics with iron catalyst, the overall performances of the NICE commercial-scale F-T SBCR, provided with 604 bundled internals and a 12 concentric-ring spargers, were also predicted using the CFD model. The simulations were carried out at four superficial gas velocities of 0.12, 0.24, 0.3 and 0.4 m/s using a catalyst concentration of 10 vol%, a pressure of 29 bar, and a temperature of 528 K. Under these conditions, the simulation results showed that the CO conversions were 48%, 59%, 58% and 55%; the H_2 conversions were 36%, 51%, 56% and 54%; and the C_5^+ products yields were 275, 576, 627 and 654 ton/day at the superficial gas velocities of 0.12, 0.24, 0.3 and 0.4 m/s, respectively.

Thus, our CFD model built and validated in this study for 3-phase non-reactive and reactive systems could be used to optimize the SBCR design and/or troubleshoot any problems associated with the internal reactor operation.

DESCRIPTORS

Absorption	Multiphase Reactors
Bubble size	Mass Transfer
Computational Fluid Dynamics	Reactor Design
Dynamic Gas Disengagement	Reactor Modeling
Fischer-Tropsch	Sauter Mean Bubble Diameter
Gas Holdup	Slurry Bubble Column Reactor
Gas-Liquid Interfacial Area	Statistical Experimental Design
Hydrodynamics	Syngas
Multiphase Flow	Volumetric Mass transfer Coefficient
Multiphase Modelling	

TABLE OF CONTENTS

DESCRIPTORS	VIII
TABLE OF CONTENTS	IX
LIST OF TABLES	XIV
LIST OF FIGURES	XVII
NOMENCLATURE	XXIV
ACKNOWLEDGEMENT	XXX
1.0 INTRODUCTION	1
2.0 LITERATURE REVIEW	9
2.1 KINETIC STUDIES OF FISCHER-TROPSCH SYNTHESIS.....	9
2.2 HYDRODYNAMIC STUDIES IN F-T SBCR	13
2.2.1 Overall Gas Holdup	14
2.2.2 Radial Distribution of Gas Holdup.....	20
2.2.3 Sauter Mean Gas Bubbles Diameter	22
2.2.4 Bubble Dynamics	25
2.2.5 Bubble Rise Velocity	28
2.3 MASS TRANSFER STUDIES IN F-T SBCR	30
2.4 HEAT TRANSFER STUDIES IN F-T SBCR	37
2.4.1 Previous Studies Investigating Effect of Internals on BCR and SBCR Performance	37
2.5 MODELING OF SBCRS FOR F-T SYNTHESIS	42
2.5.1 Axial Dispersion Models	43

2.5.2	Multiple Cell Circulation Models	51
2.5.3	Computational Fluid Dynamics (CFD) Models	56
2.5.3.1	Commonly used drag coefficient models for two-phase and three-phase systems	64
3.0	RESEARCH OBJECTIVE	68
4.0	CFD MODEL FORMULATION	70
4.1	SOLID PHASE REPRESENTATION	72
4.2	TURBULENCE MODEL	74
4.3	MOMENTUM EXCHANGE TERMS AND INTERPHASE COEFFICIENT CORRELATIONS	75
4.4	BUBBLES REPRESENTATION	77
4.4.1	Bubble Induced Turbulence	78
4.4.2	Bubble Population Balance.....	79
4.5	KINETICS AND MASS TRANSFER	82
4.6	SOLUTION METHOD AND BOUNDARY CONDITIONS.....	83
5.0	CFD MODEL VALIDATION.....	86
5.1	TESTING OF CFD MODEL USING AQUEOUS AIR-WATER-GLASS BEADS DATA BY YU AND KIM [3]	86
5.2	VALIDATION OF OUR CFD MODEL USING ORGANIC N ₂ -DRAKEOL-GLASS BEADS DATA BY CHEN ET AL. [4]	91
5.3	VALIDATION AGAINST OUR EXPERIMENTAL DATA OBTAINED FOR N ₂ -F-T REACTOR WAX-IRON-BASED CATALYST SYSTEM	93
5.3.1	Experimental Setup.....	93
5.3.2	Gas-Liquid-Solid System and Operating Conditions Used	100
5.3.2.1	Gas Phase.....	100
5.3.2.2	Liquid Phase	100
5.3.2.3	Solid Phase.....	104

		5.3.2.4 Operating Conditions Used	104
5.3.3		Hydrodynamic and Mass Transfer Parameters in the Pilot Scale SBCR under F-T Conditions	106
	5.3.3.1	Gas Holdup	106
	5.3.3.2	Sauter Mean Bubble Diameter	112
	5.3.3.3	Volumetric Mass Transfer Coefficients	116
5.3.4		Geometry and Numerical Meshing of the Pilot-Scale SBCR.....	120
5.3.5		Comparison between the CFD model predictions and our experimental data	123
6.0		CFD MODEL PREDICTIONS OF THE HYDRODYNAMICS INSIDE A SBCR.....	126
6.1		EFFECT OF THE GAS SPARGER TYPE ON THE LOCAL HYDRODYNAMICS IN THE PILOT-SCALE SBCR.....	126
	6.1.1	Effect of Sparger Design on the Gas Holdup Inside the Pilot-Scale SBCR .	130
	6.1.2	Effect of Sparger Design on the Liquid Recirculations inside the SBCR	137
	6.1.3	Effect of Sparger Design on the Liquid Turbulence Intensity inside the SBCR.....	141
	6.1.4	Effect of Sparger Orifices Orientation on the Local Hydrodynamics in the SBCR	145
	6.1.5	Sensitivity Analysis of the Model Parameters.....	154
6.2		EFFECTS OF INTERNALS ON THE LOCAL HYDRODYNAMICS IN SBCRS	157
	6.2.1	Effect of Internals in the Pilot-Scale Reactor on the Liquid Backmixing, Gas Holdup and Local Turbulence Intensity	158
	6.2.2	Effect of Parallel Internal Configurations on the Liquid Backmixing and Gas Holdup	165
	6.2.3	Effect of Bundled Internal Configurations on the Gas Holdup and Liquid Backmixing in the Conceptual Reactor.....	170
6.3		CFD MODEL PREDICTIONS OF PERFORMANCE OF A PILOT- AND LARGE- SCALE SBCRS FOR F-T SYNTHESIS.....	177

6.3.1	Prediction of the Pilot-Scale SBCR Performance	179
6.3.2	Effect of Incorporating Kinetics on the Local Hydrodynamics in the Pilot-Scale SBCR.....	182
6.3.3	Prediction of the Industrial-Scale SBCR Performance	187
7.0	CONCLUDING REMARKS.....	190
	APPENDIX A: LITERATURE REVIEW TABLES	199
	APPENDIX B: EXPERIMENTAL PROCEDURES AND CALCULATION METHODS	261
B.1	EXPERIMENTAL PROCEDURES.....	261
B.1.1	ε_G Measurement	261
B.1.2	d_{32} Measurement	262
B.1.3	k_{La} Measurement	262
B.2	CALCULATIONS.....	264
B.2.1	Peng-Robinson EOS.....	264
B.2.2	Equilibrium Solubility, C^*	266
B.2.3	Gas Holdup, ε_G	266
B.2.4	Gas Bubbles Size (d_b) and the Sauter Mean Bubble Diameter (d_{32})	268
B.2.5	Volumetric Liquid-Side Mass Transfer Coefficient, k_{La}	271
	APPENDIX C: EFFECT OF OPERATING CONDITIONS ON THE GAS BUBBLES DISTRIBUTION.....	272
C.1	EFFECT OF PRESSURE ON GAS BUBBLES DISTRIBUTION.....	273
C.2	EFFECT OF SOLID CONCENTRATION.....	275
C.3	EFFECT OF TEMPERATURE	277
C.4	EFFECT OF SUPERFICIAL GAS VELOCITY.....	280
C.5	EFFECT OF GAS DENSITY	281
	APPENDIX D: COMPARISON WITH LITERATURE GAS HOLDUP AND SAUTER BUBBLE DIAMETER DATA	283

APPENDIX E: CORRELATIONS OF THE HYDRODYNAMIC AND MASS TRANSFER PARAMETERS291

E.1 OVERALL GAS HOLDUP CORRELATION291

E.2 SAUTER MEAN DIAMETER OF GAS BUBBLES CORRELATION293

E.3 HOLDUP OF LARGE GAS BUBBLES CORRELATION.....294

E.4 DIAMETER OF LARGE GAS BUBBLES CORRELATION295

E.5 VOLUMETRIC MASS TRANSFER COEFFICIENT CORRELATION.....295

E.6 NOVEL APPROACH AND CORRELATION FOR BUBBLE SIZE DISTRIBUTION IN THE SBCR OPERATING IN THE CHURN-TURBULENT FLOW REGIME297

REFERENCES.....311

LIST OF TABLES

Table 1-1: Commercial F-T plants, catalysts and reactor technologies [12, 32].....	6
Table 2-1: Operating conditions used in the correlations for comparison purposes.....	18
Table 2-2: Correlations for the physicochemical properties of the liquid phase [126].....	18
Table 2-3: Experimental work for measuring radial gas holdups in three phase reactors	21
Table 2-4: Summary of reported effects of operating conditions on the hydrodynamic mass transfer parameters.....	35
Table 2-5: Different turbulence models available in the literature [275].....	61
Table 4-1: Momentum interphase terms used in our model.....	76
Table 4-2: Interphase coefficient expressions used in our model.....	77
Table 5-1: Experimental conditions by Yu and Kim [3] used for selecting of our CFD model parameters.....	86
Table 5-2: Model equations for the three k- ϵ turbulence models used	88
Table 5-3: Absolute average relative errors (AARE) for different turbulence and drag G-L and L-S models against experimental data by Yu and Kim [3].....	89
Table 5-4: Experimental details by Chen et al. [4]	92
Table 5-5: Comparison between average relative errors (ARE) and absolute average relative errors (AARE) between experimental results and CFD predictions.....	92
Table 5-6: Characteristics of the SBCR	94
Table 5-7: Thermodynamic properties of the gases used.....	100
Table 5-8: Correlations for predicting the physicochemical properties of the reactor wax	102
Table 5-9: Size distribution of the solid particles used	104
Table 5-10: Experimental conditions	105

Table 6-1: Description of the spargers investigated in this work	128
Table 6-2: Model performance against the radial gas holdup experimental data of.....	155
Table 6-3: Model performance against overall gas holdup data measured in our lab	156
Table 6-4: Details of parallel internal configurations used in this study	166
Table 6-5: Details of bundled internal configurations used in this study	170
Table 6-6: F-T Catalyst and kinetics provided by NICE	177
Table 6-7: Syngas composition used in this investigation	177
Table 6-8: Design data for the pilot-scale and industrial-scale SBCRs	179
Table A-1: Kinetics studies for the F-T synthesis on iron catalyst.....	200
Table A-2: Kinetics studies for the WGS reaction on iron catalyst.....	207
Table A-3: Kinetics studies for the Fischer-Tropsch synthesis on cobalt-based catalyst	210
Table A-4: Literature data on the hydrodynamics and mass transfer in SBCRs using F-T liquids	213
Table A-5: Gas holdup correlations for three-phase reactors available in literature	214
Table A-6: Bubbles diameter correlations available in the literature	221
Table A-7: Bubbles rise velocity correlations available in the literature	224
Table A-8: Gas-Liquid mass transfer correlations applicable to SBCRs.....	227
Table A-9: Heat transfer correlations applicable to SBCRs.....	232
Table A-10: Liquid-phase axial dispersion coefficient models	236
Table A-11: Liquid-phase radial dispersion coefficient investigations	239
Table A-12: Solid-phase dispersion coefficient models	240
Table A-13: Literature F-T SBCR empirical models [46, 126].....	241
Table A-14: Summary of multiple cell circulation models [285].....	244
Table A-15: CFD modeling of three-phase reactors.....	246
Table A-16: Commonly used gas-liquid drag models	255
Table A-17: Commonly used liquid-solid and gas-solid drag models.....	257

Table D-1: Gas holdup data sets used in the comparison in Figure D-1.....	287
Table D-2: Sauter bubble diameter data sets used in the comparison in Figure D-2.....	290
Table E-1: Comparison among predictions of the gas holdup correlations	292
Table E-2: Comparison among predictions of the gas bubbles Sauter mean diameter correlations	294
Table E-3: Comparison among predictions of the large gas bubbles holdup correlations.....	294
Table E-4: Comparison among predictions of the large gas bubble diameter correlations	295
Table E-5: Comparison among predictions of $k_L a$ correlations.....	296
Table E-6: Forces involved in the overall energy balance for the gas bubble [272, 323, 336, 351, 372, 647]	302

LIST OF FIGURES

Figure 1-1: Overview of XTL process	2
Figure 1-2: Commercial F-T activities worldwide as of 2016 [12, 31, 36, 37].....	3
Figure 1-3: Different F-T reactor technologies	8
Figure 2-1: Comparison among F-T rate expressions at various H ₂ /CO ratios over Iron catalysts (T = 528 K and P = 3 MPa)	11
Figure 2-2: Comparison among F-T rate expressions at various H ₂ /CO ratios over Cobalt catalysts (T = 528 K and P = 3 MPa)	12
Figure 2-3: Comparison among WGS kinetic rate expressions at various H ₂ /CO ratios (T = 528 K and P = 3 MPa)	13
Figure 2-4: Comparison among literature gas holdup correlations at various (a) superficial gas velocities, (b) Catalyst particle diameters, (c) Solid loadings and (d) h_c/d_c values	19
Figure 2-5: Comparison of various bubble diameter velocity correlations	24
Figure 2-6: Comparison among various bubble rise velocity correlations	29
Figure 2-7: Concentration profiles for mass transfer into a slurry with catalytic particles [46] ...	31
Figure 2-8: Comparison among three-phase correlations for k_{La} at various (a) superficial gas velocities, (b) Catalyst particle diameters, (c) Solid loadings and (d) h_c/d_c values	34
Figure 2-9: Comparison among the liquid axial dispersion models at various	50
Figure 2-10: Circulation cell depiction of the continuous-phase circulation patterns in BCRs and SBCRs: (a) Zehner [280, 281], (b) Groen et Al. [290], (c) Joshi And Sharma [256].....	55
Figure 2-11: Overview of CFD process	56
Figure 2-12: Comparison of various (a) Liquid-Solid and (b) Gas-Liquid drag correlation	67
Figure 4-1: Schematic of the model components and their couplings	70
Figure 5-1: Evaluation of various G-L and L-S drag model combinations using the standard $k-\varepsilon$ ((a) to (c)) and the RNG $k-\varepsilon$ ((d) to (f)) turbulence models against experimental data by Yu and Kim [3]	90

Figure 5-2: Geometry sketch and mesh of the column used by Chen et al. [4]	92
Figure 5-3: Comparison between our CFD model predictions and the experimental radial gas holdup data by Chen et al. [4].....	93
Figure 5-4: Mechanical Specifications of the SBCR	97
Figure 5-5: Schematic of the Experimental Setup	98
Figure 5-6: Photographs of the SBCR and Gas Sparger	99
Figure 5-7: Wax composition in weight fraction.....	101
Figure 5-8: Effect of temperature on the density (a), viscosity (b), surface tension (c) and vapor pressure (d) of the molten reactor wax.....	103
Figure 5-9: CCSD experimental design matrix [8, 151, 365]	105
Figure 5-10: Effect of solids concentration on ϵ_G in F-T reactor wax	108
Figure 5-11: Effect of temperature on ϵ_G in F-T reactor wax at 0-5 vol. % solid concentrations	108
Figure 5-12: Effect of temperature on ϵ_G in F-T reactor wax at 10 vol. % solid concentrations	109
Figure 5-13: Effect of temperature on ϵ_G in F-T reactor wax at 15 vol. % solid concentrations	109
Figure 5-14: Effect of pressure on ϵ_G in F-T reactor wax	110
Figure 5-15: Effect of superficial gas velocity on ϵ_G in F-T reactor wax	110
Figure 5-16: Effect of gas density on ϵ_G in F-T reactor wax.....	111
Figure 5-17: Effect of solids concentration on d_{32} in F-T reactor wax.....	113
Figure 5-18: Effect of temperature on d_{32} in F-T reactor wax at 0 – 5 vol. % solid concentrations	113
Figure 5-19: Effect of temperature on d_{32} in F-T reactor wax at 10 vol. % solid concentrations	114
Figure 5-20: Effect of temperature on d_{32} in F-T reactor wax at 15 vol. % solid concentrations	114
Figure 5-21: Effect of Pressure on d_{32} in F-T reactor wax.....	115
Figure 5-22: Effect of superficial gas velocity on d_{32} in F-T reactor wax	115

Figure 5-23: Effect of temperature on k_{LA} in F-T reactor wax at 0 – 5 vol. % solid concentrations	117
Figure 5-24: Effect of temperature on k_{LA} in F-T reactor wax at 10 vol. % solid concentrations	117
Figure 5-25: Effect of solids concentration on k_{LA} in F-T reactor wax	118
Figure 5-26: Effect of pressure on k_{LA} in F-T reactor wax.....	118
Figure 5-27: Effect of superficial gas velocity on k_{LA} in F-T reactor wax.....	119
Figure 5-28: (a) Picture and (b) Constructed geometry of the sparger used in this study	120
Figure 5-29: Mesh Independence analysis	121
Figure 5-30: Geometry and mesh details of the numerical structure employed in our simulations: (a) Cross section view, (b) Side view in sparger vicinity, (c) Side view of whole column	122
Figure 5-31: Time averaged CFD model validation vs. gas holdup data as a function of (a) temperature and (b) superficial gas velocity.....	124
Figure 5-32: Effect of mass transfer coefficients on our CFD model predictions of the gas holdup data under different operating conditions	125
Figure 6-1: (a) Picture and (b) Constructed geometry of the spider sparger used in this study ..	128
Figure 6-2: Geometry and mesh details of the spider sparger: (a) Cross-section view,	128
Figure 6-3: Geometry and mesh details of the concentric-rings sparger: (a) Built geometry,	129
Figure 6-4: Geometry and mesh details of perforated plate: (a) Cross-section view,	129
Figure 6-5: Snapshots of gas holdup contours at different times for the spider sparger.....	131
Figure 6-6: Snapshots of gas holdup contours at different times for the concentric-rings sparger	132
Figure 6-7: Snapshots of gas holdup contours at different times for the perforated plate	133
Figure 6-8: Comparison of time averaged radial profiles of gas holdup at $H/D = 0.5$ for the three gas spargers used.....	134
Figure 6-9: Comparison of time averaged radial profiles of gas holdup at $H/D = 1$ for the three gas spargers used.....	134
Figure 6-10: Comparison of time averaged radial profiles of gas holdup at $H/D = 2$ for the three gas spargers used.....	135

Figure 6-11: Comparison of time averaged radial profiles of gas holdup at $H/D = 3$ for the three gas spargers used.....	135
Figure 6-12: Comparison of time averaged radial profiles of gas holdup at $H/D = 5$ for the three gas spargers used.....	136
Figure 6-13: Comparison of time averaged radial profiles of gas holdup at $H/D = 7$ for the three gas spargers used.....	136
Figure 6-14: Snapshots of liquid velocity vectors at different times for the spider sparger	138
Figure 6-15: Snapshots of liquid velocity vectors at different times for the concentric-rings sparger	139
Figure 6-16: Snapshots of liquid velocity vectors at different times for the perforated plate	140
Figure 6-17: Snapshots of local turbulence intensity contours at different times for the spider sparger	142
Figure 6-18: Snapshots of local turbulence intensity contours at different times for the concentric-rings sparger	143
Figure 6-19: Snapshots of local turbulence intensity contours at different times for the perforated plate	144
Figure 6-20: Effect of temperature on $EoFr_{0.5}$ under the experimental conditions.....	146
Figure 6-21: Effect of sparger type and nozzles orientation on the gas holdup at different superficial gas velocities.....	149
Figure 6-22: Effect of sparger type and nozzles orientation on the Sauter bubble diameter at different superficial gas velocities	149
Figure 6-23: Comparison of axial solid loadings for different sparger nozzles orientations at $u_g = 0.1$ m/s	150
Figure 6-24: Comparison of axial solid loadings for different sparger nozzles orientations at $u_g = 0.2$ m/s	150
Figure 6-25: Comparison of axial solid loadings for different sparger nozzles orientations at $u_g = 0.3$ m/s	151
Figure 6-26: Mean axial liquid velocity profiles at $H/D = 1$ for different gas spargers at $u_g = 0.2$ m/s	152
Figure 6-27: Mean axial liquid velocity profiles at $H/D = 3$ for different gas spargers at $u_g = 0.2$ m/s	153

Figure 6-28: Mean axial liquid velocity profiles at $H/D = 6$ for different gas spargers at $u_g = 0.2$ m/s.....	153
Figure 6-29: Geometry and mesh structure used in this section: Cross sectional view (a) and view in the vicinity of the sparger (b).....	159
Figure 6-30: Snapshots of gas holdup contours at different times	160
Figure 6-31: Snapshots of turbulence intensity contours at different times.....	162
Figure 6-32: Snapshots of liquid velocity vectors at different times	163
Figure 6-33: Steady state Gas holdup (a), Local turbulence intensity (b) and liquid velocity vectors (c) of the pilot-scale reactor with vertically extended internals	164
Figure 6-34: Liquid axial velocity cross-sectional contours at different heights for the parallel internals configurations at 30 s.....	166
Figure 6-35: Liquid axial velocity cross-sectional contours at different heights for the parallel internals configurations at 300 s	167
Figure 6-36: Gas holdup cross-sectional contours at different heights for the parallel internals configurations at 30 s	168
Figure 6-37: Gas holdup cross-sectional contours at different heights for the parallel internals configurations at 300 s	169
Figure 6-38: Liquid axial velocity cross-sectional contours at different heights for the bundled internals configurations at 30 and 300 s (1-m ID, 10-m high SBCR)	171
Figure 6-39: Liquid axial velocity cross-sectional contours at different heights for the bundled internals configurations at 30 and 300 s (1-m ID, 10-m high SBCR)	172
Figure 6-40: Gas holdup cross-sectional contours at different heights for the bundled internals configurations at 30 s (1-m ID, 10-m high SBCR).....	173
Figure 6-41: Gas holdup cross-sectional contours at different heights for the bundled internals configurations at 300 s (1-m ID, 10-m high SBCR).....	174
Figure 6-42: Axial Sauter mean bubble diameter for different internals configurations.....	175
Figure 6-43: Effect of number of internal pipes and internals CSA coverage on the gas holdup.....	176
Figure 6-44: Effect of number of internal pipes and internals CSA coverage on the liquid backflow fraction.....	176
Figure 6-45: CFD model predictions of CO conversion for different H_2/CO ratios at different catalyst concentrations for F-T synthesis in the pilot-scale SBCR.....	180

Figure 6-46: CFD model predictions of H ₂ conversion for different H ₂ /CO ratios at different catalyst concentrations for F-T synthesis in the pilot-scale SBCR.....	181
Figure 6-47: CFD model predictions of the C ₅₊ products yield for different H ₂ /CO ratios at different catalyst concentrations for F-T synthesis in the pilot-scale SBCR	181
Figure 6-48: Effect of coupling kinetics on the average Sauter mean bubble diameter in the....	183
Figure 6-49: Effect of incorporating kinetics in the CFD model on the average gas holdup in the pilot-scale SBCR.....	184
Figure 6-50: Effect of incorporating kinetics in the CFD model on the gas holdup contours with and without chemical reaction at t = 60 s in the pilot-scale SBCR	185
Figure 6-51: Effect of incorporating kinetics in the CFD model on the liquid recirculation patterns with and without chemical reaction at t = 60 s in the pilot-scale SBCR.....	186
Figure 6-52: Geometry and mesh details of the industrial scale SBCR: (a) Cross-sectional view, (b) mesh structure	187
Figure 6-53: CFD model predictions of the CO conversion for different superficial gas velocities for F-T synthesis in the industrial-scale SBCR	188
Figure 6-54: CFD model predictions of H ₂ conversion for different superficial gas velocities for F-T synthesis in the industrial-scale SBCR.....	189
Figure 6-55: CFD model predictions of the C ₅₊ products yield for different superficial gas velocities for F-T synthesis in the industrial-scale SBCR.....	189
Figure B-1: Dynamic Gas Disengagement in SBCR [619].....	270
Figure C-1: Effect of pressure on bubble volume fraction.....	274
Figure C-2: Effect of pressure on bubble relative frequency	275
Figure C-3: Effect of solid concentration on bubble relative frequency.....	276
Figure C-4: Effect of solid concentration on bubble relative frequency.....	277
Figure C-5: Effect of temperature on bubble volume fraction	278
Figure C-6: Effect of temperature on bubble relative frequency.....	279
Figure C-7: Temperature on the slurry density (a) and viscosity (b) at different solid concentrations	279
Figure C-8: Effect of superficial gas velocity on bubble volume fraction.....	280
Figure C-9: Effect of superficial gas velocity on bubble relative frequency	281

Figure C-10: Effect of gas density on bubble volume fraction	282
Figure C-11: Effect of gas density on bubble relative frequency	282
Figure D-1: Comparison of measured gas holdup data with published data sets in the literature (Details provided in Table 7)	286
Figure D-2: Comparison of measured Sauter bubble diameter data with published data sets in the literature.....	289
Figure E-1: Comparison between experimental data and predicted gas holdup values using Equation (E-1).....	293
Figure E-2: Comparison between experimental data and predicted k_{LA} values using	296
Figure E-3: Pressure drop change with time as obtained from three DGD experiments	300
Figure E-4: Bubbles volume fraction distributions from the DGD under different operating conditions	304
Figure E-5: Bubbles relative frequency distributions from the DGD under different operating conditions	305
Figure E-6: Comparison between experimental and predicted values of the mean bubble diameter	308
Figure E-7: Comparison between experimental and predicted values of the bubble size variance	309
Figure E-8: Comparison between experimental and predicted values of the Sauter bubble diameter using Equation (E-21)	310

NOMENCLATURE

a	Interfacial area
A_b	Heat exchange surface, bed side (m^2)
A_f	Relative free cross-sectional area
A_m	log mean of A_b and A_u (m^2)
A_u	Heat exchange surface, heat transfer medium side (m^2)
C^*	Equilibrium concentration (solubility) in the liquid phase ($\text{mol}\cdot\text{m}^{-3}$)
C_D	Drag Coefficient
C_L	Concentration in the liquid phase ($\text{mol}\cdot\text{m}^{-3}$)
C_S	Concentration of solid particles in the slurry phase (wt.%)
$C_{s,0}$	Solid Concentration at the bottom of the reactor ($\text{kg}\cdot\text{m}^{-3}$)
C_P	Concentration of solid particles in the slurry phase ($\text{kg}\cdot\text{m}^{-3}$)
C_V	Volumetric concentration of solid particles in the slurry phase (vol.%)
d_C	Column diameter (m)
d_o	Sparger orifice diameter (m)
d_p	Particle diameter (m)
d_R	Diameter of internal pipe (m)
d_t	Tube/Column diameter (m)
d_{32}	Sauter mean bubble diameter (m)
D_{AB}	Diffusivity of phase A into B

D_{ea}	Effective diffusivity in the axial direction
D_{ra}	Effective diffusivity in the radial direction
D_{rl}	Radial dispersion coefficient in SBCR
D_{zl}	Axial dispersion coefficient in SBCR
$E\ddot{o}$	Eötvös number
f	Friction factor
F_C	Particle collision force (N)
F_D	Drag force (N)
F_k	Interphase momentum exchange (N·s)
$F_{l,m}$	Suspension inertial force (N)
F_L	Lift force (N)
F_p	Continuous phase pressure gradient force (N)
Fr	Froude number
F_{VM}	Virtual mass force (N)
g	Gravitational acceleration, m/s ²
G	Mass flow rate (kg/m ² ·s)
Ga	Galileo number
h	Reactor height (m)
h_C	Column height (m)
h_{tot}	Mean total enthalpy (kJ/mol)
ΔH	Enthalpy (kJ/mol)
\bar{J}_k	Flux
k	Turbulent kinetic energy (J/mol)

$k_L a$	Volumetric liquid side mass transfer coefficient (1/s)
k_{WGS}	WGS reaction rate constant (units depend on rate expression)
K_L	Thermal conductivity (W/m·K)
l	Packing height (m)
l_e	Characteristic length scale of the eddies
M_W	Molecular weight (kg·kmol ⁻¹)
n_R	Number of internals
P	Pressure (Pa)
P_S	Saturation vapor pressure (Pa)
Pe	Peclet number
P_m	Specific energy of dissipation per unit mass (J/kg)
Pr	Prandtl number
P_V	Liquid-phase vapor pressure, bar
r	Reaction rate (mol·kg ⁻¹ _{catalyst} ·s ⁻¹)
R	Reaction term (mol·m ⁻³ ·s ⁻¹)
Re	Reynolds number
S	Particle surface area per unit volume (m ² /m ³)
Sc	Schmidt number
Sh	Sherwood number
t	Time (s)
t_R	Tube pitch
T	Temperature (K)
u_b	Gas bubble rise velocity (m·s ⁻¹)
u_G	Superficial gas velocity (m·s ⁻¹)

U	Overall heat transfer coefficient ($\text{kJ/m}^2\cdot\text{s}\cdot^\circ\text{C}$)
v	Linear flow velocity (m/s)
$\vec{v}_{eff,rad}$	Radial momentum transfer coefficient (m^2/s)
ν_{sl}	Kinematic slurry viscosity (m^2/s)
V	Eulerian control volume fixed in space and time
X	Weight fraction of the primary liquid in the mixture (See Behkish et al. [8])
y	Mole fraction of gas component, -

Greek Letters

α_l	Heat transfer coefficient on the bed side ($\text{kJ/m}^2\cdot\text{s}\cdot^\circ\text{C}$)
α_k	Phase volume fraction
α_u	Heat transfer coefficient, heat transfer medium side ($\text{kJ/m}^2\cdot\text{s}\cdot^\circ\text{C}$)
Γ	Gas sparger coefficient (See Behkish et al. [9])
ε	Turbulence dissipation ($\text{J/kg}\cdot\text{s}$)
ε_g	Gas holdup
ε_L	Liquid holdup
η	Kinematic viscosity (m^2/s)
κ	Coefficient of bulk viscosity
λ	Dimensionless radial position at maximum downward liquid velocity
λ_{ea}	Effective axial coefficient of thermal conductivity
λ_e^0	Static contribution of effective thermal conductivity ($\text{kJ/m}^2\cdot\text{s}\cdot^\circ\text{C}$)
λ_g	Coefficient of thermal conductivity of fluid ($\text{kJ/m}^2\cdot\text{s}\cdot^\circ\text{C}$)
λ_p	Coefficient of thermal conductivity of packed bed with flowing fluid ($\text{kJ/m}^2\cdot\text{s}\cdot^\circ\text{C}$)

λ_p^0	Coefficient of thermal conductivity of packed bed with stagnant fluid (kJ/m ² ·s·°C)
λ_{ra}	Effective radial coefficient of thermal conductivity
λ_s	Coefficient of thermal conductivity of packing material (kJ/m ² ·s·°C)
μ	Viscosity kg/m·s
μ_b	Relative apparent bed viscosity
μ_T	Turbulent or eddy viscosity
v	Local velocity of the dispersed phase
ξ	Dimensionless radial position
π	3.14
ρ	Density (kg/m ³)
σ	Surface tension (N/m)
τ	Viscous stress tensor (Pa)
τ_{rz}	Reynolds shear stress
$\vec{\phi}$	Body source per unit mass

Subscripts

g or G	Gas
k	Phase
l	Liquid
s	Solid
w	Wall

Acronyms

<i>ADM</i>	Axial-Dispersion Model
<i>CFD</i>	Computational Fluid Dynamics
<i>CSA</i>	Cross Sectional Area
<i>CTL</i>	Coal to Liquid
<i>F-T</i>	Fischer Tropsch
<i>GTL</i>	Gas to Liquid
<i>L-H</i>	Langmuir-Hinshelwood
<i>MCM</i>	Mixing-Cell Model
<i>SDM</i>	Sedimentation-Dispersion Model
<i>WGS</i>	Water Gas Shift

ACKNOWLEDGEMENT

First and foremost, I want to thank my advisor Dr. Badie I. Morsi, who has been a tremendous mentor and inspiration for me, and to whom I will always be deeply grateful for his advice and guidance, both academically and personally. I would like to thank Dr. George Klinzing for encouraging my research and for his help and support throughout the past few years. I would also like to thank my committee members, Dr. Shiao-Hung Chiang, Dr. Ipsita Banerjee, Dr. Isaac Gamwo and Dr. Patrick Smolinski for serving on my committee and for their comments and suggestions.

Thanks to all the students, members and staff of the Reactor and Process Engineering Laboratory and the Department of Chemical and Petroleum Engineering at the University of Pittsburgh. I would like to acknowledge Dr. Laurent Sehabiague for his help and support in performing the experimental part of my thesis and for his guidance when I first arrived at the lab. Also, I want to acknowledge the long term, not only financial, support provided by The National Institute of Clean-and-Low-Carbon Energy (NICE).

Finally, I would like to thank my family, to whom I will always be indebted.

1.0 INTRODUCTION

Fischer-Tropsch (F-T) synthesis provides a pathway for converting carbon containing natural resources, such as natural gas, coal, heavy residue, biomass, municipal waste, etc., into liquid fuels and high value chemicals. Initially called “Synthol,” the F-T synthesis was developed in the 1920’s in Germany at the Kaiser Wilhelm Institute by two Germans, Franz Fischer and Hans Tropsch [10-14], with the intent of producing synthetic hydrocarbons based on the 1902 discovery by Sabatier and Senderens [15] that methane can be produced from H₂ and CO in the presence of nickel catalyst.

The overall F-T process involves three main steps: syngas generation, F-T catalytic reactions and product upgrading, as shown in Figure 1-1. Syngas generation involves converting the carbonaceous feedstock into a H₂-CO mixture (synthesis gas, known as syngas) via reactions with steam and optionally air or oxygen. Solid feedstocks, such as coal and biomass, are converted in a gasifier, of which various types have been already in industrial applications [16-19]. Different gasification processes and technologies have also been discussed in the literature [13, 20-30]. Natural gas, on the other hand, is converted to syngas in a reformer using either partial oxidation (POX), steam methane reforming (SMR) or auto-thermal reforming (ATR).

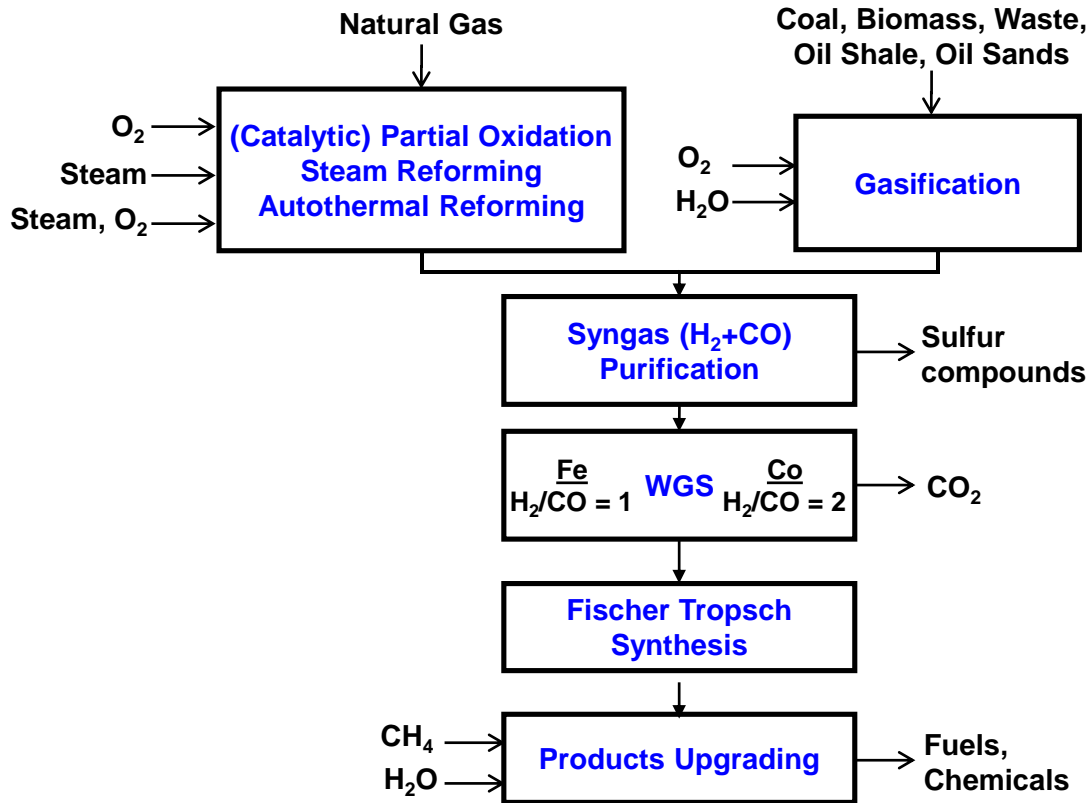


Figure 1-1: Overview of XTL process

Current worldwide commercial activities are summarized in Figure 1-2. As of 2016, the global commercial F-T capacity is 402,500 barrels per day (bpd), with an additional 216,000 bpd under construction. Although numerous planned F-T activities and plants have been put on hold or delayed due to the 2014 slump in oil prices [31, 32], there remains a significant and increased interest in GTL and CTL commercialization, once the oil market stabilizes [33-35].

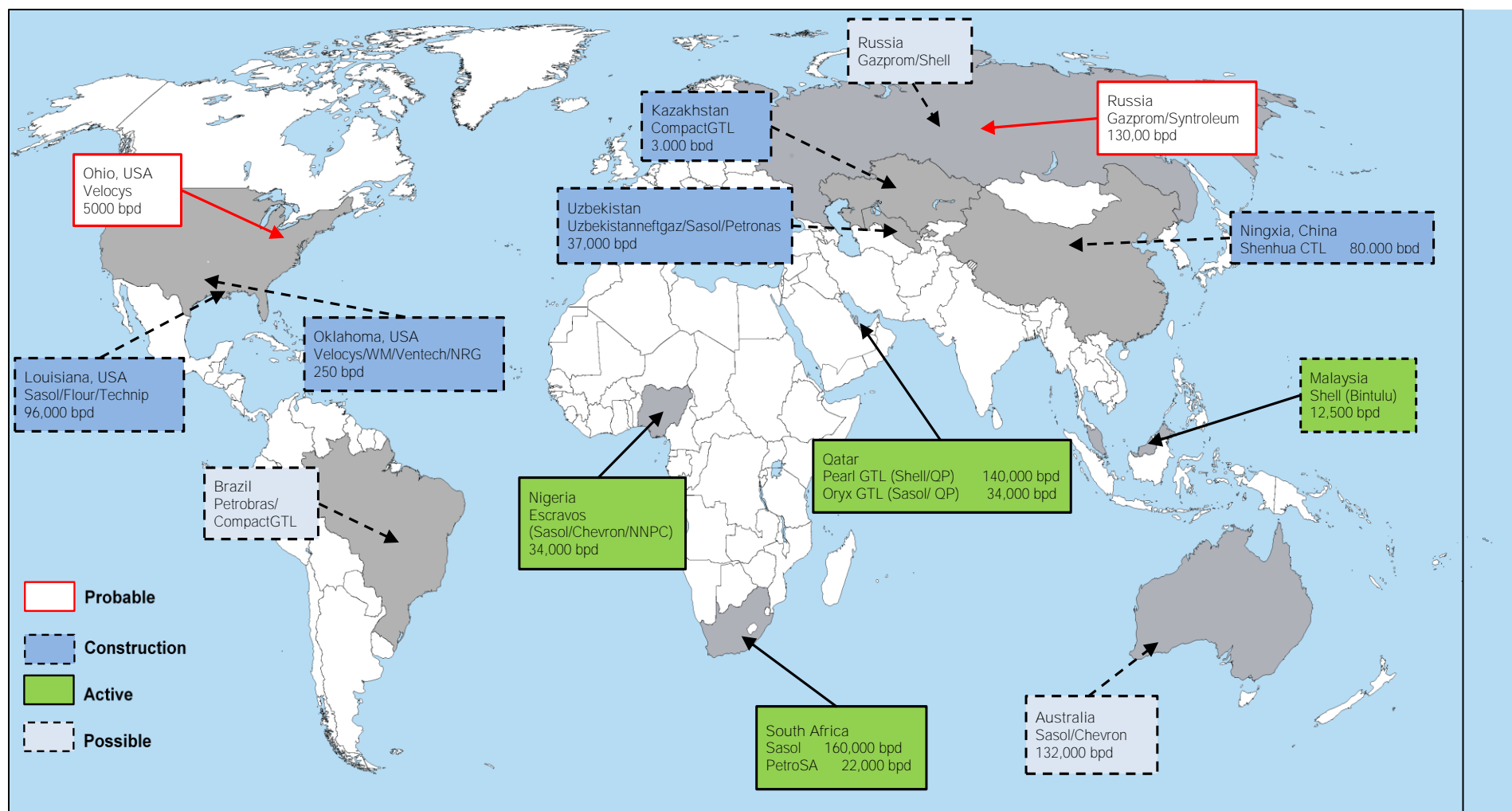
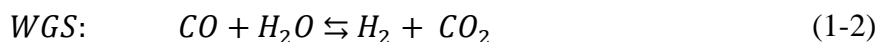
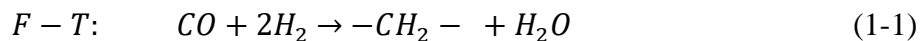


Figure 1-2: Commercial F-T activities worldwide as of 2016 [12, 31, 36, 37]

In F-T synthesis, the syngas reacts in the presence of a heterogeneous catalyst to produce a wide range of hydrocarbon products, primarily linear alkanes and alkenes. Although many metals have been identified to catalyze the F-T reactions, only iron (Fe) and cobalt (Co) have been used in industrial applications [18, 30]. Iron catalyst is cheap and has a high water-gas-shift (WGS) activity, however, it is prone to severe attrition and the water produced during the reaction appeared to decrease its activity [12, 38]. Cobalt-based catalyst, on the other hand, has higher activity than iron catalyst since it is not strongly inhibited by water. It also has longer life than iron catalyst as it is more resistant to attrition. Cobalt-based catalyst, however, is more expensive and has no WGS activity [12, 39].

During Cobalt catalyzed F-T reaction, the oxygen from CO dissociation is converted to H₂O, as shown in Equation (1-1). Conversely, Iron catalyst has a high affinity for the WGS reaction as shown in Equation (1-2), resulting in the conversion of a significant portion of the oxygen from CO dissociation into CO₂.



Thus, the extent of the WGS reaction has to be closely considered as it affects the H₂/CO ratio in the F-T process.

In the case of gas-to-liquid (GTL) applications, the produced syngas is highly rich in H₂ and any additional H₂ via the WGS reaction is undesirable. In contrast, carbon-rich feedstocks, such as coal or biomass, produce a CO-rich syngas; and would therefore require an extent of WGS in the F-T reactor. Hence, industrial GTL plants have conventionally used cobalt-based catalysts, such as the Shell (Pearl) and the Sasol (Oryx) plants in Qatar, whereas the coal-to-liquid (CTL)

plants usually use iron-based catalysts, such as the Sasol Synfuels complex in Secunda, South Africa and the planned CTL plants in China [30, 32, 40].

The F-T process configuration could ultimately dictate the type of the catalyst to be used for GTL or CTL applications. For instance, if the process is configured for recycling CO₂ or CO₂-rich tailgas to the methane reformer, this will lower the H₂/CO ratio and will allow the use of iron catalyst in GTL applications. Similarly, if the process is configured for a sour shift of the syngas from the gasifier over Cu/ZnO catalyst, followed by an acid gas (CO₂ and H₂S) removal, this will allow the use of cobalt in CTL applications. Various process configurations for Anything-to-Liquid (XTL) plants can be found elsewhere [12, 21, 32, 41-45].

Depending on the reaction temperature, the F-T process is referred to as low temperature F-T (LTFT) or high temperature F-T (HTFT). The temperature of the LTFT ranges from 180 to 260 °C and the syncrude produced is wax consisting mostly of long chain hydrocarbons, while the temperature of the HTFT process is between 290 and 360 °C and the products are mostly short chain hydrocarbons and gases. Therefore, the final products of the LTFT process consist mostly of diesel fuel, while gasoline production has been the focus of the HTFT [11]. The LTFT syncrude product is easy to upgrade by a hydroprocessing step and a fractionation step to obtain naphtha and middle distillate, whereas the HTFT syncrude requires more complex refinery facilities [11]. It should be noted that recent R&D and large-scale commercial efforts have been focused on the LTFT due to the current drive for using more diesel engines than gasoline engines, the excellent quality of sulfur-free F-T diesel, and perhaps the mild conditions of the process.

Reactor technologies used for commercial applications of the F-T synthesis are summarized in Table 1-1 and depicted in Figure 1-3. The HTFT reactors include fixed fluidized-bed reactors (FFBRs) and circulating fluidized-bed reactors (CFBRs), whereas multi-tubular

fixed-bed reactors (FBRs) and slurry bubble column reactors (SBCRs) are used for the LTFT process. Also, LTFT micro-channel reactors for small-scale applications have been recently receiving increasing attention, even though, no commercial applications are yet available.

Table 1-1: Commercial F-T plants, catalysts and reactor technologies [12, 32]

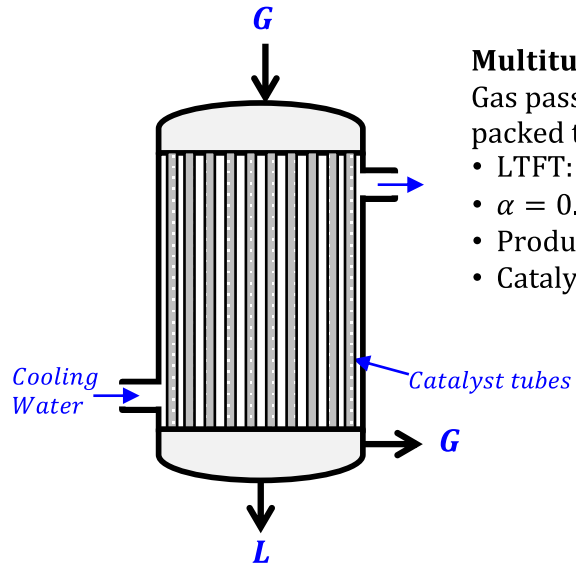
F-T Plant	Country	Date of Operation	Reactor Technology	Catalysts
CTL (14 plants active at end of WWII)	Germany	1935-1962	LTFT FB	Co/ThO ₂ /kieselguhr (100:18:100) before 1938 Co/ThO ₂ /MgO/kieselguhr (100:5:8:200) after 1938
Hydrocol GTL	USA	1951-1957	HTFT FFB	Fused Fe ₃ O ₄ /Al ₂ O ₃ /K ₂ O (97:2.5:0.5) Later replaced by natural magnetite with 0.5% K ₂ O
Sasol I CTL/GTL	South Africa	1955-present	HTFT CFB LTFT FB LTFT SBCR	Magnetite with 0.5% K ₂ O (same as Hydrocol GTL) Precipitated Fe/SiO ₂ /K ₂ O/Cu (100:25:5:5) Precipitated Fe/SiO ₂ /K ₂ O/Cu (100:25:5:5)
Sasol Synfuels CTL	South Africa	1980-present	HTFT FFB	Fused Fe (similar to Sasol I HTFT CFB catalyst)
PetroSA GTL	South Africa	1992-present	HTFT CFB LTFT SBCR	Fused Fe (same as Sasol Synfuels) Co based catalyst
Shell Bintulu	Malaysia	1993-present	LTFT FB	Co/Zr/SiO ₂
Sasol Oryx GTL	Qatar	2007-present	LTFT SBCR	Co/Pt/Al ₂ O ₃
Shell Pearl GTL	Qatar	2011-present	LTFT FB	Co/Zr/SiO ₂
Escravos GTL	Nigeria	2014-present	LTFT SBCR	Co/Pt/Al ₂ O ₃

In multi-tubular FBRs, the syngas flows through small diameter tubes packed with catalyst at small voidage, resulting in a high pressure drop and an increased operating cost. These reactors have comparatively complex heat transfer characteristics and their maximum production capacity

is limited by the amount of heat which can be removed. Hot spots would ultimately result in carbon deposits on the catalyst surfaces and serious plugging of the reactor tubes. These types of reactors, however, have been used to carry out LTFT by both Germany during WWII and Sasol since 1950's as well as by Shell at the Bintulu GTL (Malaysia) and more recently at the Pearl GTL (Qatar) [12, 20, 32, 46, 47].

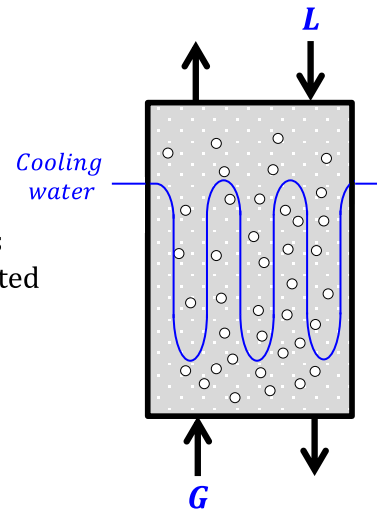
SBCRs, on the other hand, have a simpler design and allow for much higher heat removal efficiencies than multi-tubular FBRs due to the presence of a large volume of the liquid-phase. Its advantages include a much greater flexibility than FBRs and its capital cost is 20 - 40% lower than that of a multitubular FBRs [48]. However, the high mechanical shear on the catalyst resulting in particles attrition and the lack of a reliable system for the fine particles separation from the liquid products, have delayed commercial deployment of SBCRs until the 1990's. Conversely, microchannel reactors have a stationary catalyst bed combined with enhanced heat and mass transfer characteristics. Also, they are typically aimed at exploiting a different market than conventional reactors where their small size is an advantage.

The proper design and scaleup of SBCRs for LTFT synthesis require, among other, precise knowledge of the kinetics, hydrodynamics, mass transfer, heat transfer in F-T synthesis. In the following, a comprehensive literature review of the current state-of-knowledge of the mechanisms, kinetics, hydrodynamics, mass transfer, heat transfer and mathematical as well as computational fluid dynamics (CFD) modeling of LTFT synthesis in SBCRs is provided.



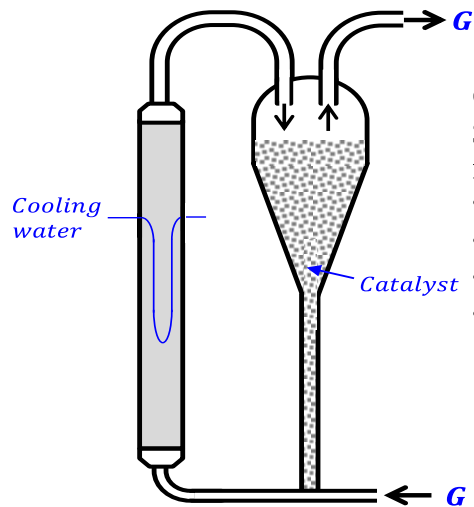
Multitubular Fixed Bed:
 Gas passes through catalyst packed tubes

- LTFT: 180–260 °C
- $\alpha = 0.70 - 0.75$
- Products: Petrol and chemicals
- Catalysts: Fused Fe, K –promoted



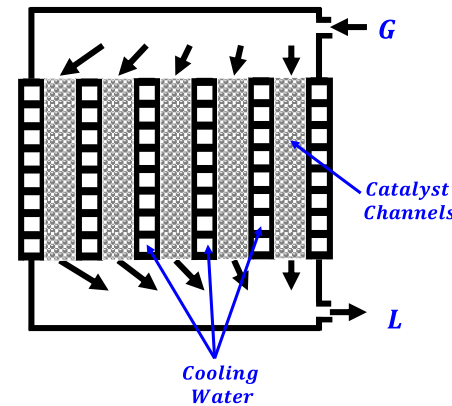
Slurry Bubble Column:
 Bubbles rise through liquid containing fine suspended solids

- LTFT: 180–260 °C
- $\alpha = 0.85 - 0.92$
- Products: Wax, diesel, naphtha
- Catalysts: Supported Co or precipitated Fe



Circulating Fluidized Bed:
 Small solid particles suspended in upward flowing gas

- HTFT: 320–350 °C
- $\alpha = 0.70 - 0.75$
- Products: Petrol and chemicals
- Catalysts: Fused Fe, K –promoted



Microchannel Reactor:
 Packed channels with highly active catalyst

- Catalysts: Supported Cobalt
- Cross flow channels for cooling

Figure 1-3: Different F-T reactor technologies

2.0 LITERATURE REVIEW

2.1 KINETIC STUDIES OF FISCHER-TROPSCH SYNTHESIS

The complexity of the F-T reaction mechanism and the numerous species involved are major obstacles to fully describe the kinetics of the F-T synthesis. In order to simplify the task, many empirical overall reaction rate equations have been developed and are available in the literature. Latest studies, however, have focused on developing comprehensive kinetics based on the Langmuir-Hinshelwood-Hougen-Watson (LHHW) approach, since the variety of the products obtained from the F-T synthesis can only be explained and modeled by detailed kinetic models, which include every elementary reaction [49]. The reaction rates available in the literature for the iron and cobalt-based catalysts are presented in the following.

Iron catalyst has a high WGS activity and therefore the rate of the WGS reaction along with that of the F-T must be taken into account for simulation purposes. Since the 1950's, numerous studies of the kinetics of the F-T on iron catalyst, conducted mostly in fixed-bed and slurry reactors, led to very different kinetic rate expressions as can be seen in Tables A-8-1 and A-8-2 (Appendix A), for F-T and WGS reactions, respectively. Only recently, however, comprehensive kinetic models, able to predict both the syngas consumption rate and products distribution, have been proposed [49-55]. The differences among the rate equations may arise from the diversity of the catalysts, reactors (mass transfer not always negligible) and the operating conditions used in these studies. As a matter of fact, when choosing one of those expressions for

modeling purposes, one has to select the correlations which have been developed within the conditions closest to the simulated ones.

Iron catalyst activity was found to increase with the partial pressure of H_2 and decrease with the partial pressure of H_2O [56, 57], suggesting a strong competition between CO and H_2O for the adsorption onto the active catalyst sites. It was therefore suggested that the F-T reaction rate over iron catalysts is inhibited by water as well as CO_2 , as reflected by the kinetic equations by Anderson [58], Huff and Satterfield [59] and Ledakowicz et al. [60]. In 2006, however, Botes et al. [61] conducted kinetic studies on a potassium-promoted precipitated iron catalyst at Sasol and concluded that neither water nor CO_2 had any significant influence on the chemical reaction kinetics. Also, in 2010, Zhou et al. [62], confirmed the findings and the proposed rate equation by Botes et al. [61].

Review articles on cobalt-catalyzed F-T kinetics are available in the literature [63, 64], whereas Zennaro et al. [65] and Das et al. [66] presented in a tabulated format the explicit rate equations, which were suggested for cobalt catalyst. Of these, the LHHW type rate equations proposed by Outi et al. [67], Sarup and Wojciechowski [68] and Yates and Satterfield [69] had been frequently cited in the literature [70]. Table A-3 (Appendix A) shows the kinetic rate expressions available in the literature for the F-T cobalt-based catalysts.

Thus, the main difference between the kinetics of cobalt-based catalysts and those of iron catalysts lies in the former's inactivity towards the WGS reaction since H_2O is not adsorbed on the catalyst active sites. As a result, the WGS reaction can be neglected when modeling the kinetics of F-T synthesis using cobalt-based catalysts. It seems that the kinetic models for cobalt are consistent with a mechanism where CO dissociation occurs before any interaction with H_2 , whereas those for iron are consistent with a mechanism of hydrogen-assisted CO dissociation.

Actually, recent results from the DFT calculations lend some support to these implications [71]. It was reported that direct CO dissociation is facile over open, high reactivity surfaces, such as corrugated or stepped cobalt surfaces, however, H₂ involvement in CO dissociation seems to be required on low reactivity surfaces, such as carbided iron, which is the predominant active phase under iron catalyzed F-T synthesis conditions [72, 73]. Figures 2-1, 2-2 and 2-3 compare various F-T and WGS rate expressions by different authors at various H₂/CO ratios; and as expected, different expressions provide different values.

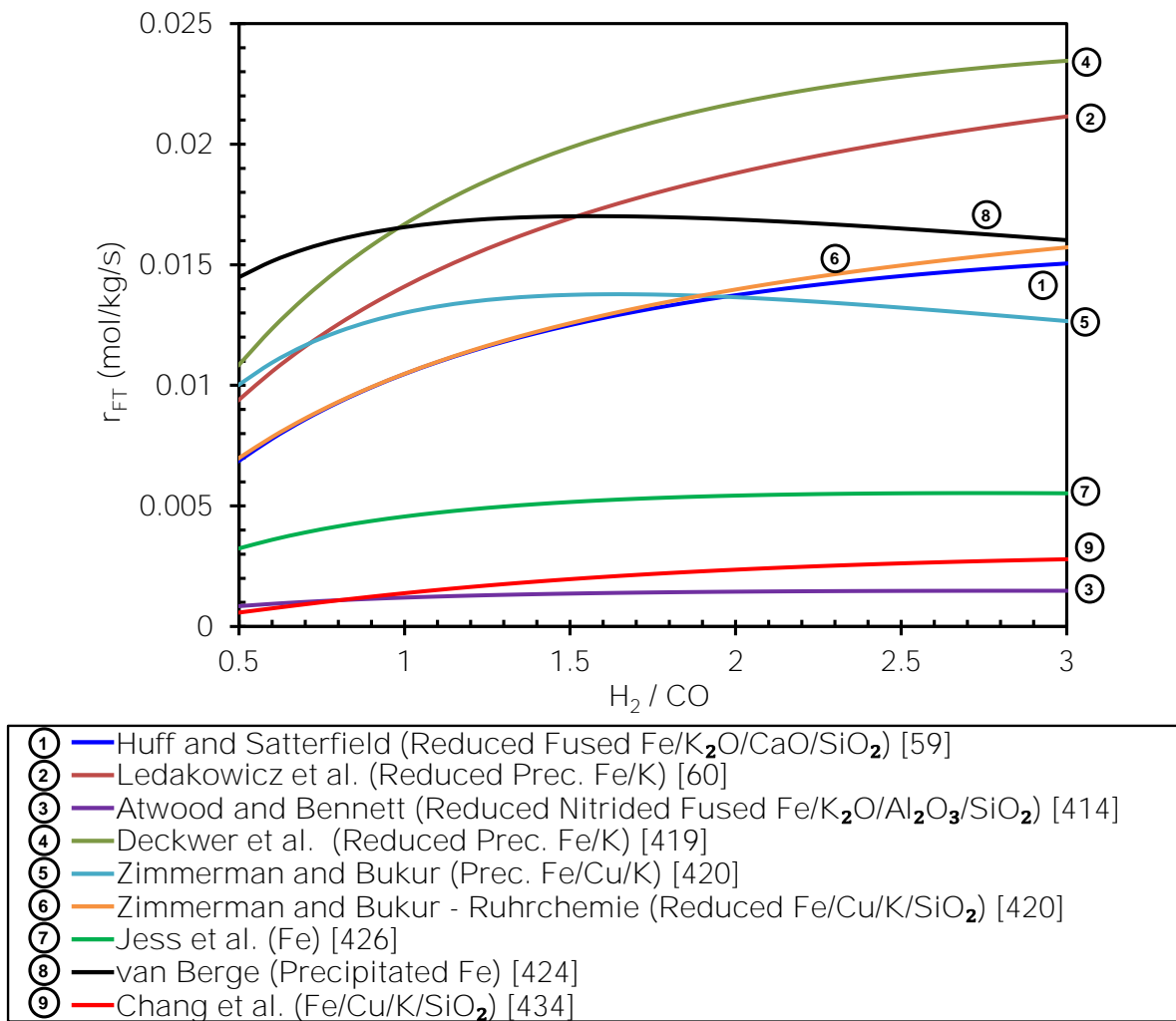


Figure 2-1: Comparison among F-T rate expressions at various H₂/CO ratios over Iron catalysts (T = 528 K and P = 3 MPa)

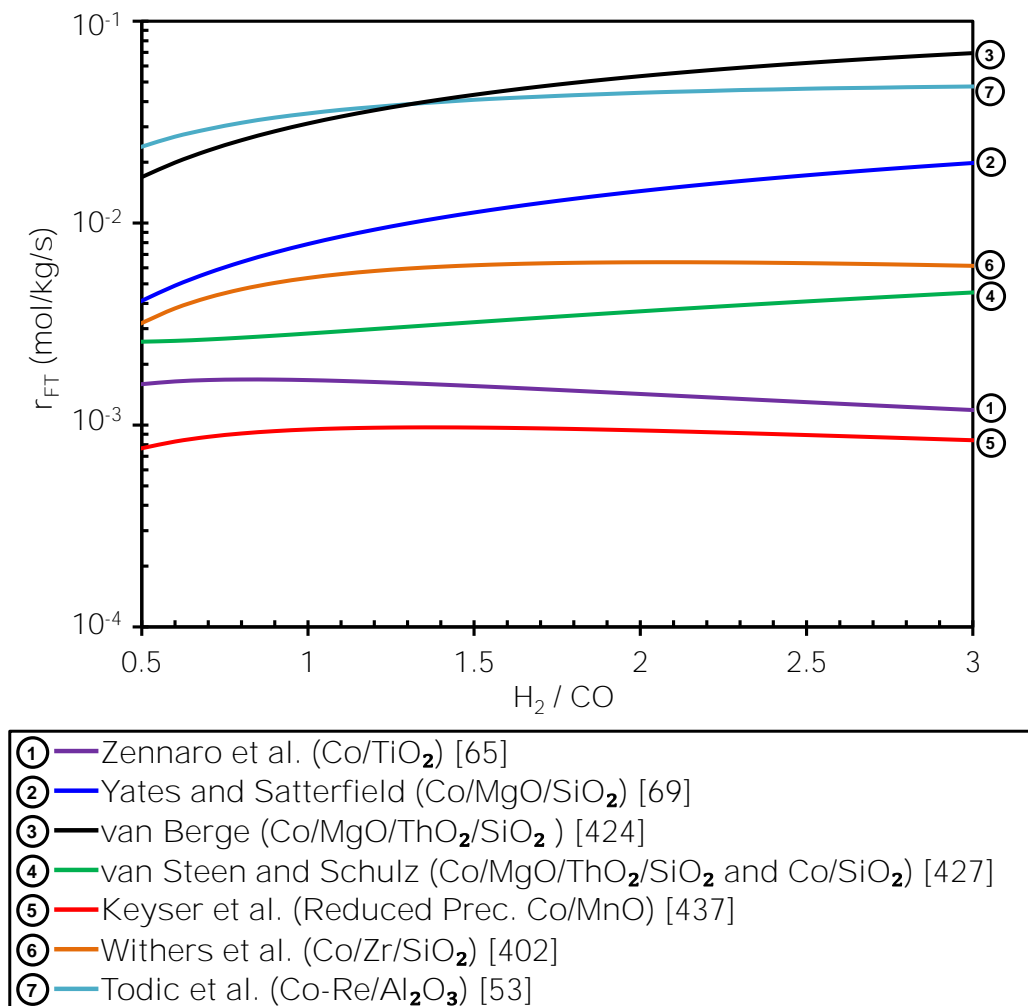


Figure 2-2: Comparison among F-T rate expressions at various H₂/CO ratios over Cobalt catalysts (T = 528 K and P = 3 MPa)

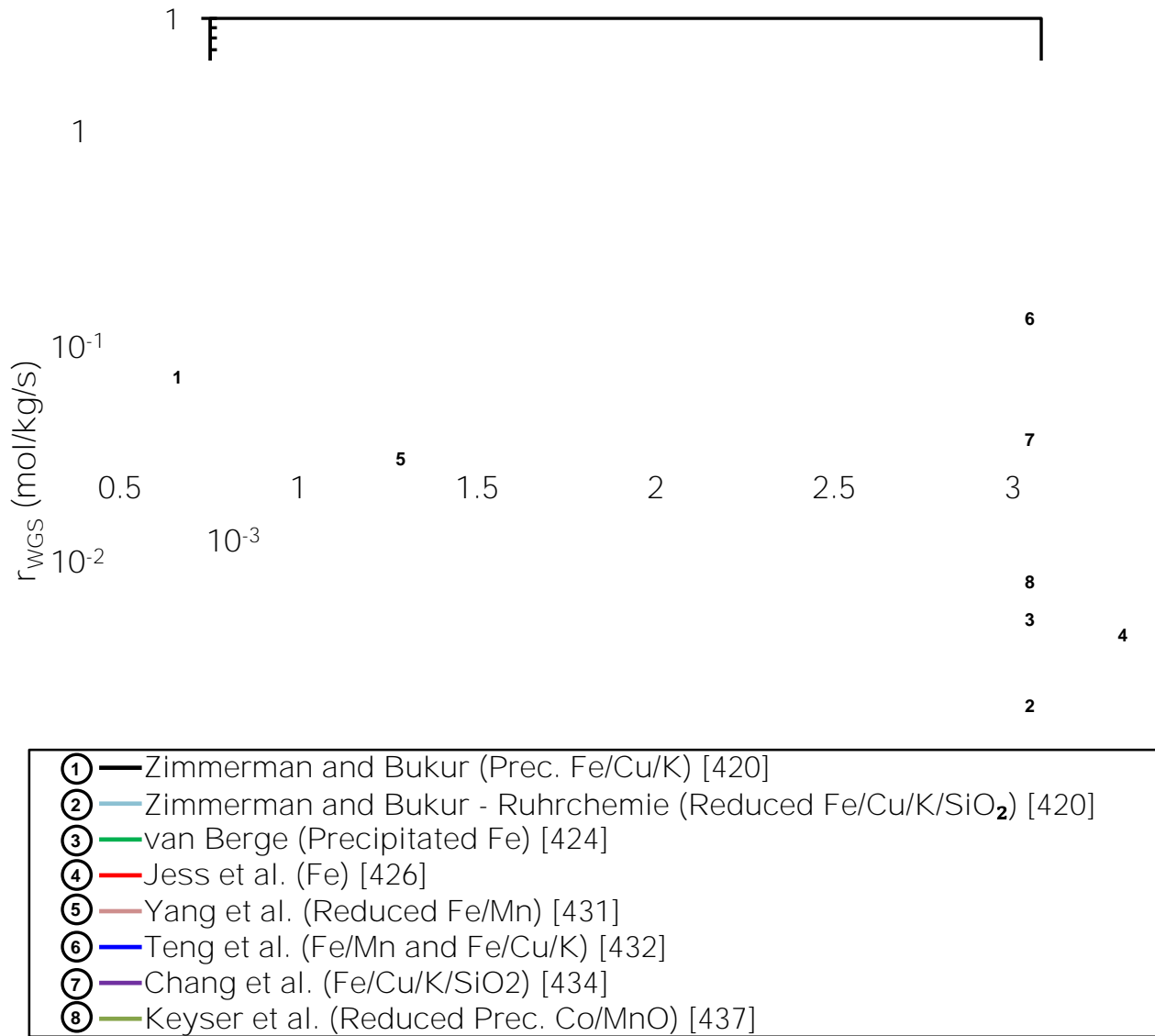


Figure 2-3: Comparison among WGS kinetic rate expressions at various H_2/CO ratios ($T = 528$ K and $P = 3$ MPa)

2.2 HYDRODYNAMIC STUDIES IN F-T SBCR

Although numerous experimental studies on the hydrodynamic and mass transfer parameters in SBCRs are available, only few, as shown in Table A-4 (Appendix A), covered conditions similar to those encountered in industrial F-T SBCRs ($P > 25$ bar, $T > 450$ K, $u_G > 0.15$ m/s, $C_V > 10$

vol.%, mixture of hydrocarbons as the liquid-phase, H₂ and CO mixture as the gas-phase, micron sized Fe or Co-based on typical catalyst support as a solid-phase). It should be mentioned that the hydrodynamics and mass transfer in SBCRs have been consistently shown to depend on the reactor size as well as operating conditions [74], and accordingly, using such available data in the literature, which were obtained in small reactor diameters (< 0.15 m) under ambient conditions or with a single gas for designing commercial-scale SBCRs, with inside diameters reaching several meters and operating in the churn-turbulent flow regime, could be risky.

2.2.1 Overall Gas Holdup

The gas holdup represents the volume fraction of the gas-phase in the reactor. Deckwer et al. [75] measured the gas holdup for N₂ in a paraffin wax in the presence of up to 16 wt.% of alumina particles at 416 and 543 K. However, their experiments were carried out in small columns of 0.04 and 0.1 m ID at low superficial gas velocities, $u_G < 0.04$ m/s and pressures, $P < 11$ bar. The gas holdup for N₂ in paraffin wax was investigated by Bukur et al. [76] who used iron oxide and silica as solid phases. Their data were measured in a small column of 0.05 m ID at low ranges of gas velocities and at low pressure (~ 1 bar). Krishna et al. [77] reported gas holdup data obtained in a relatively large column of 0.38 m ID with a three-phase system consisting of air, paraffin oil and silica particles and covered ranges of solid concentrations and gas velocities typical to those of industrial F-T reactor, nevertheless, their experiments were conducted at atmospheric pressure and ambient temperature. Vandu et al. [78] measured the gas holdup of air in a paraffin oil in the presence of alumina particles, however, they used a small SBCR of 0.1 m ID operating at atmospheric pressure and ambient temperature. Woo et al. [79] obtained gas holdup data while carrying out F-T synthesis over alumina-supported cobalt catalyst in a small SBCR of 0.05 m ID.

They reported that optimal conditions were reached when using gas velocities in the range of 0.068-0.1 m/s and catalyst concentration of 15 wt.%. It should be emphasized, however, that higher gas flow rates and solid loading would be expected in large-scale SBCRs in order to increase the reactor productivity. Behkish et al. [8, 80] measured the gas holdup for H₂, CO, N₂, CH₄ and He in Isopar-M (an iso-paraffinic liquid mixture of C₁₀ – C₁₆) in the presence of alumina particles under high pressures (up to 30 bar), temperatures (up to 473 K), gas velocities (up to 0.39 m/s) and solid concentrations (up to 36 vol.%). While typical F-T operating conditions were covered, these authors did not use gas mixtures which would mimic the syngas. Furthermore, although Isopar-M could be used as a startup liquid for an F-T reactor, its composition varies greatly from the molten reactor wax which would be present in the SBCR once steady-state operating conditions are reached. More recently, Sehabiague et al. [81] have measured gas holdup data for N₂ and He, in C₁₂-C₁₃, paraffins mixture, light F-T cut, and heavy F-T cut in a 0.3 m ID SBCR under high pressure (up to 30 bar), temperature (up to 500 K) in the presence of Alumina, Puralox Alumina, and iron oxide particles (up to 20 vol.%) at varying superficial gas velocities (up to 0.27 m/s).

The effects of various operating variables on the gas holdup have been extensively investigated in the literature; and the parameters believed to impact the gas holdup are the superficial gas velocity, liquid density, liquid surface tension, liquid viscosity, and liquid vapor pressure. Hikita et al. [82] concluded that the effects of nozzle diameter, column diameter and liquid height on the gas holdup could be neglected. Akita et al. [83] showed that the effect of liquid superficial velocity on the gas holdup could be neglected at values < 0.044 m/s. The gas holdup has been shown to increase with increasing the superficial gas velocity [46], which affects the flow regime in the reactor. The following power law expression best describes the relationship between gas holdup and superficial gas velocity.

$$\varepsilon_G \propto u_G^n \quad (2-1)$$

The value of n is dependent on the flow regime. In the homogenous flow regime, the value of n is in the range of 0.7 - 1.2 [84, 85], exhibiting an almost linear relationship between the gas holdup and the superficial gas velocity. The value of the gas holdup changes at the transition regime and as a result the value of “ n ” increases, enhancing the nonlinear dependency on the superficial gas velocity. The value of “ n ” then drops to 0.4 - 0.7 in the heterogeneous flow regime [84-87]. This change of the value of “ n ” was attributed to the variation of the system physical properties and the operating variables during the regime transition. Other studies have also reported that the effect of surface tension become more significant at low superficial gas velocities (< 0.05 m/s) [87-89].

The dependence of gas holdup on the pressure has been widely investigated and most of studies concluded that increasing pressure increases the gas holdup in SBCRs [90-92]. This dependency was attributed to the effect of increasing gas density (gas momentum) as the pressure increases. Increasing pressure is believed to reduce coalescence between the gas bubbles, and thus increases the number of small rigid gas bubbles, which translates into a high gas holdup [89, 93, 94].

The gas holdup was reported to increase with liquid viscosity and surface tension, and in some instances was reported to increase and decrease with increasing liquid density [93, 95-103]. The effect of viscosity was attributed to the rise of more bubbles coalescence in more viscous liquids. The effect of surface tension was attributed to the cohesive forces between the liquid molecules, which make it harder for the smaller bubbles to either coalesce or breakup [102, 104]. The gas holdup was found to be higher in organic liquids when compared with that in water. Moreover, for organic mixtures, the gas holdup was found to reach a maximum at a certain composition of the mixture.

The dependence of gas holdup on temperature was related primarily to the effect of temperature on the liquid physical properties. High temperatures, such as F-T synthesis, will reduce the liquid density, viscosity and surface tension, which in turn, will affect the gas holdup [105].

Increasing the solid particles density was reported to decrease the gas holdup [106-114]. The effect of solid particles size on the gas holdup was dependent on the wettability of the particles [76, 89, 103]. For non-wetting particles, the gas holdup was found to increase with the particle size, whereas the opposite was observed for wetting particles [76, 103, 106-114]. The effect of solid particles wettability on the gas holdup, however, was not clear as the values were reported to increase and also decrease [76, 103].

The reactor geometry has a strong effect on the gas holdup, depending on the location within the reactor. At the bottom of the SBCR, the gas holdup is influenced by the sparger design, whereas the values in the bulk and near the top of the reactor exhibit different dependencies [102, 115, 116]. Typically, slug flow and large gas bubbles would not occur at large reactor inside diameters (> 0.15 m) [83, 85, 102, 117-119]. In reactors with small inside diameters, slug flow and large gas bubbles would occur, decreasing the gas holdup. Similarly, the effect of reactor height, usually represented in terms of height to diameter ratio was found to be negligible for h_c/d_c values > 6 [102, 117, 120]. In addition, sparger design greatly influences the gas holdup as it affects the size and distribution of the initial bubbles generated at the bottom of the reactor [83, 94, 121-125].

There are numerous gas holdup correlations available in literature as highlighted by Behkish [9]. Many of these correlations were developed for aqueous and highly ionic systems at ambient conditions in laboratory-scale reactors, which brings into question their ability in predicting the gas holdup in industrial large-scale reactors operating under F-T conditions. Table

A-5 (Appendix A) summarizes the gas holdup correlations available in literature for three-phase reactors.

In order to graphically show the difference among these correlations, the data given in Table 2-1 were used to predict the effects of superficial gas velocity, catalyst particle diameter, solid loading and h_c/d_c on the overall gas holdup as depicted in Figure 2-4. As can be seen in this figure, there is a wide variation among the predicted values, especially at high superficial gas velocities. Also, with the exception of the correlations by Behkish et al. [9] and Sehabiague et al. [81], most correlations do not account for the effect of particle diameter, catalyst loading and h_c/d_c on the overall gas holdup.

Table 2-1: Operating conditions used in the correlations for comparison purposes

Parameter	Value
Pressure	3 MPa
Temperature	500 K
u_G	0.05 - 0.45 m/s
u_L	0.01 m/s
C_v	5-35 vol.%
d_p	40-520 micron
h_c	50 m
h_c/d_c	2.5-20
Liquid and Solid physical properties	Taken from Sehabiague and Morsi [126]

Table 2-2: Correlations for the physicochemical properties of the liquid phase [126]

$\rho_L = 978.05 - 0.5403T$	(2-2)
$\mu_L = \exp\left(\frac{2504.2}{T} - 4.3371\right)$	(2-3)
$\sigma_L = \frac{1.367 \times 10^{-4} T^2 - 0.1915T + 80.486}{1000}$	(2-4)
$\log_{10}(P_v) = -\frac{50951}{T^2} - \frac{1694.1}{T} + 3.146$	(2-5)

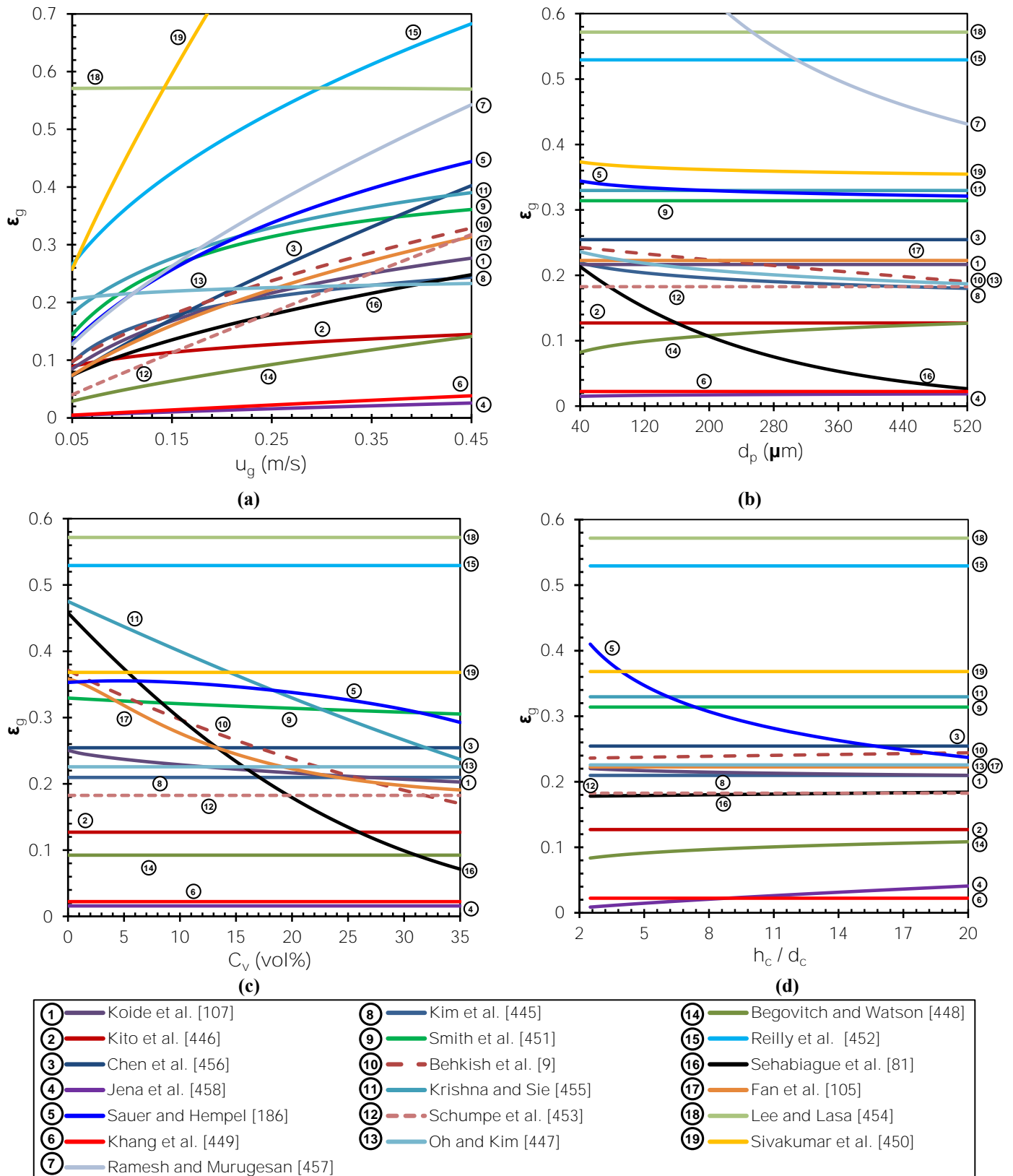


Figure 2-4: Comparison among literature gas holdup correlations at various (a) superficial gas velocities, (b) Catalyst particle diameters, (c) Solid loadings and (d) h_c/d_c values

2.2.2 Radial Distribution of Gas Holdup

The radial profile of the gas holdup in two-phase flows has been measured and reported in the literature [127-134]. Literature experiments for measuring the radial gas holdup distribution are given in Table 2-3. The exact experimental measurements have proven to be complex and time consuming, even though numerous tomographic and velocimetric techniques had been developed over the past three decades. The radial distribution of the gas holdup is generally modeled with a power law [134] (Equations (2-6) and (2-7)), based on experimental findings using Computed Tomography (CT) measurements [135, 136].

$$\varepsilon_G(\xi) = \tilde{\varepsilon}_G \left(\frac{m+2}{m} \right) (1 - c\xi^m) \quad (2-6)$$

Where $\tilde{\varepsilon}_G$ is related to the cross-sectional average holdup by the following equation:

$$\bar{\varepsilon}_G = \tilde{\varepsilon}_G \left(\frac{m+2-2c}{m} \right) \quad (2-7)$$

The value of the parameter 'm' is high for a flat gas holdup distribution (corresponding to bubbly flow regime) and decreases for the more parabolic profile prevalent in the churn-turbulent flow regime [134, 137]. This number is typically > 5 for a flat holdup profile, which exists in the bubbly-flow regime and is lower (~ 2) for the churn-turbulent flow regime. While the parameter c allows for a non-zero holdup at the wall, which was observed from CT measurements [138, 139]. The above equations have been validated by other authors to fit the experimental radial holdup profiles [140, 141].

For industrial reactors, however, it is important to obtain a few cross-sectional measurements of the gas holdup throughout the column. It is often overlooked that a single line averaged holdup, even across the centerline of the column, is not representative of the cross-

sectional mean value. Nevertheless, a line averaged gas holdup along several radial positions can be used to obtain a cross-sectional mean, provided that the holdup distribution is assumed axisymmetric. If such an assumption can be made, the radial variation of the gas holdup and hence the cross-sectional mean can be obtained by making use of the Abel integral and its inversion (Equation (2-8)) [135, 137].

$$\varepsilon_G(x, R) = 2 \int_0^{\sqrt{R^2-x^2}} f\left(\sqrt{R^2-x^2}, R\right) dy = 2 \int_0^R \frac{f(r, R)r}{\sqrt{(r^2-x^2)}} dr \quad (2-8)$$

Where $f(r, R)$ is a function of the radial position, which is not zero within the circle of radius R.

Table 2-3: Experimental work for measuring radial gas holdups in three phase reactors

Reactor dimensions	Phase properties	Operating conditions	Reference
$d_C = 0.1$ m $h_C = 0.8$ m	<ul style="list-style-type: none"> • Glass beads/ Air/Water • d_p: 0.12 – 0.47 mm • ρ_s: 2500 kg/m³ 	<ul style="list-style-type: none"> • Solid loading: 12.5 – 50% • $u_G = 0.01$ m/s 	Rigby [142]
$d_C = 0.12$ m $h_C = 2$ m	<ul style="list-style-type: none"> • Glass beads / Air/ Water • ρ_s: 2500 kg/m³ • d_p: 2.2 mm 	<ul style="list-style-type: none"> • 30 kg solid loading • $u_L = 0.05$ m/s • $u_G = 0.02 – 0.14$ m/s 	Marooka [143]
$d_C = 0.254$ m $h_C = 2.5$ m	<ul style="list-style-type: none"> • Glass beads / Air/ Water • ρ_s: 2500 kg/m³ • d_p: 2.3 mm 	<ul style="list-style-type: none"> • 30 kg solid loading • $u_L = 0.06$ m/s • $u_G = 0.01 – 0.14$ m/s 	Yu and Kim [3]
$d_C = 0.102$ m $h_C = 1.05$ m	<ul style="list-style-type: none"> • Alumina particles /Air/Water • d_p: 75 μm 	<ul style="list-style-type: none"> • Solid loading: 0 – 25% • $u_G = 0.02 – 0.13$ m/s 	Wu [144]

2.2.3 Sauter Mean Gas Bubbles Diameter

Behkish et al. [8, 80] measured the Sauter mean gas bubble diameter (d_{32}) for H₂, CO, N₂, CH₄ and He in Isopar-M (an isoparaffinic liquid mixture of C₁₀ – C₁₆) in the presence of alumina particles under high pressures (up to 30 bar), temperatures (up to 473 K), gas velocities (up to 0.39 m/s) and solid concentrations (up to 36 vol.%). While the experiments by these authors were conducted under typical F-T operating conditions, they did not use gas mixtures, mimicking the syngas; and the composition of their Isopar-M is different than that of the molten wax produced in the F-T SBCRs. More recently, Sehabiague et al. [81] have measured the Sauter mean gas bubble diameter (d_{32}) for N₂ and He, in C₁₂-C₁₃, paraffins mixture, light F-T cut, heavy F-T cut in a 0.3 m ID SBCR under high pressure (up to 30 bar), temperature (up to 500 K) and in the presence of Alumina, Puralox Alumina, and Iron oxide particles (up to 20 vol.%) at various superficial gas velocities (up to 0.27 m/s).

SBCRs are customarily operated in the churn-turbulent flow regime, which is believed to be the best mode of operation of such reactors [78, 145]. In this regime, large and small size gas bubbles were found to co-exist [145-147]. The large gas bubbles, with typical rise velocities in the order of 1.5 m/s, usually rise straight up through the reactor and disengage without any recirculation. The small bubbles, on the other hand, may experience recirculation and backmixing due to their low rise velocities.

Modeling of the gas bubbles behavior in SBCRs has received significant attention due to its effect on solid distribution and reactants conversion, Table A-6 (Appendix A) highlights commonly referenced bubble diameter correlations available in the literature, whereas Figure 2-5 depicts the behavior various correlations at various superficial gas velocities; and as can be observed, different values and trends of the bubble sizes are predicted.

In the bubbly flow regime, the gas-phase behavior can be adequately modeled assuming a uniform gas bubbles size distribution [148, 149]. On the other hand, in the Churn-turbulent flow regime, the two-class modeling approach introduced by Krishna [145, 147] was implemented by Rados [150], Sehabiague [151], and Maretto [152], among others. It assumes a generalized two-phase model, in which a dilute- and a dense-phase are identified. The dilute-phase which is dominated by large gas bubbles is virtually in plug flow, while the dense-phase experiences turbulent backmixing. The main disadvantage of this approach is that the cross flow interactions between the two-bubble classes usually are either neglected in steady state models or assumed to occur infinitely fast to quickly homogenize the composition of both classes in the transient and startup models [153, 154]. This approach gives rise to inaccuracies and deviations since it is only concerned with the limiting cases, while the actual extent of the interaction between the large and small gas bubbles would occur somewhere in the middle, which would create some differences in species concentration [136]. Moreover, intra-phase backmixing has either been accounted for using perfect mixing or by assuming plug flow [155], however, non-ideal flow models, accounting for a finite degree of backmixing, are believed to be more realistic.

It should be mentioned that the two-bubble class model in conjunction with the axial dispersion model has been accepted and used to model bubbles behavior in SBCRs [151, 152, 154-159]. In this model, the churn turbulent flow regime was assumed where large bubbles rise straight up through the reactor without recirculation, while small bubbles with lower rise velocity were entrained in the liquid and as such they followed the liquid-phase backmixing behavior.

There are two basic categories of non-ideal flow models, axial dispersion models and multi-cell models. Moreover, Iliuta [160] proposed a core annulus, multi-compartment model, which is a modified multi-cell approach that divides the reactor into compartments based on the

bubble size, and individually models the chemistry, thermodynamics and thermal effects of each compartment, while accounting for the thermo-physical interaction between the compartments.

Although many of the earlier SBCR models assumed no solids concentration gradient throughout the reactor, Kato [150] showed a gradient in the longitudinal concentration of solid particles, which was a function of the liquid micro- and macro-mixing. Therefore, the axial profile of the solids concentration is not flat and is highly dependent on the slurry properties and the operating conditions.

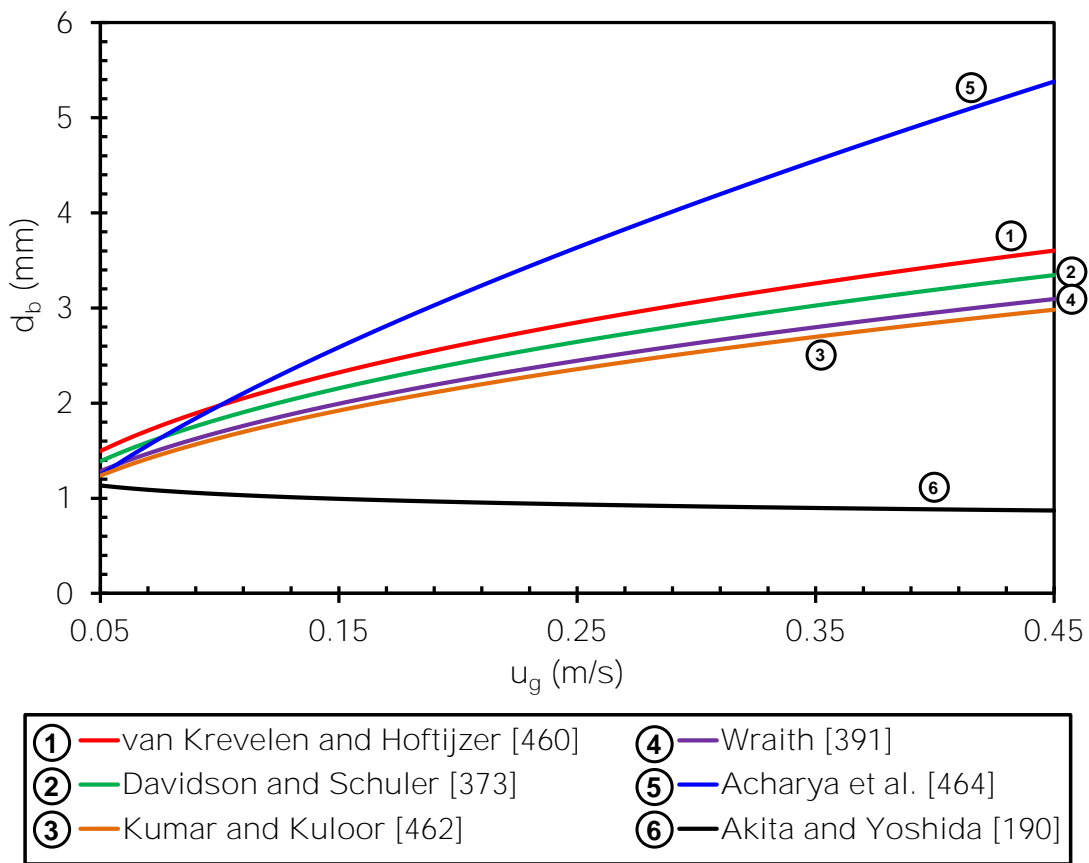


Figure 2-5: Comparison of various bubble diameter velocity correlations

2.2.4 Bubble Dynamics

Gas–liquid–solid systems have been applied extensively in industry for physical, chemical, petrochemical and biochemical processing [136, 161-163]. Current worldwide commercial activities in converting natural gas to fuels and chemicals, or gas-to-liquids technology use slurry bubble column reactors with column sizes considerably larger than those commonly considered in research investigations and in previous industrial applications [164]. Such commercial activities have prompted further fundamental research interest in fluid and bubble dynamics, transport phenomena, and the effects of high temperature and pressure conditions. .

In gas–liquid–solid systems, bubble dynamics plays a key role in dictating the transport phenomena and ultimately affects the overall rates of reactions. It has been recognized that the bubble wake, when it is present, is an important factor governing the system hydrodynamics [135]. In general, consideration of the flow associated with the bubble wake near the bubble base, whether laminar or turbulent, is essential to characterize the complete behavior of the rising bubble, including its motion. Conversely, examining the shape, rise velocity, and motion of a bubble can provide an indirect understanding of the dynamics of the liquid–solid flow around the bubble. Most of the three-phase processes with considerable commercial interest are conducted under high pressure and high temperature, for example, methanol synthesis (at $P = 5.5$ MPa and $T = 260$ °C), resin hydro-treating (at $P = 5.5$ – 21 MPa and $T = 300$ – 425 °C), Fischer–Tropsch synthesis (at $P = 1.5$ – 5.0 MPa and $T = 250$ °C), and benzene hydrogenation (at $P = 5.0$ MPa and $T = 180$ °C) [165-170]. Fundamental study of bubble dynamics in these gas–liquid–solid fluidization systems, particularly under high-pressure and high-temperature conditions, is thus crucial.

Generally, bubble-induced turbulence and shear induced turbulence are two sources of liquid phase turbulence in bubble columns. However, the dominating mechanism of the liquid phase turbulence is still not clear in such bubbly flows.

In a three-phase fluidization system, bubble size variation is intimately related to bubble–particle collisions. The collisions can yield two different consequences: the particle is ejected from the bubble surface, or the particle penetrates the bubble leading to either bubble breakage or non-breakage. Bubble–particle collisions generate perturbations on the bubble surface. After the bubble–particle collision, three factors become crucial in determining the breakage characteristics of the bubble [171]:

- (1) Shear stress, which depends on the liquid velocity gradient and the relative bubble–particle impact speed, and tends to break the bubble;
- (2) Surface tension force, which tends to stabilize the bubble and causes it to recover the bubble’s original shape;
- (3) Viscous force, which slows the growth rate of the surface perturbation, and tends to stabilize the bubble.

There are three criteria that are required for particle penetration through a bubble. These criteria were developed by neglecting the shear effects due to the liquid flow [4]. The particle will penetrate the bubble when any of the following three criteria is satisfied. The three criteria are given as follows:

- (1) The acceleration of the particle is downward;
- (2) The particle velocity relative to the bubble is downward;
- (3) The particle penetration depth is larger than the deformed bubble height.

When none of these criteria are satisfied, the particle will be ejected from the bubble surface upon contact with the bubble.

The bubble dynamics is controlled by the size and distribution of the gas bubbles present in the reactor. The bubble size controls the gas-liquid interfacial area and subsequently it influences the overall rate of reactions occurring in the reactor during commercial processes. The formation of gas bubble at the injection point is subject to the buoyancy forces due to the difference in density between the gas and liquid phases, and the surface tension forces that govern the stability of the gas bubble from the orifice and throughout the liquid/slurry phase. The behavior of the gas bubbles depends, among others, on the hydrodynamic flow regime. If a bubbly flow regime governs in the reactor, the bubbles will be narrowly distributed and low bubble-bubble interactions could be expected. In fact a uniform bubble size distribution is generally characteristics of the homogeneous bubbly flow regime. As the superficial gas velocity is increased, the high frequency of gas bubble interactions leads to coalescence and breakup and the reactor is found to be operating in the churn turbulent flow regime, and a distinguishable bimodal bubble size distribution can be observed. Consequently, bubbles in this regime can be arbitrary classified into “small”, and “large”. These bubbles appear to behave differently as the large gas bubbles rise rapidly in the reactor in a plug flow mode and create backmixing, and the small gas bubbles are entrained and re-circulate with the liquid/slurry. In the churn turbulent flow regime, bubble breakup and coalescence can occur at any moment after the formation of the gas bubble at the orifice, thus the bubble size distribution will depend on the balance between coalescence and breakup.

2.2.5 Bubble Rise Velocity

The behavior of the rising gas bubbles can be described using the rise velocity, shape and motion of the bubbles, which are related to the physical properties of the surrounding medium (solid loading, liquid viscosity and density) as well as the interfacial properties of the bubbles. The bubble rise velocity primarily depends on the bubble size for small gas bubbles and on the liquid surface tension and viscosity for large bubbles. Most studies investigating the bubble rise velocity were mainly conducted in water-based systems under ambient conditions, which bring into question the confidence in applicability to a realistic F-T SBCR conditions.

Table A-7 (Appendix A) summarizes the bubble rise velocity correlations available in literature for use in bubble columns and SBCRs modeling, whereas Figure 2-6 compares the behavior of different correlations at various superficial gas velocities. Krishna et al. [172] studied the effect of pressure on the rise velocity and found that the gas density has no noticeable effect on the bubble rise velocity. Their work, however, was conducted within a very narrow pressure range. Lin et al. [173, 174] measured the rise velocities of a single bubble of a known size in Paratherm NF heat transfer fluid under a wide range of pressures ranging from 0.1 to 14.9 MPa at three temperature 300, 320 and 350 K. They showed that the rise velocity was independent of temperature and decreased with increasing pressure. They attributed this behavior to the pressure-temperature effects on the liquids physical properties. Lou et al. [135] developed a mechanistic first principle-based correlations to predict the initial bubble size in slurries at high pressure and temperature conditions by accounting for the various competing forces at the bubble distribution source. In their model, the bubbles were assumed to be formed in two stages, expansion and detachment. During the expansion stage, the bubble initially expands with its base attached to the source nozzle; and the detachment stage occurs when the bubble's base moves away while

remaining connected to the nozzle through the neck. The bubble was assumed to be spherical during the entire formation process.

The volume of the gas bubbles can be determined using the balance of all the forces, if either of the instantaneous gas flow or the instantaneous gas velocity through the orifice is known, as has been discussed by Behkish [89].

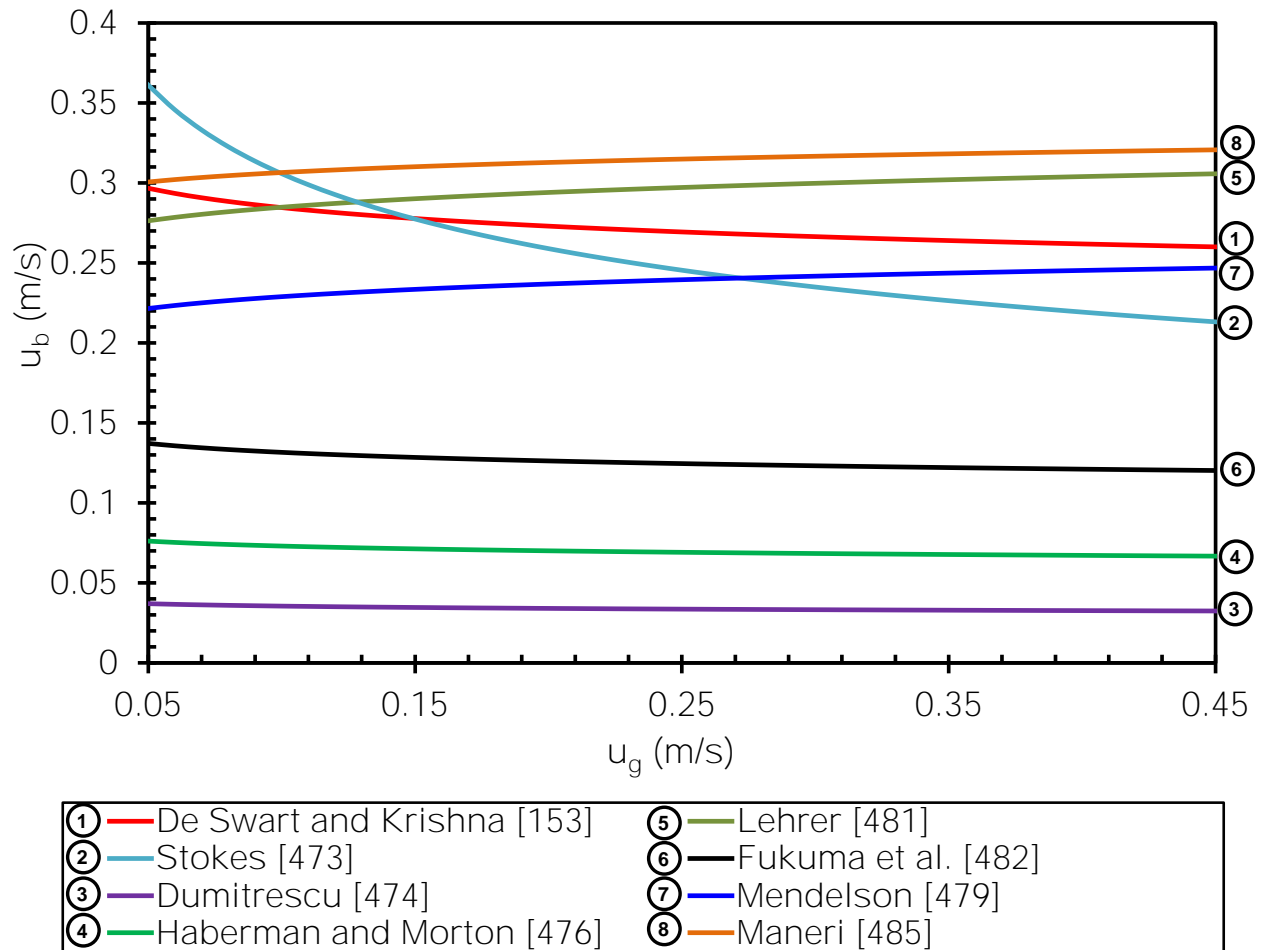


Figure 2-6: Comparison among various bubble rise velocity correlations

2.3 MASS TRANSFER STUDIES IN F-T SBCR

In F-T SBCRs, the reactants have to diffuse through the liquid produced in order to reach the catalyst active sites before the chemical reaction can take place. Figure 2-7 shows the mass transfer process in gas-liquid-solid systems, where the reaction takes place inside the pores of the solid catalyst. As can be seen, the reactants in the gas-phase have to travel from the bulk gas-phase to the gas-liquid interface and then through the liquid bulk. Once in the liquid bulk, the reactants start to mix before transferring to the external surface of the catalyst (solid) particles. After reaching the catalyst surface, the reactants have to diffuse inside the catalyst pores until they collide with an active site, where the chemical reaction can take place based on the kinetic conditions of the system. Once the products are formed, they start diffusing all the way back from the active sites to the catalyst surface, through the liquid bulk, to the gas-liquid interface, before diffusing into the gas-phase.

Since the diameter of the catalyst particles frequently used in SBCRs is very small (micron size), the interfacial area between the liquid and the catalyst surface is considerably large, and as such, the mass transfer resistance between the liquid and solid phases could be neglected. Additionally, the mass transfer resistance due to mixing of the reactants in the bulk liquid could also be neglected, if the reactor is operating in the churn-turbulent flow regime, as it provides effective mixings conditions. Furthermore, since the majority of F-T products have negligible vapor pressure, the resistance to transfer of the reactants from the bulk gas-phase to the gas-liquid interface could be neglected. Thus, the two remaining resistances which have to be considered are the reaction kinetic and the liquid-film resistances.

Generally, mass transfer between the phases can be represented using Fick's law as shown in Equation (2-9), where D_{AB} is the diffusivity of component A into component B. Vermeer and

Krishna [175], however, argued in favor of using Maxwell-Stephan's equation for representing a multicomponent mixture close to the saturation, as shown in Equation (2-10).

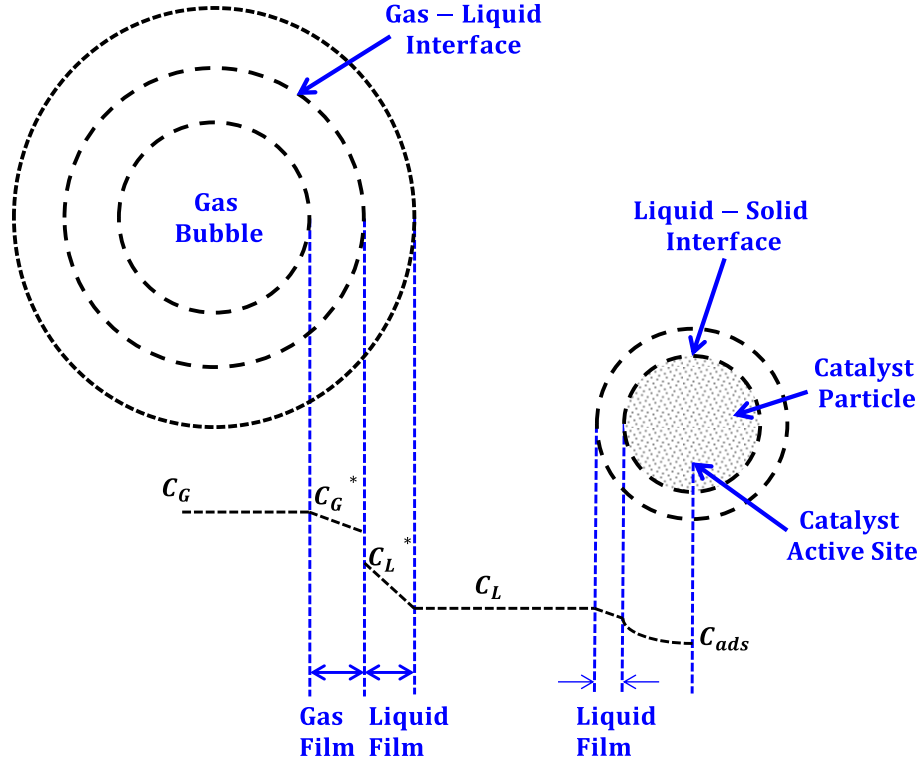


Figure 2-7: Concentration profiles for mass transfer in a three phase system [46]

$$\frac{\partial C}{\partial t} = -D_{AB} \frac{\partial^2 C}{\partial x^2} \quad (2-9)$$

$$-\phi \frac{c_i}{RT} \nabla \mu_i = \sum_{\substack{j=1 \\ j \neq i}}^n \frac{c_j N_i - c_i N_j}{c_i D_{ij}} + \frac{N_i}{D_i}, \quad i = 1, 2, \dots, n \quad (2-10)$$

The mass transfer through the liquid-film can be described by a steady-state mass transfer flux according to the two-film theory as shown in Equation (2-11).

$$J_L = k_L a (C^* - C_L) \quad (2-11)$$

Where C^* is the concentration at the gas-liquid interface, C_L is the concentration in the liquid bulk and k_L is the liquid-side mass transfer coefficient, which is often represented as a function of the gas-liquid diffusivity and the liquid film thickness by Equation (2-12).

$$k_L = \frac{D_{AB}}{\delta} \quad (2-12)$$

The volumetric liquid-side mass transfer coefficient ($k_L a$) is the product of the liquid-side mass transfer coefficient (k_L) and the gas-liquid interfacial area (a). The gas-liquid interfacial area is the area of interface between the gas bubbles and the liquid-phase, which represents the surface through which mass transfer takes place. This area can be determined from the knowledge of the gas holdup and a characteristic length for the gas bubbles assuming the bubbles to be of a specific shape.

The effects of mass transfer on three-phase reactor performance have been extensively investigated in the literature [80, 81, 176-179]. Earlier studies on the mass transfer focused on the significance of hydrogen mass transfer compared to the overall reaction resistance. This was due to the fact that F-T kinetics over iron catalyst were reported to be first order with respect to hydrogen. The principal mass transfer resistance occurs in the slurry-phase of the reactor and the extent of the effect of gas-liquid mass transfer on the reactor performance has been argued. Satterfield and Huff [180] concluded that the hydrogen mass transfer was the limiting step for reactor productivity, whereas Deckwer [75] showed that the mass transfer resistance was small compared to the kinetics resistance. Inga and Morsi [181] and Sehabiague and Morsi [81, 177] reported that F-T SBCRs operating under a kinetically-controlled regime at low catalyst concentrations could move to a mass transfer-controlled regime at high catalyst concentrations, where the reactor performance quickly declines. Nonetheless, it is generally agreed that the mass transfer strongly depends on the bubble size, where smaller gas bubbles result in a greater gas-liquid interfacial area, which improves the overall mass transfer.

The volumetric mass transfer coefficients, derived from the inlet and outlet concentrations of absorption experiments, were influenced by the dispersion in both phases. [74] Since the

dispersion is strongly dependent on the column size and geometry, the developed equations for the calculating the volumetric mass transfer coefficients appear to include geometric parameters, such as the column diameter and sparger characteristics. Behkish et al. [8, 80] measured the volumetric mass transfer coefficients ($k_L a$) for H₂, CO, N₂, CH₄ and He in Isopar-M (an isoparaffinic liquid mixture of C₁₀ – C₁₆) in the presence of alumina particles under high pressures (up to 30 bar), temperatures (up to 473 K), gas velocities (up to 0.39 m/s) and solid concentrations (up to 36 vol.%). While the experiments by these authors were conducted under typical F-T operating conditions, they did not use gas mixtures, mimicking the syngas; and the composition of their Isopar-M was greatly different than that of the molten wax produced in the SBCR. More recently, Sehabiague et al. [81] have measured the volumetric mass transfer coefficients for N₂ and He, in C₁₂-C₁₃, paraffins mixture, light F-T cut, heavy F-T cut in a 0.3 m ID SBCR under high pressure (up to 30 bar), temperature (up to 500 K) in the presence of Alumina, Puralox Alumina, Iron oxide particles (up to 20 vol.%) at various superficial gas velocities (up to 0.27 m/s).

Table A-8 (Appendix A) summarizes the few available literature studies and correlations for $k_L a$ in SBCRs. It should be mentioned, however, that numerous $k_L a$ correlations in BCRs are available in the literature as highlighted by Behkish. [89] Moreover, Figure 2-8 shows the effects of superficial gas velocity, catalyst particle diameter, solid loading and h_c/d_c on $k_L a$ using the conditions provided Table 2-1. As can be in this figure, there is a wide variation in the predicted $k_L a$ values especially at higher superficial gas velocities, which is similar to the behavior shown by gas holdup correlations presented in Figure 2-4, it should be noted that most of the correlations presented in Table A-8 do not account for the effect of particle diameter, catalyst loading and h_c/d_c on $k_L a$.

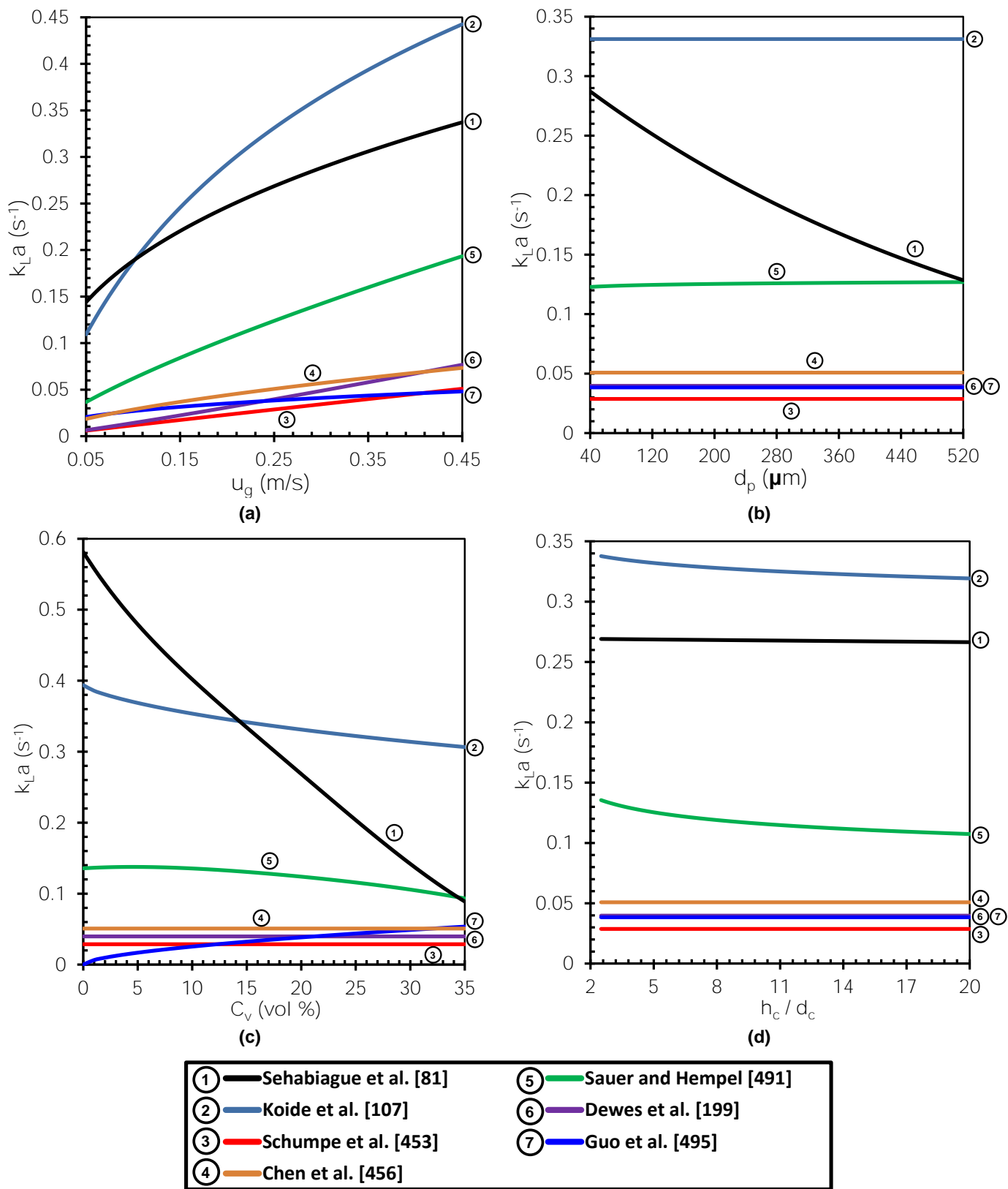


Figure 2-8: Comparison among three-phase correlations for k_{La} at various (a) superficial gas velocities, (b) Catalyst particle diameters, (c) Solid loadings and (d) h_c/d_c values

Table 2-4 summarizes the effects of various parameters on the hydrodynamics and mass transfer parameters in SBCRs based on the preceding literature review.

Table 2-4: Summary of reported effects of operating conditions on the hydrodynamic mass transfer parameters

Parameter	Effect
Gas density [74, 80, 89, 90, 105, 121, 174, 182-184]	Denser gas leads to higher gas holdups and smaller gas bubbles.
Gas molecular weight [90]	Same effect as gas density; higher molecular weights results in higher gas holdups and smaller gas bubbles
Liquid density [83, 99, 105, 107, 118, 121, 183-188]	<ul style="list-style-type: none"> • Effect is unclear, both an increase and decrease of the gas holdup has been reported. • Volumetric mass transfer coefficient decreases with decreasing liquid density.
Liquid viscosity [82, 83, 99, 101, 105, 107, 118, 183, 184, 186, 188, 189]	Increasing liquid viscosity: <ul style="list-style-type: none"> • Increases gas bubbles size • Decreases gas holdup and mass transfer coefficients
Liquid surface tension [82, 83, 90, 105, 187, 188, 190-193]	Increasing liquid surface tension: <ul style="list-style-type: none"> • Decreases gas holdup • Results in the formation of large gas bubbles • Decreases the volumetric mass transfer coefficients
Solid density [194]	Increasing solid density decreases gas holdup.
Particle Diameter [106, 194, 195]	Increasing particle diameter: <ul style="list-style-type: none"> • Increases gas holdup for non-wettable particles • Decrease/No effect on gas holdup for wettable particles
Wettability [194]	In general, have no clear effect on the gas holdup. Although some reported it to increase or decrease the gas holdup.
Temperature [183, 184, 188, 193, 196, 197]	Increasing temperature: <ul style="list-style-type: none"> • Decreases liquid surface tension; Decreases liquid viscosity • Increases gas holdup; Increases gas diffusivity; Increases volumetric mass transfer coefficients

Table 2-4 (continued)

Parameter	Effect
Pressure [80, 185, 198-200]	Increasing pressure: <ul style="list-style-type: none">• Increases gas density and gas momentum; Increases gas holdup• Increases volumetric mass transfer coefficients
Superficial gas velocity [75, 82, 83, 90, 105, 183, 184, 186-188, 196]	Increases superficial gas velocity: <ul style="list-style-type: none">• Increases gas holdup; Increases volumetric mass transfer coefficients
Liquid velocity [76, 106, 195, 201, 202]	Increasing liquid velocity decreases the gas holdup in the absence and presence of solid particles
Solid loading [8, 76, 103, 106, 107, 203]	Increasing solid loading: <ul style="list-style-type: none">• Decreases the gas holdup, despite some studies reported otherwise.• Increases slurry viscosity• Decreases the volumetric mass transfer coefficients• Leads to the formation of large gas bubbles• Increases the rate of bubble coalescence• Increases the volumetric mass transfer coefficient at low solid concentrations
Column Diameter [83, 85, 102, 118, 119, 204, 205]	Strong effect for small column diameters < 0.15 m, no effect for larger diameters.
Column Height/Diameter ratio [90, 120, 204, 206]	No effect on gas holdup for ratios > 6
Gas distributor [102, 190]	<ul style="list-style-type: none">• Increasing the size of the openings decreases the gas holdup due to the formation of large gas bubbles.• Has minimal effect on the gas bubbles size and gas holdup for orifice diameters 0.001-0.002 m.
Internal design [4, 207-215]	Some effect on increasing gas holdup has been reported; most variations lie within the range of experimental error; and no major effect was reported when internals represent the <15-20 % of reactor volume.

2.4 HEAT TRANSFER STUDIES IN F-T SBCR

One of the main advantages of SBCRs is the ease of heat removal and the uniform temperature distribution within the reactor, which makes modeling of the heat transfer a simple task. The effect of the slurry physical properties on the heat transfer is indisputable and thus the presence of water produced in F-T synthesis and its effect on the slurry properties should in turn affect the heat transfer behavior. A generalized heat balance on the SBCR can be written as:

$$\frac{\partial}{\partial z} \left[\rho_{sl} C_{p_{sl}} (1 - \varepsilon_G) D_L \frac{\partial T}{\partial z} \right] - \frac{\partial (\rho_{sl} C_{p_{sl}} u_{sl} T)}{\partial z} - U_{Heat} (T - T_{cool}) + (1 - \varepsilon_G) (-\Delta H_{FT} r_{FT}) = 0 \quad (2-13)$$

Although interphase heat exchange is not important because the inlet gas is typically preheated by the outlet gas before entering the reactor [166, 216], the continuous contact among the phases and the degree of mixing are important to allow for a uniform temperature gradient and almost isothermal operation.

In SBCRs, the intimate contact among the phases allows for an almost uniform temperature and near isothermal operation. Most of studies on the heat transfer in multiphase reactors have been focused on the determination of the effects of operating variables on the heat transfer coefficients. Table A-9 (Appendix A) summarizes the heat transfer coefficient correlations available in the literature for BCRs and SBCRs.

2.4.1 Previous Studies Investigating Effect of Internals on BCR and SBCR Performance

The vicinity of the gas sparger is highly chaotic and generally well-mixed. Krishna et al. [110] listed the typical conditions for an industrial F-T SBCR, including the heat removal by means of

cooling pipes, which are essential for controlling temperature in the highly exothermic F-T reactor [217-219]. The fact is the effect of internals on the performance of SBCRs has received little attention as of today. In addition, there is no convincing guidance on the design of internals in SBCRs. However, there have been numerous investigations on the effect of internals in BCRs, which will be discussed below.

Hulet et al. [220] reviewed the heat transfer studies in BCRs and recommended that more work involving columns with internals needs to be conducted to develop reliable models for predicting large-scale unit performance. Kölbel and Ralek [221] suggested the insertion of honeycombed cross section vertical shafts inside the column, with cooling pipes located in corners or around the shafts. They claimed this design would eliminate unfavorable backmixing, which can reduce desirable selectivities as it reduces the residence time in the BCR to that in an ideal stirred tank reactor.

Korte [222] studied heat transfer from horizontal and vertical tube bundles with an embedded heat transfer probe in BCRs of 0.19 and 0.45 m diameter and concluded that the heat transfer coefficient is very sensitive to the configuration and density of the bundle. He showed that even with high viscosity liquids, which enhance bubble coalescence, the presence of internals may inhibit any decrease of the heat transfer values by enhancing the bubble break-up rate. He also developed the following correlation:

$$St = 0.139[(Re_G Fr_G Pr_L^{2.26})^{1/3}]^{0.84} A_f^{-0.2} \left(\frac{t_R}{d_R}\right)^{0.14} \left(\frac{\mu_L}{\mu_{lw}}\right)^{0.3} \quad (2-14)$$

Where:

$$A_f = (d_c^2 - n_R d_R^2) / d_c^2 \quad (2-15)$$

From a fundamental standpoint, it is expected that similar to the heat transfer coefficients, the mass transfer coefficients are altered by the presence of internals; and accordingly mass transfer correlations and models developed in columns without internals need to be revisited. Bernemann [223] used a flywheel anemometer and found the axial component of the liquid-phase velocity to be higher in a column with internals than in a column without internals, irrespective of the gas velocity used. However, in the radial profile, the inversion point (stationary liquid velocity) between the upward and downward liquid velocities was maintained at about the same dimensionless radius of ~ 0.7 .

Saxena et al. [207] investigated the effect of internal tubes in 0.305 m diameter column, representing 1.9, 2.7 and 14.3% of the total column cross-sectional area operating with an air-water-glass beads system. The gas holdup was found to be higher for 37 tubes than for 7 tubes. They reported the overall gas holdup as a macroscopic value, with no mention of the radial profile and accordingly the effect of internals on the liquid recirculation could not be assessed using their data. Similarly, Pradhan et al. [224] studied six different volume fractions of straight tube internals ranging from 10.8 to 19.3% and helical coil internals ranging from 2.6 to 3.9% of the reactor cross-sectional area, within a 0.102 m diameter column, and found that the gas holdup increased with increasing the internals volume fraction. Moreover, helical coil internals provided higher gas holdup than vertical tubes, which was attributed to the fact that vertical inter-tubes gaps allow large bubbles to escape, decreasing the gas holdup, while in the helical coils, smaller gaps were present.

Chen et al. [4] studied the effect of internals covering $\sim 5\%$ of the total column cross-sectional area, using gamma ray Computed Tomography (CT) and Computer Automated Radioactive Particle Tracking (CARPT). They studied gas holdup, liquid recirculation, and turbulent parameters in a 0.46 m diameter column. Their data showed that the presence of internals

have no significant effect on the liquid recirculation velocity, while gas holdup increased by ~ 10% at the center of the column and less towards the wall region. Also, the turbulent stresses and eddy diffusivities were lower when the internals were added.

Modeling BCRs with internals was attempted by Forret et al. [213], who developed a 2-D model to predict the effect of internals on the liquid mixing by accounting for an axial dispersion coefficient ($D_{ax,2-D}$), a radial dispersion coefficient ($D_{rad,2-D}$), and a radially dependent axial velocity profile. They reported that the presence of internals decreased the liquid fluctuation velocity and enhanced the large-scale liquid recirculation based on their liquid tracer experiments.

Larachi et al. [225] carried out CFD simulations for the flow behavior in a column without internals and with four different internal arrangements. The occupied cross-sectional areas ranged between 2 and 16.2%; and the core-annulus flow was predicted by the simulation of the uniform internals configurations, which confirmed the results highlighted earlier by Bernemann [223, 226]. However, for non-uniform internals, a complex flow behavior was detected. Youssef et al. [227] reviewed experimental efforts investigating the effect of internals in BCRs and the following summary of the effects of horizontal and vertical arrangements of internals in BCRs was given. [228]:

1. Sectionalizing bubble columns via perforated trays leads to an increase of the gas holdup; and a similar increase of the gas holdup was observed when utilizing horizontal tubes instead [114];
2. Blass and Cornelius [229] reported a decrease in the bubble coalescence upon the addition of horizontal sectionalizing plates ranging from 1.1% to 46% of open cross-sectional area in a 3-phase system (0.14 m diameter). Kemoun et al. [230] used ~ 5% open cross-sectional

- area sieve trays in an air-water system (0.19 m diameter) and claimed that the trays induce bubble coalescence and present an obstacle to the formation of uniform bubbles;
3. Horizontal internals in bubble columns tend to reduce the overall backmixing, so that the benefits of reactor operation as an ideal cascade can be approached [231-235];
 4. Other authors [229, 236] reported an increase of the backflow ratio with increasing the perforated plate open free area, making the overall reactor behavior approach similar to that of a mixed stirred vessel. While other studies [233, 237] showed that decreasing the open free area reduced the liquid recirculation and increased the pressure drop;
 5. The mass transfer coefficients were found to increase upon sectionalization with perforated trays [238], and to decrease with the addition of more horizontal tube rows [234];
 6. Saxena et al. [113] and Pradhan et al. [224] reported that vertical internals inhibit bubble coalescence and enhance bubble breakup; however, O'Dowd et al. [208] found an increase in bubble size with the insertion of the vertical baffles;
 7. Intuitively, longitudinal tube internals tend to decrease the area available for flow, resulting in an increase in gas holdup when compared with that in empty reactors [210, 239]. The same applies when helical coils are used [224].
 8. The gap size between internals is important in the longitudinal funneling of liquid flow, as it governs the size of the large-scale eddies. This gap length is also responsible for decreasing the liquid kinetic turbulent energy [225].
 9. The large-scale liquid recirculation increased when vertical tube internals covered a large cross-sectional area (~22%) [213], while a less covered cross-sectional area (5%) did not affect the liquid recirculation; [4]

10. Forret et al. [213] proposed a 2-D model that seemed to provide good prediction for large BCRs with and without vertical tube internals; and
11. Vertical tubes increased the heat transfer coefficient more than horizontal internals did [240]. The axial dispersion coefficient also increased, especially in the bubbly flow regime, where it was a strong function of the gas velocity at the bottom of the column. This distribution was largely affected by the presence of internals [214].

2.5 MODELING OF SBCRS FOR F-T SYNTHESIS

Recent efforts have been focused on simulating F-T in SBCRs, with the aim of understanding the complex hydrodynamics and their effects on the reactor performance. Empirical 1-D models have been proposed for F-T SBCRs [126, 150, 241], which provide valuable information and predictions of the overall reactor performance. Multidimensional effects were accounted for using dispersion coefficients which cannot be calculated from first principles, but were empirically obtained for each system in question. However, the flow structures and internal recirculation zones in the SBCR were ignored in the 1-D models.

Earlier studies mainly focused on experimentally examining the macroscopic fluid dynamic behavior of three-phase fluidized beds and developing empirical correlations, however, with increasing computer power, the use of CFD has gained considerable attention. Over the past decade, significant advances have been made in numerical modeling of gas-solid and gas-liquid flow systems. However, understanding of the three-phase flows is still limited because of the complex phenomena underlying interactions among the phases, including the particle-bubble interaction and the liquid interstitial effect during particle-particle collision. Recently, several CFD

models have been reported to simulate three-phase fluidization behavior [242-244]. The following literature review indicates that modeling effort of SBCRs can be grouped as (1) Axial dispersion models (ADM); (2) multiple cell circulation models (MCCM); and (3) CFD models. Details are given in the following.

2.5.1 Axial Dispersion Models

The most common approach for modeling liquid mixing in bubble columns is the 1-D axial dispersion model (ADM), in which all mechanisms leading to liquid-phase macro-mixing are lumped into a single axial dispersion coefficient. Due to its simplicity and ease of use, the 1-D axial dispersion model has been widely implemented, however, its validity in describing multiphase flows with large degrees of backmixing, such as those present in bubble and slurry bubble columns has been scrutinized [245, 246], with investigators going as far as advising against the use of the ADM for multiphase systems [247, 248]. Hatton and Lightfoot [248] assessed the problem of dispersion and mass transfer from a generalized dispersion framework and showed that simplistic 1-D dispersion models were incapable of describing the dispersion in multiphase systems. Myers et al. [249] presented a detailed analysis of the shortcomings of the ADM in bubble columns by comparing it to a two region phenomenological model designated as the slug and cell model, which represents the gas-rich and gas-lean parts of the column. Their model accounted for the different mechanisms governing the upwards and downwards mixing within the bubble column, which was in contrast to the gradient transport nature of the ADM, predicting a symmetric rate of transport with the mean liquid velocity. Nonetheless, despite the arguments against the use of ADMs, they remain widely popular due to their ease of implementation in complex systems,

and the fact that numerous correlations were developed for gas, liquid and solid dispersion coefficients in multiphase flows as shown in Tables A-8-10 to A-8-12 (Appendix A).

It should be emphasized that these dispersion coefficient correlations vary considerably in complexity as well as details; and different correlations could predict an order of magnitude difference as reported by Rice and Littlefield. [250]. Also, a major drawback of the ADM is that most of the experiments were conducted using air-water systems at ambient conditions; and the experimental data points obtained in the churn-turbulent flow regime were limited when compared with those in the bubbly flow regime [251].

The determination of liquid-phase dispersion coefficients is based on a tracer injection method, followed by analysis of the mean and the variance of the system response curves. Electrolytes, dyes, and heat are normally applied as a tracer, which can be injected in a steady-state or an unsteady-state method; and it has been verified that both methods provide same results [86]. In the steady-state method, a tracer is injected at the exit or in another convenient point in the reactor, the axial concentration profile is measured upward in the liquid bulk, and the dispersion coefficients are then evaluated from this profile. In the unsteady-state method, a variable flow of a tracer is injected, usually at the reactor inlet and samples are then taken at the exit.

Most of the liquid-phase dispersion coefficient (D_L) correlations are function of the superficial gas velocity and column diameter and in some cases, liquid properties are accounted for. The majority of these correlations are empirical; however, attempts at theoretical or semi-theoretical derivations of the axial dispersion coefficients, based on several theories and approaches, were made [252]. Baird and Rice [253] assumed the validity of the Kolmogorov theory of isotropic turbulence [254] and used dimensional analysis to show that the liquid-phase axial dispersion coefficient can be expressed as:

$$D_L = K_r l_e^{4/3} P_m^{1/3} \quad (2-16)$$

Where l_e is the characteristic length of the eddies, which are primarily responsible for eddy diffusion effects, P_m is the specific energy dissipation per unit mass which can be expressed as $u_g g$ for bubble columns. Assuming the characteristic length is equivalent to the column diameter, Equation (2-16) can be rewritten as shown in Table A-10. This correlation is one of the most widely used to predict the liquid-phase backmixing in bubble columns.

Several investigators also correlated the axial liquid-phase dispersion coefficient in terms of the liquid circulation velocity [255, 256]. Joshi and Sharma [256] assumed the existence of axially symmetric steady multiple circulation cells in the bubble columns and used an energy balance to derive an expression for the average liquid circulation velocity. The liquid-phase axial dispersion coefficient was then directly correlated with the liquid recirculation velocity as shown in Equation (2-17).

$$D_L = 0.31 d_C^{1.5} u_{lc}^{1.5}; \quad \text{Where } u_{lc} = 1.4 [d_r g (u_G - \varepsilon_G)] \quad (2-17)$$

This correlation showed good agreement with the experimental data [256] in small column diameters, however, its applicability to large column diameters is questionable as the existence of these multiple cells in a time averaged sense has not been experimentally investigated or correlated. Similarly, Zehner [255] develop an alternative model assuming the stationary eddies are layered transversely above each other, and showed the validity of the following commonly used relationship by McHenry and Wilhelm [257]:

$$Pe = \frac{u_{lc} d_C}{D_L} \quad (2-18)$$

He then derived the following expression for the liquid-phase axial dispersion coefficient, which is similar to that by Baird and Rice [253] as:

$$D_L = 0.5f^{1/3}d_c^{1/3}(u_Gg)^{1/3} \quad (2-19)$$

Where f is the friction factor, which was empirically correlated to be 0.398.

Figure 2-9 compares the predictions of the liquid axial dispersion coefficient by different models; and as can be seen most of the models exhibit similar trends with various column diameters, whereas there is a large discrepancy among the predictions at different superficial gas velocities.

Generally, the radial dispersion in BCRs has been lumped with the axial dispersion coefficient and the latter has been widely used and almost exclusively as an indication of mixing in such reactors. As a matter of fact, while considerable information exists on axial dispersion of fluids in bubble columns, radial mixing has been almost completely ignored. The few measurements cited by Deckwer [137] suggested that the radial dispersion coefficient is always less than one-tenth of the value of the axial dispersion coefficient.

Based on the assumptions that the velocities and holdups of individual phases are uniform in the radial and axial directions, and the axial (D_{zL}) as well as the radial (D_{rL}) dispersion coefficients were assumed to be constant throughout the fluidized bed, and the two-dimensional unsteady-state dispersion model can be expressed as:

$$\frac{\partial(\varepsilon C)}{\partial t} + \frac{\partial(\varepsilon u_z C)}{\partial z} + \frac{1}{r} \frac{\partial(r\varepsilon u_r C)}{\partial r} = \frac{1}{r} \frac{\partial}{\partial r} \left[r\varepsilon D_{rL} \frac{\partial C}{\partial r} \right] + \frac{\partial}{\partial z} \left[\varepsilon D_{zL} \frac{\partial C}{\partial z} \right] \quad (2-20)$$

Equation (2-20) is usually reduced to the axial dispersion (1-D) model, since the radial dispersion coefficient (D_{rL}) is often assumed to be negligible when compared with the axial dispersion coefficient.

Table A-13 (Appendix A) shows a summary of the ADM models in three-phase reactors available in the literature; and as can be seen in all models, three distinct phases (gas-phase, liquid-phase and solid-phase) are used. In most of these models, the gas-phase is described in terms of

‘large’ and ‘small’ bubbles [56, 150, 153, 241, 258, 259] and in other studies, a single-bubble model is assumed [157, 260, 261]. The solid-phase dispersed in the liquid-phase is referred to as the “slurry-phase”.

The solid (catalyst) concentration in the reactor is often assumed constant, and in several models, the Sedimentation-Dispersion Model (SDM) is used to estimate the catalyst concentration profile. Also, the syngas consumption is not always considered or is estimated using a linear relationship between the gas consumption and the syngas conversion; and in several models, an overall mass balance on the gas-phase is formulated in order to simulate the effect of syngas consumption [151, 158, 262-267].

Early models treated the gas-phase as plug-flow, while the slurry-phase is often assumed to be perfectly-mixed [247, 248, 253, 268-270]. This latter assumption is inappropriate for simulating small-scale reactors, however, it could be viable for large-scale ones since the liquid-phase backmixing and the dispersion coefficients were reported to increase with reactor diameter [253]. Recent models have introduced the dispersion coefficients in the mass balance equations when using the ADM for the gas and slurry phases [46, 150, 265]. Rados et al. [265] showed that utilizing the ADM to model backmixing in the F-T SBCR is more versatile than the combination of ideal reactor models, such as plug-flow and perfectly-mixed. Nonetheless, for large-scale F-T reactors, considering the gas-phase moves in a plug-flow and the slurry-phase moves as perfectly-mixed appeared to give the closest results to those obtained from the ADM [265].

Visual observations and photographic methods revealed the coexistence of distinctly two classes of gas bubbles (small and large) in Bubble Column Reactors (BCRs) operating in the churn-turbulent (heterogeneous) flow-regime [8, 175, 178, 185, 271]. This finding led to the separation of the gas-phase into two distinct classes, large gas bubbles and small gas bubbles. The large gas

bubbles class is often modeled as plug-flow while the small gas bubbles class is assumed to be perfectly-mixed, similar to the slurry-phase. This is an adequate assumption, since in large-scale F-T SBCRs operating in the churn-turbulent flow regime, the fast-rising large gas bubbles induce strong circulations and create backmixing or re-circulation zones wherein the small gas-bubbles are entrained [145, 175].

Few models employed the ADM for the large and small gas bubble classes as well as for the slurry-phase. de Swart and Krishna [153] used the ADM and 1st order reaction kinetics with respect to H₂ to simulate the F-T SBCR. These authors estimated the gas consumption using a simple linear relationship for the syngas conversion. Rados et al. [150] also used the ADM for both classes, however, they introduced a gas bubbles term to account for the interactions among gas bubbles of different classes. Moreover, they assumed that the magnitude of the interaction is proportional to a dimensionless cross-flow coefficient and the slip velocity between the two interacting classes of gas bubbles; however, they only provided a guessed value for this coefficient corresponding to moderate interactions between the small and large gas bubbles. In addition, these authors included the change of gas holdup and gas velocity due to the syngas consumption and in their derivation, they considered all of the variables as space-dependent of the mass balances.

Thus, it is obvious that the reactor model developed by Rados et al. [150] is quite different from the earlier models which assumed constant parameters along the reactor height or used a linear relationship between the syngas conversion and the gas velocity to represent the gas consumption. However, like de Swart and Krishna [153], Rados et al. [150] used 1st order reaction kinetics with respect to H₂ in order to simulate the F-T reaction and assumed the catalyst to be uniformly distributed. Iliuta et al. [160] introduced a pseudo 2-dimensional model based on the two-class bubbles model and the ADM by separating the reactor radially into a core region and an

annulus region; and they included the gas bubbles interactions term previously introduced by Rados et al. [150]. They considered the WGS reaction and used detailed kinetics for the F-T reaction. They also estimated the gas consumption from the overall mass balance, and the gas-phase and liquid-phase concentrations from the vapor-liquid-equilibria (VLE). Although the empirical reactor model by Iliuta et al. [160] appears to be the most complete to date, it requires the knowledge of many parameters which are not readily available, especially for high-pressure, high-temperature reactors operating with organic liquids, such as F-T synthesis. Obviously, this could be a disadvantage, since the estimation of so many unknown parameters may compound the errors, leading to significant uncertainties in the reactor model predictions.

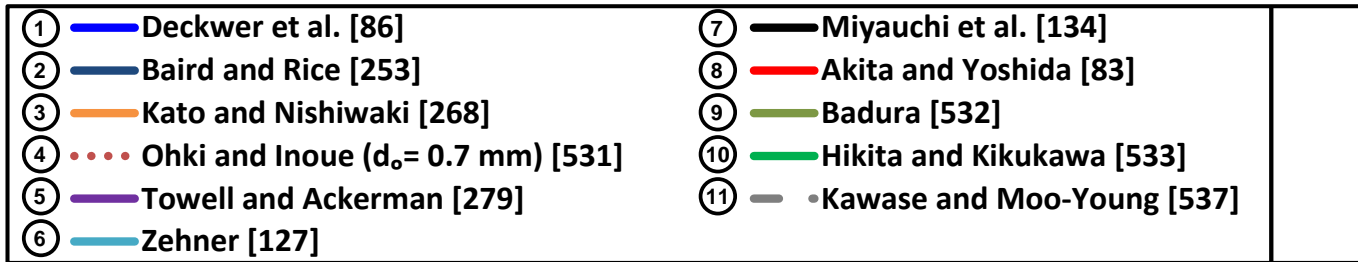
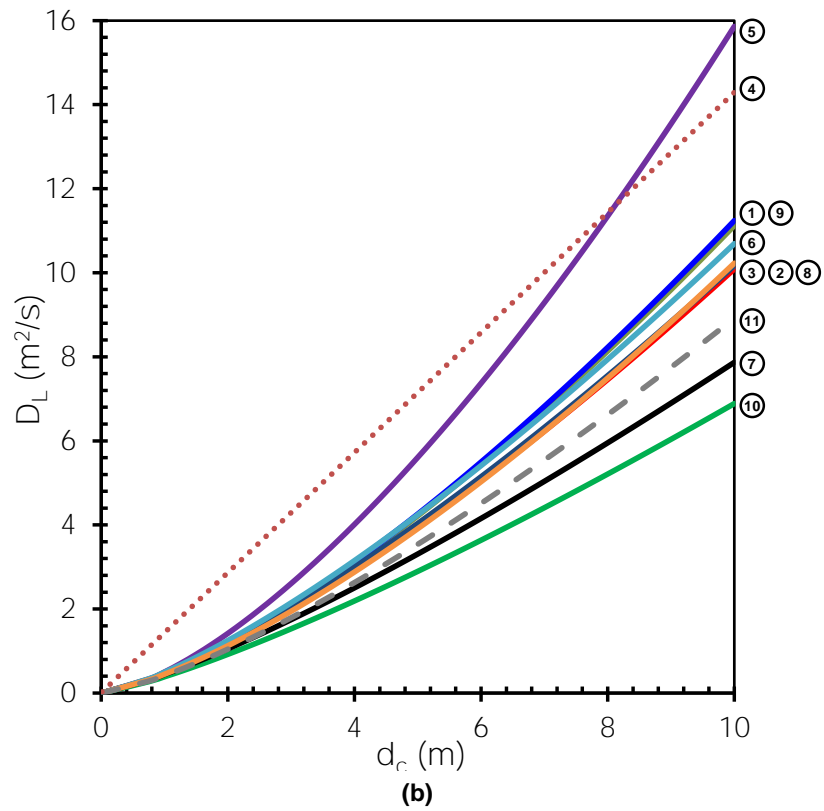
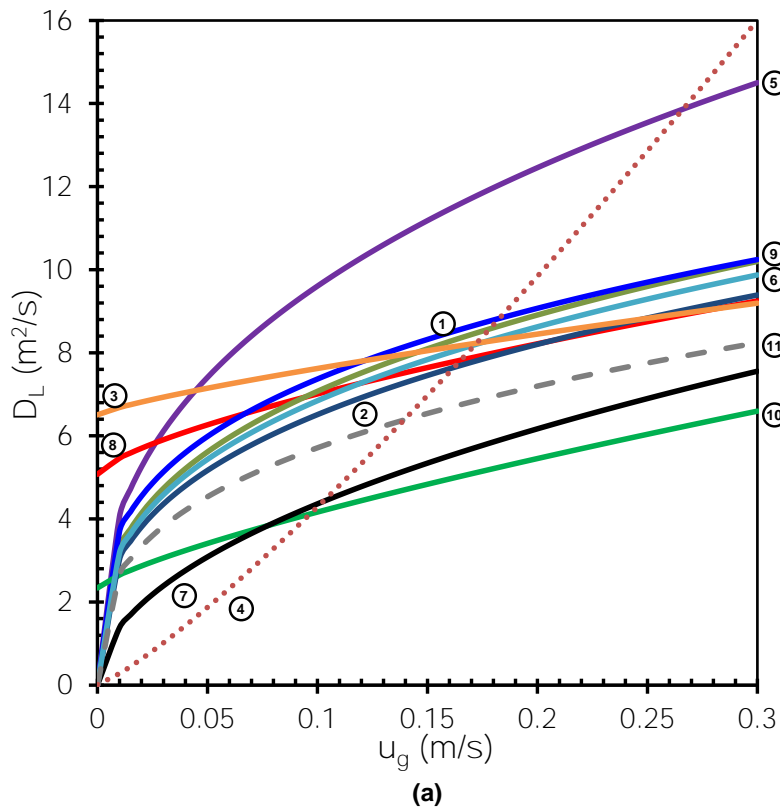


Figure 2-9: Comparison among the liquid axial dispersion models at various
 (a) column diameters for $u_g = 0.25$ m/s, (b) gas velocities for $d_c = 3.5$ m

2.5.2 Multiple Cell Circulation Models

Multiple cell circulation models (MCCM) were very popular in early modeling attempts aimed at understanding the hydrodynamics of bubble and slurry bubble column reactors. These models are based on the idea that the flow instability can be described mathematically using flow disturbances in the dispersed-phase, which can be accounted for in the mass balance as follows:

$$\frac{\partial(\varepsilon + \delta\varepsilon)}{\partial t} + \nabla \cdot [(\varepsilon + \delta\varepsilon)(v + \delta v)] = 0 \quad (2-21)$$

Mixing of the liquid-phase is attributed to various phenomena, such as turbulent vortices, liquid entrainment in the wakes of rising bubbles, liquid circulation and radial exchange flows. Generally, liquid mixing in bubble columns and SBCRs is a resultant of three major contributing mechanisms [140, 272-276]: (1) global convective circulation of the liquid-phase induced by the non-uniform radial gas holdup distribution [277]; (2) turbulent diffusion due to the presence of large and small eddies generated by the rising bubbles [135]; and (3) molecular diffusion is negligible when compared with the other diffusion mechanisms.

In SBCRs operating in the churn-turbulent flow regime, the gas flow generates significant backmixing in the slurry-phase (dense-phase). This backmixing of the dense-phase is caused by the gas-induced eddies, which derive their energy from the large fast-rising bubbles. The maximum size of eddies, for reactors with $h_c/d_c > 1$ is limited by the column diameter d_c [135]. The induced circulation patterns have a strong impact on the mass transfer and productivity and are especially vital in eliminating the concentration gradients within the SBCRs. Therefore, the design of SBCRs will require consideration of the liquid-phase backmixing. In BCRs operating in the churn-turbulent flow regime, the large gas bubbles tend to concentrate in the middle of the column,

the liquid-phase is drawn upwards in the central region and when the bubbles disengage at the top, the liquid returns down the column in the wall region.

Despite the availability of ample experimental data on the liquid-phase backmixing in the literature for different column diameters and superficial gas velocities, it is somewhat difficult to compare the results due to the differences in the reactor dimensions and the physicochemical properties of the liquids used. Generally, the circulations consist of an upward flow region where the liquid-rich of entrained gas bubbles moves upward and a compensating region where a liquid-poor of gas bubbles moves downward [278]. The liquid circulations are driven by the buoyancy of the gas-phase as it rises and drags the liquid. The bubbles-driven circulations can occur with or without net superficial liquid motion, but it requires a net upward motion of the gas.

Although the liquid circulation is desirable for some applications, such as gas lift, thermosiphon devices, or in the downcomers of distillation columns, it is undesirable in BCRs or SBCRs, because it decreases the gas retention time and causes liquid backmixing, which decrease the gas-liquid mass transfer. For instance, the widely used simplification that the flow is uniform across any horizontal cross-sectional area of the BCR or SBCR consistently predicts greater gas holdup and better mass transfer values than those actually observed [278, 279]. Also, the assumption that large gas bubbles are completely backmixed [279] may not be true for columns with significant h_c/d_c ratios, wherein many liquid circulations are prevailing. The liquid circulation phenomenon, has been claimed by many authors to be analogous to the natural convection [161, 280-284]. Yet, this analogy is inaccurate, because in natural convection, the mixing of streams with different densities eliminates the driving force by producing a stream with intermediate density, which cannot regroup spontaneously into low- and high-density streams. However, if a bubble-rich and a bubble-lean streams are mixed to produce one stream of intermediate bubble content, this stream

can regroup (due to buoyancy forces) to reform bubble-rich and bubble-poor streams. Therefore, circulation in bubble columns does not permanently eliminate the driving forces of bubble-induced circulations as it does in natural convection.

Millies and Mewes [285] argued that the liquid recirculation in bubble columns is a turbulence-induced flow instability due to the disturbance or non-uniformity of the gas distribution profile, and hence they used the MCCM similar to that by Joshi and Sharma [256] to calculate the flow fields in their bubble column. This effect was firstly reported by De Nevers [278], who stated that the liquid circulation pattern is induced by density differences caused by the uneven distribution of the bubbly-phase across the cross-sectional area of the BC. In the central area of the BC, however, the local gas holdup values are greater than those close to the wall, resulting in liquid up-flow in the central region and liquid down-flow along the wall.

When there are no baffles or internals, the length of the circulation cell will depend on the difference between the gas and slurry viscosities and densities in the SBCRs. It is typically smaller for low viscosity liquids, such as water, and much larger for high viscosity systems, such as F-T slurries [278]. This makes the use of water-based empirical models, representing circulation or turbulence parameters, inaccurate for representing the F-T SBCRs. When the gas velocity inside the column is increased, the bubble flow ceases to be uniform and strong circulation was observed within the gas-slurry mixed phase and the column operated in the circulation flow regime [139, 140]. This circulation is once again due to the existence of a bubble-rich phase near the center of the column and a bubble-lean phase near the wall of the column, which creates a difference in buoyancy forces.

The 1-D circulation models are based on solving the one-dimensional continuity and momentum balance equations, which are simplified versions of the two-fluid model equations

[272]. These models are typically applicable to the middle of the SBCR with an $h_c/d_c > 5$, where experimental evidence shows the presence of 1-D profiles [277]. The model equations for the conservation of momentum are:

$$\frac{1}{r} \frac{d}{dr} (r\tau_{rz}) = \frac{dP}{dz} + \rho_l (1 - \varepsilon_g(r)) g \quad (2-22)$$

$$-\frac{dP}{dz} = \frac{2\tau_{rz}}{R} + \rho_l (1 - \bar{\varepsilon}_g) g \quad (2-23)$$

Where ε_g is the gas holdup and τ_{rz} is the Reynolds shear stress.

The Reynolds shear stress distribution is commonly described using the following procedure by Rice and Geary [141]:

$$\begin{aligned} \tau_{rz}(\xi) &= \frac{\rho_L g d_c}{2} \left(\frac{2\bar{\varepsilon}_G}{m\lambda^2} \right) \xi \left[1 - \left(\frac{\xi}{\lambda} \right)^m \right] & \xi \leq \lambda \\ \tau_{rz}^*(\xi) &= \frac{\rho_L g d_c}{2} \left(\frac{\bar{\varepsilon}_G}{\lambda^2} \right) \xi \left[\frac{\lambda^2 - \xi^2}{\xi} \right] & \xi \geq \lambda \end{aligned} \quad (2-24)$$

The solution of the above model requires the knowledge of the gas holdup profile and a closure model for the Reynolds shear stress. Several variations of the above 1-D circulation model as shown in Figure 2-10 have been discussed in the literature [139-141, 286-288]. The variations of these models are mostly due to the boundary conditions and the Reynolds shear stress turbulence models used. Table A-14 (Appendix A) provides a summary of the various MCCM published in the literature.

Generally, the 1-D circulation model has been proven to be successful in studying liquid circulation in BCRs and SBCRs [289]. Kumar et al. [139] compared the existing variations of the 1-D circulation model to study liquid recirculation in BCRs; and they concluded that there is a lack of literature correlations for eddy viscosity and mixing length to predict the 1-D liquid velocity profiles under a wide range of operating conditions. They correlated a mixing length profile from

the experimental measurements of the Reynolds shear stress and liquid velocity gradient and showed that the mixing length in a 0.19 m diameter column can be used along with the measured holdup profile to predict recirculation in large diameter columns, up to 0.30 m. Their model was validated for gas velocities ranging from 0.02 – 0.12 m/s. The use of the power law expression was later introduced to predict the radial gas holdup profiles, as discussed in Section 2.2.2. The above system of equation is usually solved using numerical integration and details of the solutions can be found elsewhere [243, 285, 288, 290].

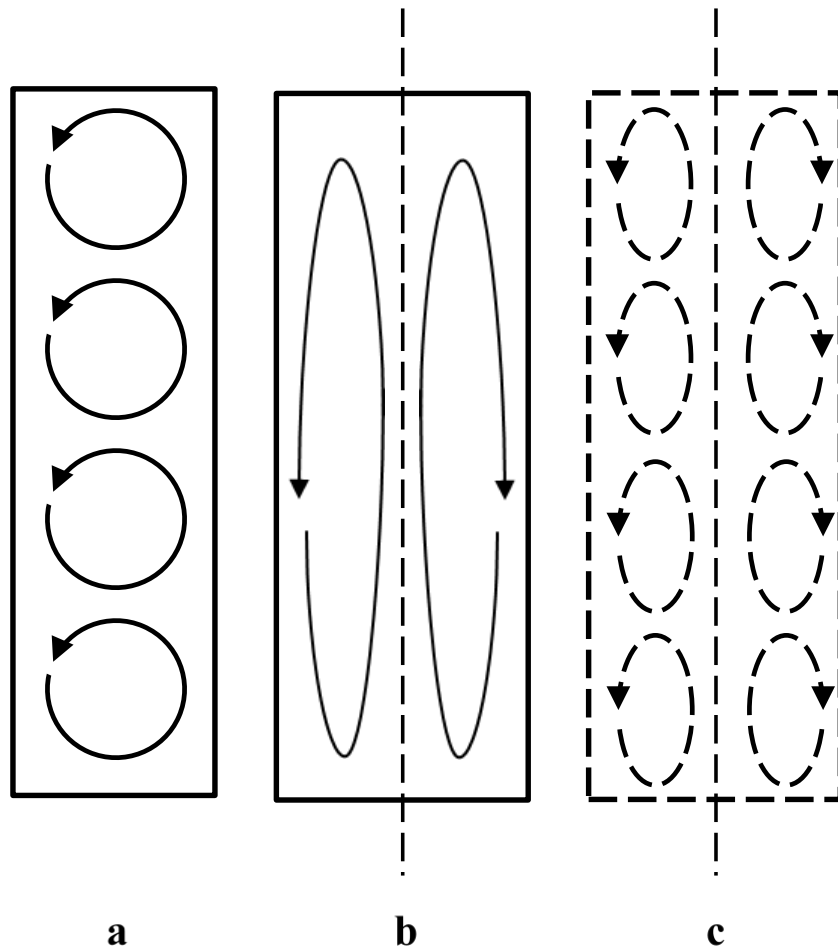


Figure 2-10: Circulation cell depiction of the continuous-phase circulation patterns in BCRs and SBCRs: (a) Zehner [280, 281], (b) Groen et Al. [291], (c) Joshi And Sharma [256].

2.5.3 Computational Fluid Dynamics (CFD) Models

CFD modeling of multiphase systems can be successful, if the calculations are carefully validated. A general overview of a CFD model development is shown in Figure 2-11. It is typically composed of three main stages: pre-processing, solver development, and post processing. Pre-processing involves the development of the geometry to be investigated and defining the meshing procedure over which the model will be solved. Solver development describes all activities related to defining model structures, properties, parameters, boundary and initial conditions, and solution methods. Once the model is solved for a specific case, the raw data is then post processed to generate analyzable figures and graphics.

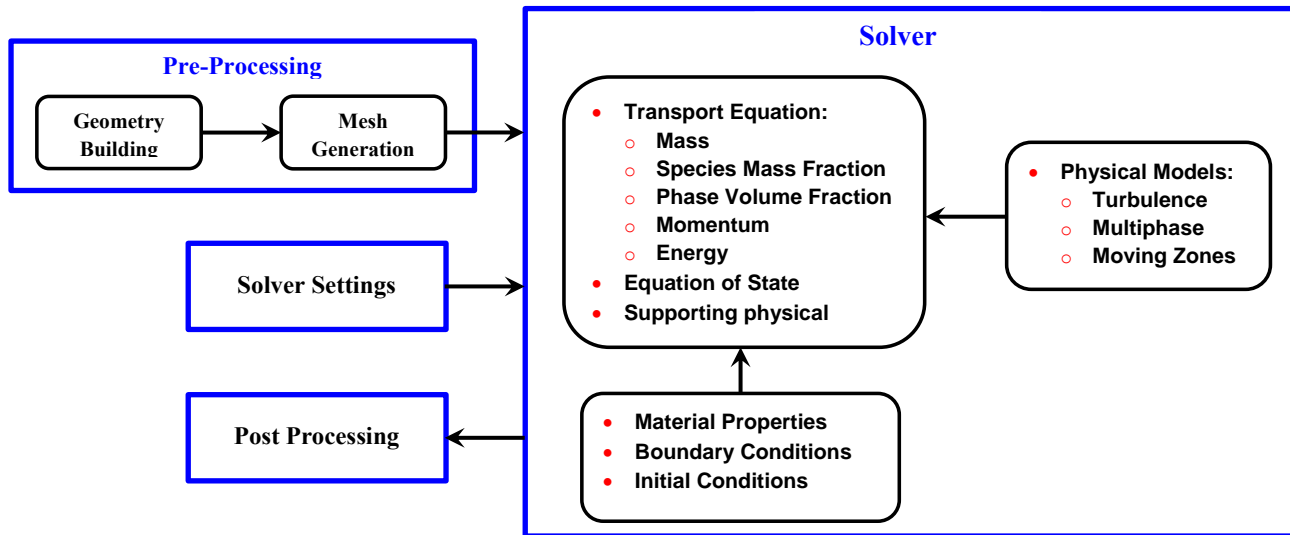


Figure 2-11: Overview of CFD process

The two most commonly used CFD approaches [292] are the Eulerian-Eulerian or Multi-fluid Eulerian approach [293] and the Eulerian-Lagrangian approach [294]. The Eulerian-Eulerian approach assumes that the dispersed and continuous phases are interpenetrating continua, and a set of Navier-Stokes equations is solved for each of the phases. The coupling between the motion

of the dispersed and continuous phases is achieved by implementing momentum exchange terms into the respective phase's momentum balance equations, which are based on drag consideration. On the other hand, the Eulerian-Lagrangian approach assumes that the dispersed-phase consists of representative particles transported with the continuous-phase and a set of Navier-Stokes equations, which include coupling between the continuous and dispersed phases, is solved only for the continuous-phase, whereas the dispersed-phase particles are tracked by solving the individual motion equations for each particles. Table A-15 (Appendix A) shows a summary of the CFD modeling efforts in three-phase reactors using 2-D and 3-D Multi-fluid Eulerian and Eulerian-Lagrangian models. In general, the Eulerian-Lagrangian model is best suited for fundamental studies, such as bubble-bubble and bubble-liquid interactions and its applications are limited only to cases where the gas superficial velocities are low and the phase holdups are small. Thus, this model is not viable when the dispersed-phase occupies a large volume fraction of the reactor, such as in many industrial applications. As a result, the Multi-fluid Eulerian approach is typically preferred for modeling large-scale applications, including SBCRs, which often operate in the churn-turbulent flow regime [295], where gas holdup values are high. Additional simplifications, such as 2-D Cartesian with axisymmetry and isothermal flow, are usually implemented in order to lower the computational cost [201, 243, 244, 293, 294, 296-302]. Details of the various modeling approaches can be found elsewhere [242, 275, 298, 303-308].

The momentum balance equation in the Multi-fluid Eulerian approach is:

$$\frac{\partial(\alpha_k \rho_k u_k)}{\partial t} + \nabla \cdot (\alpha_k \rho_k u_k u_k) = -\alpha_k \nabla p - \nabla \cdot (\alpha_k \tau_k) + \alpha_k \rho_k g + F_D + F_G \quad (2-25)$$

In the Eulerian-Lagrangian approach, the force balance equation used to track individual particles is:

$$m_p \frac{du_p}{dt} = F_p + F_D + F_{VM} + F_L + F_G \quad (2-26)$$

Among the above forces, Becker [309] and Oey et al. [310] reported that the drag force (F_D) is the most critical, whereas the other forces only have a minor or “tuning” effect.

The drag force between any two phases can be written as:

$$F_D = \frac{1}{2} C_D \pi r_d^2 \rho_c |u_s| u_s \quad (2-27)$$

Where, C_D is the drag coefficient.

The CFD modeling of multiphase reactors strongly depends on the closure drag model; and the effects of using different drag coefficient correlations on the modeling results have been reported in literature [302, 311, 312]. The most commonly used drag coefficients for two-phase and three-phase systems are given in Section 2.5.3.1.

In most CFD reactor modeling, the simulation domain is typically restricted to the reactor and the general flow within the feed, whereas spargers and cooling pipes are not accounted for. Furthermore, although the inlet volumetric flow rates are known, the velocity distribution is not specified. The most widely used practice is to use the knowledge of fully developed flow in pipes to specify the inlet velocity distribution. Therefore, for laminar flow through a cylindrical inlet pipe, one can specify a parabolic velocity profile as a boundary condition at the inlet, however, if the feed pipes have complex shapes, which is typical of bubble columns and SBCRS, it is necessary to develop an additional model, which include appropriate boundary conditions. The outlet is the surface of the solution domain through which the flow exits. Usually the outlet boundary condition implies that the gradients normal to the outlet boundary are zeros for all the variables, except pressure. In order to predict the effects of turbulence, CFD models primarily concentrate on the methods which make use of turbulence models. These methods have been specifically developed

to account for the effects of turbulence without recourse to a prohibitively fine mesh and direct numerical simulation.

Generally, liquid mixing in SBCRs is a resultant of three major contributing mechanisms [140, 272-276]: (1) global convective circulation of the liquid-phase induced by the non-uniform radial gas holdup distribution [277]; (2) turbulent diffusion due to the presence of large and small eddies generated by the rising bubbles [135]; and (3) molecular diffusion is negligible when compared with the other diffusion mechanisms.

Scaling laws are an important tool for describing turbulence. Most of the conclusions and observations regarding turbulence are based on the order of magnitude estimates, which follow from logical applications of scaling laws and dimensional analysis. Generally, the turbulent length scale is a physical quantity related to the size of the large eddies, containing the energy in the turbulent flow. A variety of length scales (eddy sizes) exists within the turbulent flow, wherein the size of the largest eddies are typically denoted by L , and those of the smallest eddies are denoted by η . The largest eddies in the flow account for most of the momentum and energy transport, and their size is only constrained by the physical boundaries of the flow. Thus, L is referred to as the integral length scale. The size of the smallest eddies (η), on the other hand, is determined by the viscosity. Therefore, the effect of viscosity increases with decreasing length scales. The smallest length scales are those where the kinetic energy is dissipated into heat. The turbulence eddies are visualized as molecules, constantly colliding and exchanging momentum and obeying laws similar to the kinetic theory of gases. Most models of Reynolds stress, using an eddy viscosity hypothesis based on an analogy between the molecular and turbulent motions, are described as follows:

$$-\overline{\rho u_i u_j} = \mu_T \left(\frac{\partial u}{\partial x_i} + \frac{\partial u}{\partial x_j} \right) - \frac{2}{3} \delta_{ij} \left(\mu_T \frac{\partial u}{\partial x_k} + \rho k \right) \quad (2-28)$$

Where μ_T is the turbulent or eddy viscosity, which unlike molecular viscosity, is not a fluid property, but depends on the local state of flow or turbulence; μ_T is a scalar quantity, which varies significantly within the flow domain; and k is the turbulent kinetic energy.

Although there are numerous turbulence models as outlined in Table 2-5, the most widely used is the two-equation, k - ε , model; in which the turbulence viscosity is related to k and ε by the following equation:

$$\mu_T = \frac{C_\mu \rho k^2}{\varepsilon} \quad (2-29)$$

Where C_μ is an empirical coefficient; and the modified form of the transport equation for the k - ε model becomes:

$$\frac{\partial \rho k}{\partial t} + \frac{\partial(\rho u_i k)}{\partial x_i} = \frac{\partial}{\partial x_i} \left(\frac{\mu_T}{\sigma_k} \frac{\partial k}{\partial x_i} \right) + G - \rho \varepsilon \quad (2-30)$$

$$\frac{\partial \rho \varepsilon}{\partial t} + \frac{\partial(\rho u_i \varepsilon)}{\partial x_i} = \frac{\partial}{\partial x_i} \left(\frac{\mu_T}{\sigma_\varepsilon} \frac{\partial \varepsilon}{\partial x_i} \right) + \frac{\varepsilon}{k} (C_1 G - C_2 \rho \varepsilon) \quad (2-31)$$

Where G is the turbulence generation term expressed as:

$$G = \frac{1}{2} \mu_T [\nabla \bar{u} + (\nabla \bar{u})^T]^2 \quad (2-32)$$

The values of the empirical parameters in the above turbulence equations are obtained using experimental data and can be found in the literature.

Table 2-5: Different turbulence models available in the literature [275]

Model	Advantages	Disadvantages
Zero-equation models (Mixing length model)	<ul style="list-style-type: none"> • Cost-effective 	<ul style="list-style-type: none"> • Applicable to very limited number of flows • $v_T \rightarrow 0$ as $\partial U / \partial y = 0$ • Lack of transport of turbulent scales. • Estimation of mixing lengths is difficult. • Cannot be used as a turbulence model.
One-equation model (k-algebraic model)	<ul style="list-style-type: none"> • Cost-effective model 	<ul style="list-style-type: none"> • Applicable to limited number of flows • The use of an algebraic equation to represent length scale is too restrictive. • Transport of the length scale is not accounted for.
Reynolds Stress Model (RSM)	<ul style="list-style-type: none"> • Most general model • Can well predict many complex flow scenarios such as non-circular ducts and curved flows 	<ul style="list-style-type: none"> • Solves for seven additional PDE's, increased computational load • Not good for round gets and flows involving significant curvature, swirl, sudden acceleration, separation and low Re regions.
Two-equation models ($k-\varepsilon$: standard, RNG, realizable)	<ul style="list-style-type: none"> • Can predict velocity and length scales with transport equations. • Good results for numerous flow applications. • Robust economically and easy to implement. 	<ul style="list-style-type: none"> • Limited to an eddy viscosity assumption. • Turbulent viscosity is assumed to be isotropic. • Convection and diffusion of the shear stress are neglected.
Standard $k-\varepsilon$	<ul style="list-style-type: none"> • Very widely used and heavily validated. 	<ul style="list-style-type: none"> • Performs poorly in certain scenarios same as RSM.
RNG $k-\varepsilon$	<ul style="list-style-type: none"> • Enhancement of the standard $k-\varepsilon$ model primarily to improve prediction of swirling flows and flow separation. 	<ul style="list-style-type: none"> • Not as stable as the standard $k-\varepsilon$ model, not suitable for round jets.
Realizable $k-\varepsilon$	<ul style="list-style-type: none"> • Enhancement of the standard $k-\varepsilon$ model to handle both swirling flows and round jets. 	<ul style="list-style-type: none"> • Can be very unstable and susceptible to divergence.

Grevskott [243] modeled water-TiO₂ nanoparticles as a single pseudo-homogenous-phase, assuming that the nanoparticles are sufficiently small to behave as liquid molecules, and accordingly the water and solid particles were assumed to have the same local velocity. The momentum and continuity equations were then solved using a 3-D, two-fluid Eulerian model with per phase k - ε turbulence in order to investigate the local holdups and velocities of the phases. Fan et al. [294, 313] developed a 2-D Eulerian-Lagrangian model for three-phase systems using: (1) the averaged Navier-Stokes equation for the liquid-phase (Euler), (2) the volume of fluid (VOF) method for the gas-phase, and (3) the discrete particle method (DEM) for the solid-phase (Lagrange). Their simulations, however, were limited to 100 solid particles, and they investigated the behavior of a single-bubble rise. A similar approach was used by Zhang and Ahmadi [298].

Mitra-Majumdar et al. [244] used a 2-D axisymmetric model with a modified drag coefficient model between the liquid and gas phases to represent the effect of gas bubbles, and another modified drag coefficient model between liquid and solid phases to simulate the effect of solid particles. Matonis et al. [297] applied the kinetic theory of granular flow (KTGF) for the solid-phase and the k - ε turbulence model for the continuous-phase. Schallenberg et al. [299] accounted for the interphase momentum between the two dispersed phases (gas and solid) and extended the k - ε turbulence model to account for the bubble induced turbulence. Panneerselvam et al. [293] used the multi-fluid Eulerian model to investigate the gas holdup and axial solid velocity patterns in three-phase fluidized beds. They used the closure law for modeling the liquid turbulence as well as the interphase momentum exchange and the k - ε turbulence for modeling the turbulence induced by the phases. They also used the constant viscosity model for calculating the solid pressure term, instead of using the kinetic theory of granular flow.

Matos et al. [301] used an axisymmetric two-fluid Eulerian approach for modeling a three-phase slurry reactor for petroleum hydrodesulfurization. They combined the solid and liquid phases into a pseudo-liquid-phase and assumed that the difference between the densities of the catalyst and the slurry-phase was so small that the catalyst did not settle, and that the fluid velocity was so small that a 2-D axisymmetric model was justified. They used friction terms to couple the momentum balance of the gas-phase and the pseudo-liquid-phase; the overall mass balance to couple both phases; the k - ε turbulence model to describe the behavior of the continuous-phase; and the axial velocities at the entrance of the reactor were set using the experimental results by Torvik and Svendsen [314]. They also added simplified hydro-desulfurization kinetics to the mass balance. They then investigated the radial variations of the gas and liquid holdups and the results were validated against the experimental values reported by Grienberger and Hofmann [315] for a two-phase, air-water system. They also, investigated the effects of the grid size and simulation time on the kinetic results.

Troshko and Zdravistch [316] employed a two-fluid Eulerian approach to model a three-phase SBCR for F-T synthesis. They used a population balance model to predict the bubble size distribution throughout the reactor and a turbulence was described using the two-equation RNG k - ε turbulence model. They used the interphase drag exchange coefficient by Ishii and Mishima [272] and incorporated the heterogeneous and homogenous kinetic reaction rates by Yates and Satterfield [317], representing a simplified F-T synthesis. They predicted the time-averaged Sauter mean bubble diameter at different elevations from the inlet of the SBCR, the gas holdup at different catalyst concentration, and the axial variation of the time-averaged Sauter mean bubble diameter along the reactor axis at different catalyst concentrations. Their results were then validated against the experimental data by Kulkarni et al. [318] for air-water bubble columns at standard

atmospheric conditions. Moreover, they also modeled the effect of the syngas inlet velocity on its conversion and reactor productivity; however, these results were not validated against any experimental data.

It should be emphasized that around half of the CFD multi-phase modeling efforts shown in Table A-15 (Appendix A) have not been experimentally validated and that, except for the work by Matos et al. [301], almost all experimental validations were conducted using small-scale air-water-solid systems at ambient pressures and temperatures, which brings into question the validity of extrapolating the conclusions to large-scale industrial reactors, operating under high pressures and temperatures with organic liquids and slurries, such as F-T synthesis.

2.5.3.1 Commonly used drag coefficient models for two-phase and three-phase systems

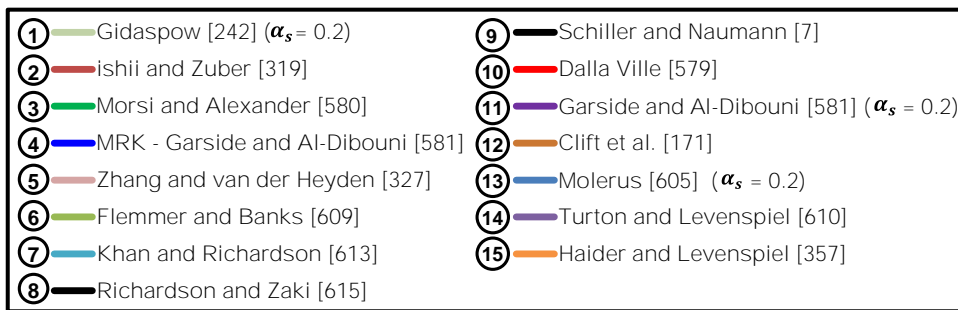
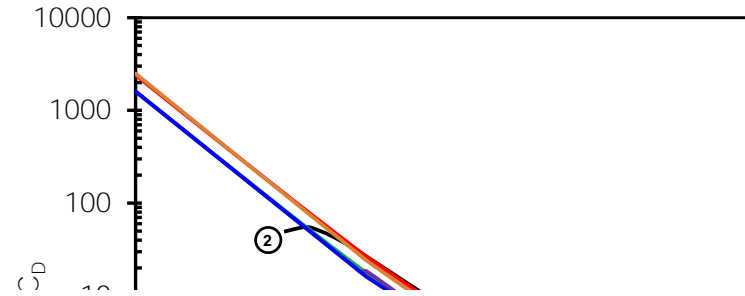
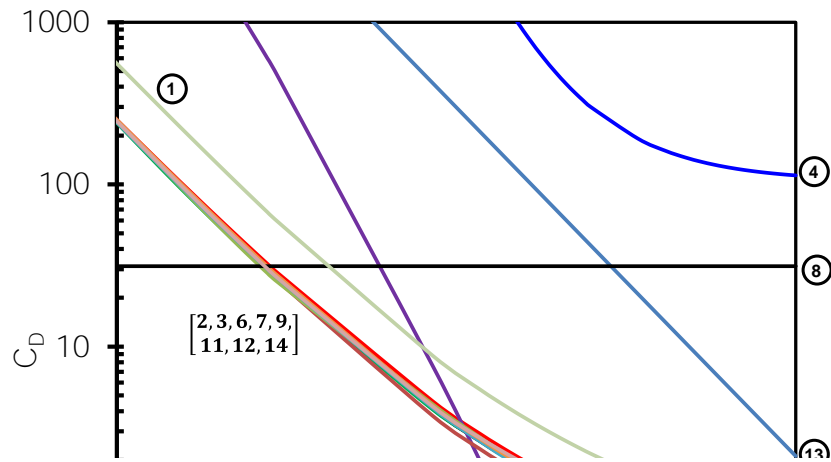
While there is extensive work on two-phase flow systems, studies investigating three-phase hydrodynamics are rather limited. Tables A-8-16 and A-8-17 (Appendix A) show the gas-liquid and solid-fluid drag coefficient models, respectively, which are commonly used in CFD modeling of multiphase flows. In general, the drag coefficient (CD), is a function of the bubble (or particle) Reynolds Number and the void fraction. Table A-16 (Appendix A) shows the gas-liquid drag coefficient correlations obtained using experiments in two-phase systems by Clift et al. [171], Ishii and Zuber [319], Kurose et al. [320], Lain et al. [321] and in three-phase systems by Grevskott et al. [243] and Tomiyama et al. [322]. Also, the model by Mei and Klausner [323] was based on a derivation for spherical bubble in an unbounded shear flow and the model by Snyder et al. [324] was based on the statistical analysis of small bubbles in isotropic turbulence. The solid loading used by Grevskott et al. [243] was 7 – 20 wt.% and the solid holdup used by Tsuchiya et al. [325] was up to 57 vol.%. Moreover, Figure 2-12 (b) compares a few gas-liquid drag correlations, and

as can be seen most correlations predict very similar values for the drag coefficient at varying bubble Reynolds numbers. It should be noted that all the gas-liquid drag coefficient correlations presented in Table A-16 (Appendix A) were developed under ambient conditions.

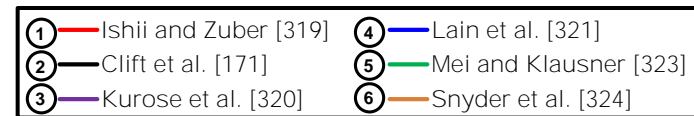
Table A-17 (Appendix A) shows the gas-solid and liquid-solid drag coefficient correlations; and as can be seen all correlations were derived from experimental data, except those by Ma and Ahmadi [326] who used thermodynamic derivation for multiphase turbulent flows; Gidaspow [242] who used theoretical derivation; and Zhang and Van der Heyden [327] who used numerical simulation for gas-solid flows. This difference among the correlations is primarily due to the nature of the experiments conducted or to the assumptions made to develop these correlations. For instance, the model by Ishii and Zuber [319] assumes the slip velocity is independent of the gas bubble diameter, while that by Schiller and Nauman [6] does not account for the bubble deformation effects. This in fact, limits these models applicability beyond the systems used in their development. Figure 2-12 (a), compares various liquid-solid drag correlations at various particle Reynolds numbers, and unlike the gas-liquid drag correlations, the liquid solid drag coefficients appear to vary greatly at similar values of the Reynolds Number .which amplifies the confusion about the selection of solid-liquid and/or gas-solid drag coefficient models for CFD modeling of SBCRs.

Thus, the gas-liquid and liquid solid drag models available were obtained mostly using air-water or air-water-glass beads flows under ambient conditions, which again bring into question their applicability for modeling large-scale industrial SBCRs, operating with organic media under high pressures and temperatures. Moreover, Zhang and Ahmadi [298] and more recently Hamidipour et al. [292] underscored the need for better and more representative drag correlations for their CFD modeling of the hydrodynamics in three-phase reactors. In addition, in some CFD

modeling efforts, the gas-liquid drag coefficients were justified by lumping the liquid and solid phases into one pseudo-homogenous phase (slurry), assuming the particle-liquid slip velocity is too small, which reduces the gas-liquid-solid system to a two-phase system [158, 292, 294, 298, 301, 302]. This is definitely a gross oversimplification of the three-phase flow since the gas-liquid drag coefficients were used instead of gas-slurry drag coefficients. Therefore, there is a great need to develop pertinent and applicable drag coefficient correlations for modeling SBCRs.



(a)



(b)

Figure 2-12: Comparison of various (a) Liquid-Solid and (b) Gas-Liquid drag correlation

3.0 RESEARCH OBJECTIVE

Modeling of 3-phase Slurry Bubble Column Reactors (SBCRs) requires, among others, detailed description of the hydrodynamics, reaction kinetics and mass as well as heat transfer parameters. Over the past 20 years, our research group has been measuring macroscopic values of these parameters in a pilot-scale (0.3-m ID and 3-m height) hot SBCR, available in our Reactor and process Engineering Laboratory (RAPEL) at the University of Pittsburgh. These data were used as input in 1-D and 2-D steady-state empirical reactor models which were incorporated into a working simulator in our laboratory [301, 328]. These empirical models, however, are incapable of predicting the local hydrodynamic or mass transfer values, flow patterns, radial velocities, species distribution or solid concentration profiles, which makes it difficult to interpret the hydrodynamic behavior and overall performance of SBCRs. Computational Fluid Dynamics (CFD), which could provide such data, have been recently used in modeling SBCRs, as 2-D and 3-D CFD multiphase systems are available in the literature. Many CFD modeling frameworks, however, have not been properly validated since, except for the work by Matos et al. (2009) [301], almost all validations were carried out with data obtained in small-scale reactors for air-water-solid systems at ambient conditions. Therefore, the predictions of the current CFD models cannot offer any proper interpretation of the complex hydrodynamic behavior of large-scale SBCRs operating at high-pressures and high-temperatures, and often provided with cooling internals.

The overall objective of this study is to develop a more comprehensive CFD model in ANSYS for LTFT synthesis in SBCRs. This three-phase model is based on the principles of conservation of mass and momentum in turbulent flow, and includes many complexities, such as gas-liquid-solid contacts, momentum exchange, solid-phase representation, bubble induced turbulence, bubble population balance, and actual reaction kinetics and gas-liquid mass transfer data for F-T synthesis. The CFD model is used to predict the volume fractions, species distribution and velocity profiles for the three phases in space and time. These predictions are validated against actual experimental hydrodynamic data available in the literature and those obtained for F-T synthesis in our pilot-scale SBCR. Upon successful validation, the CFD model is used to thoroughly investigate the effects of the three main spatio-temporal complexities, namely gas sparger design, cooling internals layout, and reaction kinetics, on the hydrodynamic and overall behavior of SBCRs for F-T synthesis.

In order to achieve this objective, the following tasks are proposed:

Task 1: Develop a three-phase CFD model for the slurry bubble column reactor.

Task 2: Validate the CFD model predictions against our experimental data and those available in the literature for multi-phase systems.

Task 3: Use the CFD model to investigate the effects of spargers on the local hydrodynamics in the pilot-scale SBCR:

Task 4: Use the CFD model to predict the effects of internals on the local hydrodynamics in the pilot-scale and a conceptual large-scale SBCRs

Task 5: Incorporate the F-T reaction kinetics into the CFD model and use it to predict the performance as well as the local hydrodynamics in the pilot-scale and a commercial-scale F-T SBCRs.

4.0 CFD MODEL FORMULATION

The 3-D transient model built in the present study is based on the Eulerian multi-fluid approach for the three phases (gas-liquid-solid). The model equations are based on the ensemble averaging of the local instantaneous equations for a single-phase flow [274, 329]. The complete mathematical model is based on an a multi-Eulerian approach and consists of three main components: (i) the core hydrodynamics model consisting of the Navier-Stokes equations; (ii) the multiple-fluid model based on an analog of Boussinesq approximation to represent the natural convection; and (iii) the population balance equations to describe the size distribution of the dispersed gas-phase. A schematic diagram of the model components and their couplings is given in Figure 4-1.

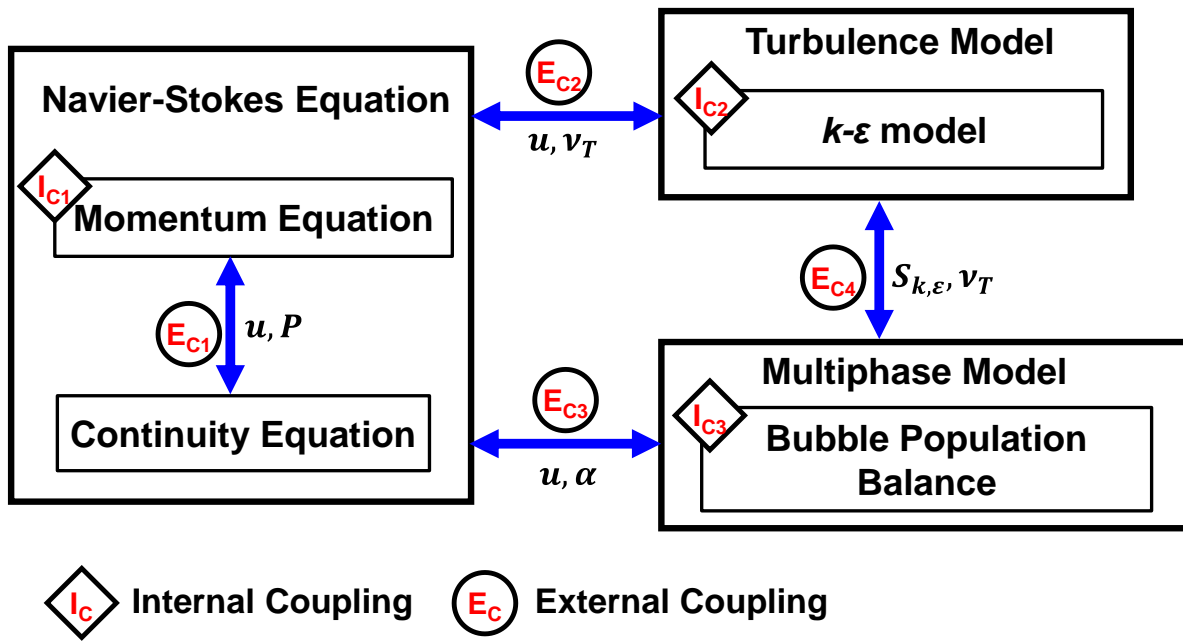


Figure 4-1: Schematic of the model components and their couplings

The mass and momentum conservation equations are:

$$\frac{\partial(\rho_k \alpha_k)}{\partial t} + \nabla(\rho_k \alpha_k \vec{u}_k) = \dot{m}_{kn} \quad (4-1)$$

$$\frac{\partial(\rho_k \alpha_k \vec{u}_k)}{\partial t} + \nabla(\rho_k \alpha_k \vec{u}_k \vec{u}_k) = -\alpha_k \cdot \nabla p_f + \nabla(\alpha_k \vec{\tau}_k) + \alpha_k \rho_k g + \vec{u}_{kn} \dot{m}_{kn} + \vec{M}_k \quad (4-2)$$

Where k indicates the phase (G for gas, L for liquid and S for solid); $\vec{u}_k = (u, v, w)$ is the velocity of phase k ; \dot{m}_{kn} is the mass transfer rate between phases k and n ; \vec{u}_{kn} is the relative velocity between phases k and n ; α is the volume fraction of each phase; \vec{M}_k is the overall interfacial momentum, p_f is the fluid pressure; and τ is the stress tensors.

The stress tensor $\vec{\tau}_k$ is represented as:

$$\vec{\tau}_{k=G,L} = \alpha_k \mu_{k,eff} \left(\nabla \vec{u}_k + (\nabla \vec{u}_k)^T - \frac{2}{3} \vec{I} (\nabla \cdot \vec{u}_k) \right) \quad (4-3)$$

μ_{eff} , is the effective viscosity, which is typically the sum of molecular and turbulent viscosities.

For the liquid-phase, the effective viscosity, which accounts for the three contributions (1) molecular viscosity, $\mu_{L,M}$, (2) shear induced turbulence viscosity, $\mu_{L,T}$ and (3) additional term due to the bubble induced turbulence, $\mu_{L,B}$ is represented as:

$$\mu_{eff} = \mu_{L,M} + \mu_{L,T} + \mu_{L,B}. \quad (4-4)$$

The turbulent viscosity is expressed as:

$$\mu_{L,T} = C_{\mu,B} \rho_L \left(\frac{k^2}{\varepsilon} \right), \quad \text{with } C_{\mu,B} = 0.6 \quad (4-5)$$

For the gas-phase, the effective viscosity is represented as the sum of the molecular viscosity $\mu_{G,M}$ and the turbulence induced viscosity:

$$\mu_{eff} = \mu_{G,M} + \mu_{G,T}. \quad (4-6)$$

Where the turbulence induced viscosity for the gas-phase is represented as:

$$\mu_{G,T} = \frac{\rho_L}{\rho_G} (\mu_{L,T}) \quad (4-7)$$

4.1 SOLID PHASE REPRESENTATION

For the solid-phase, the effect of particle-particle interactions will be accounted for by introducing additional terms to the stress tensor. The kinetic theory of granular flow (KTGF) is used to represent the solids behavior in the system. The stress tensor for the solid-phase is represented as:

$$\tau_S = \alpha_S \mu_S (\nabla \vec{u}_S + (\nabla \vec{u}_S)^T) - P_S \vec{I} + \alpha_S \mu_S \left(\lambda_S - \frac{2}{3} \right) \vec{I} (\nabla \cdot \vec{u}_S) \quad (4-8)$$

λ_S , is the solids bulk viscosity, which describes the resistance of the particle suspension against compression; and is expressed as:

$$\lambda_S = \frac{4}{3} \alpha_S^2 \rho_S d_p g_0 (1 + e_p) \sqrt{\frac{\theta}{\pi}} \quad (4-9)$$

P_S , is the solids pressure, which represents the normal solid-phase forces due to particle-particle interactions; and is expressed as: [330]

$$P_S = \rho_S \alpha_S \theta + 2g_0 \rho_S \alpha_S^2 \theta (1 + e_p) \quad (4-10)$$

The first term in the right-hand-side of the solid pressure equation represents the kinetic contribution, which accounts for the momentum transferred through the system by particles moving across imaginary shear layers in the flow. The second term represents the collisional contribution, which represents the momentum transferred by direct collisions.

e_p , is the restitution coefficient, which represents the ratio of normal relative velocity after and before the collision, and it is taken as 0.9 as proposed by Ding and Gidaspow [331].

g_0 , is the radial distribution function, which accounts for the increase in the probability of collisions when the particle density increases; and is expressed as [171, 331]:

$$g_0 = 0.6 \left[1 - \left(\frac{\alpha_s}{\alpha_{s,max}} \right)^{1/3} \right]^{-1} \quad (4-11)$$

Where $\alpha_{s,max} = 0.62$, and beyond this value, the radial distribution function goes to infinity.

Θ , represents the granular temperature, which is a measure of the kinetic energy contained in the fluctuating velocity for the solid particles and it is defined using the algebraic model by Ding and Gidaspow, [331] which helps minimize the computational load by avoiding to solve an additional differential equation along with its closure models:

$$\Theta = \frac{d_p^2}{30(1 - e_p)} (\nabla u_s + (\nabla u_s)^T) \quad (4-12)$$

μ_s , represents the solids shear viscosity, which is an elastic force, arising from the solid-phase the response to shear, compression and extension stresses exerted on it by the continuous liquid-phase. It should not be confused with the viscous forces, which arise during the fluid flow, as fluid viscosities are proportional to the rate of deformation over time, whereas the solid viscosity is proportional to the amount of shear deformation. The following model by Gidaspow [242] is used to describe the solid-phase viscosity as follows:

$$\mu_s = \frac{4}{5} \alpha_s^2 \rho_s d_p g_0 (1 + e_p) \sqrt{\frac{\Theta}{\pi}} + \frac{2 \frac{5\sqrt{\pi}}{96} \rho_s d_p \sqrt{\Theta}}{g_0 (1 + e_p)} \cdot \left[1 + \frac{4}{5} \alpha_s g_0 (1 + e_p) \right]^2 \quad (4-13)$$

4.2 TURBULENCE MODEL

As the mass and momentum balances are obtained through the ensemble averaging formulations, the terms u_k and u_k' represent the mean and fluctuating components of the velocity, thus the unclosed terms in the stress Equation (4-3) should be modeled. It is decided to use the RNG k - ε turbulence model after a comparison between various k - ε turbulence schemes was conducted [332]. The turbulent kinetic energy (k) and the turbulent energy dissipation (ε) are calculated based on the following governing equations, respectively:

$$\frac{\partial(\rho k)}{\partial t} + \nabla(\rho K \vec{u}) = \nabla(Pr_{eff,k}^{-1} \mu_{eff} \nabla k) + G_k + G_b - \rho \varepsilon - Y_M + S_k \quad (4-14)$$

$$\frac{\partial(\rho \varepsilon)}{\partial t} + \nabla(\rho \varepsilon \vec{u}) = \nabla(Pr_{eff,\varepsilon}^{-1} \mu_{eff} \nabla \varepsilon) + C_{\varepsilon 1} \frac{\varepsilon}{k} (G_k + C_{\varepsilon 3} G_b) - C_{\varepsilon 2} \rho \frac{\varepsilon^2}{k} - R_\varepsilon + S_\varepsilon \quad (4-15)$$

Where G_k represents the generation of turbulence kinetic energy due to the mean velocity gradients; G_b is the generation of turbulence kinetic energy due to buoyancy; Y_M is the contribution of the fluctuating dilation in compressible turbulence to the overall dissipation rate; $C_{\varepsilon 1}$, $C_{\varepsilon 2}$, $C_{\varepsilon 3}$ are constants set as 1.44, 1.92 and 0.09, respectively. $Pr_{eff,k}^{-1}$ and $Pr_{eff,\varepsilon}^{-1}$ are the inverse effective Prandtl numbers for K and ε , respectively derived analytically using the RNG theory. In addition, S_k and S_ε are user-defined source term. The equations used to calculate some of the above parameters are:

$$G_k = \mu_t \left(\frac{\partial \vec{U}_i}{\partial x_j} + \frac{\partial \vec{U}_j}{\partial x_i} \right) \frac{\partial \vec{U}_i}{\partial x_j} - \frac{2}{3} \frac{\partial \vec{U}_k}{\partial x_k} \left(3\mu_t \left(\frac{\partial \vec{U}_k}{\partial x_k} \right) + \rho k \right) \quad (4-16)$$

$$G_b = \begin{cases} \frac{\mu_t}{\rho \sigma_p} g_i \frac{\partial p}{\partial x_i} & \text{full bouyancy model} \\ \frac{\mu_t}{\rho \sigma_p} \rho \beta g_i \frac{\partial T}{\partial x_i} & \text{Boussinesq bouyance model} \end{cases} \quad (4-17)$$

$$\left| \frac{Pr_{eff}^{-1} - 1.3929}{\alpha_0 - 1.3929} \right|^{0.6321} \cdot \left| \frac{Pr_{eff}^{-1} + 2.3929}{\alpha_0 + 2.3929} \right|^{0.3679} = \frac{\mu_{mol}}{\mu_{eff}}, \quad \alpha_0 = 1 \quad (4-18)$$

Where $\alpha_0 = 1$, (μ_{mol}) is the molecular viscosity. In the high Reynolds number limit where $\left(\frac{\mu_{mol}}{\mu_{eff}} \ll 1\right)$, and $Pr_{eff,\varepsilon}^{-1} = Pr_{eff,k}^{-1} \approx 1.393$ [333].

4.3 MOMENTUM EXCHANGE TERMS AND INTERPHASE COEFFICIENT CORRELATIONS

The momentum exchange term in the momentum balance Equation (4-2), which describes the interface forces between the phases has been described as follows:

$$\vec{M}_k = \vec{M}_D + \vec{M}_L + \vec{M}_{VM} + \vec{M}_W + \vec{M}_{TD} \quad (4-19)$$

The right hand terms of Equation (4-19) represent the interphase drag, lift, virtual mass, wall force, and turbulence dispersion, respectively. A brief description of each of the momentum (force per unit volume), in addition to the expression used to describe them in this model is presented in Table 4-1. The terms for the various coefficients used in these terms are presented in Table 4-2.

Table 4-1: Momentum interphase terms used in our model

Force Term	Equation used in model	Reference
Drag	$\vec{M}_{D,G} = \vec{M}_{D,G-L} + \vec{M}_{D,G-S}, \quad \vec{M}_{D,L} = \vec{M}_{D,L-G} + \vec{M}_{D,L-S},$ $\vec{M}_{D,S} = \vec{M}_{D,S-G} + \vec{M}_{D,S-L}$ $G - L: \vec{M}_{D,G-L} = \frac{3}{4} \frac{C_{D,G-L}}{d_b} \alpha_G \alpha_L \rho_L \vec{u}_G - \vec{u}_L (\vec{u}_G - \vec{u}_L)$ $S - L: \vec{M}_{D,G-L} = \frac{3}{4} \frac{C_{D,S-L}}{d_p} \alpha_S \alpha_L \rho_L \vec{u}_S - \vec{u}_L (\vec{u}_S - \vec{u}_L)$ $S - G: \vec{M}_{D,G-S} = \frac{3}{4} \frac{C_{D,S-G}}{d_p} \alpha_S \rho_G \vec{u}_S - \vec{u}_G (\vec{u}_S - \vec{u}_G)$	Clift et al. [171] Schallenberg et al. [299]
Lift	$\vec{M}_{L,L} = \alpha_G \rho_L C_L (\vec{u}_G - \vec{u}_L) \times (\nabla \times \vec{u}_L)$	Drew et al. [334, 335]
Virtual Mass.	$\vec{M}_{VM} = \alpha_G \rho_L C_{VM} \left(\frac{D\vec{u}_G}{Dt} - \frac{D\vec{u}_L}{Dt} \right), \quad C_{VM} = 0.5$	Auton et al. [336]
Lateral	$\vec{M}_W = \begin{cases} \frac{\alpha_G \rho_L (\vec{u}_G - \vec{u}_L)}{D_S} \max \left(0, C_{w1} + C_{w2} \frac{D_S}{y_w} \right) n_w & y_w < \left(\frac{C_{w2}}{C_{w1}} \right) D_S \\ 0 & y_w > \left(\frac{C_{w2}}{C_{w1}} \right) D_S \end{cases}$ <p>y_w: distance from wall, n_w = vector normal to wall, $C_{w1} = -0.0064, C_{w2} = 0.0166$</p>	Antal et al. [337] Krepper et al. [338]
Turbulence dispersion	$M_{TD} = C_{TD} \rho_L k \nabla \alpha_G$ $C_{TD} = 0.2$	Bertodano [339] Burns et al. [340]

Table 4-2: Interphase coefficient expressions used in our model

Term	Model	Reference
Gas-Liquid Drag	$C_{D,G-L} = \begin{cases} \left(\frac{24}{Re_b}\right)(1 + 0.1Re_b^{0.75}) & N_\mu < 36\sqrt{2} \frac{(1 + 0.1Re_b^{0.75})}{Re_b^2} \\ \frac{2}{3}\sqrt{E\ddot{o}_b} & N_\mu \geq 36\sqrt{2} \frac{(1 + 0.1Re_b^{0.75})}{Re_b^2} \end{cases}$	Ishii and Zuber [319]
Gas-Solid Drag	$C_{D,G-S} = \begin{cases} \left(\frac{24}{Re_p}\right)(1 + 0.15Re_p^{0.687}) & Re_p < 1000 \\ 0.44 & Re_p \geq 1000 \end{cases}$	Schiller and Naumann [6]
Liquid-Solid Drag	$C_{D,L-S} = \alpha_s^{-1.65} \max\left(\frac{24}{\alpha_s Re_{S-L}}(1 + 0.15(\alpha_s Re_{S-L})^{0.687}), 0.44\right),$ $Re_{S-L} = \frac{\rho_L u_S - u_L d_p}{\mu_L}$	Wen and Yu [5]
Liquid-Gas Lift	$C_{L,L-G} = \begin{cases} \min[0.288 \tanh(0.12Re), f(E\ddot{o}_d)] & E\ddot{o}_d < 4 \\ f(E\ddot{o}_d) = 0.00105E\ddot{o}^3 - 0.0159E\ddot{o}_d^2 - 0.0204E\ddot{o}_d + 0.474 & 4 \leq E\ddot{o}_d \leq 10 \\ -0.29 & E\ddot{o}_d > 10 \end{cases}$ $E\ddot{o} = \frac{g\Delta\rho d_B^2}{\sigma}, \quad E\ddot{o}_d = E\ddot{o}(1 + 0.163E\ddot{o}^{0.757})^{2/3}$	Tomiyama [7]

4.4 BUBBLES REPRESENTATION

In a three-phase fluidized system, bubble size variation is intimately related to bubble-particle collisions. The collisions can yield two different consequences: the particle is ejected from the bubble surface, or the particle penetrates the bubble leading to either bubble breakage or non-breakage. Bubble-particle collisions generate perturbations on the bubble surface. After the bubble-particle collision, three factors become crucial in determining the coalescence and breakage characteristics of the bubble [171]: (1) shear stress, which depends on the liquid velocity gradient and the relative bubble-particle impact speed, and tends to break the bubble; (2) surface

tension force, which tends to stabilize the bubble and drive it to recover its original shape; and (3) viscous force, which slows the growth rate of the surface perturbation, and tends to stabilize the bubble. Accordingly, bubble coalescence and breakage models are classified into four main categories [341]: (1) turbulent fluctuation and collision; (2) viscous shear stress; (3) shearing-off process; and (4) interfacial stability. The bubbles induced turbulence and bubble population balance are discussed below.

4.4.1 Bubble Induced Turbulence

The bubble induced turbulence is represented by introducing two source terms, S_k and S_ε , into the k - ε equation as [310, 342]:

$$S_k = \left(\frac{\rho_G}{\rho_G + C_{VM}\rho_G} \right) \alpha_G \left(\frac{3 C_D}{4 d_B} \right) |\vec{u}_G - \vec{u}_L| (q_{LG} - 2k_L + \vec{u}_d \cdot \vec{u}_r); \quad S_\varepsilon = C_{\varepsilon 3} \frac{\varepsilon}{k} S_k \quad (4-20)$$

Where q_{LG} is the covariance of the liquid-phase and the dispersed gas-phase velocities; u_r and u_d are the relative and drift velocities, respectively; and $C_{\varepsilon 3} = 1.2$.

This model is rigorously derived by writing the equation of motion for a single bubble and rearranging it in terms of the fluid velocity, where the drag and mass coefficients (C_D and C_{VM}) appear in the formulation. The equations for the relative and drift velocities are:

$$\vec{u}_r = [\vec{u}_G - \vec{u}_L] - \vec{u}_d, \quad \vec{u}_d = -\vec{D}_{12}^t \left[\frac{\Delta\alpha_2}{\alpha_2} - \frac{\Delta\alpha_1}{\alpha_1} \right] \quad (4-21)$$

The drift velocity (\vec{u}_d) is a statistical quantity due to the conditional averaging; and may not be negligible as it accounts for the dispersion effects due to the bubbles transport by the turbulent fluid motion. \vec{D}_{12}^t is the fluid-bubble dispersion tensor, which is expressed in terms of the fluid bubble velocity covariance [q_{LG}] and the fluid-bubble turbulent interaction time scale [τ_{12}^t]. For

the purpose of practical computations [212], the dispersion tensor is simplified to its diagonal form [273, 310, 343, 344] as:

$$\vec{D}_{12}^t = \frac{1}{3} \vec{\tau}_{12}^t q_{LG} \cdot I, \quad \text{Where } I \text{ is a } 3 \times 3 \text{ identity matrix} \quad (4-22)$$

4.4.2 Bubble Population Balance

It is necessary to take into account bubble breakup and coalescence phenomena in the CFD model when a bubble column or a slurry bubble column operates in the heterogeneous flow regime. The usual approach is to use population balance models, which describe the variation in a given population property over the space and time within a velocity field. Therefore, a population balance model is used to represent the bubble size distribution. Assuming that each bubble class travels at the same mean algebraic velocity, the individual number density of a bubble class i can be expressed as [345]:

$$\frac{\partial n_i}{\partial t} + \nabla(u_G n_i) = \left(\sum_J R_J \right)_i = B_C + B_B - D_C - D_B \quad (4-23)$$

Where $(\sum_J R_J)_i$ represents the net change in the number density distribution due to the coalescence and breakup of bubbles; and $B_C, B_B,$ and $D_C, D_B,$ represent the birth and death rates, respectively due to coalescence and breakup.

The model proposed by Lou and Svendsen [346] for the breakup rate of bubbles is used in this work. Their model was developed based on the assumption of bubble binary breakup (each bubble breaks up into two distinctly smaller bubbles) under isotropic turbulence. The ‘daughter’ bubble sizes were accounted for using a dimensionless variable (f_{BV}):

$$f_{BV} = \frac{v_I}{v} = \frac{d_I^3}{d} = \frac{d_I^3}{d_I^3 + d_{II}^3} \quad (4-24)$$

Where v_I , d_I and d_{II} , represent the volumes and diameters of the daughter bubbles in the binary breakage of a parent bubble of diameter d and volume v . The breakup rate of the bubbles can be represented as:

$$\Omega_B(v: v f_{BV}) = 0.923(1 - \alpha_G)n \left(\frac{\varepsilon}{d^2}\right)^{1/3} \int_{\xi_{min}}^1 \frac{(1 + \xi)^2}{\xi^{11/3}} \exp\left(-\frac{12c_f\sigma}{\beta\rho_L\varepsilon^{2/3}d^{5/3}\xi^{11/3}}\right) d\xi \quad (4-25)$$

Where $\xi_{min} = \lambda_{min}/d$ and $\xi = \lambda/d$, representing the size ratio between an eddy and a bubble in the inertial subrange, and β is a constant derived from fundamental consideration and it equals 2. Subsequently, the birth and death rates due to breakup are represented as:

$$B_B = \sum \Omega_B(v_j: v_i) n_i, \quad (4-26)$$

$$D_B = \Omega_i n_i \text{ where } \Omega_i = \sum_{m=1}^N \Omega_{mi} \quad (4-27)$$

On the other hand, bubble coalescence occurring due to bubble collision is caused by three major phenomena (1) wake entrainment, (2) buoyancy and (3) random turbulence. Wake entrainment has been widely accepted to be negligible [347] and the effect of buoyancy is eliminated as all bubbles of the same class have been assumed to travel at the same mean velocity. Therefore, the only remaining driving force is that of the random turbulence. The coalescence rate due to random turbulent collision is adopted from Prince and Blanch as given below [348]:

$$\chi_{ij} = \frac{\pi}{4} [d_i + d_j]^2 (u_{Ti}^2 + u_{Tj}^2)^{0.5} \exp\left(-\frac{t_{ij}}{\tau_{ij}}\right) \quad (4-28)$$

u_T , is the turbulent velocity in the inertial subrange of isotropic turbulence and can be estimated as: [349]

$$u_T = \frac{r_{ij}^{2/3}}{\varepsilon^{1/3}} \quad (4-29)$$

τ_{ij} , is the contact time between two colliding bubbles:

$$\tau_{ij} = \frac{r_{ij}^{2/3}}{\varepsilon^{1/3}} \quad (4-30)$$

t_{ij} , is the time for two bubbles with radii r_i and r_j to coalesce:

$$t_{ij} = \left(\frac{r_{ij}^3 \rho_l}{16\sigma} \right)^{0.5} \ln \left(\frac{h_0}{h_f} \right) \quad (4-31)$$

Where h_0 and h_f represent the initial bubble film thickness and the critical film thickness were reported to be 10^{-4} and 10^{-8} m, respectively.

r_{ij} , is the equivalent radius:

$$r_{ij} = \frac{2r_i r_j}{(r_i + r_j)} \quad (4-32)$$

Subsequently, the number density for individual bubble groups governed by birth and death due coalescence can be expressed as:

$$B_C = \frac{1}{2} \sum_{k=1}^i \sum_{j=1}^i \eta_{jki} \chi_{ij} n_i n_j \quad (4-33)$$

$$\text{Where } \eta_{jki} = \begin{cases} (v_j + v_k) - v_{i-1} / (v_i - v_{i-1}) & \text{if } v_{i-1} < v_j + v_k < v_i \\ v_{i+1} - (v_j + v_k) / (v_{i+1} - v_i) & \text{if } v_i < v_j + v_k < v_{i+1} \\ 0 & \text{if } \text{neither} \end{cases}$$

$$D_C = \sum_{m=1}^N \chi_{ij} n_i n_j \quad (4-34)$$

It is important to note that this model will be developed for a SBCR operating under typical pressures and temperatures of F-T synthesis; and it is possible that other correlations/parameters would provide a better fit for different circumstances and scenarios.

4.5 KINETICS AND MASS TRANSFER

The interphase mass-transfer rate depends on the mass-transfer coefficient, the interfacial area concentration, and the rate of chemical reaction. The mass-transfer coefficient is a function of the local hydrodynamics, which are influenced on one hand by the bubble shrinkage due to physical or chemical absorption and on the other hand by the change of the physical properties due to the heterogeneous distributions of the chemical species.

In calculating the gas-liquid mass transfer in the transient CFD simulation, it is not possible to obtain the mass transfer coefficients from the hydrodynamic data generated using our multi-Eulerian simulation. This is primarily due to the limitations at the interface in the jump boundary conditions from the gas to liquid, which ideally require empirical mass transfer data or correlations to be incorporated in the CFD model.

Using CFD to model mass transfer and interfacial phenomena from the first principles is feasible at a very small scale, such a single droplet, using a Lagrangian or a Volume of Fluid (VOF) scheme. However, it should be noted that Gidaspow et al. [242, 331] used the granular temperature approach to derive the mass transfer coefficients in multiphase systems. Nonetheless, this would not be possible for our large-scale SBCR. Actually, attempting multi-fluid Eulerian to perform multiphase-multicomponent mass transfer would result in numerically unstable sources and sinks.

Therefore, the species mass transfer rate from the dispersed-phase to the continuous-phase per unit volume, which appeared in Equations (4-1) and (4-2) above, is defined as:

$$\dot{m}_{kn} = k_L a \cdot (C^* - C_L) \quad (4-35)$$

Where $k_L a$ is the volumetric liquid-side mass transfer coefficient, which was represented using an empirical correlation developed using numerous experimental data for different three-phase F-T systems obtained under elevated pressures and temperatures in our pilot-scale SBCR [350]:

$$k_L a = 7.99 \times 10^{-9} \frac{\rho_L^{1.82} \rho_G^{0.27} u_G^{0.387} \Gamma^{0.173}}{\mu_L^{0.25} \sigma_L^{0.976} M_w^{0.02}} \left(\frac{P}{P - P_V} \right)^{0.242} \left(\frac{d_c}{d_c + 0.3} \right)^{0.1} \quad (4-36)$$

$$\times \exp[-1.3C_p + 0.8C_p^2 - C_p^3 - 1675.7d_p + 0.176X_w]$$

The multi-formulation described above was implemented into the commercial CFD code, ANSYS Fluent v14.5, where the governing equations were solved using a multiphase-Eulerian segregated solver algorithm.

When accounting for chemical reactions, an additional species conservation equation has to be considered as follows:

$$\frac{\partial(\rho_k \alpha_k y_k^i)}{\partial t} + \nabla(\rho_k \alpha_k u_k y_k^i) = \nabla(\alpha_k \rho_k D_k^i \nabla y_k^i) + r_k^i - r_{kn}^{ij} \quad (4-37)$$

Where y_k^i represents the mass fraction of species i in phase k , whereas r_k^i and r_{kn}^{ij} represent the F-T reaction kinetics rate and the rate of chemical absorption.

4.6 SOLUTION METHOD AND BOUNDARY CONDITIONS

The multi-formulation described above was implemented into ANSYS Fluent v 14.5, where the governing equations are solved using an Eulerian multiphase segregated solver algorithm. The 3-D time-dependent simulations are conducted, both due to the nature of the geometry investigated and the bubble plume oscillations, which are characteristic of the churn-turbulent flow regime [351]. The RNG k - ε turbulence model is used, as it provides the best validation results as previously demonstrated elsewhere [332]. At the bottom of the column, Dirichlet velocity and volume fraction conditions for all phases are set, and a second order spatially accurate QUICK scheme [352-354] is employed to discretize all equations.

$$u_k(z = 0, t) = \beta, \text{ where } \beta \text{ is a constant} \quad (4-38)$$

Moreover, a multiphase variant of the SIMPLE scheme is used for pressure-velocity coupling [355]. The first order implicit time stepping is then used to advance the solution in time. Before each simulation, mesh and time independence studies are carried out in order to optimize the solution and computational time. In all simulations quasi-steady state numerical solutions are obtained. This means that at the end of the calculations, all variables exhibit small oscillations around steady-state values, indicating that the statistical averages were reached for all variables.

Additionally, outlet boundary conditions are implemented taking into account the following [301, 316]: (1) F-T SBCR reactors are typically operated in semi-batch mode where the liquid level may reach the top of the reactor [209]; and (2) Due to the F-T reaction, the liquid (mainly hydrocarbon products) formed inside the reactor is continuously removed using appropriate filtration devices within the reactor. Therefore, the following outlet boundary conditions are executed to account for the two aforementioned considerations:

1. The real computation domain is selected to be taller than the initial height of the reactor, similar to the work by Troshko and Zdravistch [316].
2. The initial liquid height is set by initializing the liquid volume fraction to 1 in the zone up to a known initial liquid height, while the gas volume fraction will be set to 1 in the region above that.
3. The ambient media in the computational zone above the reactor is set to be stagnant CO, such that the values for the pressure, backflow gas volume fraction, backflow CO gas species concentration and backflow turbulent parameters, are 1 atmosphere, 1, 1, and 0, respectively [316].

The implementation of these outlet boundary conditions allows for modeling of the slurry-phase height expansion due to the gas holdup and heterogeneous reactions without being affected by the gas-phase backflow. Moreover, due to the strong non-linear characteristics of the model, relaxation coefficients (Patankar [356]) are introduced in the momentum conservation equations. The convergence criterion adopted from Patankar [356], based on the pressure, is given by:

$$\left| \sum_{j=2}^N \sum_{i=2}^N P_{ij}^{(n+1)} - \sum_{j=2}^N \sum_{i=2}^N P_{ij}^{(n)} \right| < 10^{-9} \quad \text{Where } N \text{ is the mesh size} \quad (4-39)$$

5.0 CFD MODEL VALIDATION

The CFD model proposed above was implemented into ANSYS Workbench v. 13.0 and 14.5 and was systematically validated as follows:

5.1 TESTING OF CFD MODEL USING AQUEOUS AIR-WATER-GLASS BEADS

DATA BY YU AND KIM [3]

The CFD model was initially tested against the radial gas holdup data by Yu and Kim [3] obtained for an air-water-glass beads system in a 0.254 m ID and 2.5 m height column using various superficial gas velocities under ambient conditions. More details of their study are given in Table 5-1.

Table 5-1: Experimental conditions by Yu and Kim [3] used for selecting of our CFD model parameters

Reactor Diameter	0.254 m
Reactor Length	2.5 m
Liquid Velocity	0.06 m/s
System	Air-Water-Glass Beads
Particle Diameter	2.3 mm
Solid Concentration	9.47%
Solid Density	2500 kg/m ³
Gas Velocity	0.01; 0.06; 0.14 m/s

The aim of this study was to select the gas-liquid and liquid-solid drag models and the most accurate and effective turbulence model to be used in the CFD model in order to predict the experimental data with high accuracy. Three gas-liquid drag models by (1) Wen and Yu [3], (2) Haider and Levenspiel [357] and (3) Gidaspow [242], listed in Table A-16 (Appendix A), along with two liquid-solid drag models by (1) Schallenberg et al. [299] and (2) Schiller-Naumann [6], also listed in Table A-17 (Appendix A) were investigated. Three turbulence models, (1) Standard k - ϵ , (2) Realizable k - ϵ and (3) RNG k - ϵ summarized in Table 5-2 were also investigated. For each turbulence model, six combinations of the gas-liquid and liquid-solid drag models were used and the CFD model predictions were performed at three different superficial gas velocities of 0.01, 0.06 and 0.14 m/s. The comparisons between experimental and predicted data using the CFD model are illustrated in Figure 5-1 and the absolute average relative errors (AARE) are presented in Table 5-3 for the three superficial gas velocities. From these figures and tables, the following observations can be made:

1. For all gas-liquid and liquid-solid drag model combinations, the Realizable k - ϵ turbulence model gives the worst predictions (highest AARE), which is in agreement with previous studies [292, 302];
2. The RNG k - ϵ turbulence model, coupled with the gas-liquid drag model by Wen-Yu [5] and the liquid-solid drag model by Schiller Naumann [6], gives the most accurate predictions of the experimental data (the lowest AARE); and
3. The accuracy of our CFD model predictions using the RNG k - ϵ turbulence model, at 0.01 and 0.06 m/s superficial gas velocities was not satisfactory, since their corresponding AARE values varied from 17.5% to 35.1% and from 9.6% to 28.7%, respectively. This behavior was expected since under such low velocities in an aqueous system, the bubbly flow regime prevails

in the SBCR. At the superficial gas velocity of 0.14 m/s, however, the churn turbulent flow regime prevails and our CFD model predictions were in good agreement with the experimental data where the AARE using the RNG k-ε turbulence varied between 4.9 and 8.2%.

Table 5-2: Model equations for the three k-ε turbulence models used

Standard k-ε
$\frac{\partial(\rho k)}{\partial t} + \frac{\partial}{\partial x_j}(\rho k U_j) = \frac{\partial}{\partial x_j} \left[\left(\mu + \frac{\mu_t}{\sigma_k} \right) \frac{\partial k}{\partial x_j} \right] + G_k + G_b - \rho \varepsilon - Y_M + S_k$ $\frac{\partial(\rho \varepsilon)}{\partial t} + \frac{\partial}{\partial x_j}(\rho \varepsilon U_j) = \frac{\partial}{\partial x_j} \left[\left(\mu + \frac{\mu_t}{\sigma_\varepsilon} \right) \frac{\partial \varepsilon}{\partial x_j} \right] + C_{1\varepsilon} \frac{\varepsilon}{k} (G_k + C_{3\varepsilon} G_b) - C_{2\varepsilon} \rho \frac{\varepsilon^2}{k} + S_\varepsilon$ $C_{1\varepsilon} = 1.44, C_{2\varepsilon} = 1.92, C_{3\varepsilon} = 0.09, \sigma_k = 1 \text{ and } \sigma_\varepsilon = 1.3.$ $G_k = \mu_t \left(\frac{\partial U_i}{\partial x_j} + \frac{\partial U_j}{\partial x_i} \right) \frac{\partial U_i}{\partial x_j} - \frac{2}{3} \frac{\partial U_k}{\partial x_k} \left(3\mu_t \frac{\partial U_k}{\partial x_k} + \rho k \right); G_b = \begin{cases} \frac{\mu_t}{\rho \sigma_p} g_i \frac{\partial p}{\partial x_i} & \text{full bouyancy model} \\ \frac{\mu_t}{\rho \sigma_p} \rho \beta g_i \frac{\partial T}{\partial x_i} & \text{Boussinesq bouyance model} \end{cases}$ $\mu_t = C_\mu \rho \frac{k^2}{\varepsilon}; C_\mu = 0.09 \text{ [358]}$
Realizable k-ε
$\frac{\partial(\rho k)}{\partial t} + \frac{\partial}{\partial x_j}(\rho k U_j) = \frac{\partial}{\partial x_j} \left[\left(\mu + \frac{\mu_t}{\sigma_k} \right) \frac{\partial k}{\partial x_j} \right] + G_k + G_b - \rho \varepsilon - Y_M + S_k$ $\frac{\partial(\rho \varepsilon)}{\partial t} + \frac{\partial}{\partial x_j}(\rho \varepsilon U_j) = \frac{\partial}{\partial x_j} \left[\left(\mu + \frac{\mu_t}{\sigma_\varepsilon} \right) \frac{\partial \varepsilon}{\partial x_j} \right] + \rho C_1 S_\varepsilon - \rho C_2 \frac{\varepsilon^2}{k + \sqrt{\nu \varepsilon}} + C_{1\varepsilon} \frac{\varepsilon}{k} C_{3\varepsilon} G_b + S_\varepsilon$ $C_1 = \max \left[0.43, \frac{\eta}{\eta + 5} \right], \eta = S \frac{k}{\varepsilon}, S = \sqrt{2S_{ij}S_{ij}}$
RNG k-ε
$\frac{\partial(\rho k)}{\partial t} + \frac{\partial}{\partial x_j}(\rho k U_j) = \frac{\partial}{\partial x_j} \left[\alpha_k \mu_{eff} \frac{\partial k}{\partial x_j} \right] + G_k + G_b - \rho \varepsilon - Y_M + S_k$ $\frac{\partial(\rho \varepsilon)}{\partial t} + \frac{\partial}{\partial x_j}(\rho \varepsilon U_j) = \frac{\partial}{\partial x_j} \left[\alpha_\varepsilon \mu_{eff} \frac{\partial \varepsilon}{\partial x_j} \right] + C_{1\varepsilon} \frac{\varepsilon}{k} (G_k + C_{3\varepsilon} G_b) - \left(C_{2\varepsilon} + \frac{C_\mu \eta^3 (1 - \eta/\eta_0)}{1 + \beta \eta^3} \right) \rho \frac{\varepsilon^2}{k} + S_\varepsilon$ $C_{1\varepsilon} = 1.42, C_{2\varepsilon} = 1.68.$ $\left \frac{\alpha - 1.3929}{\alpha_0 - 1.3929} \right ^{0.6321} \left \frac{\alpha + 2.3929}{\alpha_0 + 2.3929} \right ^{0.3679} = \frac{\mu_{mol}}{\mu_{eff}}$ $\alpha_0 = 1, \text{ except in the high Reynolds number limit i.e } \frac{\mu_{mol}}{\mu_{eff}} \ll 1, \alpha_k = \alpha_\varepsilon \approx 1.393$ $d \left(\frac{\rho^2 k}{\sqrt{\varepsilon} \mu} \right) = 1.72 \frac{\left(\frac{\mu_{eff}}{\mu} \right)}{\sqrt{\left(\frac{\mu_{eff}}{\mu} \right)^3 - 1 + C_v}} d \left(\frac{\mu_{eff}}{\mu} \right); C_v \approx 100; R_\varepsilon = \frac{C_\mu \rho \eta^3 (1 - \eta/\eta_0) \varepsilon^2}{1 + \beta \eta^3 k}; \eta_0 = 4.38, \beta = 0.012$ $\mu_t = C_\mu \rho \frac{k^2}{\varepsilon}; C_\mu = 0.0845$

Table 5-3: Absolute average relative errors (AARE) for different turbulence and drag G-L and L-S models against experimental data by Yu and Kim [3]

u_g (m/s)	Gas-Liquid/Liquid-Solid Drag models	AARE (%)		
		RNG k - ϵ	Realizable k - ϵ	Standard k - ϵ
0.01	Wen-Yu [5] /Schallenberg et al. [299]	30.83	56.94	25.71
	Haider-Levenspiel [357]/ Schallenberg et al. [299]	27.28	57.98	17.14
	Gidaspow [242]/ Schallenberg et al. [299]	35.08	61.11	36.27
	Wen-Yu [5] /Schiller Naumann [6]	30.69	62.15	17.38
	Haider-Levenspiel [357]/ Schiller Naumann [6]	17.51	59.02	12.70
	Gidaspow [242]/ Schiller Naumann [6]	24.01	60.07	17.03
0.06	Wen-Yu [5] /Schallenberg et al. [299]	11.63	63.20	13.27
	Haider-Levenspiel [357]/ Schallenberg et al. [299]	28.73	64.24	15.19
	Gidaspow [242]/ Schallenberg et al. [299]	10.54	53.81	9.56
	Wen-Yu [5] /Schiller Naumann [6]	9.61	54.85	13.07
	Haider-Levenspiel [357]/ Schiller Naumann [6]	12.80	55.90	25.44
	Gidaspow [242]/ Schiller Naumann [6]	18.29	51.20	18.38
0.14	Wen-Yu [5] /Schallenberg et al. [299]	6.7	27.7	14.2
	Haider-Levenspiel [357]/ Schallenberg et al. [299]	8.2	29.4	10.4
	Gidaspow [242]/ Schallenberg et al. [299]	7.1	28.7	11.6
	Wen-Yu [5] /Schiller Naumann [6]	4.9	30.1	8.0
	Haider-Levenspiel [357]/ Schiller Naumann [6]	5.9	31.6	13.0
	Gidaspow [242]/ Schiller Naumann [6]	5.6	33.5	8.8

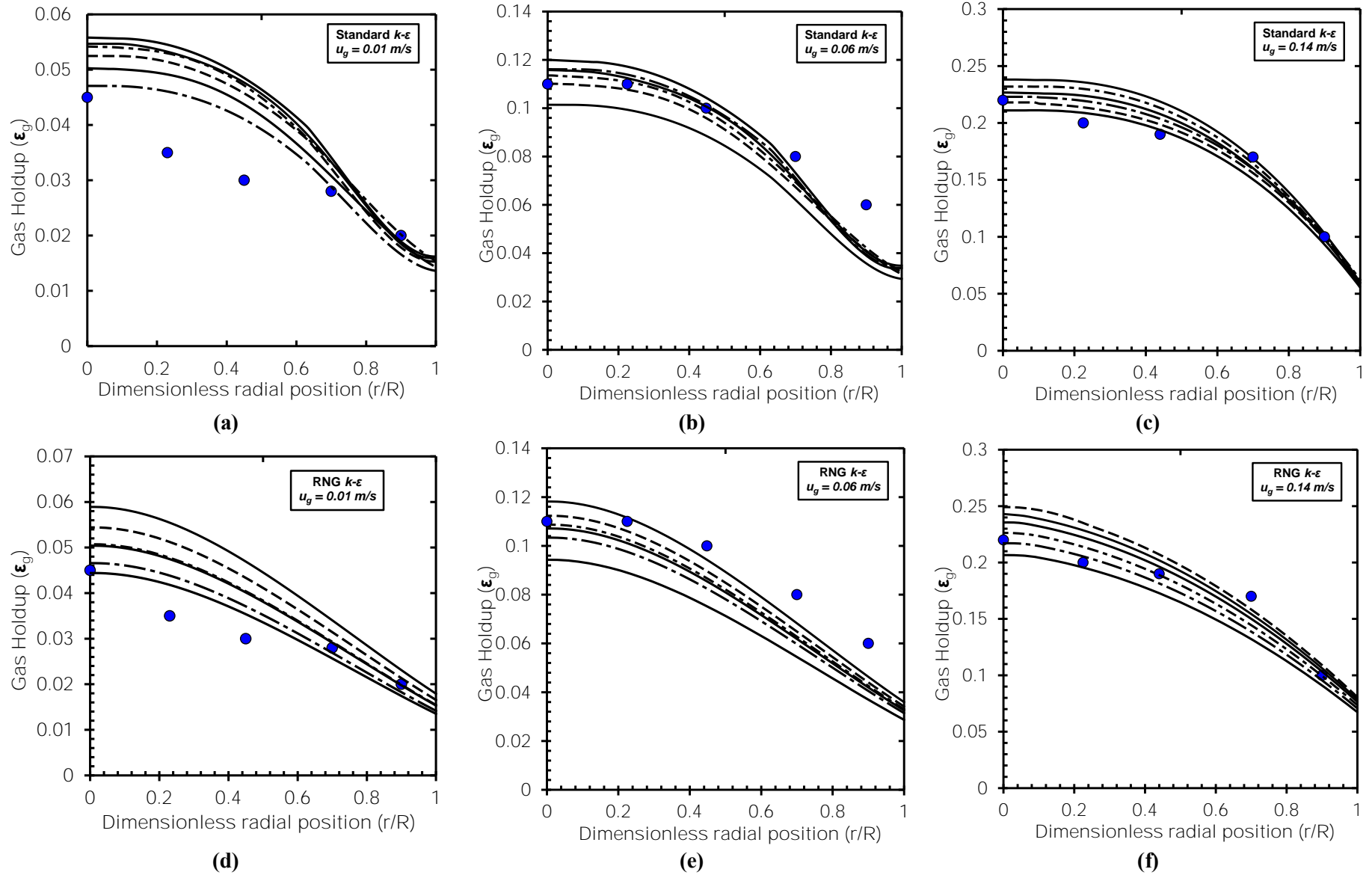


Figure 5-1: Evaluation of various G-L and L-S drag model combinations using the standard $k-\epsilon$ ((a) to (c)) and the RNG $k-\epsilon$ ((d) to (f)) turbulence models against experimental data by Yu and Kim [3]

5.2 VALIDATION OF OUR CFD MODEL USING ORGANIC N₂-DRAKEOL-GLASS BEADS DATA BY CHEN ET AL. [4]

Our CFD model was subsequently validated against the experimental data by Chen et al. [4] for an organic system, N₂-Drakeol-Glass beads as detailed in Table 5-4. The experimental data were conducted inside a bubble column reactor of 0.44 m ID and 2.44 m height. Inside this bubble column, 1-inch pipe internals are arranged in two concentric rings as shown in Figure 5-2 (a). This geometry is reconstructed in ANSYS Fluent as displayed in Figure 5-2 (b). It should be noted that the mesh size shown is very refined as the simulation was conducted at small mesh size to investigate the mesh dependency. This work was one of the first CFD simulation with internals.

The aim of the validation was to test the viability of our CFD model when using organic liquids and to check its ability in handling reactor internals. Three simulations were performed using our CFD model with the RNG k - ϵ turbulence model, coupled with the gas-liquid drag model by Wen-Yu [5] and the liquid-solid drag model by Schiller Naumann [6], at inlet superficial gas velocities of 0.02, 0.05 and 0.1 m/s. Since the sparger has not yet been configured in our CFD model, the inlet boundary conditions were set at 70% of the total cross-sectional area at the bottom of the column similar to that used by Silva et al. [302]. The CFD modeling was conducted for 60 seconds with time steps of 0.01 s in order to investigate the effect of internals as shown in Table 5-5 and Figure 5-3; and as can be seen our CFD model is able to predict the radial gas holdup with an absolute average relative error between 4.45% and 15%. Although the real computation time for this simulation was relatively long, requiring around 220 hours for completion, no computational difficulties or divergences were exhibited, which provided confidence in using our CFD model for investigating different internal configurations.

Table 5-4: Experimental details by Chen et al. [4]

Reactor diameter	0.44 m
Reactor length	2.44 m
Liquid velocity	0 m/s
System	Air-Drakeol-glass beads
Internals fraction of the reactor cross-sectional area	5.33%
Pipe diameter	0.0254 m
Number of internal pipes	16
Gas velocity	0.02; 0.05; 0.1 m/s

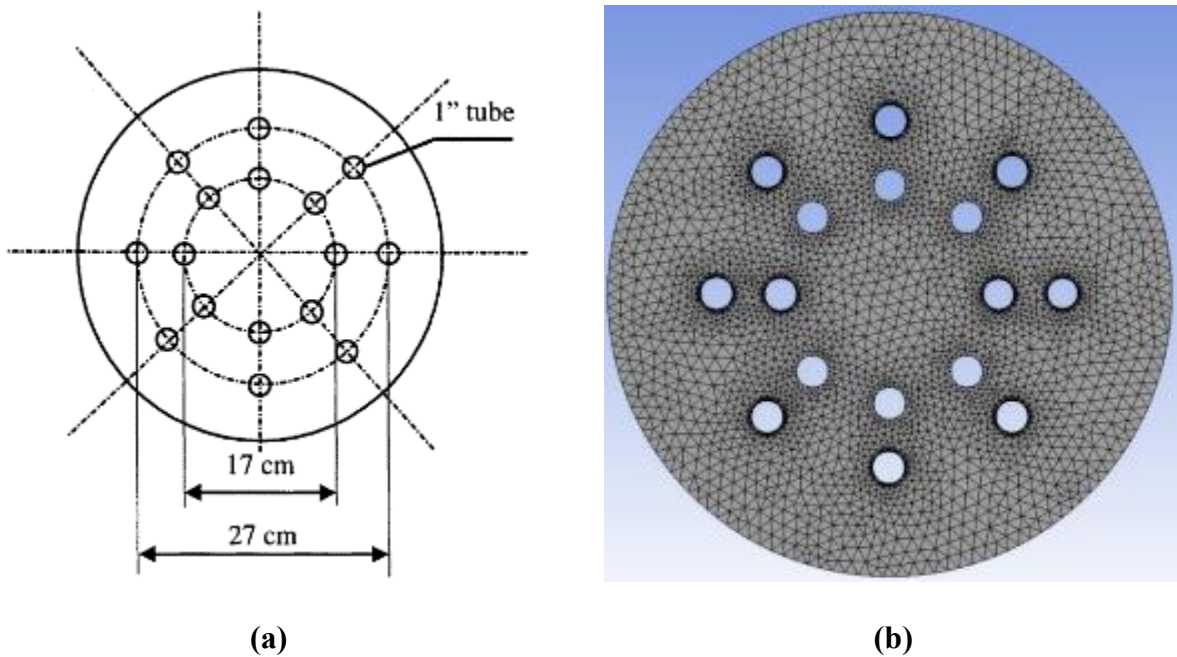


Figure 5-2: Geometry sketch and mesh of the column used by Chen et al. [4]

Table 5-5: Comparison between average relative errors (ARE) and absolute average relative errors (AARE) between experimental results and CFD predictions

Gas Velocity	AARE
0.02 m/s	11.78%
0.05 m/s	4.45%
0.10 m/s	15%

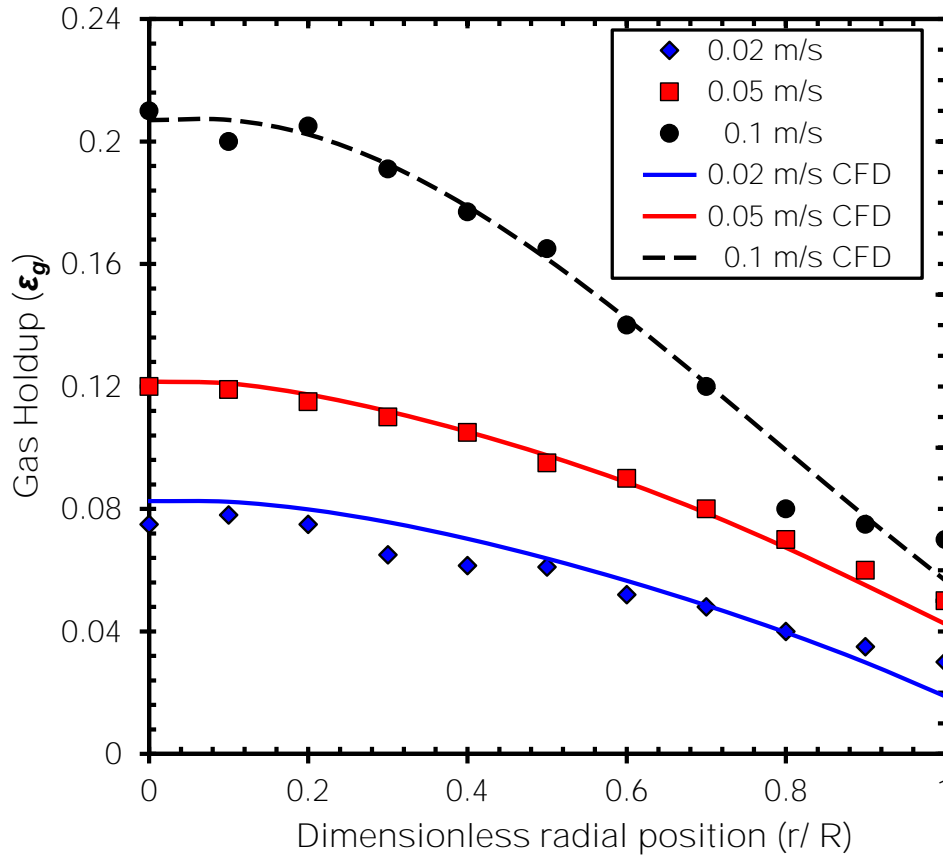


Figure 5-3: Comparison between our CFD model predictions and the experimental radial gas holdup data by Chen et al. [4]

5.3 VALIDATION AGAINST OUR EXPERIMENTAL DATA OBTAINED FOR N₂-F-T REACTOR WAX-IRON-BASED CATALYST SYSTEM

5.3.1 Experimental Setup

The characteristics of the SBCR used in this study are shown in Figure 5-4 and given in Table 5-6, and a schematic diagram of the experimental setup and photographs of the SBCR and gas sparger are shown in Figures 5-5 and 5-6, respectively. The SBCR consists mainly of: reactor (column), gas sparger, damper, filter, demister, compressor, Coriolis mass flow-meter, gas supply vessel, and

gas cylinder. The reactor is provided with two Jerguson sight-windows in order to enable recording the bubbles size/behavior under a given operating condition. The reactor's hydro-pressure is 85.5 bar at 295 K and its maximum allowable working pressure is 57 bar at a maximum temperature of 590 K. The reactor is equipped with 8 heating elements and an internal cooling coil of 0.306 m² total contact area. The heating elements, covered with a heavy-duty insulation jacket, operate with 460 V and are controlled by Solid State Contactors rated up to 50 A. The gas is introduced from a supply vessel through the bottom of the column using a six-arm spider-type gas distributor. The gas is recycled through the reactor using a single-stage compressor built by Fluitron Inc., Ivy land, USA. The compressor has a nominal displacement of 4.8x10⁻³ m³/rev. using 30 Horsepower, 1160 rpm electric motor. The gas flow rate is measured using a Coriolis mass and density meter model CMF100M330NU that gives a current output signal through a transmitter model RFT9739E4SUJ, manufactured by MicroMotion, USA. The gas velocity can be adjusted with a needle valve through a bypass line around the compressor inlet and outlet. The damper vessel is placed at the compressor's outlet in order to dampen the vibrations and fluctuations created by the movements of the piston.

Table 5-6: Characteristics of the SBCR

Nominal Diameter	12 in (0.3048 m)
Schedule	80
Material	Stainless Steel
Outside diameter, m	0.324
Inside diameter, m	0.3
Wall thickness, m	0.017
Inside cross sectional area, m ²	0.066
Outside surface area, m ² /m	1.017
Inside surface area, m ² /m	0.908
Weight, kg/m	131.895
Height, m	3.00
Height/Diameter ratio	10.38

The demister is placed at the outlet of the column in order to prevent the liquid and solid particles from entering the compressor. In addition, a filter manufactured by Parker Hannifin Corp., USA is inserted between the demister and the compressor as a second stage device to prevent any solid particles or liquid mist from entering the compressor. There are two differential pressure cells (dP), model IDP10-V20A11F manufactured by Foxboro, USA rated at 7.5 kPa connected at different positions on the reactor, which allow the measurement of the hydrostatic pressure head between any two levels in the reactor. The pressure and the temperature in the system are recorded with 5 pressure transducers manufactured by Wika, Germany, and 7 thermocouples type J manufactured by Omega Engineering Inc., USA. The design of the entire unit allows the gas to flow through or bypass the liquid using the two pneumatically actuated valves (AV-1 and AV-2); and permits up to 60% of the gas in the reactor to be sent back to the supply vessel without venting to the hood.

An online data acquisition from the thermocouples, pressure transducers, dP cells and the Coriolis mass flow meter is performed using the National Instrument FieldPoint modules FP-TC-120 and FP-AI-110, which are connected to a serial bus module (FP-1000) with RS-232 interface to a host PC. The output signals from the host PC are received by the FieldPoint module FP-AO-V10 for controlling the pneumatically activated valves and the heating elements of the reactor. The LabView software is used to monitor the entire process and perform the appropriate programs for I/O applications.

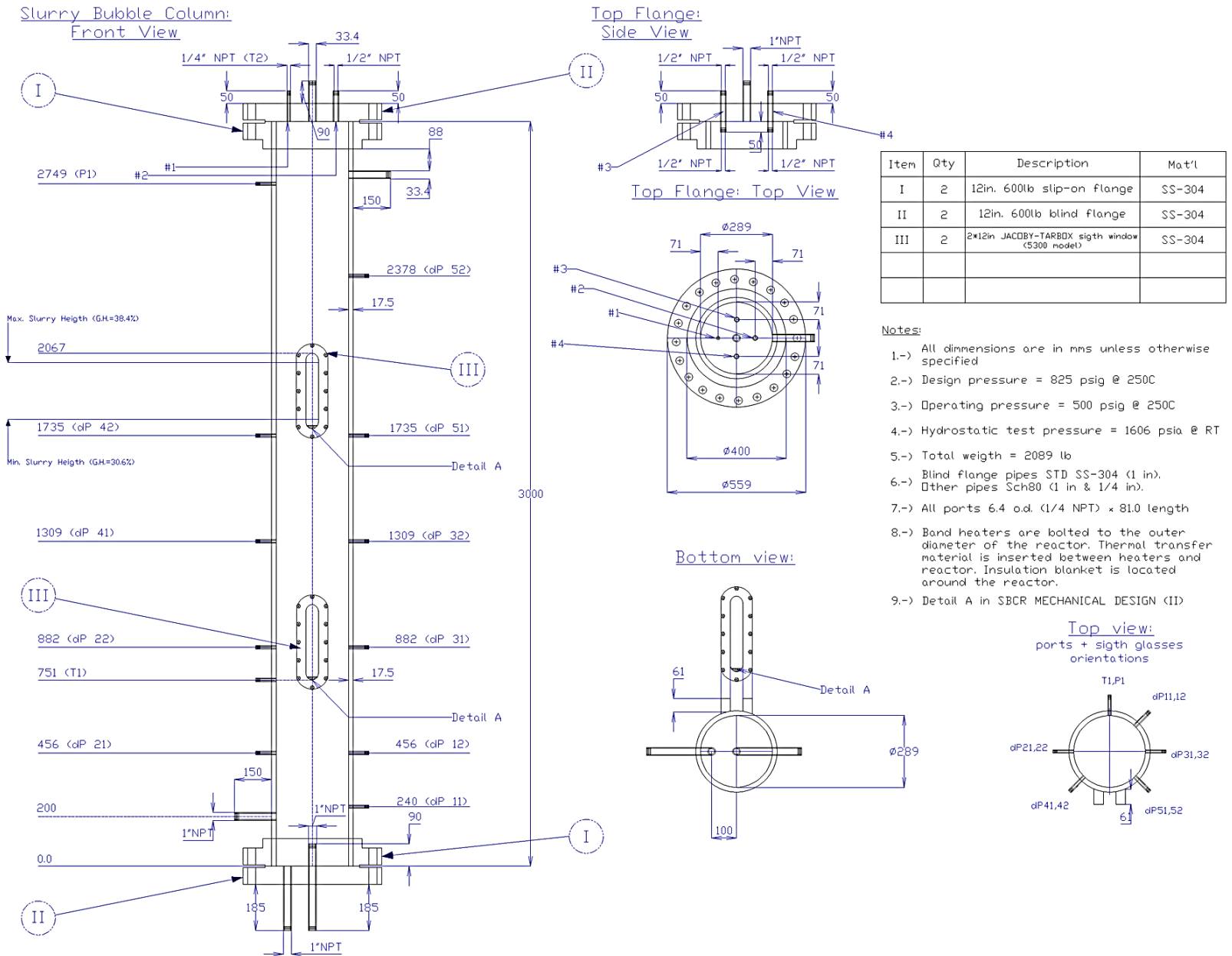
The gas sparger used in the SBCR is a spider-type with six identical legs. Each leg has 6 orifices of 0.005 m inside diameter (ID) on each side and on the bottom, totaling 18 holes in each leg and a total of 108 on the sparger. There are no orifices oriented towards the top of the legs so that solid particles could not block the orifices and the gas should be able to lift any solid particles

which might settle at the bottom flange. The gas sparger is screwed to a 0.0254 m ID pipe and its height from the bottom of the column is about 0.102 m (4 in).

This gas sparger is designed so that the reactor could operate in the fully developed hydrodynamic regime. This condition is attained if Weber number defined in Equation (5-1) is maintained at a value > 2 within the range of sparger geometry in combinations with the operating conditions [359].

$$We = \frac{\rho_G U_{G,o}^2 d_o}{\sigma} = \frac{\rho_G U_G^2 d_R^4}{N_o^2 d_o^3 \sigma} > 2 \quad (5-1)$$

Where N_o is the number of openings on the sparger and d_o is the inside diameter of the orifice.



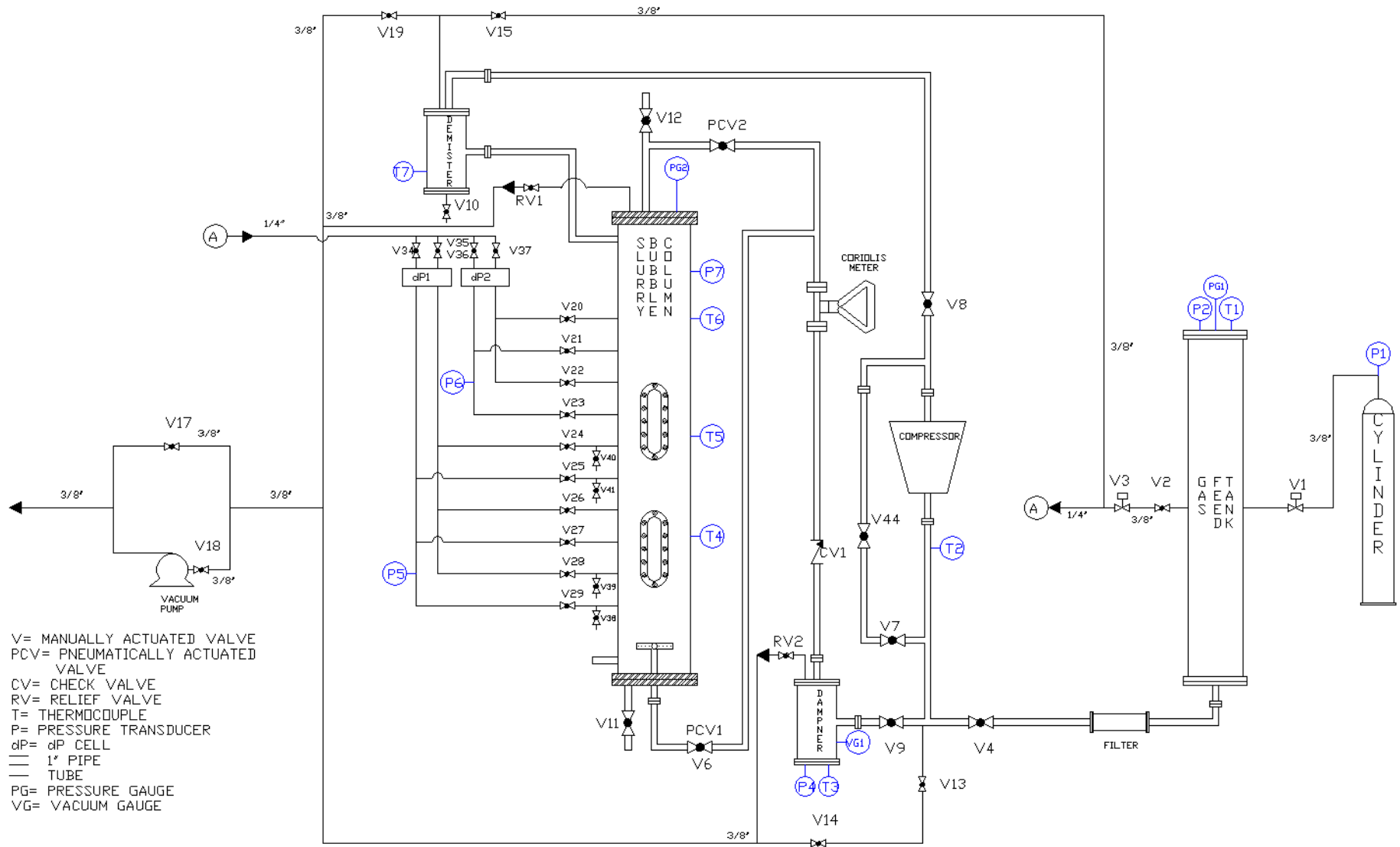


Figure 5-5: Schematic of the Experimental Setup



Figure 5-6: Photographs of the SBCR and Gas Sparger

5.3.2 Gas-Liquid-Solid System and Operating Conditions Used

5.3.2.1 Gas Phase The gases used were He and N₂ as surrogates of H₂ and CO, respectively. N₂ and He were purchased from Valley National Gases (USA). Some thermodynamic parameters [360] of these gases are given in Table 5-7.

Table 5-7: Thermodynamic properties of the gases used

Gases	MW (kg/kmol)	T _b (K)	T _c (K)	P _c (bar)	V _c (m ³ /kmol)	Z _c	ω
N ₂	28.013	77.35	126.10	33.94	0.0901	0.292	0.040
He	4.003	4.22	5.20	2.28	0.0573	0.302	-0.390
H ₂	2.016	20.39	33.18	13.13	0.0642	0.305	-0.220
CO	28.010	81.70	132.92	34.99	0.0931	0.295	0.066

5.3.2.2 Liquid Phase The liquid phase used is a molten reactor wax provided by NICE, China using the F-T process. The molten reactor wax is solid at room temperature with a melting point above 90 °C. It consists of saturated and straight chains hydrocarbons with almost no branches. The wax composition in weight fraction is shown in Figure 5-7. The components containing less than 14 carbon atoms as well as those containing more than 82 carbon atoms were grouped into 2 pseudo components consisting of C₇ and C₁₀₁ respectively, as shown in Equation (5-2). Assuming the composition before C₁₄ and beyond C₈₂ follows the well-known geometric progression that is the Anderson-Schulz-Flory distribution the properties of algebraic series were used to estimate the numbers of carbon atoms in those 2 pseudo components [361]:

$$n = \begin{cases} 1 + \frac{\alpha}{1 - \alpha} - \frac{14\alpha^{14}}{1 - \alpha^{14}}; & CN < 14 \\ 82 + \frac{\alpha}{1 - \alpha}; & CN > 82 \end{cases} \quad (5-2)$$

Jager and Espinoza [362] reported that for an existing pilot reactor, new iron and cobalt catalysts have shown α values between 0.8 and 0.95. Since 1955 Sasol, using iron based catalyst in their

tubular fixed bed Arge reactors, have been producing a product slate with an alpha value of about 0.95. An average chain growth probability factor for the NICE wax of 0.95 was used for the calculation of the pseudo components carbon numbers. It should be noted that in the next sections when density, viscosity and surface tension of the molten wax are calculated, the first pseudo component for CN < 14 which was vaporizing at the higher temperature was omitted.

The molecular weight of the reactor wax is 507.64 kg/kmol, as calculated from its compositions according to the following equation:

$$MW_{Wax} = \sum_{i=1}^n x_i MW_i \quad (5-3)$$

Where x_i represents the mole fraction of species i .

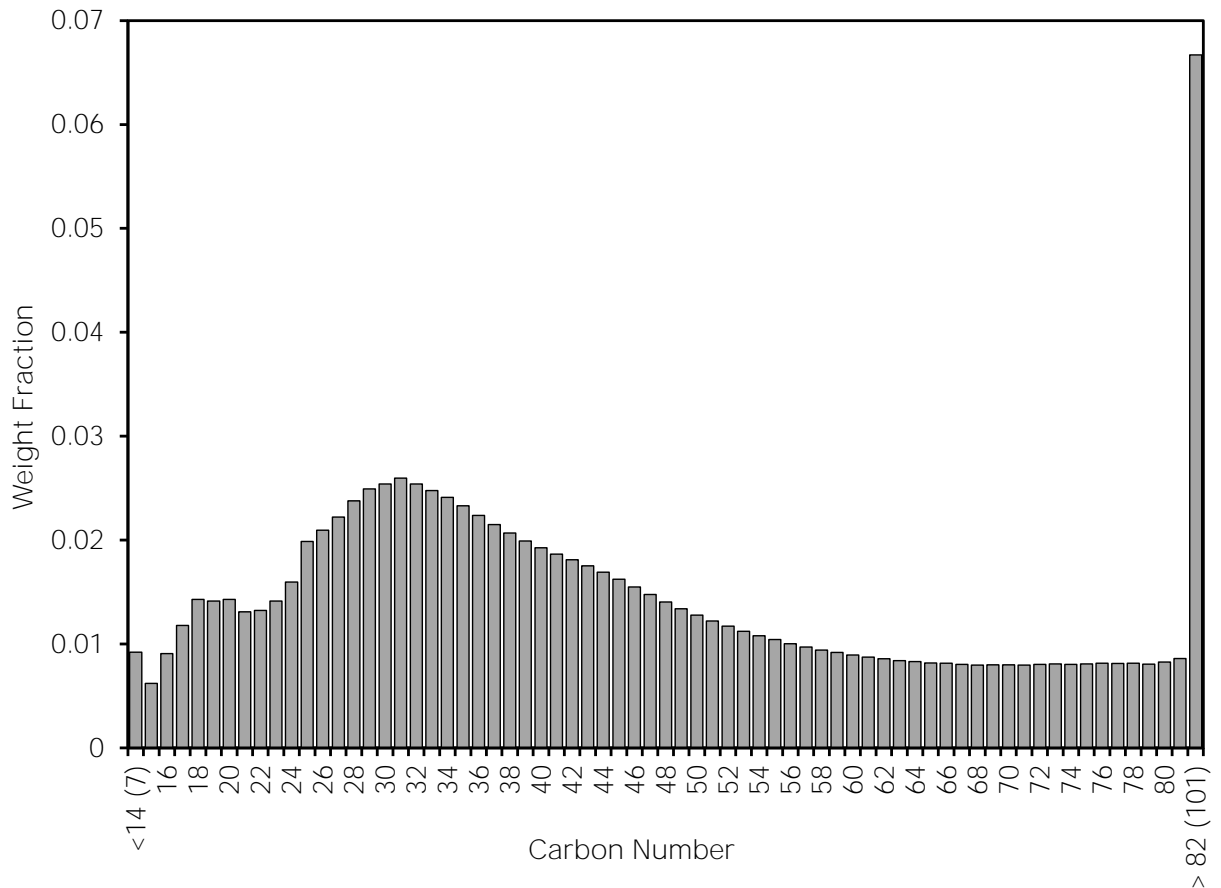


Figure 5-7: Wax composition in weight fraction

The density, viscosity and surface tension of the molten wax were measured in our laboratory at different temperatures ranging from 380 to 460 K using graduated flasks, Cannon-Fenske routine viscometers and a Fisher Surface Tensiomat, respectively. These experimental data were modeled as a function of temperature and predictive correlations were developed. The vapor pressure was predicted with the Asymptotic Behavior Correlations (ABC) developed by Marano and Holder [363, 364], assuming the wax composition consists mainly of linear paraffins. From the values obtained a simple equation was developed for calculating the vapor pressure as a function of temperature. The different correlations for predicting the physical properties of the molten reactor wax as a function of temperature are grouped in Table 5-8 and comparisons between the predicted and experimental values are shown in Figure 5-8.

Table 5-8: Correlations for predicting the physicochemical properties of the reactor wax

$\rho_L = 978.05 - 0.5403 \cdot T$	(5-4)
$\mu_L = \exp\left(\frac{2504.2}{T} - 4.3371\right)$	(5-5)
$\sigma_L = \frac{1.367 \times 10^{-4} T^2 - 0.1915 T + 80.486}{1000}$	(5-6)
$\log_{10}(P_V) = -\frac{50951}{T^2} - \frac{1694.1}{T} + 3.146$	(5-7)

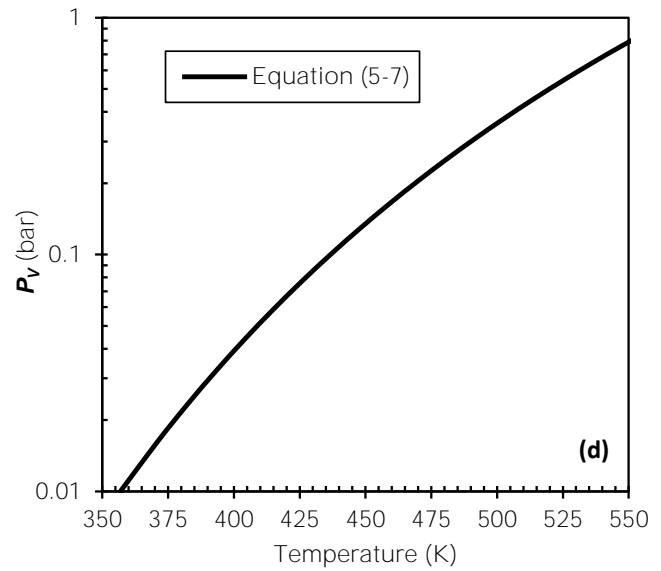
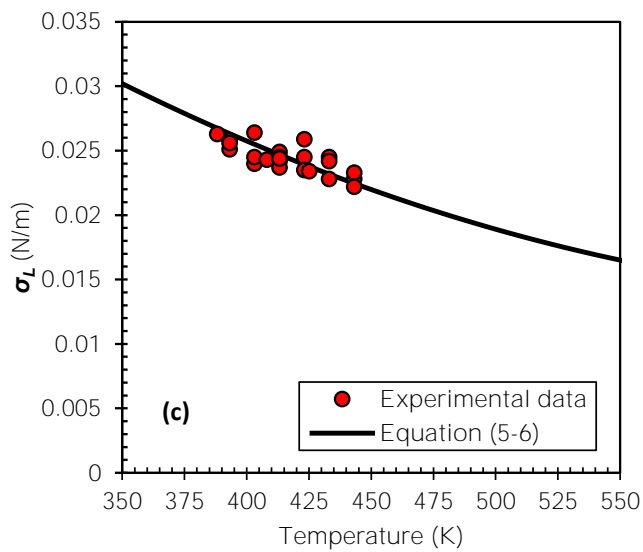
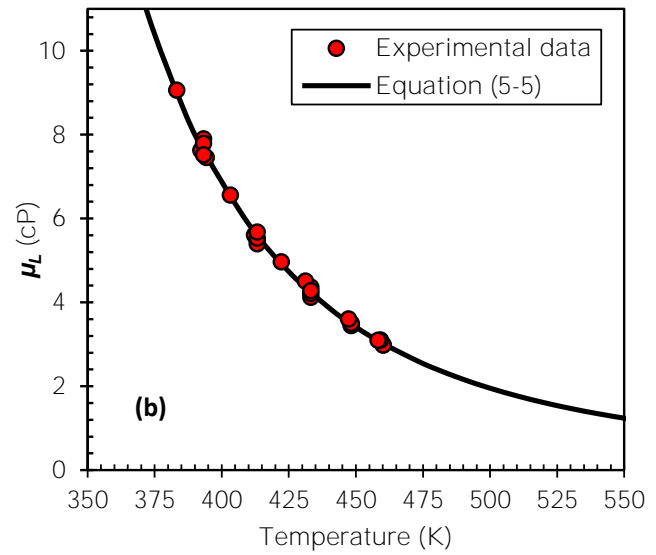
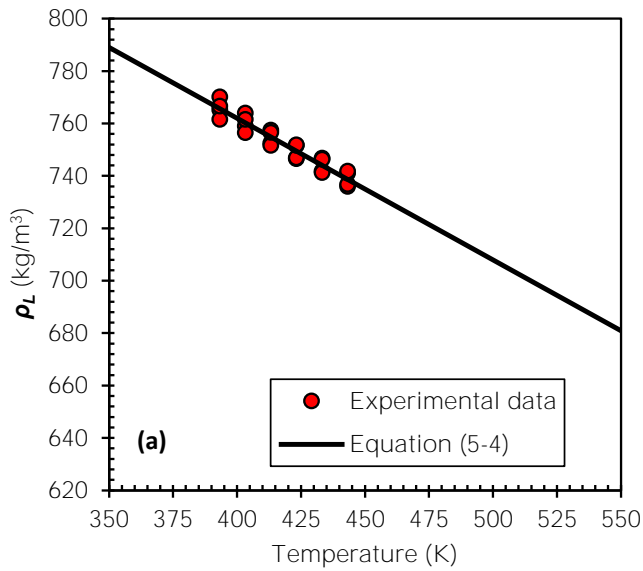


Figure 5-8: Effect of temperature on the density (a), viscosity (b), surface tension (c) and vapor pressure (d) of the molten reactor wax

5.3.2.3 Solid Phase The solid-phase used in the experiments is an iron-based catalyst with a skeletal density of 3,380 kg/m³. The particle size distribution of the catalyst is listed in Table 5-9 and accordingly the average particle diameter = 81 μm.

Table 5-9: Size distribution of the solid particles used

Diameter	Volume % finer than
39 μm	10%
56 μm	30%
80 μm	60%
169 μm	95%

5.3.2.4 Operating Conditions Used The gas holdup, bubble size and mass transfer coefficients were measured under the operating conditions listed in Table 5-10, which are typical to those of F-T synthesis. A test matrix covering these conditions was devised following the Central Composite Statistical Design (CCSD) developed at the University of Pittsburgh. Repeat runs were also carried out in order to ensure the reproducibility of the experimental data. The distribution of experiments according to this Central Composite Statistical Design is given in Figure 5-9. The experimental procedures and calculation methods used in the experimental portion of this work are provided in Appendix B.

Table 5-10: Experimental conditions

Variable	Value
Pressure (MPa)	1, 1.5, 2, 2.5, 3
Temperature (°C)	140, 155, 170, 185, 200
He/N ₂ Ratio	0, 1, 2, 3
Superficial Gas Velocity (m/s)	0.1, 0.15, 0.2, 0.25, 0.3
Solid Concentration (vol. %)	5, 10, 15

		S ₁					S ₂					S ₃					S ₄					S ₅				
		P ₁	P ₂	P ₃	P ₄	P ₅	P ₁	P ₂	P ₃	P ₄	P ₅	P ₁	P ₂	P ₃	P ₄	P ₅	P ₁	P ₂	P ₃	P ₄	P ₅	P ₁	P ₂	P ₃	P ₄	P ₅
T ₁	U ₁																									
	U ₂																									
	U ₃													■												
	U ₄																									
	U ₅																									
T ₂	U ₁																									
	U ₂							■		■								■		■						
	U ₃																									
	U ₄							■		■								■		■						
	U ₅																									
T ₃	U ₁													■												
	U ₂																									
	U ₃			■									■		■									■		
	U ₄																									
	U ₅													■												
T ₄	U ₁																									
	U ₂							■		■								■		■						
	U ₃																									
	U ₄							■		■								■		■						
	U ₅																									
T ₅	U ₁																									
	U ₂																									
	U ₃													■												
	U ₄																									
	U ₅																									

P: Pressure; S: Solid Concentration; T: Temperature; U: Superficial Gas Velocity

Figure 5-9: CCSD experimental design matrix [8, 151, 365]

5.3.3 Hydrodynamic and Mass Transfer Parameters in the Pilot Scale SBCR under F-T Conditions

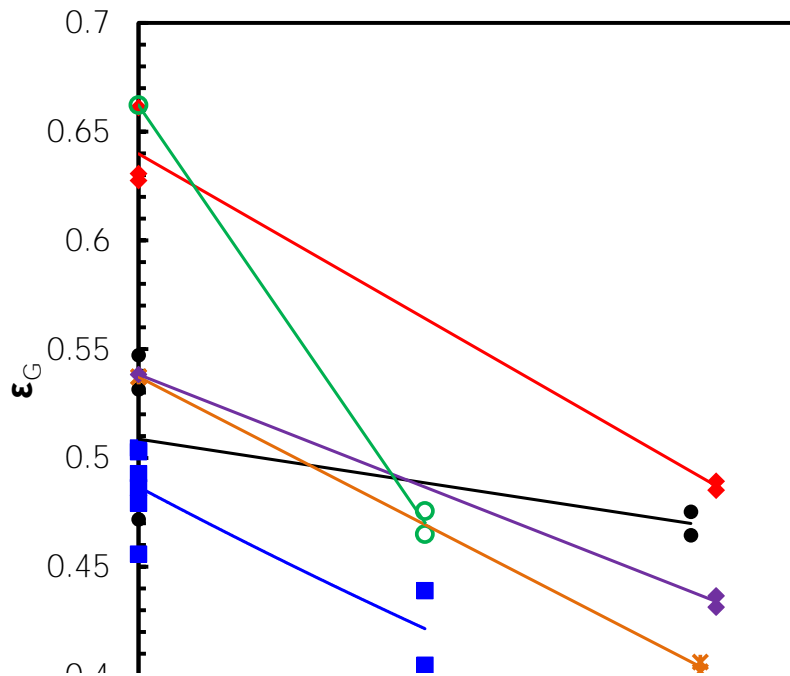
In this section, the effects of pressure, temperature, gas and liquid velocities, gas nature and composition, solid concentration, liquid and solid phases natures on the hydrodynamics (ϵ_G and d_{32}) and mass transfer (k_{LA}) parameters for N₂ and He as single components as well as for different mixtures of these two gases obtained in the NICE molten reactor wax in the presence and absence of iron-based catalyst using the pilot-scale SBCR are discussed.

5.3.3.1 Gas Holdup The gas holdup values for N₂ and He/N₂ gas mixtures in molten reactor wax generally decrease with increasing the solid concentration under the various operating conditions as shown in Figure 5-10. This is due to the increase of the slurry viscosity and density, resulting in low gas momentum/mass of slurry and large gas bubbles. This behavior is in agreement with previous findings by Vandu et al. [366] using alumina particles in a C₉-C₁₁ paraffins mixture; Deckwer et al. [75, 367] using alumina particles in paraffin wax; Krishna et al. [368] using silica particles in paraffins oil, Behkish et al. [8] using alumina particles in iso-paraffins mixture (Isopar-M), and Sehabiague and Morsi [81] using alumina and iron oxide particles in C₁₂-C₁₃ paraffins mixture and F-T cuts. Moreover, in the absence and presence of solid particles up to 15 vol. %, the gas holdup for N₂ in molten reactor wax appear to increase with temperature as depicted in Figures 5-11 to 5-13, which is in accord with other literature data [8, 81]. This behavior can be attributed to the

decrease of the liquid-phase viscosity and surface tension with increasing temperature which led to high gas holdup values.

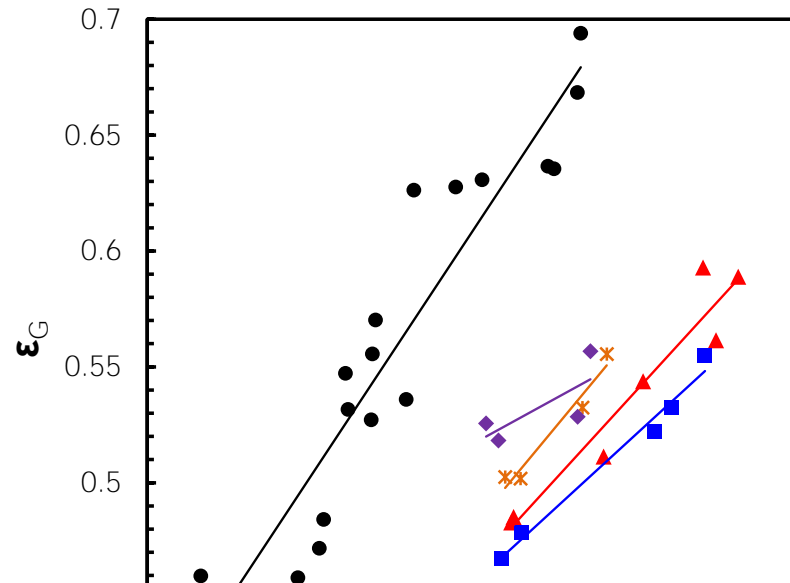
Moreover, as shown in Figure 5-14, gas holdup values are found to increase with reactor pressure, which is in agreement with other reported findings [8, 81, 369]. This behavior can be attributed to the increase of the gas density and the gas-phase momentum, which led to the increase of the gas holdup. Similarly, the gas holdup of N₂ in the molten reactor wax appear to increase with the superficial gas velocity, as shown in Figure 5-15.

The gas holdup values are also found to increase with increasing the mole fraction of N₂ or decreasing the mole fraction of He in the gas mixture, as shown in Figure 5-16, which is in agreement with earlier findings for He, N₂ and He/N₂ mixtures in an iso-paraffinic mixture (Isopar-M), and in 3 different F-T liquids [8, 81]. The presence of the heavier gas (N₂) increases the density and thus the momentum of the gaseous mixture which led to the increase of the gas holdup and to the formation of smaller gas bubbles, which resulted in a greater gas-liquid interfacial area and consequently k_{La} . Indeed, k_{La} values increased with increasing the mole fraction of N₂ in the gas mixture, with the highest k_{La} values observed for N₂ as a single component.



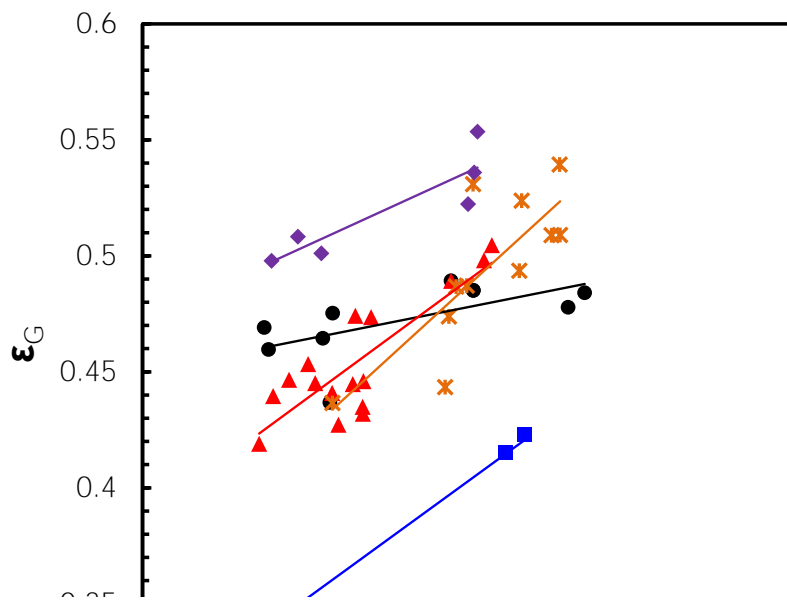
- T=415 K; P=20.6 bar; Ug=0.20 m/s
- ◆ T=440 K; P=20.4 bar; Ug=0.19 m/s
- T=441 K; P=21.6 bar; Ug=0.20 m/s; xHe=0.50
- ✕ T=443 K; P=10.6 bar; Ug=0.20 m/s
- ◆ T=444 K; P=20.6 bar; Ug=0.12 m/s
- T=447 K; P=14.4 bar; Ug=0.20 m/s

Figure 5-10: Effect of solids concentration on ϵ_G in F-T reactor wax



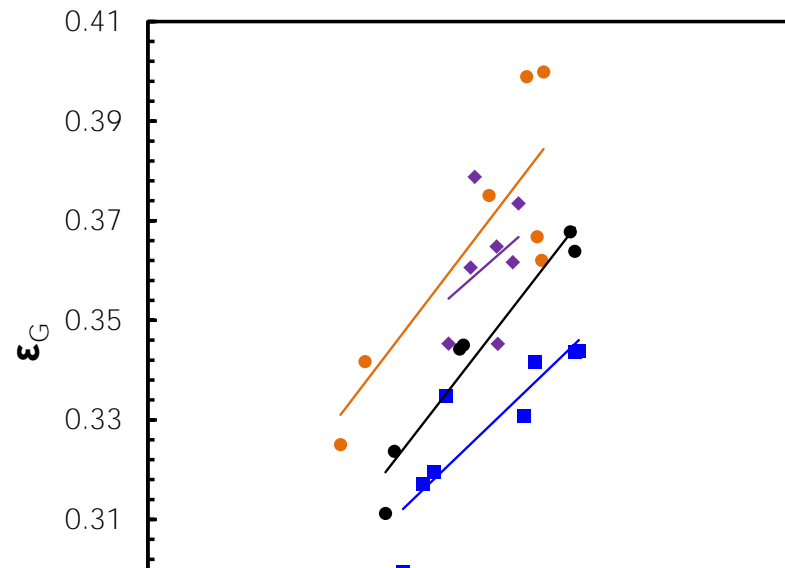
- Cs=0 vol.%; P=20.3 bar; Ug=0.20 m/s
- ▲ Cs=5 vol.%; P=21.7 bar; Ug=0.20 m/s
- Cs=5 vol.%; P=21.1 bar; Ug=0.20 m/s; xHe=0.25
- ✕ Cs=5 vol.%; P=25.9 bar; Ug=0.15 m/s
- ◆ Cs=5 vol.%; P=25.9 bar; Ug=0.25 m/s

Figure 5-11: Effect of temperature on ϵ_G in F-T reactor wax at 0-5 vol. % solid concentrations



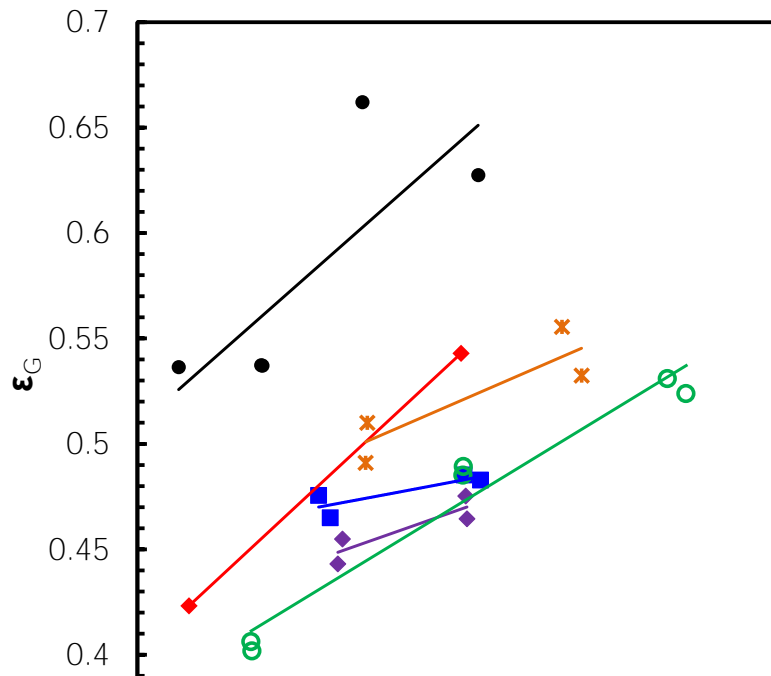
- Cs=10 vol.%; P=20.5 bar; Ug=0.20 m/s
- ▲ Cs=10 vol.%; P=21.7 bar; Ug=0.24 m/s
- Cs=10 vol.%; P=21.4 bar; Ug=0.15 m/s
- ✕ Cs=10 vol.%; P=27.7 bar; Ug=0.21 m/s
- ◆ Cs=10 vol.%; P=28.3 bar; Ug=0.27 m/s

Figure 5-12: Effect of temperature on ϵ_G in F-T reactor wax at 10 vol. % solid concentrations



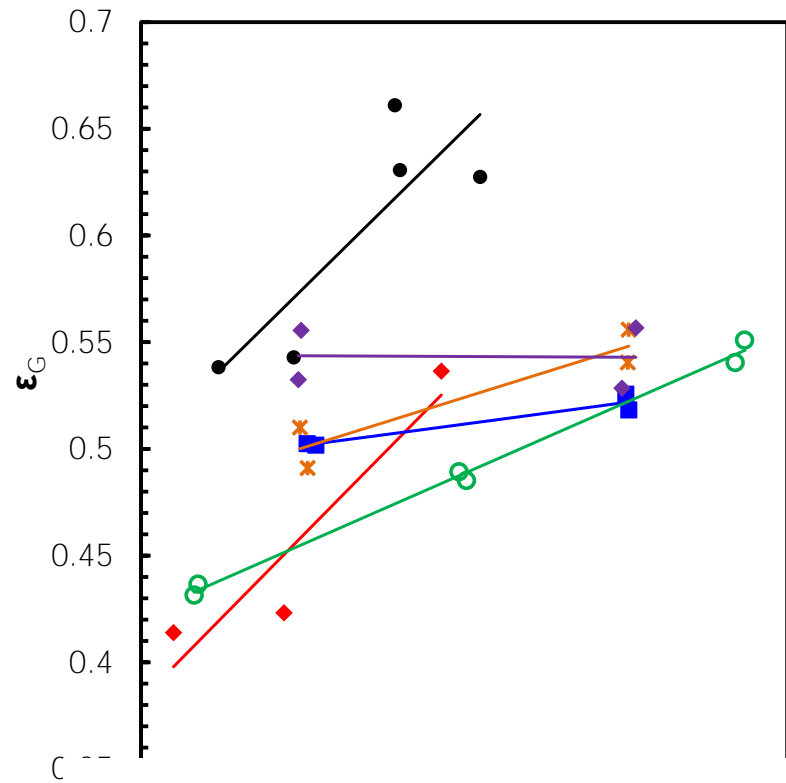
- Cs=15 vol.%; P=15.4 bar; Ug=0.25 m/s
- Cs=15 vol.%; P=20.9 bar; Ug=0.20 m/s
- Cs=15 vol.%; P=27.1 bar; Ug=0.20 m/s
- ◆ Cs=15 vol.%; P=29.4 bar; Ug=0.20 m/s
- ▲ Cs=15 vol.%; P=21.7 bar; Ug=0.24 m/s

Figure 5-13: Effect of temperature on ϵ_G in F-T reactor wax at 15 vol. % solid concentrations



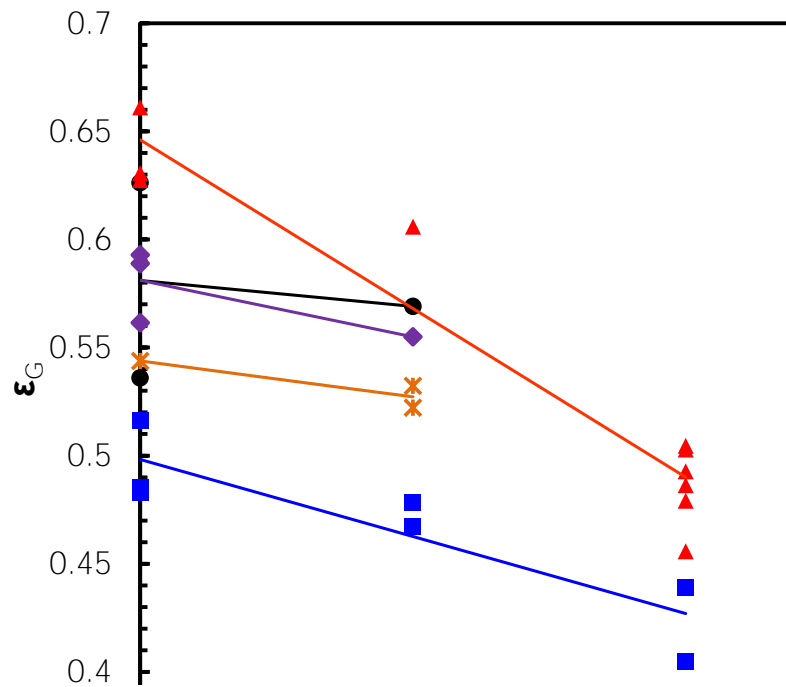
- Cs=0 vol.%; T=443 K; Ug=0.20 m/s
- ◆ Cs=0 vol.%; T=446 K; Ug=0.15 m/s
- Cs=5 vol.%; T=448 K; Ug=0.20 m/s
- ✕ Cs=5 vol.%; T=462 K; Ug=0.15 m/s
- ◆ Cs=10 vol.%; T=417 K; Ug=0.20 m/s
- Cs=10 vol.%; T=443 K; Ug=0.20 m/s

Figure 5-14: Effect of pressure on ϵ_G in F-T reactor wax



- Cs=0 vol.%; T=443 K; P=20.5 bar
- ◆ Cs=0 vol.%; T=447 K; P=7.3 bar
- Cs=5 vol.%; T=446 K; P=26.0 bar
- ✕ Cs=5 vol.%; T=461 K; P=15.6 bar
- ◆ Cs=5 vol.%; T=462 K; P=25.9 bar
- Cs=11 vol.%; T=443 K; P=20.5 bar

Figure 5-15: Effect of superficial gas velocity on ϵ_G in F-T reactor wax



- Cs=0 vol.%; T=430 K; P=21.1 bar; $U_g=0.20$ m/s
- ▲ Cs=0 vol.%; T=441 K; P=21.2 bar; $U_g=0.20$ m/s
- Cs=5 vol.%; T=448 K; P=21.2 bar; $U_g=0.20$ m/s
- × Cs=5 vol.%; T=474 K; P=21.8 bar; $U_g=0.20$ m/s
- ◆ Cs=5 vol.%; T=485 K; P=22.1 bar; $U_g=0.20$ m/s

Figure 5-16: Effect of gas density on ϵ_G in F-T reactor wax

5.3.3.2 Sauter Mean Bubble Diameter The Sauter-mean diameter (d_{32}) of gas bubbles appear to increase with increasing the concentration of solid particles under the operating conditions used as shown in Figure 5-17, which is in agreement with other findings [8, 81]. This behavior is due to the increased slurry viscosity at higher solid concentrations, which increases the rate of gas bubbles coalescence, leading to the formation of large gas bubbles and consequently large Sauter mean bubble diameters. It seems that the addition of solid particles prevented the breakup of gas bubbles.

Figures 5-18 and 5-19 also show that in the absence and presence of solid particles up to 10 vol%, the values of the Sauter mean bubble diameters decrease with increasing temperature, which can be attributed to the decrease of the liquid viscosity and surface tension with increasing temperature, leading to the formation of small gas bubbles. [8] Figure 5-18 also shows that a minimum Sauter mean bubble diameter of about 0.2 mm is reached for solid concentrations up to 5 vol%. Also, at the highest solid concentration of 15 vol%, as shown in Figure 5-20, the temperature has no effect on the gas bubble size.

Moreover, as shown in Figures 5-21 and 5-22, both the superficial gas velocity and the pressure appear to have an insignificant effect on the Sauter-mean gas bubble diameter for N_2 in wax in the presence of solid particles up to 15 vol%.

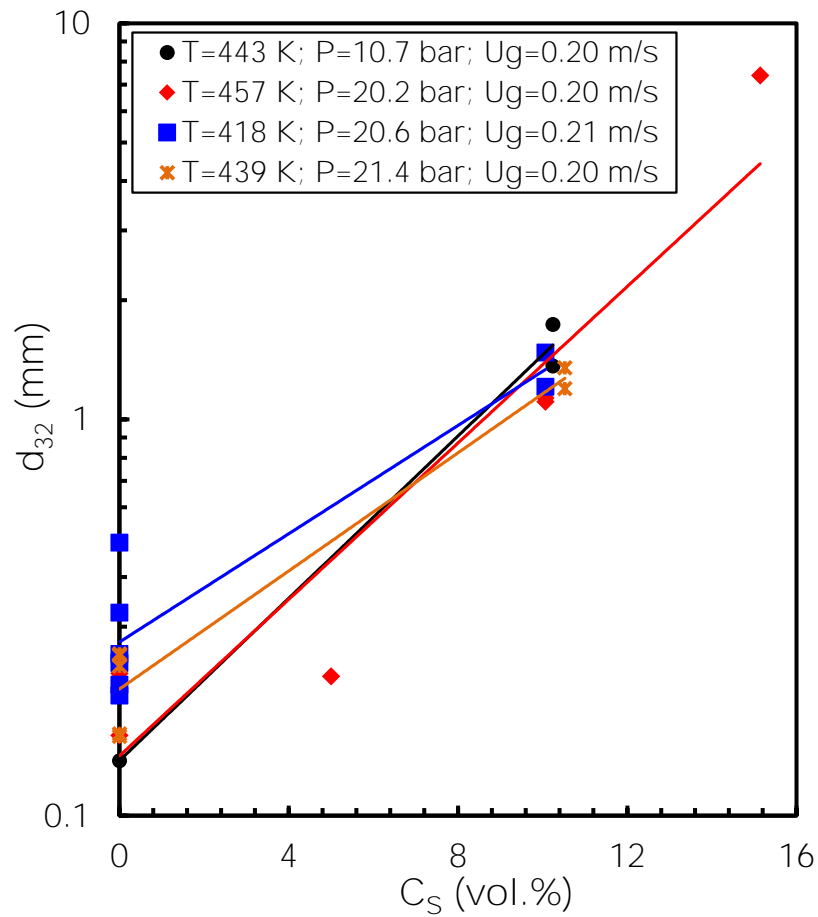


Figure 5-17: Effect of solids concentration on d_{32} in F-T reactor wax

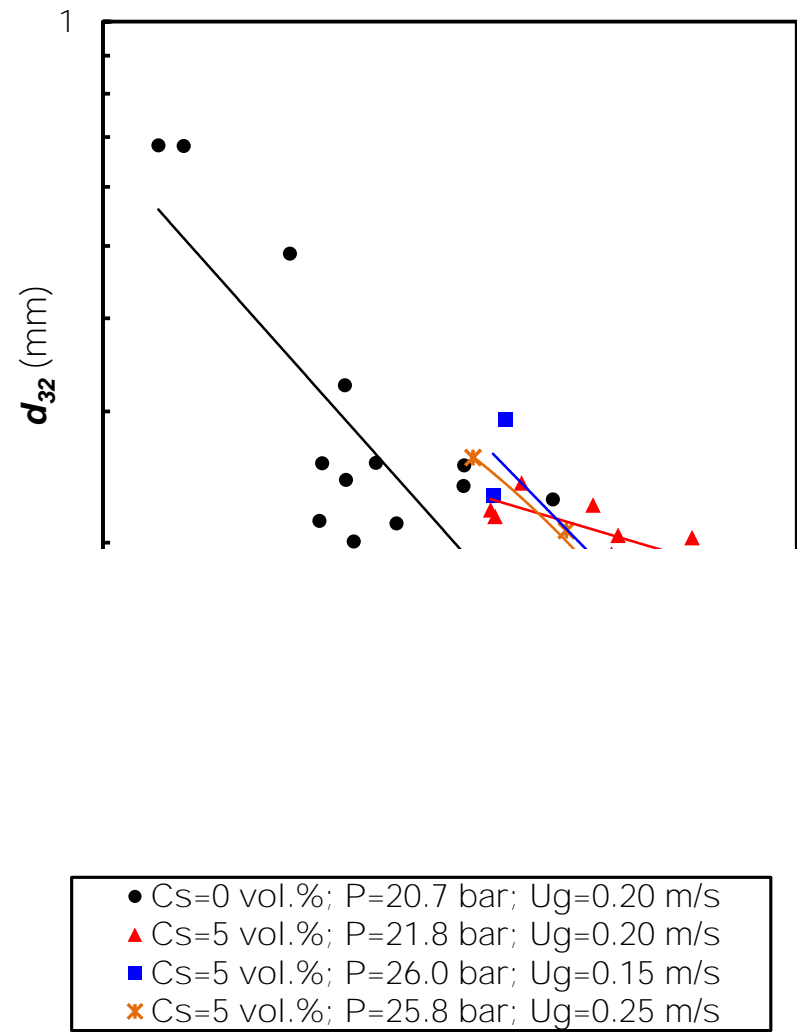
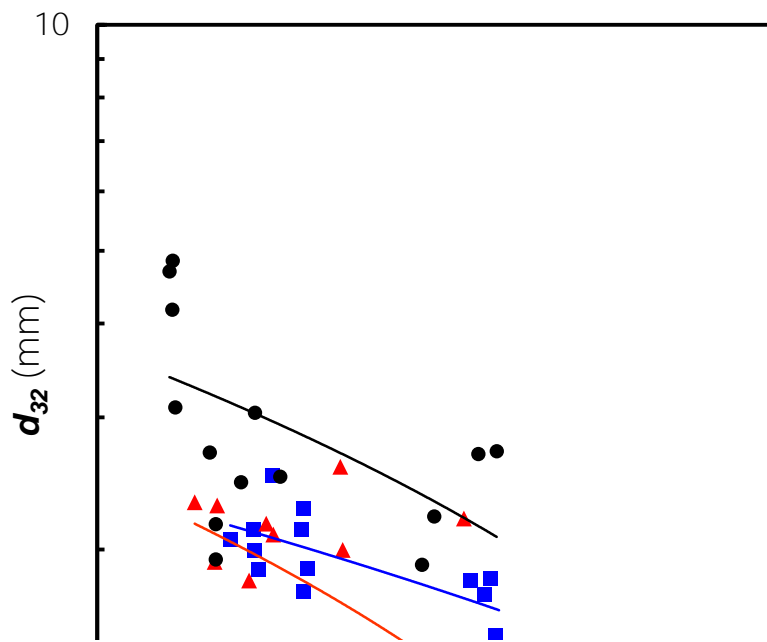
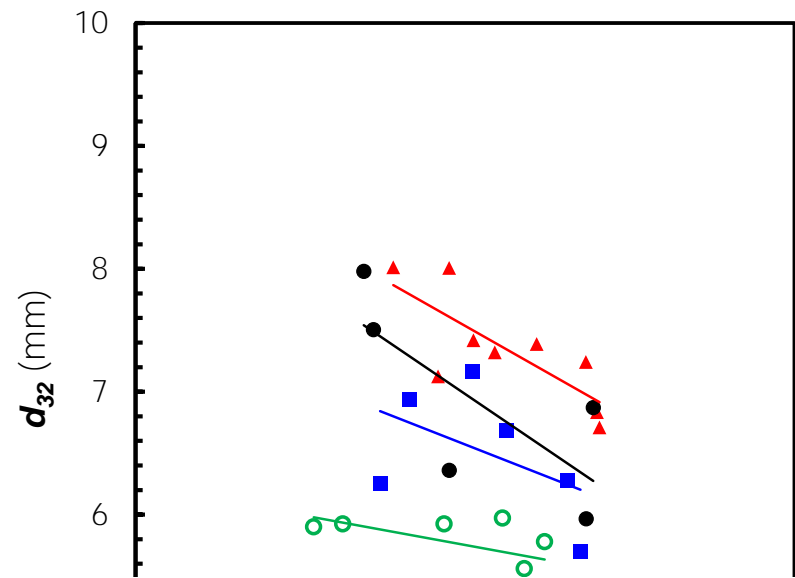


Figure 5-18: Effect of temperature on d_{32} in F-T reactor wax at 0 – 5 vol. % solid concentrations



- Cs=10 vol.%; P=14.1 bar; Ug=0.12 m/s
- ▲ Cs=10 vol.%; P=20.8 bar; Ug=0.20 m/s
- Cs=10 vol.%; P=11.9 bar; Ug=0.25 m/s

Figure 5-19: Effect of temperature on d_{32} in F-T reactor wax at 10 vol. % solid concentrations



- Cs=15 vol.%, P =1.53 bar; Ug=0.26 m/s
- ▲ Cs=15 vol.%; P=20.8 bar; Ug=0.20 m/s
- Cs=15 vol.%;P=21.4 bar; Ug=0.26 m/s
- Cs=15 vol.%; P=28.2 bar; Ug=0.20 m/s

Figure 5-20: Effect of temperature on d_{32} in F-T reactor wax at 15 vol. % solid concentrations

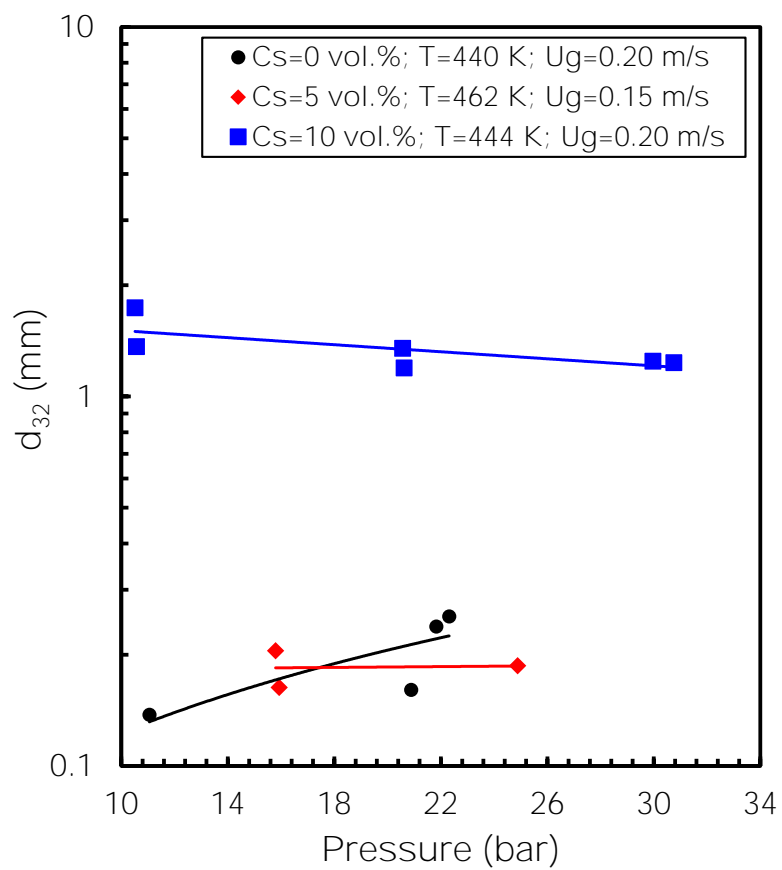


Figure 5-21: Effect of Pressure on d_{32} in F-T reactor wax

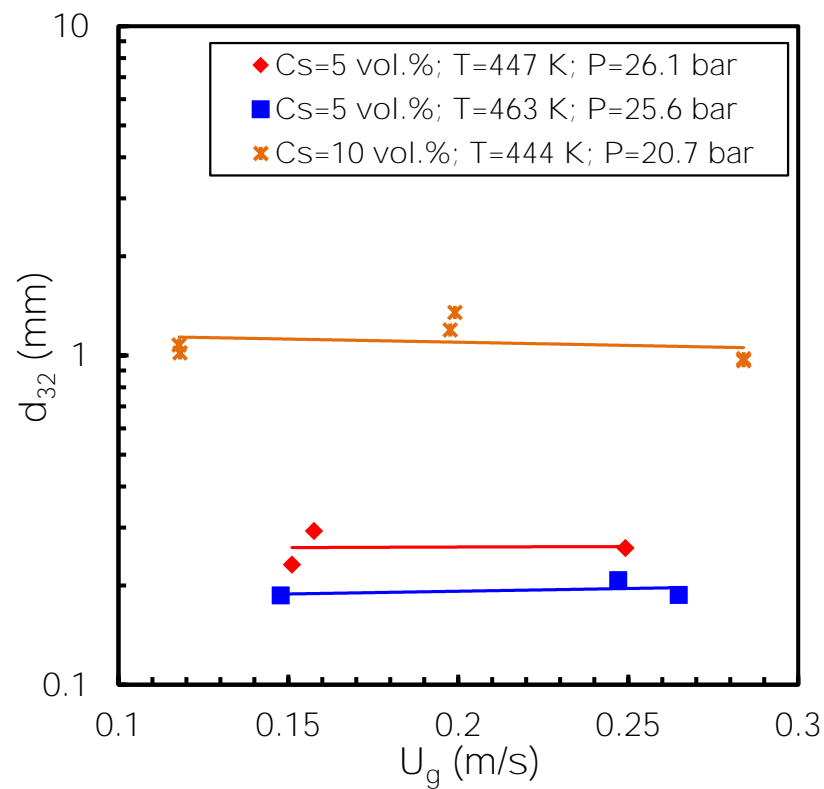
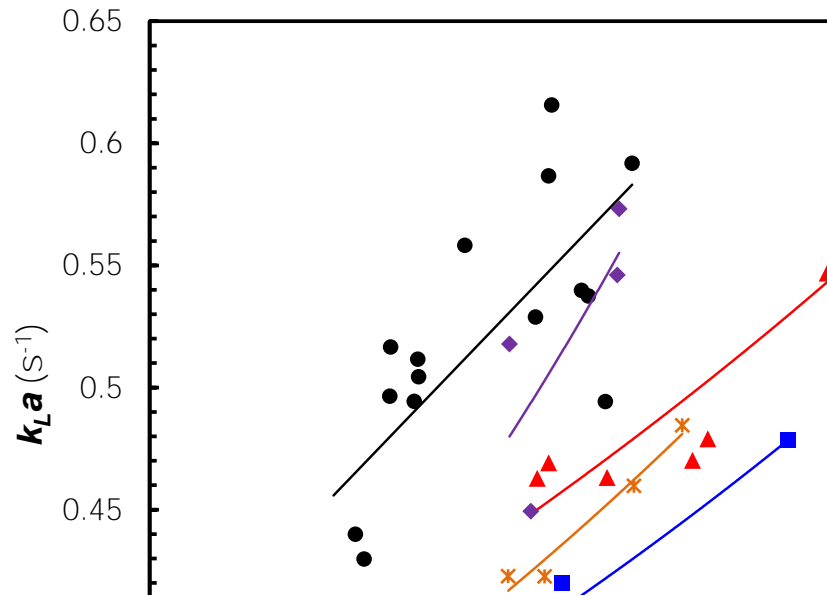


Figure 5-22: Effect of superficial gas velocity on d_{32} in F-T reactor wax

5.3.3.3 Volumetric Mass Transfer Coefficients Figures 5-23 and 5-24 show that in the absence and presence of solid particles up to 10 vol.%, the volumetric mass transfer coefficients (k_{LA}) values for N₂ and He/N₂ mixtures in NICE molten wax increase with increasing temperature. However, at high solid concentrations of 15 vol.%, the effect of temperature on k_{LA} , seems to be governed by the pressure, where at low pressures k_{LA} values increase with increasing temperatures, whereas at higher k_{LA} values the effect of temperature is insignificant.

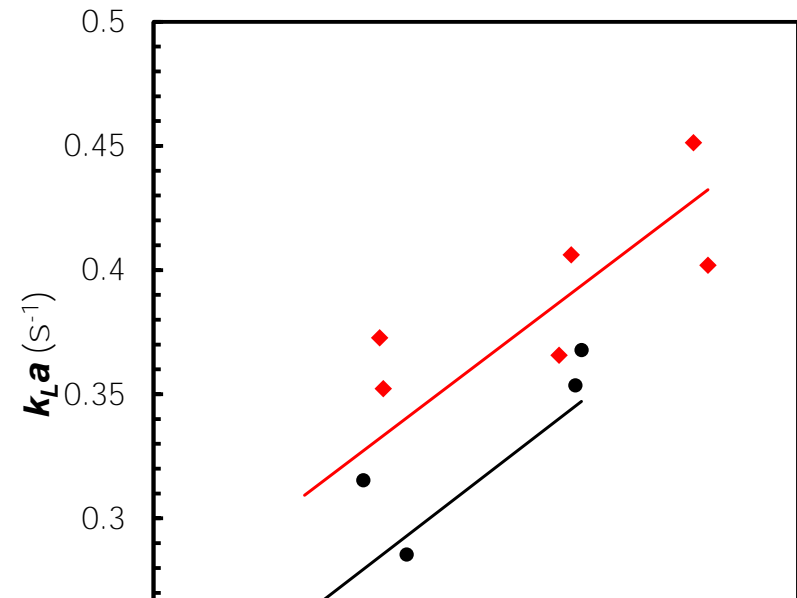
Also, at similar temperatures, k_{LA} values for the same gas-liquid system decrease with increasing solid concentration, as shown in Figure 5-25, which is in agreement with other findings [80, 81]. This behavior can be related to the decrease of the gas holdup and the increase of the Sauter mean bubble diameter with increasing solid concentration as shown in Figures 1 and 8.

The k_{LA} for N₂ in NICE molten wax, with and without solid particles, also appear to increase with increasing pressure, as shown in Figure 5-26, which is due to the increase of the gas holdup and the decrease of the Sauter mean gas bubble diameter, which led to the increase of the gas-liquid interfacial area (a). Moreover, as expected, k_{LA} for N₂ in NICE molten reactor wax always increased with increasing the superficial gas velocity (Figure 5-27), which was attributed to an increase of the gas holdup and turbulences, which increased the gas-liquid interfacial area (a) and the mass transfer coefficient (k_L), respectively.



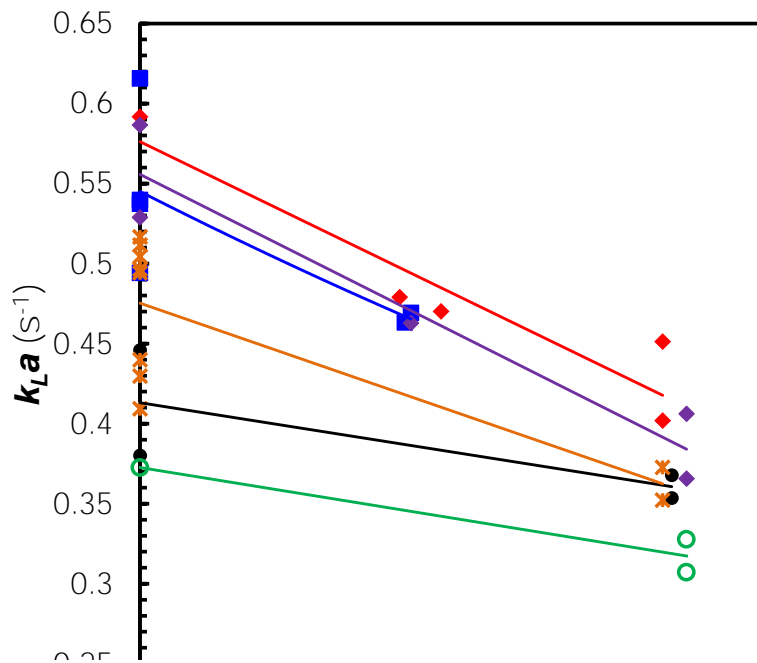
- Cs=0 vol.%; P=20.4 bar; Ug=0.19 m/s
- ▲ Cs=5 vol.%; P=21.7 bar; Ug=0.20 m/s
- Cs=5 vol.%; P=20.6 bar; Ug=0.20 m/s; yHe=0.25
- × Cs=5 vol.%; P=26.2 bar; Ug=0.14 m/s
- ◆ Cs=5 vol.%; P=25.9 bar; Ug=0.25 m/s

Figure 5-23: Effect of temperature on k_{La} in F-T reactor wax at 0 – 5 vol. % solid concentrations



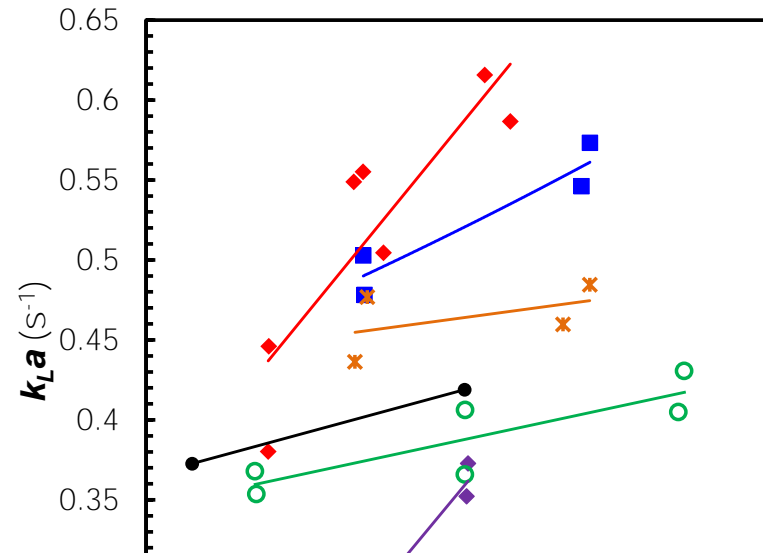
- Cs=10 vol.%| P=13.6 bar; Ug=0.19 m/s
- ◆ Cs=10 vol.%; P=20.5 bar; Ug=0.20 m/s

Figure 5-24: Effect of temperature on k_{La} in F-T reactor wax at 10 vol. % solid concentrations



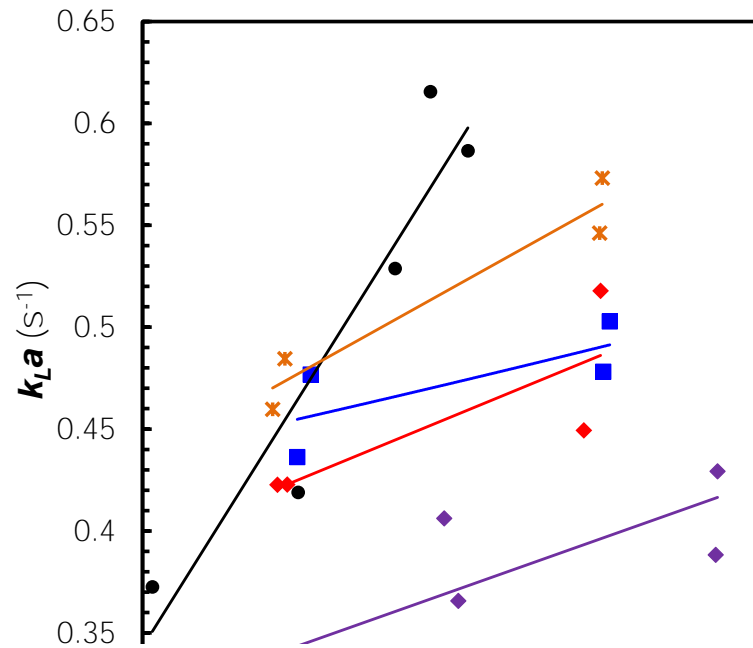
- T=454 K; P=10.6 bar; U_g=0.20 m/s
- ◆ T=470 K; P=20.5 bar; U_g=0.20 m/s
- T=456 K; P=20.6 bar; U_g=0.19 m/s
- × T=420 K; P=20.7 bar; U_g=0.19 m/s
- ◆ T=447 K; P=20.7 bar; U_g=0.20 m/s
- T=448 K; P=20.7 bar; U_g=0.11 m/s

Figure 5-25: Effect of solids concentration on k_{LA} in F-T reactor wax



- Cs=0 vol.%; T=458 K; U_g=0.15 m/s
- ◆ Cs=0 vol.%; T=460 K; U_g=0.20 m/s
- Cs=5 vol.%; T=463 K; U_g=0.25 m/s
- × Cs=5 vol.%; T=468 K; U_g=0.15 m/s
- ◆ Cs=10 vol.%; T=419 K; U_g=0.20 m/s
- Cs=10 vol.%; T=446 K; U_g=0.20 m/s

Figure 5-26: Effect of pressure on k_{LA} in F-T reactor wax



- Cs=0 vol.%; T=451 K; P=21.1 bar
- ◆ Cs=5 vol.%; T=446 K; P=26.2 bar
- Cs=5 vol.%; T=465 K; P=15.4 bar
- × Cs=5 vol.%; T=466 K; P=25.9 bar
- ◆ Cs=10 vol.%; T=446 K; P=20.5 bar

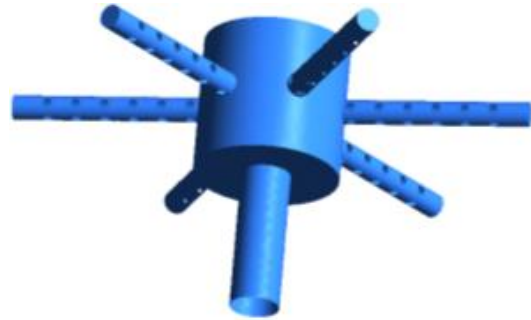
Figure 5-27: Effect of superficial gas velocity on k_{La} in F-T reactor wax

5.3.4 Geometry and Numerical Meshing of the Pilot-Scale SBCR

A picture of the gas sparger described above is given in Figure 5-28 (a). The gas sparger is screwed onto a 0.0254 m ID pipe to a height of 0.102 m from the bottom flange of the reactor. Also, its maximum height from the bottom of the reactor is about 0.152 m. The constructed geometry of this gas sparger is shown in Figure 5-28 (b).



(a)



(b)

Figure 5-28: (a) Picture and (b) Constructed geometry of the sparger used in this study

The numerical meshing structure used is shown in Figure 6. A quadrilateral/hexahedral meshing combination is generated in order to discretize the domain limited by the geometry. After preliminary numerical tests, it was proved that around 1,150,000 control volumes are enough to obtain mesh numerical independence, as shown in Figure 5-29. Also, due to the strong non-linear characteristics of our model, relaxation coefficients (Patankar [356]) are introduced in the momentum conservation equations as previously discussed by Silva Jr. et al. [302]. The convergence criterion adopted from Patankar [356], based on the pressure, is shown in Equation (4-39).

The simulations were carried out with a 0.01 s time step for a duration of 60 s, or until steady state is reached. An upwind QUICK (Quadratic Upstream Interpolation for Convective Kinematics) scheme was used to solve the model equations. This is because the upwind QUICK is superior than the second order upwind since QUICK has less dispersion and dampens the high frequency components much less. Typically, the simulations took around 220 hours to complete.

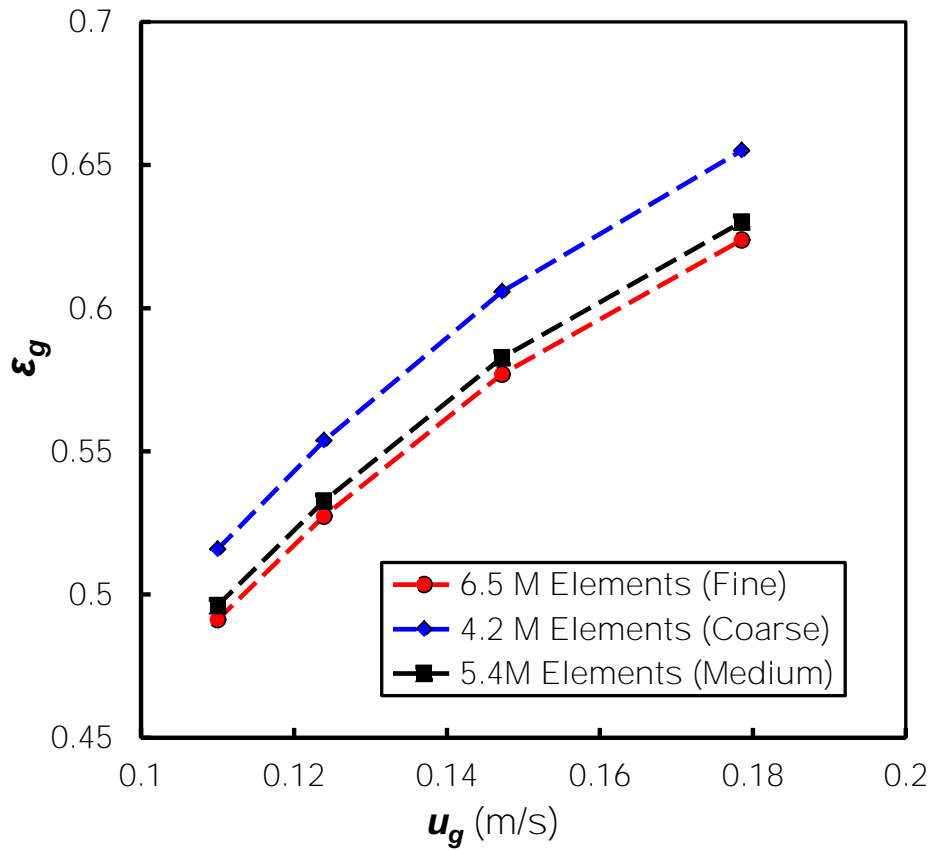
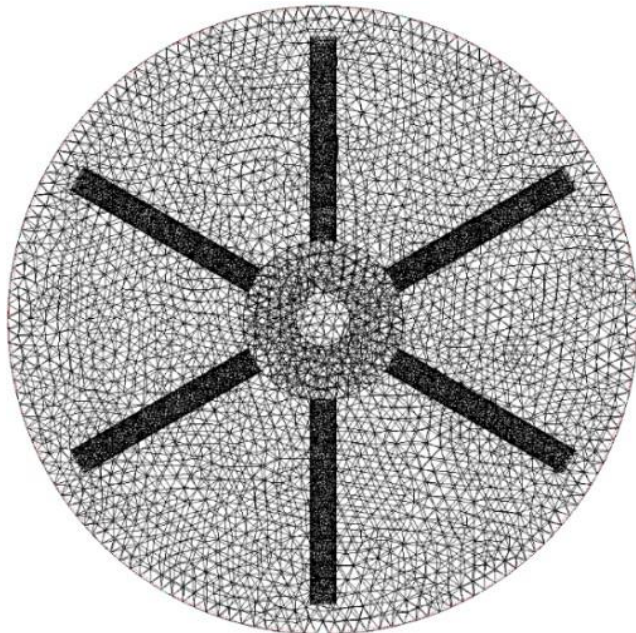
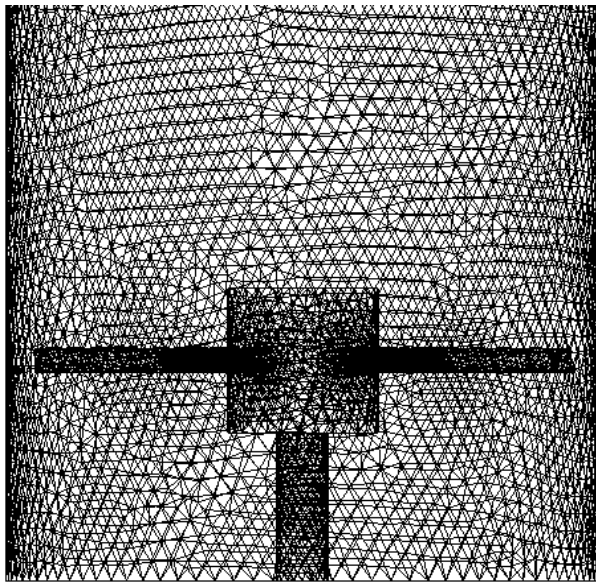


Figure 5-29: Mesh Independence analysis



(a)



(b)

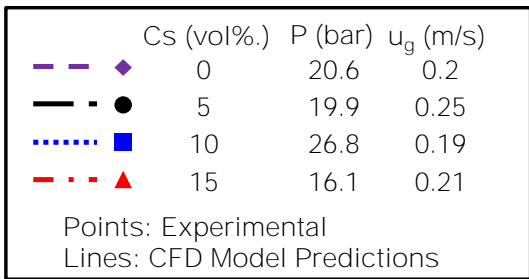
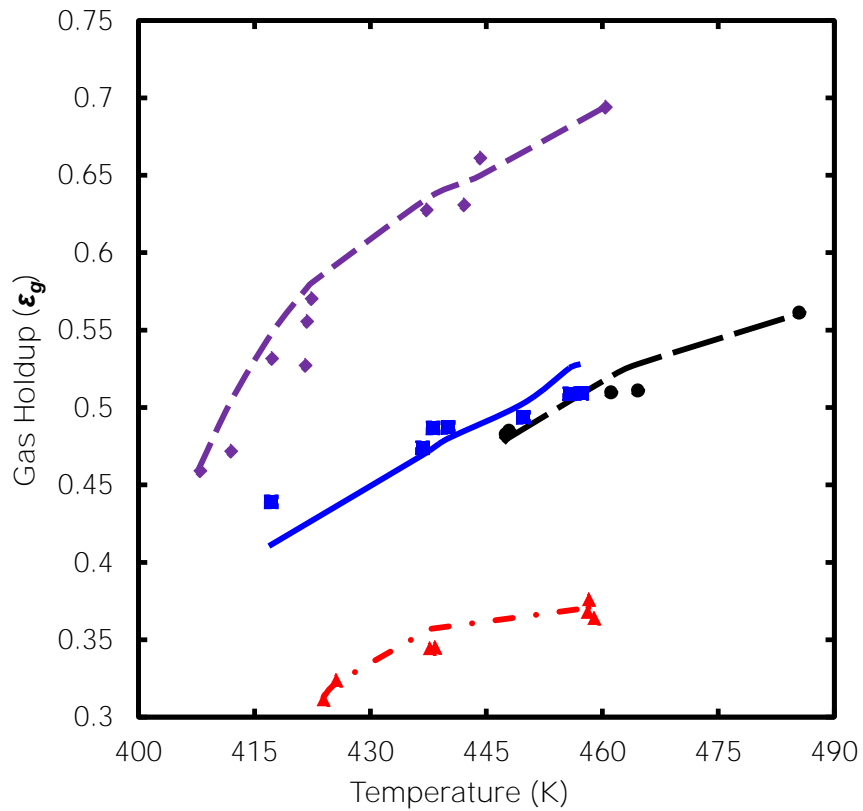


(c)

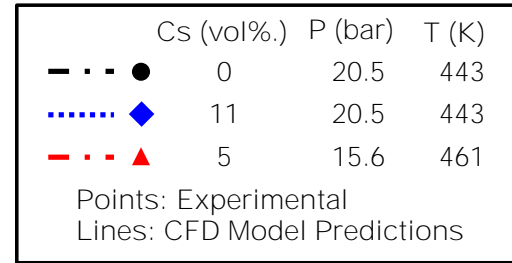
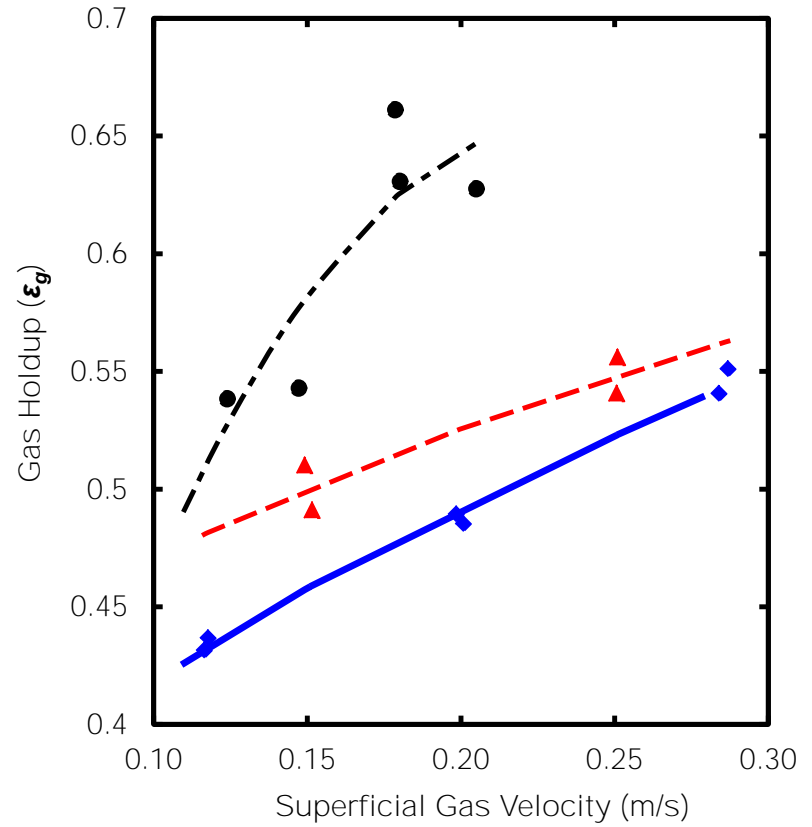
Figure 5-30: Geometry and mesh details of the numerical structure employed in our simulations: (a) Cross section view, (b) Side view in sparger vicinity, (c) Side view of whole column

5.3.5 Comparison between the CFD model predictions and our experimental data

The aim of this validation was to test our CFD model, with its optimized interphase drag coefficients, turbulence models, mesh size and structure, step size and solution method, using actual gas holdup data obtained under typical F-T conditions. All simulations were performed for a time period of 60 s with a time step of 0.01 s, which was enough to obtain quasi-steady state values of the hydrodynamic parameters. The model predictions were compared with the experimental data as shown in Figure 5-31. As can be observed in Figure 5-31 (a), our CFD model is capable of predicting the gas holdup as a function of temperature under different superficial gas velocities, solid concentrations, and pressures with an absolute averaged relative error (AARE) of 4.8%. Similarly, Figure 5-31 (b) shows that the model was able to predict the gas holdup data as a function of superficial gas velocities under different solid concentrations, temperatures and pressures with an AARE of 6.8%.



(a)



(b)

Figure 5-31: Time averaged CFD model validation vs. gas holdup data as a function of (a) temperature and (b) superficial gas velocity

Moreover, the performance of the CFD model with and without incorporating mass transfer coefficients was validated against the experimental data measured in our pilot-scale reactor at a pressure of 20.5 bars, temperature of 443 K and solid concentration of 11 vol% at different superficial gas velocities as illustrated in Figure 5-32. As can be seen in this figure, when ignoring mass transfer coefficients, the model predictions of the experimental data were with AARE of 11.1%, whereas when considering the mass transfer coefficients, the predictions were more accurate with only AARE of 1.3 %. This underscores the importance of incorporating the mass transfer coefficients in our CFD model in order to obtain precise and accurate predictions.

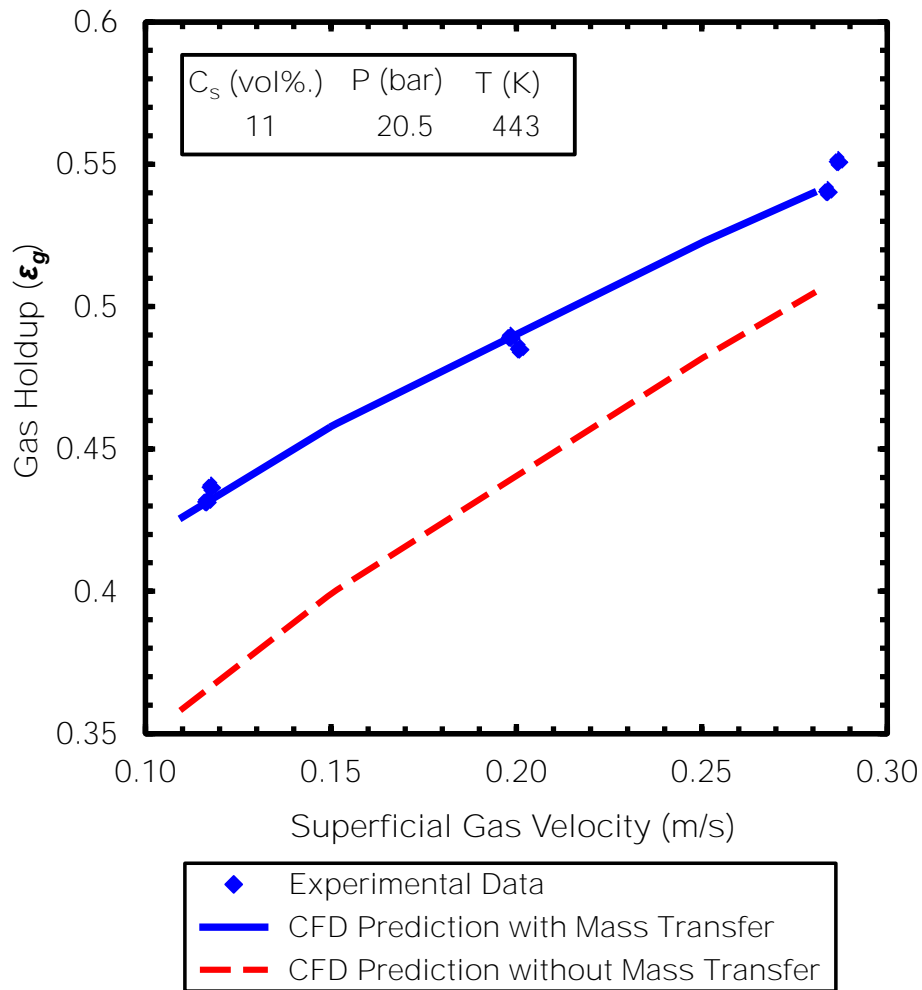


Figure 5-32: Effect of mass transfer coefficients on our CFD model predictions of the gas holdup data under different operating conditions

6.0 CFD MODEL PREDICTIONS OF THE HYDRODYNAMICS INSIDE A SBCR

Following the model testing and validation, the CFD model was used to predict the local phase holdups, liquid velocity vectors, solids distribution, axial distribution of the Sauter mean bubble diameter, and the local turbulence intensity and contours within the reactor as detailed below.

6.1 EFFECT OF THE GAS SPARGER TYPE ON THE LOCAL HYDRODYNAMICS IN THE PILOT-SCALE SBCR

Gas sparger type is an integral component in SBCRs as it can alter the bubble characteristics and consequently the gas holdup, gas-liquid interfacial area and many other parameters affecting the performance of the reactor. Some common gas spargers used in literature include perforated plates, porous plates, porous membranes, rings type distributors and multiple-arms spargers [370]. Although significant work has been done investigating bubbles formation at the orifice [371-391], the effect of sparger design on the performance of bubble columns and SBCRs has received little attention. An efficient sparger design should aim at minimizing the pressure drop across the sparger while maintaining a uniform distribution of gas bubbles at the orifices, which would translate into significant savings in operating costs and overall process energy requirements. Generally, when the diameter of the SBCR is large (> 1 m) multi-arms spiders or concentric-rings spargers are preferred over perforated plates [392]. Moreover, some studies reported that the

effects of sparger type on the gas holdup and bubble diameter were more significant at low superficial gas velocities (10 cm/sec), however, such effects become insignificant at higher superficial gas velocities or in the churn-turbulent flow regime [393, 394].

In this section, the effect of three different distributors, namely 6-arms spider, concentric-rings and perforated plate, on the gas holdup, bubble size and liquid-phase recirculation within the pilot-scale SBCR are investigated using the built CFD model. The spider-type sparger used consists of six arms, each arm has 6 orifices of 5 mm ID on each side and on the bottom, totaling 18 orifices. Thus, there are a total of 108 orifices on the 6-arms spider gas sparger. It should be emphasized that there are no orifices at the top of the arms so that the solid particles could not plug them and the gas downward jets should be able to lift any solid particles, which might settle at the bottom flange of the reactor. The gas sparger is screwed onto a 0.0254 m ID pipe to a height of 0.102 m from the top of the bottom flange. Also, its maximum height from the bottom of the reactor is about 0.152 m. A picture of the spider-type sparger is shown in Figure 6-1 and the geometry and numerical mesh details are shown in Figure 6-2.

The concentric ring sparger consists of three concentric rings with 30, 15 and 10 orifices per ring, respectively, totaling 55 identical orifices. Each orifice has an ID of 7 mm. The geometry and numerical mesh details of the concentric ring sparger are shown in Figure 6-3.

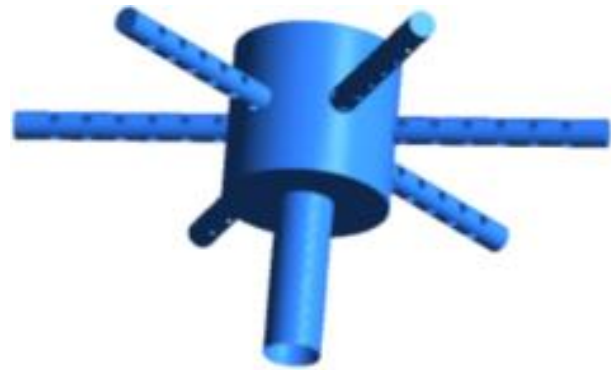
The perforated plate consists of 1580 identical orifices of 1.3 mm ID, as shown in Figure 6-4. It should be noted that the dimensions of the concentric ring and perforated plate spargers were selected such that the total orifice area for gas sparging is the same (2.12 m²). Moreover, the effect of nozzles orientation on the flow dynamics within the SBCR for both the multi-arms spider and concentric-rings sparger are investigated.

Table 6-1: Description of the spargers investigated in this work

Sparger type	Description
Spider-type sparger	Six arms, each arms has 6 orifices of 5 mm ID on each side and on the bottom, totaling 18 orifices. Thus, there are a total of 108 orifices on the gas sparger.
Concentric-rings	Three concentric-rings, with 30, 15 and 10 orifices per ring, respectively, totaling 55 identical orifices. Each orifice has an ID of 7 mm.
Perforated plate	1580 identical orifices of 1.3 mm ID

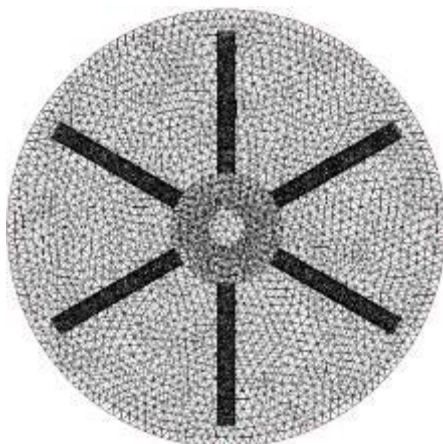


(a)

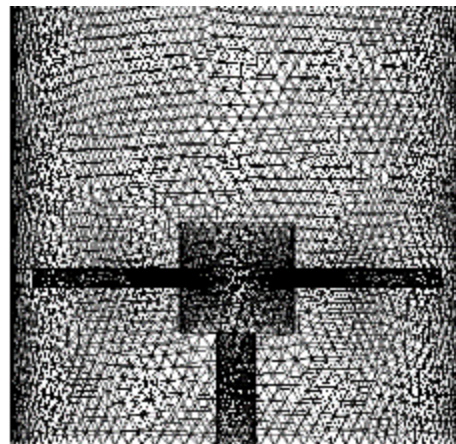


(b)

Figure 6-1: (a) Picture and (b) Constructed geometry of the spider sparger used in this study

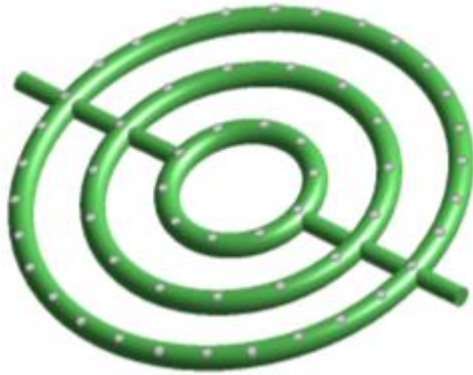


(a)

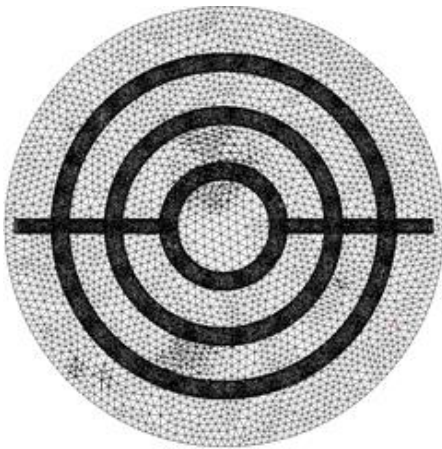


(b)

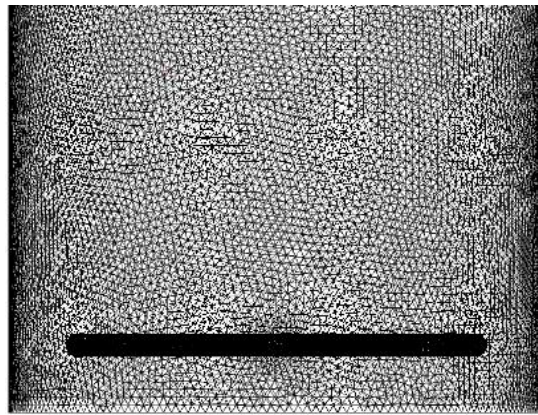
Figure 6-2: Geometry and mesh details of the spider sparger: (a) Cross-section view, (b) Side- view



(a)

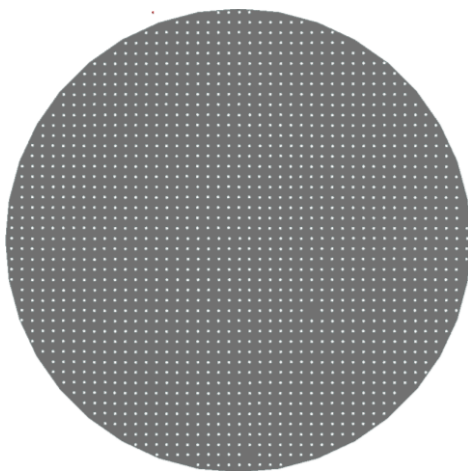


(b)

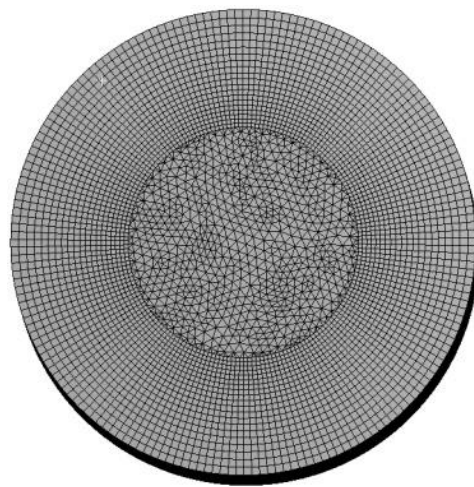


(c)

Figure 6-3: Geometry and mesh details of the concentric-rings sparger: (a) Built geometry, (b) Cross-section view of the mesh, (c) Side-view of the mesh



(a)



(b)

Figure 6-4: Geometry and mesh details of perforated plate: (a) Cross-section view, (b) Mesh structure

6.1.1 Effect of Sparger Design on the Gas Holdup Inside the Pilot-Scale SBCR

The spatial variations of the local gas holdup in the SBCR give rise to the local pressure variations, which induce liquid recirculations inside the reactor. These liquid recirculations are crucial as they govern the rate of mixing, affecting the heat and mass transfer characteristics. Our CFD model predictions illustrated in Figures 6-5, 6-6 and 6-7 for the spider, concentric-rings and perforated plate spargers, respectively, show several snapshots of the gas holdup inside the reactor at different times of 1, 20, 40 and 60 s. Also, Figures 6-8 to 6-14 compare the radial gas holdup profiles while using the three spargers at H/D values of 0.5, 1, 2, 3, 5 and 7, respectively. These data were obtained using an inlet superficial gas velocity of 0.20 m/s at temperature of 443 K, pressure of 20.5 bar and catalyst concentration of 11 vol%. Under these operating conditions, the overall gas holdup in the SBCR were 0.42, 0.36 and 0.45 for the spider, concentric-rings and perforated plate, respectively.

As can be seen in these figures, the gas holdups obtained using the three spargers vary with the axial and radial positions in the SBCR and the radial gas holdup exhibits a non-linear behavior at any axial position as illustrated by the gradual variation in the color shades of the gas holdup from the center to the wall of the reactor. It should be pointed out that the maximum gas holdup value can be mainly seen near the center of the reactor before it gradually decreases along the radii with various profiles in the axial direction. Also, the 6-arms spider and concentric-rings spargers showed distinctly steeper radial gas holdup profiles, whereas, the perforated plate showed a more uniform gas holdup distribution, which reached the steady-state much sooner than the other two spargers.

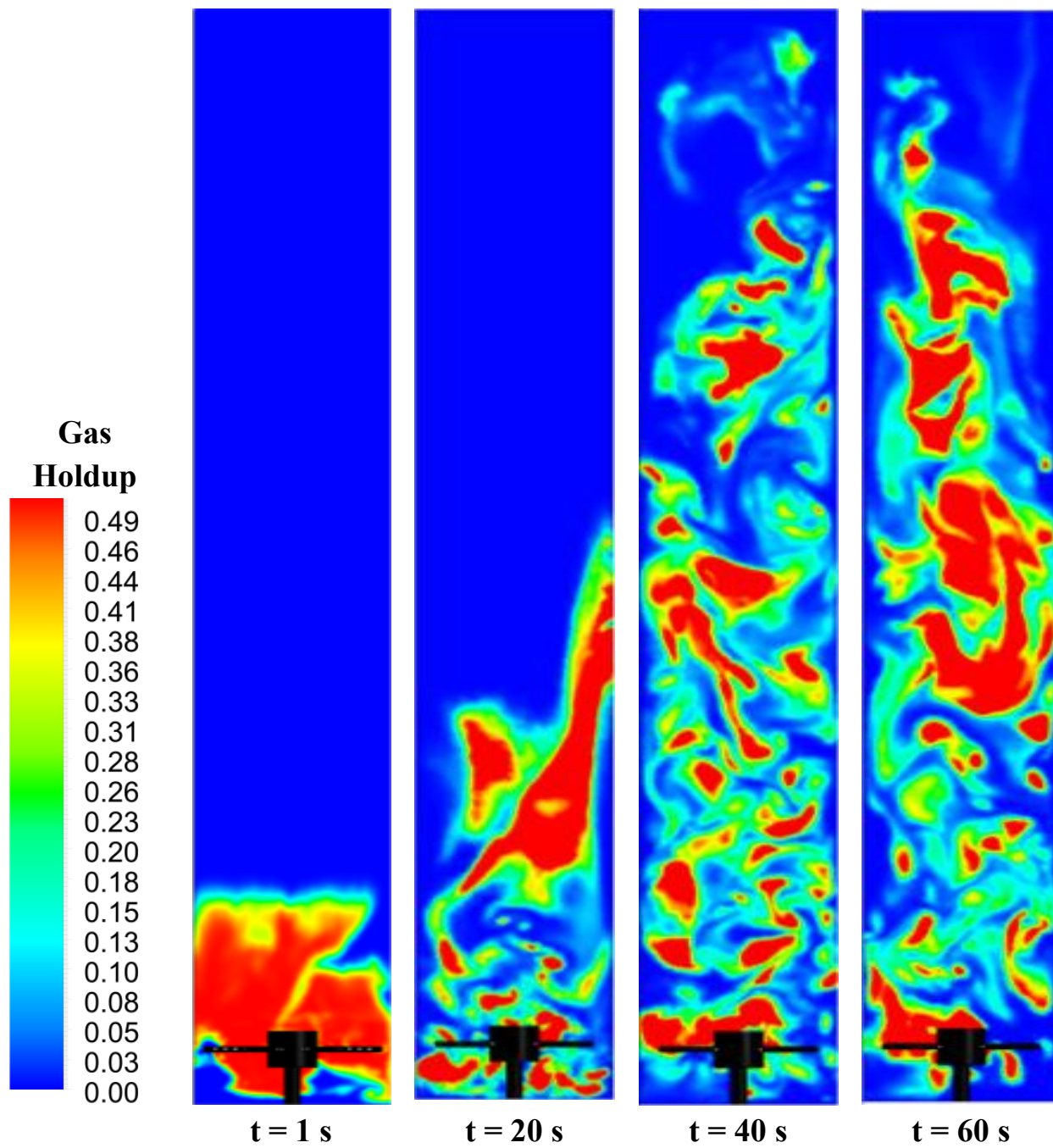


Figure 6-5: Snapshots of gas holdup contours at different times for the spider sparger

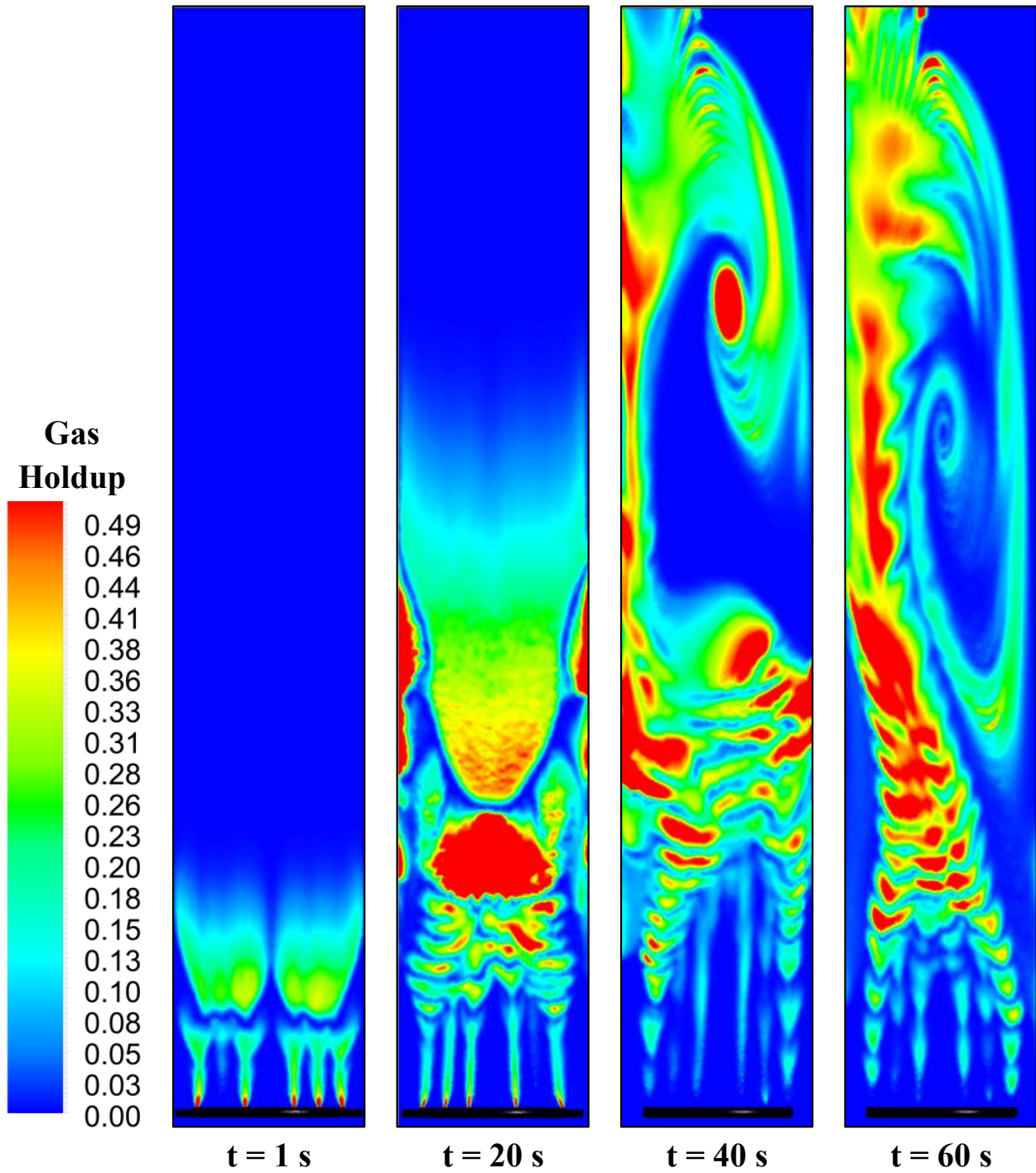


Figure 6-6: Snapshots of gas holdup contours at different times for the concentric-rings sparger

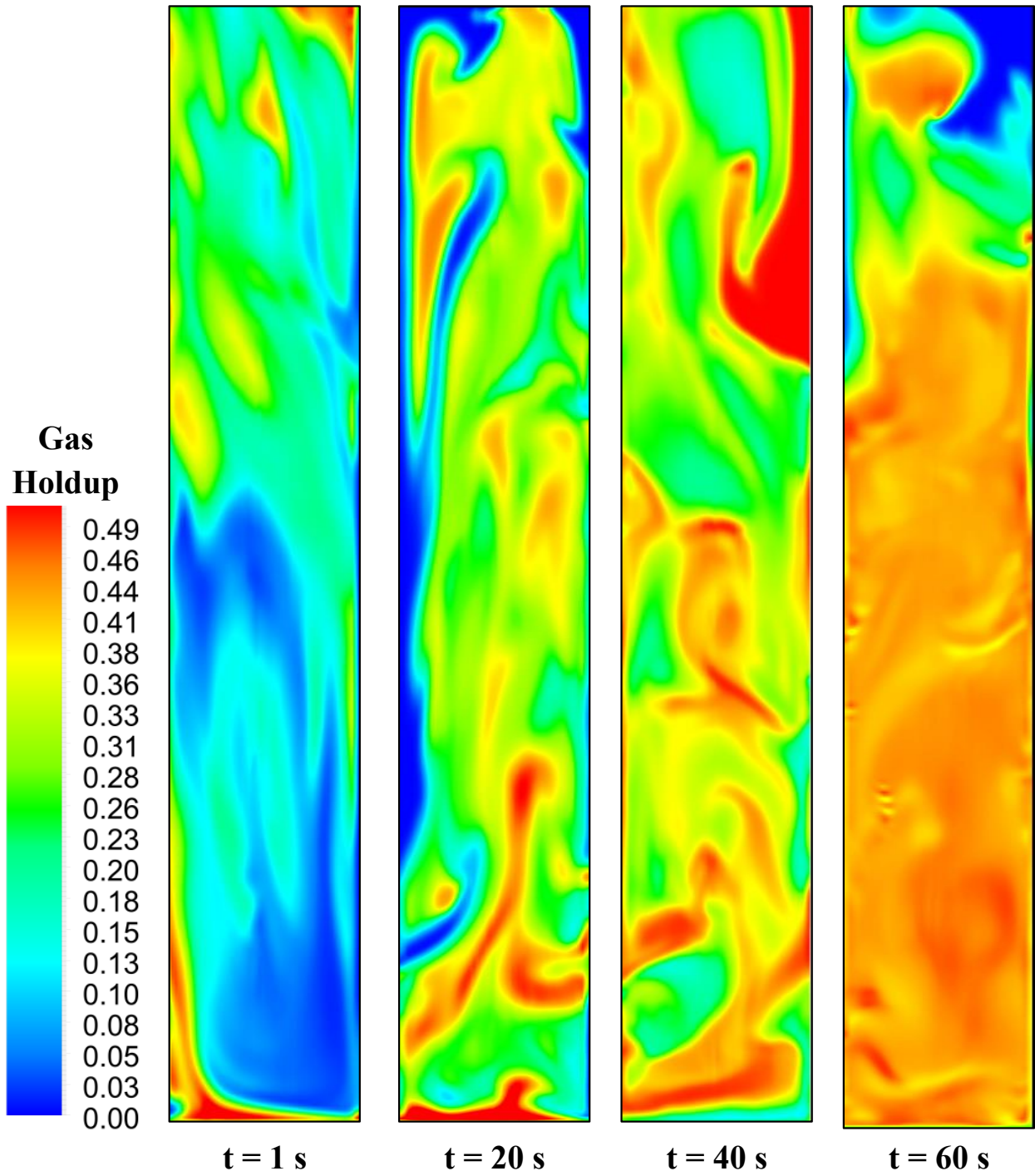


Figure 6-7: Snapshots of gas holdup contours at different times for the perforated plate

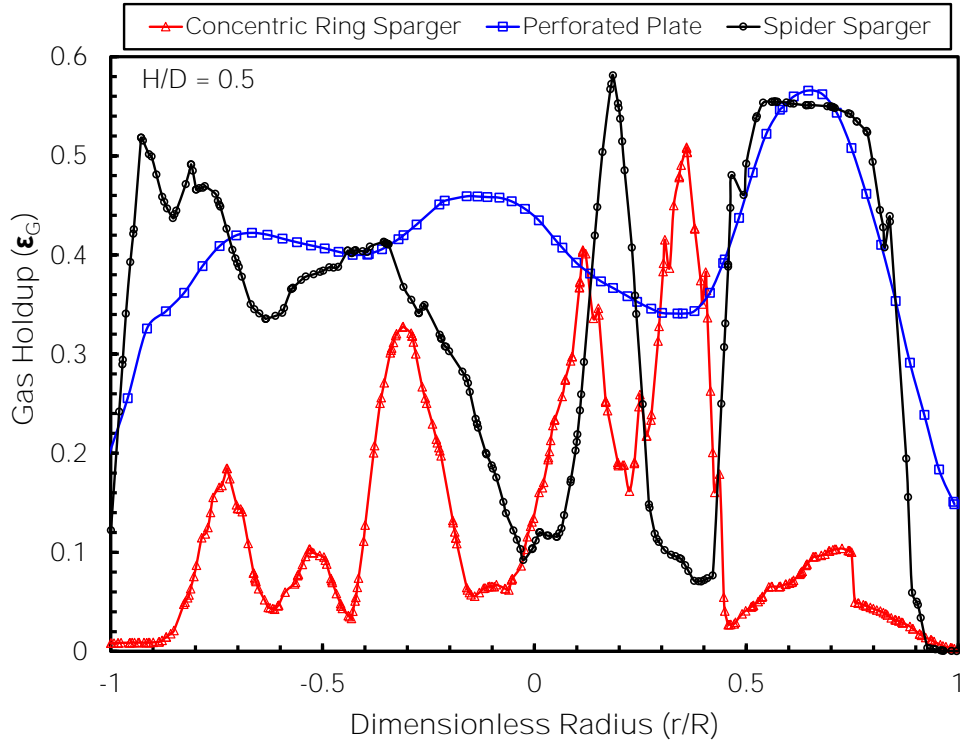


Figure 6-8: Comparison of time averaged radial profiles of gas holdup at $H/D = 0.5$ for the three gas spargers used

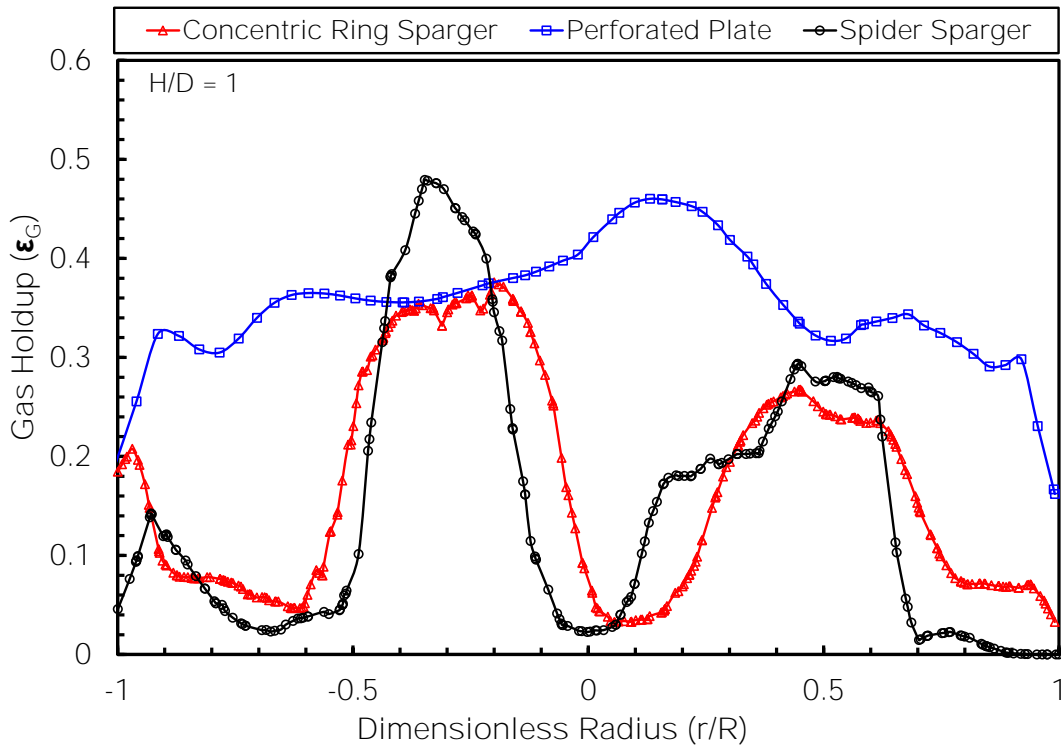


Figure 6-9: Comparison of time averaged radial profiles of gas holdup at $H/D = 1$ for the three gas spargers used

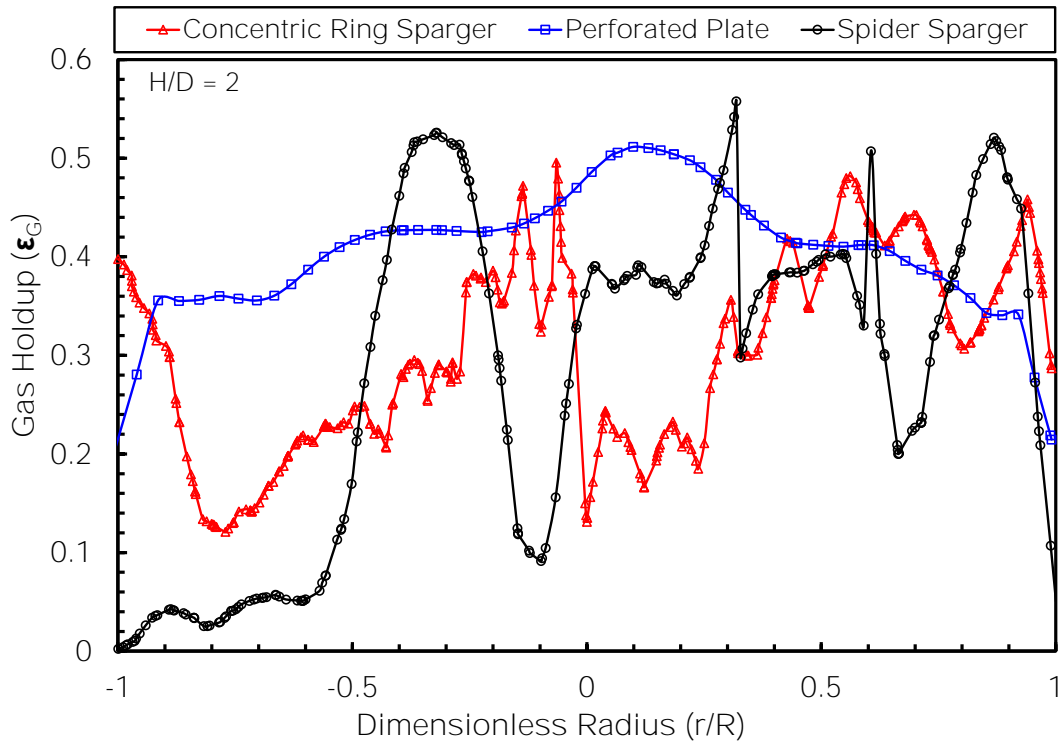


Figure 6-10: Comparison of time averaged radial profiles of gas holdup at $H/D = 2$ for the three gas spargers used

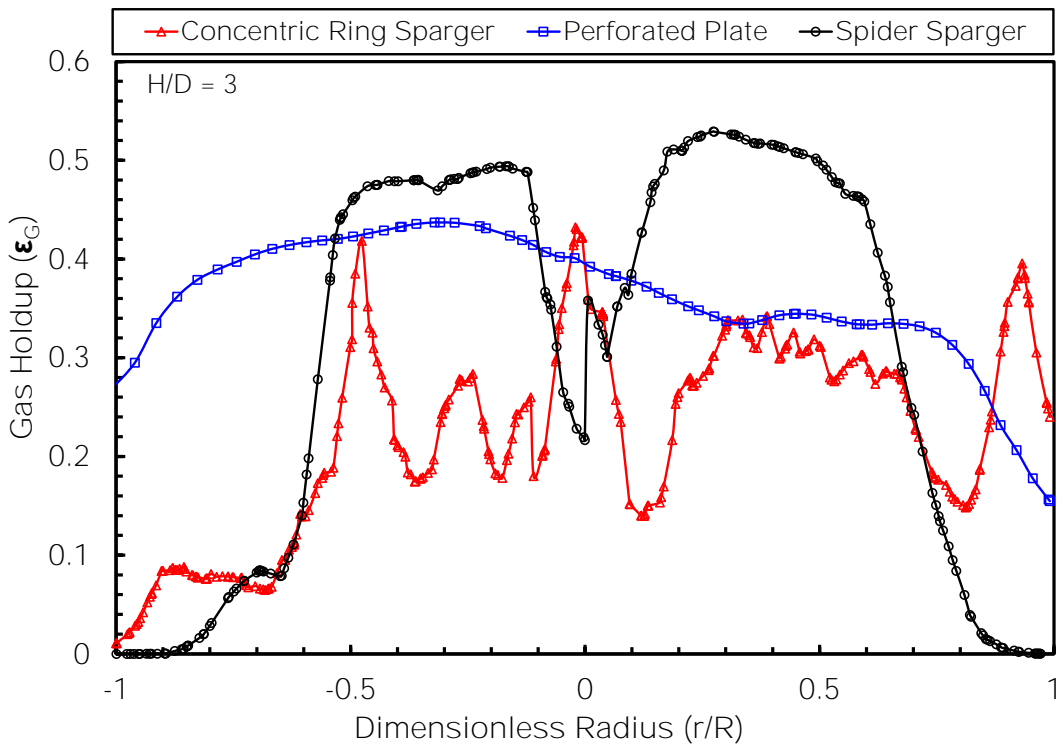


Figure 6-11: Comparison of time averaged radial profiles of gas holdup at $H/D = 3$ for the three gas spargers used

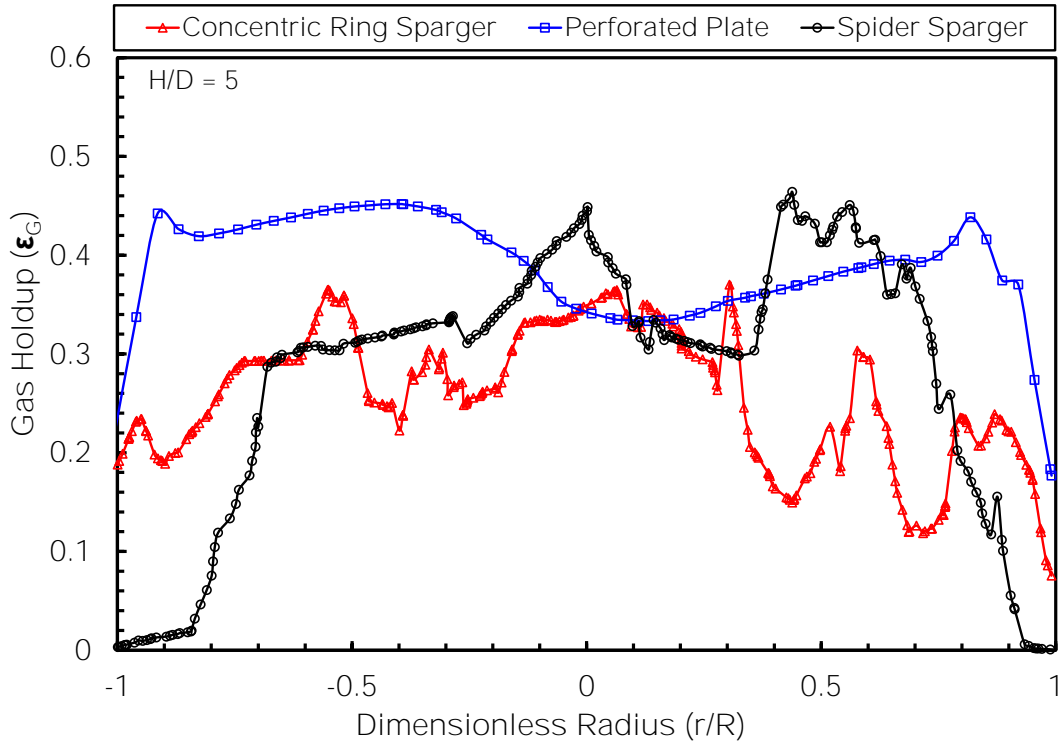


Figure 6-12: Comparison of time averaged radial profiles of gas holdup at $H/D = 5$ for the three gas spargers used

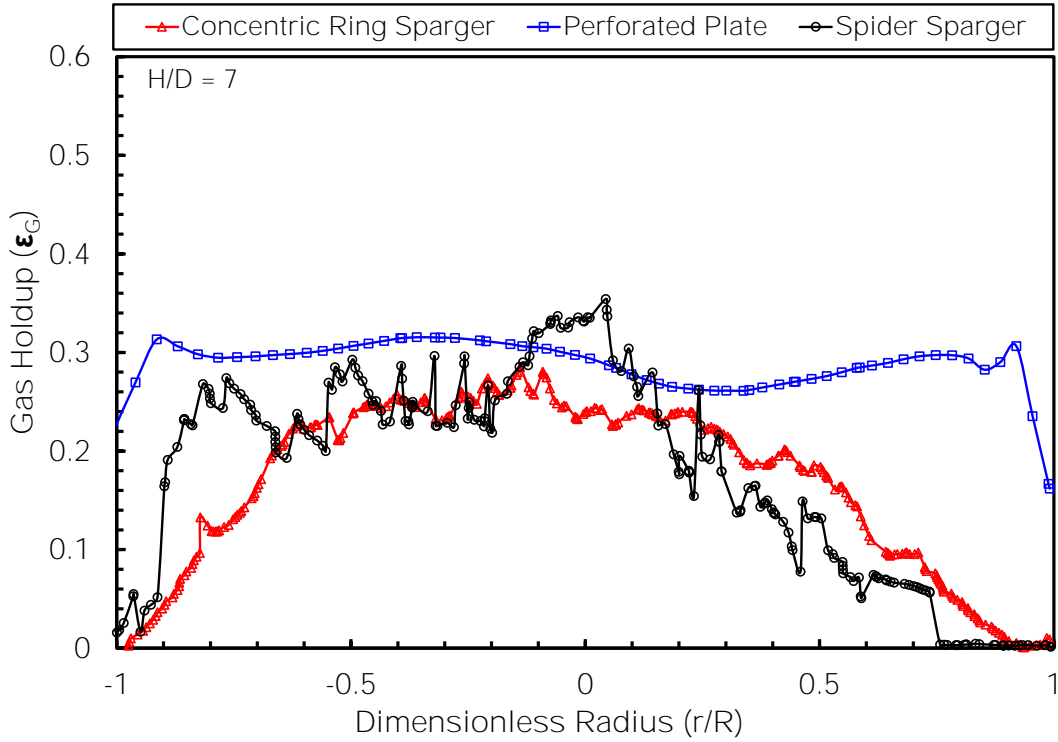


Figure 6-13: Comparison of time averaged radial profiles of gas holdup at $H/D = 7$ for the three gas spargers used

6.1.2 Effect of Sparger Design on the Liquid Recirculations inside the SBCR

The CFD model was also used to predict the liquid circulations as shown in Figures 6-14, 6-15 and 6-16 for the 6-arms spider, concentric-rings and perforated plate, respectively, which shows snapshots of liquid velocity vectors in the SBCR at 1, 20, 40 and 60 s. In general, these figures show strong liquid recirculations and backmixing are present near the reactor walls because the liquid-phase rises upward with the gas bubbles at the center of the reactor and then flows downward near the reactor wall.

Figure 6-14 shows that for the 6-arms spider sparger, smaller and faster liquid recirculation cells are present in the vicinity of the sparger from the startup until the steady-state. Also, larger and slower liquid recirculation cells appeared after about 0.36 m measured from the bottom flange. These smaller and faster liquid recirculations in the vicinity of the sparger are primarily due to the geometry of this sparger type because all gas sparging orifices are located on the sides and bottom and none on the top of each sparger arms.

Figures 6-15 and 6-16 show that for the concentric-rings and perforated plate spargers, only large and slow recirculation cells are present throughout the column above the distributor zone, which is in contrast with liquid velocity vectors observed when using the 6-arms spider, Figure 6-14.

It is important to mention also that the CFD model predictions indicated that the solid-phase velocity vectors followed very closely those of the liquid-phase, which is due primarily to the small particle-liquid slip velocity.

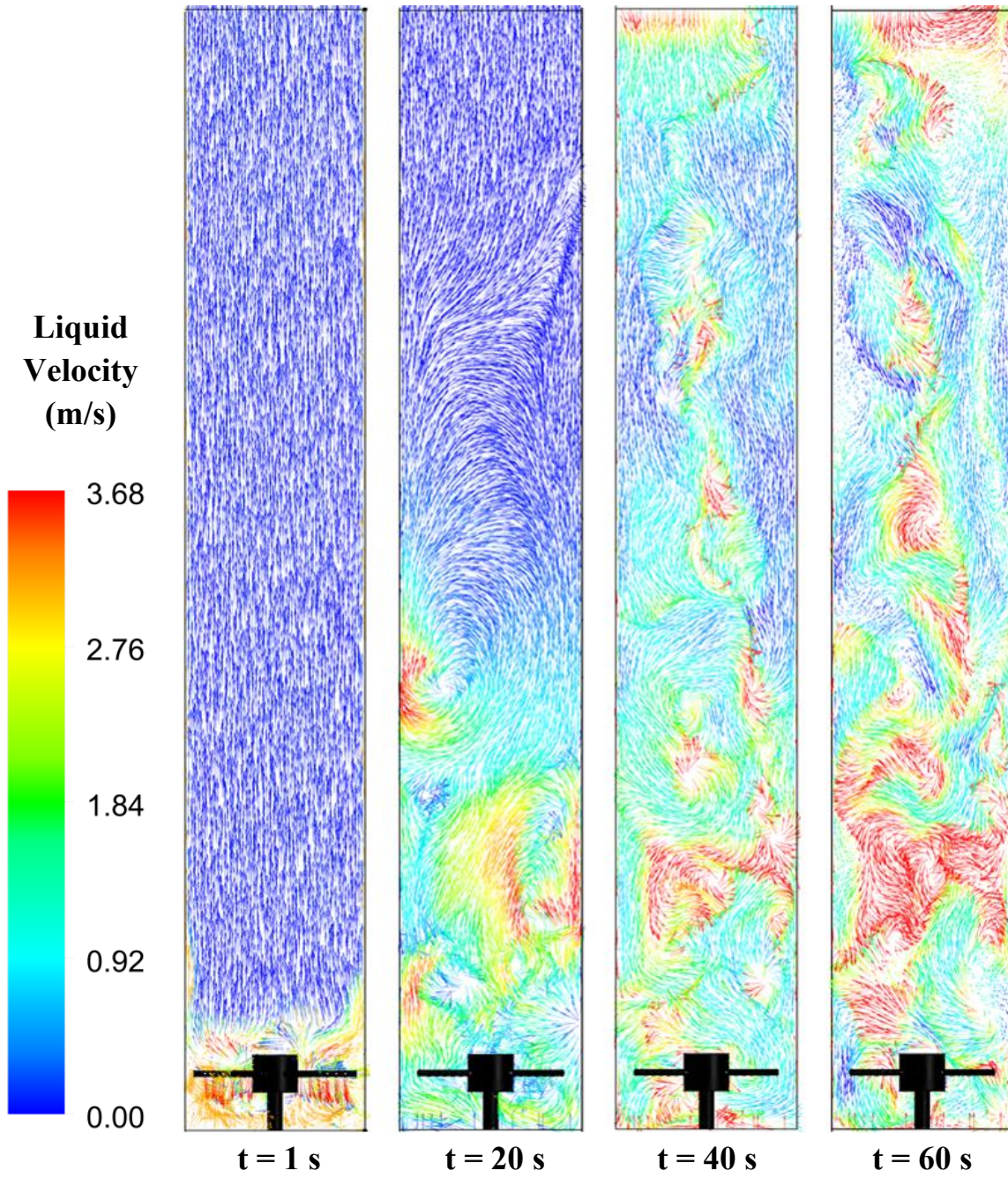


Figure 6-14: Snapshots of liquid velocity vectors at different times for the spider sparger

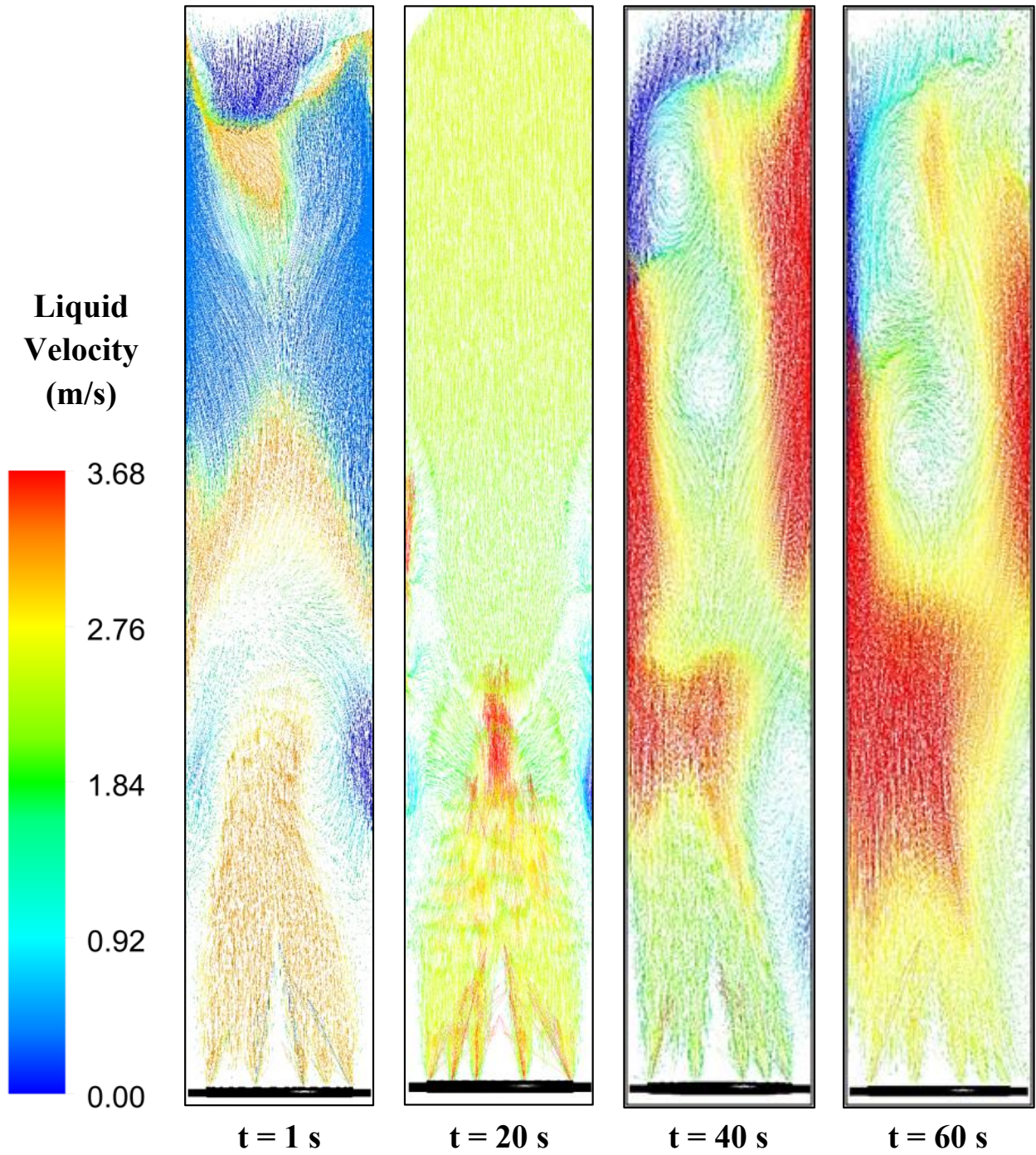


Figure 6-15: Snapshots of liquid velocity vectors at different times for the concentric-rings sparger

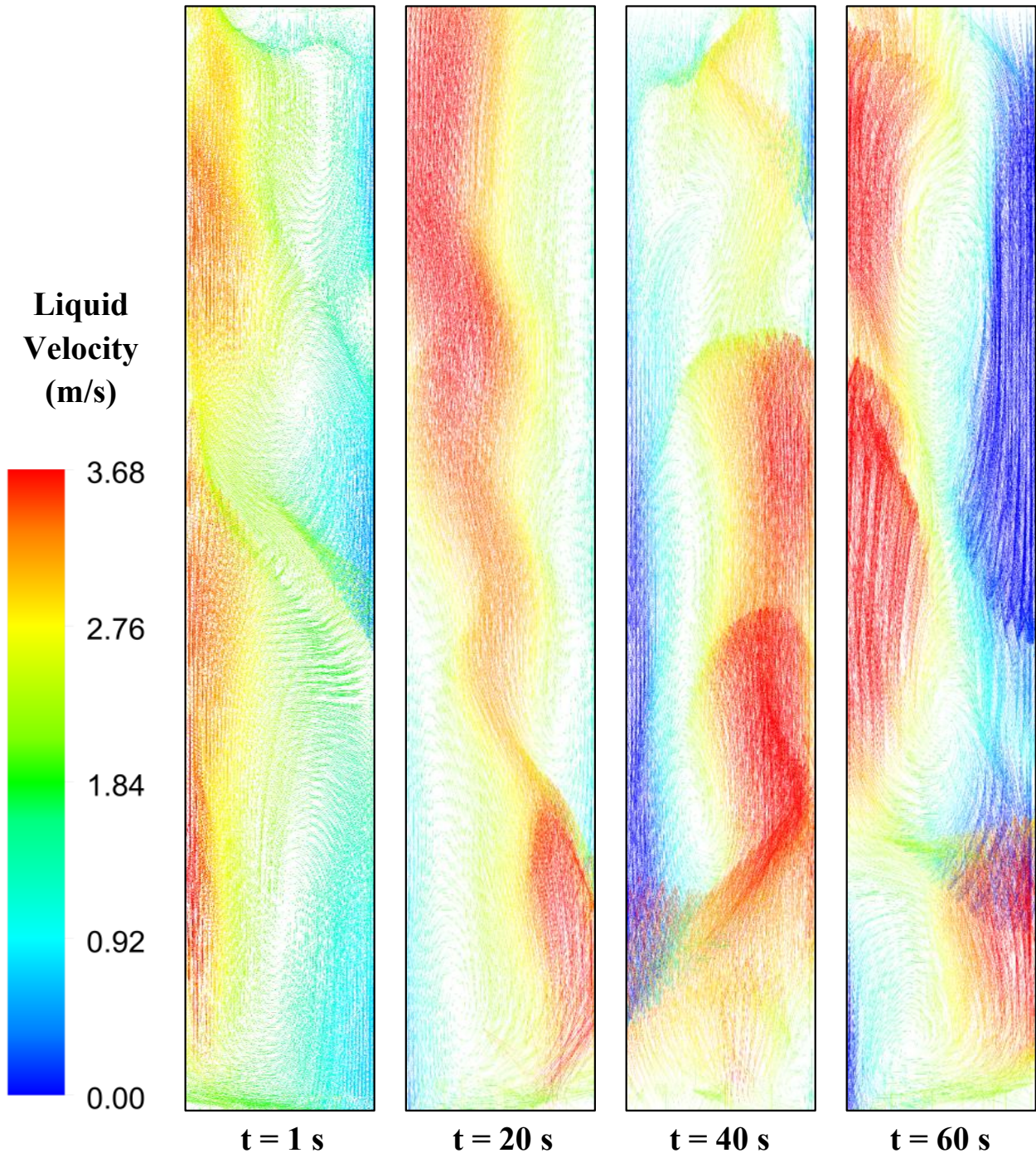


Figure 6-16: Snapshots of liquid velocity vectors at different times for the perforated plate

6.1.3 Effect of Sparger Design on the Liquid Turbulence Intensity inside the SBCR

The CFD model was also used to predict the turbulence intensity profiles inside the pilot-scale SBCR using the three different spargers. The turbulence intensity is defined as the root-mean-square of the velocity fluctuations to the mean flow velocity. It is expressed as:

$$I = \frac{u'}{U} = \frac{\sqrt{\frac{1}{3}(u_x'^2 + u_y'^2 + u_z'^2)}}{\sqrt{U_x^2 + U_y^2 + U_z^2}} \quad (6-1)$$

In general, a turbulence intensity of $\leq 1\%$ is considered low and that of $\geq 10\%$ is considered high [395]. The CFD model turbulence intensity predictions for the 6-arms spider, concentric-rings and perforated plate are shown in Figures 6-17, 6-18 and 6-19, respectively. As can be seen in these figures, the turbulence intensities for the three spargers throughout the reactor appear to increase with time.

Figure 6-17 shows that for the 6-arms spider, relatively high liquid turbulence intensities can be observed in the vicinity of the sparger during the startup time, however, after reaching steady-state, the turbulence intensities become more evenly distributed throughout the reactor. Figure 6-18 shows that for the concentric-rings sparger, the turbulence intensities are more uniform throughout the reactor during the first 40 s, however, their values increase drastically near the walls at 60 s, due to the development of large recirculation cells as shown in Figure 6-15. On the other hand, Figure 6-19 shows that the perforated plate exhibits higher turbulence intensities throughout the reactor with higher values near the top after 40 s, which is different from those shown using the other two spargers.

Thus, the CFD model confirmed that the sparger design and configuration have significant impact on the local hydrodynamics. This is a critical criterion for optimizing mixing characteristics inside the SBCR, which directly impact its overall performance.

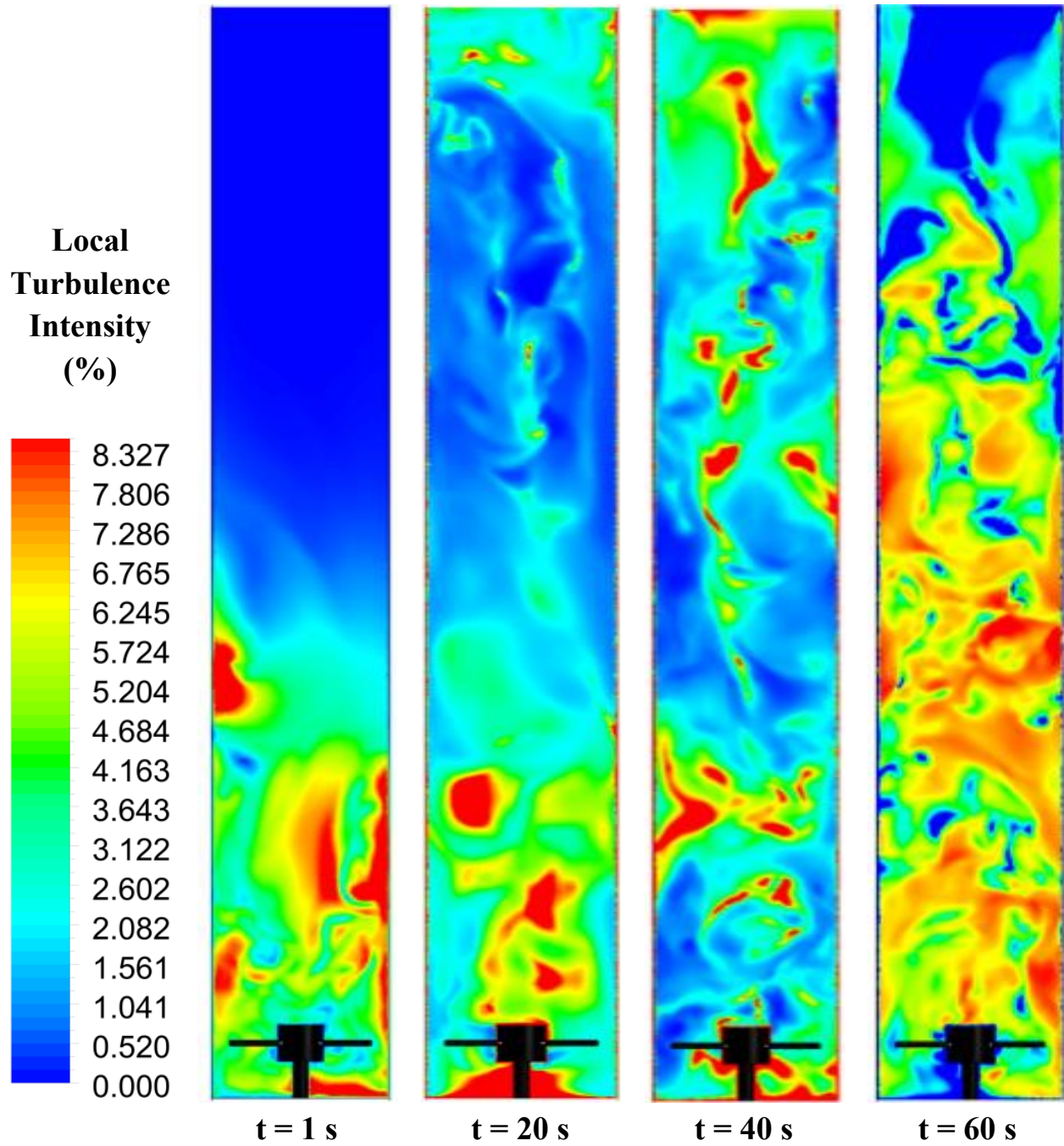


Figure 6-17: Snapshots of local turbulence intensity contours at different times for the spider sparger

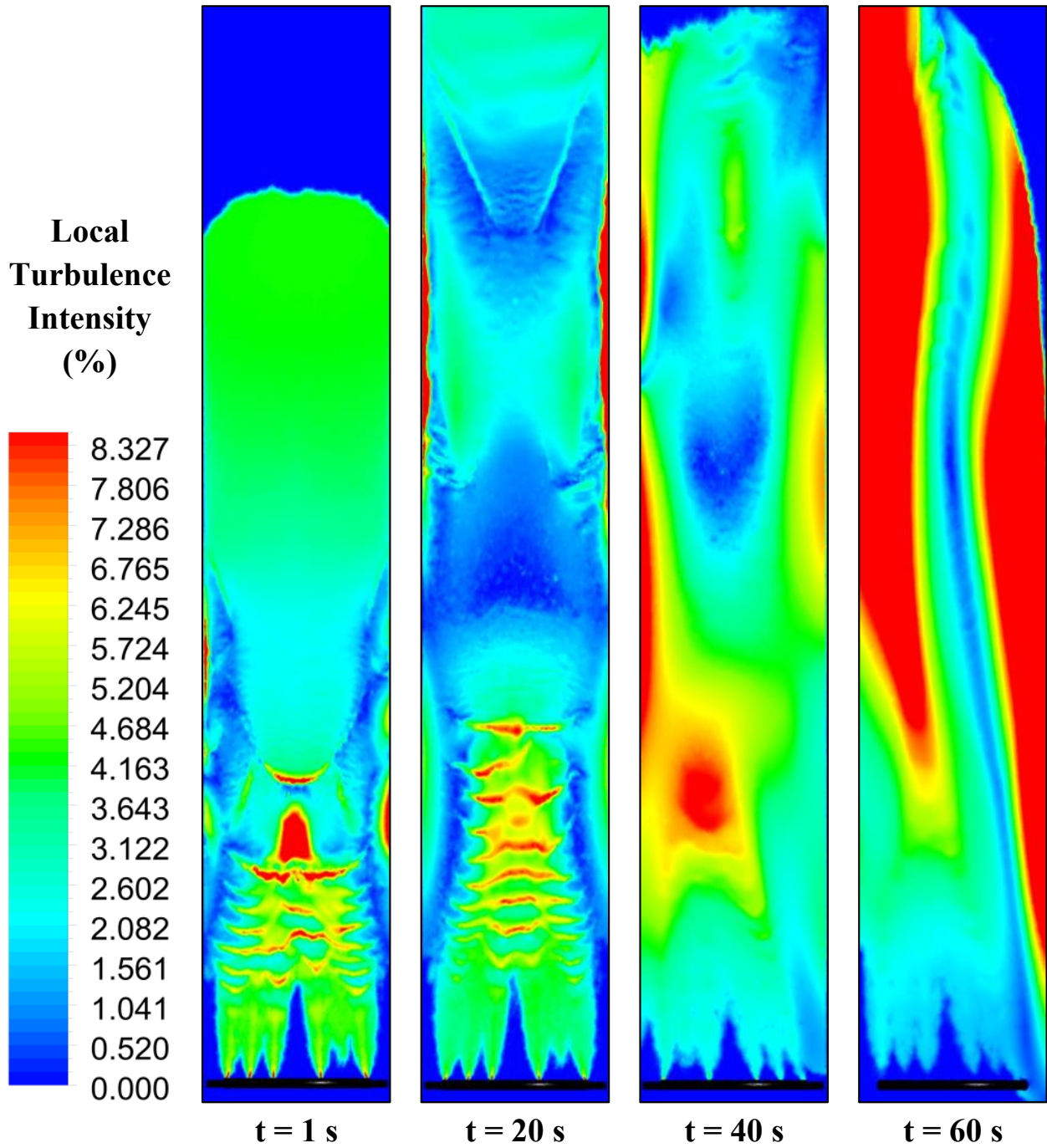


Figure 6-18: Snapshots of local turbulence intensity contours at different times for the concentric-rings sparger

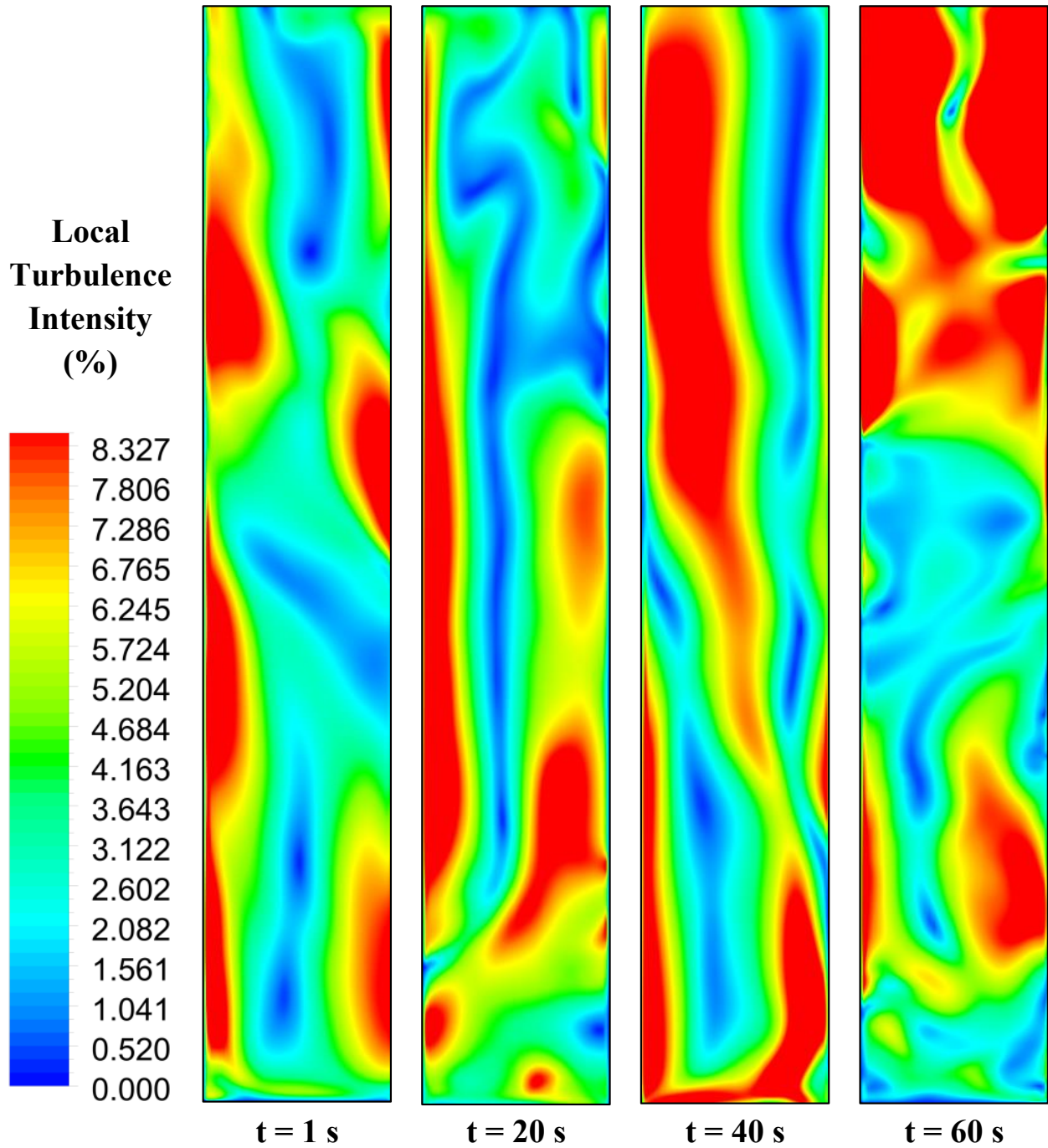


Figure 6-19: Snapshots of local turbulence intensity contours at different times for the perforated plate

6.1.4 Effect of Sparger Orifices Orientation on the Local Hydrodynamics in the SBCR

The effect of the sparger nozzles orientation on the overall gas holdup and the axial solids dispersion was investigated using our CFD model. The 6-arms spider sparger similar to that shown in Figure 6-1, provided with upward pointing orifices and the concentric-rings sparger shown in Figure 6-3 with downward pointing orifices were used in this investigation. The effect of the sparger design and orientation on the overall gas holdup, axial solid loadings and axial bubble size variation were investigated using three different superficial gas velocities of 0.1, 0.2 and 0.3 m/s at temperature of 443 K, pressure of 20.5 bar and catalyst concentration of 11 vol%.

A sparger with downward pointing orifices or nozzles is expected to be more effective in solids dispersion in a SBCR when compared with a similar sparger provided with upward pointing orifices or nozzles. It is argued that the gas jets from downward facing orifices or nozzles provide the agitation to facilitate solids dispersion. Also, the sparger used definitely determines the bubble sizes observed in the reactor, hence small orifices or nozzles enable the formation of small gas bubbles.

A general rule-of-thumb used for the determination of the effect of sparger design on the bubble size in a SBCR is given in Equation (6-2) [393, 394]. For the experimental conditions used in this study, this rule seems to hold only at high solid concentrations and superficial gas velocities > 0.2 m/s as shown in Figure 6-20. Nonetheless, at low solid concentrations or low superficial gas velocities, the effect of sparger type will remain significant.

$$EöFr^{0.5} > 16 \quad (6-2)$$

Where

$$E\ddot{o} = \frac{\Delta\rho g d_o^2}{\sigma} \quad (6-3)$$

$$Fr = \frac{U_G^2}{\sqrt{g d_o}} \quad (6-4)$$

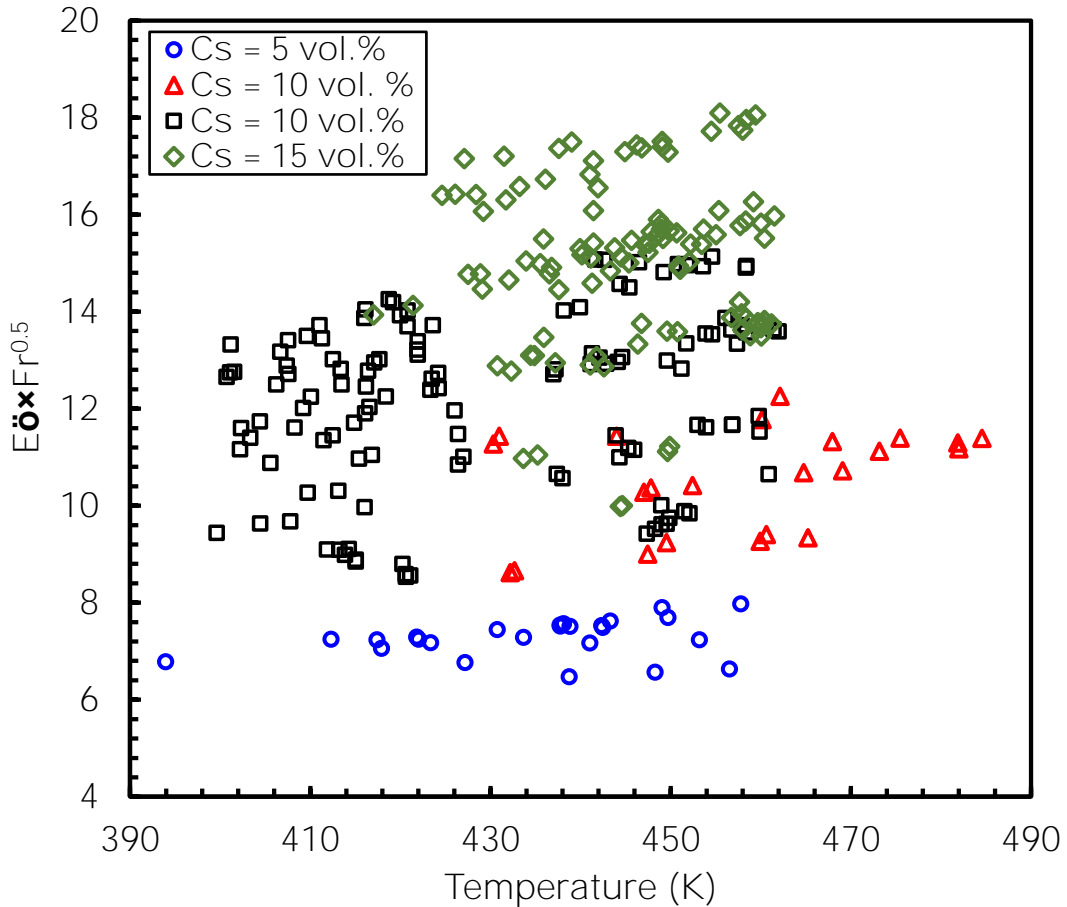


Figure 6-20: Effect of temperature on $E\ddot{o}Fr^{0.5}$ under the experimental conditions used in this study

(NICE reactor wax, $P = 4-31$ bar, $T = 380-500$ K, $u_G = 0.1-0.3$ m/s, and $C_s = 5-15$ vol.%)

Figure 6-21 shows the effect of the 6-arms sparger orifice orientations on the overall gas holdup at different superficial gas velocities. As can be observed in this figure, both the upward and downward 6-arms spider orifice orientations give higher gas holdup values when compared with those of the concentric-rings spargers. The 6-arms spider with upward facing orifices resulted in the highest gas holdups. However, at low superficial gas velocities ($u_G < 0.15$ m/s), the concentric-

rings sparger with downward facing orifices gives higher gas holdup values than those using the sparger provided with upward facing orifices.

Figure 6-22 shows the effect of the sparger orifice orientations on the Sauter mean bubble diameter (d_{32}) at different superficial gas velocities. As can be observed in this figure, the concentric-rings spargers resulted in greater d_{32} when compared with those of the 6-arms spider, which can be attributed to the larger orifice size (7 mm ID) for the concentric-rings sparger versus 5 mm ID for the 6-arms spider. The effect of the superficial gas velocity on the d_{32} obtained with the 6-arms spider was insignificant, which is in agreement with the experimental data presented in Section 5.3.3.4. The effect of superficial gas velocity on the d_{32} , however, was more significant for the concentric-rings upward facing orifices sparger as a result of the turbulent eddies created, which enhanced the bubbles coalescence. This is because bubbles coalescence and breakup mechanisms is primarily governed by the turbulent eddies, which in turn, are controlled by the liquid and gas velocities [288]. The bubble breakup, however, is governed by the turbulent stresses, which are controlled by the pressure variations within the fluid and subsequently are related to the physical property gradients within the continuous-phase [348]. This behavior also explains why the temperature changes, affecting the physical properties, have a stronger influence on bubbles breakup than on the bubbles coalescence.

Figures 6-23 to 6-25 show the effects of the sparger orifices orientations on the axial solid concentration profiles at superficial gas velocities of 0.1, 0.2 and 0.3 m/s, respectively. As can be seen in these figures, the downward facing orifices spargers give a more uniform axial solids distribution, whereas, the upward facing orifices spargers result in a solid accumulation near the bottom of the reactor. Actually, high solid concentrations (up to 17.2 vol %) can be seen at the

bottom of the reactor at superficial gas velocity 0.2 m/s, leading to lower solid concentrations above and far from the sparger.

It is important to note that the concentric-rings sparger with upward facing orifices resulted in higher solid concentrations at the bottom of the reactor when compared with those of the 6-arms spider with upward facing orifices. This behavior could be due to the fact that the 6-arms spider has also nozzles on the sides of each arms, which helped in enhancing mixing around this sparger. The effect of sparger orifices orientation on the axial solids distribution profile at an axial position (z) to the total height (H) ratio (z/H) greater than 0.2 appear to decrease with increasing the superficial gas velocity. Generally, the spargers with downward facing orifices were more effective in solids distribution when compared with those with upward facing orifices. This is due to the increased mixing provided by the gas jets from the downward facing orifices, which increased the solid particles distribution.

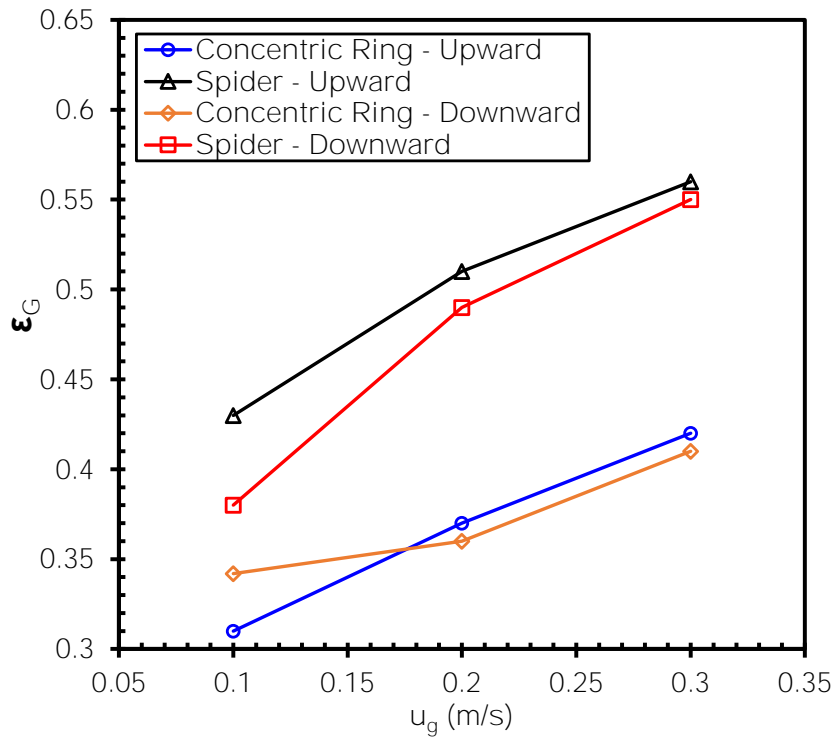


Figure 6-21: Effect of sparger type and nozzles orientation on the gas holdup at different superficial gas velocities

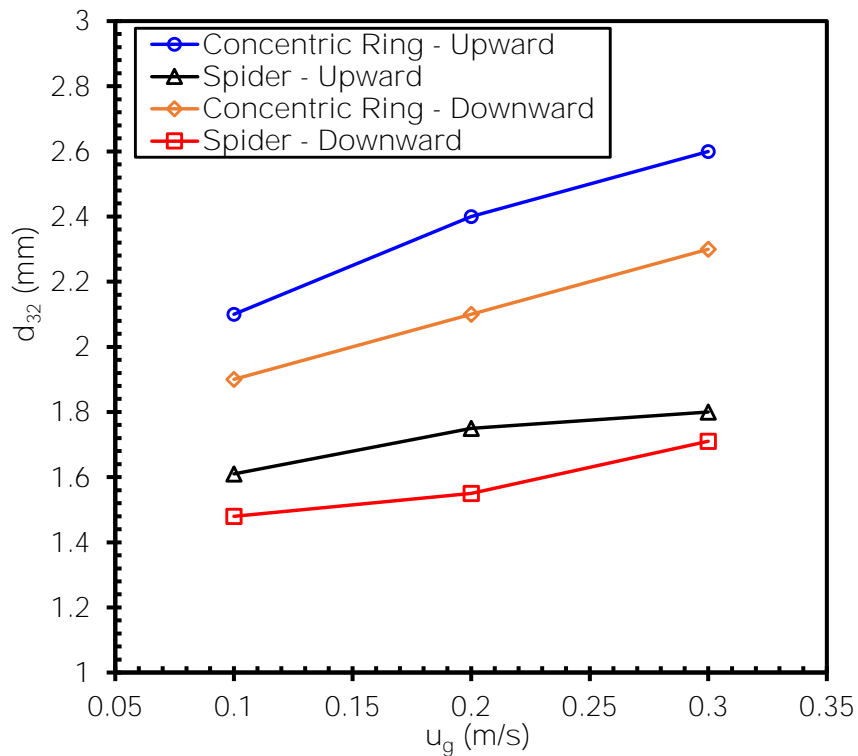


Figure 6-22: Effect of sparger type and nozzles orientation on the Sauter bubble diameter at different superficial gas velocities

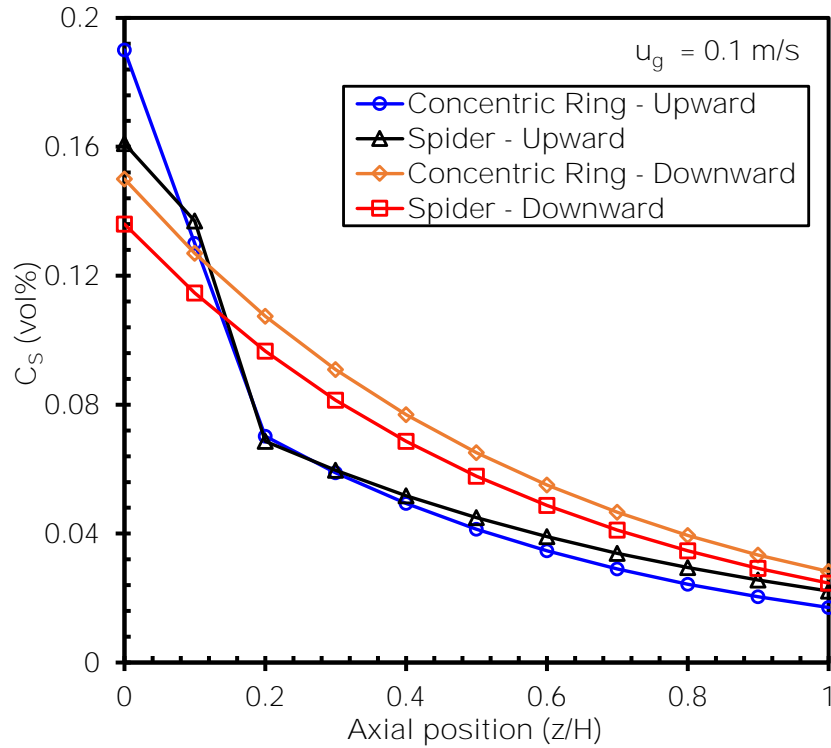


Figure 6-23: Comparison of axial solid loadings for different sparger nozzle orientations at $U_G = 0.1 \text{ m/s}$

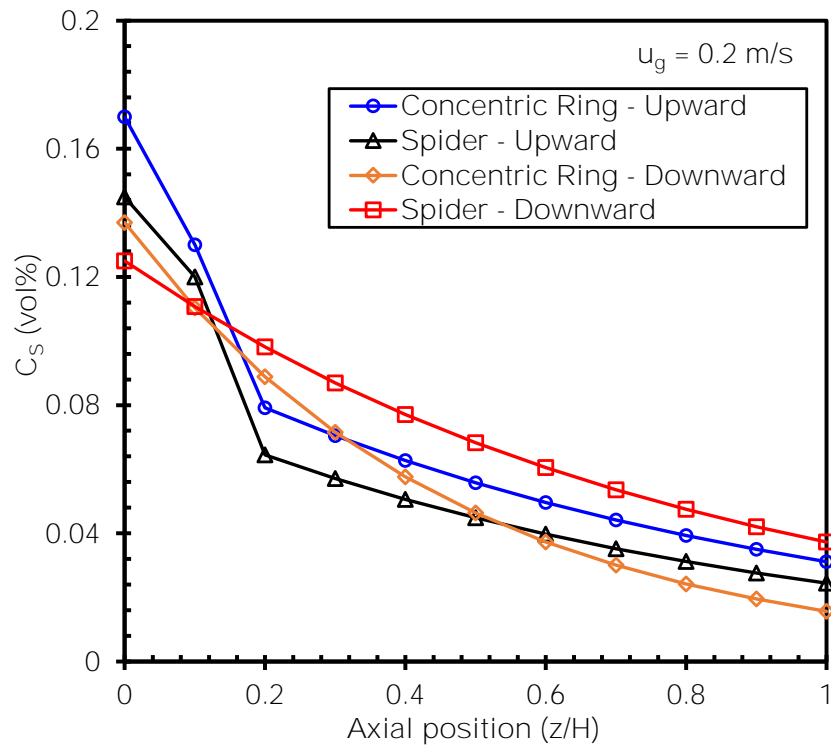


Figure 6-24: Comparison of axial solid loadings for different sparger nozzle orientations at $u_g = 0.2 \text{ m/s}$

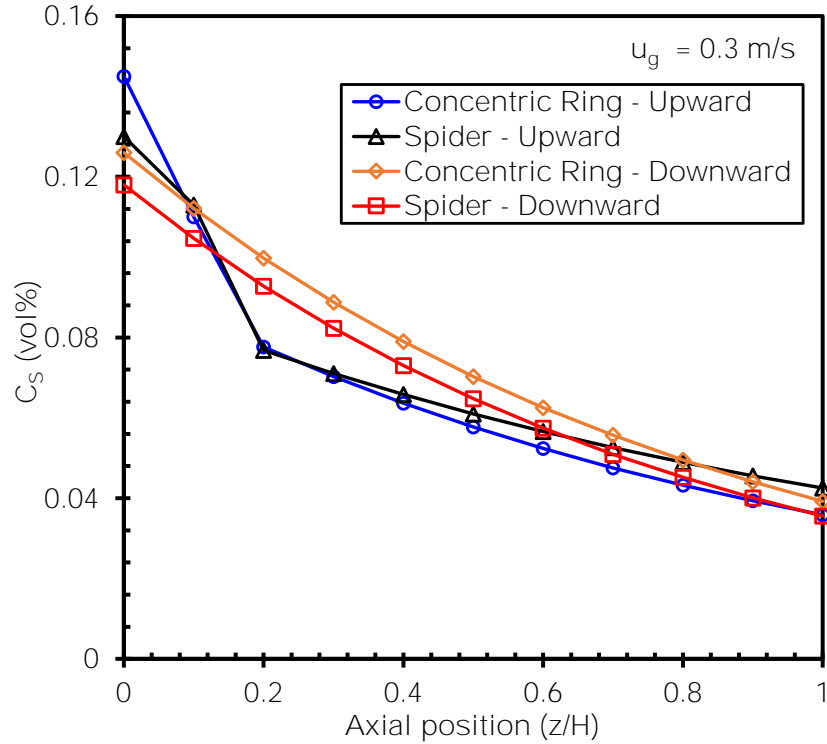


Figure 6-25: Comparison of axial solid loadings for different sparger nozzle orientations at $u_g = 0.3$ m/s

Basha et al. [2] classified the different liquid recirculation profiles typically observed in bubble columns and SBCRs into three patterns as discussed in Section 2.5.2. Pattern (a) is characterized by large segmented liquid recirculations along the height of the reactor, pattern (b) is characterized by a single large liquid recirculation flow structure across the entire reactor, and pattern (c) is characterized by smaller and faster liquid recirculations throughout the reactor.

The CFD model predictions of the mean axial velocity profiles in the SBCR are presented in Figures 6-26 through 6-28 for the different gas spargers used at a superficial gas velocity of 0.2 m/s for height to diameter ratios (H/D) of 1, 3 and 6, respectively. As can be observed in these figures, the sparger design and orifices orientation appear to significantly affect the mean axial velocity profiles throughout the entire length of the reactor. Thus, the previous claims that the sparger design has no effect on the flow structure at high superficial gas velocities in bubble

columns and SBCRs, which were based on experiments conducted at ambient temperature [393, 394], are not applicable to the SBCRs operating under typical Fischer-Tropsch conditions.

Furthermore, these figures show that the concentric-rings and the 6-arms spider with downward facing orifices exhibit flow profiles which are similar to the circulation pattern (c). Also, the concentric-rings and 6-arms spider spargers with upward facing orifices follow the circulation pattern (a). It should be mentioned, however, that the perforated plate exhibited a unique flow profile, which follows the circulation pattern (b).

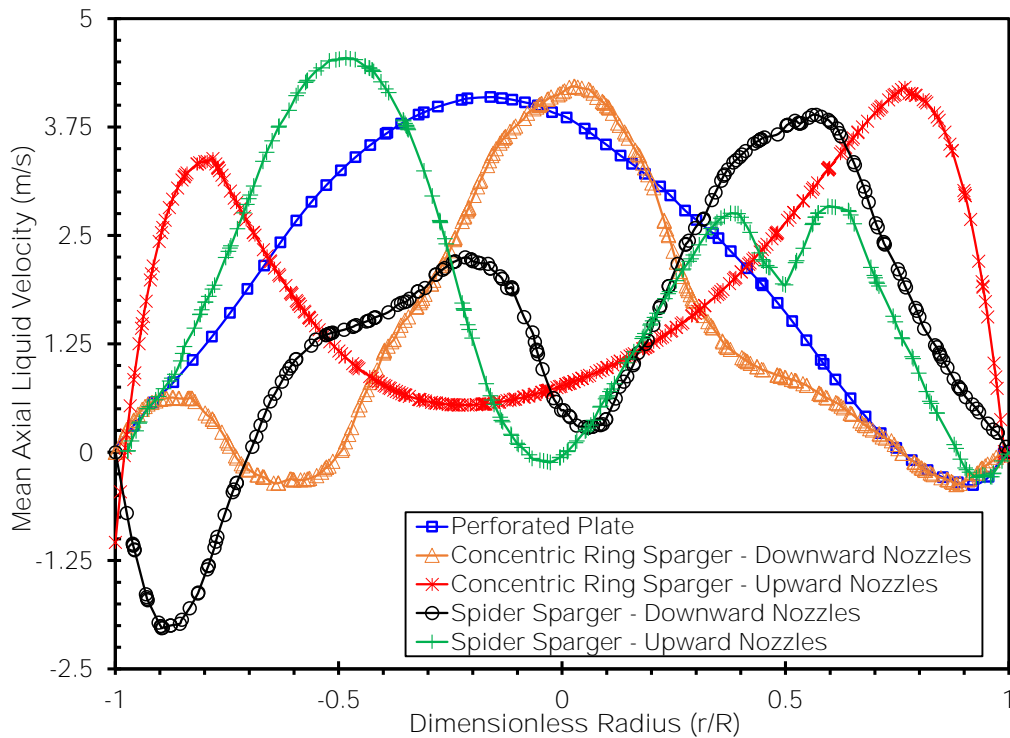


Figure 6-26: Mean axial liquid velocity profiles at $H/D = 1$ for different gas spargers at $u_g = 0.2$ m/s

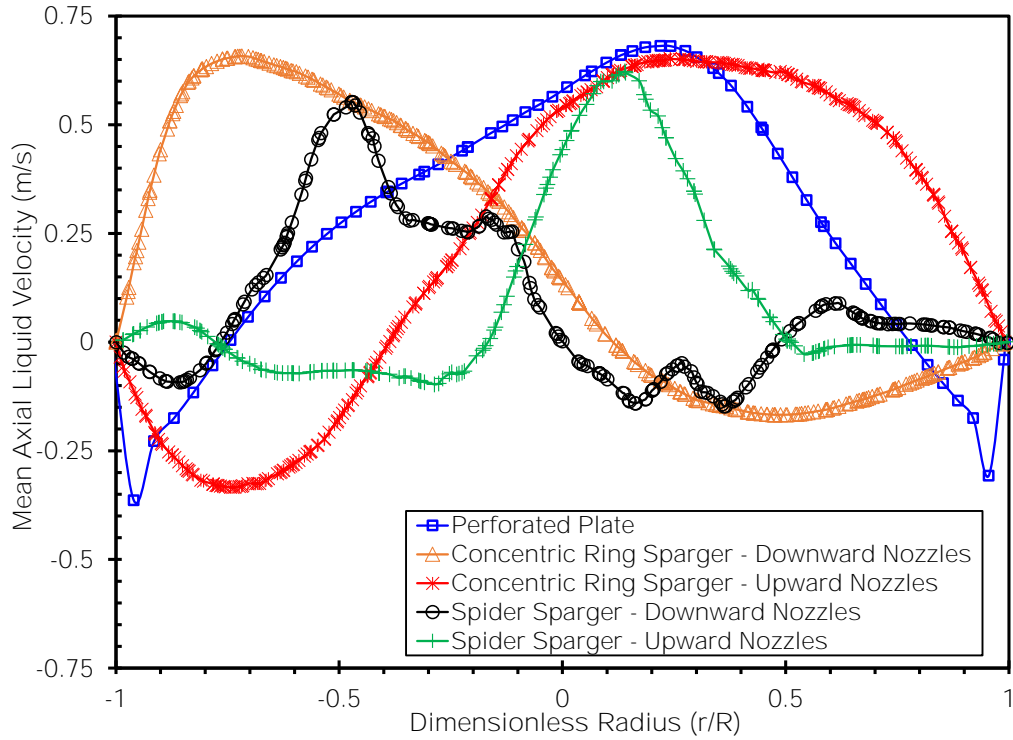


Figure 6-27: Mean axial liquid velocity profiles at $H/D = 3$ for different gas spargers at $u_g = 0.2$ m/s

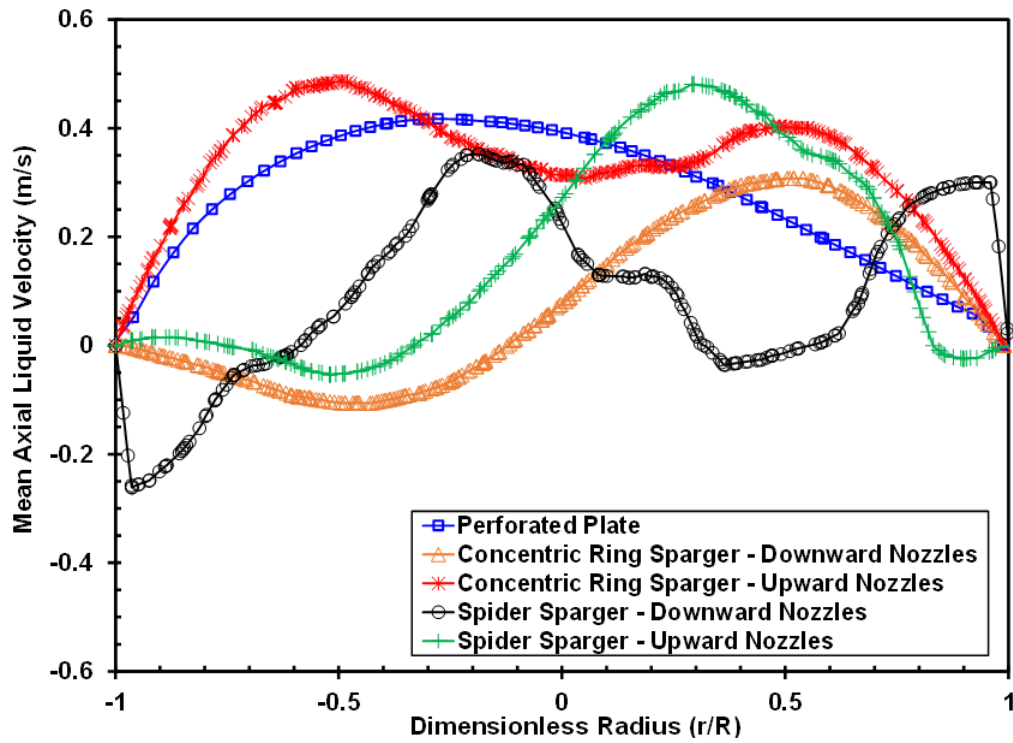


Figure 6-28: Mean axial liquid velocity profiles at $H/D = 6$ for different gas spargers at $u_g = 0.2$ m/s

6.1.5 Sensitivity Analysis of the Model Parameters

In order to use our model as an efficient design tool, it is critical to identify the relative importance of each of the incorporated sub-models and parameters, and to eventually eliminate any unnecessary terms that needlessly increase the computational time without an acceptable increase in the prediction accuracy. In this work, the effect of incorporating a bubble population balance (Equation (4-23)) and the effect of incorporating momentum exchange terms (Equation (4-19)), on the model predictions were investigated. More precisely, the predictions were carried out under six different cases were compared with those of the original model described in Section 4 (Base Case). These cases are: 1. eliminating the bubble population balance; 2. accounting for the bubble population balance with only the coalescence kernel activated; 3. accounting for the bubble population balance with only the breakup kernel activated; 4. accounting only for the drag in the momentum exchange terms; 5. accounting only for Drag and Lift; and 6. accounting only for Drag, Lift and Virtual Mass.

The cases were validated against two sets of experimental data to test both the spatial and overall model predictions. The data of Chen et al. [4] for N₂-Drakeol-Glass beads system at superficial gas velocities of 0.05 as described in Section 6.6.3, were used to investigate the model's prediction of the radial gas holdup profiles. Also, our experimental data, as described in Section 6.6.4, were used to investigate the overall model performance at an inlet superficial gas velocity = 0.20 m/s, temperature = 443 K and catalyst concentration = 11 vol%. Three main criteria were used to evaluate the relative importance of each of those parameters: (i) the overall computational time, (ii) the Absolute Average Relative Error (AARE), and (iii) the Percent Bias (PBIAS), which is used to identify the model's bias to underestimate or overestimate the data [396] as shown in Equation (6-5):

$$PBIAS = \frac{\sum_1^n(\text{Pred.} - \text{Exp.})}{\sum_1^n(\text{Pred.})} \times 100\% \quad (6-5)$$

Positive values indicate the model's underestimation bias, whereas positive values indicate the model's overestimation bias.

Tables 6-2 and 6-3 show the model performance using the two sets of experimental data. As can be seen in these tables, the greatest reduction in computation time for two sets was achieved by accounting only for the drag momentum exchange term, while eliminating the other terms (Case # 4), which resulted in a decrease of computational time by 25.5% and 27.1% for set 1 and set 2, respectively, with an almost insignificant change in the AARE. Moreover, eliminating the bubble population balance significantly reduced the computation time by 19% and 23.3% for set 1 and set 2, respectively, however, a significant increase in AARE of 9.47% and 6.57% was observed. Thus, the degree of complexity employed in our model is dependent on the required prediction accuracy. Obviously, increased accuracy will significantly increase the required computational time.

Table 6-2: Model performance against the radial gas holdup experimental data of Chen et al. [4]

Case #	Eliminated sub-model	AARE	PBIAS	Computation Time (hrs)	Time Reduction
Base	-	4.45%	1.07%	220	-
1	Bubble population balance	13.92%	-1.3%	178	19.1%
2	Breakup kernel	7.98%	0.07%	184	16.4%
3	Coalescence kernel	11.21%	1.21%	192	12.7%
4	Lift, Virtual Mass, Wall, Turbulence dispersion	4.75%	1.12%	164	25.5%
5	Virtual Mass, Wall, Turbulence dispersion	4.69%	1.09%	207	5.9%
6	Wall, Turbulence dispersion	4.56%	1.06%	214	2.7%

Table 6-3: Model performance against overall gas holdup data measured in our lab

Case #	Eliminated sub-model	AARE	PBIAS	Computation time (hrs)	Time Reduction
Base	-	2.75%	0.32%	218	-
1	Bubble population balance	9.32%	8.1%	167	23.4%
2	Breakup kernel	5.64%	6.5%	181	17.0%
3	Coalescence kernel	7.21%	8.1%	173	20.6%
4	Lift, Virtual Mass, Wall, Turbulence dispersion	2.86%	0.44%	159	27.1%
5	Virtual Mass, Wall, Turbulence dispersion	3.07%	3.70%	203	6.9%
6	Wall, Turbulence dispersion	3.22%	3.63%	217	0.5%

6.2 EFFECTS OF INTERNALS ON THE LOCAL HYDRODYNAMICS IN SBCRS

Reactor internals with different shapes and configurations are an integral part of the design and optimization of numerous industrial applications. For instance, different types of internals, such as rings, inverse-cone tubes, horizontal ring-type baffles, and perforated plates were used in the circulating fluidized bed (CFB) to improve the solids radial distribution [397]. Fixed and floating internals were used in the fast fluidized-beds to reduce the agglomerate size in cohesive powders for fluidization improvement [398]. Porous draft tubes, open-sided draft tubes and non-porous draft tubes were used in conical spouted beds to increase the gas flow rate from the spout into the annulus and enhance heat transfer [399, 400]. Different internals were also used in SBCRs to maintain a near isothermal operation using the highly exothermic processes.

Generally, heat transfer rate in multiphase systems is controlled by many variables, such as heat transfer area, heat transfer coefficient, superficial gas velocity, liquid circulation velocity, and bubble dynamics, including the local and overall phase holdups, bubble velocities, bubble sizes, and bubble frequency.

In SBCRs, the good mixing and high heat capacity of the slurry-phase allow for excellent temperature control, making it ideal for the F-T synthesis process, which is highly exothermic. Kolbel and Ralek [221] reported a temperature difference of less than 1 °C over the total length of a pilot-scale SBCR (1.29-m ID, 8-m height) used for F-T synthesis at 268 °C. The cooling surface requirements in slurry bubble reactor reactors have been reported to be less than a quarter of those used in a multitubular fixed bed reactors, due to the improved heat transfer film coefficient in addition to a higher permissible ΔT between reactant and coolant [165, 401].

In this section, the effect of internals on the internal hydrodynamics in our pilot-scale SBCR are investigated using the CFD model in two steps. In the first step, the effect of internals on the experimental and predicted hydrodynamics previously discussed in Section 6.1 was investigated. In the second step, the effect of different internals configurations on the gas holdup structure and liquid backmixing was investigated.

6.2.1 Effect of Internals in the Pilot-Scale Reactor on the Liquid Backmixing, Gas Holdup and Local Turbulence Intensity

The internals configuration used in the pilot-scale SBCR, shown in Figure 6-29 consists of a bundled arrangement of one, 2.5-inch pipe at the center of the reactor, surrounded by 6, 1.75-inch pipes in a hexagonal pattern. The overall cross sectional areal coverage of the internals was 17.65%. The internal pipes were 2.1-m in length each, and extended from the top of the reactor up to 70% of the total length of the reactor, with a volume fraction of 12.3%.

In the CFD modeling, a tetrahedral mesh was used with 4.95 million nodes and 2.85 million cells. The mesh has an average element quality of 0.84 and the cross-sectional contour of the mesh is shown in Figure 6-29. The simulations were carried out at an inlet superficial gas velocity = 0.20 m/s, temperature = 443 K, pressure = 20.5 bar and catalyst concentration = 11 vol. %. The local values of the gas holdup, local turbulence intensity and liquid velocity were determined over 60 s, which is the time required to achieve a steady-state within the pilot-scale reactor.

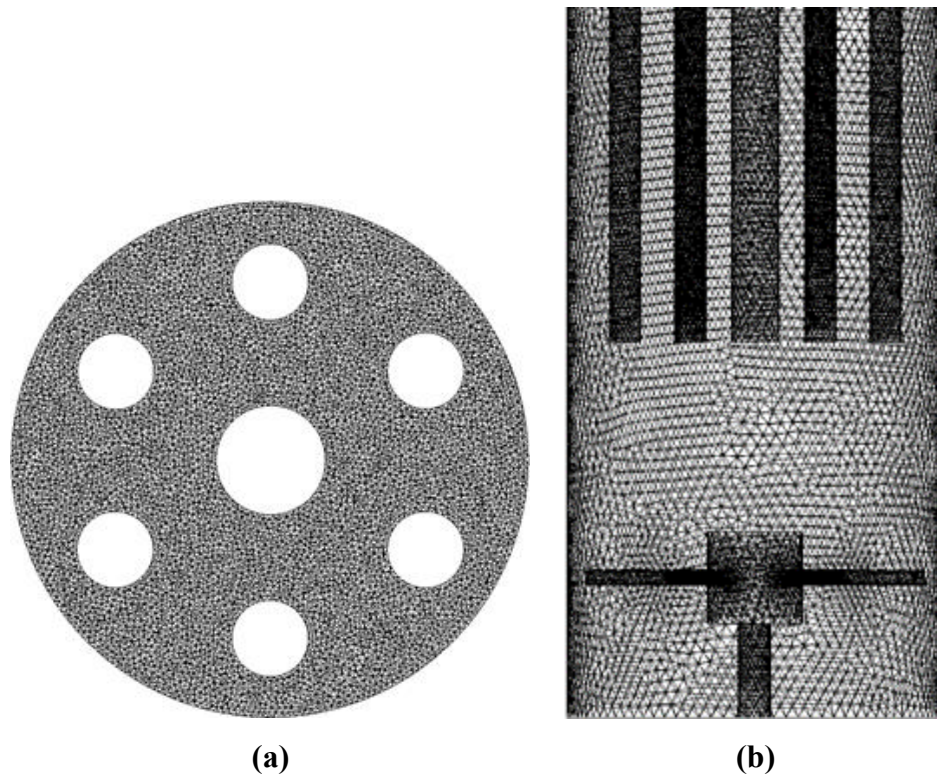


Figure 6-29: Geometry and mesh structure used in this section: Cross sectional view (a) and view in the vicinity of the sparger (b)

Figure 6-30 shows snapshots of gas holdup contours at different times. As can be observed in this figure, the presence of internals generally increases the gas holdup when compared with the reactor without internals shown in Figure 6-5. This behavior could be due to a decrease of the area available for gas flow. Moreover, there is a significant effect on the radial distribution of the gas holdup, as more even radial distribution can be seen in the presence of internals.

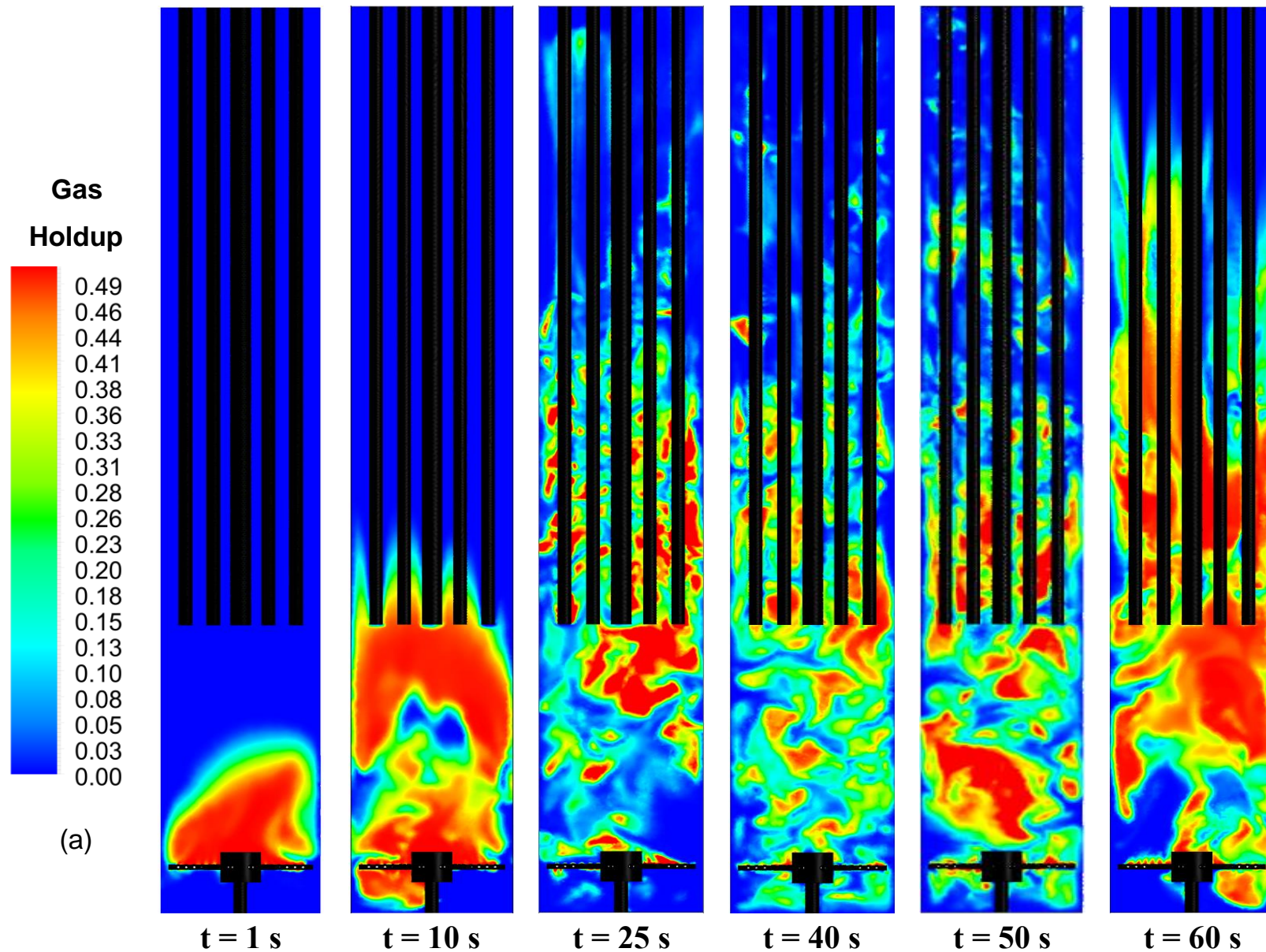


Figure 6-30: Snapshots of gas holdup contours at different times

Figure 6-31 shows snapshots of turbulence intensity contours at different times in the pilot-scale SBCR and as can be observed the presence of internals does not have a significant effect on the turbulence intensity during the first 40 s, when compared with the case without internals shown in Figure 6-17. However, after 40 s, there is a significant increase in the turbulence intensity in the presence of internals, particularly in the upper region of the reactor where the internals are present. This is primarily due to the effect of internals on the longitudinal funneling of the flow, which tends to control the size of large scale eddies, resulting in a more turbulent flow. This effect is also supported by Figure 6-32 which shows snapshots of the liquid velocity vectors at different times in the SBCR. As shown in this figure, the presence of internals results in a significantly different flow structure throughout the reactor after the 40 s, with smaller and faster liquid recirculation cells in the vicinity of the sparger, and larger liquid recirculation in the upper part of the reactor where the internals are present.

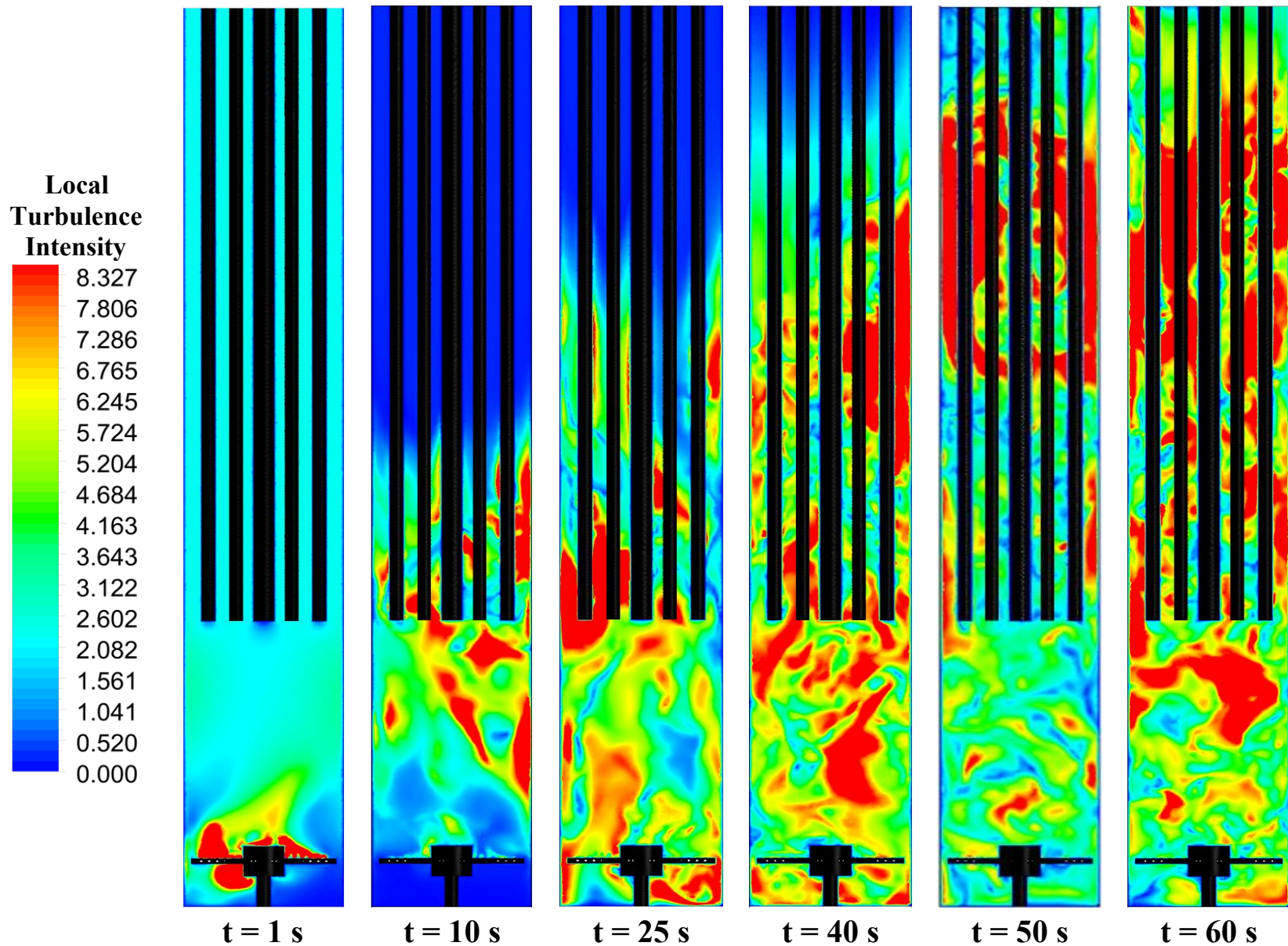


Figure 6-31: Snapshots of turbulence intensity contours at different times

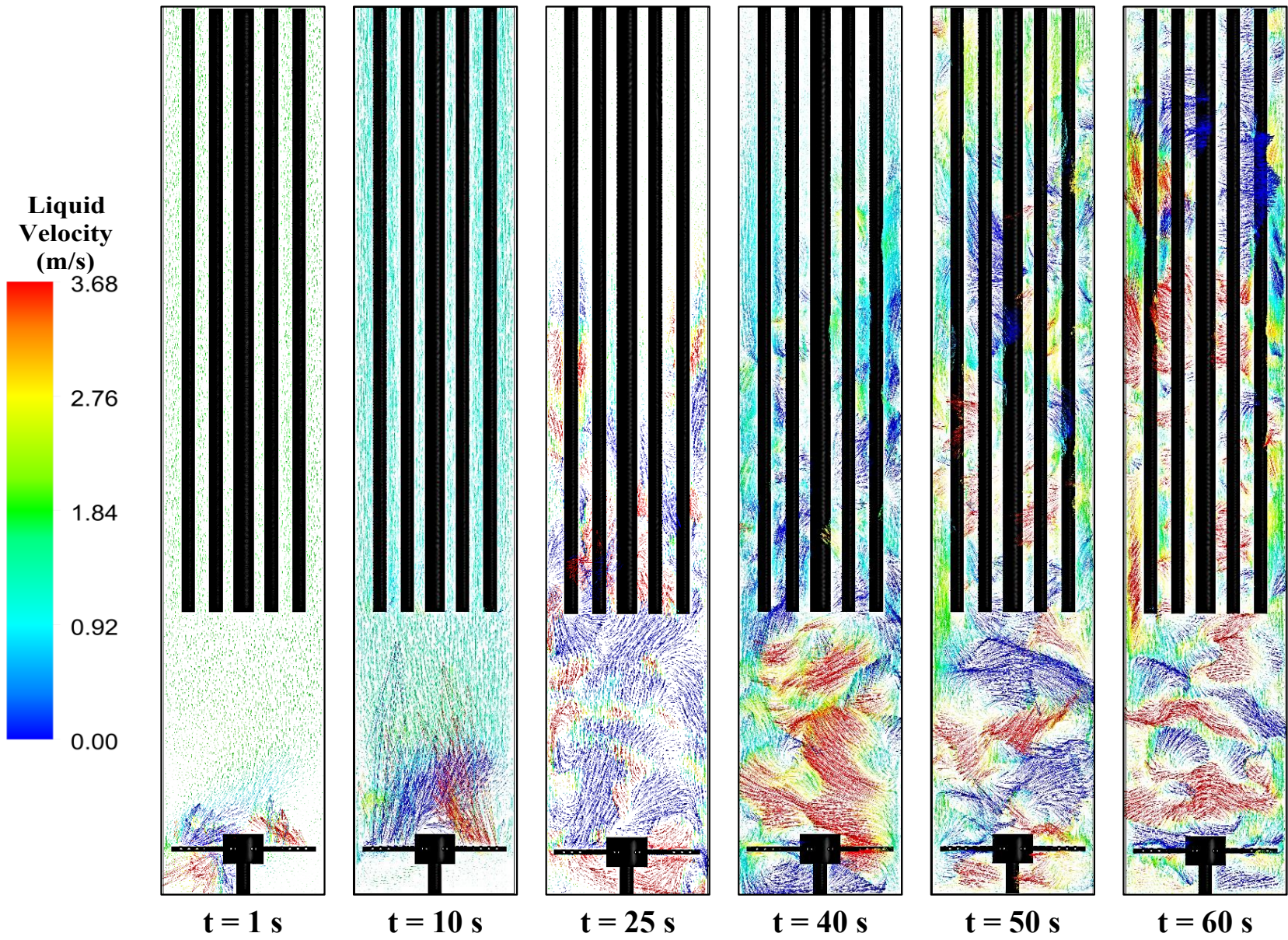


Figure 6-32: Snapshots of liquid velocity vectors at different times

The effect of internals length on the local hydrodynamics was also investigated. The simulations were carried out in the pilot-scale SBCR under the same operating conditions, however, the internals were extended from 2.1 m to 2.6 m, covering 86% of the total reactor length and representing a volume fraction of 15.3%, as shown in Figure 6-33. As can be observed in the figure, increasing the internals length increases the overall gas holdup and results in less steep radial gas holdup profiles in the vicinity of the internals. Also, there is a general increase of the turbulence intensity, primarily in the upper regions of the reactor. Moreover, there is a significant liquid funneling and larger recirculations at the internals zone and smaller, faster recirculations in the vicinity of the sparger.

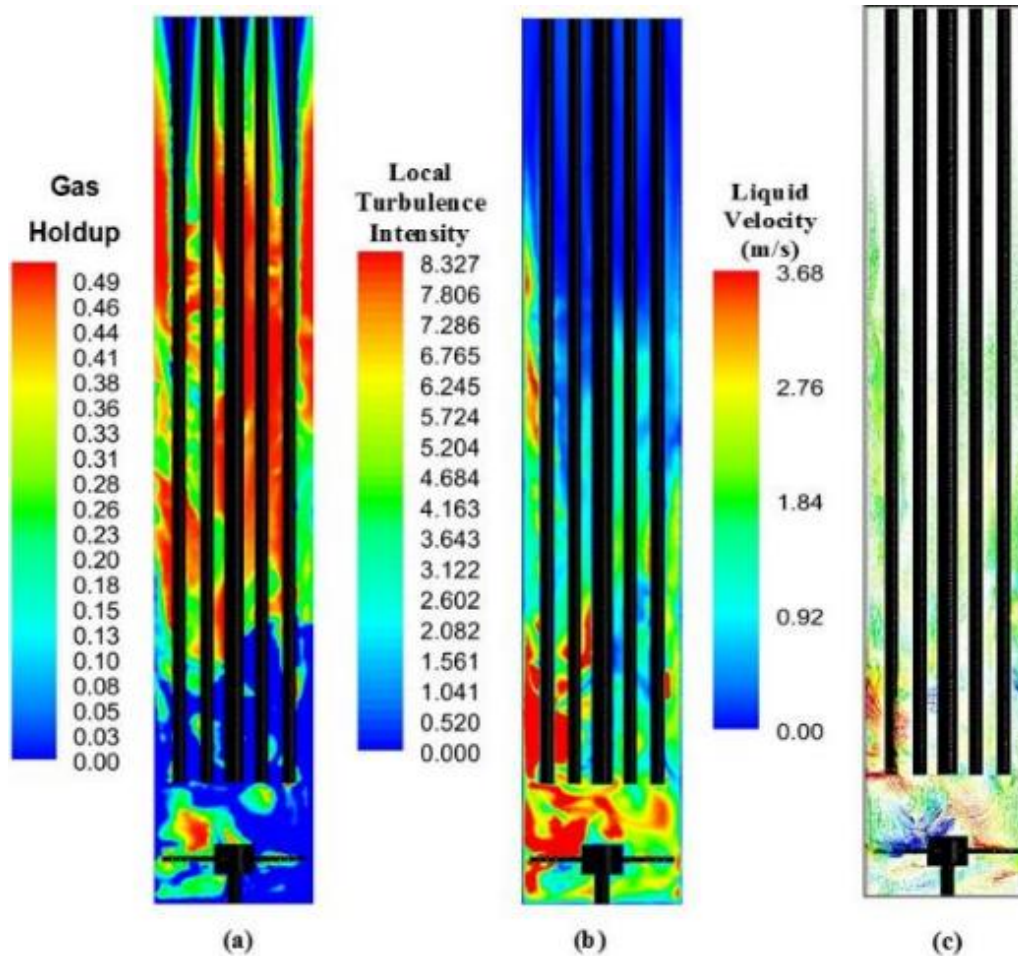


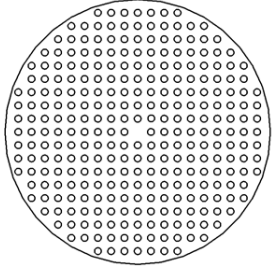
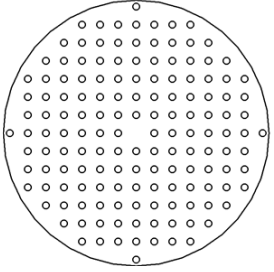
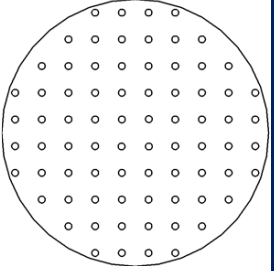
Figure 6-33: Steady state Gas holdup (a), Local turbulence intensity (b) and liquid velocity vectors (c) of the pilot-scale reactor with vertically extended internals

6.2.2 Effect of Parallel Internal Configurations on the Liquid Backmixing and Gas Holdup

The effect of internals configurations on the liquid backmixing and gas holdup was predicted using our CFD model in three different parallel (baffled) configurations inside a conceptual large-scale reactor (1-m ID and 10-m height). The areal coverage and volume fraction of the internals in both reactors are shown in Table 6-4. In all the cases investigated, the internals extended from the top of the reactor up to 86% of the reactor height. The gas was introduced using a concentric-ring sparger, consisting of 3 concentric-rings with 333, 167 and 111 orifices, totaling 611 identical orifices, each with an ID of 7-mm.

The simulations were carried out at an inlet superficial gas velocity of 0.20 m/s, temperature of 443 K, pressure of 20.5 bar and catalyst concentration of 11 vol. %. In order to prevent numerical problems, however, the calculations were carried out with a 0.05 s increment for the first 1000 time steps, increased to 0.1 s for the next 1000 time steps, then increased to 0.25 s until the end of the simulation time. The simulated physical time was for 300 s, at which the statistical quasi-steady state was attained, i.e. once the converging time averages of the local holdups and axial velocities were stabilized. The cross-sectional contours for both the liquid axial velocity and gas holdup at different z/D points throughout the reactor are shown in Figures 6-34 to 6-37.

Table 6-4: Details of parallel internal configurations used in this study

Parallel Arrangement		
P-1	P-2	P-3
		
19% CSA Coverage 16.34% Volume coverage 293 – 1 in internal pipes 1 m –ID, 10 m high SBCR	10% CSA Coverage 8.6% Volume Coverage 155 – 1 in internal pipes 1m –ID, 10 m high SBCR	5% CSA Coverage 4.3% Volume Coverage 77 – 1 in internal pipes 1m –ID, 10 m high SBCR

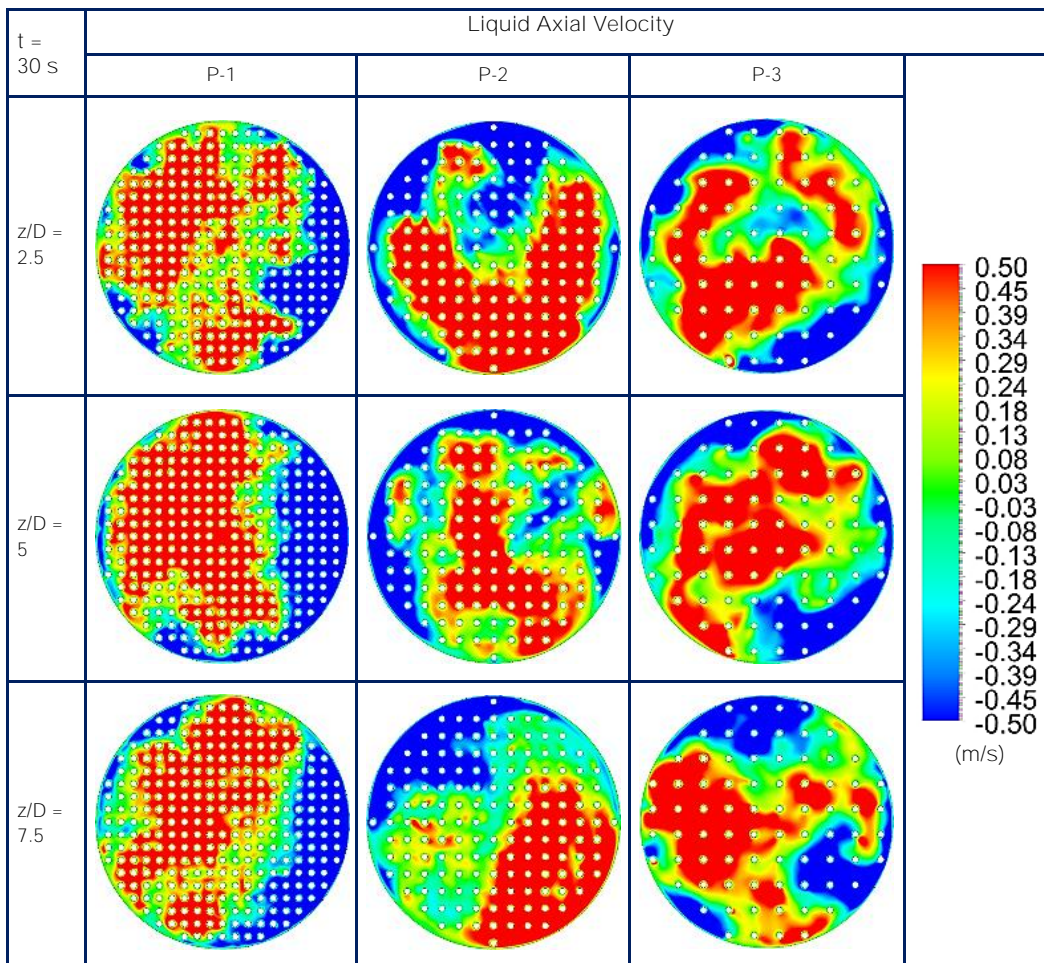


Figure 6-34: Liquid axial velocity cross-sectional contours at different heights for the parallel internals configurations at 30 s

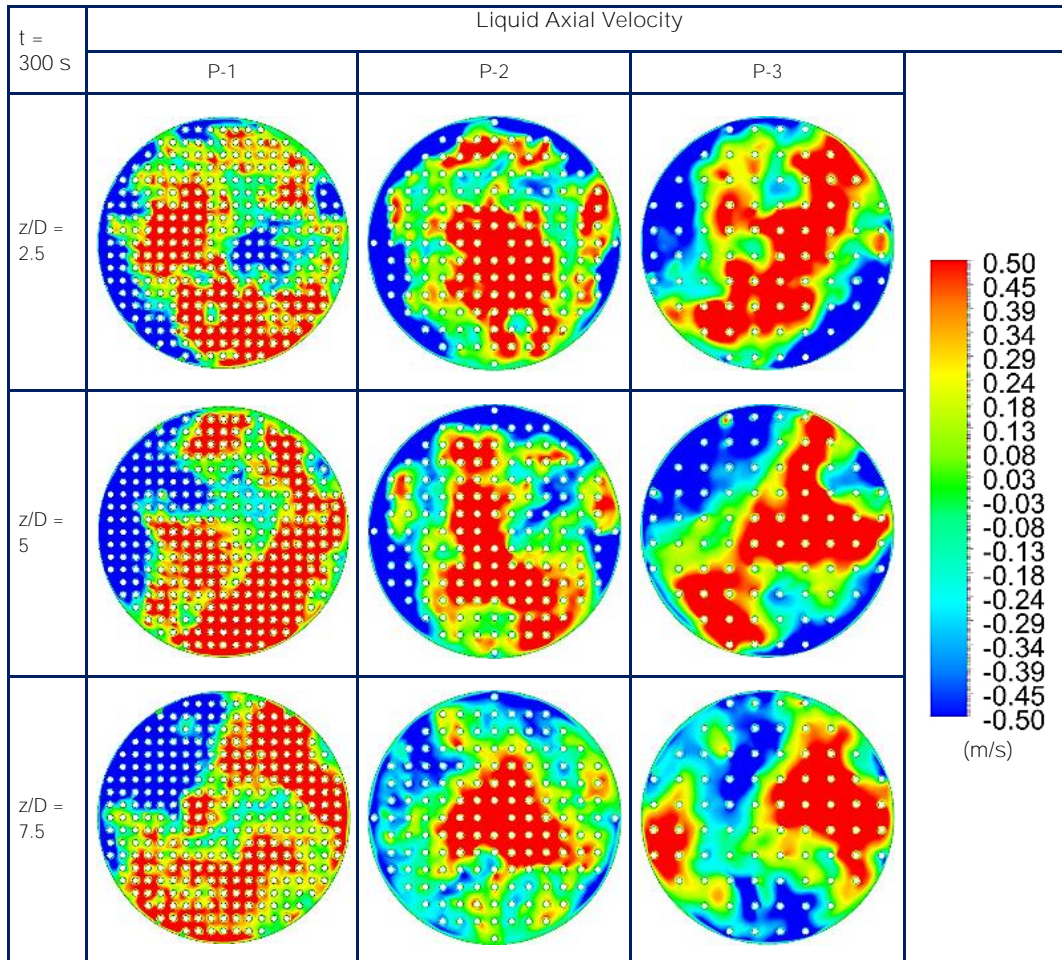


Figure 6-35: Liquid axial velocity cross-sectional contours at different heights for the parallel internals configurations at 300 s

Figures 6-34 and 6-35 show the axial liquid velocity contours for cases P-1 through P-3. As can be seen in this Figure, strong liquid recirculations are exhibited at a much earlier time, marked by smaller scale liquid circulations throughout the reactor, which eventually grow into large scale recirculation cells with positive axial velocity near the reactor center and strong backmixing near the reactor wall at steady-state conditions. Similar flow structure and behavior is also exhibited for cases P-1 and P-2, in which the liquid recirculations develop at a much faster rate, and eventually result in large liquid recirculations throughout the reactor. This behavior is primarily due to liquid funneling because of the presence of internals in the reactor, which

significantly affect the flow structure, resulting in large, fast and more turbulent liquid recirculations.

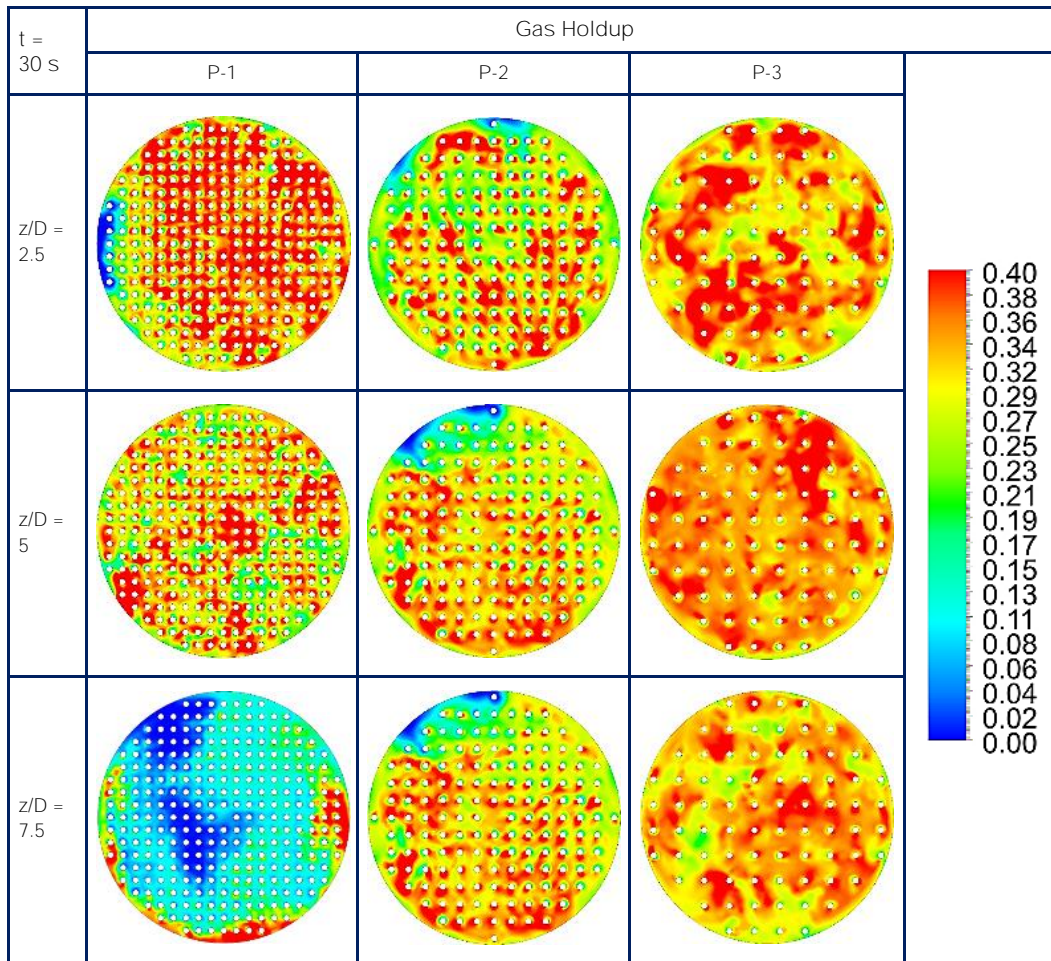


Figure 6-36: Gas holdup cross-sectional contours at different heights for the parallel internals configurations at 30 s

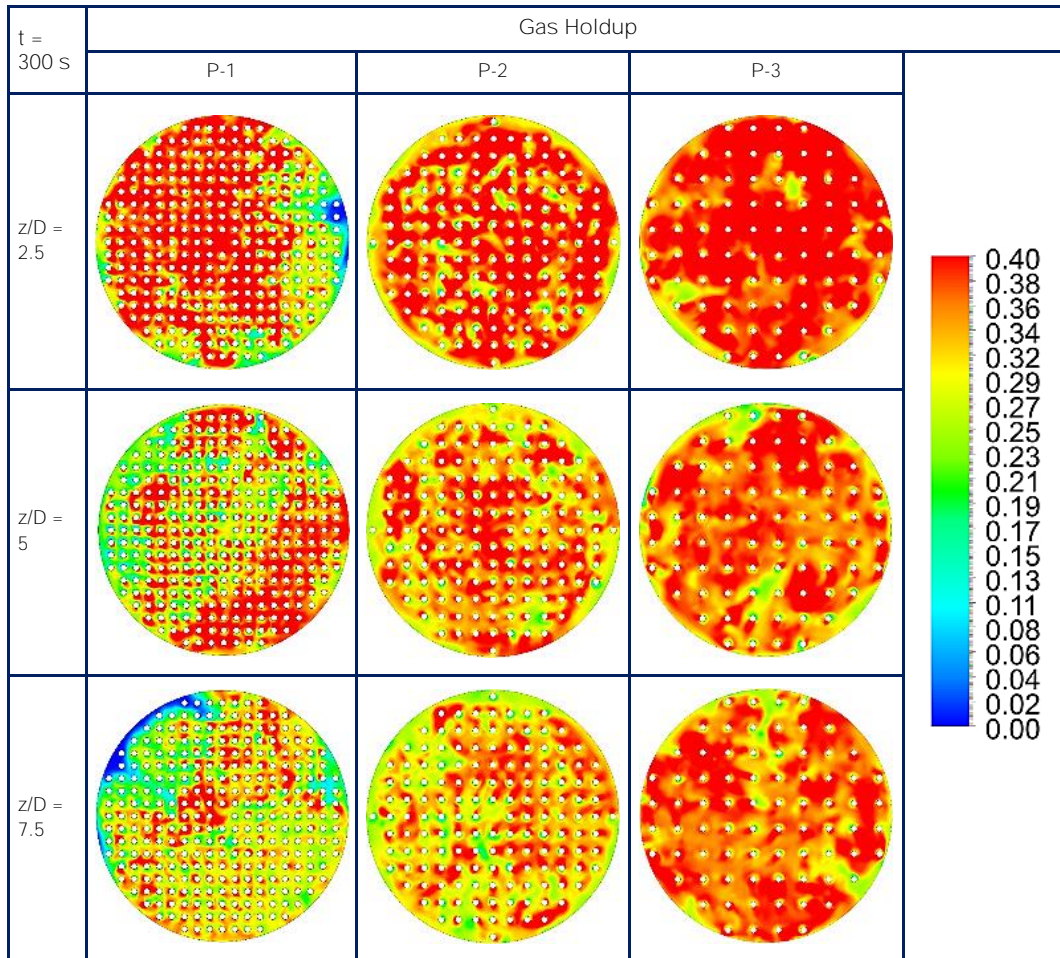


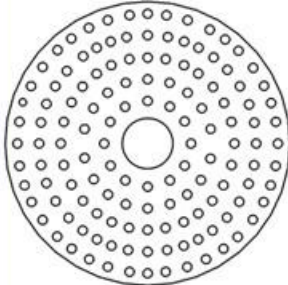
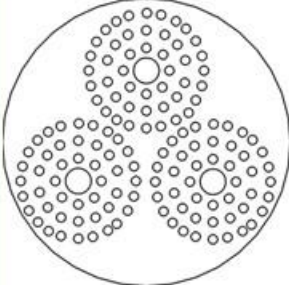
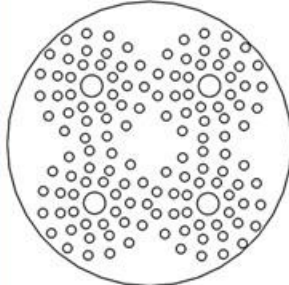
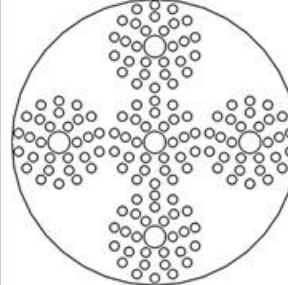
Figure 6-37: Gas holdup cross-sectional contours at different heights for the parallel internals configurations at 300 s

Figures 6-36 and 6-37 shows the presence of internals increases the gas holdup throughout the reactor, which is in agreement with earlier findings [223, 226]. Also, in all cases at z/D value of 2.5, the radial gas holdup profiles exhibit higher values near the reactor center and lower values near the reactor wall, which eventually flatten along the reactor height, with more distinctly flatten gas holdup profiles at higher z/D values of 5 and 7.5.

6.2.3 Effect of Bundled Internal Configurations on the Gas Holdup and Liquid Backmixing in the Conceptual Reactor

Four different bundled configurations in the conceptual reactor (1-m ID and 10-m height) with 1, 3, 4 and 5 bundles, as shown in Table 6-5, were investigated. This was performed to investigate the effect of the reactor geometry on the local hydrodynamics in the presence of internals, and the impact of inserting a large number of internals inside the reactor. In all the cases investigated, the internals extended from the top of the reactor up to 86% of the reactor height, which is equivalent to 2.58 m for the 3 m height reactor and 8.6 m for the 10 m reactor. The simulations were carried out at an inlet superficial gas velocity of 0.20 m/s, temperature of 443 K, pressure of 20.5 bar and catalyst concentration of 11 vol. %. The cross-sectional contours for both the liquid axial velocity and gas holdup at different z/D points throughout the reactor are shown in Figures 6-38 and 6-8.

Table 6-5: Details of bundled internal configurations used in this study (1-m ID, 10-m high SBCR)

Bundled Arrangement			
B-1	B-2	B-3	B-4
			
16.7% CSA Coverage 14.3% Volume Coverage 1 - 7 in bundle center 134 - 1.25 in internal pipes 1 m-ID, 10 m high SBCR	16.3% CSA Coverage 14.0% Volume Coverage 3, 3.5 in bundle centers 138, 1.25 in internal pipes 1 m-ID, 10 m high SBCR	16% CSA Coverage 13.8% Volume Coverage 4, 3 in bundle centers 136, 1.25 in internal pipes 1 m-ID, 10 m high SBCR	17.5% CSA Coverage 15.1% Volume Coverage 5, 3 in bundle centers 145, 1.25 in internal pipes 1 m-ID, 10 m high SBCR

Figures 6-38 and 6-39 show the axial liquid velocity contours for cases B-1 through B-4; and as can be seen the presence of bundled internals results in significantly different backmixing profiles. Strong liquid recirculations are exhibited for cases B-1 and B-2 for the 1 and 3 bundle configurations, whereas weaker liquid recirculations are shown for cases B-3 and B-4 for the 4 and 5 bundle configurations. Generally, backmixing zones in the bundled arrangements seem to be affected by the presence of wall clearance zones, especially in the configurations which promote large wall clearances, such as the 3 bundle and 5 bundle arrangements, where the large wall clearance zones generated unique backmixing profiles.

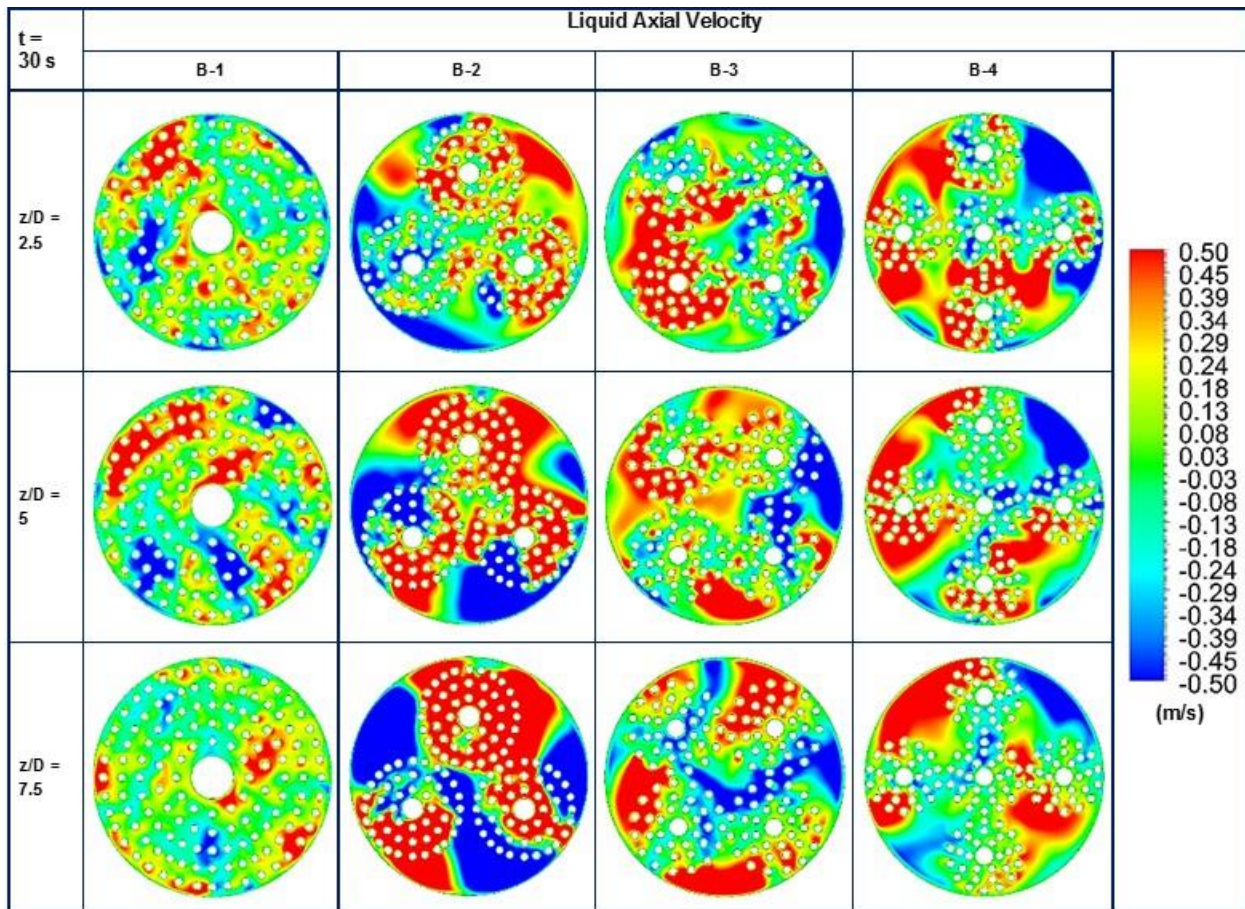


Figure 6-38: Liquid axial velocity cross-sectional contours at different heights for the bundled internals configurations at 30 and 300 s (1-m ID, 10-m high SBCR)

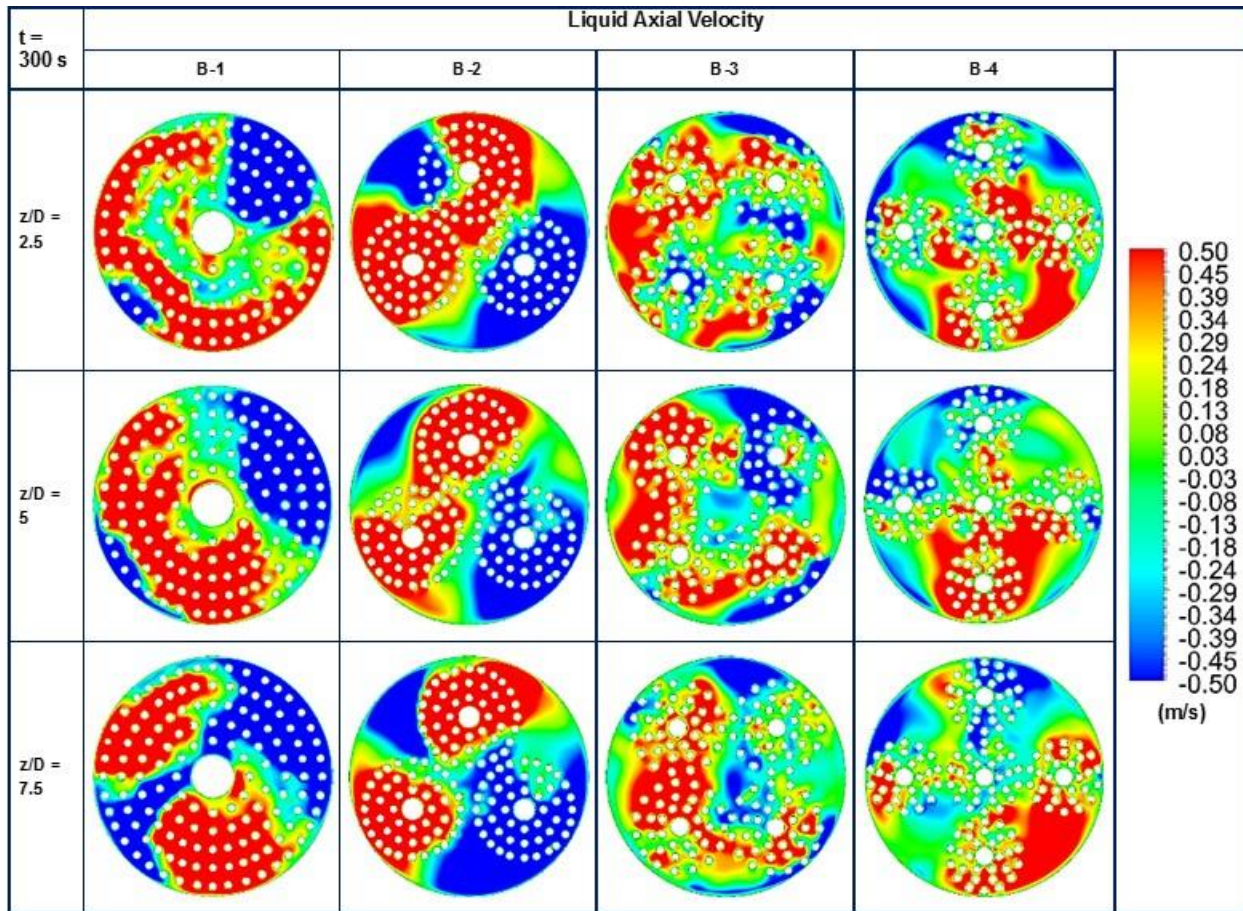


Figure 6-39: Liquid axial velocity cross-sectional contours at different heights for the bundled internals configurations at 30 and 300 s (1-m ID, 10-m high SBCR)

Figures 6-40 and 6-41 show the gas holdup contours for cases B-1 to B-4, at 30 and 300 s, respectively. As can be observed for all cases, the presence of internals results in smoother radial gas holdup profiles, however, the local gas holdup values were lower than those exhibited for the parallel configurations (Figure 6-36). This behavior is primarily due to the increase of the average bubble size for bundled internals when compared with those for parallel internals, as shown in in Figure 6-42.

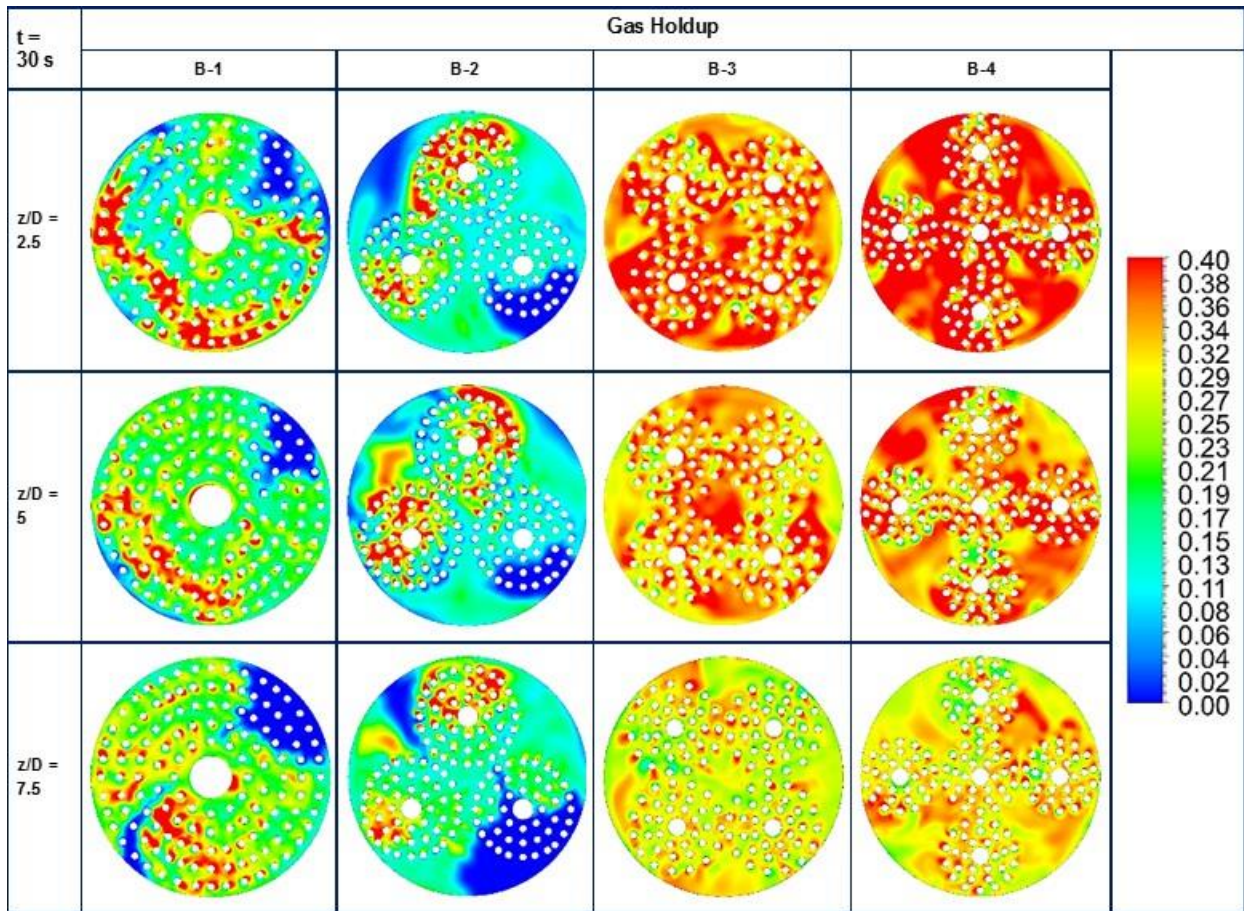


Figure 6-40: Gas holdup cross-sectional contours at different heights for the bundled internals configurations at 30 s (1-m ID, 10-m high SBCR)

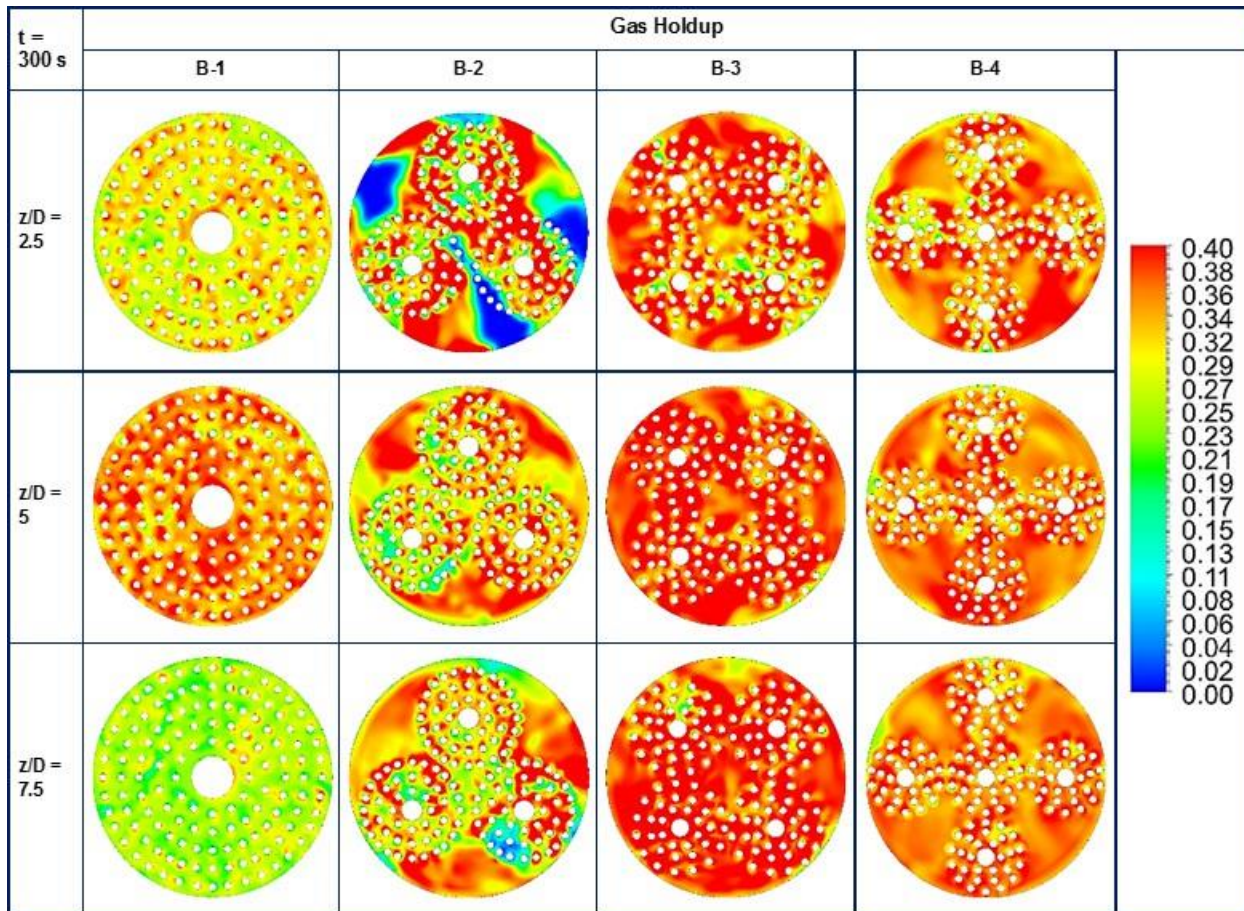


Figure 6-41: Gas holdup cross-sectional contours at different heights for the bundled internals configurations at 300 s (1-m ID, 10-m high SBCR)

Figure 6-42 shows that the bundled internals result in higher Sauter mean bubble diameter (d_{32}) values when compared with those for the parallel internals. This behavior could be due to the fact that the presence of parallel internals enhances bubble breakup and inhibits bubble coalescence, whereas the presence of bundled internals enhances bubble coalescence. This is clearly shown when comparing the bubble diameters of case P-1 to the values obtained with no internals (Figure 6-42). Moreover, the bubble size appears to increase with decreasing the cross-sectional area for the parallel internals and increasing the number of bundled internals. This behavior could be related to the effect of the distance between the internals in the case of parallel configurations, where lower cross-sectional area coverages result in wider distance between the

internals, leading to the formation of large gas bubbles. For bundled internals, on the other hand, this effect is due to the wall clearance, where bigger clearances resulted in increased bubble diameter.

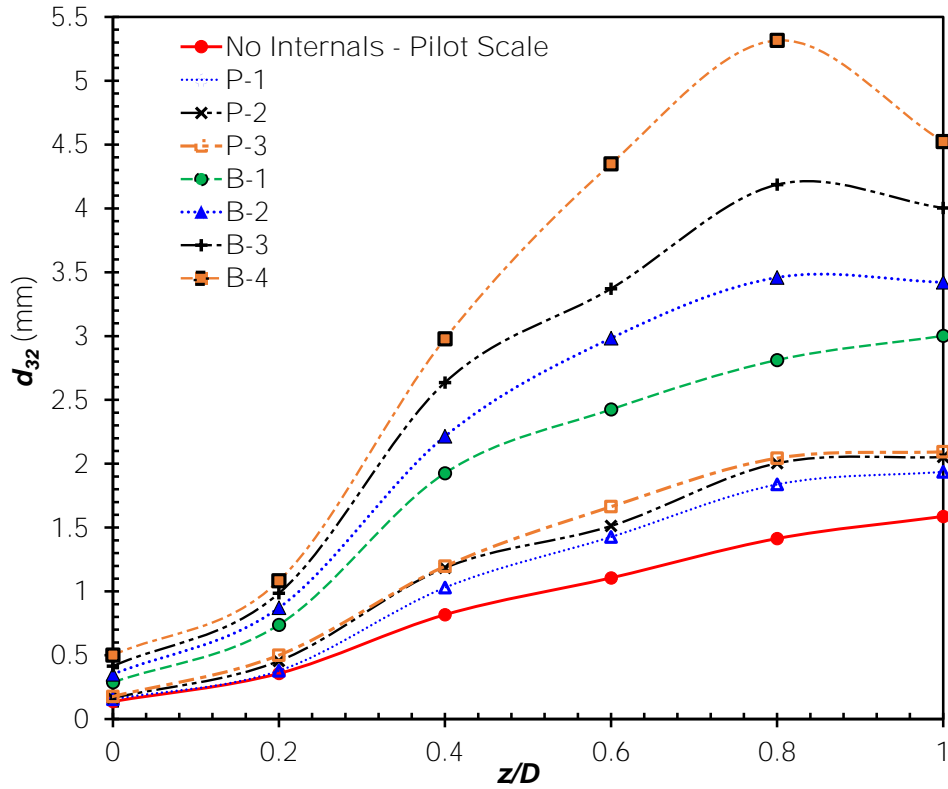


Figure 6-42: Axial Sauter mean bubble diameter for different internals configurations

Additionally, the effect of the number of internals and the internals cross-sectional area coverage on both the gas holdup and backflow fraction, has been investigated, as shown in Figures 6-43 and 5-21. As shown in these figures, the number of internals does not have a significant effect on the gas holdup, which seems to be governed by the internal cross-sectional areal coverage of the internals. On the other hand, the number of internals appears to have significant effect on enhancing liquid backmixing when compared with that of the cross-sectional area coverage. Thus, the presence of internals and their combination can increase or decrease backmixing depending on their design and arrangement.

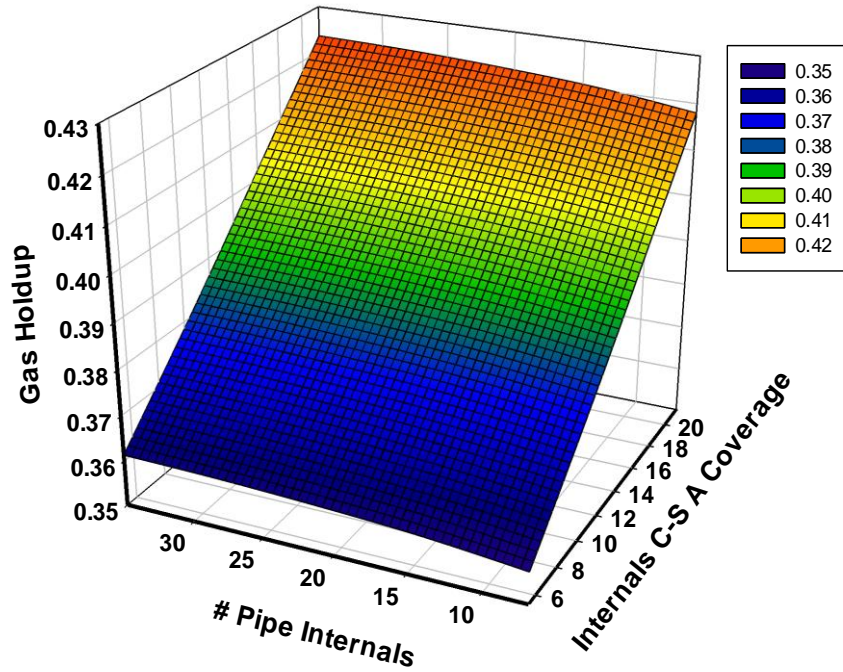


Figure 6-43: Effect of number of internal pipes and internals CSA coverage on the gas holdup

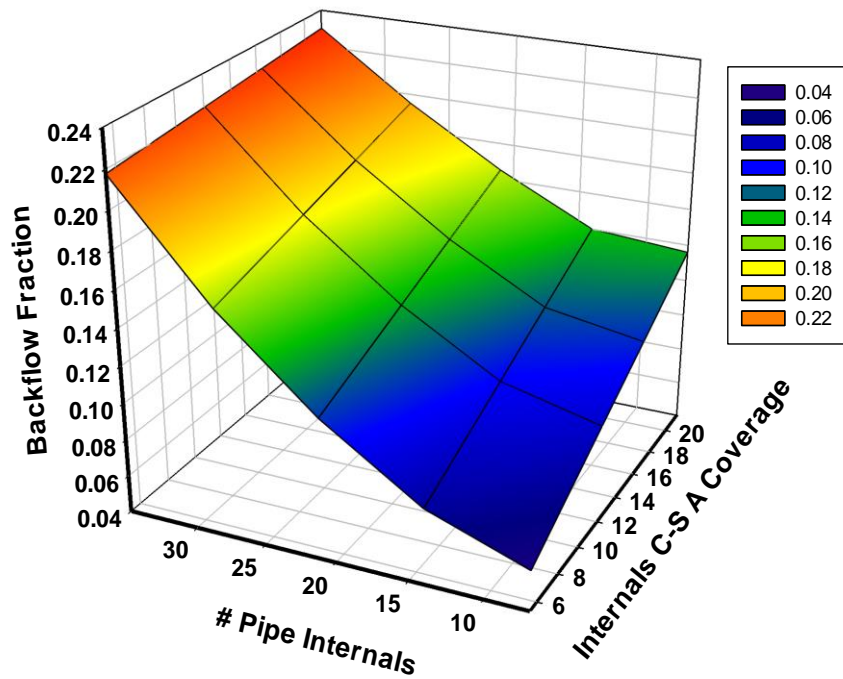


Figure 6-44: Effect of number of internal pipes and internals CSA coverage on the liquid backflow fraction

6.3 CFD MODEL PREDICTIONS OF PERFORMANCE OF A PILOT- AND LARGE-SCALE SBCRs FOR F-T SYNTHESIS

The use of CFD models to predict the F-T reactor performance at relatively large scales has been rarely attempted as previously discussed in Section 2.5.3, due to the computational and physical complexity of the process. Most modeling attempts have been limited to 1-D axial dispersion models. In this investigation, our CFD model was used to predict the performance of the pilot-scale SBCR reactor available in our laboratory and an industrial-scale SBCR for F-T synthesis using iron catalyst. The kinetic rate expressions used for both the F-T and WGS reactions are given in Table 6-6.

Table 6-6: F-T Catalyst and kinetics provided by NICE

Catalyst	Reaction	Equation	Parameters
NICE Catalyst (Fe)	F-T	$r_{FT} = \frac{kP_{CO}P_{H_2}}{P_{CO} + aP_{H_2} + bP_{CO_2}}$	k = 0.118 mol·kg ⁻¹ ·s ⁻¹ ·MPa ⁻¹ at 528 K a = 5.9 b = 5.9
	WGS	$r_{WGS} = \frac{k \left(P_{CO}P_{H_2} - \frac{P_{H_2}P_{CO_2}}{K_p} \right)}{\left(P_{CO} + aP_{H_2} + bP_{CO_2} \right)^2}$	k = 0.083 mol·kg ⁻¹ ·s ⁻¹ a = 1.9 b = 1.9 K _p = 79.7 at 528 K

The composition of the syngas used in the CFD simulation is given in Table 6-7.

Table 6-7: Syngas composition used in this investigation

Composition	Mol. %
H ₂	52.47
O ₂ /Ar	0.27
N ₂	12.72
CO	34.46
CO ₂	0.02
CH ₄	0.03

The F-T products distribution was determined using the 2- α model [46]. The mole fraction of the products with an n carbons is calculated using Equation (6-6):

$$x_n = \frac{\alpha_1^{n-1} + \left(\frac{\alpha_1}{\alpha_2}\right)^{\zeta-1} \alpha_2^{n-1}}{\frac{1}{1-\alpha_1} + \left(\frac{\alpha_1}{\alpha_2}\right)^{\zeta-1} \frac{1}{1-\alpha_2}} \quad (6-6)$$

Where ζ represents the break point of the products distribution in the 2- α model.

The products selectivities obtained by Withers et al. [402] were used to fit the values of the parameters ζ , α_1 and α_2 and they were found to be 13, 0.79 and 0.91, respectively. Furthermore, the literature data by Chang et al. [403] available for an iron-based catalyst, similar to the one used in this study, were used to develop Equation (6-7) in order to predict the ratio of α -olefins to paraffins (*Rop*).

$$\begin{aligned} n < 5 & \quad Rop_n = -1.06n^2 + 7.18n - 6.25 \\ n \geq 5 & \quad Rop_n = -0.000115n^4 + 0.00804n^3 - 0.188n^2 + 1.4n + 1.47 \end{aligned} \quad (6-7)$$

The solubilities of gases, other than H₂ and CO, were calculated using the Marano and Holder [361, 363, 364, 404] correlations for the multi-component vapor-liquid equilibrium model. The design data and operating conditions for the pilot-scale and the industrial-scale SBCRs used in this CFD modeling are given Table 6-8.

Table 6-8: Design data for the pilot-scale and industrial-scale SBCRs

Parameter	Pilot-scale	Industrial-Scale
Reactor inside diameter (D_R)	0.3	5.8 m
Reactor effective height (H_R)	3 m	42 m
Sparger Type	6-arms spider	Concentric circles
Orifices inside diameter (ID_{orifice})	5 mm	3 mm
Number of orifices (N_{orifice})	108	29,000
Cooling Pipes	Stainless Steel	Stainless Steel
Number of cooling pipes × Cooling pipe size	1 × 63.5 mm OD (58.42 mm ID)	151 × 89 mm OD (77 mm ID)
	6 × 44.45 mm OD (39.37 mm ID)	453 × 57 mm OD (47 mm ID)
Pressure	20.5 bar	29 bar
Temperature	443 K	528 K
Superficial gas velocity	0.24 m/s	0.12, 0.24, 0.30 and 0.40 m/s
Slurry or Liquid flow rate	0.00015 m/s	0.00015 m/s
Catalyst	Iron (Table 6-6)	Iron (Table 6-6)
Average particle size	81 micron	81 micron
Particle skeletal density (NICE catalyst)	3,380 kg/m ³ (Iron)	3,380 kg/m ³ (Iron)
Catalyst loading (solid concentration)	0-15 vol% (0-45 wt. %)	10 vol% (34 wt. %)

6.3.1 Prediction of the Pilot-Scale SBCR Performance

Our CFD model was first used to predict the performance of the pilot-scale SBCR for F-T synthesis. The effect of catalyst concentration on the H₂ and CO conversions and the overall C₅⁺ products yield was investigated at three solid concentrations of 5, 10 and 15 vol% for three H₂/CO ratios of 1, 1.5 and 2. The simulations were carried out at a pressure of 20.5 bar, a temperature of 443 K, and superficial gas velocity of 0.24 m/s. The geometry used is shown in Figure 6-29.

The simulations were carried out for a period of 120 minutes, using a 0.25 s time step, for a total of 28,800 time steps per simulation. Each simulation took an average of 270 hours to

complete. It should be noted that the addition of the reaction kinetics resulted in significant convergence difficulties and that the simulation had to be initialized using a first order steady state solution before advancing the transient solution. The results for the yield were ultimately expressed in tons of C_5^+ products per day.

Our CFD model was able to predict the performance of the pilot-scale SBCR as shown in Figures 6-45 through 6-47. The predictions indicated that increasing catalyst concentration increases the CO and H_2 conversions. Also, Figure 6-47 shows that this pilot-scale SBCR could produce a maximum of 1.87 tons/day of C_5^+ products when using a catalyst concentration of 15 vol. % under the operating conditions given in Table 6-8.

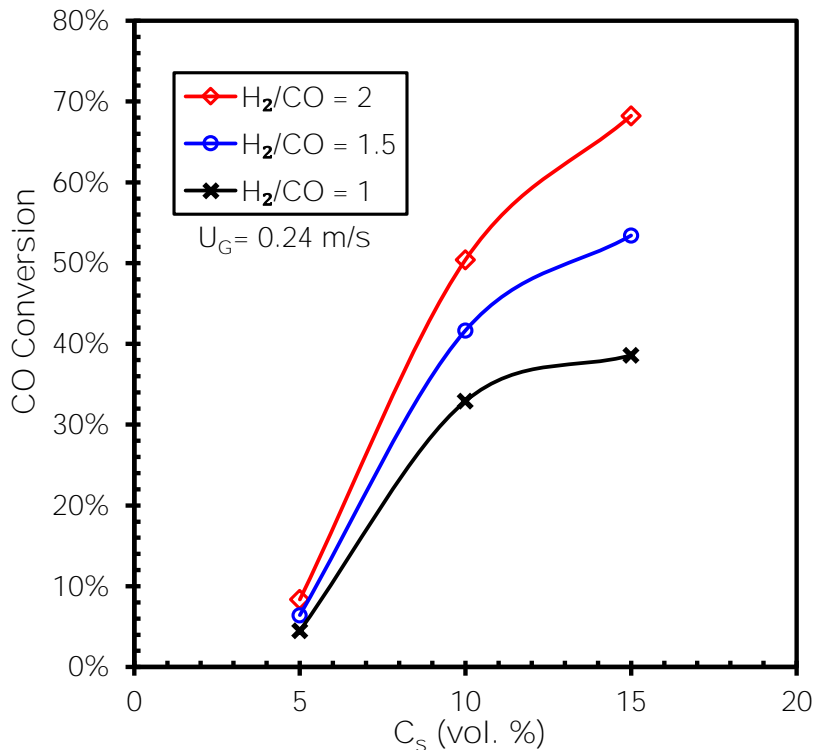


Figure 6-45: CFD model predictions of CO conversion for different H_2/CO ratios at different catalyst concentrations for F-T synthesis in the pilot-scale SBCR

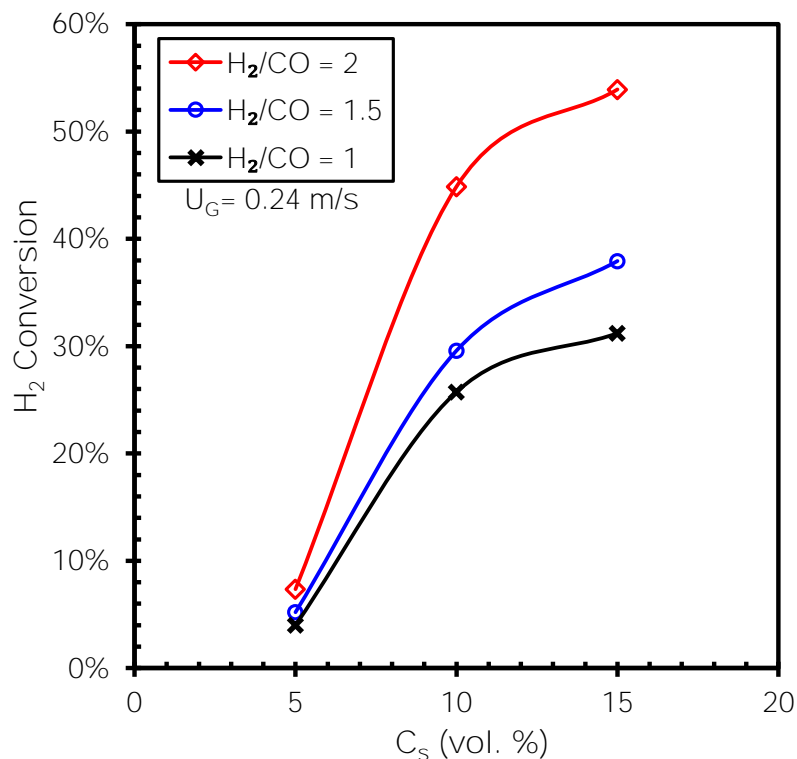


Figure 6-46: CFD model predictions of H₂ conversion for different H₂/CO ratios at different catalyst concentrations for F-T synthesis in the pilot-scale SBCR

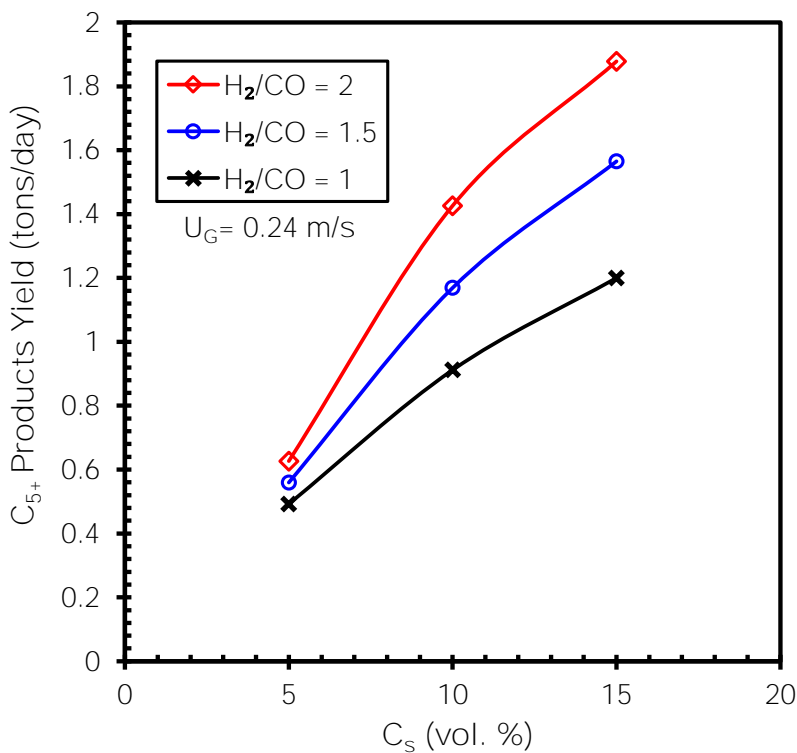


Figure 6-47: CFD model predictions of the C₅₊ products yield for different H₂/CO ratios at different catalyst concentrations for F-T synthesis in the pilot-scale SBCR

6.3.2 Effect of Incorporating Kinetics on the Local Hydrodynamics in the Pilot-Scale SBCR

The impact of incorporating the F-T reaction kinetics on the hydrodynamics in the pilot scale SBCR was investigated. Generally, the effect of the chemical reaction on the hydrodynamics in a SBCR is expected, primarily due to gas and liquid velocity changes along the reactor axial position, and the net molar gas consumption or production as the reaction proceeds. The changes in the local gas velocities are expected to change the gas holdup and bubble size, which in turn affect the gas-phase continuity equation, and the momentum balance for the gas and liquid phases. In this analysis the CFD results, with and without F-T reaction kinetics, were compared at pressure = 20.5 bar, temperature = 443 K, inlet superficial gas velocity = 0.20 m/s, catalyst concentration = 10 vol. %, and at H₂/CO ratio = 2. The geometry used in this work is shown in Figure 6-29. It includes a 6-arms spider sparger, and one bundled internal, consisting of one, 2.5-inch pipe at the center of the reactor, surrounded by 6, 1.75-inch pipes in a hexagonal pattern. The internals had a cross sectional areal coverage of 17.65% and extended for 86% of the overall reaction length, representing a volume fraction of 15.3%.

Figure 6-21 shows the axial average Sauter mean bubble diameters profiles of in the pilot-scale SBCR with and without chemical reactions. As can be seen in this figure incorporating the F-T reaction kinetics into the CFD model decreases the average d_{32} values along the reactor by an average of 17.63%. Similarly, Figure 6-49 shows axial average gas holdup profiles in the pilot-scale SBCR with and without chemical reactions. As can be observed in this figure incorporating the F-T reaction kinetics into the CFD model decreases the average gas holdup along the reactor by an average of 15.4%. Moreover, Figure 6-50 shows the cross sectional contours of the gas holdup in the pilot-scale SBCR. It is important to note that despite the changes of the average d_{32} and gas holdup values along the reactor in the presence of chemical reaction, the liquid

recirculation patterns exhibited in the pilot-scale SBCR under these conditions was similar to that obtained in the absence of chemical reaction as can be observed in Figure 6-51.

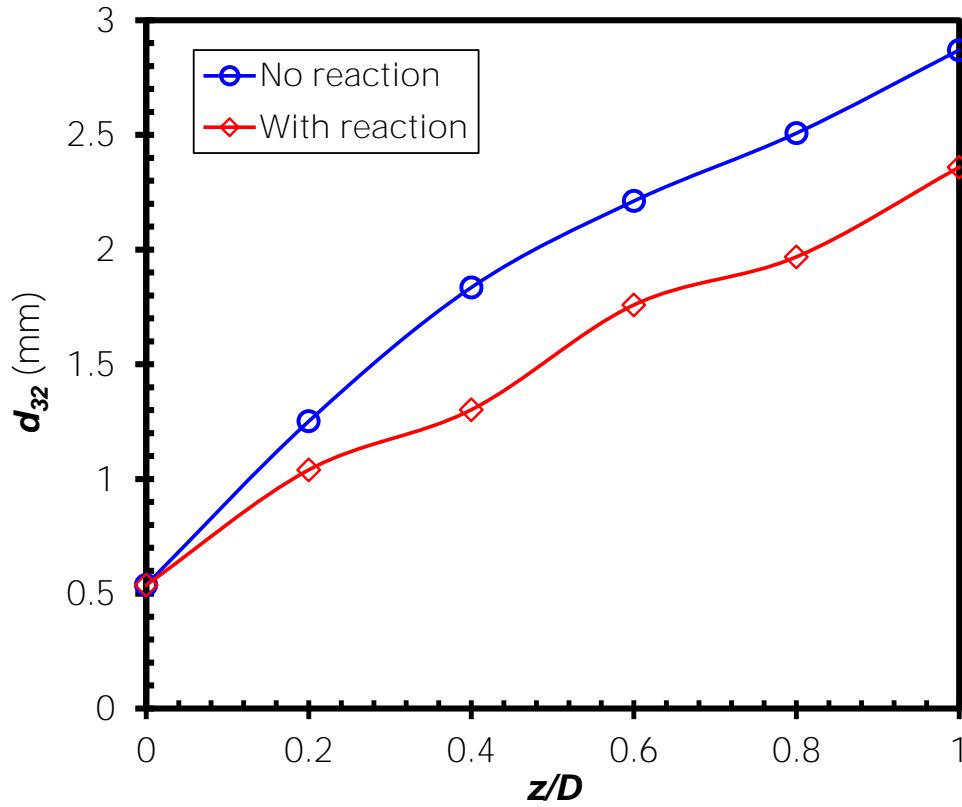


Figure 6-48: Effect of coupling kinetics on the average Sauter mean bubble diameter in the Pilot-scale SBCR

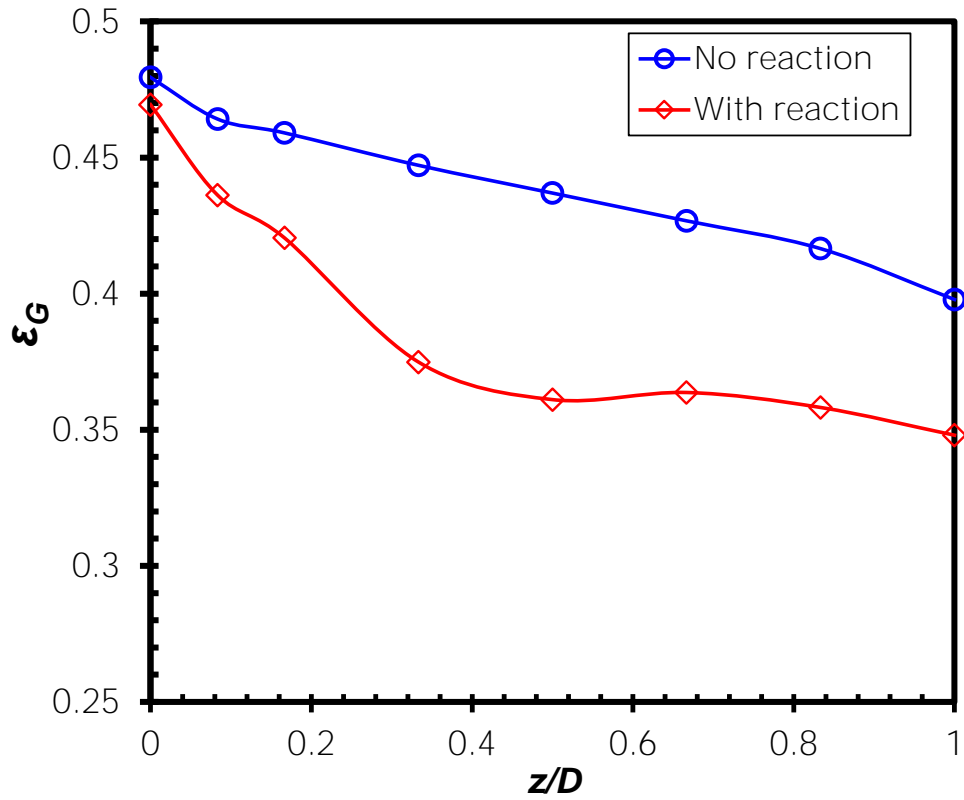


Figure 6-49: Effect of incorporating kinetics in the CFD model on the average gas holdup in the pilot-scale SBCR

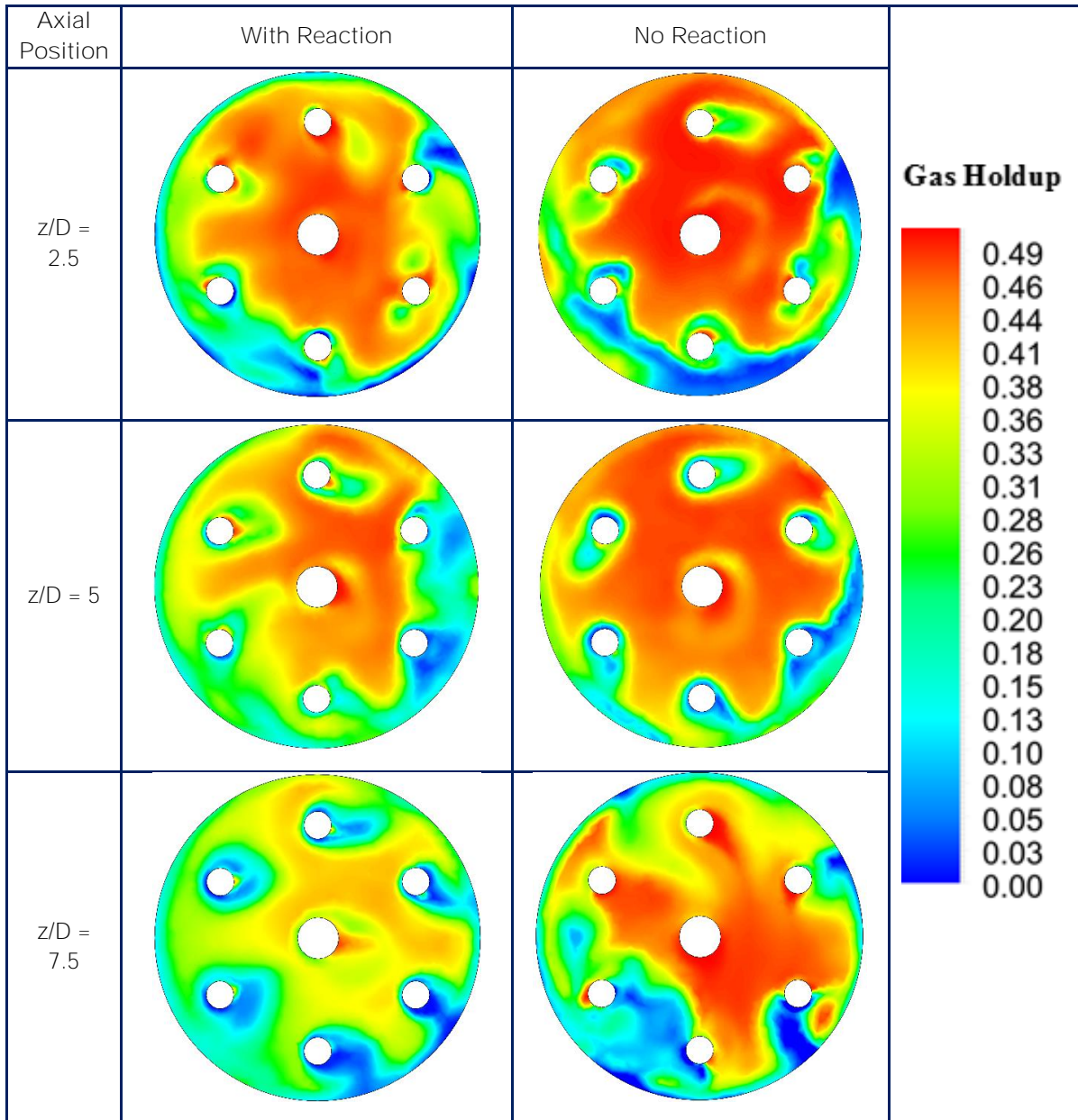


Figure 6-50: Effect of incorporating kinetics in the CFD model on the gas holdup contours with and without chemical reaction at $t = 60$ s in the pilot-scale SBCR

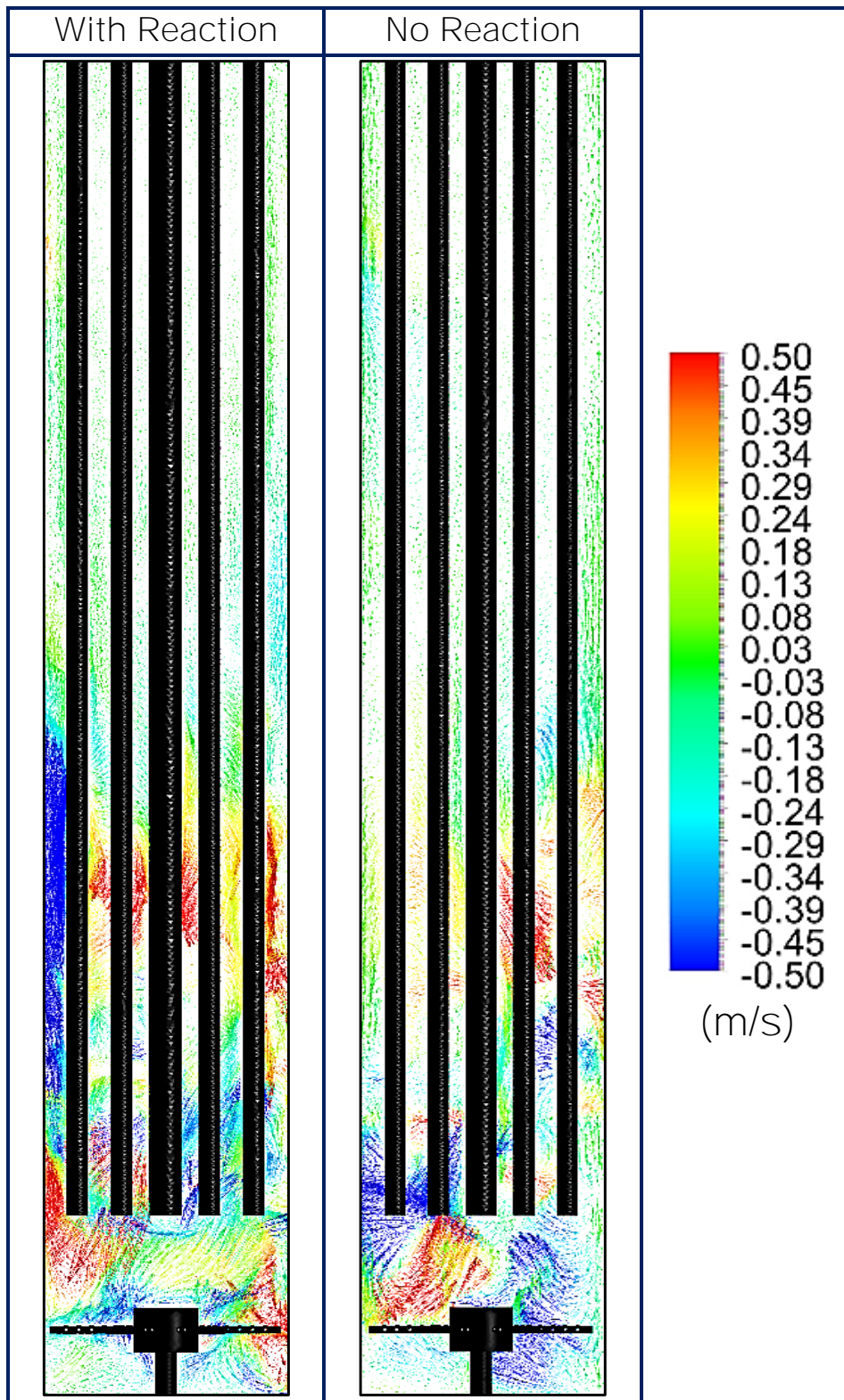


Figure 6-51: Effect of incorporating kinetics in the CFD model on the liquid recirculation patterns with and without chemical reaction at $t = 60$ s in the pilot-scale SBCR

6.3.3 Prediction of the Industrial-Scale SBCR Performance

Our CFD model was then used to predict the performance of the industrial-scale SBCR with the design data and operating conditions given in Table 6-8. Due to the huge number of sparger orifices required, 12 concentric-ring spargers were built at the inlet of the reactor. A cross-section view of the geometry and mesh structure of the reactor is shown in Figure 6-52. The mesh consisted of 8.8 million elements, in addition to a mixed-element grid consisting of 71% tetrahedral, 16% prism, 9% pyramid and 4% hexahedral elements. The average element quality was 0.84 and the minimum element quality was 0.167. It should be noted that although a relatively coarse mesh was selected due to the large size of the reactor, this mesh satisfied the convergence criteria set by Patankar [356] for highly non-linear relaxation coefficients, as previously discussed in Section 6.5.

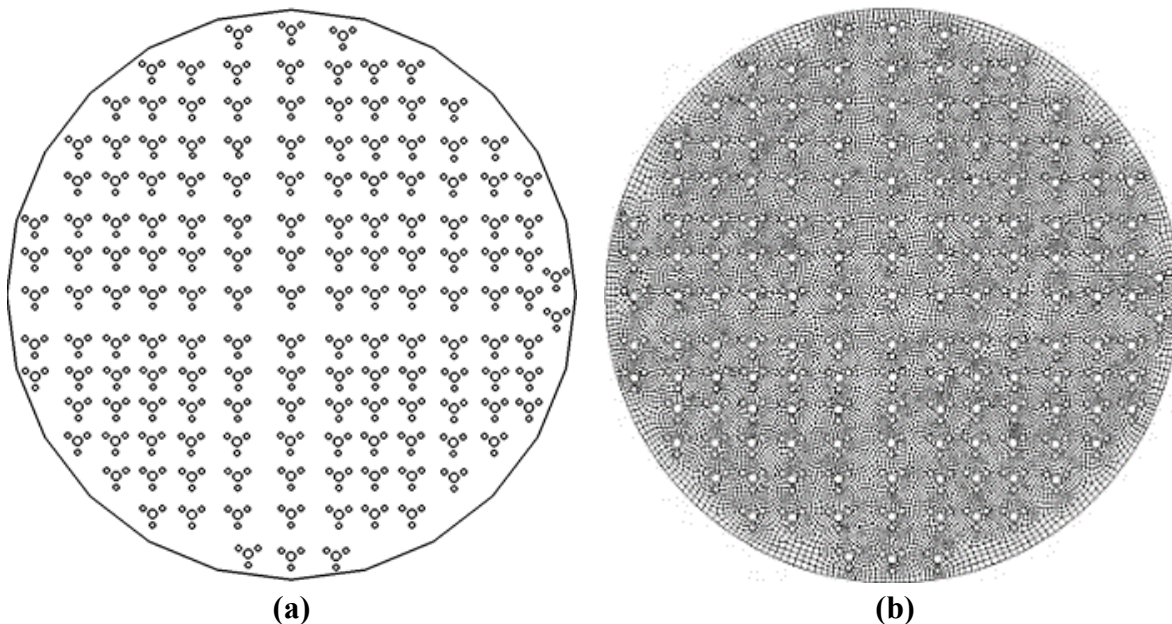


Figure 6-52: Geometry and mesh details of the industrial scale SBCR: (a) Cross-sectional view, (b) mesh structure

The CFD simulations were conducted at four superficial gas velocities of 0.12, 0.24, 0.30 and 0.40 m/s. Figures 6-53 through 6-55 show the simulation results for the CO conversion, H₂ conversion and C₅⁺ products yields, respectively. Under these conditions, the results indicated that the CO conversions are 48%, 59%, 58% and 55% at the superficial gas velocities of 0.12, 0.24, 0.3 and 0.4 m/s, respectively. Similarly, the H₂ conversions are 36%, 51%, 56% and 54% at the superficial gas velocities of 0.12, 0.24, 0.3 and 0.4 m/s, respectively. The C₅₊ products yields are 275, 576, 627 and 654 ton/day at superficial the gas velocities of 0.12, 0.24, 0.3 and 0.4 m/s, respectively.

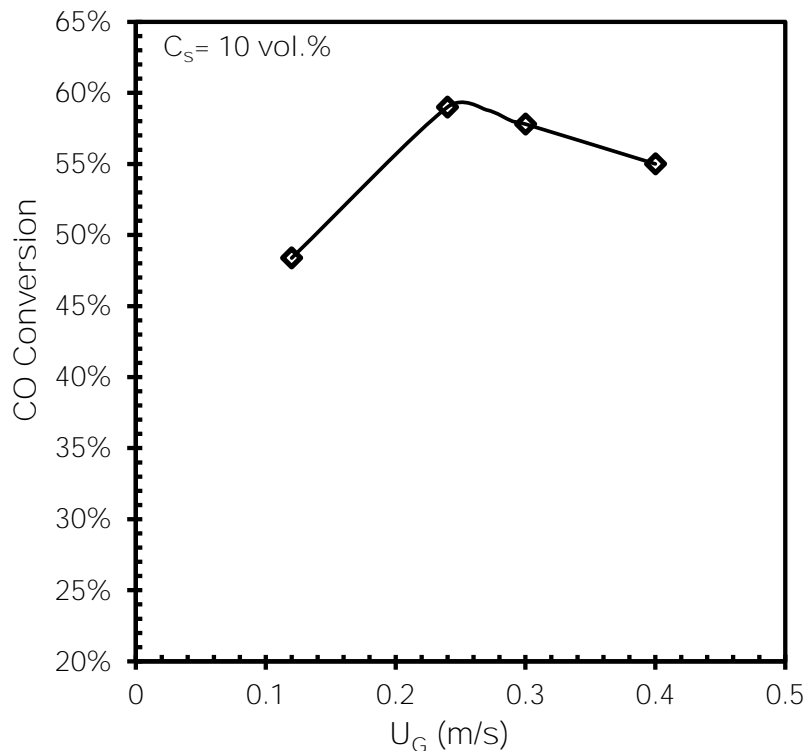


Figure 6-53: CFD model predictions of the CO conversion for different superficial gas velocities for F-T synthesis in the industrial-scale SBCR

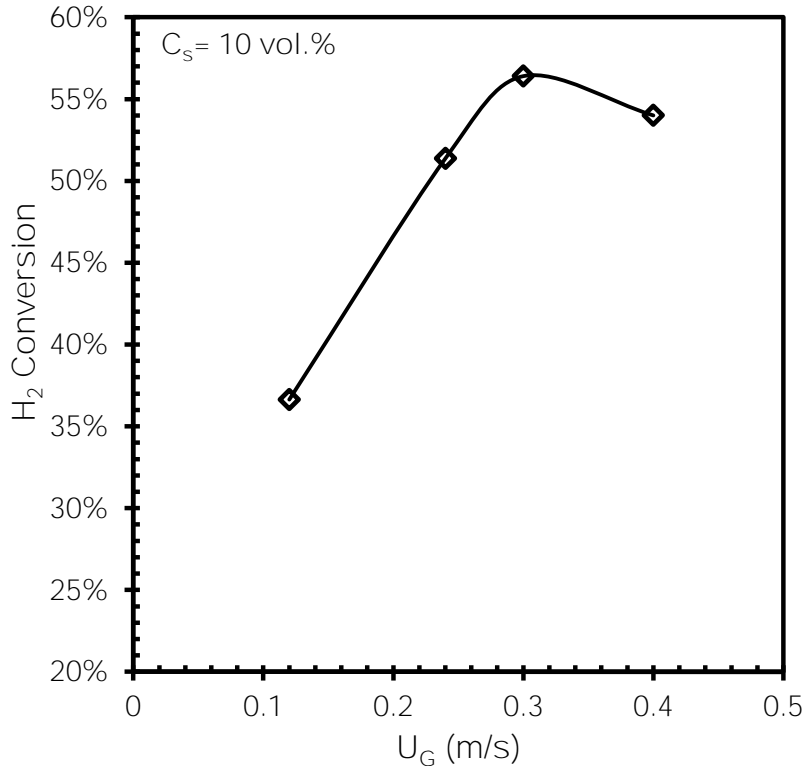


Figure 6-54: CFD model predictions of H_2 conversion for different superficial gas velocities for F-T synthesis in the industrial-scale SBCR

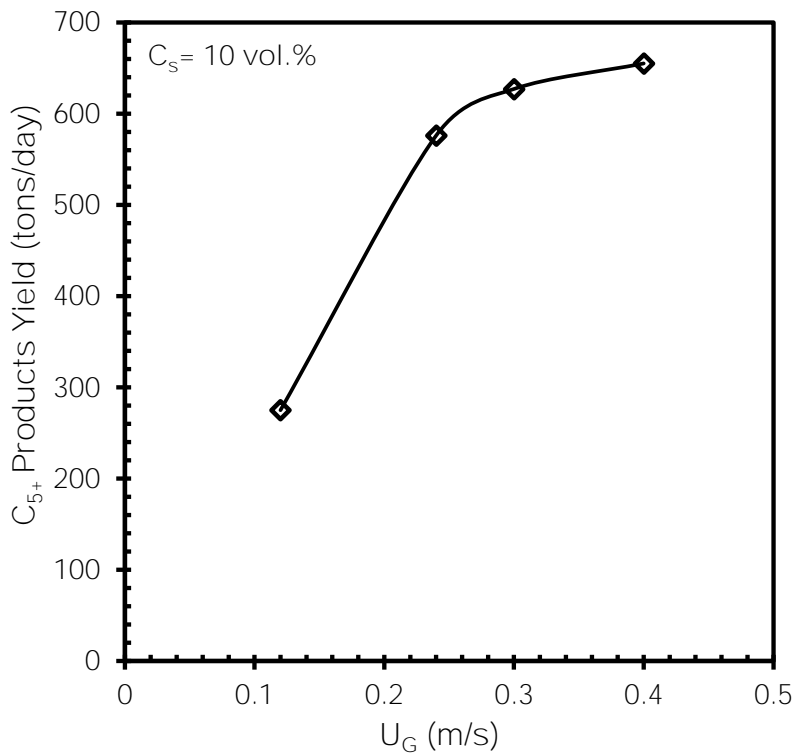


Figure 6-55: CFD model predictions of the C_{5+} products yield for different superficial gas velocities for F-T synthesis in the industrial-scale SBCR

7.0 CONCLUDING REMARKS

1. A three-phase, 3-D comprehensive CFD model to predict the local hydrodynamics and performance of SBCRs for F-T synthesis was developed. The kinetic theory of granular flow (KTGF) was used to represent the solid-phase behavior, and the model by Gidaspow [242] was used to describe the solid viscosity. The bubbles induced turbulence was considered by introducing two source terms, S_k and S_ε , into the k - ε equation to account for the covariance of the liquid- and dispersed-phase velocities as well as the relative and drift velocity effects. Also, a bubble population balance was included to represent the bubble size distribution. In addition, the model incorporated the breakup and coalescence models by Lou and Svendsen [405] and Prince and Blanch [348], respectively. The CFD model was developed in ANSYS and a first order implicit time stepping was used to advance the solution in time. Moreover, due to the strong non-linear characteristics of the model, relaxation coefficients, as proposed by Patankar [356], were introduced in the momentum conservation equations.
2. The CFD model predictions, in the absence of F-T reactions, were tested against the experimental data by Yu and Kim [3] for air-water-glass beads system and by Chen et al. [4] for N₂-Drakeol-glass beads system in order to select the turbulence and drag models. Based on these validations, of inclusion of the RNG k - ε turbulence model coupled with the gas-liquid drag model by Wen-Yu [5], the liquid-solid drag model by Schiller Naumann [6] and the lift

coefficient by Tomiyama [7] in the CFD model, allowed the most accurate predictions of these experimental data.

3. Due to the absence of adequate hydrodynamics and mass transfer data in the literature to validate our CFD model, an experimental program was devised to measure the gas holdup (ϵ_G), Sauter mean bubble diameter (d_{32}), and volumetric mass transfer coefficients (k_{LA}) for gaseous mixtures of He/N₂ as surrogates for H₂/CO in F-T reactor wax containing iron catalyst in a pilot-scale (0.3-m ID, 3-m height) SBCR. These data were measured under various operating conditions, pressures (4-31 bar), temperatures (380-500 K), superficial gas velocities (0.1-0.3 m/s) and catalyst concentrations (0-15 vol. %), which are typical to those of the F-T synthesis. The gas distributor used for gas sparging was a 6-arms spider. The F-T reactor wax was provided by the National Institute of Clean and Low-Carbon Energy (NICE), China; and was obtained from a large-scale (5.8-m ID, 30-m height) SBCR operating with iron catalyst under actual F-T industrial conditions. The CFD model predictions, in the absence of F-T chemical reactions, were validated against the gas holdup data obtained in this study under actual F-T conditions, and this validation underscored the importance of including the k_{LA} correlation in the CFD model in order to precisely predict the gas holdup data in the pilot-scale SBCR.
4. After validation, the CFD model was used to predict the effect of internals on the local hydrodynamics (local gas hold up, liquid and gas velocity vectors, mixing intensities) inside the pilot-scale SBCR reactor (0.3-m ID, 3-m height) provided with the 6-arms spider for gas sparging. From the simulation results obtained in the absence of F-T reactions, the following remarks can be made:
 - a. The presence of internals generally increases the gas holdup when compared with the reactor without internals. This behavior could be due to a decrease of the area available for

gas flow. Moreover, there is a significant effect on the radial distribution of the gas holdup, as more even radial distribution can be seen in the presence of internals.

- b. The presence of internals does not have a significant effect on the turbulence intensity during the first 40 s, when compared with the case without internals. However, after 40 s, there is a significant increase in the turbulence intensity in the presence of internals, particularly in the upper region of the reactor where the internals are present. This is primarily due to the effect of internals on the longitudinal funneling of the flow, which tends to control the size of large scale eddies, resulting in a more turbulent flow. Moreover, the presence of internals results in a significantly different flow structure throughout the reactor after the 40 s, with smaller and faster liquid recirculation cells in the vicinity of the sparger, and larger liquid recirculation in the upper part of the reactor where the internals are present.
- c. Increasing the internals length increases the overall gas holdup and results in less steep radial gas holdup profiles in the vicinity of the internals. Also, there is a general increase of the turbulence intensity, primarily in the upper regions of the reactor. Moreover, there is significant liquid funneling and larger recirculations at the internals zone and smaller, faster recirculations in the vicinity of the sparger.
- d. The number of internals does not have a significant effect on the gas holdup, which seems to be governed by the internal cross-sectional areal coverage of the internals. On the other hand, the number of internals appears to have significant effects on enhancing liquid backmixing when compared with that of the cross-sectional area coverage. Thus, the presence of internals and their combination can increase or decrease backmixing depending on their design and arrangement

- e. Increasing the number internals for the same cross-sectional areal coverage did not have a significant effect on the overall gas holdup inside the reactor. The internal mixing and the backmixing fraction, nonetheless, increased significantly (about 50% higher) with increasing the number of internals.
 - f. The local gas holdup and liquid backmixing fraction inside the SBCR provided with internals appeared to increase with increasing the inlet superficial gas velocity and temperature for all internals configurations used.
5. The CFD model was then used to investigate the effect of the gas sparger type and orientation on the gas holdup, Sauter mean bubble diameter, axial concentration profiles, mean axial velocity profiles and the flow structure in the pilot-scale (0.3-m ID, 3-m height), with no internals and no F-T reactions. A 6-arms spider, a concentric ring sparger, with upward and downward facing orifices, and a perforated plate distributor were used in this investigation. The following conclusions can be drawn:
- a. The gas holdups obtained using the three spargers vary with the axial and radial positions in the SBCR and the radial gas holdup exhibits a non-linear behavior at any axial position as illustrated by the gradual variation in the color shades of the gas holdup from the center to the wall of the reactor. It should be pointed out that the maximum gas holdup value can be mainly seen near the center of the reactor before it gradually decreases along the radii with various profiles in the axial direction. Also, the 6-arms spider and concentric-rings spargers showed distinctly steeper radial gas holdup profiles, whereas, the perforated plate showed a more uniform gas holdup distribution, which reached the steady-state much sooner than the other two spargers.

- b. The CFD model confirmed that the sparger design and configuration have significant impact on the local hydrodynamics. For the 6-arms spider, relatively high liquid turbulence intensities can be observed in the vicinity of the sparger during the startup time, however, after reaching steady-state, the turbulence intensities become more evenly distributed throughout the reactor. For the concentric-rings sparger, the turbulence intensities are more uniform throughout the reactor during the first 40 s, however, their values increase drastically near the walls at 60 s, due to the development of large recirculation cells. On the other hand, the perforated plate exhibits higher turbulence intensities throughout the reactor with higher values near the top after 40 s, which is different from those shown using the other two spargers.
- c. For the 6-arms spider sparger, smaller and faster liquid recirculation cells are present in the vicinity of the sparger from the startup until the steady-state. Also, larger and slower liquid recirculation cells appear to develop after around 1.2 time the reactor diameter (measured from the bottom flange). These smaller and faster liquid recirculations in the vicinity of the sparger are primarily due to the geometry of this sparger type because all gas sparging orifices are located on the sides and bottom and none on the top of each sparger arms. For the concentric-rings and perforated plate spargers, only large and slow recirculation cells are present throughout the column above the distributor zone, which is in contrast with liquid velocity vectors observed when using the 6-arms spider.
- d. Both the upward and downward 6-arms spider orifice orientations give higher gas holdup values when compared with those of the concentric-rings spargers. The 6-arms spider with upward facing orifices resulted in the highest gas holdups. However, at low superficial gas velocities ($U_g < 0.15$ m/s), the concentric-rings sparger with downward facing orifices

gives higher gas holdup values than those using the sparger provided with upward facing orifices.

- e. The concentric-rings spargers resulted in greater d_{32} values when compared with those of the 6-arms spider, which can be attributed to the larger orifice size (7 mm ID) for the concentric-rings sparger versus 5 mm ID for the 6-arms spider. The effect of the superficial gas velocity on the d_{32} obtained with the 6-arms spider was insignificant, which is in agreement with the experimental data.
- f. The effect of superficial gas velocity on the d_{32} , however, was more significant for the concentric-rings upward facing orifices sparger as a result of the turbulent eddies created, which enhanced the bubbles coalescence. This is because bubbles coalescence and breakup mechanisms is primarily governed by the turbulent eddies, which in turn, are controlled by the liquid and gas velocities [288]. The bubble breakup, however, is governed by the turbulent stresses, which are controlled by the pressure variations within the fluid and subsequently are related to the physical property gradients within the continuous-phase [348].
- g. The downward facing orifices spargers give a more uniform axial solids distribution, whereas, the upward facing orifices spargers result in a solid accumulation near the bottom of the reactor. Actually, high solid concentrations (up to 17.2 vol %) can be seen at the bottom of the reactor at superficial gas velocity 0.2 m/s, leading to lower solid concentrations above and far from the sparger.
- h. The concentric-rings sparger with upward facing orifices resulted in higher solid concentrations at the bottom of the reactor when compared with those of the 6-arms spider with upward facing orifices. This behavior could be due to the fact that the 6-arms spider

has also nozzles on the sides of each arms, which helped in enhancing mixing around this sparger.

- i. The effect of sparger orifices orientation on the axial solids distribution profile at an axial position (z) to the total height (H) ratio (z/H) greater than 0.2 appear to decrease with increasing the superficial gas velocity. Generally, the spargers with downward facing orifices were more effective in solids distribution when compared with those with upward facing orifices. This is due to the increased mixing provided by the gas jets from the downward facing orifices, which increased the solid particles distribution.
6. The CFD model was then used to study the effect of four parallel and four bundled internals configurations on the gas holdup and liquid axial velocity inside a Conceptual SBCR (1-m ID, 10 m high), and in the absence of F-T reactions, the following remarks can be made:
- a. For the parallel internals, in the larger Conceptual reactor, faster, larger liquid recirculations were exhibited at a much earlier time, when compared to similar simulations inside the Pilot Scale SBCR. Moreover, the presence of internals significantly enhanced liquid funneling in the Conceptual reactor when compared to pilot-scale SBCR. On the other hand, the gas holdup profiles were found take a longer time to develop in the pilot-scale SBCR when compared to the Conceptual reactor.
 - b. On the other hand, in the presence of bundled internals, strong liquid recirculations are exhibited for the 1 and 3 bundle configurations, whereas, weaker liquid recirculations were shown for the 4 and 5 bundle configurations. Also, backmixing zones in the bundled arrangements seem to be affected by the presence of wall clearance zones, especially in the configurations which promote large wall clearances, such as the 3 bundle and 5 bundle arrangements, where the large wall clearance zones generated unique backmixing profiles.

Bundled internals also exhibited smoother radial gas holdup profiles, with lower local gas holdup values when compared to the parallel internals. This behavior is primarily due to the increase of the average bubble size for bundled internals when compared with those for parallel internals.

- c. The bundled internals result in higher Sauter mean bubble diameter (d_{32}) values when compared with those for the parallel internals. This behavior could be due to the fact that the presence of parallel internals enhances bubble breakup and inhibits bubble coalescence, whereas, the presence of bundled internals enhances bubble coalescence. Also, the bubble size appears to increase with decreasing the cross-sectional area for the parallel internals and increasing the number of bundled internals. This behavior could be related to the effect of the distance between the internals in the case of parallel configurations, where lower cross-sectional area coverages result in wider distance between the internals, leading to the formation of large gas bubbles. For bundled internals, on the other hand, this effect is due to the wall clearance, where bigger clearances resulted in increased bubble diameter.
7. The CFD model was also used to simulate the performance of the pilot-scale SBCR reactor available in our laboratory and an industrial-scale SBCR for F-T synthesis using iron catalyst. The kinetic expressions of the F-T synthesis and water-gas-shift provided by NICE were included in the CFD model. The CO and H₂ conversions and C₅⁺ yields were calculated at different operating conditions. The following remarks can be made:
- a. The CFD model was used to simulate the performance of the pilot-scale (0.3-m, 3-m height) F-T SBCR, provided with internals in a single bundled arrangement of one, 2.5-inch pipe at the center of the reactor, surrounded by 6, 1.75-inch pipes in a hexagonal pattern and a six arm spider sparger and operating with NICE iron catalyst. The CFD

model was capable of predicting the overall performance and the local hydrodynamics in this pilot-scale SBCR. The simulations were carried out with a catalyst concentrations of 5, 10 and 15 vol% and three H₂/CO ratios of 1, 1.5 and 2, at temperature of 443 K, pressure of 20.5 bar, and a superficial gas velocity of 0.24 m/s. The Simulation results showed that the CO and H₂ conversions increase with increasing the catalyst concentration. Also, the pilot scale SBCR can produce a maximum of 1.87 tons/day of C₅⁺ products when using a catalyst concentration of 15 vol%.

- b. The CFD model was also used to simulate the performance of a commercial-scale (5.8-m ID, 42-m height) F-T SBCR, provided with 604 internals and a concentric ring sparger, and operating with NICE iron catalyst. The CFD model was capable of predicting the overall performance and the local hydrodynamics in this commercial-scale SBCR. The simulations were conducted at a catalyst loading of 10 vol% at a temperature of 528 K, pressure of 29 bar and four superficial gas velocities of 0.12, 0.24, 0.3 and 0.4 m/s. Under these conditions, the simulation results indicated that the CO conversions were 48%, 59%, 58% and 55%; the H₂ conversions were 36%, 51%, 56% and 54% and the C₅⁺ products yields were are 275, 576,627 and 654 ton/day at the superficial gas velocities of 0.12, 0.24, 0.3 and 0.4 m/s, respectively.
- c. Thus, the CFD model built and validated in this work could be used to optimize the SBCR design and/or troubleshoot any problems associated with the internal reactor operation.

APPENDIX A

LITERATURE REVIEW TABLES

Table A-1: Kinetics studies for the F-T synthesis on iron catalyst

Catalyst	Reactor	Operating Conditions			Equation	Reference
		T (°C)	P, MPa	H ₂ /CO feed		
Fe	Fixed Bed	-	-	-	$r_{FT} = k_{FT} P_{H_2}^2 P_{CO}$	Brotz [406]
Reduced Fused Fe/K ₂ O/MgO	Fixed Bed, Fluidized Bed, Slurry	250-320	2.2-4.2	2.0	$r_{FT} = k_{FT} P_{total}$	Hall et al. [407]
Reduced Nitrided Fe	Fixed Bed	-	-	-	$r_{FT} = k_{FT} \frac{P_{H_2} P_{CO}}{P_{CO} + a P_{CO_2}}$	Anderson [408]
Reduced Nitrided Fused Fe	Fixed Bed	225-240	2.2	0.25-2.0	$r_{FT} = a P_{H_2}^{0.6} P_{CO}^{0.4} - b P_{H_2O}^{0.5} r_{FT}^{0.5}$	Anderson and Karn [409]
Fused Fe & Prec. Fe/Cu/MgO/K ₂ CO ₃	Fixed Bed	200-280	10	3.1 ²	$r_{FT} = a P_{H_2}^{1.5} P_{CO}^{0.2} - b P_{H_2O}^{0.2} r_{FT}^{0.5}$	Kolbel et al. [410]
Reduced Nitrided Fused Fe/Cr ₂ O ₃ /SiO ₂ /MgO/K ₂ O	Fixed Bed	225-255	2.2	0.25-2.0	$r_{FT} = P_{H_2}^{0.66} P_{CO}^{0.34}$	Anderson et al. [411]
Reduced Fused Fe/K ₂ O/Al ₂ O ₃ /SiO ₂	Fixed Bed	225-265	1.0-1.8	1.2-7.2	$r_{FT} = k_{FT} P_{H_2}$	Dry et al. [412]
Fe	Fixed Bed, Fluidized Bed	200-340	0.5-4.0	1.0-7.3	$r_{FT} = k_{FT} \frac{P_{H_2} P_{CO}}{P_{CO} + a P_{H_2O}}$	Dry [413]
Reduced Nitrided Fused Fe/K ₂ O/Al ₂ O ₃ /SiO ₂	Gradientless Fixed Bed	250-315	2.0	2.0	$r_{FT} = k_{FT} \frac{P_{H_2} P_{CO}}{P_{CO} + a P_{H_2O}}$	Atwood and Bennett [414]

Table A-1 (continued)

Catalyst	Reactor	Operating Conditions			Equation	Reference
		T (°C)	P, MPa	H ₂ /CO feed		
Plasma Sprayed Fe	Recirculating Reactor	250-300	0.77-3.1	1.5-3.9	$r_{FT} = k_{FT} \frac{P_{H_2} P_{CO}}{P_{CO} + aP_{H_2O}}$	Thomson et al. [415]
Reduced Prec. Fe/Cu/K ₂ O	Fixed Bed	220-270	1.0-2.0	1.0-6.0	$r_{FT} = k_{FT} \frac{P_{H_2}}{P_{CO}^{0.25}}$	Feimer et al. [416]
Reduced Fused Fe/K ₂ O/CaO/SiO ₂	Slurry	232-263	0.4-1.5	0.5-1.8	$r_{FT} = k_{FT} \frac{P_{H_2}^2 P_{CO}}{P_{CO} P_{H_2} + aP_{H_2O}}$	Huff and Satterfield [59]
Fe/Cu/K	-	265	-	-	$r_{FT} = k_{FT} \frac{P_{H_2} P_{CO}}{P_{CO} + aP_{CO_2}}$	Leib and Kuo [417]
Reduced Prec. Fe/K	Slurry	220-260	1.0	0.5-0.6	$r_{FT} = k_{FT} \frac{P_{H_2} P_{CO}}{P_{CO} + aP_{CO_2}}$	Ledakowicz et al. [60]
Prec. Fe & Fused Fe	Slurry	210-280	0.5-5.5	0.5-3.5	$r_{FT} = k_{FT} \frac{P_{H_2} P_{CO}}{P_{CO} + aP_{H_2O}}$ $r_{FT} = k_{FT} \frac{P_{H_2} P_{CO}}{P_{CO} + aP_{CO_2}}$	Nettelhoff et al. [418]
Reduced Prec. Fe/K	Slurry	220-260	-	0.5-2.0	$r_{FT} = k_{FT} \frac{P_{H_2} P_{CO}}{P_{CO} + aP_{CO_2}}$ $r_{FT} = k_{FT} \frac{P_{H_2}^2 P_{CO}}{P_{CO} P_{H_2} + aP_{H_2O}}$	Deckwer et al. [419]
Prec. Fe/Cu/K & Reduced Fe/Cu/K/SiO ₂	Slurry	235-265	1.5-3.0	0.6-1.0	$r_{FT} = k_{FT} P_{H_2}$ $r_{FT} = k_{FT} \frac{P_{H_2} P_{CO}}{P_{CO} + aP_{H_2O}}$	Zimmerman and Bukur [420]
Prec. Fe/Cu/K	Gradientless	230-264	1.0-2.6	1.1-2.4	$r_{FT} = k_{FT} \frac{P_{H_2} P_{CO}}{P_{CO} + aP_{H_2O}}$ $r_{FT} = k_{FT} \frac{P_{H_2}^2 P_{CO}}{P_{CO} P_{H_2} + aP_{H_2O}}$	Shen et al. [421]

Table A-1 (continued)

Catalyst	Reactor	Operating Conditions			Equation	Reference
		T (°C)	P, MPa	H ₂ /CO feed		
Reduced Prec. Fe/Cu/K	Fixed Bed	220-300	1.0-3.2	1.1-2.8	$r_{FT} = k_{FT} \frac{P_{H_2} P_{CO}}{P_{CO} + aP_{H_2O}}$	Liu et al. [422]
Reduced Prec. Fe/Cu/K/SiO ₂	Slurry	250	1.2-4.0	0.25-4.0	$r_{FT} = k_{FT} \frac{P_{H_2}^{0.5} P_{CO}}{(1 + aP_{CO} + bP_{CO_2})^2}$	van der Laan [423]
Reduced Prec. Fe/CuO/K ₂ O/Na ₂ O/SiO ₂	Fixed Bed	250-350	0.6-2.1	3.0-6.0	$r_{C_n H_{2n+2}} = k_5 \frac{P_{H_2} \left(\frac{k_1 P_{CO}}{k_1 P_{CO} + k_5 P_{H_2}} \right) \alpha^{n-1}}{1 + \left(\frac{k_1 P_{CO}}{k_1 P_{CO} + k_5 P_{H_2}} \right) \frac{1}{\alpha - 1}}$ $r_{C_n H_{2n}} = k_6 \frac{P_{H_2} \left(\frac{k_1 P_{CO}}{k_1 P_{CO} + k_5 P_{H_2}} \right) \alpha^{n-1}}{1 + \left(\frac{k_1 P_{CO}}{k_1 P_{CO} + k_5 P_{H_2}} \right) \frac{1}{1 - \alpha}}$ $\alpha = \frac{k_1 P_{CO}}{k_1 P_{CO} + k_5 P_{H_2} + k_6}$	Lox and Froment [50, 51]
Precipitated Fe	Slurry	210-250	1.38-4.12	1-7	$r_{FT} = \frac{k_{FT} P_{CO} P_{H_2}^{0.5}}{P_{CO} + aP_{H_2O}}$	van Berge [424]
Reduced Prec. Fe/Cu/K/SiO ₂	Spinning Basket	250	0.8-4.0	0.25-4.0	$r_{FT} = k_{FT} \frac{P_{H_2} P_{CO}}{1 + aP_{CO} + bP_{H_2O}}$ $r_{FT} = k_{FT} \frac{P_{H_2} P_{CO}}{(1 + aP_{CO} + bP_{H_2O})^2}$ $r_{FT} = k_{FT} \frac{P_{H_2}^{0.5} P_{CO}}{(1 + aP_{CO} + bP_{H_2O})^2}$	van der Laan and Beenackers [425]
Fe	Fixed Bed	220-260	2.4	1.87-2.0 ⁵	$r_{FT} = k_{FT} C_{H_2} \frac{1}{1 + 1.6 \frac{C_{H_2O}}{C_{CO}}}$	Jess et al. [426]
Fe & Fe/Al ₂ O ₃ /Cu/K ₂ O & Fe/Mn/Cu/K ₂ O	Slurry	225-275	P _{H₂} =0.26-3.02 P _{CO} =0.02-1.94-		$r_{c,org} = \frac{k_{FT} (P_{H_2}^{1.5} P_{CO} / P_{H_2O})}{(1 + a(P_{H_2} P_{CO} / P_{H_2O}))^2}$	van Steen and Schulz [427]

Table A-1 (continued)

Catalyst	Reactor	Operating Conditions			Equation	Reference
		T (°C)	P, MPa	H ₂ /CO feed		
Fe & Fe/K	Slurry	200-240	1.0	1.0-3.0	$r_{FT} = k_{FT}(P_{H_2})^x(P_{CO})^y$	Eliason and Bartholomew [428]
Fe/Cu/K	-	-	-	-	$r_{CH_4} = \frac{k_{5M}P_{H_2}\alpha_1}{1 + \left(1 + \frac{1}{K_2K_3K_4} \frac{P_{H_2O}}{P_{H_2}^2} + \frac{1}{K_2K_3P_{H_2}} + \frac{1}{K_4}\right) \sum_{i=1}^N (\prod_{j=1}^i \alpha_j)}, (n = 1)$ $r_{C_nH_{2n+2}} = \frac{k_5P_{H_2} \prod_{j=1}^i \alpha_j}{1 + \left(1 + \frac{1}{K_2K_3K_4} \frac{P_{H_2O}}{P_{H_2}^2} + \frac{1}{K_2K_3P_{H_2}} + \frac{1}{K_4}\right) \sum_{i=1}^N (\prod_{j=1}^i \alpha_j)}, (n \geq 2)$ $r_{C_nH_{2n}} = \frac{k_6(1 - \beta_n) \prod_{j=1}^i \alpha_j}{1 + \left(1 + \frac{1}{K_2K_3K_4} \frac{P_{H_2O}}{P_{H_2}^2} + \frac{1}{K_2K_3P_{H_2}} + \frac{1}{K_4}\right) \sum_{i=1}^N (\prod_{j=1}^i \alpha_j)}, (n \geq 2)$ $r_{CO_2} = \frac{k_V \left(\frac{P_{CO}P_{H_2O}}{P_{H_2}^{0.5}} - \frac{P_{CO_2}P_{H_2}^{0.5}}{K_p} \right)}{1 + \frac{K_V P_{CO} P_{H_2O}}{P_{H_2}^{0.5}}}$ $\alpha_1 = \frac{k_1 P_{CO}}{k_1 P_{CO} + k_{5M} P_{H_2}}, (n = 1)$ $\alpha_n = \frac{k_1 P_{CO}}{k_1 P_{CO} + k_5 P_{H_2} + k_6(1 - \beta_n)}, (n \geq 2)$ $\beta_n = \frac{\frac{k_{-6}}{k_6} P_{C_nH_{2n}}}{\left[\alpha_A^{n-1} \frac{k_1 P_{CO}}{k_1 P_{CO} + k_5 P_{H_2}} + \frac{k_1 P_{CO}}{k_1 P_{CO} + k_5 P_{H_2} + k_6} \sum_{i=2}^n \alpha_A^{i-1} P_{C_{(n-i+2)}H_{2(n-i+2)}} \right]}, (n \geq 2)$ $\alpha_n = \frac{k_1 P_{CO}}{k_1 P_{CO} + k_5 P_{H_2} + k_6}, (n \geq 2)$ $K_p = \frac{5078.0045}{T} - 5.8972089 + 13.958689 \times 10^{-4} T - 27.592844 \times 10^{-8} T^2$	Wang et al. [52, 429]

Table A-1 (continued)

Catalyst	Reactor	Operating Conditions			Equation	Reference
		T (°C)	P, MPa	H ₂ /CO feed		
Reduced Fe/Cu/K	Fixed Bed	220-269	1.1-3.1	1.0-3.0	$r_{CH_4} = \frac{k_{5M} P_{H_2} \alpha_1}{1 + \left(1 + \frac{1}{K_2 K_3 K_4} \frac{P_{H_2 O}}{P_{H_2}^2} + \frac{1}{K_3 K_4 P_{H_2}} + \frac{1}{K_4}\right) \sum_{i=1}^N (\prod_{j=1}^i \alpha_j)}$ $(n = 1)$ $r_{C_n H_{2n+2}} = \frac{k_5 P_{H_2} \prod_{j=1}^i \alpha_j}{1 + \left(1 + \frac{1}{K_2 K_3 K_4} \frac{P_{H_2 O}}{P_{H_2}^2} + \frac{1}{K_3 K_4 P_{H_2}} + \frac{1}{K_4}\right) \sum_{i=1}^N (\prod_{j=1}^i \alpha_j)}$ $(n \geq 2)$ $r_{C_n H_{2n}} = \frac{k_6 (1 - \beta_n) \prod_{j=1}^i \alpha_j}{1 + \left(1 + \frac{1}{K_2 K_3 K_4} \frac{P_{H_2 O}}{P_{H_2}^2} + \frac{1}{K_3 K_4 P_{H_2}} + \frac{1}{K_4}\right) \sum_{i=1}^N (\prod_{j=1}^i \alpha_j)}$ $(n \geq 2)$ $r_{CO_2} = \frac{k_V \left(\frac{P_{CO} P_{H_2 O}}{P_{H_2}^{0.5}} - \frac{P_{CO_2} P_{H_2}^{0.5}}{K_p} \right)}{1 + \frac{K_V P_{CO} P_{H_2 O}}{P_{H_2}^{0.5}}}$	Wang et al. [430]
Reduced Fe/Mn	Fixed Bed	267-327	1.0-3.0	1.0-3.0	$r_{CH_4} = \frac{k_{7M} K_4 K_6 K_3' P_{CO} P_{H_2}^3}{P_{H_2 O} \left[1 + \sqrt{K_4 P_{H_2}} + K_1 P_{CO} + \frac{K_3' P_{CO} P_{H_2}^2}{P_{H_2 O}} + K_1 K_2 P_{CO} P_{H_2} + \frac{K_6 K_4^{0.5} K_3' P_{CO} P_{H_2}^{2.5}}{P_{H_2 O}} + \frac{K_3' P_{CO} P_{H_2}^2}{P_{H_2 O}} \left(1 + K_6 \sqrt{K_4 P_{H_2}} \right) \sum_{i=1}^N \left(\prod_{j=1}^i \alpha_j \right) \right]^2}$	Yang et al. [431]

Table A-1 (continued)

Catalyst	Reactor	Operating Conditions			Equation	Reference
		T (°C)	P, MPa	H ₂ /CO feed		
					$r_{C_nH_{2n+2}} = \frac{k_7 K_4 K_6 K_3' P_{CO} P_{H_2}^3}{P_{H_2O}} \prod_{j=1}^i \alpha_j$ $\left[1 + \sqrt{K_4 P_{H_2}} + K_1 P_{CO} + \frac{K_3' P_{CO} P_{H_2}^2}{P_{H_2O}} + K_1 K_2 P_{CO} P_{H_2} + \frac{K_6 K_4^{0.5} K_3' P_{CO} P_{H_2}^{2.5}}{P_{H_2O}} + \frac{K_3' P_{CO} P_{H_2}^2}{P_{H_2O}} \left(1 + K_6 \sqrt{K_4 P_{H_2}} \right) \sum_{i=1}^N \left(\prod_{j=1}^i \alpha_j \right) \right]^2$ $r_{C_nH_{2n}} = \frac{k_8^+ (1 - \beta_n) K_3' P_{CO}}{P_{H_2O}} \prod_{j=1}^i \alpha_j$ $\left[1 + \sqrt{K_4 P_{H_2}} + K_1 P_{CO} + \frac{K_3' P_{CO} P_{H_2}^2}{P_{H_2O}} + K_1 K_2 P_{CO} P_{H_2} + \frac{K_6 K_4^{0.5} K_3' P_{CO} P_{H_2}^{2.5}}{P_{H_2O}} + \frac{K_3' P_{CO} P_{H_2}^2}{P_{H_2O}} \left(1 + K_6 \sqrt{K_4 P_{H_2}} \right) \sum_{i=1}^N \left(\prod_{j=1}^i \alpha_j \right) \right]^2$	
Fe/Mn & Fe/Cu/K	Spinning Basket	260-300	1.1-2.6	0.67-2.05	$r_{CH_3OH} = k_{9,1} K_1 K_4 K_7 K_8 P_{CO} P_{H_2}^2 [s]^2$ $r_{CH_4} = k_{11,1} \alpha_{T,1} K_2 P_{H_2} [s]^2$ $r_{C_nH_{2n+1}OH} = k_9 K_1 K_4 K_7 K_8 P_{CO} P_{H_2}^2 \prod_{i=1}^{n-1} \alpha_{T,1} [s]^2$ $r_{C_nH_{2n-1}OOH} = \frac{k_{10} K_1 K_7 P_{CO} P_{H_2O}}{K_6} \prod_{i=1}^{n-1} \alpha_{T,1} [s]^2$	Teng et al. [432]

Table A-1 (continued)

Catalyst	Reactor	Operating Conditions			Equation	Reference
		T (°C)	P, MPa	H ₂ /CO feed		
					$r_{C_nH_{2n+2}} = k_{11}K_4P_{H_2} [S]^2 \prod_{i=1}^n \alpha_{T,1}$ $r_{C_nH_{2n}} = k_{12} \sqrt{K_4P_{H_2}} [S] \prod_{i=1}^n \alpha_{T,1} (1 - \beta_n)$	
Precipitated Fe	Slurry	-	-	-	$r_{FT} = \frac{k_{FT}P_{CO}P_{H_2}^{0.5}}{(1 + k_{CO}P_{CO})^2}$	Botes et al. [433]
Fe/Cu/K/SiO ₂	Slurry	250-290	1.0-2.5	0.67-1.5	$r_{CH_4} = K_1K_2K_3K_6k_{7,M}K_4^{0.5} \frac{P_{CO}P_{H_2}^{2.5}}{P_{H_2O}} [S]^2$ $r_{C_nH_{2n+2}} = K_1K_2K_3K_6k_7K_4 \frac{P_{CO}P_{H_2}^3}{P_{H_2O}} \prod_{i=2}^n \alpha_i [S]^2$ $+ P_{H_2}k_h \frac{k_{8,-}P_{C_nH_{2n}}^*[\sigma]}{k_hP_{H_2} + k_{8,+}}, \quad (n \geq 2)$ $r_{C_nH_{2n}} = K_1K_2K_3k_{8,+}(1 - \beta_n) \frac{P_{CO}P_{H_2}^2}{P_{H_2O}} \prod_{i=2}^n \alpha_i [S]^2$ $- P_{H_2}k_h \frac{k_{8,-}P_{C_nH_{2n}}^*[\sigma]}{k_hP_{H_2} + k_{8,+}}, \quad (n \geq 2)$	Chang et al. [434]
Reduced Fe	Slurry	260	1-3	0.8-3.2	$r_{FT} = \frac{k_{FT}C_{CO}C_{H_2}^{0.5}}{(1 + k_{CO}C_{CO})^2}$ $r_{FT} = \frac{k_{FT}C_{CO}C_{H_2}}{(1 + k_{CO}C_{CO})}$	Zhou et al. [435]

Table A-2: Kinetics studies for the WGS reaction on iron catalyst

Catalyst / Promoter	Reactor	Operating Conditions			Equation	Reference
		T (°C)	P, MPa	H ₂ /CO feed		
Fe	Fixed Bed, Fluidized Bed	200-340	0.5-4.0	1.0-7.3	$r_{WGS} = k_{WGS}P_{CO}$	Dry [413]
Reduced Prec. Fe/Cu/K ₂ O	Fixed Bed	220-270	1.0-2.0	1.0-6.0	$r_{WGS} = k_{WGS}P_{CO}$	Feimer et al. [416]
Fe/Cu/K	-	265	-	-	$r_{WGS} = k_{WGS} \frac{\left(P_{CO}P_{H_2O} - \frac{P_{CO_2}P_{H_2}}{K_{eq}}\right)}{P_{CO} + aP_{H_2O}}$	Leib and Kuo [417]
Prec. Fe/Cu/K & Reduced Fe/Cu/K/SiO ₂	Slurry	235-265	1.5-3.0	0.6-1.0	$r_{WGS} = k_{WGS} \frac{\left(P_{CO}P_{H_2O} - \frac{P_{CO_2}P_{H_2}}{K_{eq}}\right)}{P_{CO} + aP_{H_2O}}$ $r_{WGS} = k_{WGS} \frac{\left(P_{CO}P_{H_2O} - \frac{P_{CO_2}P_{H_2}}{K_{eq}}\right)}{P_{CO}P_{H_2} + aP_{H_2O}}$	Zimmerman and Bukur [420]
Reduced Prec. Fe/CuO/K ₂ O/Na ₂ O/SiO ₂	Fixed Bed	250-350	0.6-2.1	3.0-6.0	$r_{WGS} = k_{WGS} \frac{\left(P_{CO}P_{H_2O} - \frac{P_{CO_2}P_{H_2}^{0.5}}{K_{eq}}\right)}{\left(1 + a\frac{P_{H_2O}}{P_{H_2}^{0.5}}\right)^2}$	Lox and Froment [50, 51]
Prec. Fe/Cu/K	Gradientless	230-264	1.0-2.6	1.1-2.4	$r_{WGS} = k_{WGS} \frac{\left(P_{CO}P_{H_2O} - \frac{P_{CO_2}P_{H_2}}{K_{eq}}\right)}{P_{CO}P_{H_2} + aP_{H_2O}}$ $r_{WGS} = k_{WGS} \frac{\left(P_{CO}P_{H_2O} - \frac{P_{CO_2}P_{H_2}}{K_{eq}}\right)}{P_{CO} + aP_{H_2O} + bP_{CO_2}}$	Shen et al. [436] ²

Table A-2 (continued)

Catalyst / Promoter	Reactor	Operating Conditions			Equation	Reference
		T (°C)	P, MPa	H ₂ /CO feed		
Precipitated Fe	Slurry	210-250	1.38-4.12	1-7	$r_{WGS} = a \left(P_{CO} - \frac{P_{CO_2} P_{H_2}}{k_{WGS} P_{H_2O}} \right)$	van Berge [424]
Reduced Prec. Fe/Cu/K/SiO ₂	Spinning Basket	250	0.8-4.0	0.25-4.0	$r_{WGS} = k_{WGS} \frac{\left(P_{CO} P_{H_2O} - \frac{P_{CO_2} P_{H_2}}{K_{eq}} \right)}{\left(1 + a P_{CO} + b P_{H_2O} \right)^2}$ $r_{WGS} = k_{WGS} \frac{\left(\frac{P_{CO} P_{H_2O}}{P_{H_2}^{0.5}} - \frac{P_{CO_2} P_{H_2}^{0.5}}{K_{eq}} \right)}{\left(1 + a P_{CO} + b P_{H_2O} \right)^2}$	van der Laan and Beenackers [56, 423, 425]
Reduced Prec. Fe/Cu/K/SiO ₂	Slurry	250	1.2-4.0	0.25-4.0	$r_{WGS} = k_{WGS} \frac{\left(P_{CO} P_{H_2O} - \frac{P_{CO_2} P_{H_2}}{K_{eq}} \right)}{\left(P_{CO} + a P_{H_2O} \right)^2}$	van der Laan [423]
Fe	Fixed Bed	220-260	2.4	1.87-2.0 ⁵	$r_{WGS} = k_{WGS} P_{H_2O}$	Jess et al. [426]
Reduced Prec. Co/MnO	Micro-Fixed Bed	210-250	0.6-2.6	1.6-4.1	$r_{WGS} = k_{WGS} P_f \left(P_{CO} - \frac{P_{CO_2} P_{H_2}}{K_{eq} P_{H_2O}} \right)$ where $P_f = P^{\left(\frac{0.5-P}{250} \right)}$	Keyser et al [437]
Fe/Cu/K	-	-	-	-	$r_{WGS} = k_{WGS} \frac{\left(\frac{P_{CO} P_{H_2O}}{P_{H_2}^{0.5}} - \frac{P_{CO_2} P_{H_2}^{0.5}}{K_{eq}} \right)}{\left(1 + b \frac{P_{CO} P_{H_2O}}{P_{H_2}^{0.5}} \right)^2}$	Wang et al [52, 429]

Table A-2 (continued)

Catalyst / Promoter	Reactor	Operating Conditions			Equation	Reference
		T (°C)	P, MPa	H ₂ /CO feed		
Reduced Fe/Cu/K	Fixed Bed	220-269	1.1-3.1	1.0-3.0	$r_{WGS} = k_{WGS} \frac{\left(\frac{P_{CO}P_{H_2O}}{P_{H_2}^{0.5}} - \frac{P_{CO_2}P_{H_2}^{0.5}}{K_{eq}} \right)}{\left(1 + b \frac{P_{CO}P_{H_2O}}{P_{H_2}^{0.5}} \right)^2}$	Wang et al. [54]
Reduced Fe/Mn	Fixed Bed	267-327	1.0-3.0	1.0-3.0	$r_{WGS} = a \frac{\left(\frac{P_{CO}P_{H_2O}}{P_{H_2}^{0.5}} - \frac{P_{CO_2}P_{H_2}^{0.5}}{K_{eq}} \right)}{\left(1 + b \frac{P_{CO}P_{H_2O}}{P_{H_2}^{0.5}} \right)^2}$	Yang et al. [431]
Fe/Mn & Fe/Cu/K	Spinning Basket	260-300	1.1-2.6	0.67-2.05	$r_{WGS} = a \frac{\left(P_{CO}P_{H_2O} - \frac{P_{CO_2}P_{H_2}}{K_{eq}} \right)}{cP_{H_2}^{0.5} + P_{H_2} + d \frac{P_{CO}P_{H_2O}}{P_{H_2}}}$	Teng et al. [432]
Fe/Cu/K/SiO ₂	Slurry	250-290	1.0-2.5	0.67-1.5	$r_{WGS} = a \frac{\left(\frac{P_{CO}P_{H_2O}}{P_{H_2}^{0.5}} - \frac{P_{CO_2}P_{H_2}^{0.5}}{K_{eq}} \right)}{\left(1 + b \frac{P_{CO}P_{H_2O}}{P_{H_2}^{0.5}} \right)^2}$	Chang et al. [434]
Sasol commercial spray dried precipitated Iron Catalyst	Slurry	240-250	5-40	1.55	$r_{WGS} = \frac{a \left(P_{CO}P_{H_2O} - \left(\frac{P_{H_2}P_{CO_2}}{K_{WGS}} \right) \right)}{\left(1 + 1.1P_{H_2O} + 6.3 \left(\frac{P_{H_2O}}{P_{H_2}^{0.5}} \right) \right)^2}$	Botes [438]

¹ as reported in [420]
² as reported in [439]

Table A-3: Kinetics studies for the Fischer-Tropsch synthesis on cobalt-based catalyst

Catalyst	Reactor	Operating Conditions			Equation	Reference
		T (°C)	P (MPa)	H ₂ /CO _{feed}		
Co	-	-	-	-	$r_{FT} = k_{FT} \frac{P_{H_2}^2}{P_{CO}}$	Brotz [406]
Co/ThO ₂ /kieselguhr	-	-	-	-	$r_{FT} = k_{FT} \frac{P_{H_2}^2 P_{CO}}{1 + aP_{CO} P_{H_2}^2}$	Anderson [408]
Co	-	-	-	-	$r_{FT} = k_{FT} P_{H_2} P_{CO}^{0.5}$	Yang et al. [440]
Co	-	-	-	-	$r_{FT} = k_{FT} \frac{P_{H_2}^{0.55}}{P_{CO}^{0.33}}$	Pannell et al. [441]
Reduced Prec. Co/Al ₂ O ₃	Fixed Bed	250	0.015-0.1	0.25-5	$r_{FT} = k_{FT} \frac{P_{H_2} P_{CO}^{0.5}}{1 + aP_{CO}^{0.5} + bP_{H_2}^{1.5}}$	Outi et al. [67]
Co/Kieselguhr	Berty internal recycle reactor	190	0.2-1.5	0.5-8.3	$r_{FT} = k_{FT} \frac{P_{H_2}^{0.5} P_{CO}^{0.5}}{(1 + aP_{CO}^{0.5} + bP_{H_2}^{0.5})^2}$ $r_{FT} = k_{FT} \frac{P_{H_2}^{0.5} P_{CO}}{(1 + aP_{CO} + bP_{H_2}^{0.5})^2}$	Sarup and Wojciechowski [68]
Co/Zr/SiO ₂	Slurry	220-280	2.1	0.5-2.0	$r_{FT} = k_{FT} \frac{P_{H_2}^2 P_{CO}}{P_{CO} P_{H_2} + aP_{H_2}^2}$	Withers et al. [402]
Co/MgO/SiO ₂	Slurry	220-240	1.5-3.5	1.5-3.5	$r_{FT} = k_{FT} \frac{P_{CO} P_{H_2}}{(1 + aP_{CO})^2}$	Yates and Satterfield [69]
Co/MgO/ThO ₂ /SiO ₂	Slurry	210-250	1.38-4.12	1-7	$r_{FT} = k_{FT} \frac{P_{CO} P_{H_2}}{(1 + aP_{CO})^2}$	van Berge [424]
Co/MgO/ThO ₂ /SiO ₂ & Co/SiO ₂	Slurry	190-210	$P_{H_2} = 0.01-1.93$ $P_{CO} = 0.05-2.54$		$r_{c,org} = \frac{k_{FT} (P_{H_2}^{1.5} P_{CO} / P_{H_2}^2)}{(1 + a(P_{H_2} P_{CO} / P_{H_2}^2))^2}$	van Steen and Schulz [427]

Table A-3 (continued)

Catalyst	Reactor	Operating Conditions			Equation	Reference
		T (°C)	P (MPa)	H ₂ /CO feed		
CO/TiO ₂	Differential fixed bed reactor	180-240	2.0265	1-3.5	$r_{FT} = \frac{k_{FT} P_{CO} P_{H_2}^{0.74}}{(1 + aP_{CO})^2}$	Zennaro et al. [65]
Reduced Prec. Co/MnO ₃	Micro-Fixed Bed	210-250	0.6-2.6	1.6-4.1	$r_{FT} = k_{FT} \frac{P_{H_2} P_{CO}}{P_{CO} + P_{H_2O}}$	Keyser et al. [437]
Co/Al ₂ O ₃	Fixed Bed (micro)	210-235	0.8-2.5	1.8-2.7	$r_{1,N} = k_{1N} \theta_{CH_2^*} \theta_{H^*}$ $r_{CH_4} = k_{CH_4} \theta_{CH_3^*} \theta_{H^*}$ $r_{G,n} = k_G \theta_{R_n^*} \theta_{CH_2^*}, n: 1, 49$ $r_{P,n} = k_{P_n} \theta_{R_n^*} \theta_{H^*}, n: 2, 50$ $r_{O,n} = k_{O_n,dx} \theta_{R_n^*} - k_{O_n,sx} x_{O_n} \theta_{H^*}, n: 3, 50$ $r_{O,2} = k_{O_2,dx} \theta_{R_2^*} - k_{O_2,sx} x_{O_2} \theta_{H^*}, n: 3, 50$	Visconti et al. [442]
Co/Al ₂ O ₃	Slurry	220	2.0	1.6-3.35	<p><i>Detailed kinetics based on hydrocarbon productions considering olefin re-adsorption based on van Steen and Schulz</i></p> $r_{c,org} = k_{FT} \frac{P_{H_2}^{1.5} P_{CO}}{(P_{H_2O} + aP_{H_2} P_{CO})^2}$	Anfray et al. [443]
Co-Re/Al ₂ O ₃	Batch	205, 220, 230	1.5, 2.5	1.4, 2.1	$r_{CH_4} = k_{SM} K_7^{0.5} P_{H_2}^{1.5} \alpha_1 [S]$ $r_{C_2H_4} = k_{6E,0} e^{2c} \sqrt{K_7 P_{H_2} \alpha_1 \alpha_2 [S]}$ $r_{C_n H_{2n+2}} = k_5 K_7^{0.5} P_{H_2}^{1.5} \alpha_1 \alpha_2 \prod_{i=3}^n \alpha_i [S] \quad n \geq 2$	Todic et al. [53]

Table A-3 (continued)

Catalyst	Reactor	Operating Conditions			Equation	Reference
		T (°C)	P (MPa)	H ₂ /CO feed		
					$r_{C_nH_{2n}} = k_{6,0} e^{cn} \sqrt{K_7 P_{H_2}} \alpha_1 \alpha_2 \prod_{i=3}^n \alpha_i [S] \quad n \geq 3$ $[S] = 1 / \left\{ 1 + \sqrt{K_7 P_{H_2}} + \sqrt{K_7 P_{H_2}} \left(1 + \frac{1}{K_4} + \frac{1}{K_3 K_4 P_{H_2}} + \frac{1}{K_2 K_3 K_4} \frac{P_{H_2 O}}{P_{H_2}^2} \right) \left(\alpha_1 + \alpha_1 \alpha_2 + \alpha_1 \alpha_2 \sum_{i=3}^n \prod_{j=3}^i \alpha_j \right) \right\}$	
Co/Al ₂ O ₃	Tubular fixed bed reactor	190 - 220	1 - 2.5	1.5 - 3	$r_{FT} = k_{FT} \frac{P_{H_2} P_{CO}}{(1 + a P_{CO})}$	Kaiser et al. [444]

Table A-4: Literature data on the hydrodynamics and mass transfer in SBCRs using F-T liquids

Reference	Gas-Liquid-Solid System	Reactor Geometry	Operating Conditions	Parameter Measured
Deckwer et al. [75]	N ₂ - Paraffin Wax - Al ₂ O ₃	$d_C = 0.04, 0.1 \text{ m}$	P up to 11 bar; T = 416 K & 543 K; u_g up to 0.04 m/s; C _S up to 16 wt. %	ε_g, k_{LA}
Bukur et al. [76]	N ₂ - FT-300 Paraffin Wax - Iron Oxide, Silica	$d_C = 0.05 \text{ m};$ $h_C = 3 \text{ m}$	P _{atm} ; T = 538 K; $u_g = 0.02\text{-}0.12$ m/s; C _S = 10-30 wt. %	ε_g
Krishna et al. [77]	Air - Paraffin Oil - Silica	$d_C = 0.38 \text{ m}$	P _{atm} ; T _{amb} ; u_g up to 0.5 m/s; C _S up to 36 vol. %	ε_g
Vandu et al. [366]	Air - C ₉ -C ₁₁ Paraffin Oil - Puralox (Al ₂ O ₃)	$d_C = 0.1 \text{ m}$	P _{atm} ; T _{amb} ; u_g up to 0.4 m/s; C _S up to 25 vol. %	ε_g, k_{LA}
Behkish et al. [8, 80]	H ₂ , CO, N ₂ , He, CH ₄ - Isopar-M - Glass Beads, Al ₂ O ₃	$d_C = 0.3 \text{ m};$ $h_C = 3 \text{ m}$	P up to 30 bar; T up to 473 K; u_g up to 0.39 m/s; C _S up to 36 vol. %	$\varepsilon_g, d_{32}, k_{LA}$
Woo et al. [79]	Actual F-T reactive system with Al ₂ O ₃ supported Co catalyst	$d_C = 0.05 \text{ m};$ $h_C = 1.5 \text{ m}$	P = 10 - 30 bar; T = 480–520 K; $u_g = 0.017\text{-}0.136$ m/s; C _S = 9-27 wt. %	ε_g
Sehabiague et al. [81]	N ₂ , He – C ₁₂ -C ₁₃ , Paraffins mixture, Light F-T cut, Heavy F-T cut – Alumina, Puralox Alumina, Iron oxide	$d_C = 0.3 \text{ m};$ $h_C = 3 \text{ m}$	P up to 30 bar; T up to 500 K; u_g up to 0.27 m/s; C _S up to 20 vol. %	$\varepsilon_g, d_{32}, k_{LA}$

Table A-5: Gas holdup correlations for three-phase reactors available in literature

System	Conditions	Correlation	Reference
Air Sugar solution Carboxymethylcellulose Water-acetone Glass beads Irregular gravel	$d_c: 0.66 \text{ m}$ $h_c: 2.438 \text{ m}$ $u_g: 0.007 - 0.161 \text{ m/s}$ $d_p: 1 - 6 \text{ mm}$ $\rho_s: 2300 - 2950 \text{ kg/m}^3$ $\rho_l: 960 - 1170 \text{ kg/m}^3$ $\mu_l: 0.001 - 0.07 \text{ Pa} \cdot \text{s}$ $\sigma_l: 0.0398 - 0.0738 \text{ N/m}$	ε_l $= 1.40 \left(\frac{u_l^2}{gd_p} \right)^{0.170} \left(\frac{\mu_l u_l}{\sigma_l} \right)^{0.078}$ $- 1.504 \left(\frac{u_l^2}{gd_p} \right)^{0.234} \left(\frac{u_g^2}{gd_p} \right)^{-0.086} \left(\frac{u_l d_p \rho_l}{\mu_l} \right)^{-0.082} \left(\frac{\mu_l u_l}{\sigma_l} \right)^{0.092}$	Kim et al. [445]
Air Ethanol Aqueous Glycerol Methanol Water Solid	$u_g: 0.05 - 4 \text{ m/s}$ $d_c: 0.05 - 0.1 \text{ m}$ $d_p: 0.011 - 0.0287 \text{ m}$ $h_c: 0.05 - 0.2 \text{ m}$ $\rho_l: 797 - 1165 \text{ kg/m}^3$ $\mu_l: 1.01 - 14.45 \text{ cP}$ $\sigma_l: 0.0233 - 0.0728 \text{ N/m}$	$\varepsilon_g = 0.19 \left(\frac{u_g^2 d_p \rho_l}{\sigma_l} \right)^{0.11} \left(\frac{u_l}{\sqrt{gd_p}} \right)^{0.22}$	Kito et al. [446]
Air Water Glass beads	$u_g: 0.02 - 0.12 \text{ m/s}$ $u_l: 0.03 - 0.14 \text{ m/s}$ $\rho_s: 2500 \text{ kg/m}^3$ $d_p: 1.63 - 7.85 \text{ mm}$ $d_c: 0.15 \text{ m}$ $h_c: 2.5 \text{ m}$	$\varepsilon_g = 0.46 \left(\frac{u_l^2}{gd_p} \right)^{0.19} \left(\frac{u_g^2}{gd_p} \right)^{0.01} \left(\frac{u_l d_p \rho_l}{\mu_l} \right)^{0.026}$ $- 0.26 \left(\frac{u_l^2}{gd_p} \right)^{0.44} \left(\frac{u_g^2}{gd_p} \right)^{-0.032} \left(\frac{u_l d_p \rho_l}{\mu_l} \right)^{-0.006}$	Oh and Kim [447]
Air Water Alumina beads Glass beads Alumino silicate Plexiglas	$u_g: 0 - 0.173 \text{ m/s}$ $u_l: 0 - 0.12 \text{ m/s}$ $\rho_l: 100 - 1200 \text{ kg/m}^3$ $\rho_s: 1720 - 2440 \text{ kg/m}^3$ $d_p: 1.9 - 6.3 \text{ mm}$ $d_c: 0.076 - 0.152 \text{ m}$ $h_c: 0.22 - 0.45 \text{ m}$	$\varepsilon_g = 1.61 u_g^{0.72} d_p^{0.168} d_c^{-0.125}$	Begovich and Watson [448]

Table A-5 (continued)

System	Conditions	Correlation	Reference
Air Kerosene Solids	$u_g: 0 - 0.0022 \text{ m/s}$ $d_p: 1.1 \text{ mm}$ $\rho_s: 1330 \text{ kg/m}^3$ $\rho_l: 810 \text{ kg/m}^3$ $\mu_l: 1.4 \text{ mPa} \cdot \text{s}$	$(1 - \varepsilon_g)u_g + \varepsilon_g u_l = \varepsilon_g(22.67\varepsilon_g + 10.44)$	Khang et al. [449] taken from [450]
Air Glycerol Glycol Barium chloride Sodium sulfate Glass spheres Bronze spheres	$u_g: 0.03 - 0.15 \text{ m/s}$ $\rho_s: 2500, 8770 \text{ kg/m}^3$ $d_p: 47.5 - 192 \text{ }\mu\text{m}$ $\rho_l: 997 - 1178 \text{ kg/m}^3$ $\mu_l: 0.894 - 17.6 \text{ mPa} \cdot \text{s}$ $\sigma_l: 0.0515 - 0.073 \text{ N/m}$ $d_c: 0.1 - 0.3 \text{ m}$ $h_c: 2.3 - 3 \text{ m}$	$\frac{\varepsilon_g}{(1 - \varepsilon_g)^4} = \frac{A \left(\frac{u_g \mu_l}{\sigma_l}\right)^{0.918} \left(\frac{g \mu_l^4}{\rho_l \sigma_l^3}\right)^{-0.252}}{1 + 4.35 \left(\frac{C_s}{\rho_p}\right)^{0.748} \left(\frac{\rho_p - \rho_l}{\rho_l}\right)^{0.881} \left(\frac{d_c u_g \rho_l}{\mu_l}\right)^{-0.168}}$ $A = \begin{cases} 0.277 & \text{Water and aq. solution of glycerol and glycol} \\ 0.364 & \text{Aq. solution of inorganic electrolytes} \end{cases}$	Koide et al. [107]
N ₂ Water Aqueous ethanol (95%) Silicone oil Ethylene glycol Glass beads	$u_g: 0.02 - 0.22 \text{ m/s}$ $\rho_s: 2420, 3990 \text{ kg/m}^3$ $d_p: 19.4 - 96.5 \text{ }\mu\text{m}$ $C_v: 2.8 - 5 \text{ vol}\%$ $\rho_l: 820 - 1100 \text{ kg/m}^3$ $\mu_l: 0.82 - 17.1 \text{ mPa} \cdot \text{s}$ $\sigma_l: 17.4 - 71.5 \text{ mN/m}$ $d_c: 0.108 \text{ m}$ $h_c: 1.94 \text{ m}$	$\varepsilon_g = \left[2.25 + \left(\frac{33.9}{0.01 u_g} \right) \left(\frac{\rho_{sl} \sigma_l}{72} \right)^{0.31} (1000 \mu_{sl})^{0.016} \right]^{-1}$ $\mu_{sl} = 0.001 \mu_l \exp \left[\frac{5 \varepsilon_s}{3(1 - \varepsilon_s)} \right]$	Smith et al. [451]
Air Water Trichloroethylene Glass beads	$u_g: 0.02 - 0.2 \text{ m/s}$ $\rho_g: 0.168 - 1.34 \text{ kg/m}^3$ $C_v: \text{up to } 10 \text{ vol.}\%$ $\rho_s: 1510 - 4470 \text{ kg/m}^3$ $d_p: 71 - 745 \text{ }\mu\text{m}$	$\varepsilon_g = 296 u_g^{0.44} \rho_l^{-0.98} \sigma_l^{-0.16} \rho_g^{0.19} + 0.009$	Reilly et al. [452]

Table A-5 (continued)

System	Conditions	Correlation	Reference										
	$\rho_l: 788 - 1450 \text{ kg/m}^3$ $\mu_l: 0.522 - 1.452 \text{ mPa}$ $\sigma_l: 0.0283 - 0.072 \text{ N/m}$ $d_c: 0.3 \text{ m}$ $h_c: 0.5 \text{ m}$												
N ₂ , O ₂ Water Na ₂ SO ₄ Activated Carbon Diatomite Al ₂ O ₃	P_{atm}, T_{atm} $u_G < 0.07 \text{ ms}^{-1}$ $C_v: 0.51 - 15.22 \text{ vol}\%$ $d_p: 5.4, 6.6, 8.1 \mu\text{m}$ $d_c: 0.095 \text{ m}$ $h_c: 0.85 \text{ m}$	$\varepsilon_g = F \cdot u_g^{0.87} \mu_{eff}^{-0.18}$ $F = \begin{cases} 0.81 & \text{for salt solution} \\ 0.43 & \text{for tap water} \end{cases}$ $\mu_{eff} = k(2800u_g)^{n-1}$ <p><i>k</i> is the fluid consistency index = 1.97 <i>n</i>: empirical constant $1 \geq n \geq 0.18$</p>	Schumpe et al. [453]										
Air H ₂ O Various Plastics Sand	$u_g: 0.01 - 0.08 \text{ m/s}$ $d_p: 0.11 - 2.8 \text{ mm}$ $C_v: 0 - 20 \text{ vol}\%$ P_{atm} $\rho_s: 1020 - 2780 \text{ kg/m}^3$ <i>PfP, SP Sparger</i>	$\frac{\varepsilon_g'''}{1 - \varepsilon_g'''} = K \left(\frac{u_g}{(v_{sl} g u_g)^{1/4}} \right)^{B1} \left(\frac{v_{sl}}{\vec{v}_{eff,rad}} \right)^{B2} \left(\frac{\vec{C}_s}{C_{so}} \right)^{B3}$ <p><i>The values of constant K and of exponents B1-B3 are as follows:</i></p> <table style="width: 100%; border: none;"> <thead> <tr> <th style="text-align: center;"><i>Sieve plate</i></th> <th style="text-align: center;"><i>Perforated Plate</i></th> </tr> </thead> <tbody> <tr> <td style="text-align: center;">$K = 0.00476$</td> <td style="text-align: center;">$K = 0.0277$</td> </tr> <tr> <td style="text-align: center;">$B1 = 0.888$</td> <td style="text-align: center;">$B1 = 0.844$</td> </tr> <tr> <td style="text-align: center;">$B2 = -0.258$</td> <td style="text-align: center;">$B2 = -0.136$</td> </tr> <tr> <td style="text-align: center;">$B3 = 0.0407$</td> <td style="text-align: center;">$B3 = 0.0392$</td> </tr> </tbody> </table> $v_{sl} = \frac{\mu_L(1 + 2.5\varepsilon_s + 10.05\varepsilon_s^2 + 0.00273e^{16.6\varepsilon_s})}{\rho_{sl}}$ $\vec{v}_{eff,rad} = 0.011 d_c \sqrt{g d_c} \left(\frac{u_g^3}{g \eta_l} \right)^{1/8}$	<i>Sieve plate</i>	<i>Perforated Plate</i>	$K = 0.00476$	$K = 0.0277$	$B1 = 0.888$	$B1 = 0.844$	$B2 = -0.258$	$B2 = -0.136$	$B3 = 0.0407$	$B3 = 0.0392$	Sauer and Hempel [186]
<i>Sieve plate</i>	<i>Perforated Plate</i>												
$K = 0.00476$	$K = 0.0277$												
$B1 = 0.888$	$B1 = 0.844$												
$B2 = -0.258$	$B2 = -0.136$												
$B3 = 0.0407$	$B3 = 0.0392$												

Table A-5 (continued)

System	Conditions	Correlation	Reference
		$\frac{\bar{C}_s}{C_{so}} = \frac{u_{ss} h_c}{u_g d_c} \frac{13 Fr_g (1 + 0.09 Re_p Fr_g^{-0.8})}{1 + 8 Fr_g^{0.85}}$ $\rho_{sl} = \varepsilon_s \rho_s + (1 - \varepsilon_s) \rho_l$	
Air Water Glass beads	$u_g: 0.0057 - 0.02 \text{ m/s}$ $u_l: 0.0039 - 0.0195 \text{ m/s}$ $C_v: 0.1 - 0.9 \text{ vol. \%}$ $d_p: 250 \mu\text{m}$ $d_c: 0.2 \text{ m}$ $h_c: 3.35 \text{ m}$	$\varepsilon_g = 0.794 - 0.04 X_1^2 - 0.034 X_2^2 - 0.006 (u_l)^{0.246} (u_g)^{-0.059}$ $X_1 = 0.409 (u_l - 3.01) - 0.913 (u_g - 2.12)$ $X_2 = 0.973 (u_l - 3.01) - 0.229 (u_g - 2.12)$	Lee and Lasa [454]
N ₂ FT-300 Paraffin Wax, Iron Oxide Silica	P_{atm} $u_g: 0.02 - 0.12$ $C_s: 10 - 30 \text{ wt. \%}$ $T: 538$ $d_c: 0.05 \text{ m}$ $h_c: 3 \text{ m}$ <i>S-ON Sparger</i>	$\langle \varepsilon_g \rangle_{ij} = 1 - \frac{\Delta P_{ij} / (S_{sl})_{ij}}{\Delta h_{ij}}$ $i = 1 \text{ to } 5, \quad j = i + 1$ <p style="text-align: center;"><i>where</i></p> $(S_{sl})_{ij} = \frac{1 / \rho_{water}}{\langle W_s \rangle_{ij} / \rho_p + (1 - \langle W_s \rangle_{ij} / \rho_l)}$ <p style="text-align: center;"><i>The average gas holdup for the entire dispersion is estimated using a weighted average of the gas holdups in the individual sections</i></p> $\varepsilon_g = \frac{\sum_{i=1}^5 \langle \varepsilon_g \rangle_{ij} \Delta h_{ij}}{\sum_{i=1}^5 \Delta h_{ij}}$	Bukur et al. [262]
Various Experimental data for three phase systems	$\rho_l: 683 - 2965 \text{ kg/m}^3$ $\mu_l: 0.29 - 30 \text{ mPa} \cdot \text{s}$ $\sigma_l: 0.019 - 0.073 \text{ N/m}$ $\rho_g: 0.2 - 90 \text{ kg/m}^3$ $\varepsilon_s: 0 - 40 \text{ vol\%}$ $d_p: 20 - 143 \mu\text{m}$ $\rho_s: 2200 - 5730 \text{ kg/m}^3$	$\frac{\varepsilon_g}{1 - \varepsilon_g} = \frac{2.9 (u_g^4 \rho_g / \sigma_l g)^\alpha (\rho_g / \rho_{sl})^\beta}{[\cosh(Mo_m^{0.054})]^{4.1}}$ $Mo_m = \frac{g (\rho_{sl} - \rho_g) (\xi \mu_l)^4}{\rho_{sl}^2 \sigma_l^3}$	Fan et al. [105]

Table A-5 (continued)

System	Conditions	Correlation	Reference
	$u_g: 0.05 - 0.69 \text{ m/s}$ $u_l: 0$ $d_c: 0.1 - 0.61 \text{ m}$ $h_c/d_c > 5$	$Mo = \frac{g(\rho_l - \rho_g)(\mu_l)^4}{\rho_l^2 \sigma_l^3}$ $\alpha = 0.21 Mo_m^{0.0079}, \beta = Mo_m^{-0.011}$ $\ln \xi = 4.6 \varepsilon_s \{ 5.7 \varepsilon_s^{0.58} \sinh[-0.71 \exp(-5.8 \varepsilon_s) \times \ln(Mo)^{0.22}] + 1 \}$	
Air Paraffin oil Tellus oil Silica	$u_g < 0.5 \text{ m/s}$ $C_v: 0 - 36 \text{ vol. \%}$ $d_c: 0.1, 0.19, 0.38, 0.63 \text{ m}$	$\varepsilon_g = \varepsilon_{g-large} + \varepsilon_{df}(1 - \varepsilon_{g-large})$ $\varepsilon_{g-large} = \frac{u_g - u_{g-df}}{u_{b-large}}$ $u_{b-large} = 0.71(gd_b)^{0.5}(DF)(SF)(AF)$ $SF: \begin{cases} 1 \text{ for } \frac{d_b}{d_c} < 0.125 \\ 1.13 e^{\left(\frac{-d_b}{d_c}\right)} \text{ for } 0.125 < \frac{d_b}{d_c} < 0.6, \\ 0.496 \left(\frac{d_b}{d_c}\right)^{-0.5} \text{ for } \frac{d_b}{d_c} > 0.6 \end{cases}$ $AF = \alpha + \beta(u_g - u_{g-df}), DF = \left(\frac{1.29}{\rho_g}\right)^{0.5}$ $d_b = \gamma(u_g - u_{g-df})^\delta, u_{g-df} = u_{b-small} \varepsilon_{df}$ $\varepsilon_{df} = \varepsilon_{df,0} \left(\frac{\rho_g}{\rho_{g,ref}}\right)^{0.48} \left(1 - \frac{0.7}{\varepsilon_{df,0}} C_v\right)$ $u_{b-small} = u_{b-small,0} \left(1 - \frac{0.8}{u_{b-small,0}} C_v\right)$ $\varepsilon_{df,0}, u_{b-small,0}: \text{function of liquid nature}$	Krishna and Sie [455]
Air Water Nickel Slurry	$u_g: 0.02 - 0.04 \text{ m/s}$ $u_l: 0.018 - 0.037 \text{ m/s}$ $C_S: 5.7 \text{ vol\%}$	$\varepsilon_g = 0.75 u_g^{0.78} \exp[8.12 \times 10^{-6} h_c]$	Chen et al. [456]

Table A-5 (continued)

System	Conditions	Correlation	Reference
	$d_p: 177 - 210 \mu\text{m}$ $\rho_s: 8900 \text{ kg/m}^3$ $d_c: 0.05 \text{ m}$ $h_c: 0.5 \text{ m}$		
Air 55% Glycerol 25% Glycerol Water Mono ethanol amine (MEA) Solids of various sizes and shapes	$u_g: 0 - 0.13 \text{ m/s}$ $\rho_g: 0.168 - 1.34 \text{ kg/m}^3$ $\rho_s: 2030 - 2480 \text{ kg/m}^3$ $d_p: 4.11 - 6.8 \text{ mm}$ $u_l: 0 - 0.13 \text{ m/s}$ $\rho_l: 100 - 1150 \text{ kg/m}^3$ $\mu_l: 0.85 - 15 \text{ mPa}$ $\sigma_l: 0.049 - 0.072 \text{ N/m}$ $d_c: 0.072 \text{ m}$ $h_c: 1.0 \text{ m}$	$\varepsilon_g =$ $0.17 \left(\frac{u_g^2}{g d_p} \right)^{0.33} \left(\frac{d_p u_l \rho_l}{\mu_l} \right)^{-0.065} \left(\frac{d_p^3 \rho_l (\rho_s - \rho_l) g}{\mu_l^2} \right)^{0.125} \left(\frac{\mu_l^4 g}{\rho_l \sigma_l^3} \right)^{0.05}$ <p style="text-align: center;"><i>for</i> $\frac{d_p u_l \rho_l}{\mu_l} \leq 100$</p> $0.11 \left(\frac{u_g^2}{g d_p} \right)^{0.35} \left(\frac{d_p u_l \rho_l}{\mu_l} \right)^{0.2} \left(\frac{d_p^3 \rho_l (\rho_s - \rho_l) g}{\mu_l^2} \right)^{0.11} \left(\frac{\mu_l^4 g}{\rho_l \sigma_l^3} \right)^{0.075}$ <p style="text-align: center;"><i>for</i> $\frac{d_p u_l \rho_l}{\mu_l} > 100$</p>	Ramesh and Murugesan [457]
H ₂ CO N ₂ CH ₄ Isopar-M Hexanes Glass beads Iron Oxide	$u_g: 0.0035 - 0.574 \text{ m/s}$ $C_s: 0 - 36 \text{ vol. \%}$ $T: 275 - 538 \text{ K}$ $P: 0.1 - 15 \text{ MPa}$ $\rho_s: 700 - 4000 \text{ kg/m}^3$ $d_p: 5 - 300 \mu\text{m}$ $\rho_l: 633.4 - 1583 \text{ kg/m}^3$ $\mu_l: 0.189 - 398.8 \text{ mPa} \cdot \text{s}$ $\sigma_l: 8.4 - 75 \text{ mN/m}$ $d_c: 0.0382 - 5.5 \text{ m}$	$\varepsilon_g = 4.94$ $\times 10^{-3} \left(\frac{\rho_l^{0.415} \rho_g^{0.177}}{\mu_l^{0.174} \sigma_g^{0.27}} \right) u_g^{0.553} \left(\frac{P_T}{P_T - P_S} \right)^{0.203} \left(\frac{d_c}{d_c + 1} \right)^{-0.117} \Gamma^{0.053}$ $\times \exp[-2.23 C_v - 0.16 \rho_s d_p - 0.24 X_W]$ $\Gamma = K_d \times N_o d_o^\alpha$ $K_d, \alpha: \text{Function of gas sparger}$ $\varepsilon_{g\text{-large}} = \varepsilon_g^{0.84} (F) = \varepsilon_g^{0.84} (1 - 3.04 \times 10^{-6} \frac{\rho_l^{0.97}}{\mu_l^{0.16}} \times \exp[-4.59 C_s])$ $\varepsilon_{G\text{-small}} = \begin{cases} \varepsilon_G - \varepsilon_{G\text{-large}} & \text{for } \varepsilon_G > F^{25/4} \\ 0 & \text{for } \varepsilon_G < F^{25/4} \end{cases}$	Behkish et al. [9]

Table A-5 (continued)

System	Conditions	Correlation	Reference
Air Water CCl ₄ Glass beads	$u_g: 0 - 0.107 \text{ m/s}$ $u_l: 0.021 - 0.169 \text{ m/s}$ $T: 305 \text{ K}$ $C_s: 13.8 - 24.3 \text{ vol. \%}$ $\rho_s: 2216 - 2270 \text{ kg/m}^3$ $d_p: 2.18 - 4.05 \text{ mm}$ $\rho_l: 998.4 - 1600 \text{ kg/m}^3$ $\mu_l: 0.8 - 0.94 \text{ mPa} \cdot \text{s}$ $d_c: 0.1 \text{ m}$ $h_c: 1.24 \text{ m}$	$\varepsilon_g = 5.53 \left(\frac{u_g^2}{gd_c} \right)^{0.4135} \left(\frac{\rho_l u_l d_c}{\mu_l} \right)^{-0.1808} \left(\frac{h_c}{d_c} \right)^{0.0597} \left(\frac{d_p}{d_c} \right)^{0.0873}$	Jena et al. [458]
Air Water, 20% glycerol, 60% glycerol, 90% glycerol, 65% glycerol, 85% glycerol, MEA, Butyric acid, 0.1 % Carboxymethylcellulose (CMC), 0.5 % CMC, 1% CMC, Spheres, Berl Saddles, Raschig Rings	$u_g: 0.00375 - 0.1375 \text{ m/s}$ $u_l: 0.008 - 0.2487 \text{ m/s}$ $T: 305 \text{ K}$ $C_s: 13.8 - 24.3 \text{ vol. \%}$ $\rho_s: 2216 - 2270 \text{ kg/m}^3$ $d_p: 1 - 13.66 \text{ mm}$ $\rho_l: 1245 - 2960 \text{ kg/m}^3$ $\mu_l: 0.85 - 32 \text{ mPa} \cdot \text{s}$ $\sigma_l: 0.025 - 0.072 \text{ N/m}$ $d_c: 0.005 - 0.15 \text{ m}$ $h_c: 1.8 \text{ m}$	$\varepsilon_g = 0.98 \left(\frac{u_g^2}{gd_p} \right)^{0.382} \left(\frac{u_l^2}{gd_p} \right)^{0.0438} \left(\frac{\rho_s}{\rho_l} \right)^{-0.529} \left(\frac{d_p}{d_c} \right)^{0.0339} \left(\frac{g\mu_l^4}{\rho_l \sigma_l^3} \right)^{0.0265} \phi_s^{-0}$ <p style="text-align: center;">ϕ_s: Particle Sphericity</p>	Sivakumar et al. [450]
He, N ₂ Paraffins mixture, C ₁₂ -C ₁₃ , Light F-T Cut, Heavy F-T-Cut, Alumina, Puralox Alumina, Iron oxide	$u_g: 0.14 - 0.26 \text{ m/s}$ $C_p: 0 - 20 \text{ vol. \%}$ $T: 330 - 530 \text{ K}$ $P: 8 - 30 \text{ MPa}$ $\rho_s: 3218 - 4000 \text{ kg/m}^3$ $d_p: 1.5 - 140 \mu\text{m}$ $\rho_l: 631.3 - 779.5 \text{ kg/m}^3$ $\mu_l: 0.27 - 9.96 \text{ mPa} \cdot \text{s}$ $\sigma_l: 13 - 27 \text{ mN/m}$ $d_c: 0.3 \text{ m}$ $h_c: 3 \text{ m}$	$\varepsilon_g = 11241.6 \left(\frac{\rho_g^{0.174} u_g^{0.553} \Gamma^{0.053}}{\mu_l^{0.025} \sigma_l^{0.105} \rho_l^{1.59}} \right) \left(\frac{P}{P - P_s} \right)^{0.203} \left(\frac{d_c}{d_c + 1} \right)^{-0.117}$ $\times \exp[-1.2 \times 10^{-3} C_s - 0.4 \times 10^{-6} C_s^2 - 4339 d_p + 0.434 X_W]$	Sehabiague et al. [81]

Table A-6: Bubbles diameter correlations available in the literature

Correlation	Reference
$d_{b,o} = 81.18 \frac{\sigma_l}{P_o g}$	Eversole et al. [459]
$d_b = \left(1.722 \frac{Q^{6/5} 6}{g^{3/5} \pi} \right)^{1/3}$	Van Krevelen and Hoftijzer [460]
$d_{b,o} = 1.82 \frac{d_o \sigma_l^{0.25}}{g d_o^2 \rho_l}$	Benzing and Mayers [371]
$d_{b,o} = 0.19 d_o^2 Re_b^{0.32}$	Leibson et al. [380, 381]
$d_b = (l^2 h)^{1/3}$ $\left. \begin{aligned} l &= \frac{d_b}{1.14 Ta^{-0.176}} \\ h &= 1.3 d_b Ta^{-0.352} \end{aligned} \right\} \text{ for } 2 < Ta < 6,$ $\left. \begin{aligned} l &= \frac{d_b}{1.36 Ta^{-0.28}} \\ h &= 1.85 d_b Ta^{-0.56} \end{aligned} \right\} \text{ for } 6 < Ta < 16.5$ $Ta = Re_b Mo^{0.23},$ $Re_b = \frac{d_b u_b \rho_l}{\mu_l}$ $Mo = \frac{g \mu_l^4}{\rho_l \sigma_l^3}$	Nedeltchev and Schumpe [461]
<p><i>Viscous Liquids:</i></p> $V_b = 1.378 \frac{Q^{6/5}}{g^{3/5}}$ $d_b = \left(1.378 \frac{Q^{6/5} 6}{g^{3/5} \pi} \right)^{1/3}$ <p><i>Inviscid liquids:</i></p> $d_{b,o} = \frac{32g}{11} \left[\frac{t^2}{4} + \frac{V_o t}{2Q} - \frac{V_o^2}{2Q^2} \ln \left(\frac{Qt + V_o}{V_o} \right) \right]$ $V_o = \frac{\pi d_o^2}{3}$	Davidson and Schuler [373]

Table A-6 (continued)

Correlation	Reference
$V_b = \left(\frac{4\pi}{2}\right)^{0.25} \left(\frac{15\mu_l Q}{2\rho_l g}\right)^{0.75}$	Kumar and co-workers [378, 385, 462, 463]
$V_b = 1.09Q^{6/5}g^{-3/5}$	Wraith [391]
$V_{b,o} = \frac{\pi d_o \sigma_l}{\Delta\rho g}$	Park et al. [384]
$V_b = 0.976 \left(\frac{Q^2}{g}\right)^{3/5}$	Acharya et al. [464]
$d_{b,o} = \left(\frac{3\sigma_l d_o}{\rho_l} + \sqrt{\left(\frac{3\sigma_l d_o}{\rho_l}\right)^2 + \frac{K d_o}{g}}\right)^{\frac{1}{3}}$ <i>K: pulsation parameter</i>	Rabiger and Vogelpohl [465]
$V_{b,o} = \frac{4\pi\sigma_l d_o}{\rho_l g} + 2\frac{G^2}{g} \left(\frac{3}{4\pi V_f^2}\right)^{0.33}$	Rice and Lakhani [466]
$d_{b,o} = \left[\left(\frac{6d_o\sigma_l}{\rho_l g}\right) + \frac{81\eta_l u_b}{\pi g} + \left(\frac{135u_b^2}{4\pi^2 g}\right)^{5/3}\right]^{0.25}$	Gaddis and Vogelpohl [467]
$d_b = 6.9 \left(\frac{\sigma_l}{\rho_l}\right)^{0.5} u_g^{0.44}$ $V_b = \frac{\pi d_o \sigma_l}{\Delta\rho g}$	Tsuge et al. [386-388, 468]
$d_b = (a^2 b)^{\frac{1}{3}}$ <i>a: maximum bubble diameter; b = minimum bubble diameter</i>	Sada et al. [469]
$V_{b,o} = \frac{\pi d_o^3}{12}$	Wilkinson and van Dierendonck [390]
$d_{b,o} = d_o A \sqrt{\frac{We_l(\rho_l - \rho_g)}{(We_l - 8)}}$ $A = \sqrt{\frac{4}{Re_o} + \frac{0.124}{\sqrt{Re_o}}}; Re_o = \frac{2u_b d_o}{\eta_l}$	Pamperin and Rath [383]

Table A-6 (continued)

Correlation	Reference
$d_{b,o} = \left[\frac{5}{Bd_o^{1.08}} + \frac{9.26Fr_l^{0.36}}{Ga_l^{0.39}} + 2.147Fr_l^{0.51} \right]^{0.33}$ $Bd_o = 4 \frac{\rho_l g d_b^2}{\sigma_l}$	Jamialahmedi et al.[377]
$d_b = 26d_c \left(\frac{d_c^2 g \rho_l}{\sigma_l} \right)^{-0.5} \left(\frac{g d_c^3}{\eta_l^2} \right)^{-0.12} \left(\frac{u_g}{\sqrt{g d_c}} \right)^{-0.12}$	Akita and Yoshida [190]
$d_{b,o} = \left[\left(\frac{6d_o \sigma_l}{\rho_l g} \right)^{4/3} + \left(\frac{81Q\eta_l}{\pi g} \right) + \left(\frac{135Q^2}{4\pi^2 g} \right)^{4/5} \right]^{1/4}$	Gaddis and Vogelpohl [467]
$d_b = \left(0.976 \frac{Q^{6/5} 6}{g^{3/5} \pi} \right)^{1/3}$	Kumar and Kuloor [462]
$d_b = 0.725 \frac{\sigma_l^{3/5}}{\rho_l^{1/5} p^{2/5}}$	Hinze [470]
$d_b = We_c^{3/5} \frac{\sigma_l^{3/5}}{\rho_g^{1/5} p^{2/5}} \left(\frac{\mu_l}{\mu_g} \right)^{0.1}$ $We_c = \frac{\rho_l \bar{u}_{rms}^2 d_b}{\sigma_l}; \bar{u}_{rms}^2 = \left(\frac{p d_b}{\rho_l} \right)^{2/3}$	Lin et al. [174]
$d_b = 1.817 \frac{2\sigma_l}{u_b^{2/3} \sqrt{\rho_g \rho_l^2}}$	Levich [471]
$d_b = k \sqrt{\frac{\sigma_l}{g \rho_g}}$ $k = \begin{cases} 2.53 & \text{Liquid} \\ 3.27 & \text{Slurry} \end{cases}$	Luo et al. [472]
$d_b = \frac{2\pi \sqrt{\frac{\sigma_l}{g \Delta \rho}}}{\left(\frac{\rho_l}{\Delta \rho} \right) \frac{\rho_g u_r^2}{2\sqrt{\sigma_l g \Delta \rho}} + \left(1 + \frac{\left(\frac{\rho_l \rho_g u_r^2}{2} \right)^2}{(\rho_l + \rho_g)^2 \sigma_l g \Delta \rho} \right)^{0.5}}$	Wilkinson and van Dierendonck [90]

u_r : relative velocity between the gas and liquid phase at the interface

Table A-7: Bubbles rise velocity correlations available in the literature

Correlation	Reference
$u_b = \frac{g\rho_l d_b^2}{18\mu_l}$	Stokes [473]
$u_{b\infty} = 0.35\sqrt{gd_b}$	Dumitrescu [474]
$u_b = \frac{g\rho_l d_b^2}{18\mu_l} \quad Re < 2$ $u_b = \frac{0.33g^{0.76}\rho_l^{0.52}r_b^{1.28}}{10\mu_l^{0.52}} \quad 2 < Re < 4.02Mo^{-0.214}$ $u_b = 1.35\left(\frac{2\sigma_l g}{d_b\rho_l}\right)^{0.5} \quad 4.02Mo^{-0.214} < Re < 3.1Mo^{-0.25}$ $u_b = 1.18\left(\frac{\sigma_l g^2}{\rho_l}\right) \quad 3.1Mo^{-0.25} < Re$ <p style="text-align: center;"> $626 < \rho_l < 1071 \frac{kg}{m^3}$ $0.016 < \sigma_l < 0.72 N/m$ $0.22 < \mu_l < 31 cP$ </p>	Peebles and Garber [475]
$u_b = 0.721\sqrt{gd_b} \quad 782 < \rho_l < 1480 \frac{kg}{m^3}$ $0.02 < \sigma_l < 0.72 N/m$ $0.52 < \mu_l < 18000 cP$	Haberman and Morton [476]
$u_{b\infty} = 1.53\left[\frac{g\Delta\rho\sigma_l}{\rho_l^2}\right]^{0.25} \quad \text{Moderately distorted ellipsoids}$ $u_{b\infty} = \lambda_l \sqrt{\frac{g\Delta\rho d_b}{\rho_l}} \quad \text{Cylindrical Slugs}$	Harmathy [477]
$u_b = K \frac{(0.5d_b^3)^m}{6}$ $m = 0.167(1 + 0.34Mo^{0.24})$ $K = 25/(1 + 0.33Mo^{0.29})$	Angelino [478]
$u_b = \sqrt{\frac{2\sigma_l}{d_b\rho_l} + 0.5gd_b} \quad 782 < \rho_l < 1480 \frac{kg}{m^3}$ $0.02 < \sigma_l < 0.72 N/m$ $0.52 < \mu_l < 18000 cP$	Mendelson [479]
$u_b = \left(\frac{\mu_l}{\rho_l d_{b,e}}\right) Mo^{-0.149}(J - 0.857)$ $J = \begin{cases} 0.94H^{0.757} & (2 < H \leq 59.3) \\ 3.24H^{0.441} & (H > 59.3) \end{cases}$ $H = \frac{4}{3}EoMo^{-0.149}\left(\frac{\mu_l}{\mu_w}\right)^{-0.14}$	Grace et al. [480]
$u_b = \sqrt{\frac{3\sigma_l}{d_b\rho_l} + \frac{gd_b\Delta\rho}{\rho_l}} \quad 782 < \rho_l < 1480 \frac{kg}{m^3}$ $0.02 < \sigma_l < 0.72 N/m$ $0.52 < \mu_l < 18000 cP$	Lehrer [481]

Table A-7 (continued)

Correlation	Reference
$u_b = \frac{\mu_l}{\rho_l d_p} M^{-0.149} (J - 0.857)$ $M = \frac{g \mu_l^4 (\rho_l - \rho_g)}{\rho_l^2 \sigma_l^3}$ $J = \begin{cases} 0.94 H^{0.747} & \text{for } 2 < H \leq 59.3 \\ 3.42 H^{0.441} & \text{for } H > 59.3 \end{cases}$ $H = \frac{4}{3} E \ddot{o} M^{-0.149} \left(\frac{\mu_l}{\mu_{\text{water}}} \right)^{-0.14}$ $M < 10^{-3}, \quad E \ddot{o} < 40, \quad Re > 0.1$	<p>Clift et al. [171]</p>
$u_b = 1.3 (g d_b)^{0.5}$	<p>Fukuma et al. [482]</p>
$u_b = 0.361 (1 + 4.89 / E \ddot{o})^{0.25}$	<p>Nickens et al. [483]</p>
$u_b \left(\frac{\rho_l}{g \sigma_l} \right)^{0.25} = \left\{ \left(\frac{M o^{-0.25}}{K_b} \left(\frac{\rho_l - \rho_g}{\rho_l} \right)^{1.25} d_b^2 \frac{g \rho_l}{\sigma_l} \right)^{-n} + \left(\frac{2c}{d_b} \left(\frac{g \rho_l}{\sigma_l} \right)^{-0.5} + \frac{(\rho_l - \rho_g) d_b}{2 \rho_l} \left(\frac{g \rho_l}{\sigma_l} \right)^{0.5} \right)^{-0.5n} \right\}^{-\frac{1}{n}}$ <p>$n = 0.8$ (contaminated liquid), 1.6 (pure liquid) $c = 1.2$ (monocomponent liquid), 1.4 (multicomponent liquid) $K_b = \max(K_{b,0} M o^{-0.038}, 12)$ $K_{b,0} = 14.7$ (aqueous solution), 10.2 (organic)</p>	<p>Fan and Tsuchiya [135]</p>
$u_b = \frac{u_{b,sph} u_{b,wav}}{(u_{b,sph}^2 + u_{b,wav}^2)^{0.5}}$ $u_{b,sph} = \frac{g d_b^2 (\rho_l - \rho_g)}{18 \mu_l} \left(\frac{3 \mu_l + 3 \mu_g}{2 \mu_l + 3 \mu_g} \right); \quad u_{b,wav} = \left(\frac{2 \sigma}{d_b (\rho_l + \rho_g)} + \frac{g d_b}{2} \right)^{0.5}$	<p>Jamialahmedi et al. [194]</p>
$u_b = 1.16 \left[\frac{d_B g^{0.5} \rho_l^{b'} M o^{0.23 b'}}{\mu_l^{b'} C_D^{0.5}} \right]^{1/(1-b')}$ $C_D = 24(1 + 0.173 Re^{0.65}) Re + 0.143 / (1 + 16300 Re^{-1.089})$	<p>Karamanev [484]</p>
$u_b = \left(\frac{g(\rho_l - \rho_g) d_b}{2 \rho_l} + \frac{2c \sigma_l}{d_b \rho_l} \right)^{0.5}$ $c = 0.449 \frac{\rho_l^{0.128}}{\mu_l^{0.019} \sigma_l^{0.083}}$ <p>$1301 \leq \rho_l (\text{kg/m}^3) \leq 2927$ $4.23 \leq \mu_l (10^{-4} \text{Pa} \cdot \text{s}) \leq 83.6$ $0.024 \leq \sigma_l (\text{N/m}) \leq 0.049$</p>	<p>Maneri [485]</p>
$u_b = d_B \left[\left(\frac{g \mu_l}{\rho_l} \right)^{0.33} \left(\frac{4 a' M o^{0.46 b'}}{2.85^{0.5-2b'}} \right) \left(\frac{\rho_l^2 g}{\mu_l^2} \right)^{\frac{(2-2b')}{(6-6b')}} \right]^{\frac{(2-2b')}{(2b'+1)}}$	<p>Nguyen [486]</p>

Table A-7 (continued)

Correlation	Reference
$u_{b-large} = 0.71(gd_b)^{0.5}(DF)(SF)(AF)$ $SF: \begin{cases} 1 & \text{for } \frac{d_b}{d_c} < 0.125 \\ 1.13 e^{\left(\frac{-d_b}{d_c}\right)} & \text{for } 0.125 < \frac{d_b}{d_c} < 0.6 \\ 0.496 \left(\frac{d_b}{d_c}\right)^{-0.5} & \text{for } \frac{d_b}{d_c} > 0.6 \end{cases}$ $AF = \alpha + \beta(u_g - u_{g-df}); DF = \left(\frac{1.29}{\rho_g}\right)^{0.5}$	<p>Krishna et al. [487]</p>
$u_b \left(\frac{\rho_l}{g\sigma_l}\right)^{0.25} = \left\{ \left(\frac{Mo^{-0.25}}{K_b} \left(\frac{\rho_l - \rho_g}{\rho_l} \right)^{1.25} d_b^2 \frac{g\rho_l}{\sigma_l} \right)^{-n} + \left(\frac{2c}{d_b} \left(\frac{g\rho_l}{\sigma_l} \right)^{-0.5} + \frac{(\rho_l - \rho_g)d_b}{2\rho_l} \left(\frac{g\rho_l}{\sigma_l} \right)^{0.5} \right)^{-0.5n} \right\}^{-\frac{1}{n}}$ <p>$n = 0.8$ (contaminated liquid), 1.6 (pure liquid) $c = 1.2$ (monocomponent liquid), 1.4 (multicomponent liquid) $K_b = \max(K_{b,0} Mo^{-0.038}, 12)$ $K_{b,0} = 14.7$ (aqueous solution), 10.2 (organic) $Mo = g \left(\frac{(\rho_l - \rho_g)\mu_l^4}{\rho_l^4 \sigma_l^3} \right)$</p>	<p>Luo et al. [472]</p>
$u_b = \alpha \left[\frac{u_g(1 - \varepsilon_g)}{\varepsilon_g} \right]^\beta$	<p>Yang et al. [488]</p>
$u_b = \sqrt{\frac{2\sigma_l}{\rho_l d_b} + \frac{g d_b}{2}}$	<p>Nedelchev and Schumpe [461]</p>
$u_B = \frac{Vr\mu_l^{0.33}\sigma_l^{0.33}}{(d_B)^{2/3}\rho_l^{2/3}}$ <p>$722 < \rho_l < 1380 \frac{kg}{m^3}$ $0.015 < \sigma_l < 0.091 N/m$ $0.0022 < \mu_l < 18 Pa \cdot s$</p>	<p>Rodrigue [489]</p>
$u_b = 1.95d_c^{1/6}(gd_b)^{0.5} \text{ for } d_b \geq 0.005 \text{ m}$	<p>De Swart and Krishna [153]</p>

Table A-8: Gas-Liquid mass transfer correlations applicable to SBCRs

System	Conditions	Correlation	Reference										
135 data sets of 7 different groups	-	$k_L = 0.00163 u_g^{0.21} \left(\frac{h_C}{d_C}\right)^{-0.261} \left(\frac{\rho_l \sigma_l^3}{g \mu_l^4}\right)^{0.119}$	Gestrich et al. [490]										
N ₂ – Water, Glycerol, Glycol, BaCl ₂ , Na ₂ SO ₄ – Glass, Bronze	P_{atm} $u_G: 0.03 - 0.15 \text{ ms}^{-1}$ $C_S: 0 - 200 \text{ kg/m}^3$ $d_C: 0.1 - 0.3 \text{ m}$ $h_C: 2.3 - 3 \text{ m}$	$k_L a = \left(\frac{g \rho_l D_{AB}}{\sigma_l}\right)^{2.11} \left(\frac{\mu_l}{\rho_l D_{AB}}\right)^{0.5} \left(\frac{g \mu_l^4}{\rho_l \sigma_l^3}\right)^{-0.159} \varepsilon_g^{1.18}$ $A = 1 + 1.47 \times 10^4 \left(\frac{C_S}{\rho_S}\right)^{0.612} \left(\frac{u_{t\infty}}{(g d_C)^{0.5}}\right)^{0.486} \left(\frac{d_C g \rho_l}{\sigma_l}\right)^{-0.477} \left(\frac{d_C u_g \rho_l}{\mu_l}\right)^{-0.345}$	Koide et al. [107]										
N ₂ , O ₂ – Water, Na ₂ SO ₄ /Activated Carbon – Diatomite, Al ₂ O ₃	P_{atm}, T_{atm} $u_G < 0.07 \text{ ms}^{-1}$ $C_V: 0.51 - 15.22 \text{ vol\%}$ $d_p: 5.4, 6.6, 8.1 \mu\text{m}$ $d_C: 0.095 \text{ m}$ $h_C: 0.85 \text{ m}$	$k_L a = K u_g^{0.82} \mu_{eff}^{-0.39}$ $K = \begin{cases} 0.063 & \text{for Salt Solutions} \\ 0.042 & \text{for Salt free Systems} \end{cases}$ $\mu_{eff} = k(2800 u_g)^{n-1}$ $k \text{ is the fluid consistency index} = 1.97; n: \text{empirical constant } 1 \geq n \geq 0.18$	Schumpe et al [453]										
Air – Water – 10 different solid particles	$u_g: 0.01 - 0.08 \text{ m/s}$ $C_V: 0 - 20 \text{ vol\%}$ $d_p: 0.11 - 2.8 \text{ mm}$ P_{atm} $\rho_S: 1020 - 2780 \text{ kg/m}^3$ <i>PfP, SP Sparger</i>	$k_L a \left(\frac{v_{sl}}{g u_g}\right)^{1/2} = K \left(\frac{u_g}{(v_{sl} g u_g)^{1/4}}\right)^{B1} \times \left(\frac{v_{sl}}{\vec{v}_{eff,rad}}\right)^{B2} \times \left(\frac{\vec{C}_S}{C_{SO}}\right)^{B3}$ <i>The values of constant K and of exponents B1-B3 are as follows:</i> <table style="width: 100%; border: none;"> <tr> <td style="text-align: center;">Sieve plate</td> <td style="text-align: center;">Perforated plate</td> </tr> <tr> <td style="text-align: center;">$K = 0.231 \times 10^{-4}$</td> <td style="text-align: center;">$K = 0.197 \times 10^{-4}$</td> </tr> <tr> <td style="text-align: center;">$B1 = 0.305$</td> <td style="text-align: center;">$B1 = 0.385$</td> </tr> <tr> <td style="text-align: center;">$B2 = -0.0746$</td> <td style="text-align: center;">$B2 = -0.0712$</td> </tr> <tr> <td style="text-align: center;">$B3 = -0.0127$</td> <td style="text-align: center;">$B3 = -0.0114$</td> </tr> </table>	Sieve plate	Perforated plate	$K = 0.231 \times 10^{-4}$	$K = 0.197 \times 10^{-4}$	$B1 = 0.305$	$B1 = 0.385$	$B2 = -0.0746$	$B2 = -0.0712$	$B3 = -0.0127$	$B3 = -0.0114$	Sauer and Hempel [491]
Sieve plate	Perforated plate												
$K = 0.231 \times 10^{-4}$	$K = 0.197 \times 10^{-4}$												
$B1 = 0.305$	$B1 = 0.385$												
$B2 = -0.0746$	$B2 = -0.0712$												
$B3 = -0.0127$	$B3 = -0.0114$												

Table A-8 (continued)

System	Conditions	Correlation	Reference
Air – Water – Glass beads	$d_p: 0.056 - 2.8 \text{ mm}$ $u_g: \text{up to } 0.1 \text{ ms}^{-1}$ $C_V: 9 - 40 \text{ vol}\%$	$\frac{k_L d_{32}^2}{6 \varepsilon_g D_{AB}} = 4.5 \times 10^{-4} Sc^{0.5} Ga^{0.8} Bo^{-0.2}$	Fukuma et al. [492]
Air, N ₂ – Water, Alcohols, Calcium alginate, Polystyrene	P_{atm} $u_g \text{ up to } 0.15 \text{ ms}^{-1}$ $C_V \text{ up to } 20 \text{ vol}\%$ $d_C: 0.14, 0.218, 0.3 \text{ m}$ $h_C: 1.5 \text{ m}$	$k_L a = 12.9 Sc^{0.5} Mo^{-0.159} Bo^{-0.184} \varepsilon_g^{1.3} \left(\frac{g \rho_l D_{AB}}{\sigma_l} \right) \times \left(0.47 + 0.53 \exp \left(-41.4 \frac{\Pi_\infty k_l}{\mu_l u_p} Re_B^{-0.5} \right) \right) (1 + 0.62 C_V)^{-1}$ $\Pi_\infty = -C_B \left(\frac{d\sigma}{dC_B} \right)$	Salvacion et al [203]
O ₂ , CO ₂ – Glycol, Water, Brine, Aqueous Polyacrylamide	<i>Sieve and Sintered plate</i>	$k_L = \alpha \left(\frac{(\rho_l - \rho_g) \mu_l g}{\rho_l^2} \right)^{\frac{1}{3}} \left(\frac{\mu_l}{\rho_l D_{AB}} \right)^{-\frac{2}{3}}$ $\alpha = \begin{cases} 0.31 & \text{for } d_p < 1.0 \text{ mm} \\ 0.0031 & \text{for } 1.0 < d_p < 2.5 \text{ mm} \\ 0.0042 & \text{for } d_p > 2.5 \text{ mm} \end{cases}$	Calderbank et al. [493]
CO ₂ – NaHCO ₃ , Na ₂ CO ₃ surfactants	$d_C = 0.113 \text{ m}$ $h_C = 1.086 \text{ m}$ $u_g < 0.002 \text{ ms}^{-1}$	$k_L = K_4 u_g^{0.5} \sigma_l^{1.35}$ <i>K₄ is a function of the bubble plate size</i>	Vazquez et al. [494]
He, N ₂ , SF ₆ , Air – 0.8 M Na ₂ SO ₄ – Xanthan gum, Diatomite, Alumina suspensions	$P: 0.1 - 1 \text{ MPa}$ $u_G: 0.01 - 0.08 \text{ ms}^{-1}$ $C_V: \text{Upto } 18\% \text{ vol}$ $d_p: 7, 22 \mu\text{m}$ $d_C: 0.115 \text{ m}$ $h_C: 1.37 \text{ m}$	$k_L a = u_g^{0.9} \mu_{eff}^{-0.55} \rho_g^{0.46}$ $K = \begin{cases} 0.063 & \text{for Salt Solutions} \\ 0.042 & \text{for Salt free Systems} \end{cases}$ $\mu_{eff} = k(2800 u_g)^{n-1}$ <i>k is the fluid consistency index = 1.97; n: empirical constant</i> $1 \geq n \geq 0.18$	Dewes et al. [199]

Table A-8 (continued)

System	Conditions	Correlation	Reference
N ₂ /Fe(CN) - NaOH, CMC, HNaCO ₃ - Na ₂ CO ₃ /glass, diatomite, silicon carbide, alumina	$u_g: 0.007 - 0.09 \text{ ms}^{-1}$ $C_V: 1.3 - 12.4 \text{ vol}\%$ $d_p: 44 - 105 \text{ }\mu\text{m}$ $\rho_s: 2448 - 3965 \text{ kg/m}^3$ $\rho_l: 1026 - 1121 \text{ kg/m}^3$ $\mu_l: 0.99 - 6.27 \text{ mPa}\cdot\text{s}$ $d_C: 0.05 \text{ m}$ $h_C: 0.75 \text{ m}$	$\frac{k_L}{u_g} = 0.103(ReFrSc^2)^{-0.265}$	Neme et al. [101]
Air - Water - Lexan, PS, Glass	$u_g: 0.0025 - 0.05 \text{ ms}^{-1}$ $\rho_s: 1170 - 2460 \text{ kg/m}^3$ $C_V: 0.9 - 2.5 \text{ vol}\%$ $d_p: 2.3 - 3 \text{ mm}$ $d_C: 0.06 \text{ m}$ $h_C/d_C: 22 - 30.2$	$k_L a = 4.49u_g^{0.338}C_s^{0.595}\left(1 - \frac{\rho_l}{\rho_s}\right)^{0.337}$	Guo et al. [495]
Air - Water - Nickel	$u_g: 0.02 - 0.04 \text{ m/s}$ $u_l: 0.018 - 0.037 \text{ m/s}$ $C_s: 5.7 \text{ vol}\%$ $d_p: 177 - 210 \text{ }\mu\text{m}$ $\rho_s: 8900 \text{ kg/m}^3$ $d_C: 0.05 \text{ m}$ $h_C: 0.5 \text{ m}$	$k_L a = 0.4u_g^{0.625}u_l^{0.26}\times\exp[1.477 \cdot 10^{-5}h_C]$	Chen et al. [456]
H ₂ /CO - Paraffin oil - Silica gel	$T: 293 - 523 \text{ K}$ $P: 1 - 5 \text{ MPa}$ $d_p: 134 \text{ }\mu\text{m}$ $C_V: 5 - 20 \text{ vol}\%$ $d_C: 0.037 \text{ m}$ $h_C: 0.48 \text{ m}$	$H_2: \frac{k_L d_{32}}{D_{AB}} = 1.546 \times 10^{-2} Eu^{0.052} Re^{0.076} Sc^{-0.231}$ $CO: \frac{k_L d_{32}}{D_{AB}} = 8.748 \times 10^{-2} Eu^{-0.012} Re^{0.024} Sc^{-0.133}$	Yang et al. [496]

Table A-8 (continued)

System	Conditions	Correlation	Reference
<p>H₂, CO, N₂, CH₄, Isopar-M, Hexanes – Glass beads, Iron Oxide</p>	<p>u_g: 0.0035 – 0.574 m/s C_S: 0 – 36 vol. % T: 275 – 538 K P: 0.1 – 15 MPa ρ_S: 700 – 4000 kg/m³ d_p: 5 – 300 μm ρ_l: 633.4 – 1583 kg/m³ μ_l: 0.189 – 398.8 mPa · s σ_l: 8.4 – 75 mN/m d_c: 0.0382 – 5.5 m</p>	$\frac{k_L}{(1 - \varepsilon_g)} = 6.14 \times 10^4 \cdot \frac{\rho_l^{0.26} \mu_l^{0.12} \varepsilon_g^{1.21} D_{AB}^{0.5}}{\sigma_l^{0.52} \rho_g^{0.06} u_g^{0.12} d_p^{0.05} T^{0.68}} \Gamma^{0.11} \left(\frac{d_c}{d_c + 1} \right)^{0.4}$	<p>Lemoine et al. [179]</p>
<p>Semi-Theoretical approach based on Kolmogorov theory of isotropic turbulence</p>	<p>-</p>	$k_L a = f_c \sqrt{\frac{4 D_{AB} R_{sf}}{\pi S_B} \frac{f_B S_B}{A_c u_b}}$ $R_{sf} = \pi \sqrt{\frac{l_b^2 + h_b^2}{2} - \frac{(l_b - h_b)^2}{8}} u_b;$ $S_B = \pi \frac{l^2}{2} \left[1 + \left(\frac{h}{l} \right)^2 \frac{1}{2e} \ln \frac{(1+e)}{(1-e)} \right]; e = \sqrt{1 - \left(\frac{h}{l} \right)^2}$ $\left. \begin{aligned} l &= \frac{d_b}{1.14 Ta^{-0.176}} \\ h &= 1.3 d_b Ta^{-0.352} \end{aligned} \right\} \text{for } 2 < Ta < 6; \quad \left. \begin{aligned} l &= \frac{d_b}{1.36 Ta^{-0.28}} \\ h &= 1.85 d_b Ta^{-0.56} \end{aligned} \right\} \text{for } 6$ $Ta = Re_b Mo^{0.23}; Re_b = \frac{d_b u_b \rho_l}{\mu_l}; Mo = \frac{g \mu_l^4}{\rho_l \sigma_l^3}$	<p>Nedeltchev and Schumpe [461]</p>

Table A-8 (continued)

System	Conditions	Correlation	Reference
		$f_c = 0.124E\ddot{o}^{0.94} \left(\frac{\rho_g}{\rho_g^{ref}} \right)^{0.15} = 0.124 \left(\frac{g(\rho_l - \rho_g)d_b^2}{\sigma_l} \right)^{0.94} \left(\frac{\rho_g}{1.2} \right)^{0.15}$ $f_B = \frac{u_g A_c}{V_b}; V_b = \frac{\pi d_b^3}{6} = \frac{4}{3} \pi \left(\frac{l}{2} \right)^2 \frac{h}{2}$	
H ₂ , CO, N ₂ CH ₄ , Isopar-M. Hexanes – Glass beads, Iron Oxide	$u_g: 0.0035 - 0.574 \text{ m/s}$ $C_V: 0 - 36 \text{ vol. \%}$ $T: 275 - 538 \text{ K}$ $P: 0.1 - 15 \text{ MPa}$ $\rho_s: 700 - 4000 \text{ kg/m}^3$ $d_p: 5 - 300 \text{ }\mu\text{m}$ $\rho_l: 633.4 - 1583 \text{ kg/m}^3$ $\mu_l: 0.189 - 398.8 \text{ mPa}\cdot\text{s}$ $\sigma_l: 8.4 - 75 \text{ mN/m}$ $d_c: 0.0382 - 5.5 \text{ m}$	$k_L a = 0.18 Sc^{0.6} \left(\frac{\rho_l \eta_g}{Mw_l} \right)^{-2.84} (\rho_g u_g)^{0.49} \times \exp[-2.66 C_V]$	Behkish et al. [9]
He, N ₂ – Paraffins mixture, C ₁₂ -C ₁₃ , Light F-T Cut, Heavy F-T- Cut – Alumina, Puralox Alumina, Iron oxide	$u_g: 0.14 - 0.26 \text{ m/s}$ $C_S: 0 - 20 \text{ vol. \%}$ $T: 330 - 530 \text{ K}$ $P: 8 - 30 \text{ MPa}$ $\rho_s: 3218 - 4000 \text{ kg/m}^3$ $d_p: 1.5 - 140 \text{ }\mu\text{m}$ $\rho_l: 631.3 - 779.5 \text{ kg/m}^3$ $\mu_l: 0.27 - 9.96 \text{ mPa}\cdot\text{s}$ $\sigma_l: 13 - 27 \text{ mN/m}$ $d_c: 0.3 \text{ m}; h_c: 3 \text{ m}$	$k_L a$ $= 7.99 \times 10^{-9} \frac{\rho_l^{1.82} \rho_g^{0.27} u_g^{0.387} \Gamma^{0.173}}{\mu_l^{0.25} \sigma_l^{0.976} Mw_g^{0.02}} \left(\frac{P_T}{P_T - P_S} \right)^{0.242} \left(\frac{d_c}{d_c + 0.3} \right)^{0.1}$ $\times \exp[-1.3C_p + 0.8C_p^2 - C_p^3 - 1675.7d_p + 0.176X_W]$	Sehabiague et al. [81]

Table A-9: Heat transfer correlations applicable to SBCRs

Correlation	Reference
$Nu_{(d_R)} = 34.7Re_{G,d_R}^{0.22} \text{ for } Re_{G,d_R} > 150$ $Nu_{(d_R)} = 22.4Re_{G,d_R}^{0.36} \text{ for } Re_{G,d_R} > 150$	Kölbel et al. [497]
$St_{sus} = 0.124 \left[(Re_G Fr_G Pr_{sus}^{2.5})^{1/3} \right]^{-0.66}$	Kölbel and Langemann [498]
$\alpha_W = 8850u_G^{0.22}$	Fair et al. [118]
$St = 0.1 \left[(Re_G Fr_G Pr_L^2)^{1/3} \right]^{-2/3}$	Kast [499]
$St = 0.11 \left[(Re_G Fr_G Pr_L^{2.48})^{1/3} \right]^{-0.69}$	Burkel [500]
$St = 0.11 \times 1.25 \left[(Re_G Fr_G Pr_L^{2.5})^{1/3} \right]^{-0.667}$	Shaykhutdinov et al. [501]
$St = 0.418 (Re_G Fr_G Pr_L^2)^{-1/3} u_g^{1/4} \left(\frac{\rho_l - \rho_g}{\rho_l} \right)^{1/3} \left(\frac{\eta_L}{\eta_{L,W}} \right)^{-0.05}$ $St = 0.3 (Re_G Fr_G Pr_L^2)^{-1/3} \left(\frac{\rho_l - \rho_g}{\rho_l} \right)^{1/3} \left(\frac{\eta_L}{\eta_{L,W}} \right)^{-0.05}$ $St = 1.2 (Re_G Fr_G Pr_L^2)^{-1/3} (u_G u_L)^{1/4} \left(\frac{\rho_L - \rho_G}{\rho_L} \right)^{1/3} \left(\frac{\eta_L}{\eta_{L,W}} \right)^{-0.05}$	Nishikawa et al. [502]
$h = 1977 u_l^{0.070} u_G^{0.059} d_p^{0.106}$	Baker et al. [503]
$St = 0.136 \left[(Re_G Fr_G Pr_L^{1.94})^{1/3} \right]^{-0.81}$	Louisi [504]
$St = 0.1 \left[(Re_G Fr_G Pr_L^{1.94})^{1/3} \right]^{-0.75}$	Deckwer et al. [367, 505]
$\frac{hd_C}{k_L} = 0.4 \left(\frac{d_C v_C \rho_L}{\eta_L} \right)^{2/3} \left(\frac{\mu_l}{\mu_{l,w}} \right) \left(\frac{C_{p,l} \mu_l}{k_l} \right)^{1/3}$ $v_C = 1.31 [gd_C (u_G - \varepsilon_G v_{b\infty})]^{1/3}$	Joshi and Sharma [506]
$Nu' = 0.044 (Re' Pr)^{0.78} + 2.0 Fr_g^{0.17}$	Kato et al. [507]

Table A-9 (continued)

Correlation	Reference
$Nu' = \frac{hd_p \varepsilon_l}{K_L(1 - \varepsilon_l)} \quad , \quad Re' = \frac{\rho_l d_p u_l \varepsilon_l}{\mu_l(1 - \varepsilon_l)}$ $Pr = \frac{\mu_l C_{p_l}}{K_l} \quad , \quad Fr_g = \frac{u_g^2}{gd_p}$	
$\frac{hl_B}{k_L} = 0.18(1 - \varepsilon_G) \left(\frac{v_c l_B}{\eta_L} \right)^{\frac{2}{3}} \left(\frac{C_{p,l} \mu_l}{k_l} \right)^{\frac{1}{3}}$ $v_c = \sqrt[3]{\frac{1}{2.5} \left(\frac{\rho_L - \rho_G}{\rho_L} \right) gd_c u_G}; \quad l_B = d_B \sqrt[3]{\frac{\pi}{6\varepsilon_G}}$	Zehner [255, 508]
$St = 0.0371 Re_G^{-0.17} Fr_G^{-0.32} Pr_L^{-0.46}$	Wendt [509]
$St = 0.11 [(Re_G Fr_G Pr_L^2)^{1/3}]^{-0.75}$ $St_{sus} = 0.12 [(Re_{G,sus} Fr_G Pr_{sus}^2)^{1/3}]^{-0.75}$	Michael [510]
$St_{m3} = St_{m2} = 0.1234 Re_{m2}^{-0.305} Pr^{-2/3}$	Chiu and Ziegler [511]
$h = 2290 u_g^{0.1} u_g^{0.05} \mu_l^{-0.18} d_p^{0.04}$	Kang et al. [512]
$\frac{h_3}{h_2} = 1 + 0.0413 \left(\frac{u_g}{u_l} \right)^{0.3} \left(\frac{(d_p/D_c)(\rho_s - \rho_l)}{\rho_l} \right)^{0.61}$	Muroyama et al. [513]
$Nu = 0.762 Re_m^{0.646} Pr^{0.638} U_R^{0.266} \phi_s^{-1} \left(1 - \frac{\varepsilon_{l,2}}{\varepsilon_{l,3}} \right)$	Chiu and Ziegler [514]
$Nu = 0.036 Re_l^{0.81} Pr^{0.65}$	Kang et al. [515]
$h = 2.13 (10^{-4}) u_g^{0.338} u_l^{0.54} \rho_l^{1.235} \mu_l^{0.162} K_L^{0.04} C_{p,l}^{1.04} d_l^{0.930} \cdot (\rho_s - \rho_l)^{-0.357}$	Saberian-Broudjenni et al. [516]

Table A-9 (continued)

Correlation	Reference
$h = 0.0647 \left[K_L \rho_l C_{p,l} \left(\frac{((u_l + u_g)(\varepsilon_l \rho_l + \varepsilon_g \rho_g + \varepsilon_s \rho_s) - u_l \rho_l)}{\varepsilon_l \mu_l} \right)^{0.5} \right]^{0.5}$	Suh et al. [517]
$h = 0.0722 \left[K_L \rho_l C_{p,l} \left(\frac{((u_l + u_g)(\varepsilon_l \rho_l + \varepsilon_g \rho_g + \varepsilon_s \rho_s) - u_l \rho_l)}{\varepsilon_l \mu_l} \right)^{0.5} \right]^{0.5}$	Kim et al. [518]
$j'_H = 0.137 Re'_{l,g}{}^{-0.271}$ $j'_H = \left(\frac{h_w}{\rho_l C_{p,l} u_l} \right) \varepsilon_l Pr^{2/3}, \quad Re'_{l,g} = Re_l \left(\frac{(\varepsilon_l - \varepsilon_g)}{\varepsilon_l (1 - \varepsilon_l - \varepsilon_g)} \right)$	Muroyama et al. [519, 520]
$\frac{Nu Pr_l^{-1/3} \left(\frac{\mu_b}{\mu_w} \right)^{-0.14}}{Re_l^{0.2} Re_g^{0.055}} = 10.5 e^{-3.18(10^{-4})(C_s - 22)^2}$	Hatate et al. [521]
$St = 0.12 [(Re_G Fr_G Pr_L^{2.2})^{1/3}]^{-0.83} \left(\frac{D_R}{d_R} \right)^{0.15} \left(\frac{\eta_L}{\eta_{L,W}} \right)^{0.3}$	Korte [222, 522]
$h = 0.1 \left(K_L \rho_l C_{p,l} \left(\frac{P_v}{v_l} \right)^{0.5} \right)^{0.5} + 0.285 \left(\left(\frac{K_L \rho_l C_{p,l} \varepsilon_s^{1/3} (u_l - u_{mf})}{\varphi_s d_{eq}} \right) \right)^{0.5}$	Magiliotou et al. [523]
$h = 0.0685 \left(K_L \rho_l C_{p,l} \left(\frac{(u_l + u_g) \left\{ \left[1 - \left(\frac{V_f/V_s}{1 + V_f/V_s} \right) \right] \varepsilon_s \rho_s + \varepsilon_f \rho_f + \varepsilon_g \rho_g + \varepsilon_l \rho_l \right\} g}{\varepsilon_l \mu_l} \right)^{0.5} \right)^{0.5}$ <p style="text-align: center;"> $0.02 \leq u_g \leq 0.14 \text{ ms}^{-1}, \quad 0.02 \leq u_l \leq 0.09 \text{ ms}^{-1}$ $1 \leq d_p \leq 6 \text{ mm}, \quad 0 \leq \frac{V_f}{V_s} \leq 0.2, \quad 1500 \leq \rho_f \leq 1800 \text{ kg/m}^3$ </p>	Kim et al. [524]
$Nu = 0.042 Re_l^{0.72} Pr_l^{0.86} Fr_g^{0.067}$ <p style="text-align: center;"> $0.01 \leq u_g \leq 0.14 \text{ ms}^{-1}, \quad 1.27 \leq u_l \leq 9 \text{ cms}^{-1}$ $3.7 \leq \mu_l \leq 300 \text{ mPa}, \quad d_p = 3, 5 \text{ mm}$ </p>	Zaidi et al. [525]

Table A-9 (continued)

Correlation	Reference
$h = 1800u_g^{0.11}\mu_{eff}^{-0.14}u_l^{1.03(0.65-\varepsilon_l)}d_p^{0.58(\varepsilon_l-0.68)}$ $0.01 \leq u_g \leq 0.14 \text{ ms}^{-1}, \quad 0.013 \leq u_l \leq 0.09 \text{ ms}^{-1}$	
$h_w = 0.0035(k_{sl}\rho_{sl}C_{p,sl})^{0.5} \left(\frac{\rho_{sl}g}{\mu_{sl}}\right)^{0.47} u_G^{0.25}$	Saxena [526]
$Nu' = 5.56(10)^2(Re'Pr)^{0.709} \left(\frac{\rho_s - \rho_l}{\rho_s}\right)^{0.156}$ $Nu' = \frac{h_{av,2}d_p\varepsilon_l}{K_L(1-\varepsilon_l)}, \quad Re'Pr = \frac{d_p u_l \rho_l C_{p,l}}{K_L(1-\varepsilon_l)}$ $59.96 \leq Re'Pr \leq 15,472.7 \text{ (for } Pr = 5.83) \quad , \quad 1.04 \leq \rho_s \leq 2.5 \text{ gcm}^{-3}$	Kumar et al. [527]
$St = 0.037 \left[\left(Re_{sl} Fr Pr_{sl}^{1.87} \left(\frac{\varepsilon_g}{1-\varepsilon_g} \right) \right) \right]^{-0.22}$	Yang et al. [488]
$St = A(ReFr)^B Pr^C \left(\frac{x}{H}\right)^D \left(\frac{r}{R}\right)^E$	Kantarci et al. [528]
$St = 0.1 \left[Pr^2 Re Fr \frac{\mu_b}{\mu_l} \frac{P_V}{g \rho_l u_l} \right]^{-0.25}$	Kskrao [529]
$\frac{hd_c}{k_l} = 0.084 \left(\frac{d_c v_c \rho_L}{\eta_L}\right)^{0.8} \left(\frac{C_{p,l} \mu_l}{k_l}\right)^{1/3} \left(\frac{\mu_l}{\mu_{l,w}}\right)^{0.14}$ $v_c = 0.21 \sqrt{gd_c} \left(\frac{u_g^3}{g \eta_l}\right)^{0.125}$ $h(r) = h \left(1 - \left(\frac{n-1}{n}\right) \left(\frac{r}{R}\right)^n\right)$ <p>Where recommended value of $n = 1.4$</p>	Jhawar and Prakash [530]

Table A-10: Liquid-phase axial dispersion coefficient models

Model	Conditions	u_g (cm/s)	u_l (cm/s)	d_c (cm)	Reference
$D_L = \frac{d_c(2u_g + u_{b\infty})}{Pe_l}$	Air-tap water systems. Concentrated NaCl was injected via 20 holes in a spiral tube, tracer concentrations were measured using a conductivity meter.	45	0.88-2.18	5.08, 14, 29	Reith et al. [129]
$D_L = \begin{cases} 75.4d_c^2u_g^{1.2} + 17000d_o & 0 \leq u_g \leq 0.07 \text{ m/s} \\ \frac{0.14d_c}{(1 - \varepsilon_g)^2} & u_g \geq 0.1 \text{ m/s} \end{cases}$	Air-tap water systems. The tracer, 4 N aqueous solution of potassium chloride, was poured instantaneously and uniformly on the liquid surface at the top of column from the tracer injector.	2-26	0	4-16	Ohki and Inoue [531]
$D_L = \frac{g^{0.5}d_c^{1.5}}{13} \left[1 + 6.5 \left(\frac{u_g}{\sqrt{gd_c}} \right)^{0.8} \right]$	Used zero order reaction analysis under continuous flow conditions of the liquid.	4-20	0.52	3, 4.5, 6.6, 12.2	Kato and Nishiwaki [268]
$D_L = 1.23d_c^{1.5}u_g^{0.5}$	Steady-state experiments with large diameter bubble columns.	0.9-8.92	0.6-1.5	40.64, 106.68	Towell and Ackerman [279]
$D_L = g^{0.5}d_c^{1.5} \left[0.06 + 0.55 \left(\frac{u_g}{\sqrt{gd_c}} \right)^{0.7} \right]$	Various gas-liquid systems, liquids were water, glycol, methanol and aqueous NaCl, gases were air, oxygen, helium and CO ₂	0.53-41.9	3.5	15.2, 30.1, 60	Akita and Yoshida [83]
$D_L = 0.692d_c^{1.4}u_g^{1/3}$	Air-Water system. The dispersion coefficient was measured using the stationary method using both a dye and a heat source.	0.5-15	0.2-0.8	15	Badura [532]
$D_L = d_c^{1.25} (0.15 + 0.69u_g^{0.77}) \left(\frac{10^{-3}}{\eta_l} \right)^{0.12}$	Impulse injection with KCl solution as tracer. Two bubble columns (19 and 10 cm diameter, 240 and 150 cm high). Air was used for the gas phase, water, aqueous methanol and aqueous cane sugar solutions used for the liquid phase. Temperature range of 12.5 – 20 °C.	4.3-33.8	0	10, 19	Hikita and Kikukawa [533]

Table A-10 (continued)

Model	Conditions	u_g (cm/s)	u_l (cm/s)	d_c (cm)	Reference
$D_L = 0.678d_c^{1.4}u_g^{0.3}$	Different gas distributors. Liquid phases investigated were tap water, aqueous solutions of sodium sulfate and sodium chloride, as well as aqueous solutions of molasses with various concentrations. Gas phase was oxygen. Steady and impulse injection with NaCl solution as tracer.	5-12	0.71	15, 20	Deckwer et al. [86]
$D_L = 0.33d_c^{4/3}(gu_g)^{1/3}$	Semi theoretical model based on isotropic turbulence model for eddy diffusivity, correlated to experimental data from literature.	0.3-45	-	8.2-107	Baird and Rice [253]
$D_L = 0.9d_c^{1.5}[h_c(u_g - \varepsilon_g V_s)]^{1/3}$ $V_s = 0.164(1 - \varepsilon_g)^{1.39}(1 + 2.25\varepsilon_g^3)$	N/A	-	-	-	Field and Davidson [269]
$D_L = 0.33(V_C + u_L)d_C$ $V_C = 1.31 \left[gd_C \left(u_g - \frac{\varepsilon_g}{1 - \varepsilon_g} u_l - \varepsilon_g u_{b\infty} \right) \right]^{1/3}$	Theoretical derivation based on the multiple circulation cell model of a bubble column. The height to diameter ratio of the circulation cell and the column was taken to be 0.8 rather than 1.0.	-	-	-	Joshi and Shah [534]
$D_L = d_c^{1.5}u_g^{0.25} \left(0.291 + \frac{0.341}{(1 - 0.5u_g^{0.5})^2} \right)$	Theoretical derivation.	-	-	-	Miyauchi et al. [134]
$D_L = 0.068(gu_g)^{3/8}d_c^{1.5}u_l^{-1/8}$	Theoretical derivation based on the assumption of the validity of the $Pe = 2$ analogy, developed for fixed bed, to bubble columns.	-	-	-	Riquarts [535]
$D_L \propto D_c^{1.5}$ $D_L \propto u_g^{1/3}$	Steady injection, heat tracer method. Systems investigated were air/water/CO ₂ , N ₂ /n-propanol/CO ₂ and air/glycol.	0.5-18	0-6	10	Mangartz and Pilhofer [536]

Table A-10 (continued)

Model	Conditions	u_g (cm/s)	u_l (cm/s)	d_c (cm)	Reference
$D_L = 0.5 \times 0.368 g^{1/3} d_c^{4/3} u_g^{1/3}$	Theoretical calculation based on the multiple circulation cell model of a bubble column.	-	-	-	Zehner [127]
$D_L = 0.606 d_c \left(\frac{g u_g h_{lo}}{4 + \frac{70}{Re^{0.25}} \frac{h_{lo}}{d_c}} \right)^{1/3}$ $Re > 1000, \quad \frac{h_{lo}}{d_c} > 3$	Theoretical calculation using microscopic and macroscopic balances.	-	-	-	Walter and Blanch [133]
$D_L \propto d_c^{1.4}$	Steady injection method using both heat and NaCl as tracers.	1.5-30	0.2-4.5	6.3	Wendt et al. [509]
$D_L = 0.343 n^{-8/3} g^{1/3} d_c^{4/3} u_g^{1/3}$	Measured dispersion coefficients in several Newtonian and non-Newtonian liquids (water, MC, CMC-1, CMC-2, and Separan) in a 0.23 m diameter, 1.22 m high bubble column. Solid tracer particles suspended freely in the liquid were used to determine the dispersion coefficient.	0.01-5	-	23	Kawase and Moo-Young [537]
$D_L = 0.208 u_g^{0.4} (d_c + n_t d_t)^{1.48} A_f^{1.8} u_l^{-0.12}$	N/A	-	-	-	Bernemann [226]
$D_L = 0.632 d_c^{1.25} \frac{u_g}{\varepsilon_g}$	Tap water, aqueous alcohol and CMC solutions of lower concentrations were used as the liquid phase. Dispersion coefficients were measured by detecting tracer gas concentration in the quadrupole mass spectrometer. Helium, argon and carbon dioxide were used as the tracer gases.	1-18		15, 25	Kantak [130]
$D_L \propto d_c^n, \quad \frac{n}{n_o} = 1 - 0.11 \ln \left(\frac{\rho_g}{\rho_{g,o}} \right)$	Thermal dispersion, water and hydrocarbon as the liquid phase, air as the gas phase.	2-20	0.34 - 1.0	5.08	Yang et al. [55]

Table A-11: Liquid-phase radial dispersion coefficient investigations

Description	u_g (cm/s)	u_l (cm/s)	d_c (cm)	Reference
Air-tap water systems. A steady tracer stream was introduced by a single tube at the axis of the column; radial dispersion was obtained by measuring the concentration downstream of the injection point at several distances from the axis of the column. The radial dispersion coefficient was found to be a factor 10 smaller than the axial dispersion coefficient at the same superficial gas velocity.	45	0.88-2.18	14, 29	Reith et al. [129]
Air-tap water system in a 5-cm co-current air-water bubble column were investigated using the steady-state, point-source tracer injection technique. Radial dispersion coefficients were found to be a factor of 10 times smaller than the axial dispersion coefficient for the same gas and liquid velocities.	1.41 - 6.72	0.748 - 1.275	5	Eissa et al. [128]
Air-tap water and air/sea water systems were used. Measured radial dispersion in a 2.3 m tall, 0.193 m diameter bubble column bioreactor. For otherwise equal conditions, the radial dispersion coefficient value was typically only about 1% of the axial value	0.062 -5.1	0	19.3	Rubio et al. [131]

Table A-12: Solid-phase dispersion coefficient models

Model	Conditions	Reference
$Pe_s = \frac{u_g d_c}{d_p}$ $= \left[1 + 0.009 Re_s \left(\frac{u_g}{g d_c} \right)^{-0.8} \right] \frac{13 (u_g / \sqrt{g d_c})}{1 + 8 (u_g / \sqrt{g d_c})^{0.85}}$	<p>For low Froude number and large particle diameters. Glass beads, $\rho_p = 2520 \text{ kg/m}^3$, $75.5 < d_p < 163 \text{ }\mu\text{m}$ $C_s = 48 - 202 \text{ kg/m}^3$</p>	<p>Kato and Nishiwaki [268]</p>
$\frac{u_g d_c}{d_p} = 10 \left(\frac{u_g}{g d_c} \right)^{0.76}$	<p>Glass beads, $1 < d_p < 125 \text{ }\mu\text{m}$, $C_s = 3.1 - 62 \text{ kg/m}^3$</p>	<p>Kojima et al. [108]</p>
$\frac{u_g d_c}{d_p} = 7.7 \left(\frac{Fr_g^6}{Re_g} \right)^{0.098} + 0.019 Re_p^{1.1}$	<p>Glass beads, $\rho_p = 2420 \text{ kg/m}^3$, $88 < d_p < 105 \text{ }\mu\text{m}$ $C_s = \text{up to } 420 \text{ kg/m}^3$</p>	<p>O'Dowd et al. [208]</p>
$\frac{u_g d_c}{d_p} = 9.6 \left(\frac{Fr_g^6}{Re_g} \right)^{0.1114} + 0.019 Re_p^{1.1}$	<p>Glass beads, $\rho_p = 2420, 3990 \text{ kg/m}^3$, $48.5 < d_p < 164 \text{ }\mu\text{m}$ $C_s = \text{up to } 420 \text{ kg/m}^3$</p>	<p>Smith and Reuther [538]</p>

Table A-13: Literature F-T SBCR empirical models [46, 126]

Authors/Ref.	Kinetics	Species involved in MB	Gas Phase		Liquid/Slurry Phase	Solid Phase	Energy	Gas Consumption	Steady-State or Transient?
			LB	SB					
Calderbank et al. [539]	F-T, 1 st order	H ₂	PF		PF	Uniform	-	-	-
Satterfield and Huff [540]	F-T, 1 st order	H ₂	PF		PM	Uniform	Isothermal	No	Steady-State
Deckwer et al. [541]	F-T, 1 st order	H ₂	PF		PM	Uniform	Isothermal	Linear f(X)	Steady-State
Deckwer et al. [542]	F-T, 1 st order	H ₂	ADM		ADM	SDM	ADM	Linear f(X)	Steady-State
Bukur [148]	F-T, 1 st order	H ₂	PF		PM; PF	Uniform	Isothermal	Linear f(X)	Steady-State
Kuo [543]	F-T, 1 st order	H ₂	PF		PF; PM; ADM	Uniform	Isothermal	Linear f(X)	Steady-State
	F-T, L-H WGS, L-H	H ₂ , CO, H ₂ O, CO ₂							
Stern et al. [176]	F-T, 1 st order	H ₂	PF		PM	Uniform	Isothermal	No	Steady-State
Leib and Kuo [417]	F-T, L-H WGS, L-H	H ₂ , CO, H ₂ O, CO ₂	PF		Unmixed	SDM	-	Linear f(X)	Steady-State
Stern et al. [267]	F-T, 1 st order WGS, 2 nd order	H ₂ , CO, H ₂ O, CO ₂ , C _n H _m	ADM		ADM	SDM	Isothermal	Overall gas MB	Steady-State
Bukur and Zimmerman [262]	F-T, L-H WGS, L-H	H ₂ , CO, H ₂ O, CO ₂ , C _n H _m	PF		Unmixed	SDM	Isothermal	Overall gas MB	Steady-State
Turner and Mills [270]	F-T, 1 st order	H ₂	MCM; PF		MCM	Uniform	Isothermal	Linear f(X)	Steady-State
			ADM		ADM	SDM	ADM		
Prakash [264]	F-T, L-H WGS, L-H	H ₂ , CO, H ₂ O, CO ₂	ADM		ADM	SDM	Isothermal	Overall gas MB	Steady-State

Table A-13 (continued)

Authors/Ref.	Kinetics	Species involved in MB	Gas Phase		Liquid/Slurry Phase	Solid Phase	Energy	Gas Consumption	Steady-State or Transient?
			LB	SB					
Leib et al. [544]	F-T, 1 st order	H ₂	MCM		MCM	Uniform	Isothermal	Linear f(X)	Steady-State
Inga and Morsi [181]	F-T, L-H WGS, L-H	H ₂ , CO, H ₂ O, CO ₂	PF		MCM	Uniform	Isothermal	No	Steady-State
Mills et al. [261]	F-T, 1 st order	H ₂	ADM		ADM	SDM	ADM	Linear f(X)	Steady-State
Maretto and Krishna [241]	F-T, L-H	H ₂ , CO	PF	PM	PM	Uniform	Isothermal	No	Steady-State
van der Laan et al. [56]	F-T, L-H WGS, L-H	H ₂ , CO, H ₂ O, CO ₂ , n-products	PF	PM	PM	Uniform	Isothermal	Linear f(X)	Steady-State
de Swart and Krishna [153]	F-T, 1 st order	H ₂	ADM	ADM	ADM	SDM	ADM	Linear f(X)	Transient
Rados et al. [150, 265]	F-T, 1 st order	H ₂ , CO, H ₂ O, pseudo-product	ADM	ADM	ADM	Uniform	ADM	Overall gas MB	Transient
Song et al. [266]	F-T, L-H	H ₂ , CO, H ₂ O, pseudo-product	PF		PM	Uniform	Isothermal	Overall gas MB	Steady-State
Song et al. [545]	F-T, L-H	H ₂ , CO, H ₂ O, CO ₂	PM		PM	Uniform	Isothermal	No	Steady-State
Fernandes [258]	F-T, L-H WGS, L-H	H ₂ , CO, H ₂ O, CO ₂ , n-products	PF	PM	PM	Uniform	Isothermal	Linear f(X)	Steady-State
Iliuta et al. [160, 263]	F-T, L-H WGS, L-H	H ₂ , CO, H ₂ O, CO ₂ , n-pseudo-products	Core & Annulus ADM				ADM	Overall gas MB	Steady-State

Table A-13 (continued)

Authors/Ref.	Kinetics	Species involved in MB	Gas Phase		Liquid/Slurry Phase	Solid Phase	Energy	Gas Consumption	Steady-State or Transient?
			LB	SB					
Sehabiague et al. [151]	F-T, L-H	H ₂ , CO, H ₂ O, CO ₂ , N ₂ , n products	ADM	ADM	ADM	SDM	ADM	Overall gas MB	Steady-State
Wang et al. [158]	F-T, L-H WGS, L-H	H ₂ , CO, H ₂ O, CO ₂ , N ₂ , n-products	PF	PM	PM	Uniform	Isothermal	Overall gas MB	Steady-State
Guettel and Turek [546]	F-T, 1 st order	H ₂	PF		PM	Uniform	PF	Linear f(X)	Steady-State

L-H: Overall reaction rate based on Langmuir-Hinshelwood kinetics.
 ADM: Axial-Dispersion Model
 MCM: Mixing-Cell Model
 SDM: Sedimentation-Dispersion Model
 PF: Plug-Flow
 PM: Perfectly Mixed
 MB: Mass Balance
¹ as reported by Mills et al. [261]
² as reported by Bukur and Zimmerman [262]

Table A-14: Summary of multiple cell circulation models [285]

Reference	Numerical method for the continuous phase	Numerical method for the dispersed phase	Height of circulation cells	Liquid circulation driving force
Freedman [547]	Vortex function equation	Bubble path calculated in the known velocity field	Equal to the column height	Gas distribution partially covering cross section
Rietema and Ottengraf [548, 549]	Laminar, viscous	Maximum of the energy dissipation function	Only one circulation cell	N/A
Whalley and Davidson [550]	Equation for the vortex function	Bubble path calculated in the known velocity field	Equal to the column diameter	Gas distribution partially covering cross section
Ueyama and Miyauchi [140]	Analytical with constant apparent liquid viscosity	Assumed distribution profile	N/A	N/A
Joshi and Sharma [256, 551]	Equation for the vortex function	Bubble path calculated in the known velocity field	Equal to the column diameter	Gas distribution partially covering cross section
Zehner [127, 255]	Circulation velocity calculated from the drag coefficient	Algebraic equation derived using mass balance	Equal to the column diameter	N/A
Clark et al. [286, 552]	Difference method, mixing lengths	Bubble path integrated	N/A	N/A
Anderson and Rice [287]	Von Karman	Assumed distribution profile	N/A	N/A
Gasche et al. [553]	Finite volume, $k-\varepsilon$	Finite volume	N/A	N/A
Geary and Rice [141, 290, 554]	Mixing lengths	Assumed distribution profile	N/A	N/A
Grienberger and Hoffmann [315]	Finite volume, $k-\varepsilon$	Finite volume	Only one circulation cell along column	N/A

Table A-14 (continued)

Reference	Numerical method for the continuous phase	Numerical method for the dispersed phase	Height of circulation cells	Liquid circulation driving force
Svendsen et al. [405]	Finite volume, $k-\varepsilon$	Finite volume	Only one circulation cell along column height	N/A
Ranade [555]	Finite volume, $k-\varepsilon$	Finite volume	Only one circulation cell along column diameter	N/A
Sokolichin et al. [556]	Finite volume, Laminar flow	Finite volume	Only one circulation cell along column height	Gas distribution partially covering cross section
Millies et al. [285, 557]	Explicit difference method, mixing length	Transient assumptive functions, integrated along the characteristics	Calculated	Small disturbances of the gas distribution
Delnoij et al. [283, 284]	Finite elements, Volume averaged mass and momentum balance equations	Individual Bubble path integrated by accounting for force balance	20 circulation cell per L/D along column height	Gas distribution partially covering cross section

Table A-15: CFD modeling of three-phase reactors

Multiphase model	Supporting models/ Simulation conditions	Parameters investigated	Author
Multi-fluid Eulerian approach for three phase fluidized bed	<ul style="list-style-type: none"> - Both symmetric and axisymmetric - Kinetic theory granular flow model applied for solid phase - Gas phase treated as a particulate phase with 4 mm diameter 	<ul style="list-style-type: none"> - Compared time averaged axial solid velocity with experimental data - Verified different flow regimes in fluidized beds. 	Bahary et al. [558]
Two fluid Eulerian-Eulerian model for three phase bubble column	<ul style="list-style-type: none"> - 3-D - Liquid phase and solid particles modelled as pseudo-homogeneous phase by modifying the viscosity and density. - Included bubble size distribution based on the bubble induced turbulent length scale and the local turbulent kinetic energy level. 	<ul style="list-style-type: none"> - Liquid circulation - Solid movement - Studied variation of bubble size distribution 	Grevskott et al. [243]
Multi fluid Eulerian approach for three phase bubble column	<ul style="list-style-type: none"> - 2-D axisymmetric - Modified drag correlation between liquid and gas phase to account for effect of solid particles. - Modified drag correlation between solid and liquid phase to account for the effect of gas bubbles. - Standard $k-\epsilon$ turbulence model - Accounted for effect of bubbles on liquid phase turbulence 	<ul style="list-style-type: none"> - Studied axial variation of gas holdup and solid holdup profiles for a wide range of superficial gas velocities and solid circulation velocities. 	Mitra-Majumdar et al. [244]
Eulerian-Eulerian approach for three phase bubble column	<ul style="list-style-type: none"> - 2-D - Pseudo two phase fluid dynamics model based on the time averaged Navier-Stokes equation. - $k_{sus}-\epsilon_{sus}-k_b-\epsilon_b$ turbulence model used to describe and calculate the local flow (sus: suspension phase, b: gas phase). 	<ul style="list-style-type: none"> - Studied effects of: <ul style="list-style-type: none"> o Solid loading o Superficial liquid velocity o Superficial gas velocity - On local flow characteristics such as axial liquid velocity and gas holdup. - Validated local axial liquid velocity and local gas holdup with experimental data from tap water-compressed air-resin particles system. 	Jianping and Shonglin [201]

Table A-15 (continued)

Multiphase model	Supporting models/ Simulation conditions	Parameters investigated	Author
Eulerian-Lagrangian model for three phase fluidization	<ul style="list-style-type: none"> - 2-D CFD-VOF-DPM - Eulerian fluid dynamics method to account for liquid phase flow. - Dispersed particle method (DPM) to account for solid particles behavior. - Volume of fluid (VOF) method to account for gas phases. - Continuum surface force (CSF) model to account for gas-liquid coupling. - Surface tension force model to account for particle-bubble coupling - Newton's third law to account for particle liquid coupling. - Included a close distance interaction model in the particle-particle collision analysis to account for the liquid interstitial effects between colliding particles. 	<p>Studied:</p> <ul style="list-style-type: none"> - Single bubble rise velocity in a liquid solid fluidized bed. - Bubble wake structure and bubble rise velocity in liquid and liquid-solid mediums. 	Li et al. [294]
Multi fluid Eulerian approach for three phase draft tube bubble column	<ul style="list-style-type: none"> - 3-D - Extended multiphase $k-\varepsilon$ turbulence model as developed by Kashiwa [559] - Drag between solid grains and the gas bubbles was modelled identically to drag between liquid and gas bubbles – based on the notion that solid particles in the vicinity of gas bubbles tend to follow the liquid. 	<ul style="list-style-type: none"> - Simulated gas volume fractions and liquid circulation in draft tube bubble column. - Validated simulation results with experimental measurements of gas holdups for three and two fluid flow systems (tap water-air-siliceous sand) in a an air lift draft tube by Pironti et al. [560] 	Padial et al. [561]
Eulerian-Lagrangian model for three phase fluidized bed	<ul style="list-style-type: none"> - 2-D - Eulerian volume averaged method to describe the liquid phase - Lagrangian dispersed particle method (DPM) to describe the solid particles - Volume of fluid (VOF) method to describe the gas bubbles. 	<ul style="list-style-type: none"> - Studied the effect of pressure and solid holdup on the bubble size rise characteristics such as the bubble rise velocity, bubble shape and bubble trajectory. 	Zhang et al. [313]

Table A-15 (continued)

Multiphase model	Supporting models/ Simulation conditions	Parameters investigated	Author
	<ul style="list-style-type: none"> - Bubble induced force model to describe the particle –bubble coupling interaction - Continuum surface force (CSF) model to describe the gas liquid coupling interaction - Newton’s third law to describe the particle-liquid coupling interaction 	<ul style="list-style-type: none"> - Validated simulation results with experimental measurements of bubble rise velocities of a gas-liquid system. 	
Eulerian-Lagrangian model for three phase fluidized bed	<ul style="list-style-type: none"> - 2-D - Eulerian volume averaged method to describe the liquid phase - Lagrangian dispersed particle method (DPM) to describe the solid particles - Volume of fluid (VOF) method to describe the gas bubbles. - Bubble induced force model to describe the particle –bubble coupling interaction - Continuum surface force (CSF) model to describe the gas liquid coupling interaction - Newton’s third law to describe the particle-liquid coupling interaction 	<ul style="list-style-type: none"> - Studied: <ul style="list-style-type: none"> o Single bubble rise behavior in a liquid solid suspension. o Bubble entrainment by a bubble on the surface of the bed. o Validated simulation results with experimental measurements of bed expansion and pressure drop in a water-air-Pliolite particles fluidized bed by Lin et al. [562] 	Zhang et al. [563]
Multi fluid Eulerian approach for slurry bubble column	<ul style="list-style-type: none"> - 3-D - Kinetic theory granular flow (KTGF) model for describing particulate phase - Standard $k-\varepsilon$ turbulence model for liquid phase turbulence 	<ul style="list-style-type: none"> - Studied: <ul style="list-style-type: none"> o Time averaged solid velocity o Volume fraction profiles o Normal and shear Reynolds stress - Validated simulation results with experimental measurements of velocity profiles and gas and solid volume fractions for a three phase air-water-Ballotini leaded glass beads system. 	Matonis et al. [297]

Table A-15 (continued)

Multiphase model	Supporting models/ Simulation conditions	Parameters investigated	Author
Multi fluid Eulerian approach for slurry bubble column	<ul style="list-style-type: none"> - Standard $k-\varepsilon$ turbulence model for liquid phase turbulence - Accounted for the momentum transfer between the dispersed phases (gas-solid) through the modified drag model of Padial et al. [561] - Used a very course grid with average grid length of 0.059 m to limit computational load 	<ul style="list-style-type: none"> - Studied gas and solid holdups throughout the SBCR at different superficial gas velocities. - Validated gas holdup simulations against the data of Dziallas [564] 	Michele and Hempel [565]
Multi-phase Eulerian-Eulerian model for three phase flow in a bubble column	<ul style="list-style-type: none"> - 2-D - Standard $k-\varepsilon$ turbulence model for liquid phase turbulence. - Kinetic theory granular flow (KTGF) model for describing particulate phase 	<ul style="list-style-type: none"> - Studied the effect of solid loading and superficial gas velocity on solid distribution. - Qualitatively validated simulation results with experimental values from an air-water-glass beads system 	Rampure et al. [566]
Multi-phase Eulerian-Eulerian model for three phase flow in a slurry bubble column	<ul style="list-style-type: none"> - 2-D - Used the kinetic theory of granular flow with a measured restitution coefficient to model particulate viscosity - Simplified kinetics to incorporate the reaction between carbon monoxide and hydrogen to produce methanol - Operating conditions are based on the Air Products/DOE La Porte's slurry reactor for methanol synthesis 	<ul style="list-style-type: none"> - Solids distribution - Reactor performance 	Gamwo et al. [567]
Eulerian-Lagrangian model for three phase fluidized bed	<ul style="list-style-type: none"> - 3-D - Locally averaged Navier-Stokes equations are used to describe the liquid phase flow outside the gas bubble and the gas phase floe inside the gas bubble. - Employed a Sub-Grid Scale (SGS) stress model with modified coefficients to account for the effect of the bubble induced turbulence. - Level set method to describe the motion and topological variation of the gas bubbles. - 	<ul style="list-style-type: none"> - Studied air bubble formation from an orifice and bubble rise velocity - Validated simulation results with experimental measurements of bubble rise velocity for air-water and air-heat transfer fluid (Paratherm NF)-solid systems. 	Chen and Fan [372]

Table A-15 (continued)

Multiphase model	Supporting models/ Simulation conditions	Parameters investigated	Author
	<ul style="list-style-type: none"> - Lagrangian dispersed particle method (DPM) to describe the solid particles 	-	
Modified transport equation approach for three phase bubble column	<ul style="list-style-type: none"> - 2-D - Modified mixture model for the volume fraction of the dispersed phase - Ignored particle interactions - Implemented Reynolds stress turbulence model. 	<ul style="list-style-type: none"> - Investigated the time averaged vertical mixture velocity and the volume fraction of the gas and solid phases. 	Glover and Generalis [568]
Multi fluid Eulerian approach for three phase bubble column	<ul style="list-style-type: none"> - 3-D - Liquid and solid phases modelled as a pseudo homogenous phase because of ultrafine nanoparticles. - Interface model used for drag, lift and virtual mass. - Standard $k-\varepsilon$ turbulence model 	<ul style="list-style-type: none"> - Compared the local time averaged liquid velocity and gas holdup profiles along the radial position 	Feng et al. [296]
Multi fluid Eulerian approach for three phase bubble column	<ul style="list-style-type: none"> - 2-D - Multi fluid Eulerian model coupled with a population balance equation. (Solid and gas phases considered Eulerian) - Accounted for bubble breakup and coalescence using source terms in the mass balance - Modified $k-\varepsilon$ turbulence model for the liquid phase - Kinetic theory granular flow (KTGF) model for describing particulate phase pressure and stress tensor. 	<ul style="list-style-type: none"> - Studied back mixing in the liquid and gas phase - Presented an alternate approach to the modeling of three phase floe for an L/D ratio of 5. 	Wieman and Mewes [569]
Multi fluid Eulerian approach for three phase bubble column.	<ul style="list-style-type: none"> - 3-D - Modified gas-liquid drag coefficient based on single bubble rise, modified for the effect of the solid phase. - Standard $k-\varepsilon$ turbulence model for bubble induced turbulence - Accounted for interphase momentum between the two dispersed phases. 	<ul style="list-style-type: none"> - Validated simulation results with experimental measurements of local gas and liquid holdup, and liquid velocities for a three phase air-water-solid particles system by Dziallas et al. [564] 	Schallenberg et al. [299]

Table A-15 (continued)

Multiphase model	Supporting models/ Simulation conditions	Parameters investigated	Author
Multi scale Eulerian Lagrangian model for three phase flow	<ul style="list-style-type: none"> - 3-D - Combined front tracking approach for gas bubbles - Discrete particle (DP) approach for solid particles - Staggered rectangular 3-D grid using a two-step projection-correction method with explicit treatment of the convection and diffusion terms and implicit treatment of the pressure gradient. 	<ul style="list-style-type: none"> - Studied bubble rise behavior and bubble-particle interaction for single and multiple bubble scenarios 	Annaland and Kuipers [570]
Eulerian-Lagrangian model for three phase slurry reactor	<ul style="list-style-type: none"> - Liquid flow modeled using a volume averaged system of governing equations - Bubbles and particles modelled using a Lagrangian trajectory analysis procedure - Bubble-bubble and particle-particle collision are included using a hard sphere collision model. - Two way phase coupling. Coupling between fluid and dispersed phases is implemented using a momentum interaction term from the discrete phase to the fluid phase. - Accounted for drag, lift, buoyancy and virtual mass forces. - Bubble coalescence included in the model using a critical Webber number approach. 	<p>Studied:</p> <ul style="list-style-type: none"> - Transient characteristics of the gas, liquid and solid phase flows in terms of flow structure and instantaneous velocities. - Effect of bubble size on variation of flow patterns. 	Zhang and Ahmadi [298]
Multi fluid Eulerian approach for three phase fluidized bed	<ul style="list-style-type: none"> - 2-D - Gidaspow model for drag - Isothermal, reaction free model for mass and momentum balances 	<p>Studied:</p> <ul style="list-style-type: none"> - Phase holdups and velocity profiles - Effect of liquid velocity on pressure drop - Effect of liquid velocity on bed porosity - 	Nguyen et al. [571]
Multi fluid Eulerian approach for three phase fluidized bed reactor	<ul style="list-style-type: none"> - 2-D and 3-D - Pressure field is assumed to be shared by all three phases, in proportion to their volume fraction. - 	<ul style="list-style-type: none"> - Validated simulation results with experimental measurements of solid phase mean and turbulent velocities for a three phase air/tap water/ solid (glass, PVC and 	Panneerselvam et al. [293]

Table A-15 (continued)

Multiphase model	Supporting models/ Simulation conditions	Parameters investigated	Author
	<ul style="list-style-type: none"> - Momentum of each phase is governed by respective mass and momentum conservation equations. - Applied closure law to model liquid turbulence, solid pressure and interphase momentum exchange - Modelled gas-solid interphase drag in the same way as that between the continuous and dispersed phase using the model developed by Wang et al. [572] 	acetate) bead system by Kiared et al. [573], and with experimental measurements of gas and liquid phase velocities and holdups for a three phase air-water-glass beads system by Yu and Kim [3, 574]	
Multi fluid Eulerian-Lagrangian approach for a three phase circulating fluidized bed	<ul style="list-style-type: none"> - 2-D - Two fluid model used for coupling between gas and liquid phases. - Lagrangian Distinct element method (DEM) used to describe solid particle motion. - Standard $k-\varepsilon$ turbulence model 	<ul style="list-style-type: none"> - Studied: <ul style="list-style-type: none"> o Radial distribution of local liquid velocity at various liquid viscosities and at various superficial gas velocities. o Variation of local solid hold-up in radial direction for various superficial gas velocities - Qualitatively validated simulation results with experimental values from an air-water-styrene resin beads system 	Cao et al. [575]
Two fluid Eulerian approach for a three phase slurry reactor for petroleum hydrosulfurization	<ul style="list-style-type: none"> - 2-D - Axisymmetric - Solid and Liquid combined into a pseudo-liquid phase - Difference in density between the catalyst and the slurry phase is so small that the catalyst does not settle and the fluid velocity is sufficiently small to assume axial symmetry. - Mass balance for the two phases (pseudo-liquid and gas) is coupled by an overall mass balance. - Friction terms used to couple the momentum balance of both phases. - Standard $k-\varepsilon$ turbulence model - 	<ul style="list-style-type: none"> - Validated simulation results with experimental measurements of the radial variation of the gas and liquid holdups for a two phase air-water system by Grienberger and Hofmann [315] - Studied effect of grid size and simulation time on kinetics results 	Matos et al. [301]

Table A-15 (continued)

Multiphase model	Supporting models/ Simulation conditions	Parameters investigated	Author
	<ul style="list-style-type: none"> - Implemented hydro-sulfurization reaction kinetics into the mass balance - Axial velocities at the entrance of the reactor set using experimental results by Torvik and Svendsen [314] 	-	
Multi fluid Eulerian approach for three phase fluidized bed contactor	<ul style="list-style-type: none"> - 3-D - Isothermal energy conditions, no energy equations - Neglected momentum transfer between dispersed phases - Bubbles are assumed as rigid spheres with a constant diameter - $k-\varepsilon$ turbulence model for liquid phase 	<ul style="list-style-type: none"> - Investigated the effect of various drag force models on phase velocities - Studied the effect of : <ul style="list-style-type: none"> o Liquid superficial velocity on the axial solid velocity o Particle size and density on the axial solid velocity o Gas velocity and liquid viscosity on bed porosity o Column diameter on gas holdup, liquid holdup and bed porosity. 	Muthiah et al. [576]
Multiphase Eulerian approach for three phase fluidized bed	<ul style="list-style-type: none"> - 2-D - Introduced the Multiphase particle-in-cell (MP-PIC) method for modeling particle dynamics and collisional exchange. Solved the solid phase particle distribution function. 	Studied: <ul style="list-style-type: none"> - Mass averaged velocities of solid and liquid phases - Particle velocity fluctuations - Collision time - Liquid droplet distribution 	O'Rourke et al. [577]
Two fluid Eulerian approach for a three phase slurry reactor for Fischer Tropsch synthesis	<ul style="list-style-type: none"> - 2-D/3-D - Bubble size distribution predicted using a population balance model. - Incorporated heterogeneous and homogenous reaction rates representing simplified F-T synthesis from Yates and Satterfield [317] - Turbulence is described by the two equation RNG $k-\varepsilon$ model 	Studied: <ul style="list-style-type: none"> - Time averaged Sauter diameter at different elevations from inlet - Gas holdup at different catalyst concentrations - Inlet velocity on syngas conversion and reactor productivity 	Troshko and Zdarvistch [316]

Table A-15 (continued)

Multiphase model	Supporting models/ Simulation conditions	Parameters investigated	Author
	<ul style="list-style-type: none"> - Interphase drag exchange coefficient from Ishii and Mishima [272] 	<ul style="list-style-type: none"> - Axial variation of time averaged Sauter diameter along the reactor axis for different catalyst concentrations 	
<p>Multi-phase mixture approach for three phase fluidized bed reactor</p>	<ul style="list-style-type: none"> - Discrete phase method (DPM) to account for gas phase behavior. - Solid and liquid phases modelled using a simplified mixture model in: phases move at different velocities, but assume local equilibrium over short spatial length scales - Second order upwind scheme for discretization of the momentum equations. 	<ul style="list-style-type: none"> - Studied effect of different porous models (porous jump vs porous zone) on liquid and solid phase velocities. - Validated simulation results with experimental measurements of pressure drop for a three phase air/water/solid system. 	<p>Sivaguru et al. [300]</p>
<p>Multi fluid Eulerian approach for three phase fluidized bed reactor</p>	<ul style="list-style-type: none"> - 3-D pressure based solver - Triple Euler model - Applied closure law to model liquid turbulence, solid pressure and interphase momentum exchange - Isothermal, reaction free model for mass and momentum balances - Accounted for liquid-solid, gas-liquid and gas –solid drag forces. - $k-\varepsilon$ turbulence model 	<ul style="list-style-type: none"> - Studied: <ul style="list-style-type: none"> o Significance of implementing different numerical schemes. o Accuracy of different $k-\varepsilon$ turbulence models (standard, RNG, realizable) o Solid wall boundary conditions o Granular temperature models - Validated simulation results with experimental measurements of axial solid velocity and gas holdup for a three phase air-tap water-glass bead system by Kiared et al. [573], and Yu and Kim [3] 	<p>Hamidipour et al. [292]</p>
<p>Multi fluid Eulerian approach for three phase slurry bubble column</p>	<ul style="list-style-type: none"> - 3-D transient simulation - Wen-Yu and Gidaspow models used for liquid-solid drag force correlations [578]. - Schallenberg and Syamlal-O’Brien models used for gas-solid drag force correlations [299] - Turbulence is described by the two equation RNG $k-\varepsilon$ model. - Disregarded heat and mass transfer effects. 	<ul style="list-style-type: none"> - Validated simulation results using different drag models with experimental measurements of axial gas velocity and holdup for a three phase air-water-catalyst system by Wu et al. [144] 	<p>Silva Jr. et al. [302]</p>

Table A-16: Commonly used gas-liquid drag models

System	Drag Coefficient Correlation	Reference
Various experimental data for air-water	$C_D = \begin{cases} \frac{29.1667}{Re_b} - \frac{3.8889}{Re_b^2} + 1.222 & 1 < Re_b < 10 \\ \left(\frac{24}{Re_b}\right)(1 + 0.15Re_b^{0.687}) & 10 < Re_b < 200 \end{cases}$	Clift et al. [171]
Ambient air-water, air-dilute NO ₂ SO ₃	$C_D = \begin{cases} \left(\frac{24}{Re_b}\right)(1 + 0.1Re_b^{0.75}) & N_\mu < 36\sqrt{2} \frac{(1 + 0.1Re_b^{0.75})}{Re_b^2} \\ \frac{2}{3}\sqrt{E\ddot{o}_b} & N_\mu \geq 36\sqrt{2} \frac{(1 + 0.1Re_b^{0.75})}{Re_b^2} \end{cases}$	Ishii and Zuber [319]
Derivation for spherical bubble in an unbounded shear flow	$C_D = \left(\frac{16}{Re_b}\right) \left\{ 1 + \left[\frac{8}{Re_b} + 0.5 \left(1 + \frac{3.315}{\sqrt{Re_b}} \right) \right]^{-1} \right\}$	Mei and Klausner [323]
Ambient air-tap water-glass beads/ non-spherical silica	<p style="text-align: center;"><i>For Pure Liquid:</i></p> $C_D = \max \left[\min \left(\frac{16}{Re_b} (1 + 0.15Re_b^{0.687}), \frac{48}{Re_b} \right), \frac{8}{3} \frac{E\ddot{o}_b}{E\ddot{o}_b + 4} \left(\frac{1 + 17.67\alpha_s^{\frac{9}{7}}}{18.67\alpha_s^{\frac{3}{2}}} \right)^2 \right]$ <p style="text-align: center;"><i>For a slightly contaminated liquid:</i></p> $C_D = \max \left[\min \left(\frac{24}{Re_b} (1 + 0.15Re_b^{0.687}), \frac{72}{Re_b} \right), \frac{8}{3} \frac{E\ddot{o}_b}{E\ddot{o}_b + 4} \left(\frac{1 + 17.67\alpha_s^{\frac{9}{7}}}{18.67\alpha_s^{\frac{3}{2}}} \right)^2 \right]$ <p style="text-align: center;"><i>For contaminated systems:</i></p> $C_D = \max \left[\frac{24}{Re_b} (1 + 0.15Re_b^{0.687}), \frac{8}{3} \frac{E\ddot{o}_b}{E\ddot{o}_b + 4} \right]$	Tomiyama et al. [322]
Air-water system at 12-70 °C Ambient air-water-glass beads system with solid loading of 7 – 20%	$C_D = \frac{5.645}{E\ddot{o}_b^{-1} + 2.835}$	Grevskott et al. [243]

Table A-16 (continued)

System	Drag Coefficient Correlation	Reference
Iron particle in glycerin/water shear flow	$C_D = \begin{cases} \frac{16}{Re_b} & Re_b < 1 \\ \left(\frac{16}{Re_b}\right)(1 + 0.15Re_b^{0.5}) & Re_b \geq 1 \end{cases}$	Kurose et al. [320]
Air-tap water/ propanol	$C_D = \begin{cases} \frac{16}{Re_b} & Re_b \leq 1.5 \\ \frac{14.9}{Re_b^{0.78}} & 1.5 \leq Re_b \leq 80 \\ \frac{48}{Re_b} \left(1 - \frac{2.21}{\sqrt{Re_b}}\right) + (1.86 \times 10^{-15})Re_b^{4.756} & 80 \leq Re_b \leq 1500 \\ 2.61 & Re_b \geq 1500 \end{cases}$	Lain et al. [321]
Statistical analysis of small bubbles in isotropic turbulence	$C_D = \begin{cases} \frac{24}{Re_b} & Re_b \leq 1 \\ \left(\frac{24}{Re_b}\right) \left(1 + \frac{3.6}{Re_b^{0.313}} \left(\frac{Re - 1}{19}\right)^2\right) & 1 \leq Re_b \leq 20 \\ \left(\frac{24}{Re_b}\right) (1 + 0.15Re_b^{0.687}) & Re_b > 20 \end{cases}$	Snyder et al. [324]

Table A-17: Commonly used liquid-solid and gas-solid drag models

System	Drag Coefficient Correlation	Reference
Smooth spherical particle in stagnant fluid	$C_D = \begin{cases} \left(\frac{24}{Re_p}\right) (1 + 0.15Re_p^{0.687}) & Re_p < 1000 \\ 0.44 & Re_p \geq 1000 \end{cases}$	Schiller and Naumann [6]
Sand/silt-Water system $d_p = 0.001 - 0.01 \text{ m}$	$C_D = \left(0.63 + \frac{4.8}{\sqrt{Re_p}}\right)^2$	Dalla Ville [579]
Smooth spherical particle in stagnant fluid $d_p = 0.0025 \text{ m}$	$C_D = \begin{cases} \frac{24}{Re_p} & Re_p < 0.1 \\ \frac{22.73}{Re_p} + \frac{0.0903}{Re_p^2} + 3.69 & 0.1 < Re_p < 1 \\ \frac{29.1667}{Re_p} - \frac{3.8889}{Re_p^2} + 1.222 & 1 < Re_p < 10 \\ \frac{46.5}{Re_p} - \frac{116.67}{Re_p^2} + 0.6167 & 10 < Re_p < 100 \\ \frac{98.33}{Re_p} - \frac{2778}{Re_p^2} + 0.3644 & 100 < Re_p < 1000 \\ \frac{148.62}{Re_p} - \frac{4.75 \times 10^4}{Re_p^2} + 0.357 & 1000 < Re_p < 5000 \\ \frac{-490.546}{Re_p} + \frac{57.87 \times 10^4}{Re_p^2} + 0.46 & 5000 < Re_p < 10000 \\ \frac{-1662.5}{Re_p} + \frac{5.4167 \times 10^6}{Re_p^2} + 0.5191 & 10000 < Re_p < 50000 \end{cases}$	Morsi and Alexander [580]

Table A-17 (continued)

System	Drag Coefficient Correlation	Reference
<p>Various published experimental data for glass beads/spheres-water/ glycol/ glycerol systems $d_p = 0.006$ m</p>	$C_D = \frac{1}{f^2} \left(0.63 + \frac{4.8}{\sqrt{Re_p/f}} \right)^2$ $f = 0.5 \left[A - 0.06Re_p + \sqrt{0.036Re_p^2 + 0.12Re_p(2B - A) + A^2} \right]$ $A = \alpha_s^{4.14} ; B = \begin{cases} 0.8\alpha_s^{1.28} & \alpha_s \leq 0.85 \\ \alpha_s^{2.65} & \alpha_s > 0.85 \end{cases}$	<p>Garside and Al-Dibouni [581]</p>
<p>Various published experimental data for glass beads/spheres-water/ glycol/ glycerol systems $d_p = 0.006$ m</p>	$C_D = \frac{0.44}{\alpha_s^{2(n-1)}} ; n = \frac{5.1 + 0.27Re_p^{0.9}}{1 + 0.1Re_p^{0.9}}$ <p>(Richardson and Zaki)</p>	<p>Garside and Al-Dibouni [581]</p>
<p>478 points from various published experimental data for a wide range of Reynolds [395, 582-604]</p>	$C_D = \frac{24}{Re_p} + \frac{3}{16} \quad Re_p < 0.01$ $C_D = \frac{24}{Re_p} \left[1 + 0.1315Re_p^{(0.82-0.05w)} \right] \quad 0.01 \leq Re_p \leq 20$ $C_D = \frac{24}{Re_p} \left[1 + 0.195Re_p^{0.6305} \right] \quad 20 \leq Re_p \leq 260$ $\log(C_D) = 1.6435 - 1.1242w + 0.1558w^2 \quad 260 \leq Re_p \leq 1500$ $\log(C_D) = -2.4571 + 2.5558w - 0.929w^2 + 0.1049w^3 \quad 1500 \leq Re_p \leq 1.2 \times 10^4$ $\log(C_D) = -1.9181 + 0.6370w - 0.0636w^2 \quad 1.2 \times 10^4 \leq Re_p \leq 4.4 \times 10^4$ $\log(C_D) = -4.3390 + 1.5809w - 0.1546w^2 \quad 4.4 \times 10^4 \leq Re_p \leq 3.8 \times 10^5$ $w = \log(Re_p)$	<p>Clift et al.[171]</p>

Table A-17 (continued)

System	Drag Coefficient Correlation	Reference
Glass spheres - Ethylene glycol glass spheres - water	$C_D = \left(\frac{24}{Re_p}\right) \left(1 + 0.347 \left(\frac{r_o}{\delta} + \frac{1}{2} \left(\frac{r_o}{\delta}\right)^2\right)\right)$ $\frac{r_o}{\delta} = \frac{1}{(0.9/(1 - \alpha_s)^{1/3}) - 1}$	Molerus [605]
Glass Spheres in Glycerin-Water 10 cm ID column $d_p = 0.036$	$C_D = \begin{cases} \left(\frac{24}{Re_p}\right) (1 + 0.1Re_p^{0.75}) & Re_p < 1000 \\ 0.45 & 1000 \leq Re_p \leq 2 \times 10^5 \end{cases}$	Ishii and Zuber [319]
Derived using the experimental data from Heywood [606, 607] and Lapple and Shepherd [608] for a wide range of spherical particles in Newtonian fluids	$C_D = \frac{24}{Re_p} 10^E$ $E = 0.261Re_p^{0.369} - 0.105Re_p^{0.431} - \frac{0.124}{1 + (\log(Re_p))^2}$	Flemmer and Banks [609]
Derived using the same experimental data used by Clift et al. [171]	$C_D = \frac{24}{Re_p} (1 + 0.173Re_p^{0.657}) + \frac{0.413}{1 + 16300Re_p^{-1.09}} \quad Re_p < 2.6 \times 10^5$	Turton and Levenspiel [610]
Fitted experimental data [599, 602, 608, 611]1-5 using the modified Rosenbrock method [612]	$C_D = (2.25Re_p^{-0.31} + 0.36Re_p^{0.06})^{3.45} \quad 0.01 \leq Re_p \leq 3 \times 10^5$	Khan and Richardson [613]
Derived using the same experimental data used by Clift et al. [171]	$C_D = \frac{24}{Re_p} (1 + 0.1806Re_p^{0.6459}) + \frac{0.4251}{1 + 6880.95Re_p^{-1}} \quad Re_p < 2.6 \times 10^5$	Haider and Levenspiel [357]
Thermodynamic derivation for multiphase turbulent flows	$C_D = \left(\frac{24}{Re_p}\right) (1 + 0.1Re_p^{0.75}) \left[\frac{1}{\left(1 - \left(\frac{1 - \alpha_s}{0.64356}\right)\right)^{1.6089}} \right]$	Ma and Ahmadi [326]

Table A-17 (continued)

System	Drag Coefficient Correlation	Reference
Theoretical derivation	<p>$\varepsilon_g < 0.8$ (Derived using the Wen and Yu[5] Fluidization model)</p> $\beta = 150 \frac{(1 - \alpha_g)^2 \mu_g}{\alpha_g d_p^2} + 1.75 \frac{\rho_g (1 - \alpha_g) v_g - v_s }{d_p}$ <p>$\varepsilon_g \geq 0.8$ (Derived using the Ergun Pressure Drop correlation [614])</p> $\beta = \frac{3}{4} C_D \frac{\alpha_g v_g - v_s \rho_g (1 - \alpha_g)}{d_p}$ $C_D = \begin{cases} \left(\frac{24}{\alpha_g Re_b} \right) (1 + 0.15 (\alpha_g Re_b)^{0.687}) \alpha_g^{-2.65} & \alpha_g Re_p < 1000 \\ 0.44 \alpha_g^{-2.65} & \alpha_g Re_p \geq 1000 \end{cases}$	Gidaspow [242]
Glass ballotini/ Lead shot-bromoform 0.062 m ID column $d_p = 0.031754$ m	$C_D = 0.44 \alpha_s^{-2.65}$	Richardson and Zaki [615]
Numerical simulation for two phase gas-solid flows	$C_D = 0.44 + \frac{24}{Re_p} + \frac{6}{1 + \sqrt{Re_p}}$	Zhang and van der Heyden [327]

APPENDIX B

EXPERIMENTAL PROCEDURES AND CALCULATION METHODS

B.1 EXPERIMENTAL PROCEDURES

The experimental procedures to obtain the volumetric liquid-side mass transfer coefficients (k_{LA}), gas holdup (ε_G), and the Sauter-mean bubble diameter (d_{32}) are detailed in the following.

B.1.1 ε_G Measurement

The hydrostatic method, known also as the manometric method, was used to obtain the gas holdup. Once the system reaches thermodynamic equilibrium (steady state), the following procedure for obtaining the gas holdup was followed:

1. The dP cells legs were purged of liquid or slurry and pressurized with the gas which was being used.
2. The hydrostatic pressure was measured at different positions along the height of the reactor by opening and closing the corresponding valves.
3. The computer collected the dP cell readings and calculates the gas holdup at any given position along the reactor.

B.1.2 d_{32} Measurement

The Dynamic Gas Disengagement (DGD) technique was employed to obtain the bubble size and the bubble size distribution. Once k_{LA} and ε_G measurements were successfully completed at given temperature, the following procedure was followed:

1. The dP cell legs at given positions were opened.
2. Using the pneumatically actuated valves, the inlet valve for the gas flow at the bottom of the reactor was closed, while the valve located at the top of the reactor was opened, directing the gas from the bottom to the top of the reactor, and as a result the gas retained in the liquid disengaged.
3. The dP cell readings were recorded until all the gas bubbles were completely disengaged from the liquid or slurry and the pressure leveled off.
4. The computer collected the dP cell readings and calculated the gas holdup.
5. The bubble sizes were then calculated using the gas holdup versus time data.

B.1.3 k_{La} Measurement

The Transient Physical Gas Absorption technique (TPGA) was employed to obtain k_{La} for the gases into the liquid phase or slurry phase under the operating conditions used. The experimental procedure is described below:

1. A predetermined amount of liquid or slurry was charged into the reactor (95 liters).
2. The entire system was vacuumed to remove any gases which might be dissolved in the liquid-phase. Once the pressure in the reactor reaches the vapor pressure of the liquid phase, the vacuum was stopped.

3. The reactor content was heated to the desired temperature.
4. The gas was charged into the supply vessel and an initial mass balance was built.
5. The gas was then charged to the reactor until the desired pressure was reached.
6. The cooling water and the drain valves for the compressor were opened.
7. Once the gas was charged, the compressor was turned on and the gas was being recirculated only through the top of the reactor with valve AV-2 open and valve AV-1 closed. The gas velocity was adjusted to the desired flow rate, regulated by the gas bypass valve.
8. The top valve AV-2 was closed while simultaneously opening the bottom gas valve AV-1 allowing the gas to flow through the liquid or slurry. The reactor pressure was recorded as a function of time during the gas absorption in the liquid or slurry phase until thermodynamic equilibrium is reached.
9. Once the system reaches thermodynamic equilibrium, data collection was stopped.
10. k_La was then calculated from the transient part of the pressure-time data and the gas solubility (C^*) is obtained from the equilibrium part.

In order to obtain different k_La at various conditions, Steps 2-8 are repeated.

B.2 CALCULATIONS

The equilibrium solubility (C^*) for the each gas used in the molten reactor wax was calculated from the steady-state portion of the pressure decline (Pressure -Time) curve, whereas the volumetric liquid-side mass transfer coefficient (k_{LA}) was obtained from the transient portion of the same curve. The calculations were performed by building mass balances on the supply vessel of the SBCR and the reactor, coupled with the Peng-Robinson Equation of State (PR-EOS).

The following assumptions were made in order to calculate C^* and k_{LA} :

1. The gas-phase in the preheater (or supply vessel) and reactor behaves as non-ideal gas and the Peng-Robinson Equation-of-State (PR-EOS) is applicable.
2. The gas and liquid phases are well mixed, resulting in homogeneous concentrations for each phase.
3. No gas absorption prior to mixing.
4. The liquid volume is constant during the absorption process, which is true, if the gas has low solubility in liquid-phase.

B.2.1 Peng-Robinson EOS

The PR-EOS was used to calculate the number of moles of gas in the feed tank before and after charging the reactor, and to calculate the number of moles remaining in the reactor after gas absorption. A general form of the PR-EOS can be written as:

$$P = \frac{RT}{v - b} - \frac{a}{v^2 + 2bv - b^2} \quad (\text{B-1})$$

This equation can be expressed in terms of the compressibility factor, Z as:

$$Z^3 - (1 - B)Z^2 + (A - 3B^2 - 2B)Z - (AB - B^2 - B^3) = 0 \quad (\text{B-2})$$

Where:

$$A = \frac{aP}{R^2T^2} \quad (\text{B-3})$$

$$B = \frac{bP}{RT} \quad (\text{B-4})$$

$$z = \frac{Pv}{RT} \quad (\text{B-5})$$

For a multi-component, one-phase system, the solution of Equation (B-2) results in three real roots or one real (single-phase) and two imaginary roots. The coefficients in Equations (B-3) and (B-4) are listed below.

$$a = \sum_i \sum_j y_i y_j a_{ij} \quad (\text{B-6})$$

$$b = \sum_i y_i b_i \quad (\text{B-7})$$

$$a_{ij} = (1 - \delta_{ij}) \sqrt{a_i a_j} \quad (\text{B-8})$$

$$a_i = 0.45724 \frac{R^2 T_c^2}{P_c^2} [1 + \kappa [1 - T_R^{0.5}]] \quad (\text{B-9})$$

$$b_i = 0.0778 \frac{RT_c}{P_c} \quad (\text{B-10})$$

$$\kappa = 0.37464 + 1.5422\omega - 0.26992\omega^2 \quad (\text{B-11})$$

Equation (B-1) was used to calculate the number of moles before and after absorption in the gas-phase in order to calculate the gas solubility.

B.2.2 Equilibrium Solubility, C^*

The equilibrium solubility (C^*) is defined as the number of moles of gas absorbed into the liquid at equilibrium and can be defined by:

$$C_i^* = \frac{N_{i,I} - N_{i,F}}{V_L} \quad (\text{B-12})$$

Where $N_{i,I}$ is the initial number of moles of the gaseous species (i) in the reactor prior to absorption and $N_{i,F}$ is the number of moles of the gaseous species (i) remaining in the reactor at thermodynamic equilibrium. $N_{i,I}$ and $N_{i,F}$ are calculated as follows:

$$N_{i,I} = \frac{V_G}{Z_{i,I} R T_I} (P_{i,I} - P^S) \quad (\text{B-13})$$

$$N_{i,f} = \frac{V_G}{Z_{i,F} R T_{F,avg}} (P_{Fi,I} - P^S) \quad (\text{B-14})$$

Where T_I is the initial temperature before the start of the absorption and $T_{F,avg}$ is the average temperature of the gas phase during the absorption. The volume of the gas phase, V_G , is calculated by subtracting the reactor volume and the liquid volume as follow:

$$V_G = V_{reactor} - \left(\frac{m_{liquid}}{\rho_{liquid}} \right) \quad (\text{B-15})$$

In the above equation, m_{liquid} and ρ_{liquid} are the mass and density of the liquid-phase, respectively. The solubility, C^* is then obtained by substituting Equations (B-13) or (B-14) into Equation (B-15).

B.2.3 Gas Holdup, ε_G

The gas holdup was determined using the manometric method (also known as the hydrostatic head method) with the following assumptions: (1) the reactor is operating under steady-state condition;

(2) the liquid or slurry and gas phases are well mixed in the volume between the 2 dP cell legs; and (3) the impact of the frictional effects on the pressure drop is negligible [616, 617].

The passage of gas bubbles throughout the slurry phase alters the pressure drop along the column which can be expressed by the following expression:

$$\frac{dP}{dh} = -\rho_D g \quad (\text{B-16})$$

Where ρ_D is the density of the dispersed phase containing gas, liquid and solid and can be derived as:

$$\rho_D = \varepsilon_G \rho_G + \varepsilon_L \rho_L + \varepsilon_S \rho_S \quad (\text{B-17})$$

Introducing c_V as the volumetric concentration of catalyst in the slurry-phase, the equation above becomes:

$$\rho_D = \varepsilon_G \rho_G + (1 - \varepsilon_G)[c_V \rho_S + (1 - c_V) \rho_L] \quad (\text{B-18})$$

Replacing this expression of ρ_D in Equation (B-17), the latter can be integrated as follows:

$$\int_{P_B}^{P_T} dP = - \int_{h_B}^{h_T} (\varepsilon_G \rho_G + (1 - \varepsilon_G)[c_V \rho_S + (1 - c_V) \rho_L]) g dh \quad (\text{B-19})$$

The lower and higher limits are defined by the position of the dP cell legs on the column. If assumption #2 is used, the gas holdup and the catalyst concentration can be considered constant between the two dP cell legs leading to:

$$P_T - P_B = -[\varepsilon_G \rho_G + (1 - \varepsilon_G)[c_V \rho_S + (1 - c_V) \rho_L]] g (H_T - H_B) \quad (\text{B-20})$$

The pressure difference between the lower and the upper legs is directly measured by the dP cell and since the distance between the legs is known, the following expression for gas holdup can be written:

$$\varepsilon_G = \frac{c_V \rho_S + (1 - c_V) \rho_L}{c_V \rho_S + (1 - c_V) \rho_L - \rho_G} \left(1 - \frac{\Delta P_{cell}}{(c_V \rho_S + (1 - c_V) \rho_L) g \Delta H_{cell}} \right) \quad (\text{B-21})$$

B.2.4 Gas Bubbles Size (d_b) and the Sauter Mean Bubble Diameter (d_{32})

The Dynamic Gas Disengagement (DGD) technique was used to obtain the Sauter-mean bubble diameter. The corresponding gas holdups of the small and large gas bubbles in the SBCR were calculated using the technique introduced by Inga and Morsi [369] and successfully used by Behkish et al. [618, 619] and Lemoine et al. [620]. This technique relies on the assumption that large gas bubbles have greater rise velocity and therefore disengage first, whereas small gas bubbles, retained within the slurry or entrained in the wakes created by the flow of the large gas bubbles, have smaller rise velocity and therefore they disengage in a later stage.

The following assumptions were made in order to derive the equations needed for calculating the gas bubble sizes: (1) the rate of gas disengagement of each bubble is constant under given experimental conditions; (2) once the gas flow is stopped, there is no coalescence or breakup of gas bubbles, meaning that the bubbles sizes remain constant as they disengage; and (3) the liquid internal circulation does not affect the bubble rise velocity. [621]

The assessment of the ε_G with time after the gas flow inside the SBCR has been stopped using Equation (B-21) can lead to the estimation of the rate of disengagement of each bubble size. An example of the behavior of ε_G with time is shown in Figure B-1. From $t = 0$ to t_1 , the dP cell shows no decline in ε_G , however, no more gas is entering the bottom of the reactor. This means that the amount of gas that leaves the dP cell section (from H_B to H_T) is the same as the one which leaves the lower section (from H_0 to H_B). From t_1 to t_2 , the large gas bubbles having a bubble rise velocity (U_b) ranging from $\Delta H_{cell}/t_1 = (H_T - H_B)/t_1$ to $\Delta H_{cell}/t_2$ disengage from the cell region and

during this period, the small gas bubbles present in the lower section (H_0 to H_B) do not affect the dP cell reading. From t_2 to t_3 , the small gas bubbles are disengaging from the cell region (H_B to H_T) and the dP cell reflects the small gas bubbles with U_b ranging from $\Delta H_{cell}/t_2$ to $\Delta H_{cell}/t_3$.

The volume of the gas bubbles that leaves the dP cell region ($\Delta H_{cell} = H_T - H_B$) can therefore be represented by the decrease of the total gas holdup as follows:

$$\Delta \varepsilon_{G,i} = \int_{t_{i-1}}^{t_i} \frac{d\varepsilon_G}{dt} dt \quad (\text{B-22})$$

Consequently the total gas holdup is:

$$\varepsilon_G = \sum_{i=1}^n \Delta \varepsilon_{G,i} \quad (\text{B-23})$$

The rise velocity of each size of the bubbles can then be calculated at any time (t) from:

$$U_{b,i} = \frac{\Delta H_{cell}}{t} \quad (\text{B-24})$$

This method is valid when dealing with gas-liquid system, however, the presence of solids should be accounted for, due to the settling velocity of the solid particles. In this study, the correlation proposed by Fukuma et al. [622], who used up to 50 vol.% glass beads, was used to calculate the bubble size $d_{b,i}$:

$$d_{b,i} = \frac{U_{b,i}^2}{1.69g} \quad (\text{B-25})$$

The Sauter-mean bubble diameter (d_{32} or d_S) was then calculated using the following equation:

$$d_{32} = \frac{\sum_i n_i d_{b,i}^3}{\sum_i n_i d_{b,i}^2} \quad (\text{B-26})$$

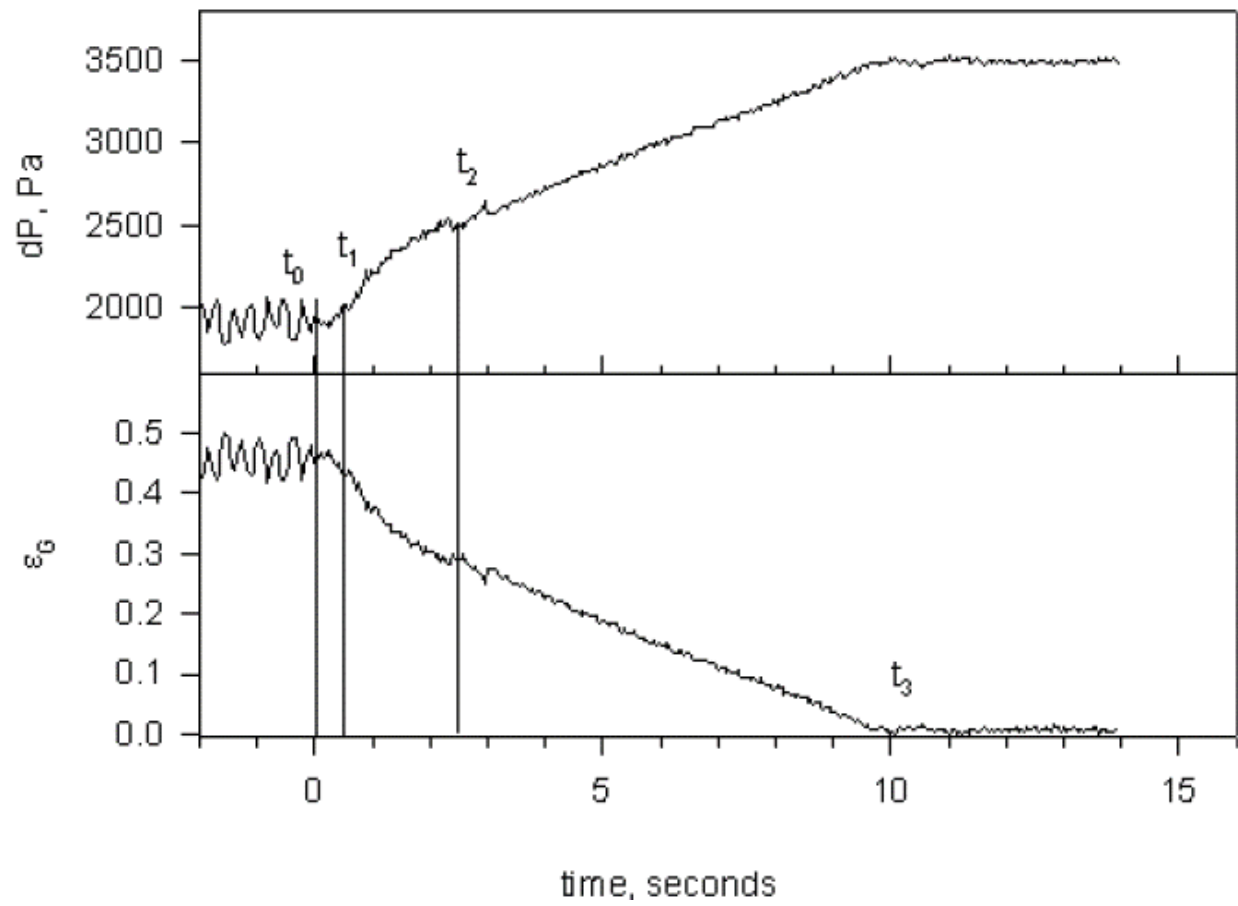
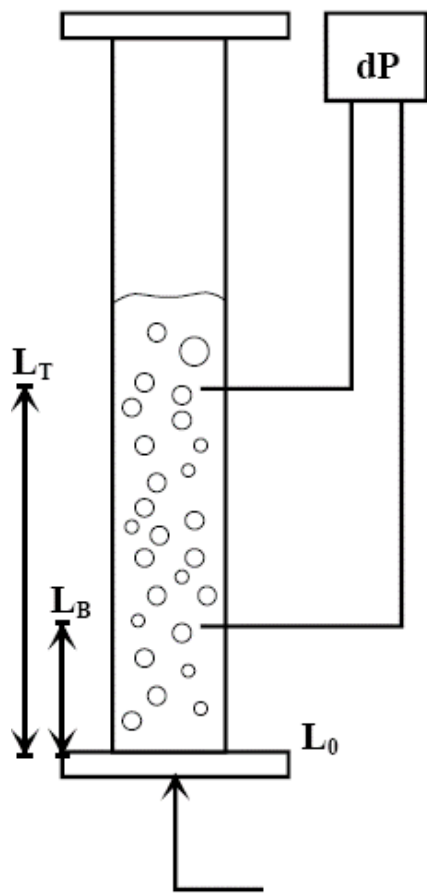


Figure B-1: Dynamic Gas Disengagement in SBCR [619]

B.2.5 Volumetric Liquid-Side Mass Transfer Coefficient, $k_L a$

The volumetric mass transfer coefficient, $k_L a$, was calculated using the Transient Physical Gas Absorption technique. During the absorption of the gas into the liquid, the decline of reactor pressure was recorded as a function of time until the equilibrium was reached.

The rate of mass transfer of the solute gas into the liquid phase can be calculated using the two-film model as:

$$\frac{dn_L}{dt} = k_L a (C^* - C_L) V_L \quad (\text{B-27})$$

The interface gas concentration (C^*) at a given gas partial pressure was estimated assuming the validity of Henry's law. At any time (t), the gas concentration in the liquid-phase (C_L) was calculated by building a mass balance on the gas-phase inside the reactor with the Peng-Robinson Equation of State (P-R EOS), which uses the experimental pressure decline data and the temperature recorded during the gas absorption. The $k_L a$ values were then calculated by numerically solving Equation (B-27), i.e., by fitting the C_L/C^* values as function of time.

APPENDIX C

EFFECT OF OPERATING CONDITIONS ON THE GAS BUBBLES DISTRIBUTION

The dynamic gas disengagement (DGD) technique was used to calculate the bubble size and distribution using the data obtained in this study as presented in Section 6.1. The bubble size was determined using the bubble rise velocity, which is dependent on the positions of the pressure transducers or on the liquid height, as shown in Equation (C-1), and a correlation relating the bubble rise velocity to the bubble diameter, such as that by Fukuma et al. [622] (Equation (C-2)).

$$U_{b,i} = \frac{\Delta H_{cell}}{\Delta t} \quad (C-1)$$

$$d_{b,i} = \frac{U_{b,i}^2}{1.69(g)} \quad (C-2)$$

Eight different classes were identified in the SBCR based on the bubble diameter as follows: < 1 mm, 1-3 mm, 3-5 mm, 5-10 mm, 10-15 mm, 15-20 mm, 20-30 mm and > 30 mm. The volume fraction and relative frequency of each bubble-class were calculated using Equations (C-3) and (C-4), respectively.

$$Volume\ fraction_i = \frac{\sum_{d_{b,i-lower\ bound}}^{d_{b,i-upper\ bound}} V_{G,i}}{V_{G,total}} \quad (C-3)$$

$$\text{Relative frequency}_i = \frac{\sum_{d_{b,i-\text{lower bound}}}^{d_{b,i-\text{upper bound}}} n_i}{n_{\text{total}}} \quad (\text{C-4})$$

The volume fraction represents the ratio between the volume of a certain bubble-class and the total volume of the bubbles in the reactor, whereas, the relative frequency represents the ratio between the number of bubbles in a certain bubble-class and the total number of bubbles in the reactor. Although the relative frequency may not have a direct effect on gas holdup, it is an important factor in characterizing the fluid flow and turbulent behavior within the reactor, where the bubbles induced turbulences play a significant role.

C.1 EFFECT OF PRESSURE ON GAS BUBBLES DISTRIBUTION

Figure C-1 shows that increasing pressure increases the volume fraction of larger gas bubble sizes (> 30 mm) and decreases the volume fraction of the intermediate and small gas bubble sizes. Figure C-2 also shows that increasing pressure significantly decreases the relative frequency of small gas bubbles (< 1 mm) and increases those of the intermediate and large gas bubbles. This behavior can be attributed to the fact that increasing pressures decreases the gas bubbles size at the distributor, resulting in the formation of more frequent smaller gas bubbles. Also, increasing pressure increases the gas momentum, which imparts a greater upward force on the bubbles, thus enhancing their departure from the sparger zone. Thus, increasing pressure increases the frequency and momentum of gas bubbles, which enhance their coalescence and interaction in the vicinity of the gas sparger, resulting in significantly high frequency of the 1-3 mm bubbles. It is important to note that the relative frequency of bubbles has a significant effect on the hydrodynamics and flow regimes within the reactor.

At low pressures, however, the high frequency of small gas bubbles results in low interphase pressure gradients and weak turbulence forces, leading to strong tendencies of gas bubbles movement towards the reactor walls with low liquid-backmixing.

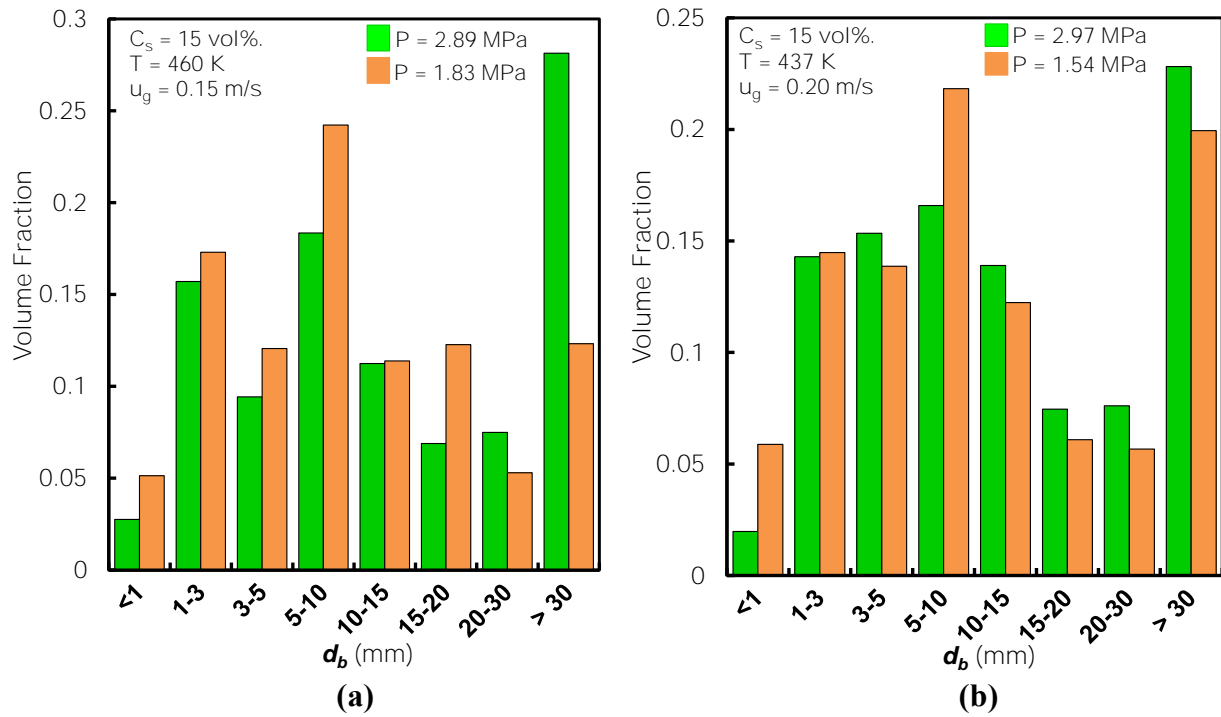


Figure C-1: Effect of pressure on bubble volume fraction

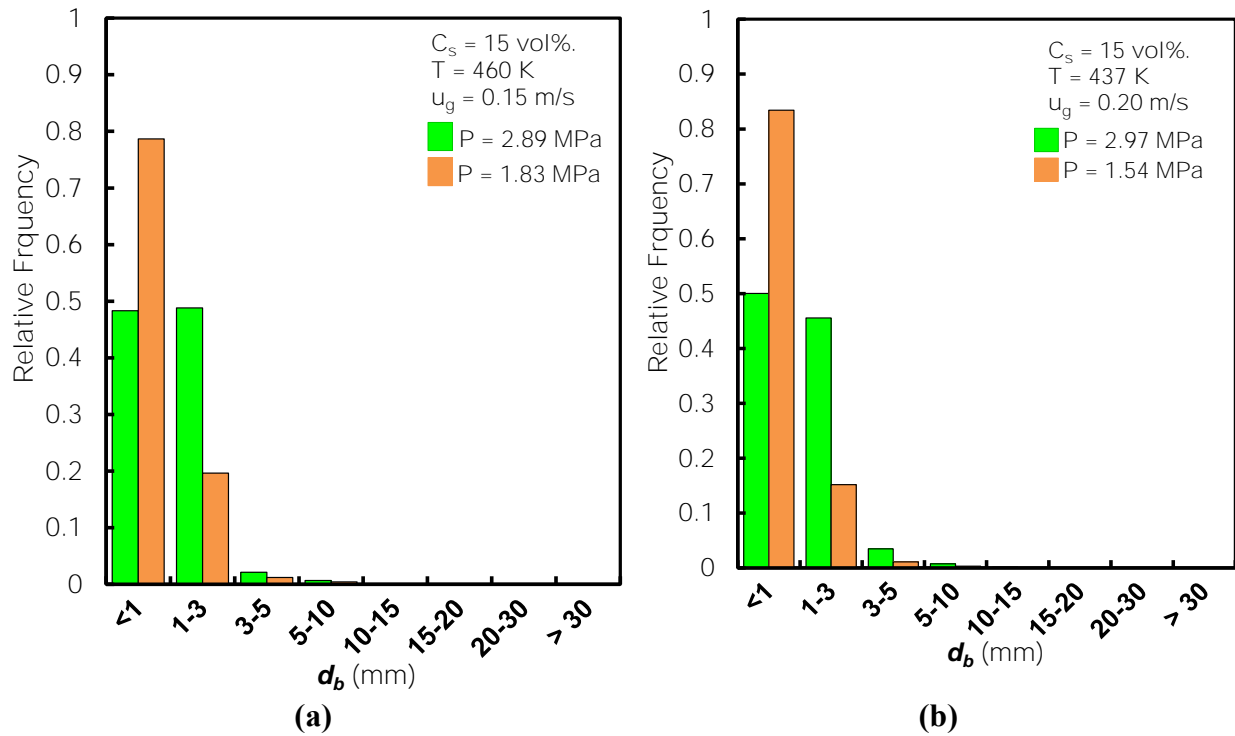


Figure C-2: Effect of pressure on bubble relative frequency

C.2 EFFECT OF SOLID CONCENTRATION

Figures C-3 and 10-4 show that increasing solids concentration increases the volume fraction of the larger gas bubbles and decreases the relative frequency of smaller gas bubbles. This behavior is primarily due to the fact that increasing solid concentration increases the slurry viscosity and density, which enhance the gas bubbles coalescence and accordingly the formation of large gas bubbles.

It should be noted that the effect of solid particle-bubble interaction in the SBCR was insignificant due to the small particle sizes used in this study (100 μm), which are an order of magnitude smaller than that of the lowest bubble-class size present in the reactor. When using

large solid particle sizes, however, the effect of particle-bubble interactions on enhancing the gas bubbles breakup becomes significant [623].

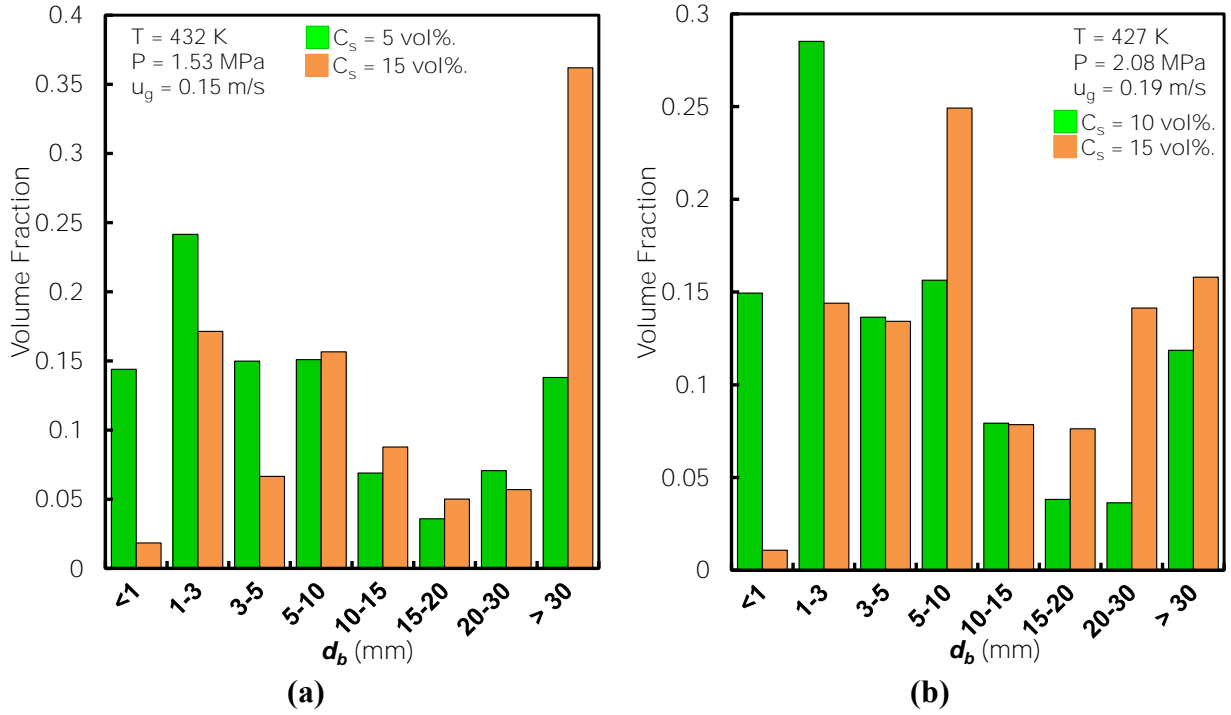


Figure C-3: Effect of solid concentration on bubble relative frequency

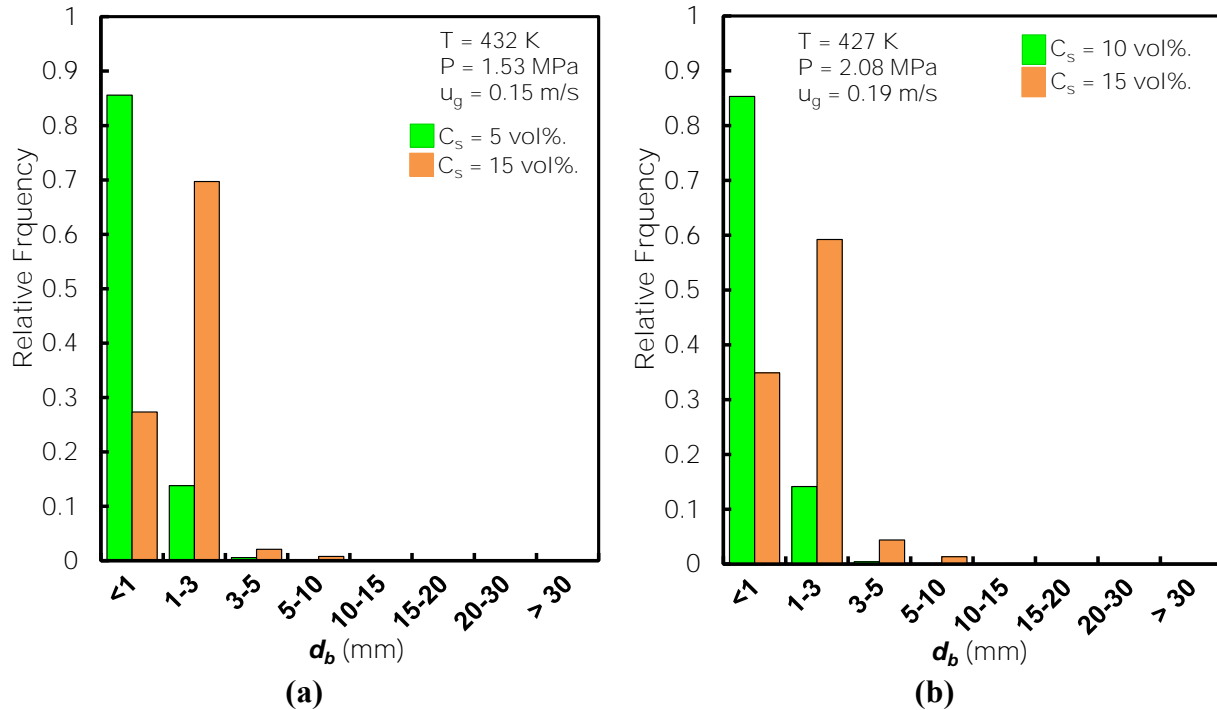


Figure C-4: Effect of solid concentration on bubble relative frequency

C.3 EFFECT OF TEMPERATURE

Figure C-5 (a) shows that increasing temperature at low solid concentration increases the volume fractions of the small gas bubbles, and decreases that of the large gas bubbles, however, Figure C-5 (b) shows that increasing temperature at high solid concentrations increases the volume fraction of the large gas bubbles (> 30 mm) and decreases that of the small gas bubbles.

Similarly, Figure C-6 show that increasing temperature at low solid concentrations slightly increases the relative frequency of the smallest gas bubble-class and slightly decreases the relative frequency of the rest of the gas bubble classes. Increasing temperature at high solid concentrations, however, significantly decreases the relative frequency of the smallest bubble-class and increases the relative frequency of the other gas bubble classes. These results are supported by Figures 5-18

to 5-20, where increasing temperature at low solid concentrations increased the Sauter mean bubble diameter (d_{32}), while increasing temperature at high solid concentrations did not have clear effect on d_{32} .

At high temperatures and high solid concentrations, the change of the gas bubbles behavior is primarily due to the competing effects of both temperature and solid concentration on the slurry physical properties. Increasing temperature decreases the liquid surface tension and viscosity, whereas, increasing solid concentration increase the slurry viscosity. It should be pointed out, however, that at high temperatures, the effect of solid concentrations on the slurry viscosity decreases significantly as shown in Figure C-7.

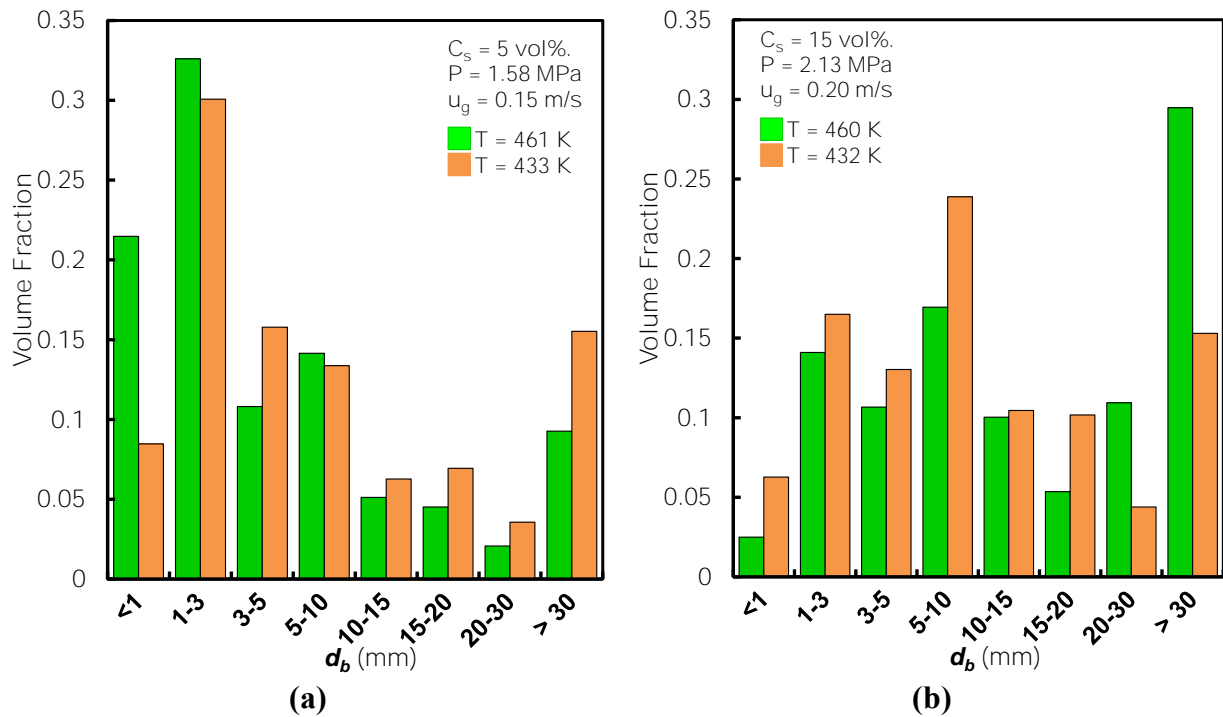


Figure C-5: Effect of temperature on bubble volume fraction

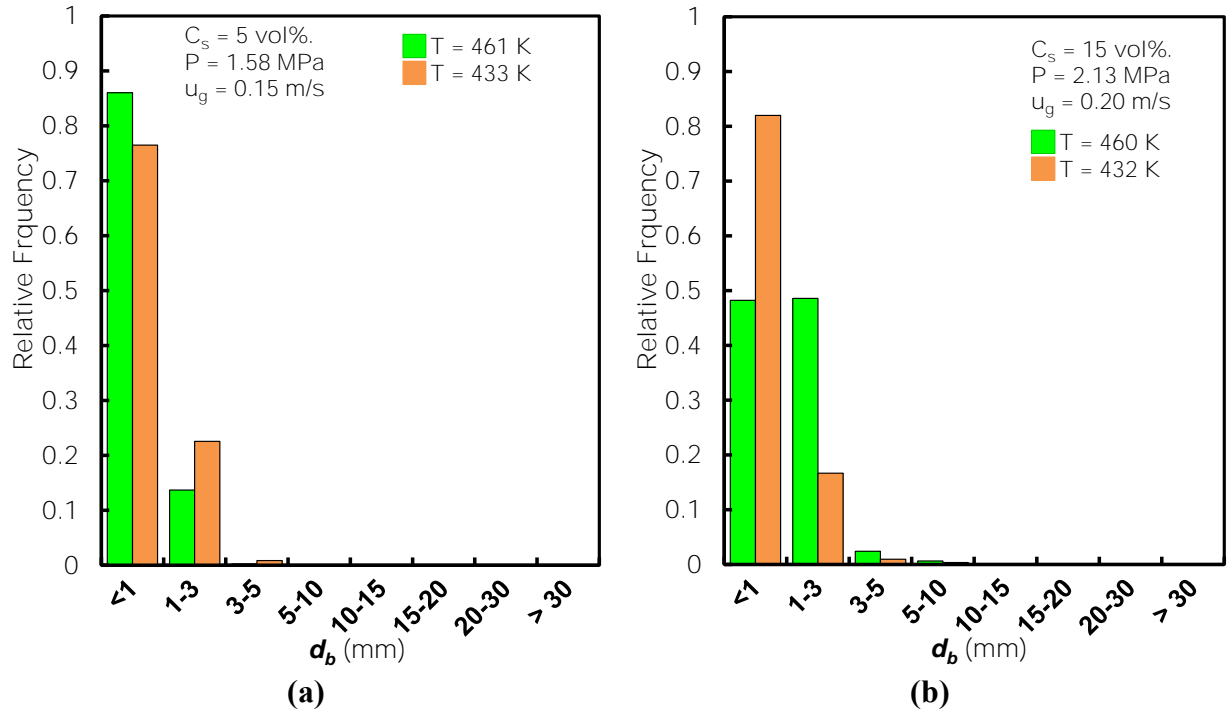


Figure C-6: Effect of temperature on bubble relative frequency

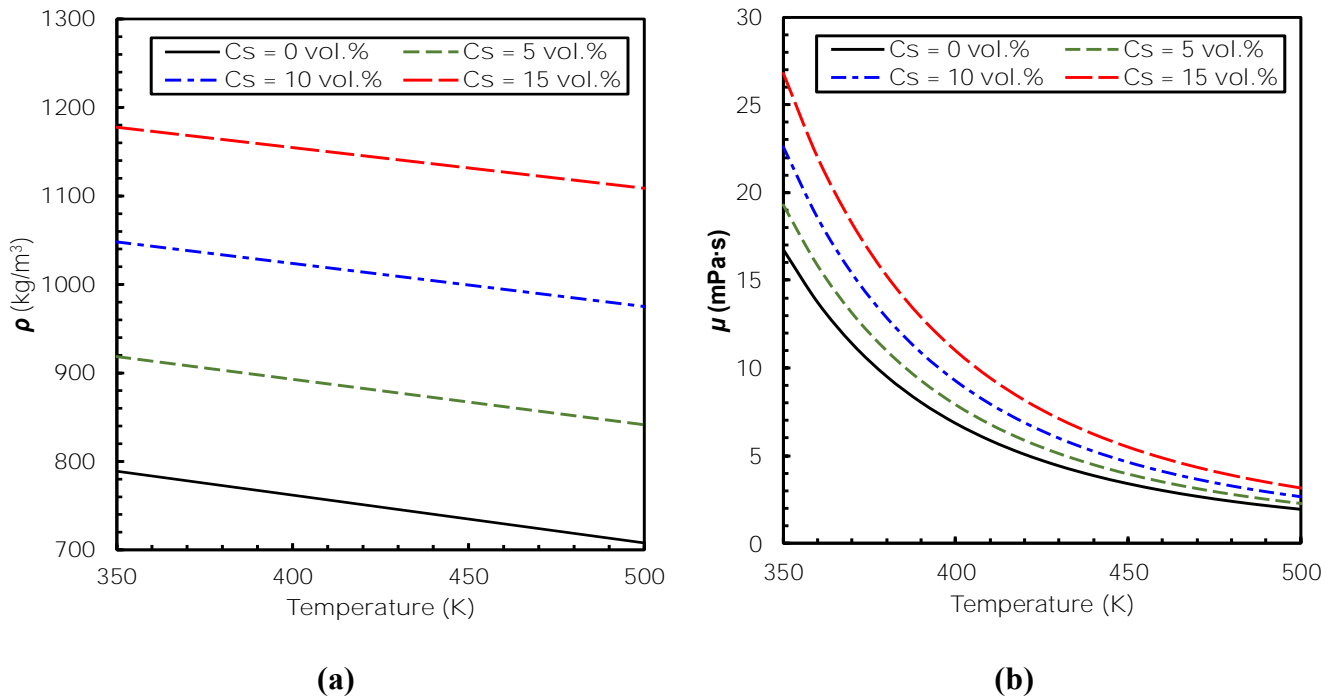


Figure C-7: Temperature on the slurry density (a) and viscosity (b) at different solid concentrations

C.4 EFFECT OF SUPERFICIAL GAS VELOCITY

Figures C-8 and C-9 show that increasing the superficial gas velocity does not have a significant effect on either the bubble size volume fraction or the relative bubble frequency, which is an agreement with Figure 5-22, which indicated that the superficial gas velocity did not have a noticeable effect on the gas bubbles size within the experimental conditions used.

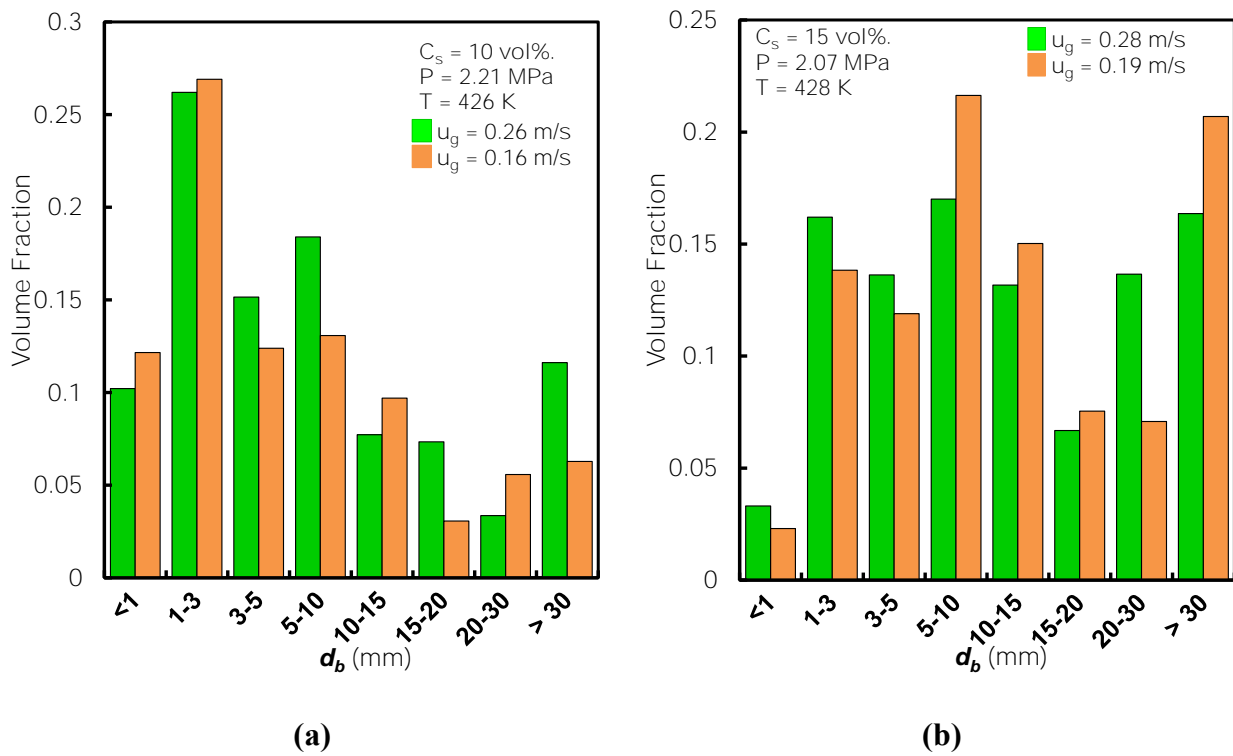


Figure C-8: Effect of superficial gas velocity on bubble volume fraction

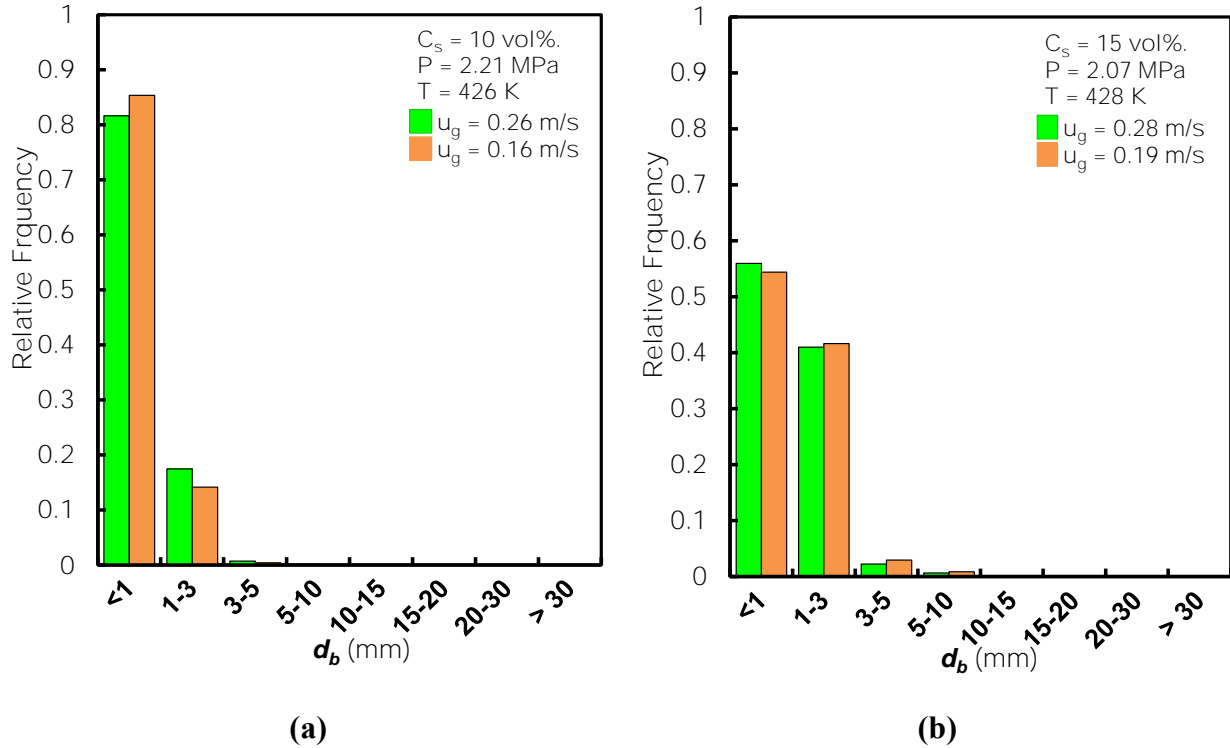


Figure C-9: Effect of superficial gas velocity on bubble relative frequency

C.5 EFFECT OF GAS DENSITY

Figure C-10 shows that increasing gas density increases the volume fraction of the large (> 30 mm) and small (< 5 mm) gas bubbles, and decreases the volume fraction of the intermediate gas bubbles. Also, Figure C-11 shows that increasing gas density increases the relative frequency of the smallest gas bubbles and decreases the relative frequency of the remaining gas bubble classes. This behavior is primarily due to the effect of gas density on the bubble momentum, where at high gas densities the increased bubble momentum enhances bubble breakup and accordingly the frequency of the large gas bubbles dramatically decreases as shown in Figure C-11.

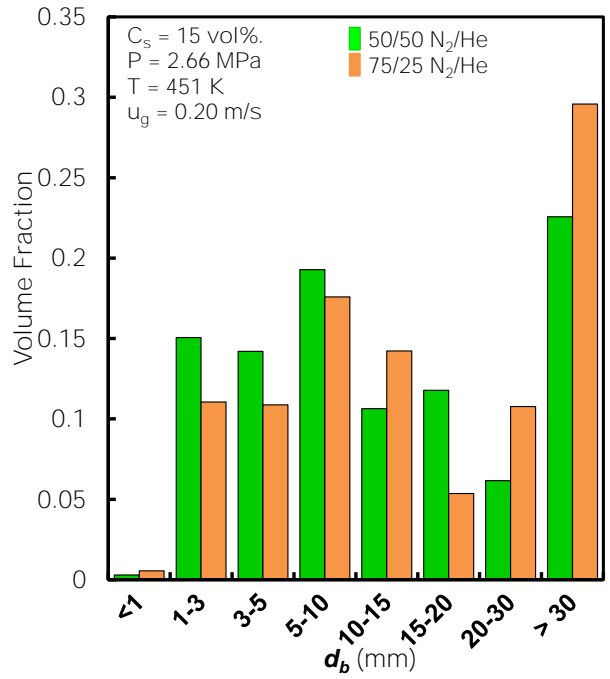
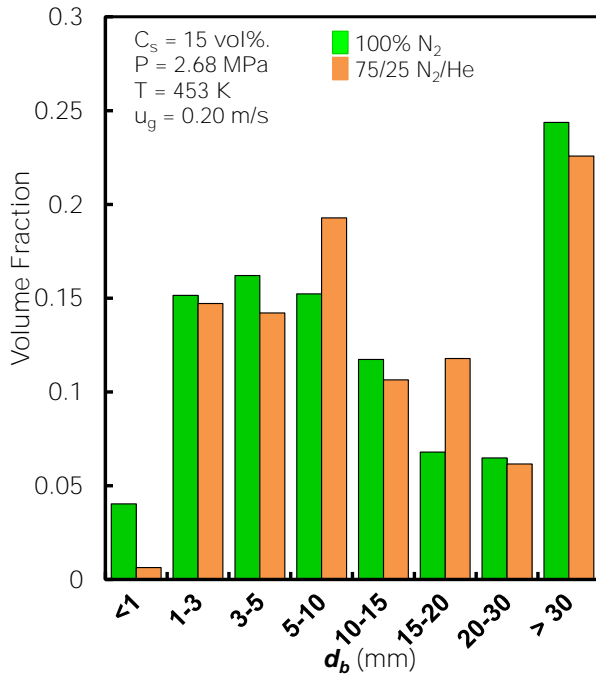


Figure C-10: Effect of gas density on bubble volume fraction

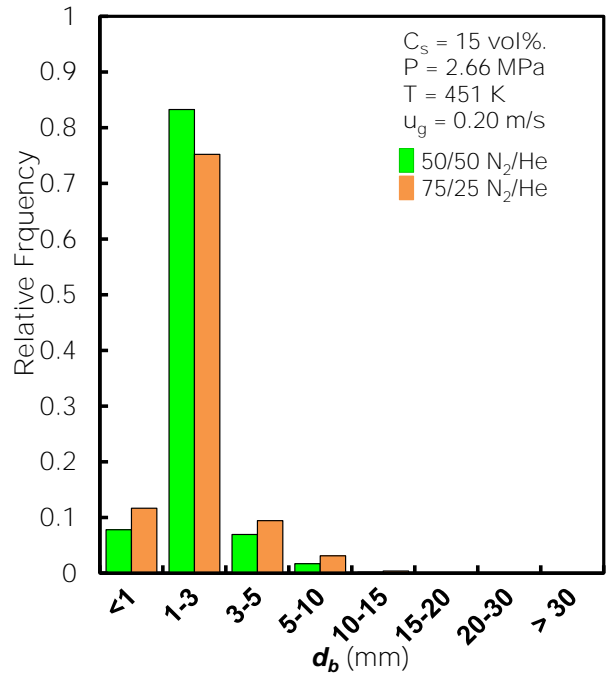
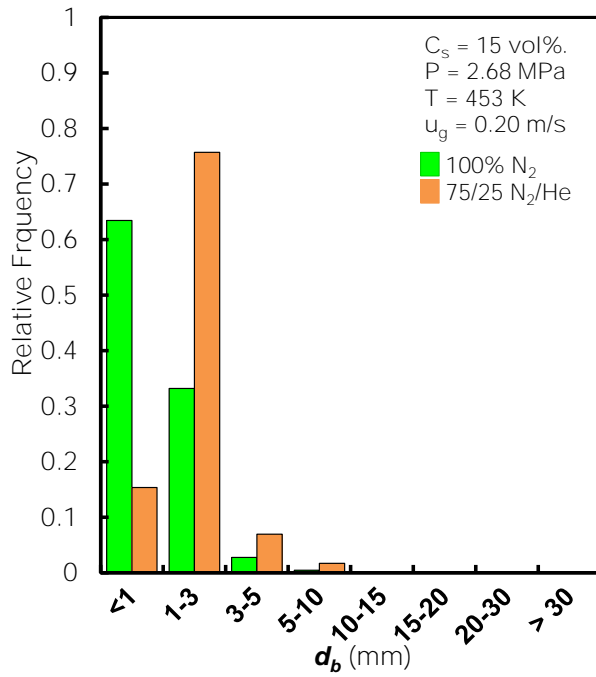


Figure C-11: Effect of gas density on bubble relative frequency

APPENDIX D

COMPARISON WITH LITERATURE GAS HOLDUP AND SAUTER BUBBLE DIAMETER DATA

Figure 7 shows a comparison between our gas holdup data and available experimental values obtained by numerous investigators under different operating conditions as given in Table 7. As can be observed, the gas holdup data obtained in this work are notably greater than all other data depicted in the figure. This behavior can be attributed to the high pressure values used in this work (15.6 and 20.5 bar), which increased the gas density, momentum, and thus the gas holdup [121]. This behavior is further supported by the behavior of data sets 5 and 6 obtained at lower pressures of 11.7 and 7.5 bar by Behkish et al. [8, 80]. Also, the relatively high gas holdup (data set 8) by Deckwer et al. [75] obtained at 8 bar and 523 K were measured at low gas velocities (0.005-0.03 m/s) and no direct comparison with our data could be made.

The gas holdup (data sets 9 and 15) by Bukur et al. [624-627] obtained at ambient pressure (1 bar) and high temperature (538 K) in 0.05 and 0.21 m ID reactors are greater than those (data set 7) by Behkish et al. [8, 80] and those (data sets 16 and 17) by Krishna et al. [77] obtained under about 1 bar at 298 K. This behavior was expected since increasing temperature decreases the liquid properties (viscosity, surface tension and density), which enhance the gas bubbles breakup, leading

to the formation of numerous small bubbles, thus increasing the gas holdup. As a matter of fact, under 1 bar, Bukur et al. [624-627] reported small bubble diameters between 0.9 to 1.4 mm at 538 K, whereas Behkish et al. [8, 80] reported bubble diameters between 2-3 mm at 400 K. On the other hand, increasing temperature decreases the gas density and its momentum, thus decreasing the gas holdup. It appears that the effect of decreasing liquid properties on the gas holdup was more significant than that of decreasing the gas momentum, since the gas holdup was found to increase with temperature.

Figure 8 shows a comparison between our Sauter mean bubble diameter (d_{32}) and experimental values obtained by Patel et al. [628, 629] and Bukur et al. [624-627, 629] under different conditions as given in Table 8. It should be emphasized that their data were measured under ambient pressure (1 bar) and high temperature (538 K) in different waxes using the Dynamic Gas Disengagement technique in the absence of solid particles. As can be observed in this figure, our (d_{32}) values (data sets 1-6) vary between 0.18 and 6 mm; and the values (data sets 7-10) by Patel et al., [628, 629] obtained at superficial gas velocities (< 0.12 m/s) in a small diameter column (0.05 m), varied from 0.37 to 5.6 mm. However, d_{32} values (data set 11) by Patel et al. [628, 629] and (data set 12) by Bukur et al. [624-627, 629] measured in a 0.23 and 0.21 m diameter columns, respectively, at gas velocities (< 0.12 m/s) were between 0.27 and 1.7 mm. As mentioned above, increasing temperature enhances gas bubbles breakup, leading to the formation of numerous small bubbles; and increasing pressure shrinks further these gas bubbles, leading to small values of d_{32} . On the other hand, increasing solid concentration, increases the slurry viscosity thereby increasing the bubble coalescence and the formation of large bubbles, resulting in high values of d_{32} . Thus, these two opposing effects should dictate the resultant value of the Sauter mean bubble diameter. Based only on the temperature effect, our d_{32} values were supposed to be greater than those by

Patel et al.[628, 629] and Bukur et al.[624-627, 629] in the large column since our temperature is lower. Also, based on the presence of solids in addition to the higher viscosity of the reactor wax used in this work, our d_{32} were supposed to be greater than those by these authors. However, the much greater pressure used in this work appeared to suppress the bubble growth and reduce the bubble size, leading to d_{32} in the range of from 0.18 to 6 mm, which is in agreement with previous findings.[46]

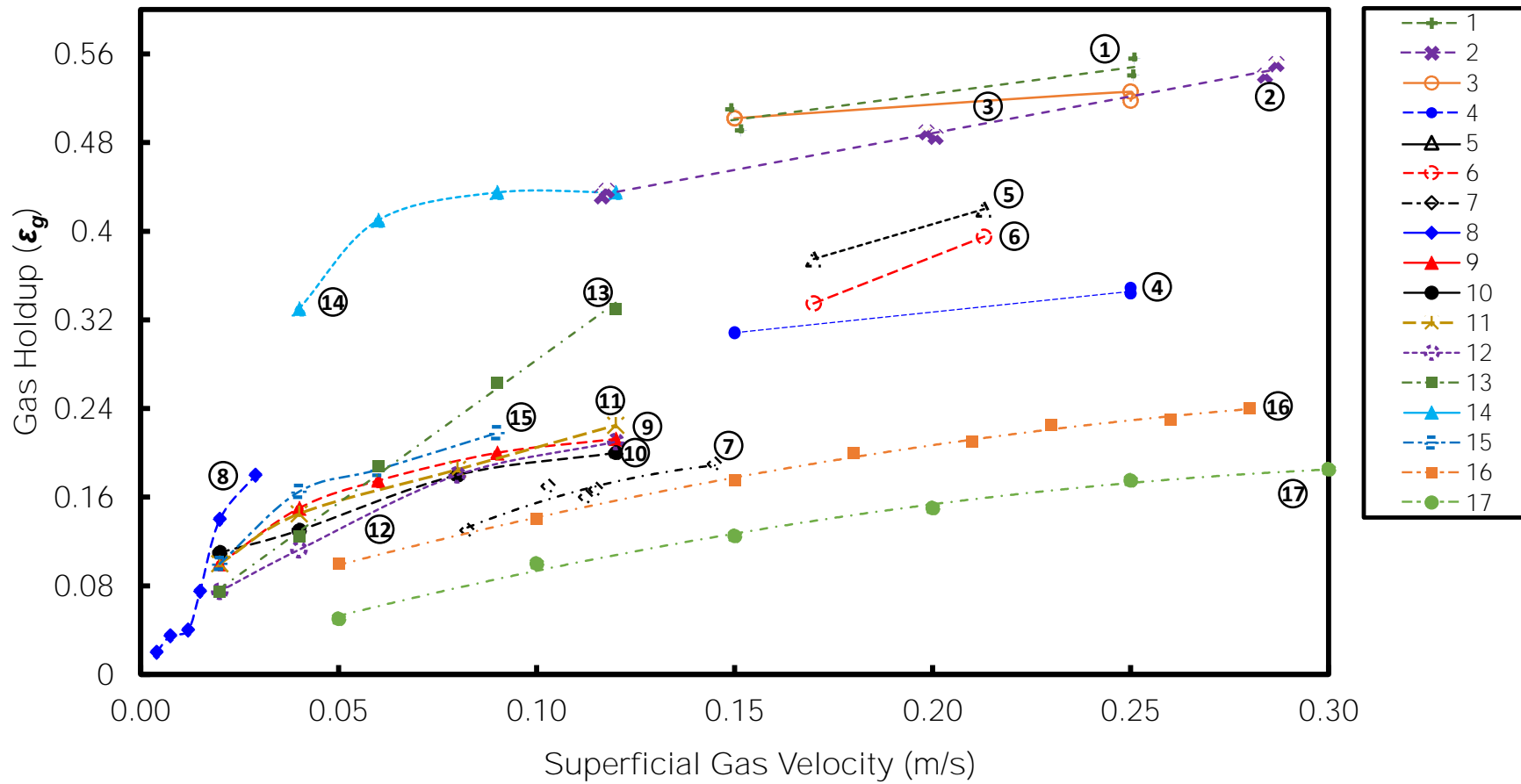


Figure D-1: Comparison of measured gas holdup data with published data sets in the literature

Table D-1: Gas holdup data sets used in the comparison in Figure D-1

#	Reference	Operating Conditions			Reactor Dimensions			Liquid				Solid			Gas
		T (K)	P (bar)	C_v (wt%)	D_C (m)	H_C (m)	Gas distributor, d_o (mm)	Type	ρ_L (kg/m ³)	μ_L (mPa·s)	σ_L (Nm ⁻¹)	Type	ρ_s (kg/m ³)	d_P (μm)	
1	This work	461	15.6	20	0.29	3	Spider, 5	Reactor Wax	728.97	2.989	0.0213	Fe-based	3380	81	N ₂
2	This work	443	20.5	34	0.29	3	Spider, 5	Reactor Wax	738.70	3.727	0.0225	Fe-based	3380	81	N ₂
3	This work	445.9	25.9	20	0.29	3	Spider, 5	Reactor Wax	737.13	3.593	0.0223	Fe-based	3380	81	N ₂
4	This work	459.5	20.7	45	0.29	3	Spider, 5	Reactor Wax	729.78	3.043	0.0214	Fe-based	3380	81	N ₂
5	Behkish et al. [8, 80]	400	11.7	32.8	0.29	3	Spider, 5	Isopar-M	733.21	0.909	0.0213	Alumina powder	3218.3	42.4	N ₂
6	Behkish et al. [8, 80]	400	7.5	32.8	0.29	3	Spider, 5	Isopar-M	733.21	0.909	0.0213	Alumina powder	3218.3	42.4	N ₂
7	Behkish et al. [8, 80]	298	1.75	41.2	0.316	2.82	Spider, 5	Isopar-M	783.343	2.705	0.0277	Glass beads	2500	19	N ₂
8	Deckwer et al. [75]	523	8	16	0.1	0.6-1 ¹	Sintered plate, 0.075	Molten Paraffin	670	2.0	0.021	Alumina powder	1284	≤5	N ₂
9	Bukur et al. [624-627, 629]	538	1	20	0.21	3	Perforated Plate, 2	Sasol Wax	655	2.0	0.016	Iron Oxide	5100	20-44	N ₂
10	Bukur et al. [624-627, 629]	538	1	20	0.21	3	Perforated Plate, 2	Sasol Wax	655	2.0	0.016	Iron Oxide	5100	0-5	N ₂
11	Bukur et al. [624-627, 629]	538	1	20	0.21	3	Perforated Plate, 2	Sasol Wax	655	2.0	0.016	Silica	2650	20-44	N ₂

Table D-1 (continued)

#	Reference	Operating Conditions			Reactor Dimensions			Liquid				Solid			Gas
		T (K)	P (bar)	C_v (wt%)	D_C (m)	H_C (m)	Gas distributor, d_o (mm)	Type	ρ_L (kg/m ³)	μ_L (mPa·s)	σ_L (Nm ⁻¹)	Type	ρ_s (kg/m ³)	d_P (μm)	
12	Bukur et al. [624-627, 629] ²	538	1	20	0.21	3	Perforated Plate, 2	FT-300 Wax	681	2.7	0.017	Iron Oxide	5100	20-44	N ₂
13	Bukur et al. [624-627, 629] ²	538	1	20	0.05	3	Orifice, 2	FT-300 Wax	681	2.7	0.017	Silica	2650	0-5	N ₂
14	Bukur et al. [624-627, 629]	538	1	20	0.05	3	Orifice, 2	FT-300 Wax	681	2.7	0.017	Iron Oxide	5100	0-5	N ₂
15	Bukur et al. [624-627, 629]	538	1	20	0.05	3	Orifice, 2	Sasol Wax	655	2.0	0.016	Iron Oxide	5100	20-44	N ₂
16	Krishna et al. [77]	298	1	58.9	0.38	4	Sintered plate, 0.05	Paraffin Oil	790	2.9	0.028	Silica particles	2100	≤47	Air
17	Krishna et al. [77]	298	1	59.9	0.38	4	Sintered plate, 0.05	Paraffin Oil	790	2.9	0.028	Silica particles	2100	≤47	Air

¹Suspension height

²Liquid velocity = 0.005 m/s

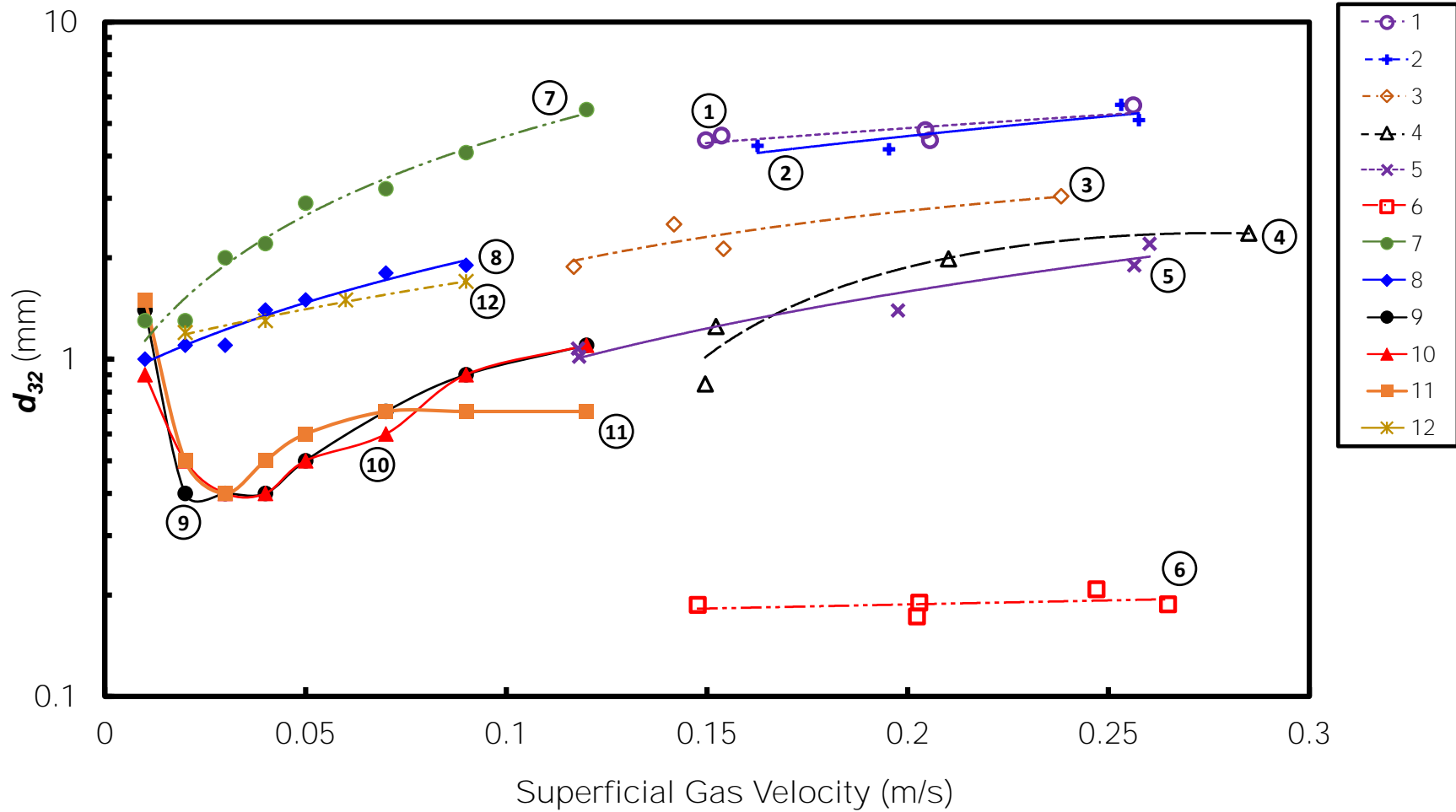


Figure D-2: Comparison of measured Sauter bubble diameter data with published data sets in the literature

Table D-2: Sauter bubble diameter data sets used in the comparison in Figure D-2

#	Reference	Operating Conditions			Reactor Dimensions			Liquid				Solid			Gas
		T (K)	P (bar)	C_v (wt%)	D_c (m)	H_c (m)	Gas distributor, d_o (mm)	Type	ρ_L (kg/m ³)	μ_L (mPa·s)	σ_L (Nm ⁻¹)	Type	ρ_s (kg/m ³)	d_p (μm)	
1	This work	429.1	14.29	34	0.29	3	Spider, 5	Reactor Wax	746.21	4.476	0.0235	Fe-based	3380	81	N ₂
2	This work	455.9	27.63	45	0.29	3	Spider, 5	Reactor Wax	731.73	3.176	0.0216	Fe-based	3380	81	N ₂
3	This work	414	14.95	34	0.29	3	Spider, 5	Reactor Wax	754.37	5.538	0.0246	Fe-based	3380	81	N ₂
4	This work	443	27.85	34	0.29	3	Spider, 5	Reactor Wax	738.69	3.727	0.0225	Fe-based	3380	81	N ₂
5	This work	444.3	21.07	34	0.29	3	Spider, 5	Reactor Wax	733.21	3.666	0.0224	Fe-based	3380	81	N ₂
6	This work	470.8	24.66	20	0.29	3	Spider, 5	Reactor Wax	723.68	2.669	0.0206	Fe-based	3380	81	N ₂
7	Patel et al. [628, 629]	538	1	0	0.05	3	Orifice, 2	Mobil Wax	674	2.3	-	-	-	-	N ₂
8	Patel et al. [628, 629]	538	1	0	0.05	3	Orifice, 2	Sasol Wax	655	2.0	0.016	-	-	-	N ₂
9	Patel et al. [628, 629]	538	1	0	0.05	3	Orifice, 2	FT-300 Wax	681	2.7	0.017	-	-	-	N ₂
10	Patel et al. [628, 629]	538	1	0	0.05	3	Orifice, 4	FT-300 Wax	681	2.7	0.017	-	-	-	N ₂
11	Patel et al. [628, 629]	538	1	0	0.23	3	Perforated Plate, 2	FT-300 Wax	681	2.7	0.017	-	-	-	N ₂
12	Bukur et al. [624-627, 629]	538	1	0	0.21	3	Perforated Plate, 2	Sasol Wax	655	2.0	0.016	-	-	-	N ₂

APPENDIX E

CORRELATIONS OF THE HYDRODYNAMIC AND MASS TRANSFER PARAMETERS

Using the experimental data obtained in the pilot scale SBCR operating with the molten reactor wax, the following parameters can be estimated: (1) overall gas holdup; (2) large and small gas bubble holdups; (3) Sauter mean bubble diameters of large and small gas bubbles; and (4) gases volumetric gas-liquid mass transfer coefficients. The hydrodynamic and mass transfer data obtained in the reactor wax were compared with the predictions of different correlations available in the literature by calculating the average relative error (ARE), the absolute average relative error (AARE) and their associated standard deviations (SD).

E.1 OVERALL GAS HOLDUP CORRELATION

The overall gas holdup data were compared with the predictions of the available literature correlations are shown in Table E-1. As can be observed in this table, the correlation by Sehabiague and Morsi [81] gives the best prediction closely followed by that of Hammer et al., [630] Joshi et al., [631] Wilkinson et al., [102] and Urseanu et al. [632] The correlation by Sehabiague and Morsi

[81] was further modified as shown in Equation (E-1) in order to enhance the accuracy of the gas holdup predictions as given in Table E-1 and Figure E-1 (a).

$$\varepsilon_G = 1.235 \times 10^4 \frac{\rho_g^{0.174} u_g^{0.553} \Gamma^{0.053}}{\rho_L^{1.59} \mu_L^{0.025} \sigma_L^{0.105}} \left(\frac{P}{P - P_v} \right)^{0.203} \left(\frac{1 + D_C}{D_C} \right)^{0.117} \quad (\text{E-1})$$

$$\times \exp(-1.5 \times 10^{-4} C_p - 1.78 \times 10^{-6} C_p^2 - 433.9 d_p + 0.434 X)$$

Table E-1: Comparison among perditions of the gas holdup correlations

Reference	ARE	SD (ARE)	AARE	SD(AARE)
Equation (E-1)	-0.9%	9.5%	7.3%	6.1%
Sehabiague and Morsi [81]	-17.9%	10.1%	18.9%	8.1%
Hammer et al. (1984) as reported in [630]	-3.0%	20.4%	17.9%	10.2%
Joshi et al. (1998) as reported in [631]	-9.9%	18.9%	18.9%	9.9%
Wilkinson et al. [102]	-13.9%	18.5%	20.7%	10.3%
Urseanu et al. [632]	6.5%	22.9%	19.1%	14.2%
Krishna et al. [87, 110, 455, 487]	23.6%	19.0%	25.5%	16.4%
Koide et al. [107]	-56.4%	7.3%	56.4%	7.3%
Gandhi et al. [631]	-53.7%	11.6%	53.7%	11.6%
Dharwadkar et al. [633]	66.2%	35.9%	66.2%	35.8%
Reilly et al. [634]	71.8%	35.4%	71.8%	35.4%
Akita and Yoshida [83]	>100%	>100%	79.3%	4.7%
Nedeltchev and Schumpe [461]	85.8%	47.6%	85.9%	47.5%

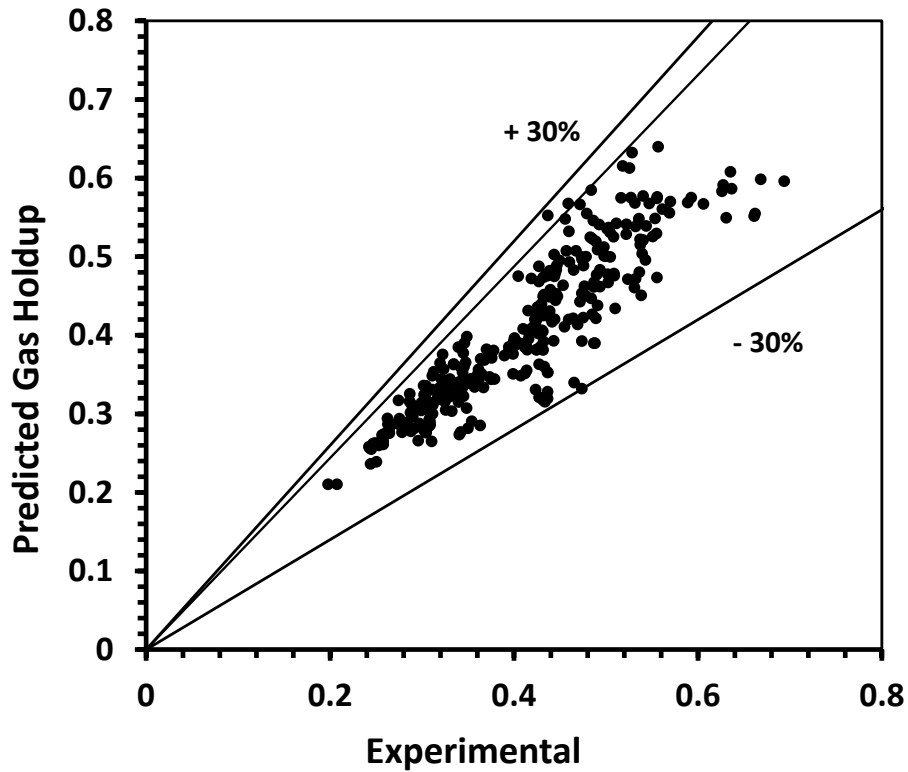


Figure E-1: Comparison between experimental data and predicted gas holdup values using Equation (E-1)

E.2 SAUTER MEAN DIAMETER OF GAS BUBBLES CORRELATION

Table E-2 shows that the correlations by Fukuma et al. [492] and Wilkinson et al., [635] which were developed for gas-liquid systems, are unable to predict the experimental data in the presence of solids which was not surprising. Similarly, the correlation by Lemoine et al. [179] could not predict the data with acceptable accuracy. Therefore, a more accurate correlation, based on the that of Lemoine et al., [179] is developed to predict the gas Sauter mean bubble diameter for catalyst volumetric concentrations less or greater than 5 vol.% as shown in Equation (E-2).

$$\begin{aligned} \text{if } C_v < 5 \text{ vol. \% } \quad d_{32} &= 0.213e^{2.81C_v}F \\ \text{if } C_v \geq 5 \text{ vol. \% } \quad d_{32} &= 0.0574e^{29C_v}F \end{aligned}$$

(E-2)

$$F = \frac{\mu_L^{0.08} \sigma_L^{1.22} \rho_G^{0.02} T^{1.66} U_G^{0.14}}{\rho_L^{1.52} MW_G^{0.12}} \left(\frac{D_C}{D_C + 1} \right) (1 - \varepsilon_G)^{1.56} \Gamma^{-0.02}$$

Table E-2: Comparison among predictions of the gas bubbles Sauter mean diameter correlations

Reference	ARE	SD(ARE)	AARE	SD(AARE)
Equation (E-2)	-34.9%	22.2%	37.4%	17.7%
Lemoine et al. [636]	>100%	>100%	>100%	>100%
Fukuma et al. [492]	>100%	>100%	>100%	>100%
Wilkinson et al. [635]	>100%	>100%	>100%	>100%

E.3 HOLDUP OF LARGE GAS BUBBLES CORRELATION

The data for the holdup of large gas bubbles were compared with the correlations by Behkish et al. [9] and by Krishna et al. [87, 110, 455, 487]. The correlation of Behkish et al. [9] was able to predict the experimental data with reasonable accuracy as shown in Table E-3.

Table E-3: Comparison among predictions of the large gas bubbles holdup correlations

Reference	ARE	SD (ARE)	AARE	SD(AARE)
Behkish et al. [9]	3.0%	24.8%	15.1%	19.9%
Krishna et al. [87, 110, 455, 487]	- 41.9%	24.5%	42.6%	23.3%

E.4 DIAMETER OF LARGE GAS BUBBLES CORRELATION

The correlation by Krishna et al. [487] proposed for gas-liquid systems could not predict the size of the large gas bubbles, whereas that by Lemoine et al. [636] under predicted the size of large gas bubbles by an average of 93%. The latter correlation was then modified as shown in Equation (E-3) to predict the experimental data with better accuracy as shown in Table E-4.

$$d_{LB} = d_{32}^{0.78} \left(1 - 10^{-5} \rho_L^{0.22} \mu_L^{0.03} \sigma_L^{8.6} U_g^{0.04} \varepsilon_G^{2.37} \varepsilon_{LB}^{2.74} \right) \quad (\text{E-3})$$

Table E-4: Comparison among predictions of the large gas bubble diameter correlations

Reference	ARE	SD (ARE)	AARE	SD(AARE)
Equation (E-3)	0.0%	51.9%	44.2%	27.0%
Lemoine et al. [637]	-93.0%	5.8%	93.0%	5.8%
Krishna et al. [487]	>100%	>100%	>100%	>100%

E.5 VOLUMETRIC MASS TRANSFER COEFFICIENT CORRELATION

The experimental k_{LA} data obtained in this study were compared with the predictions of different literature correlations shown in Table A-8; and as can be observed in Table E-5, the best prediction was obtained using the correlation by Sehabiague and Morsi,[81] which could predict the experimental data with an ARE of 9.9%. This correlation was further modified in order to increase the prediction accuracy as show in Equation (E-4) and Figure E-1 (b).

$$k_L a = 9.34 \times 10^{-9} \frac{\rho_L^{1.82} \rho_g^{0.27} U_g^{0.387} \Gamma^{0.173}}{M_g^{0.02} \mu_L^{0.25} \sigma_L^{0.976}} \left(\frac{P}{P - P_v} \right)^{0.242} \left(\frac{D_C}{0.3 + D_C} \right)^{0.1} \times \exp(-8 \times 10^{-9} C_p^3 - 1.6 \times 10^{-6} C_p^2 - 0.8 C_p + 1675.7 d_p + 0.176 X) \quad (\text{E-4})$$

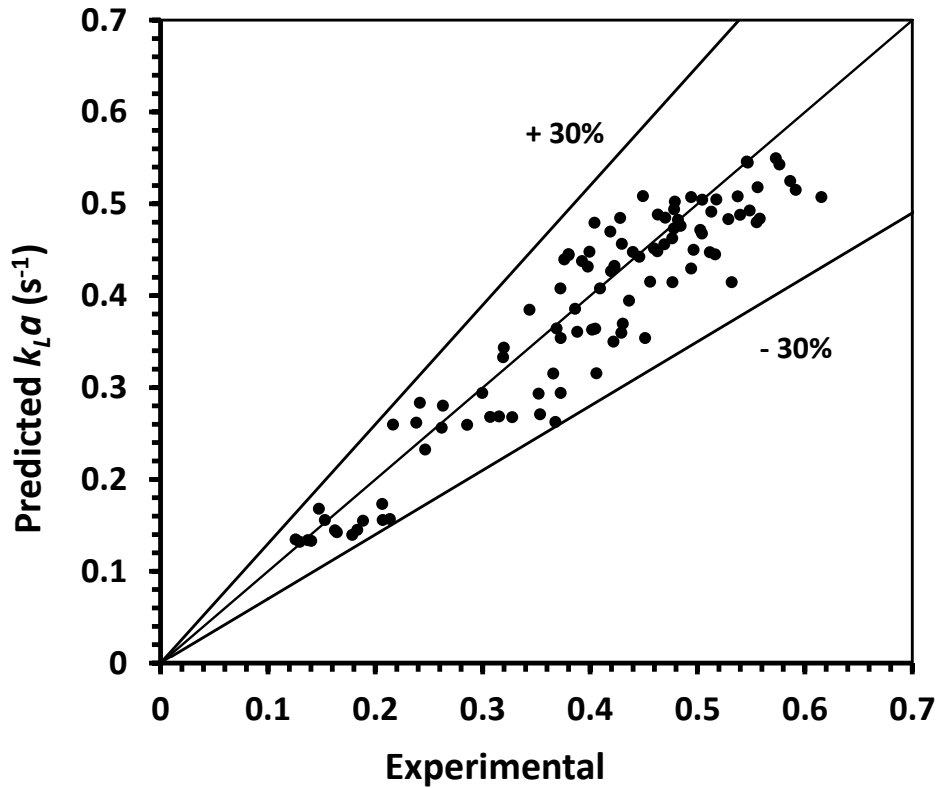


Figure E-2: Comparison between experimental data and predicted k_{LA} values using Equation (E-4)

Table E-5: Comparison among predictions of k_{LA} correlations

Reference	ARE	SD (ARE)	AARE	SD(AARE)
Equation (E-4)	0.0%	14.0%	11.1%	8.5%
Sehabiague and Morsi [81]	- 9.9%	22.0%	20.7%	12.4%
Koide et al. [107]	- 16.2%	27.4%	28.2%	14.6%
Nedeltchev and Schumpe [461]	>100%	>100%	>100%	>100%

E.6 NOVEL APPROACH AND CORRELATION FOR BUBBLE SIZE DISTRIBUTION IN THE SBCR OPERATING IN THE CHURN- TURBULENT FLOW REGIME

Over the past four decades, significant work has been done to investigate the hydrodynamics in bubble columns and SBCRs, and numerous correlations were developed for predicting the gas holdup, average bubble size, bubble rise velocity and axial dispersion coefficients, as recently summarized by Basha et al. [2]. However, investigating the bubble size distribution in bubble columns and SBCRs has been limited, despite its importance in developing proper closure models for numerical modeling as well as CFD simulation.

Previous 1-D and 2-D modeling efforts investigating bubble columns and SBCRs have frequently used the “two-bubble” or bimodal class model, which is based on convective and dispersive mechanisms [244, 638], in order to account for gas bubbles representation [155, 301, 350]. This model represents an oversimplification of the complex hydrodynamics inside the two-phase and three-phase reactors. In this model, the gas bubbles are classified into small bubbles, which are primarily controlled by the liquid- or slurry-phase motion, and large bubbles, which are independent of the liquid or slurry motion as they flow upwards in a plug-flow manner. The demarcation size of the gas bubbles classified as small has been always arbitrary.

The validity of two-bubble class model in describing the gas bubbles behavior, however, appeared to be questionable due to the fact that actual results for gas bubbles did not follow a bimodal size distribution, as demonstrated by numerous investigators [144, 145, 243, 639-642]. Also, the bimodal gas bubble distribution fails to explain the enhanced gas-phase mixing with increasing the superficial gas velocity. This is because this model assumes that the increase of the volume fraction of large gas bubbles leads the gas mixing to approach a plug-flow, which

contradicts the reported experimental data [266, 643, 644]. Therefore, there is a great need to develop a novel model for bubble size distribution, which should enable more accurate representation of the different gas bubble classes inside the SBCR.

The current practice to determine the size of gas bubbles in bubble column and SBCRs is to employ the DGD technique coupled with the correlation relating the bubble rise velocity to the bubble diameter by Fukuma et al. [622]. In this DGD technique, the disengagement profiles, which have been studied by various authors [8, 111, 645, 646], have been characterized by two straight lines, where the first line represents the disengagements of the large gas bubbles and some of the small bubbles, and the second line represents the disengagement of the small gas bubbles. It should be pointed out, however, some of the small gas bubbles disengage within the fast bubble flow region and some are hindered by the disengagement of the large bubbles; and the bubble rise velocity obtained from DGD is actually the swarm rise velocity associated with the class of gas bubbles disengaging during a given period. Thus, it is important to differentiate between the swarm properties and the gas bubble properties in order to accurately determine the bubble size distribution in the DGD process.

Schumpe and Grund [185, 453] reported some of the uncertainties and problems associated with the DGD technique. These included: (1) the subjectivity involved in obtaining an accurate disengagement profile during large gas bubbles disengagement, (2) the waterfall effect or the downward flow of liquid during bubble disengagement and its impact on the rise velocities of the small gas bubbles, which are still in the liquid-phase, and (3) the errors introduced by the bubbles entering the dispersion zone as the pressure in the plenum chamber equilibrates with the hydrostatic pressure in the reactor after the interruption of the feed gas. In addition, in a strongly coalescing or highly turbulent flow regime, the assumptions that there are no bubble-bubble interactions and that the dispersion is axially homogenous at the moment when the gas flow is

interrupted are not entirely accurate. It is important to note that in the coalescing flow regime, the bubble-bubble interactions play a significant role in bubbles formation, a behavior which is oversimplified with the assumption of a bimodal bubble size distribution. Furthermore, it should be mentioned that the correlation by Fukuma et al. [622] was developed using an air- tap water system in the presence of glass beads at ambient conditions. The glass beads used had diameters from 0.056 to 0.46 mm and exhibited solid concentrations between 13 and 50 vol.%. This brings into question the extrapolation of such a correlation to predict the bubble rise velocity and consequently the bubble diameters in SBCRs, operating under high-pressures and high-temperatures.

In this study, in order to delineate the bubble size distributions from the DGD technique, we define a minimum stable bubble size based on the assumptions that turbulences are isotropic and that bubble breakup mainly occurs due to the collision of eddies with the gas bubbles in the turbulent flow regime. We also assume that only eddies of length-scale \geq the bubble diameter would contribute to the bubbles breakup, while small eddies would transport the bubbles without breakup. This latter assumption is based on the statistical derivation of Prince and Blanch [348], which indicated that smaller eddies are unlikely to significantly contribute to the bubble breakup, due to their comparatively insignificant momentum when compared with that of large bubbles. The smallest hydrodynamic eddy length-scale at which the energy is dissipated in turbulent flow, referred to as the Kolmogorov's length-scale, is used to represent the minimum stable bubble size, which is expressed by Equation (E-5):

$$l_{min} = d_{b,min} = \left(\frac{D_c \mu_{sturry}^3}{\rho_{sturry}^3 U_G^3} \right)^{0.25} \quad (E-5)$$

Also, the semi-empirical correlation by Luo et al. [472] for high-pressure SBCRs is used to represent the maximum stable bubble size as shown in Equation (E-6):

$$d_{b,max} = 2.53 \left(\frac{\sigma_{liquid}}{g\rho_G} \right)^{0.5} \quad (E-6)$$

A typical DGD pressure-drop-time relationship, corresponding to the gas bubbles leaving the DGD cell (length), is shown in Figure E-3 for three different runs. The increase of the pressure drop at any time (t) is due to the disengagement of bubbles from the DGD cell.

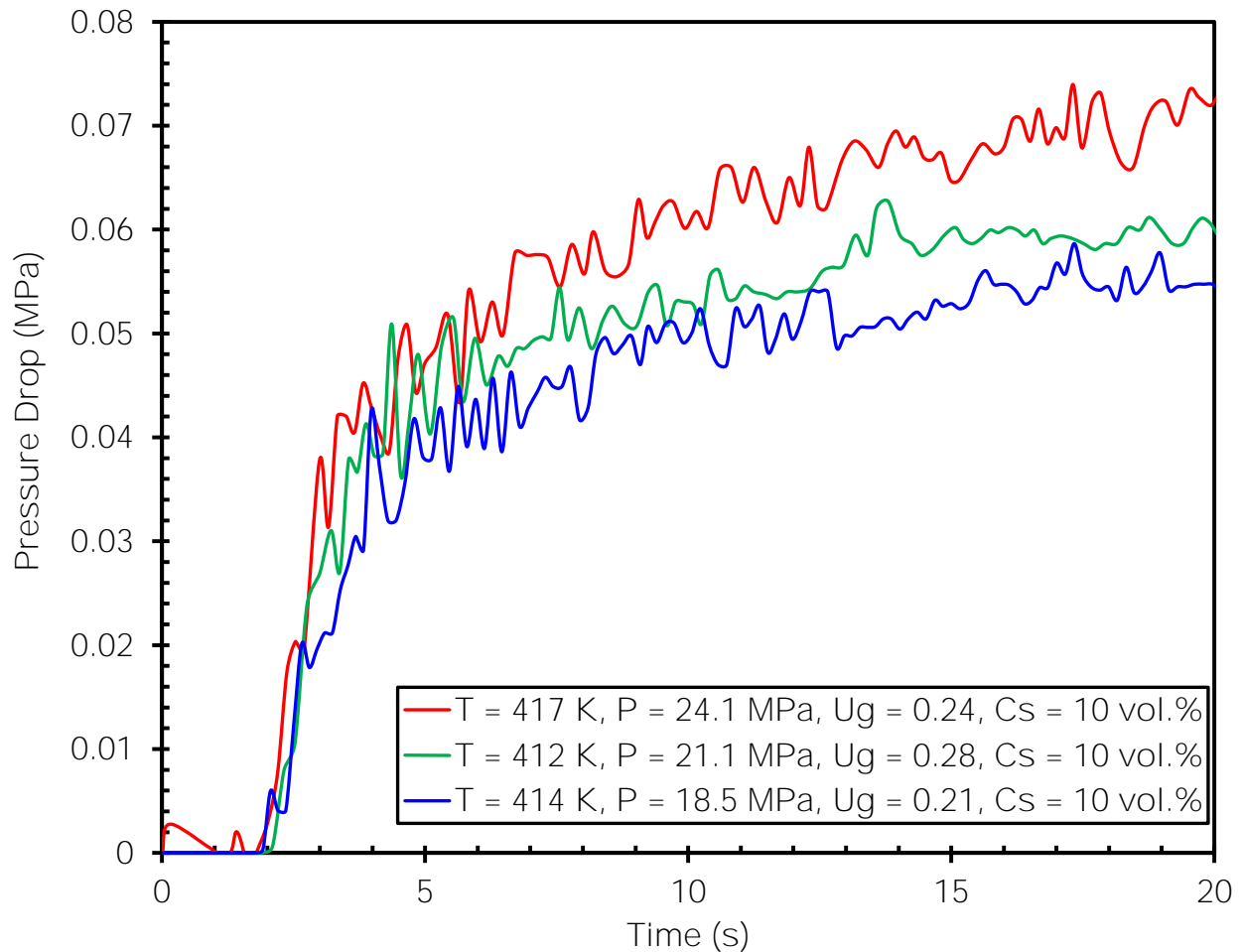


Figure E-3: Pressure drop change with time as obtained from three DGD experiments

Our novel approach considers the overall energy balance within the gas disengagement cell. During the DGD process, the pressure drop measured is primarily due to the change in the overall density within the DGD cell. In order to write the energy balance on the DGD cell, the following assumptions are made:

1. There is no dissipation of mechanical energy.
2. The bubble rise velocities, which is dependent on the bubble diameter, will determine which bubbles will disengage first. This means that at a given time (t), only a single bubble class will disengage from the DGD cell, with the largest bubbles disengaging first.
3. The gas bubbles disengage from the top of the DGD cell in the axial direction at a 0° angle

Considering these assumptions, the energy balance on the DGD cell requires that the energy lost from the cell should be equivalent to that gained by the bubbles leaving the cell, as expressed in Equation (E-7).

$$dP \cdot (V_{DGD-cell}) = (\Delta H_{DGD-cell}) \sum n_{b,i} F_{b,i} \quad (E-7)$$

Where $F_{b,i}$ refers to the force applied on the number of disengaging bubbles of class i ($n_{b,i}$).

The overall force balance on one spherical bubble (assuming no bubble deformation) with a constant bubble rise velocity ($U_{b,i}$) throughout the disengagement cell, is expressed using Equation (E-8):

$$\sum F_{b,i} = F_{Buoyancy} + F_M - F_D - F_{VM} - F_{Basset} - F_C - F_G \quad (E-8)$$

Where F_D is the liquid drag; F_{Basset} is the Basset force, $F_{Buoyancy}$ is the buoyancy force; F_C is the particle collision; F_{VM} is the virtual mass force, F_M is the force due to bubble momentum and F_G is the gravity. The description of each force is given in Table E-6.

Table E-6: Forces involved in the overall energy balance for the gas bubble [272, 323, 336, 351, 372, 647]

Force	Equation	Description
F_D : Drag	$C_D \left(\frac{\pi}{4} d_b^2 \right) \frac{\rho_{slurry} U_G^2}{2}$ $C_D = \begin{cases} \left(\frac{24}{Re_b} \right) (1 + 0.15 Re_b^{0.687}) & Re_b < 10^3 \\ 0.44 & Re_b \geq 10^3 \end{cases}$	Force accounting for the fluid resistance, acting opposite to the relative motion of the bubbles. The drag coefficient of Schiller and Naumann was used [6].
F_{VM} : Virtual Mass	$\frac{\pi}{12} \rho_{slurry} d_b^3 \frac{U_G}{\Delta t}$	Accounts for the resistance of the fluid mass that is moving at the same acceleration as the particle. It is assumed that the liquid velocity is insignificant compared to the gas velocity, Δt was taken to be 0.05 s.
F_{Basset} : Basset	$\frac{3}{2} d_b^2 (\pi \rho_{slurry} \mu_{slurry})^{0.5} \frac{U_b}{(\Delta t)^{0.5}}$	Additional drag due to vortices formed by bubble acceleration [648], Δt was taken to be 0.05 s.
$F_{Buoyancy}$: Buoyancy	$\frac{\pi}{6} d_b^3 (\rho_{slurry} - \rho_G) g$	Upward force exerted by the slurry on the bubble.
F_G : Gravity	$\frac{\pi}{6} d_b^3 \rho_G g$	Force due to gravity
F_C : Particle Collision	$\frac{\pi}{4} d_b^2 \varepsilon_s U_G^2 \rho_s$	Force imparted due to collision with solid particles [242]
F_M : Bubble Momentum	$\frac{\pi}{4} d_b^2 \rho_G U_b^2$	Accounts for the bubble momentum as it rises throughout the column.

The solution of Equation (E-8) was carried out under the constraints given in Equations (E-9) through (E-12).

$$\sum F_{b,i} = \rho_G \left(\frac{\pi d_{b,i}^3}{6} \right) \frac{U_{b,i}}{\Delta t} \quad (\text{E-9})$$

$$V_{G,i} = \varepsilon_{G,i} V_{DGD-cell} = n_{b,i} \left(\frac{\pi d_{b,i}^3}{6} \right) \quad (E-10)$$

$$d_{b,min} \leq d_b \leq d_{b,max} \quad (E-11)$$

$$d_{b,i}|_t > d_{b,i}|_{t+\Delta t} \quad (E-12)$$

It is important to note that in order to successfully use this novel method, the gas holdup for each bubble class is required, which can be simultaneously determined from the gas disengagement profile while performing the DGD experiments, as described in Sections 5.3 and 5.4.

When substituting the forces given in Table E-6 into the right-hand-side of Equation (E-8) and inserting it into Equation (E-7), the energy balance leads to a cubic equation of $d_{b,i}$, which can be used to identify the single bubble size and the number of bubbles for every bubble class disengaging at any time (t).

In this study, this novel method was followed to calculate the number of bubbles for every bubble diameter between the minimum and maximum stable sizes calculated using Equations (E-5) and (E-6), with increments of 0.5 mm. It should be mentioned that a single bubble diameter ($d_{b,i}$) and number of bubbles ($n_{b,i}$) were obtained for the majority of the experimental data. In a few cases, however, multiple solutions were found and the values, which were more in line with the rest of the data at similar operating conditions, were selected. The volume fraction of each bubble size was then calculated using Equations (E-13) and (E-14), whereas the relative frequency of each bubble size was determined using Equation (C-4).

$$Volume\ fraction_{b,i} = \frac{\sum_{d_{b,min}}^{d_{b,max}} n_{b,i} V_{b,i}}{V_{G,total}} \quad (E-13)$$

$$V_{b,i} = \frac{\pi (d_{b,i} - 0.5 \cdot \Delta d_b)^3}{6} \quad (E-14)$$

Where $\Delta d_b = 0.5$ mm in this work.

Figures 5-22 and 6-14 show the calculated volume fraction and relative frequency as a function of the bubble diameter at different operating conditions, respectively.

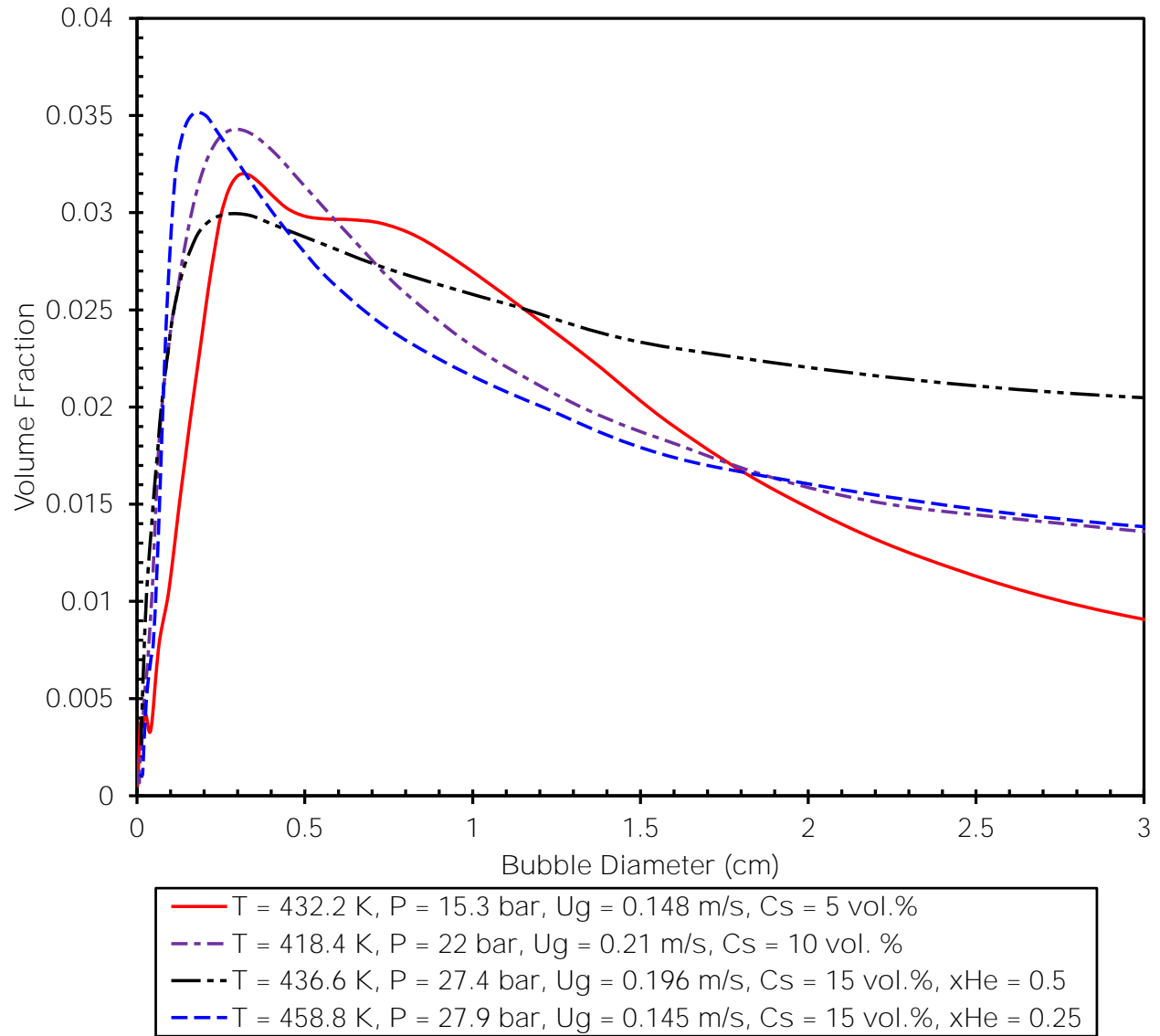


Figure E-4: Bubbles volume fraction distributions from the DGD under different operating conditions

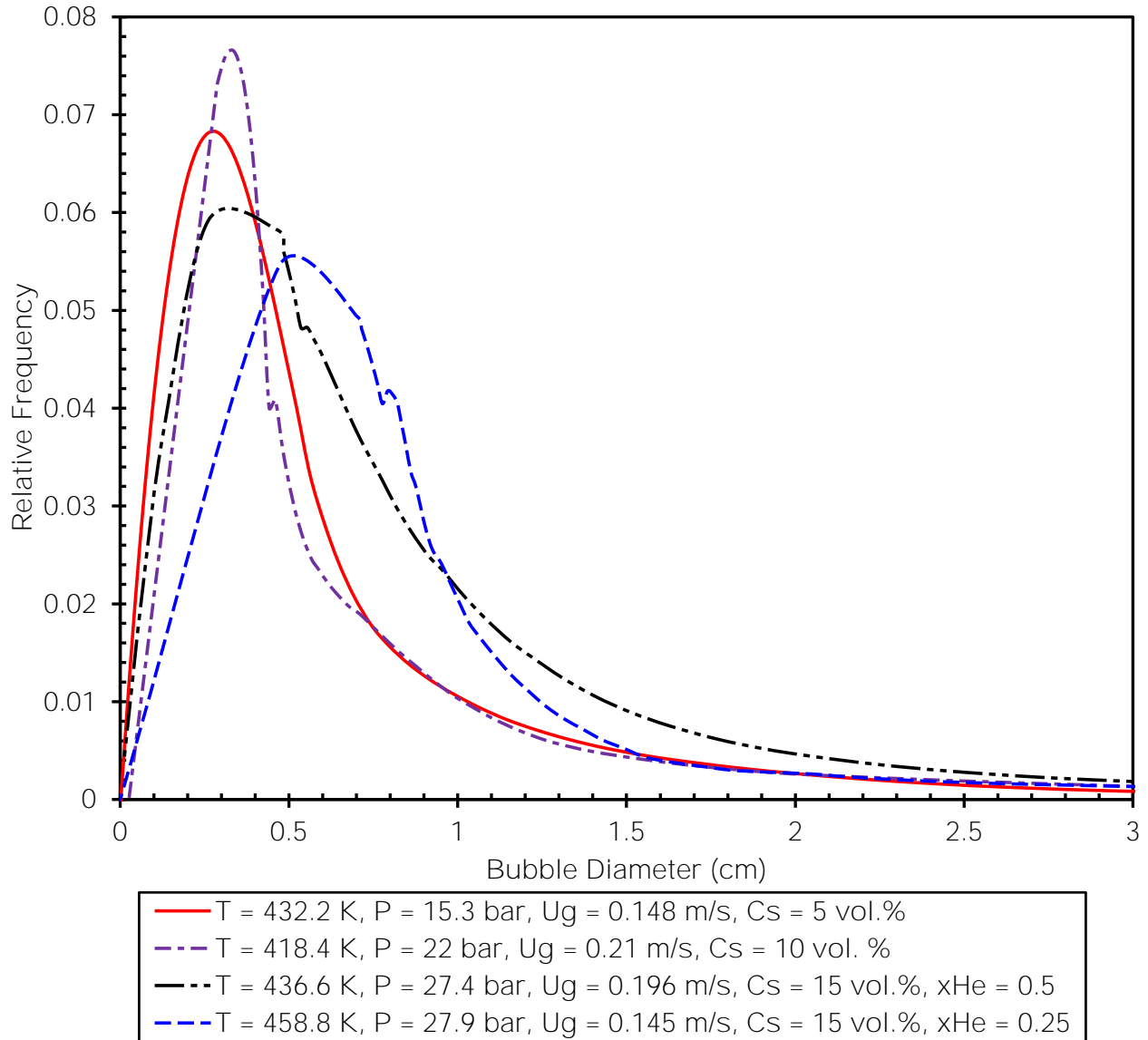


Figure E-5: Bubbles relative frequency distributions from the DGD under different operating conditions

As can be seen in these figures, the bubbles volume fraction and relative frequency distributions at each set of operating conditions (T, P, C_s , and ρ_g) can be represented using a probability distribution function, as shown in Equation (E-15).

$$f(d_{b,i}|d_{b,avg}, \beta^2)|_{T,P,u_G} = \frac{1}{\sqrt{2\beta^2\pi}} e^{-\left(\frac{(d_{b,i}-d_{b,avg})^2}{2\beta^2}\right)} \quad (\text{E-15})$$

Where $f(d_{b,i}|d_{b,avg}, \beta^2)|_{T,P,u_g}$ is the relative frequency of a bubble class i with a diameter ($d_{b,i}$) at a certain set of operating conditions (T, P, u_g); $d_{b,avg}$ is the arithmetic mean of the bubble sizes obtained from a given DGD data set at fixed pressure, temperature and gas velocity; and β^2 is the variance. It should be remembered that the variance represents the spread of the distribution, where a small variance indicates that the bubble distribution is close to the arithmetic mean, whereas a large variance indicates that the bubble distribution spreads far away from the arithmetic mean.

The experimental DGD data obtained in the pilot-scale SBCR for the gas-liquid solid systems discussed in Sections 6.1.1 to 6.1.3 along with those for paraffins mixture-Puralox alumina, reactor wax-iron oxide, and reactor wax-alumina obtained also in the SBCR [8, 46, 81, 637, 649] were used to correlate the arithmetic mean bubble size and the variance as a function of the operating conditions used in each run. A total of 772 DGD experiments were used to develop the correlations of the arithmetic mean bubble size and the bubble size variance, which are given in Equations (E-16) and (E-17), respectively.

$$d_{b,avg} = 2.03 \times 10^{-3} \frac{\mu_{slurry}^{0.159} U_G^{0.885} (\rho_{slurry} - \rho_G)^{2.05}}{\rho_{slurry}^{1.13} \sigma_{liquid}^{4.07}} \quad (E-16)$$

$$\beta^2 = 1.27 \times 10^{-3} \left(\frac{Re^{0.0358} E\ddot{o}^{0.494}}{We^{0.0198}} \right) \quad (E-17)$$

The definition of the dimensionless numbers, Re , We and $E\ddot{o}$ used in these correlations are given in Equations (E-18) through (E-20).

$$Re_b = \frac{\rho_{slurry} U_G d_b}{\mu_{slurry}} \quad (E-18)$$

$$We = \frac{\rho_{slurry} d_b U_G^2}{\sigma_{liquid}} \quad (E-19)$$

$$E\ddot{o} = \frac{g(\rho_{slurry} - \rho_G)d_b^2}{\sigma_{liquid}} \quad (E-20)$$

It should be mentioned that these correlations can only be used within the following ranges:

$$\begin{array}{lll}
 48 \geq Re_b \geq 1305 & 660 \geq \rho_{slurry} \text{ (kg/m}^3\text{)} \geq 1155 & 4.1 \geq P \text{ (bar)} \geq 31.9 \\
 0.2 \geq We \geq 31.5 & 9 \geq \sigma_{liquid} \text{ (mN/m)} \geq 27 & 323 \geq T \text{ (K)} \geq 531 \\
 0.05 \geq E\ddot{o} \geq 143 & 1.7 \geq \rho_G \text{ (kg/m}^3\text{)} \geq 23.4 & 0 \geq C_s \text{ (vol. \%)} \geq 15.2 \\
 0.2 \geq \mu_{slurry} \text{ (mPa}\cdot\text{s)} \geq 24 & 0.05 \geq U_G \text{ (m/s)} \geq 0.29 &
 \end{array}$$

The calculated arithmetic mean bubble size and variance are plotted in Figures 12-6 and 12-7 with an absolute average relative errors (AARE) of 9.49% and 5.87%, respectively.

As can be deduced, Equation (E-15), coupled with Equations (E-16) and (E-17) can be used to calculate the bubble size distribution inside the pilot-scale SBCR available in our laboratory at elevated pressures, temperatures and different gas velocities. Therefore, our novel approach overcomes the problems associated with the oversimplified method adopted when using the DGD technique data as reported by numerous investigators [144, 155, 306, 312, 348, 461, 623, 650].

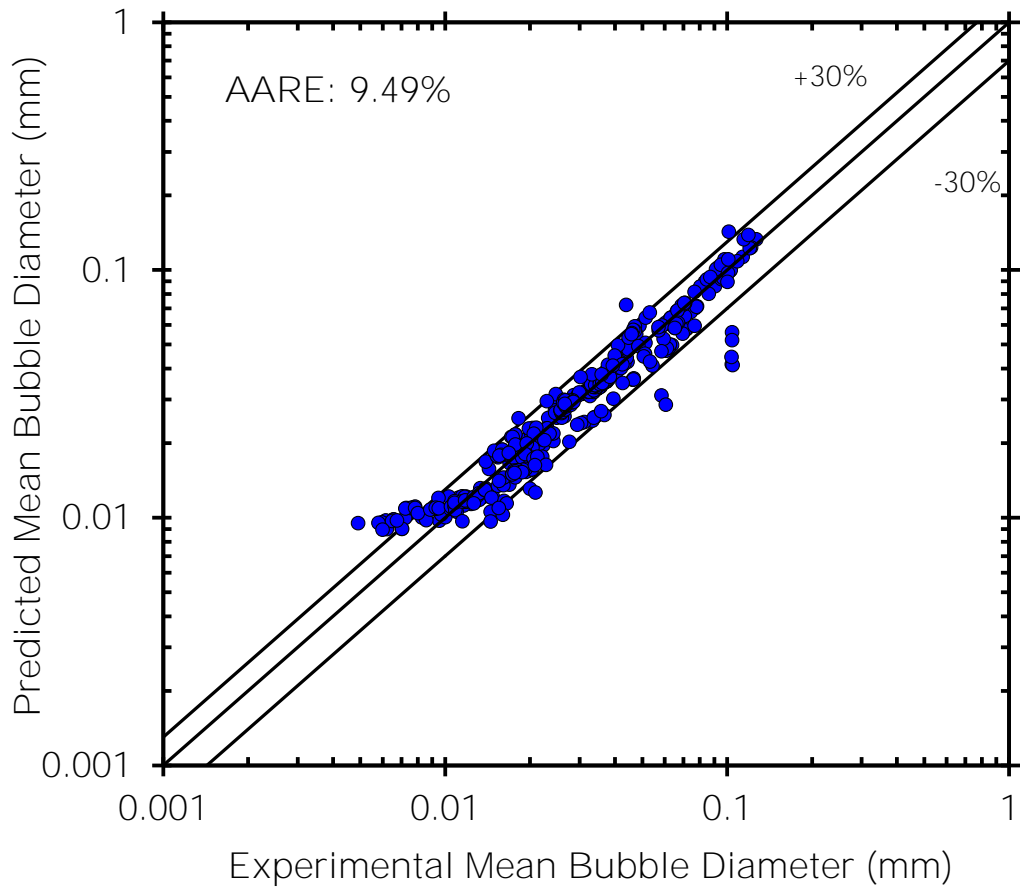


Figure E-6: Comparison between experimental and predicted values of the mean bubble diameter

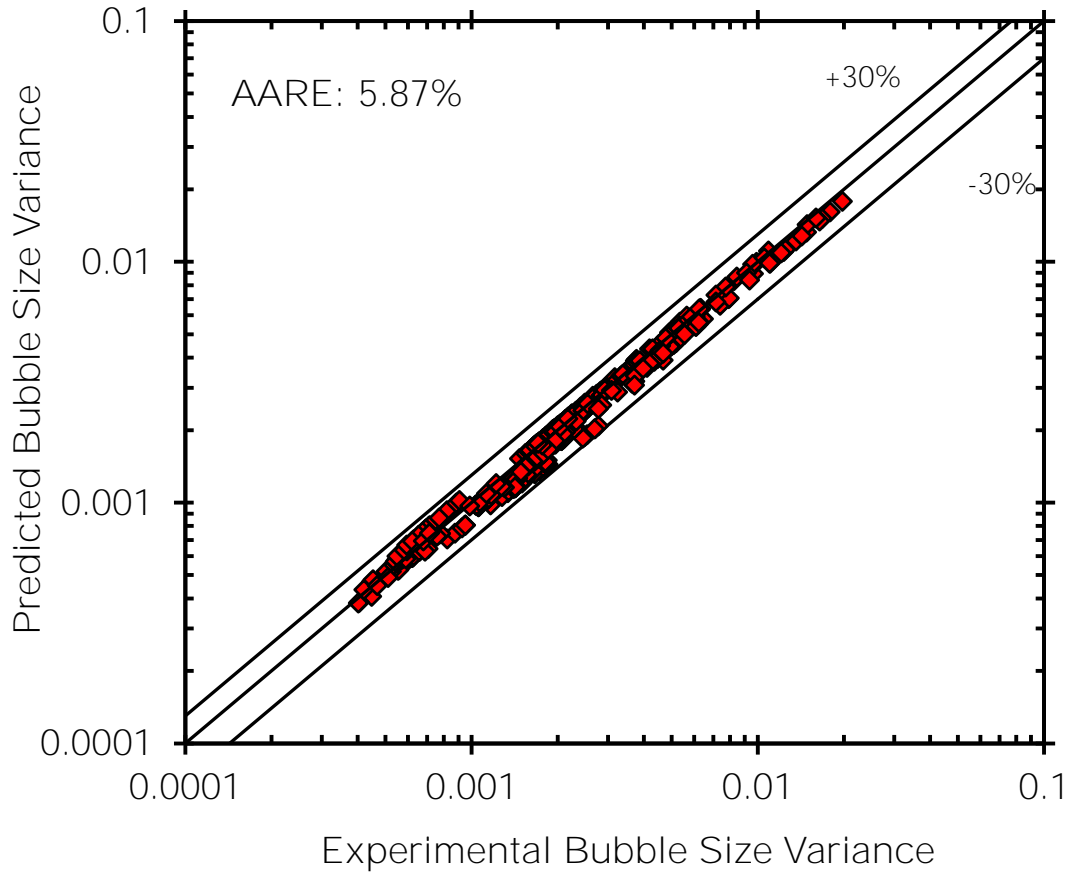


Figure E-7: Comparison between experimental and predicted values of the bubble size variance

In addition, the predicted values of $f(d_{b,i})$ and $d_{b,i}$ using Equations (E-15), (E-16) and (E-17) were used to calculate the Sauter mean bubble diameter with Equation (E-21) using the experimental data obtained in this study and those obtained for different gas-liquid-solid systems under various operating conditions inside in the same pilot-scale SBCR [8, 46, 81, 637, 649, 651].

$$d_{32} = \frac{\sum_i f(d_{b,i})d_{b,i}^3}{\sum_i f(d_{b,i})d_{b,i}^2} \quad (\text{E-21})$$

The calculated values using Equation (E-21) are plotted in Figure E-8; and as can be observed in this figure, the novel method is capable of predicting the Sauter mean bubble diameter with an absolute average relative error (AARE) of 8.87%. This is a significant improvement over

our initial correlation [651], Equation (E-22), which employed the equation by Fukuma et al. [622] to predict the intermediate bubble sizes. It should be noted that Equation (E-22) was able to predict the experimental data with an AARE of 37.4%, which was an improvement when compared with other commonly used correlations available in the literature [492, 635], as highlighted by Sehabiague et al. [651].

$$d_{32} = 0.213e^{2.81C_s} F \quad \text{if } C_s < 5 \text{ vol. \%}$$

$$d_{32} = 0.0574e^{29C_s} F \quad \text{if } C_s \geq 5 \text{ vol. \%}$$

(E-22)

$$F = \frac{\mu_{liquid}^{0.08} \sigma_{liquid}^{1.22} \rho_G^{0.02} T^{1.66} U_G^{0.14}}{\rho_{liquid}^{1.52} M_{W_G}^{0.12}} \left(\frac{D_C}{D_C + 1} \right)^{0.3} (1 - \varepsilon_G)^{1.56} (\Gamma^{-0.2})$$

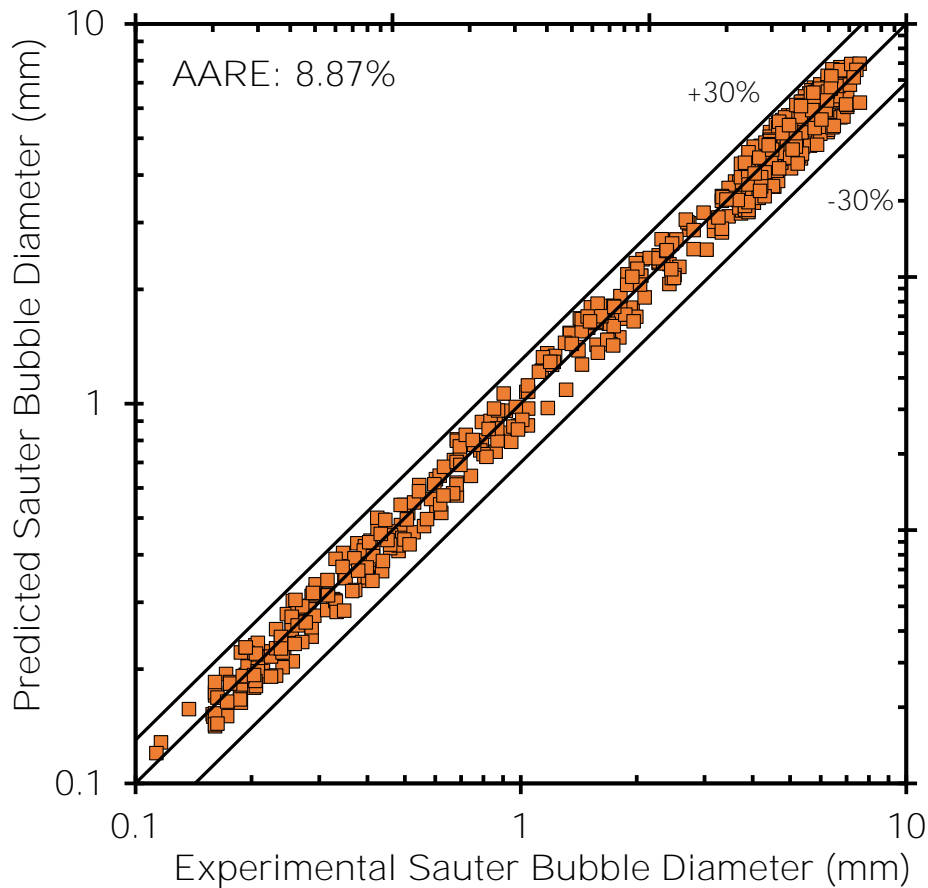


Figure E-8: Comparison between experimental and predicted values of the Sauter bubble diameter using Equation (E-21)

REFERENCES

- [1] O. M. Basha, L. Weng, Z. Men, and B. I. Morsi, "CFD Modeling with Experimental Validation of the Internal Hydrodynamics in a Pilot-Scale Slurry Bubble Column Reactor," *International Journal of Chemical Reactor Engineering*, vol. AOP, 2016.
- [2] O. M. Basha, L. Sehabiague, A. Abdel-Wahab, and B. I. Morsi, "Fischer–Tropsch Synthesis in Slurry Bubble Column Reactors: Experimental Investigations and Modeling—A Review," *International Journal of Chemical Reactor Engineering*, vol. 13, pp. 201-288, 2015.
- [3] Y. H. Yu and S. D. Kim, "Bubble characteristics in the radial direction of three-phase fluidized beds," *AIChE Journal*, vol. 34, pp. 2069-2072, 1988.
- [4] J. Chen, F. Li, S. Degaleesan, P. Gupta, M. H. Al-Dahhan, M. P. Dudukovic, and B. A. Toseland, "Fluid dynamic parameters in bubble columns with internals," *Chemical Engineering Science*, vol. 54, pp. 2187-2197, 1999.
- [5] C. Y. Wen and Y. H. Yu, "Mechanics of Fluidization," *Chem Eng Prog Symp Ser*, vol. 62, pp. 100-111, 1966.
- [6] L. Schiller and Z. Naumann, "A drag coefficient correlation," *Zeitung Ver. Deutsch. Ing.*, vol. 77, pp. 318-320, 1935.
- [7] A. Tomiyama, H. Tamai, I. Zun, and S. Hosokawa, "Transverse migration of single bubbles in simple shear flows," *Chemical Engineering Science*, vol. 57, pp. 1849-1858, 2002.
- [8] A. Behkish, R. Lemoine, L. Sehabiague, R. Oukaci, and B. I. Morsi, "Gas holdup and bubble size behavior in a large-scale slurry bubble column reactor operating with an organic liquid under elevated pressures and temperatures," *Chemical Engineering Journal*, vol. 128, pp. 69-84, 2007.
- [9] A. Behkish, R. Lemoine, R. Oukaci, and B. I. Morsi, "Novel correlations for gas holdup in large-scale slurry bubble column reactors operating under elevated pressures and temperatures," *Chemical Engineering Journal*, vol. 115, pp. 157-171, 2006.

- [10] H. Schulz, "Short history and present trends of Fischer–Tropsch synthesis," *Applied Catalysis A: General*, vol. 186, pp. 3-12, 1999.
- [11] D. Leckel, "Diesel Production from Fischer–Tropsch: The Past, the Present, and New Concepts," *Energy & Fuels*, vol. 23, pp. 2342-2358, 2009/05/21 2009.
- [12] M. E. Dry, "The Fischer-Tropsch process: 1950-2000," *Catalysis Today*, vol. 71, pp. 227-241, 2002.
- [13] A. Steynberg and M. Dry, *Fischer-Tropsch Technology*. Amsterdam: Elsevier Science, 2004.
- [14] C. L. Penniall, "Fischer-Tropsch Based Biomass to Liquid Fuel Plants in the New Zealand Wood Processing Industry Based on Microchannel Reactor Technology," 2013.
- [15] P. Sabatier and J. D. Senderens, "Nouvelles Syntheses du Methane.," *Comptes Rendus*, vol. 134, p. 514, 1902.
- [16] K. Ripfel-Nitsche, H. Hofbauer, R. Rauch, M. Goritschnig, R. Koch, P. Lehner, M. Koch, and A. Kiennemann, "BTL–Biomass to liquid (Fischer Tropsch process at the biomass gasifier in Güssing)," in *Proceedings of the 15th European Biomass Conference & Exhibition, Berlin, Germany, 2007*.
- [17] J. R. Longanbach, G. J. Stiegel, M. D. Rutkowski, T. L. Buchanan, M. G. Klett, and R. L. Schoff, "Capital and Operating Cost of Hydrogen Production from Coal Gasification," Final Report, U.S. DOE Contract No. DE-AM26-99FT40465, Subcontract No. 990700362, Pittsburgh April 2003 2003.
- [18] F. G. Botes, J. W. Niemantsverdriet, and J. van de Loosdrecht, "A comparison of cobalt and iron based slurry phase Fischer–Tropsch synthesis," *Catalysis Today*, vol. 215, pp. 112-120, 2013.
- [19] A.-G. Collot, "Matching gasification technologies to coal properties," *International Journal of Coal Geology*, vol. 65, pp. 191-212, 1/17/ 2006.
- [20] R. L. Espinoza, a. P. Steynberg, B. Jager, and a. C. Vosloo, "Low temperature Fischer–Tropsch synthesis from a Sasol perspective," *Applied Catalysis A: General*, vol. 186, pp. 13-26, 1999.
- [21] M. Dry, "The fischer-tropsch process-commercial aspects," *Catalysis today*, vol. 9570, 1990.

- [22] J. Xu and G. Froment, "Methane steam reforming, methanation and water-gas shift: I. Intrinsic kinetics," *AIChE Journal*, vol. 35, pp. 88-96, 1989.
- [23] W. Mitchell, J. Thijssen, and J. M. Bentley, "Development of a Catalytic Partial Oxidation/Ethanol Reformer for Fuel Cell Applications," *Society of Automotive Engineers*, vol. Paper No.9, 1995.
- [24] M. Bradford and M. Vannice, "Catalytic reforming of methane with carbon dioxide over nickel catalysts II. Reaction kinetics," *Applied Catalysis A: General*, vol. 142, pp. 97-122, 1996.
- [25] K. Kusakabe, K.-I. Sotowa, T. Eda, and Y. Iwamoto, "Methane steam reforming over Ce–ZrO₂-supported noble metal catalysts at low temperature," *Fuel Processing Technology*, vol. 86, pp. 319-326, 2004.
- [26] a. Berman, R. K. Karn, and M. Epstein, "Kinetics of steam reforming of methane on Ru/Al₂O₃ catalyst promoted with Mn oxides," *Applied Catalysis A: General*, vol. 282, pp. 73-83, 2005.
- [27] P. Wu, X. Li, S. Ji, B. Lang, F. Habimana, and C. Li, "Steam reforming of methane to hydrogen over Ni-based metal monolith catalysts," *Catalysis Today*, vol. 146, pp. 82-86, 2009.
- [28] A. J. de Abreu, A. F. Lucrédio, and E. M. Assaf, "Ni catalyst on mixed support of CeO₂–ZrO₂ and Al₂O₃: Effect of composition of CeO₂–ZrO₂ solid solution on the methane steam reforming reaction," *Fuel Processing Technology*, vol. 102, pp. 140-145, 2012.
- [29] H.-S. Roh, I.-H. Eum, and D.-W. Jeong, "Low temperature steam reforming of methane over Ni–Ce_(1-x)Zr_(x)O₂ catalysts under severe conditions," *Renewable Energy*, vol. 42, pp. 212-216, 2012.
- [30] D. A. Wood, C. Nwaoha, and B. F. Towler, "Gas-to-liquids (GTL): A review of an industry offering several routes for monetizing natural gas," *Journal of Natural Gas Science and Engineering*, vol. 9, pp. 196-208, 2012.
- [31] K. Arno de, "Small-Scale Fischer-Tropsch Gas-to-Liquids Facilities," in *Fischer-Tropsch Synthesis, Catalysts, and Catalysis*, ed: CRC Press, 2016, pp. 379-402.
- [32] A. de Klerk, *Fischer-Tropsch Refining*. Weinheim: Wiley-VCH Verlag & Co. KGaA, 2012.
- [33] "Gas-To-Liquid (GTL) Technology Assessment in support of AE02013," U.S. Energy Information Administration 2013.

- [34] A. E. Outlook, "Energy Information Administration," *Department of Energy*, 2014.
- [35] M. Scott, "Engineering Economic Analysis Guide: Liquid Fuels Technologies," U.S. Energy Information Administration 2015.
- [36] R. D. Soumitra, C. L. Stephen, J. R. Heinz, and D. Matthew, "Commercializing an Advanced Fischer-Tropsch Synthesis Technology," in *Fischer-Tropsch Synthesis, Catalysts, and Catalysis*, ed: CRC Press, 2016, pp. 361-378.
- [37] M. E. Dry, J. R. A. Anderson, and M. Boudart, "Catalysis: Science and Technology," p. 159, 1981.
- [38] H. Schulz, G. Schaub, M. Claeys, and T. Riedel, "Transient initial kinetic regimes of Fischer-Tropsch synthesis," *Applied Catalysis A: General*, vol. 186, pp. 215-227, 1999.
- [39] R. Deverell and M. Yu, "Long Run Commodity Prices: Where do we stand?," Credit Suisse 27 July, 2011 2011.
- [40] Z. Liu, S. Shi, and Y. Li, "Coal liquefaction technologies—Development in China and challenges in chemical reaction engineering," *Chemical Engineering Science*, vol. 65, pp. 12-17, 2010.
- [41] T. G. Kreutz, E. D. Larson, G. Liu, and R. H. Williams, "Fischer-Tropsch fuels from coal and biomass," in *25th Annual International Pittsburgh Coal Conference*, 2008.
- [42] A. de Klerk and E. Furimsky, *Catalysis in the Refining of Fischer-Tropsch Syncrude*: Royal Society of Chemistry, 2010.
- [43] B. Bao, M. M. El-Halwagi, and N. O. Elbashir, "Simulation, integration, and economic analysis of gas-to-liquid processes," *Fuel Processing Technology*, vol. 91, pp. 703-713, 2010.
- [44] M. Sudiro and A. Bertucco, "Production of synthetic gasoline and diesel fuel by alternative processes using natural gas and coal: Process simulation and optimization," *Energy*, vol. 34, pp. 2206-2214, 2009.
- [45] L. Sehabiague, O. Basha, and B. I. Morsi, "Recycling of Tail Gas in Fischer-Tropsch Bubble Column Slurry Reactor and its Impact on the Coal-to-Liquid Process," presented at the Proceedings of the 30th Annual International Pittsburgh Coal Conference, Beijing, China, 2013.

- [46] L. Sehabiague, "Modeling, Scaleup and Optimization of Slurry Bubble Column Reactors for Fischer-Tropsch Synthesis," Doctoral Dissertation, Department of Chemical and Petroleum Engineering, University of Pittsburgh, 2012.
- [47] R. Chedid, M. Kobrosly, and R. Ghajar, "The potential of gas-to-liquid technology in the energy market: The case of Qatar," *Energy Policy*, vol. 35, pp. 4799-4811, 2007.
- [48] D. Gray, A. Elsayy, G. Tomlinson, G. J. Stiegel, and R. D. Srivastava, *Proceedings of the DOE Liquefaction Contractors' Review Meeting*, p. 344, 1991.
- [49] J. Chang, L. Bai, B. Teng, R. Zhang, J. Yang, Y. Xu, H. Xiang, and Y. Li, "Kinetic modeling of Fischer-Tropsch synthesis over catalyst in slurry phase reactor," *Chemical Engineering Science*, vol. 62, pp. 4983-4991, 2007.
- [50] E. S. Lox and G. F. Froment, "Kinetics of the Fischer-Tropsch reaction on a precipitated promoted iron catalyst. 2. Kinetic modeling," *Industrial & Engineering Chemistry Research*, vol. 32, pp. 71-82, 1993/01/01 1993.
- [51] E. S. Lox and G. F. Froment, "Kinetics of the Fischer-Tropsch reaction on a precipitated promoted iron catalyst. 1. Experimental procedure and results," *Industrial & Engineering Chemistry Research*, vol. 32, pp. 61-70, 1993/01/01 1993.
- [52] Y.-N. Wang, Y.-Y. Xu, H.-W. Xiang, Y.-W. Li, and B.-J. Zhang, "Modeling of Catalyst Pellets for Fischer-Tropsch Synthesis," *Industrial & Engineering Chemistry Research*, vol. 40, pp. 4324-4335, 2001/10/01 2001.
- [53] B. Todic, T. Bhatelia, G. F. Froment, W. Ma, G. Jacobs, B. H. Davis, and D. B. Bukur, "Kinetic Model of Fischer-Tropsch Synthesis in a Slurry Reactor on Co-Re/Al₂O₃ Catalyst," *Industrial & Engineering Chemistry Research*, vol. 52, pp. 669-679, 2013/01/16 2012.
- [54] Y. N. Wang, Y. Y. Xu, Y. W. Li, Y. L. Zhao, and B. J. Zhang, "Heterogeneous modeling for fixed-bed Fischer-Tropsch synthesis: Reactor model and its applications," *Chemical Engineering Science*, vol. 58, pp. 867-875, 2003.
- [55] G. Q. Yang and L. S. Fan, "Axial liquid mixing in high-pressure bubble columns," *AIChE Journal*, vol. 49, pp. 1995-2008, 2003.
- [56] G. P. Van der Laan, A. A. C. M. Beenackers, and R. Krishna, "Multicomponent reaction engineering model for Fe-catalyzed Fischer-Tropsch synthesis in commercial scale slurry bubble column reactors," *Chemical Engineering Science*, vol. 54, pp. 5013-5019, 1999.

- [57] C. Satterfield and R. Hanlon, "Effect of water on the iron-catalyzed Fischer-Tropsch synthesis," ... *product research and ...*, pp. 407-414, 1986.
- [58] R. B. Anderson, *Catalysis* vol. 4. New York: P. H. Emmet 1956.
- [59] G. A. Huff Jr. and C. N. Satterfield, "Intrinsic Kinetics of the Fischer-Tropsch Synthesis on a Reduced Fused-Magnetite Catalyst," *Industrial & Engineering Chemistry Process Design and Development*, vol. 23, pp. 696-705, 1984.
- [60] S. Ledakowicz, H. Nettelhoff, R. Kokuun, and W. D. Deckwer, "Kinetics of the Fischer-Tropsch synthesis in the slurry phase on a potassium promoted iron catalyst," *Industrial & Engineering Chemistry Process Design and Development*, vol. 24, pp. 1043-1049, 1985/10/01 1985.
- [61] F. G. Botes and B. B. Breman, "Development and Testing of a New Macro Kinetic Expression for the Iron-Based Low-Temperature Fischer-Tropsch Reaction," *Industrial & Engineering Chemistry Research*, vol. 45, pp. 7415-7426, 2006/10/01 2006.
- [62] L.-P. Zhou, X. Hao, J.-H. Gao, Y. Yang, B.-S. Wu, J. Xu, Y.-Y. Xu, and Y.-W. Li, "Studies and Discriminations of the Kinetic Models for the Iron-Based Fischer-Tropsch Catalytic Reaction in a Recycle Slurry Reactor," *Energy & Fuels*, vol. 25, pp. 52-59, 2011/01/20 2010.
- [63] B. W. Wojciechowski, "The Kinetics of the Fischer-Tropsch Synthesis," *Catalysis Reviews*, vol. 30, pp. 629-702, 1988/12/01 1988.
- [64] G. P. Van Der Laan and A. A. C. M. Beenackers, "Kinetics and Selectivity of the Fischer-Tropsch Synthesis: A Literature Review," *Catalysis Reviews*, vol. 41, pp. 255-318, 1999/01/10 1999.
- [65] R. Zennaro, M. Tagliabue, and C. H. Bartholomew, "Kinetics of Fischer-Tropsch synthesis on titania-supported cobalt," *Catalysis Today*, vol. 58, pp. 309-319, 2000.
- [66] T. Das, W. Conner, J. Li, and G. Jacobs, "Fischer-Tropsch synthesis: Kinetics and effect of water for a CO/SiO₂ catalyst," *Energy & ...*, pp. 1430-1439, 2005.
- [67] A. Outi, I. Rautavuoma, and H. S. van der Baan, "Kinetics and mechanism of the Fischer-Tropsch hydrocarbon synthesis on a cobalt on alumina catalyst," *Applied Catalysis*, vol. 1, pp. 247-272, 1981.
- [68] B. Sarup and B. W. Wojciechowski, "Studies of the Fischer-Tropsch synthesis on a cobalt catalyst II. Kinetics of carbon monoxide conversion to methane and to higher hydrocarbons," *The Canadian Journal of Chemical Engineering*, vol. 67, pp. 62-74, 1989.

- [69] I. C. Yates and C. N. Satterfield, "Intrinsic kinetics of the Fischer-Tropsch synthesis on a cobalt catalyst," *Energy & Fuels*, vol. 5, pp. 168-173, 1991/01/01 1991.
- [70] F. G. Botes, B. van Dyk, and C. McGregor, "The Development of a Macro Kinetic Model for a Commercial Co/Pt/Al₂O₃ Fischer-Tropsch Catalyst," *Industrial & Engineering Chemistry Research*, vol. 48, pp. 10439-10447, 2009/12/02 2009.
- [71] J. van de Loosdrecht, F. G. Botes, I. M. Ciobica, A. Ferreira, P. Gibson, D. J. Moodley, A. M. Saib, J. L. Visagie, C. J. Weststrate, and J. W. Niemantsverdriet, "7.20 - Fischer-Tropsch Synthesis: Catalysts and Chemistry," in *Comprehensive Inorganic Chemistry II (Second Edition)*, J. Reedijk and K. Poepelmeier, Eds., ed Amsterdam: Elsevier, 2013, pp. 525-557.
- [72] J. Gracia, F. Prinsloo, and J. W. Niemantsverdriet, "Mars-van Krevelen-like Mechanism of CO Hydrogenation on an Iron Carbide Surface," *Catalysis letters*, vol. 133, pp. 257-261, 2009/12/01 2009.
- [73] L.-J. Deng, C.-F. Huo, X.-W. Liu, X.-H. Zhao, Y.-W. Li, J. Wang, and H. Jiao, "Density Functional Theory Study on Surface C_xH_y Formation from CO Activation on Fe₃C(100)," *The Journal of Physical Chemistry C*, vol. 114, pp. 21585-21592, 2010/12/16 2010.
- [74] J. R. Inga, "Scaleup and Scaledown of Slurry Reactors: A New Methodology," ed, 1997.
- [75] W.-D. Deckwer, Y. Louisi, A. Zaidi, and M. Ralek, "Hydrodynamic Properties of the Fischer-Tropsch Slurry Process," *Industrial & Engineering Chemistry Process Design and Development*, vol. 19, pp. 699-708, 1980/10/01 1980.
- [76] D. B. Bukur, S. A. Patel, and J. G. Daly, "Gas holdup and solids dispersion in a three-phase slurry bubble column," *AIChE Journal*, vol. 36, pp. 1731-1735, 1990.
- [77] R. Krishna, J. W. A. D. Swart, J. Ellenberger, G. B. Martina, and C. Maretto, "Gas Holdup in Slurry Bubble Columns: Effect of Column Diameter and Slurry Concentration," *AIChE Journal*, vol. 43, pp. 311-316, 1997.
- [78] C. O. Vandu and R. Krishna, "Volumetric mass transfer coefficients in slurry bubble columns operating in the churn-turbulent flow regime," *Chemical Engineering and Processing: Process Intensification*, vol. 43, pp. 987-995, 2004.
- [79] K.-J. Woo, S.-H. Kang, S.-M. Kim, J.-W. Bae, and K.-W. Jun, "Performance of a slurry bubble column reactor for Fischer-Tropsch synthesis: Determination of optimum condition," *Fuel Processing Technology*, vol. 91, pp. 434-439, 2010.

- [80] A. Behkish, Z. Men, J. R. Inga, and B. I. Morsi, "Mass transfer characteristics in a large-scale slurry bubble column reactor with organic liquid mixtures," *Chemical Engineering Science*, vol. 57, pp. 3307-3324, 2002.
- [81] L. Sehabiague and B. I. Morsi, "Hydrodynamic and Mass Transfer Characteristics in a Large-Scale Slurry Bubble Column Reactor for Gas Mixtures in Actual Fischer-Tropsch Cuts," *International Journal of Chemical Reactor Engineering*, vol. 11, pp. 83-102, 2013.
- [82] H. Hikita, S. Asai, and K. Tanigawa, "Gas hold-up in bubble columns," *The Chemical Engineering Journal*, vol. 20, pp. 59-67, 1980.
- [83] K. Akita and F. Yoshida, "Gas Holdup and Volumetric Mass Transfer Coefficient in Bubble Columns. Effects of Liquid Properties," *Industrial & Engineering Chemistry Process Design and Development*, vol. 12, pp. 76-80, 1973.
- [84] W. D. Deckwer and R. W. Field, *Bubble column reactors*: Wiley, 1992.
- [85] Y. T. Shah, B. G. Kelkar, S. P. Godbole, and W.-D. Deckwer, "Design parameters estimations for bubble column reactors," *AIChE Journal*, vol. 28, pp. 353-379, 1982.
- [86] W. D. Deckwer, R. Burckhart, and G. Zoll, "Mixing and mass transfer in tall bubble columns," *Chemical Engineering Science*, vol. 29, pp. 2177-2188, 1974.
- [87] R. Krishna and J. Ellenberger, "Gas holdup in bubble column reactors operating in the churn-turbulent flow regime," *AIChE Journal*, vol. 42, pp. 2627-2634, 1996.
- [88] K. N. Clark, "The effect of high pressure and temperature on phase distributions in a bubble column," *Chemical Engineering Science*, vol. 45, pp. 2301-2307, 1990.
- [89] A. Behkish, "Hydrodynamic and Mass Transfer Parameters in Large-Scale Slurry Bubble Column Reactors," ed, 2004.
- [90] P. M. Wilkinson and L. v. Dlerendonck, "Pressure and Gas density effects on bubble break-up and gas hold-up in bubble columns," *Chemical Engineering Science*, vol. 45, pp. 2309-2315, 1990.
- [91] P. Jiang, T.-J. Lin, X. Luo, and L.-S. Fan, "Flow visualization of high pressure (21 MPa) bubble column: bubble characteristics," *Chemical engineering research & design*, vol. 73, pp. 269-274, 1995.
- [92] P. Therning and A. Rasmuson, "Liquid dispersion, gas holdup and frictional pressure drop in a packed bubble column at elevated pressures," *Chemical Engineering Journal*, vol. 81, pp. 331-335, 2001.

- [93] M. Oyevaar, T. De La Rie, C. Van der Sluijs, and K. Westerterp, "Interfacial areas and gas hold-ups in bubble columns and packed bubble columns at elevated pressures," *Chemical Engineering and Processing: Process Intensification*, vol. 26, pp. 1-14, 1989.
- [94] G. Smith, B. Gamblin, and D. Newton, "X-ray imaging of slurry bubble column reactors: the effects of system pressure and scale," *International Journal of Multiphase Flow*, vol. 22, pp. 102-102, 1996.
- [95] Y. Soong, F. W. Harke, I. K. Gamwo, R. R. Schehl, and M. F. Zaroachak, "Hydrodynamic study in a slurry-bubble-column reactor," *Catalysis Today*, vol. 35, pp. 427-434, 1997.
- [96] S. S. öztürk, A. Schumpe, and W. D. Deckwer, "Organic liquids in a bubble column: Holdups and mass transfer coefficients," *AIChE Journal*, vol. 33, pp. 1473-1480, 1987.
- [97] D. Bhaga, B. B. Pruden, and M. E. Weber, "Gas holdup in a bubble column containing organic liquid mixtures," *The Canadian Journal of Chemical Engineering*, vol. 49, pp. 417-420, 1971.
- [98] D. Stegeman, P. A. Knop, A. J. G. Wijnands, and K. R. Westerterp, "Interfacial Area and Gas Holdup in a Bubble Column Reactor at Elevated Pressures," *Industrial & Engineering Chemistry Research*, vol. 35, pp. 3842-3847, 1996/01/01 1996.
- [99] S. P. Godbole, A. Schumpe, Y. T. Shah, and N. L. Carr, "Hydrodynamics and Mass Transfer in Non-Newtonian Solutions in a Bubble Column," *AIChE Journal*, vol. 30, pp. 213-220, 1984.
- [100] A. Yasunishi, M. Fukuma, and K. Muroyama, "Measurement of behavior of gas bubbles and gas holdup in a slurry bubble column by a dual electroresistivity probe method," *Journal of Chemical Engineering of Japan*, vol. 19, pp. 444-449, 1986 1986.
- [101] F. Neme, L. Coppola, and U. Böhm, "Gas holdup and mass transfer in solid suspended bubble columns in presence of structured packings," *Chemical Engineering & Technology*, vol. 20, pp. 297-303, 1997.
- [102] P. M. Wilkinson, A. P. Spek, and L. L. van Dierendonck, "Design parameters estimation for scale-up of high-pressure bubble columns," *AIChE Journal*, vol. 38, pp. 544-554, 1992.
- [103] J. H. J. Kluytmans, B. F. M. Kuster, and J. C. Schouten, "Gas Holdup in a Slurry Bubble Column: Influence of Electrolyte and Carbon Particles," *Industrial & Engineering Chemistry Research*, vol. 40, pp. 5326-5333, 2001.
- [104] J. R. Crabtree and J. Bridgwater, "Bubble coalescence in viscous liquids," *Chemical Engineering Science*, vol. 26, pp. 839-851, 1971.

- [105] L. Fan, G. Yang, D. Lee, K. Tsuchiya, and X. Luo, "Some aspects of high-pressure phenomena of bubbles in liquids and liquid–solid suspensions," *Chemical Engineering Science*, vol. 54, pp. 4681-4709, 1999.
- [106] S. Kara, B. G. Kelkar, Y. T. Shah, and N. L. Carr, "Hydrodynamics and axial mixing in a three-phase bubble column," *Industrial & Engineering Chemistry Process Design and Development*, vol. 21, pp. 584-594, 1982.
- [107] K. Koide, A. Takazawa, M. Komura, and H. Matsunaga, "Gas Holdup and Volumetric Liquid-Phase Mass Transfer Coefficient in Solid-Suspended Bubble Columns," *Journal of Chemical Engineering of Japan*, vol. 17, pp. 459-466, 1984.
- [108] H. Kojima, H. Anjyo, and Y. Mochizuki, "Axial mixing in bubble column with suspended solid particles," *Journal of Chemical Engineering of Japan*, vol. 19, pp. 232-234, 1986.
- [109] J. De Swart and R. Krishna, "Influence of particles concentration on the hydrodynamics of bubble column slurry reactors," *Chemical Engineering Research and Design*, vol. 73, pp. 308-313, 1995.
- [110] R. Krishna, J. M. van Baten, M. I. Urseanu, and J. Ellenberger, "Design and scale up of a bubble column slurry reactor for Fischer-Tropsch synthesis," *Chemical Engineering Science*, vol. 56, pp. 537-545, 2001.
- [111] D. J. Lee, X. Luo, and L.-S. Fan, "Gas disengagement technique in a slurry bubble column operated in the coalesced bubble regime," *Chemical Engineering Science*, vol. 54, pp. 2227-2236, 1999.
- [112] B. Gandhi, A. Prakash, and M. a. Bergougnou, "Hydrodynamic behavior of slurry bubble column at high solids concentrations," *Powder Technology*, vol. 103, pp. 80-94, 1999.
- [113] S. C. Saxena, N. S. Rao, and P. R. Thimmapuram, "Gas phase holdup in slurry bubble columns for two- and three-phase systems," *The Chemical Engineering Journal*, vol. 49, pp. 151-159, 1992.
- [114] A. Colmenares, M. Sevilla, J. J. Goncalves, and D. González-Mendizabal, "Fluid-dynamic experimental study in a bubble column with internals," *International Communications in Heat and Mass Transfer*, vol. 28, pp. 389-398, 2001.
- [115] B. N. Thorat, K. Kataria, A. V. Kulkarni, and J. B. Joshi, "Pressure Drop Studies in Bubble Columns," *Industrial & Engineering Chemistry Research*, vol. 40, pp. 3675-3688, 2001/08/01 2001.

- [116] F. Yamashita, "Effect of Clear Liquid Height and Gas Inlet Height on Gas Holdup in a Bubble Column," *JOURNAL OF CHEMICAL ENGINEERING OF JAPAN*, vol. 31, pp. 285-288, 1998.
- [117] F. Kastanek, J. Zahradnik, J. Kratochvil, and J. Cermak, "Modeling of large-scale bubble column reactors for non-ideal gas–liquid systems," vol. 1, ed: Wiley, 1984, p. 330.
- [118] J. R. Fair, A. J. Lambright, and J. W. Andersen, "Heat Transfer and Gas Holdup in a Sparged Contactor," *Industrial & Engineering Chemistry Research Process Design and Development*, vol. 1, pp. 33-36, 1962/01/01 1962.
- [119] F. Yoshida and K. Akita, "Performance of gas bubble columns: Volumetric liquid–phase mass transfer coefficient and gas holdup," *AIChE Journal*, vol. 11, pp. 9-13, 1965.
- [120] L. Z. Pino, R. B. Solari, S. Siquier, L. A. Estevez, M. M. Yepez, and A. E. Saez, "Effect of Operating Conditions on Gas Holdup in Slurry Bubble Columns with a Foaming Liquid," *Chemical Engineering Communications*, vol. 117, pp. 367-382, 1992.
- [121] I. G. Reilly, D. S. Scott, T. J. W. Debruijn, and D. Macintyre, "The Role of Gas Phase Momentum in Determining Gas Holdup and Hydrodynamic Flow Regimes in Bubble Column Operations," *Canadian Journal of Chemical Engineering*, vol. 72, pp. 3-12, 1994.
- [122] J. S. Smith, L. F. Burns, K. T. Valsaraj, and L. J. Thibodeaux, "Bubble Column Reactors for Wastewater Treatment. 2. The Effect of Sparger Design on Sublation Column Hydrodynamics in the Homogeneous Flow Regime†," *Industrial & Engineering Chemistry Research*, vol. 35, pp. 1700-1710, 1996/01/01 1996.
- [123] K. Tsuchiya, M. H. Haryono, T. Tomida, H. Hatano, and H. Oaki, "Performance of a Hollow-Fiber Spiral Disk for Effective Gas Dispersion toward High Mass Transfer Rate†," *Industrial & Engineering Chemistry Research*, vol. 35, pp. 613-620, 1996/01/01 1996.
- [124] A. Elgozali, V. Linek, M. Fialová, O. Wein, and J. Zahradník, "Influence of viscosity and surface tension on performance of gas–liquid contactors with ejector type gas distributor," *Chemical Engineering Science*, vol. 57, pp. 2987-2994, 8// 2002.
- [125] A. Mersmann, "Design and scale-up of bubble and spray columns," *Ger. Chem. Eng.*, vol. 1, pp. 1-11, 1978.
- [126] L. Sehabiague and B. I. Morsi, "Modeling and Simulation of a Fischer–Tropsch Slurry Bubble Column Reactor Using Different Kinetic Rate Expressions for Iron and Cobalt Catalysts," *Int. J. of Chem. Rctr. Eng.*, vol. 11, pp. 309-330, 2013.

- [127] P. Zehner, "Mehrphasenströmungen in Gas-Flüssigkeits-Reaktoren," *Dechema Monogr.*, vol. 114, pp. 215-233, 1989.
- [128] S. H. Eissa, M. M. El-Halwagi, and M. A. Saleh, "Axial and Radial Mixing in a Cocurrent Bubble Column," *Industrial & Engineering Chemistry Process Design and Development*, vol. 10, pp. 31-36, 1971/01/01 1971.
- [129] T. Reith, S. Renken, and B. A. Israël, "Gas hold-up and axial mixing in the fluid phase of bubble columns," *Chemical Engineering Science*, vol. 23, pp. 619-629, 1968.
- [130] M. V. Kantak, S. A. Shetty, and B. G. Kelkar, "LIQUID PHASE BACKMIXING IN BUBBLE COLUMN REACTORS—A NEW CORRELATION," *Chemical Engineering Communications*, vol. 127, pp. 23-34, 1994/01/01 1994.
- [131] F. Camacho Rubio, A. Sánchez Mirón, M. C. Cerón García, F. García Camacho, E. Molina Grima, and Y. Chisti, "Mixing in bubble columns: a new approach for characterizing dispersion coefficients," *Chemical Engineering Science*, vol. 59, pp. 4369-4376, 2004.
- [132] L. S. Pozin, M. E. Aérov, and T. A. Bystrova, "Study of Turbulent Diffusion Coefficients in Bubble-Bed Liquid Phases," *Theoretical Foundations of Chemical Engineering*, vol. 3, p. 714, 1969.
- [133] J. F. Walter and H. W. Blanch, "Liquid circulation patterns and their effect on gas holdup and axial mixing in bubble columns," *Chemical Engineering Communications*, vol. 19, pp. 243-262, 1983/01/01 1983.
- [134] T. Miyauchi, S. Furusaki, S. Morooka, and Y. Ikeda, "Transport phenomena and reaction in fluidized catalyst beds," *Advances in Chemical Engineering*, vol. 11, pp. 275-448, 1981.
- [135] L. S. Fan and K. Tsuchiya, *Bubble wake dynamics in liquids and liquid-solid suspensions*: Butterworth-Heinemann, 1990.
- [136] L. S. Fan, *Gas-liquid-solid fluidization engineering*: Butterworths, 1989.
- [137] J. Chaouki, F. Larachi, and P. Dudukovic, *Non-Invasive Monitoring of Multiphase Flows*: Elsevier Science, 1997.
- [138] D. Adkins, K. Shollenberger, T. O'Hern, and J. Torczynski, "Pressure effects on bubble column flow characteristics," in *ANS Proceedings of the 1996 National Heat Transfer Conference*, 1996, pp. 318-325.

- [139] S. B. Kumar, N. Devanathan, D. Moslemian, and M. P. Dudukovic, "Effect of scale on liquid recirculation in bubble columns," *Chemical Engineering Science*, vol. 49, pp. 5637-5652, 1994.
- [140] K. Ueyama and T. Miyauchi, "Properties of recirculating turbulent two phase flow in gas bubble columns," *AIChE Journal*, vol. 25, pp. 258-266, 1979.
- [141] R. G. Rice and N. W. Geary, "Prediction of liquid circulation in viscous bubble columns," *AIChE Journal*, vol. 36, pp. 1339-1348, 1990.
- [142] G. R. Rigby and C. E. Capes, "Bed expansion and bubble wakes in three-phase fluidization," *The Canadian Journal of Chemical Engineering*, vol. 48, pp. 343-348, 1970.
- [143] S. Morooka, K. Uchida, and Y. Kato, "Recirculating turbulent flow of liquid in gas-liquid-solid fluidized bed," *Journal of Chemical Engineering of Japan*, vol. 15, pp. 29-34, 1982.
- [144] C. Wu, K. Suddard, and M. H. Al-dahhan, "Bubble dynamics investigation in a slurry bubble column," *AIChE Journal*, vol. 54, pp. 1203-1212, 2008.
- [145] J. W. A. De Swart, R. E. Van Vilet, and R. KRishna, "Size, Structure and Dynamics of "Large" Bubbles in a Two-Dimensional Slurry Bubble Column," *Chemical Engineering Science*, vol. 51, pp. 4619-4629, 1996.
- [146] J. Ellenberger and R. Krishna, "A unified approach to the scale-up of gas—solid fluidized bed and gas—liquid bubble column reactors," *Chemical Engineering Science*, vol. 49, pp. 5391-5411, 1994.
- [147] R. Krishna and J. Ellenberger, "A unified approach to the scale-up of “fluidized” multiphase reactors," *Trans IChemE*, vol. 73, pp. 217-221, 1995.
- [148] D. Bukur, "Some comments on models for Fischer-Tropsch reaction in slurry bubble column reactors," *Chemical Engineering Science*, vol. 38, pp. 441-446, 1983.
- [149] D. Bukur and V. R. Kumar, "Effect of catalyst dispersion on performance of slurry bubble column reactors," *Chemical engineering science*, vol. 41, pp. 1435-1444, 1986.
- [150] N. Rados, M. H. Al-Dahhan, and M. P. Dudukovic, "Modeling of the Fischer-Tropsch synthesis in slurry bubble column reactors," *Catalysis Today*, vol. 79-80, pp. 211-218, 2003.
- [151] L. Sehabiague, R. Lemoine, A. Behkish, Y. J. Heintz, M. Sanoja, R. Oukaci, and B. I. Morsi, "Modeling and optimization of a large-scale slurry bubble column reactor for

- producing 10,000bbl/day of Fischer–Tropsch liquid hydrocarbons," *Journal of the Chinese Institute of Chemical Engineers*, vol. 39, pp. 169-179, 2008.
- [152] C. Maretto and R. Krishna, "Modelling of a bubble column slurry reactor for Fischer-Tropsch synthesis," *Catalysis Today*, vol. 52, pp. 279-289, 1999.
- [153] J. W. a. de Swart and R. Krishna, "Simulation of the transient and steady state behaviour of a bubble column slurry reactor for Fischer–Tropsch synthesis," *Chemical Engineering and Processing: Process Intensification*, vol. 41, pp. 35-47, 2002.
- [154] Y. Zheng and T. Gu, "Analytical solution to a model for the startup period of fixed-bed reactors," *Chemical engineering science*, vol. 51, pp. 3773-3779, 1996.
- [155] I. Iliuta, F. Larachi, and D. Desvigne, "Multicompartment hydrodynamic model for slurry bubble columns," *Chemical Engineering Science*, vol. 63, pp. 3379-3399, 2008.
- [156] G. Lozano-Blanco, J. W. Thybaut, K. Surla, P. Galtier, and G. B. Marin, "Simulation of a slurry-bubble column reactor for Fischer-Tropsch synthesis using single-event microkinetics," *AIChE Journal*, vol. 55, pp. 2159-2170, 2009.
- [157] V. R. Ahón, E. F. Costa, J. E. P. Monteagudo, C. E. Fontes, E. C. Biscaia, and P. L. C. Lage, "A comprehensive mathematical model for the Fischer–Tropsch synthesis in well-mixed slurry reactors," *Chemical Engineering Science*, vol. 60, pp. 677-694, 2005.
- [158] Y. Wang, W. Fan, Y. Liu, Z. Zeng, X. Hao, M. Chang, C. Zhang, Y. Xu, H. Xiang, and Y. Li, "Modeling of the Fischer–Tropsch synthesis in slurry bubble column reactors," *Chemical Engineering and Processing: Process Intensification*, vol. 47, pp. 222-228, 2008.
- [159] J. W. A. de Swart and R. Krishna, "Simulation of the transient and steady state behavior of a bubble column slurry reactor for Fisher-Tropsch synthesis," *Chemical Engineering and Processing*, vol. 41, pp. 35-47, 2002.
- [160] I. Iliuta, F. Larachi, J. Anfray, N. Dromard, and D. Schweich, "Multicomponent multicompartment model for Fischer-Tropsch SCBR," *AIChE Journal*, vol. 53, pp. 2062-2083, 2007.
- [161] Y. T. Shah, *Gas-liquid-solid reactor design*: McGraw-Hill International Book Co., 1979.
- [162] G. A. L'Homme, *Chemical Engineering of Gas-liquid-solid Catalyst Reactions: Proceedings of an International Symposium*. Liege: CEBEDOC, 1979.
- [163] R. V. Chaudhari and P. A. Ramachandran, "Three phase slurry reactors," *AIChE Journal*, vol. 26, pp. 177-201, 1980.

- [164] S. Sookai, P. Langenhoven, and T. Shingles, "Scale-up and commercial reactor fluidization related experience with Synthol, gas to liquid fuel, dense phase fluidized bed reactors," *Fluidization X*, pp. 621-628, 2001.
- [165] J. Fox, III, "Fischer-Tropsch reactor selection," *Catalysis letters*, vol. 7, pp. 281-292, 1990/01/01 1990.
- [166] J. Fox, B. Degen, G. Cady, F. Deslate, R. Summers, A. Akgerman, and J. Smith, "Slurry reactor design studies," Bechtel Group, Inc., San Francisco, CA (USA)1990.
- [167] B. Jager and R. Espinoza, "Advances in low temperature Fischer-Tropsch synthesis," *Catalysis Today*, vol. 23, pp. 17-28, 1995.
- [168] P. L. Mills, J. R. Turner, P. A. Ramachandran, and M. P. Dudukovic, *Three-Phase Sparged Reactors; The Fischer-Tropsch Synthesis in Slurry Bubble Column Reactors: Analysis of reactor Performance Using the Axial Dispersion Model* vol. 8. Amsterdam, The Netherlands: Gordon and Breach Science Publishers, 1996.
- [169] X. Peng, B. Toseland, and P. Tijm, "Kinetic understanding of the chemical synergy under LPDME TM conditions—once-through applications," *Chemical Engineering Science*, vol. 54, pp. 2787-2792, 1999.
- [170] S. Saxena, "Bubble column reactors and Fischer-Tropsch synthesis," *Catalysis Reviews*, vol. 37, pp. 227-309, 1995.
- [171] R. Clift, J. R. Grace, and M. E. Weber, *Bubbles, Drops, and Particles*. New York: Academic Press, 1978.
- [172] R. Krishna, J. W. A. De Swart, D. E. Hennephof, J. Ellenberger, and H. C. J. Hoefsloot, "Influence of increased gas density on hydrodynamics of bubble-column reactors," *AIChE Journal*, vol. 40, pp. 112-119, 1994.
- [173] T. J. Lin, K. Tsuchiya, and L.-S. Fan, "On the measurements of regime transition in high-pressure bubble columns," *The Canadian Journal of Chemical Engineering*, vol. 77, pp. 370-374, 1999.
- [174] T. J. Lin, K. Tsuchiya, and L. S. Fan, "Bubble flow characteristics in bubble columns at elevated pressure and temperature," *AIChE Journal*, vol. 44, pp. 545-560, 1998.
- [175] D. Vermeer and R. Krishna, "Hydrodynamics and mass transfer in bubble columns in operating in the churn-turbulent regime," *Industrial & Engineering Chemistry ...*, pp. 475-482, 1981.

- [176] D. Stern, A. T. Bell, and H. Heinemann, "Effects of Mass Transfer on the Performance of Slurry Reactors used for Fischer-Tropsch Synthesis," *Chemical Engineering Science*, vol. 38, pp. 597-605, 1983.
- [177] J. R. Inga and B. I. Morsi, "Effect of catalyst loading on gas-liquid mass transfer in a slurry reactor: A statistical experimental approach," *The Canadian Journal of Chemical Engineering*, vol. 75, pp. 872-881, 1997.
- [178] R. Lemoine, A. Behkish, and B. I. Morsi, "Hydrodynamic and Mass Transfer Characteristics in Organic Liquid Mixtures in a Large-Scale Bubble Column Reactor for the Toluene Oxidation Process," *Industrial & Engineering Chemistry Process Design and Development*, vol. 43, pp. 6195-6212, 2004.
- [179] R. Lemoine and B. I. Morsi, "Hydrodynamic and mass transfer parameters in agitated reactors part II: Gas-holdup, sauter mean bubble diameters, volumetric mass transfer coefficients, gas-liquid interfacial areas, and liquid-side mass transfer coefficients," *International Journal of Chemical Reactor Engineering*, vol. 3, p. A20, 2005.
- [180] G. A. Huff and C. N. Satterfield, "Intrinsic kinetics of the Fischer-Tropsch synthesis on a reduced fused-magnetite catalyst," *Industrial & Engineering Chemistry Process Design and Development*, vol. 23, pp. 696-705, 1984.
- [181] J. R. Inga and B. I. Morsi, "A Novel Approach for the Assessment of the Rate-Limiting Step in Fischer-Tropsch Slurry Process," *Energy & Fuels*, vol. 10, pp. 566-572, 1996/01/01 1996.
- [182] M. Letzel and J. Schouten, "Effect of gas density on large • bubble holdup in bubble column reactors," *AIChE Journal*, vol. 44, pp. 2333-2336, 1998.
- [183] U. Jordan, K. Terasaka, G. Kundu, and a. Schumpe, "Mass Transfer in High-Pressure Bubble Columns with Organic Liquids," *Chemical Engineering & Technology*, vol. 25, pp. 262-265, 2002.
- [184] U. Jordan and A. Schumpe, "The gas density effect on mass transfer in bubble columns with organic liquids," *Chemical engineering science*, vol. 56, pp. 6267-6272, 2001.
- [185] G. Grund, A. Schumpe, and W. D. Deckwer, "Gas-Liquid Mass Transfer in a Bubble Column with Organic Liquids," *Chemical Engineering Science*, vol. 47, pp. 3509-3516, 1992.
- [186] T. Sauer and D. Hempel, "Fluid dynamics and mass transfer in a bubble column with suspended particles," *Chemical engineering & technology*, vol. 10, pp. 180-189, 1987.

- [187] G. Hughmark, "Holdup and mass transfer in bubble columns," *Industrial & Engineering Chemistry Process Design and Development*, vol. 6, pp. 218-220, 1967.
- [188] R. Zou, X. Jiang, B. Li, Y. Zu, and L. Zhang, "Studies on gas holdup in a bubble column operated at elevated temperatures," *Industrial & Engineering Chemistry Research*, vol. 27, pp. 1910-1916, 1988.
- [189] S. P. Godbole, "Study of hydrodynamic and mass transfer characteristics of multiphase bubble column reactor," ed, 1983.
- [190] K. Akita and F. Yoshida, "Bubble size, interfacial area, and liquid-phase mass transfer coefficient in bubble columns," *Ind & Engineering Chemistry Process Design and Development*, vol. 13, pp. 84-91, 1974.
- [191] H. Hikita, S. Asai, K. Tanigawa, K. Segawa, and M. Kitao, "The Volumetric Liquid-Phase Mass Transfer Coefficient in Bubble Columns," *The Chemical Engineering Journal*, vol. 22, pp. 61-69, 1981.
- [192] J. H. J. Kluytmans, A. P. Markusse, B. F. M. Kuster, G. B. Marin, and J. C. Schouten, "Engineering aspects of the aqueous noble metal catalysed alcohol oxidation," *Catalysis Today*, vol. 57, pp. 143-155, 2000.
- [193] R. Pohorecki, W. Moniuk, and A. Zdrójkowski, "Hydrodynamics of a bubble column under elevated pressure," *Chemical engineering science*, vol. 54, pp. 5187-5193, 1999.
- [194] M. Jamialahmadi and H. Müller-Steinhagen, "Effect of Solid Particles on Gas Hold-Up in Bubble Columns," *Canadian Journal of Chemical Engineering*, vol. 69, pp. 390-393, 1991.
- [195] B. G. Kelkar and Y. T. Shah, "Hydrodynamics and Axial Mixing in a Three-Phase Bubble Column. Effects of Slurry Properties," *Industrial & Engineering Chemistry Process Design and Development*, vol. 23, pp. 308-313, 1984.
- [196] R. Pohorecki and W. Moniuk, "Hydrodynamics of a pilot plant bubble column under elevated temperature and pressure," *Chemical Engineering Science*, vol. 56, pp. 1167-1174, 2001.
- [197] J. Chabot and H. I. de Lasa, "Gas holdups and bubble characteristics in a bubble column operated at high temperature," *Industrial & Engineering Chemistry Research*, vol. 32, pp. 2595-2601, 1993.
- [198] I. Dewes, A. Kuksal, and A. Schumpe, "Gas density effect on mass transfer in three phase sparged reactors," *Chemical Engineering Research and Design*, vol. 73, pp. 697-700, 1995.

- [199] I. Dewes and A. Schumpe, "Gas density effect on mass transfer in the slurry bubble column," *Chemical engineering science*, vol. 52, pp. 4105-4109, 1997.
- [200] H. Kojima, J. Sawai, and H. Suzuki, "Effect of pressure on volumetric mass transfer coefficient and gas holdup in bubble column," *Chemical engineering science*, vol. 52, pp. 4111-4116, 1997.
- [201] W. Jianping and X. Shonglin, "Local hydrodynamics in a gas-liquid-solid three-phase bubble column reactor," *Chemical Engineering Journal*, vol. 70, pp. 81-84, 1998.
- [202] H. Jin, S. Yang, M. Wang, and R. A. Williams, "Measurement of gas holdup profiles in a gas liquid cocurrent bubble column using electrical resistance tomography," *Flow Measurement and Instrumentation*, vol. 18, pp. 191-196, 2007.
- [203] J. Salvacion and M. Murayama, "Effects of alcohols on gas holdup and volumetric liquid-phase mass transfer coefficient in gel-particle-suspended bubble column.," *Journal of Chemical Engineering of Japan*, vol. 28, pp. 434-442, 1995.
- [204] H. Eickenbusch, P.-O. Brunn, and a. Schumpe, "Mass transfer into viscous pseudoplastic liquid in large-diameter bubble columns," *Chemical Engineering and Processing: Process Intensification*, vol. 34, pp. 479-485, 1995.
- [205] S. Moustiri, G. Hebrard, S. Thakre, and M. Roustan, "A unified correlation for predicting liquid axial dispersion coefficient in bubble columns," *Chemical Engineering Science*, vol. 56, pp. 1041-1047, 2001.
- [206] C. Guy, P. J. Carreau, J. Paris, and P. J. C. C. Guy, J. Paris, "Mixing characteristics and gas hold-up of a bubble column," *Canadian Journal of Chemical Engineering*, vol. 64, pp. 23-35, 1986.
- [207] S. Saxena, N. Rao, and P. Thimmapuram, "Gas phase holdup in slurry bubble columns for two-and three-phase systems," *The Chemical Engineering Journal*, vol. 49, pp. 151-159, 1992.
- [208] W. O'Dowd, D. N. Smith, J. A. Ruether, and S. C. Saxena, "Gas and solids behavior in a baffled and unbaffled slurry bubble column," *AIChE Journal*, vol. 33, pp. 1959-1970, 1987.
- [209] Saxena, S. C. and Chen, Z. D., "Hydrodynamics and heat transfer of baffled and unbaffled slurry bubble column," *Reviews in Chemical Engineering*, vol. 10, pp. 195-400, 1994.
- [210] F. Yamashita, "Effects of vertical pipe and rod internals on gas holdup in bubble columns," *Journal of Chemical Engineering of Japan*, vol. 20, pp. 204-206, 1987.

- [211] S. C. Saxena, N. S. Rao, and P. R. Thimmapuram, "Gas Phase Holdup in Slurry Bubble Column for Two- and Three-Phase Systems," *The Chemical Engineering Journal*, vol. 49, pp. 151-159, 1992.
- [212] S. De, S. Ghosh, R. Parichha, and P. De, "Gas hold-up in two-phase system with internals," *Indian Chemical Engineer*, vol. 41, pp. 112-116, 1999.
- [213] A. Forret, J.-M. Schweitzer, T. Gauthier, R. Krishna, and D. Schweich, "Liquid Dispersion in Large Diameter Bubble Columns, with and without Internals," *The Canadian Journal of Chemical Engineering*, vol. 81, pp. 360-366, 2003.
- [214] Y. Shah, C. Ratway, and H. McIlvried, "Back-mixing characteristics of a bubble column with vertically suspended tubes," *Transactions of the Institution of Chemical Engineers*, vol. 56, pp. 107-112, 1978.
- [215] S. Joseph, "Hydrodynamic and mass transfer characteristics of a bubble column," University of Pittsburgh, 1985.
- [216] L. Caldwell and D. S. Van Vuuren, "On the formation and composition of the liquid phase in Fischer-Tropsch reactors," *Chemical Engineering Science*, vol. 41, pp. 89-96, // 1986.
- [217] A. P. Steynberg and H. G. Nel, "Clean coal conversion options using Fischer-Tropsch technology," *Fuel*, vol. 83, pp. 765-770, 4// 2004.
- [218] G. N. Choi, S. Kramer, S. Tam, and F. JM III, "Design and economics of a Fischer-Tropsch plant for converting natural gas to liquid transportation fuels," in *Fuel and Energy Abstracts*, 1997, pp. 222-222.
- [219] A. P. Steynberg, R. L. Espinoza, B. Jager, and A. C. Vosloo, "High temperature Fischer-Tropsch synthesis in commercial practice," *Applied Catalysis A: General*, vol. 186, pp. 41-54, 10/4/ 1999.
- [220] C. Hulet, P. Clement, P. Tochon, D. Schweich, N. Dromard, and J. Anfray, "Literature review on heat transfer in two-and three-phase bubble columns," *International Journal of Chemical Reactor Engineering*, vol. 7, 2009.
- [221] H. Kölbel and M. Ralek, "The Fischer-Tropsch synthesis in the liquid phase," *Catalysis Reviews Science and Engineering*, vol. 21, pp. 225-274, 1980.
- [222] H. Korte, "Heat transfer in bubble columns with and without internals," PhD Thesis, University of Dortmund, 1987.

- [223] K. Bernemann, "On the hydrodynamics and mixing of the liquid phase in bubble columns with longitudinal tube bundles," PhD Thesis, University of Dortmund, 1989.
- [224] A. K. Pradhan, R. K. Parichha, and P. De, "Gas hold-up in non-newtonian solutions in a bubble column with internals," *The Canadian Journal of Chemical Engineering*, vol. 71, pp. 468-471, 1993.
- [225] F. ç. Larachi, D. Desvigne, L. Donnat, and D. Schweich, "Simulating the effects of liquid circulation in bubble columns with internals," *Chemical Engineering Science*, vol. 61, pp. 4195-4206, 2006.
- [226] K. Bernemann, "Zur Fluidodynamik und zum Vermischungsverhalten der flüssigen Phase in Blasensäulen mit langsangeströmten Rohrbu," Ph.D. thesis, University Dortmund, 1989.
- [227] A. A. Youssef and M. H. Al-Dahhan, "Impact of Internals on the Gas Holdup and Bubble Properties of a Bubble Column," *Industrial & Engineering Chemistry Research*, vol. 48, pp. 8007-8013, 2009/09/02 2009.
- [228] A. Youssef, "Fluid dynamics and scale-up of bubble columns with internals," 2010.
- [229] E. Blass and W. Cornelius, "The residence time distribution of solid and liquid in multistage bubble columns in the cocurrent flow of gas, liquid and suspended solid," *International Journal of Multiphase Flow*, vol. 3, pp. 459-469, 1977.
- [230] A. Kemoun, N. Rados, F. Li, M. H. Al-Dahhan, M. P. Dudukovic', P. L. Mills, T. M. Leib, and J. J. Lerou, "Gas holdup in a trayed cold-flow bubble column," *Chemical Engineering Science*, vol. 56, pp. 1197-1205, 2001.
- [231] K. R. Westerterp, W. P. M. van Swaaij, A. A. C. M. Beenackers, and H. Kramers, *Chemical reactor design and operation*: Wiley, 1984.
- [232] R. Mashelkar and M. Sharma, "Mass transfer in bubble and packed bubble columns," *Transactions of the Institution of Chemical Engineers*, vol. 48, pp. T162-T162, 1970.
- [233] S. N. Palaskar, J. K. De, and A. B. Pandit, "Liquid Phase RTD Studies in Sectionalized Bubble Column," *Chemical Engineering & Technology*, vol. 23, pp. 61-69, 2000.
- [234] S. A. Nosier, "Solid-Liquid Mass Transfer at Gas Sparged Tube Bundles," *Chemical Engineering & Technology*, vol. 26, pp. 1151-1154, 2003.
- [235] J. Alvaré and M. H. Al-Dahhan, "Liquid phase mixing in trayed bubble column reactors," *Chemical Engineering Science*, vol. 61, pp. 1819-1835, 2006.

- [236] T. Sekizawa and H. Kubota, "Liquid Mixing in Multistage Bubble Columns," *Journal of Chemical Engineering of Japan*, vol. 7, pp. 441-446, 1975.
- [237] Y. K. Doshi and A. B. Pandit, "Effect of internals and sparger design on mixing behavior in sectionalized bubble column," *Chemical Engineering Journal*, vol. 112, pp. 117-129, 2005.
- [238] H. Kawasaki, H. Hirano, and H. Tanaka, "Effects of Multiple Draft Tubes with Perforated Plates on Gas Holdup and Volumetric Mass Transfer Coefficient in a Bubble Column," *Journal of Chemical Engineering of Japan*, vol. 27, pp. 669-670, 1994.
- [239] V. Balamurugan, D. Subbarao, and S. Roy, "Enhancement in gas holdup in bubble columns through use of vibrating internals," *The Canadian Journal of Chemical Engineering*, vol. 88, pp. 1010-1020, 2010.
- [240] L. Aksel'rod, "Vorotnikova NI, Kozlov AA," *Heat transfer and several aspects of hydrodynamics of bubble beds on sieve trays equipped with tube bundles. Heat Transf-Soviet Research*, vol. 8, pp. 25-33, 1976.
- [241] C. Maretto and R. Krishna, "Modelling of a bubble column slurry reactor for Fischer-Tropsch synthesis," *Catalysis today*, vol. 52, pp. 279-289, 1999.
- [242] D. Gidaspow, *Multiphase flow and fluidization: continuum and kinetic theory descriptions*. San Diego: Academic Press, 1994.
- [243] S. Grevskott, B. H. Sannæs, M. P. Duduković, K. W. Hjarbo, and H. F. Svendsen, "Liquid circulation, bubble size distributions, and solids movement in two- and three-phase bubble columns," *Chemical Engineering Science*, vol. 51, pp. 1703-1713, 1996.
- [244] D. Mitra-Majumdar, B. Farouk, and Y. T. Shah, "Hydrodynamic modeling of three-phase flows through a vertical column," *Chemical Engineering Science*, vol. 52, pp. 4485-4497, 1997.
- [245] R. G. Rice, J. M. I. Tupperainen, and R. M. Hedge, "Dispersion and hold-up in bubble columns — comparison of rigid and flexible spargers," *The Canadian Journal of Chemical Engineering*, vol. 59, pp. 677-687, 1981.
- [246] C. Y. Wen and L. T. Fan, *Models for Flow Systems and Chemical Reactors*: Dekker, 1975.
- [247] O. Levenspiel and T. J. Fitzgerald, "A Warning on the misuse of the dispersion model," *Chemical Engineering Science*, vol. 38, pp. 489-491, 1983.

- [248] T. A. Hatton and E. N. Lightfoot, "Dispersion, mass transfer and chemical reaction in multiphase contactors: Part I: Theoretical developments," *AIChE Journal*, vol. 30, pp. 235-243, 1984.
- [249] K. J. Myers, M. P. Duduković, and P. A. Ramachandran, "Modelling churn-turbulent bubble columns—I. Liquid-phase mixing," *Chemical Engineering Science*, vol. 42, pp. 2301-2311, 1987.
- [250] R. G. Rice and M. A. Littlefield, "Dispersion coefficients for ideal bubbly flow in truly vertical bubble columns," *Chemical Engineering Science*, vol. 42, pp. 2045-2053, 1987.
- [251] Y. T. Shah, G. J. Stiegel, and M. M. Sharma, "Backmixing in gas-liquid reactors," *AIChE Journal*, vol. 24, pp. 369-400, 1978.
- [252] F. Kašánek and D. H. Sharp, *Chemical reactors for gas-liquid systems*: Ellis Horwood, 1993.
- [253] M. H. Baird and R. G. Rice, "Axial Dispersion in Large Unbaffled Columns," *The Chemical Engineering Journal*, vol. 9, pp. 171-174, 1975.
- [254] A. N. Kolmogorov, "The Local Structure of Turbulence in Incompressible Viscous Fluid for Very Large Reynolds Numbers," *Proceedings: Mathematical and Physical Sciences*, vol. 434, pp. 9-13, 1991.
- [255] P. Zehner, "Impuls-, Stoff- und Wärmetransport in Blasensäulen," *Chemie Ingenieur Technik*, vol. 54, pp. 248-251, 1982.
- [256] J. Joshi and M. Sharma, "A circulation cell model for bubble columns," *Chemical Engineering Research and Design*, vol. 57, pp. 244-251, 1979.
- [257] K. W. McHenry and R. H. Wilhelm, "Axial mixing of binary gas mixtures flowing in a random bed of spheres," *AIChE Journal*, vol. 3, pp. 83-91, 1957.
- [258] F. A. N. Fernandes, "Modeling and Product Grade Optimization of Fischer–Tropsch Synthesis in a Slurry Reactor," *Industrial & Engineering Chemistry Research*, vol. 45, pp. 1047-1057, 2006.
- [259] T. Wang, J. Wang, and Y. Jin, "Slurry reactors for gas-to-liquid processes: A review," *Industrial and Engineering Chemistry Research*, vol. 46, pp. 5824-5847, 2007.
- [260] E. Coselli Vasco de Toledo, P. Leite de Santana, M. Regina Wolf Maciel, and R. Maciel Filho, "Dynamic modelling of a three-phase catalytic slurry reactor," *Chemical Engineering Science*, vol. 56, pp. 6055-6061, 2001.

- [261] P. L. Mills, J. R. Turner, P. A. Ramachandran, and M. P. Dudukovic, "The Fischer-Tropsch synthesis in slurry bubble column reactors: analysis of reactor performance using the axial dispersion model," in *Three phase sparged reactors*, K. D. P. Nigam and A. Schumpe, Eds., ed Amsterdam: Gordon and Breach, 1996, pp. 339-386.
- [262] D. B. Bukur and J. G. Daly, "Gas hold-up in bubble columns for Fischer-Tropsch synthesis," *Chemical Engineering Science*, vol. 42, pp. 2967-2969, 1987.
- [263] I. Iliuta, F. Larachi, J. Anfray, N. Dromard, and D. Schweich, "Comparative Simulations of Cobalt- and Iron-Based Fischer-Tropsch Synthesis Slurry Bubble Column Reactors," *Industrial & Engineering Chemistry Research*, vol. 47, pp. 3861-3869, 2008/06/01 2008.
- [264] A. Prakash, "On the effects of syngas composition and water gas shift reaction rate on FT synthesis over iron based catalyst in a slurry reactor," *Chemical Engineering Communications*, vol. 128, pp. 143-158, 1994/01/01 1994.
- [265] N. Rados, M. H. Al-Dahhan, and M. P. Duduković, "Dynamic Modeling of Slurry Bubble Column Reactors," *Industrial & Engineering Chemistry Research*, vol. 44, pp. 6086-6094, 2005/08/01 2005.
- [266] H.-S. Song, D. Ramkrishna, S. Trinh, R. L. Espinoza, and H. Wright, "Multiplicity and sensitivity analysis of Fischer-Tropsch bubble column slurry reactors: plug-flow gas and well-mixed slurry model," *Chemical Engineering Science*, vol. 58, pp. 2759-2766, 2003.
- [267] D. Stern, A. T. Bell, and H. Heinemann, "A theoretical model for the performance of bubble-column reactors used for Fischer-Tropsch synthesis," *Chemical Engineering Science*, vol. 40, pp. 1665-1677, 1985.
- [268] Y. Kato and A. Nishiwaki, "Longitudinal dispersion coefficient of a liquid in a bubble column," *Int. Chem. Engng.*, vol. 12, pp. 182-187, 1972.
- [269] R. W. Field and J. F. Davidson, "Axial dispersion in bubble columns," *Trans. Inst. Chem. Engrs.*, vol. 58, pp. 228-236, 1980.
- [270] J. R. Turner and P. L. Mills, "Comparison of Axial Dispersion and Mixing Cell Models for Design and Simulation of Fischer-Tropsch Slurry bubble column reactors," *Chemical Engineering Science*, vol. 45, pp. 2317-2324, 1990.
- [271] R. Krishna, M. I. Urseanu, J. M. van Baten, and J. Ellenberger, "Liquid phase dispersion in bubble columns operating in the churn-turbulent flow regime," *Chemical Engineering Journal*, vol. 78, pp. 43-51, 2000.

- [272] M. Ishii and K. Mishima, "Two-fluid model and hydrodynamic constitutive relations," *Nuclear Engineering and Design*, vol. 82, pp. 107-126, 1984.
- [273] R. T. Lahey, Jr. and D. A. Drew, "The Three-Dimensional Time and Volume Averaged Conservation Equations of Two-Phase Flow," in *Advances in Nuclear Science and Technology*. vol. 20, J. Lewins and M. Becker, Eds., ed: Springer US, 1988, pp. 1-69.
- [274] D. A. Drew, "Mathematical Modeling of Two-Phase Flow," *Annual Review of Fluid Mechanics*, vol. 15, pp. 261-291, 1983.
- [275] V. V. Ranade, *Computational Flow Modeling for Chemical Reactor Engineering*. San Diego: Academic Press, 2002.
- [276] H. A. Jakobsen, *Chemical Reactor Modeling: Multiphase Reactive Flows*: Springer, 2008.
- [277] N. Devanathan, D. Moslemian, and M. P. Dudukovic, "Flow mapping in bubble columns using CARPT," *Chemical Engineering Science*, vol. 45, pp. 2285-2291, 1990.
- [278] N. De Nevers, "Bubble driven fluid circulations," *AIChE Journal*, vol. 14, pp. 222-226, 1968.
- [279] G. D. Towell and G. H. Ackerman, "Axial Mixing of liquid and gas in large bubble column reactor.," in *Proceedings of 2nd International Symposium Chem. React. Engng.*, Amsterdam, The Netherlands, 1972, pp. B3.1-B3.13.
- [280] P. Zehner, "Momentum, mass and heat transfer in bubble columns. Part 2. Axial blending and heat transfer," *Int. Chem. Eng*, vol. 26, pp. 29-35, 1986.
- [281] P. Zehner, "Momentum, mass and heat transfer in bubble columns. Part 1. Flow model of the bubble column and liquid velocities," *Int. Chem. Eng*, vol. 26, p. 22, 1986.
- [282] J. Chen, M. Jamialahmadi, and S. Li, "Effect of liquid depth on circulation in bubble columns: a visual study," *Chemical engineering research & design*, vol. 67, pp. 203-207, 1989.
- [283] E. Delnoij, J. A. M. Kuipers, and W. P. M. van Swaaij, "Dynamic simulation of gas-liquid two-phase flow: effect of column aspect ratio on the flow structure," *Chemical Engineering Science*, vol. 52, pp. 3759-3772, 1997.
- [284] E. Delnoij, F. A. Lammers, J. A. M. Kuipers, and W. P. M. van Swaaij, "Dynamic simulation of dispersed gas-liquid two-phase flow using a discrete bubble model," *Chemical Engineering Science*, vol. 52, pp. 1429-1458, 1997.

- [285] M. Millies and D. Mewes, "Calculation of circulating flows in bubble columns," *Chemical Engineering Science*, vol. 50, pp. 2093-2106, 1995.
- [286] N. N. Clark, C. M. Atkinson, and R. L. C. Flemmer, "Turbulent circulation in bubble columns," *AIChE Journal*, vol. 33, pp. 515-518, 1987.
- [287] K. G. Anderson and R. G. Rice, "Local turbulence model for predicting circulation rates in bubble columns," *AIChE Journal*, vol. 35, pp. 514-518, 1989.
- [288] H. Luo and H. F. Svendsen, "Turbulent circulation in bubble columns from eddy viscosity distributions of single-phase pipe flow," *The Canadian Journal of Chemical Engineering*, vol. 69, pp. 1389-1394, 1991.
- [289] M. M. Kumar and E. Natarajan, "CFD simulation for two-phase mixing in 2D fluidized bed," *The International Journal of Advanced Manufacturing Technology*, pp. 1-4, 2009.
- [290] N. W. Geary and R. G. Rice, "Circulation and scale-up in bubble columns," *AIChE Journal*, vol. 38, pp. 76-82, 1992.
- [291] J. S. Groen, R. G. C. Oldeman, R. F. Mudde, and H. E. A. van den Akker, "Coherent structures and axial dispersion in bubble column reactors," *Chemical Engineering Science*, vol. 51, pp. 2511-2520, 1996.
- [292] M. Hamidipour, J. Chen, and F. Larachi, "CFD study on hydrodynamics in three-phase fluidized beds—Application of turbulence models and experimental validation," *Chemical Engineering Science*, vol. 78, pp. 167-180, 2012.
- [293] R. Panneerselvam, S. Savithri, and G. D. Surender, "CFD simulation of hydrodynamics of gas–liquid–solid fluidised bed reactor," *Chemical Engineering Science*, vol. 64, pp. 1119-1135, 2009.
- [294] Y. Li, J. Zhang, and L.-S. Fan, "Numerical simulation of gas–liquid–solid fluidization systems using a combined CFD-VOF-DPM method: bubble wake behavior," *Chemical Engineering Science*, vol. 54, pp. 5101-5107, 1999.
- [295] Y. Pan and S. Banerjee, "Numerical simulation of particle interactions with wall turbulence," *Physics of Fluids (1994-present)*, vol. 8, pp. 2733-2755, 1996.
- [296] W. Feng, J. Wen, J. Fan, Q. Yuan, X. Jia, and Y. Sun, "Local hydrodynamics of gas–liquid–nanoparticles three-phase fluidization," *Chemical Engineering Science*, vol. 60, pp. 6887-6898, 2005.

- [297] D. Matonis, D. Gidaspow, and M. Bahary, "CFD simulation of flow and turbulence in a slurry bubble column," *AIChE Journal*, vol. 48, pp. 1413-1429, 2002.
- [298] X. Zhang and G. Ahmadi, "Eulerian–Lagrangian simulations of liquid–gas–solid flows in three-phase slurry reactors," *Chemical Engineering Science*, vol. 60, pp. 5089-5104, 2005.
- [299] J. Schallenberg, J. H. Enß, and D. C. Hempel, "The important role of local dispersed phase hold-ups for the calculation of three-phase bubble columns," *Chemical Engineering Science*, vol. 60, pp. 6027-6033, 2005.
- [300] K. Sivaguru, K. M. M. S. Begum, and N. Anantharaman, "Hydrodynamic studies on three-phase fluidized bed using CFD analysis," *Chemical Engineering Journal*, vol. 155, pp. 207-214, 2009.
- [301] E. M. Matos, R. Guirardello, M. Mori, and J. R. Nunhez, "Modeling and simulation of a pseudo-three-phase slurry bubble column reactor applied to the process of petroleum hydrodesulfurization," *Computers & Chemical Engineering*, vol. 33, pp. 1115-1122, 2009.
- [302] J. L. Silva Jr, E. D. Mori, R. Soccol Jr, M. A. d'Ávila, and M. Mori, "Interphase Momentum Study in a Slurry Bubble Column," *Chemical Engineering Transactions*, vol. 32, pp. 1507-1512, 2013.
- [303] J. Joshi, "Computational flow modelling and design of bubble column reactors," *Chemical Engineering Science*, vol. 56, pp. 5893-5933, 2001.
- [304] D. L. Marchisio and R. O. Fox, *Multiphase reacting flows: modelling and simulation: Modelling and Simulation*: Springer, 2007.
- [305] G. H. Yeoh and J. Tu, *Computational Techniques for Multiphase Flows*: Elsevier Science, 2009.
- [306] G. H. Yeoh, C. P. Cheung, and J. Tu, *Multiphase Flow Analysis Using Population Balance Modeling: Bubbles, Drops and Particles*: Elsevier Science, 2013.
- [307] D. Gidaspow and V. Jiradilok, *Computational Techniques: The Multiphase CFD Approach to Fluidization and Green Energy Technologies*: Nova Science Publishers, Incorporated, 2009.
- [308] L. Cheng and D. Mewes, *Advances in Multiphase Flow and Heat Transfer*: Bentham Science Publishers, 2012.

- [309] S. Becker, A. Sokolichin, and G. Eigenberger, "Gas—liquid flow in bubble columns and loop reactors: Part II. Comparison of detailed experiments and flow simulations," *Chemical Engineering Science*, vol. 49, pp. 5747-5762, 1994.
- [310] R. S. Oey, R. F. Mudde, and H. E. A. van den Akker, "Sensitivity study on interfacial closure laws in two-fluid bubbly flow simulations," *AIChE Journal*, vol. 49, pp. 1621-1636, 2003.
- [311] N. Hooshyar, J. R. van Ommen, P. J. Hamersma, S. Sundaresan, and R. F. Mudde, "Dynamics of Single Rising Bubbles in Neutrally Buoyant Liquid-Solid Suspensions," *Physical Review Letters*, vol. 110, p. 244501, 2013.
- [312] N. Hooshyar, "Hydrodynamics of Structured Slurry Bubble Columns," Ph.D. Dissertation, Delft University of Technology, 2013.
- [313] J. Zhang, Y. Li, and L.-S. Fan, "Numerical studies of bubble and particle dynamics in a three-phase fluidized bed at elevated pressures," *Powder Technology*, vol. 112, pp. 46-56, 2000.
- [314] R. Torvik and H. F. Svendsen, "Modelling of slurry reactors. A fundamental approach," *Chemical Engineering Science*, vol. 45, pp. 2325-2332, 1990.
- [315] J. Grienberger and H. Hofmann, "Investigations and modelling of bubble columns," *Chemical Engineering Science*, vol. 47, pp. 2215-2220, 1992.
- [316] A. A. Troshko and F. Zdravistch, "CFD modeling of slurry bubble column reactors for Fisher–Tropsch synthesis," *Chemical Engineering Science*, vol. 64, pp. 892-903, 2009.
- [317] I. Yates and C. Satterfield, "Intrinsic kinetics of the Fischer-Tropsch synthesis on a cobalt catalyst," *Energy & fuels*, pp. 168-173, 1991.
- [318] A. A. Kulkarni, J. B. Joshi, and D. Ramkrishna, "Determination of bubble size distributions in bubble columns using LDA," *AIChE Journal*, vol. 50, pp. 3068-3084, 2004.
- [319] M. Ishii and N. Zuber, "Drag coefficient and relative velocity in bubbly, droplet or particulate flows," *AIChE Journal*, vol. 25, pp. 843-855, 1979.
- [320] R. Kurose and S. Komori, "Drag and lift forces on a rotating sphere in a linear shear flow," *Journal of fluid mechanics*, vol. 384, pp. 183-206, 1999.
- [321] S. Lain, D. Bröder, M. Sommerfeld, and M. F. Göz, "Modelling hydrodynamics and turbulence in a bubble column using the Euler–Lagrange procedure," *International Journal of Multiphase Flow*, vol. 28, pp. 1381-1407, 2002.

- [322] A. Tomiyama, I. Kataoka, and T. Sakaguchi, "Drag Coefficients of Bubbles : 1st Report, Drag Coefficients of a Single Bubble in a Stagnant Liquid," *Transactions of the Japan Society of Mechanical Engineers. B*, vol. 61, pp. 2357-2364, 1995/07/25 1995.
- [323] R. Mei and J. F. Klausner, "Shear lift force on spherical bubbles," *International Journal of Heat and Fluid Flow*, vol. 15, pp. 62-65, 1994.
- [324] M. R. Snyder, O. M. Knio, J. Katz, and O. P. Le Maître, "Statistical analysis of small bubble dynamics in isotropic turbulence," *Physics of Fluids (1994-present)*, vol. 19, pp. -, 2007.
- [325] K. Tsuchiya, A. Furumoto, L.-S. Fan, and J. Zhang, "Suspension viscosity and bubble rise velocity in liquid-solid fluidized beds," *Chemical Engineering Science*, vol. 52, pp. 3053-3066, 1997.
- [326] G. Ahmadi and D. Ma, "A thermodynamical formulation for dispersed multiphase turbulent flows—1: Basic theory," *International Journal of Multiphase Flow*, vol. 16, pp. 323-340, 1990.
- [327] D. Z. Zhang and W. B. VanderHeyden, "The effects of mesoscale structures on the macroscopic momentum equations for two-phase flows," *International Journal of Multiphase Flow*, vol. 28, pp. 805-822, 2002.
- [328] T. O. Salmi, J. P. Mikkola, and J. P. Warna, *Chemical Reaction Engineering and Reactor Technology*. Florida: Taylor & Francis, 2011.
- [329] D. A. Drew and S. L. Passman, *Theory of Multicomponent Fluids*. New York: Springer, 1998.
- [330] C. K. K. Lun and S. B. Savage, "The effects of an impact velocity dependent coefficient of restitution on stresses developed by sheared granular materials," *Acta Mechanica*, vol. 63, pp. 15-44, 1986/11/01 1986.
- [331] J. Ding and D. Gidaspow, "A bubbling fluidization model using kinetic theory of granular flow," *AIChE Journal*, vol. 36, pp. 523-538, 1990.
- [332] O. Basha, L. Sehabiague, Z. Shi, H. Jia, L. Weng, Z. Men, K. Liu, and B. I. Morsi, "Computational Fluid Dynamics Modeling of Complex Spatio Temporal Phenomena In Slurry Bubble Columns For Fischer Tropsch Synthesis," presented at the Proceedings of 31st Annual International Pittsburgh Coal Conference, Pittsburgh, PA, 2014.
- [333] A. F. Ansys, "14.0 Theory Guide," *ANSYS inc*, pp. 218-221, 2011.

- [334] D. Drew, L. Cheng, and R. T. Lahey Jr, "The analysis of virtual mass effects in two-phase flow," *International Journal of Multiphase Flow*, vol. 5, pp. 233-242, 1979.
- [335] E. A. Ervin and G. Tryggvason, "The rise of bubbles in a vertical shear flow," *Journal of Fluids Engineering, Transactions of the ASME*, vol. 119, pp. 443-449, 1997.
- [336] T. R. Auton, J. C. R. Hunt, and M. Prud'homme, "Force exerted on a body in inviscid unsteady non-uniform rotational flow," *Journal of fluid mechanics*, vol. 197, pp. 241-257, 1988.
- [337] S. P. Antal, R. T. Lahey Jr, and J. E. Flaherty, "Analysis of phase distribution in fully developed laminar bubbly two-phase flow," *International Journal of Multiphase Flow*, vol. 17, pp. 635-652, 1991.
- [338] E. Krepper, D. Lucas, and H.-M. Prasser, "On the modelling of bubbly flow in vertical pipes," *Nuclear Engineering and Design*, vol. 235, pp. 597-611, 2005.
- [339] M. Lopez de Bertodano, R. Lahey Jr, and O. Jones, "Phase distribution in bubbly two-phase flow in vertical ducts," *International Journal of Multiphase Flow*, vol. 20, pp. 805-818, 1994.
- [340] A. D. Burns, T. Frank, I. Hamill, and J.-M. Shi, "The Favre averaged drag model for turbulent dispersion in Eulerian multi-phase flows," in *5th international conference on multiphase flow, ICMF*, 2004.
- [341] Y. Liao and D. Lucas, "A literature review of theoretical models for drop and bubble breakup in turbulent dispersions," *Chemical Engineering Science*, vol. 64, pp. 3389-3406, 2009.
- [342] S. E. Elghobashi and T. W. Abou-Arab, "A two-equation turbulence model for two-phase flows," *Physics of Fluids (1958-1988)*, vol. 26, pp. 931-938, 1983.
- [343] R. Issa and P. Oliveira, "Modelling of turbulent dispersion in two phase flow jets," *Eng Turbul Model Exp*, vol. 2, pp. 947-957, 1993.
- [344] M. R. Wells and D. E. Stock, "The effects of crossing trajectories on the dispersion of particles in a turbulent flow," *Journal of fluid mechanics*, vol. 136, pp. 31-62, 1983.
- [345] S. Kumar and D. Ramkrishna, "On the solution of population balance equations by discretization—I. A fixed pivot technique," *Chemical Engineering Science*, vol. 51, pp. 1311-1332, 1996.

- [346] H. Luo and H. F. Svendsen, "Theoretical Model for Drop and Bubble Breakup in Turbulent Dispersions," *AIChE Journal*, vol. 42, pp. 1225-1233, 1996.
- [347] G. Li, X. Yang, and G. Dai, "CFD simulation of effects of the configuration of gas distributors on gas-liquid flow and mixing in a bubble column," *Chemical Engineering Science*, vol. 64, pp. 5104-5116, 2009.
- [348] M. J. Prince and H. W. Blanch, "Bubble coalescence and break-up in air-sparged bubble columns," *AIChE Journal*, vol. 36, pp. 1485-1499, 1990.
- [349] J. C. Rotta, *Turbulente Strömungen: eine Einführung in die Theorie und ihre Anwendung* vol. 8: Universitätsverlag Göttingen, 2010.
- [350] L. Sehabiague, O. M. Basha, Y. Hong, B. Morsi, Z. Shi, H. Jia, L. Weng, Z. Men, K. Liu, and Y. Cheng, "Assessing the performance of an industrial SBCR for Fischer-Tropsch synthesis: Experimental and modeling," *AIChE Journal*, vol. 61, pp. 3838-3857, 2015.
- [351] P. Chen, J. Sanyal, and M. P. Duduković, "Numerical simulation of bubble columns flows: effect of different breakup and coalescence closures," *Chemical Engineering Science*, vol. 60, pp. 1085-1101, 2005.
- [352] B. P. Leonard, "Order of accuracy of QUICK and related convection-diffusion schemes," *Applied Mathematical Modelling*, vol. 19, pp. 640-653, 1995.
- [353] B. P. Leonard and S. Mokhtari, "Beyond first-order upwinding: The ultra-sharp alternative for non-oscillatory steady-state simulation of convection," *International Journal for Numerical Methods in Engineering*, vol. 30, pp. 729-766, 1990.
- [354] I. ANSYS, "Ansys CFX-Solver Theory Guide," *ANSYS CFX Release*, vol. 11, pp. 69-118, 2010.
- [355] S. A. Vasquez and V. A. Ivanov, "A phase coupled method for solving multiphase problems in unstructured meshes.," presented at the Proceedings of ASME FEDSM'00: ASME 2000 Fluids Engineering Division Summer Meeting, Boston, 2000.
- [356] S. Patankar, *Numerical Heat Transfer and Fluid Flow*. New York: McGraw-Hill Book Company, 1980.
- [357] A. Haider and O. Levenspiel, "Drag coefficient and terminal velocity of spherical and nonspherical particles," *Powder Technology*, vol. 58, pp. 63-70, 5// 1989.

- [358] Y. Sato, M. Sadatomi, and K. Sekoguchi, "Momentum and heat transfer in two-phase bubble flow—I. Theory," *International Journal of Multiphase Flow*, vol. 7, pp. 167-177, 1981.
- [359] A. Behkish, "Hydrodynamic and Mass Transfer Parameters in Large-Scale Slurry Bubble Column Reactors," Ph.D. Dissertation, Chemical and Petroleum Engineering Department, University of Pittsburgh, Pittsburgh, USA, 2004.
- [360] C. L. Yaws, *Chemical Properties Handbook*: McGraw-Hill, 1999.
- [361] J. J. Marano and G. D. Holder, "Characterization of Fischer-Tropsch liquids for vapor-liquid equilibria calculations," *Fluid Phase Equilibria*, vol. 138, pp. 1-21, 1997.
- [362] B. Jager and R. Espinoza, "Advances in low temperature Fischer-Tropsch synthesis," *Catalysis Today*, vol. 23, pp. 17-28, 1995.
- [363] J. J. Marano and G. D. Holder, "General Equation for Correlating the Thermophysical Properties of n -Paraffins, n -Olefins, and Other Homologous Series. 2. Asymptotic Behavior Correlations for PVT Properties," *Industrial & Engineering Chemistry Research*, vol. 36, pp. 1895-1907, 1997.
- [364] J. J. Marano and G. D. Holder, "A General Equation for Correlating the Thermophysical Properties of n -Paraffins, n -Olefins, and Other Homologous Series. 3. Asymptotic Behavior Correlations for Thermal and Transport Properties," *Industrial & Engineering Chemistry Research*, vol. 36, pp. 2399-2408, 1997.
- [365] R. Lemoine, A. Behkish, L. Sehabiague, Y. J. Heintz, R. Oukaci, and B. I. Morsi, "An algorithm for predicting the hydrodynamic and mass transfer parameters in bubble column and slurry bubble column reactors," *Fuel Processing Technology*, vol. 89, pp. 322-343, 2008.
- [366] C. O. Vandu, K. Koop, and R. Krishna, "Volumetric mass transfer coefficient in a slurry bubble column operating in the heterogeneous flow regime," *Chemical Engineering Science*, vol. 59, pp. 5417-5423, 2004.
- [367] W.-D. Deckwer, Y. Louisi, M. Ralek, and A. Zaidi, "Hydrodynamic Properties of the Fischer-Tropsch Slurry Process," *Industrial & Engineering Chemistry Process Design and Development*, vol. 19, pp. 699-708, 1980.
- [368] R. Krishna, J. W. A. de Swart, J. Ellenberg, G. B. Martina, and C. Maretto, "Gas Holdup in Slurry Bubble Columns: Effect of Column Diameter and Slurry Concentrations," *AIChE Journal*, vol. 43, pp. 311-316, 1997.

- [369] J. R. Inga and B. I. Morsi, "Effect of Operating Variables on the Gas Holdup in a Large-Scale Slurry Bubble Column Reactor Operating with an Organic Liquid Mixture," *Industrial & Engineering Chemistry Research*, vol. 38, pp. 928-937, 1999/03/01 1999.
- [370] N. Kantarci, F. Borak, and K. O. Ulgen, "Bubble column reactors," *Process Biochemistry*, vol. 40, pp. 2263-2283, 2005.
- [371] R. J. Benzing and J. E. Myers, "Low Frequency Bubble Formation at Horizontal Circular Orifices," *Industrial & Engineering Chemistry*, vol. 47, pp. 2087-2090, 1955/10/01 1955.
- [372] C. Chen and L.-S. Fan, "Discrete simulation of gas-liquid bubble columns and gas-liquid-solid fluidized beds," *AIChE Journal*, vol. 50, pp. 288-301, 2004.
- [373] J. F. Davidson and B. O. G. Schüler, "Bubble formation at an orifice in a viscous liquid," *Chemical Engineering Research and Design*, vol. 75, Supplement, pp. S105-S115, 1997.
- [374] S. E. Forrester and C. D. Rielly, "Bubble formation from cylindrical, flat and concave sections exposed to a strong liquid cross-flow," *Chemical Engineering Science*, vol. 53, pp. 1517-1527, 1998.
- [375] J. J. Heijnen and K. Van't Riet, "Mass transfer, mixing and heat transfer phenomena in low viscosity bubble column reactors," *The Chemical Engineering Journal*, vol. 28, pp. B21-B42, 1984.
- [376] K. Idogawa, K. Ikeda, T. Fukuda, and S. Morooka, "FORMATION AND FLOW OF GAS BUBBLES IN A PRESSURIZED BUBBLE COLUMN WITH A SINGLE ORIFICE OR NOZZLE GAS DISTRIBUTOR," *Chemical Engineering Communications*, vol. 59, pp. 201-212, 1987/09/01 1987.
- [377] M. Jamialahmadi, M. R. Zehtaban, H. Müller-Steinhagen, A. Sarrafi, and J. M. Smith, "Study of Bubble Formation Under Constant Flow Conditions," *Chemical Engineering Research and Design*, vol. 79, pp. 523-532, 2001.
- [378] A. K. Khurana and R. Kumar, "Studies in bubble formation — III," *Chemical Engineering Science*, vol. 24, pp. 1711-1723, 1969.
- [379] A. Kumar, T. E. Degaleesan, G. S. Laddha, and H. E. Hoelscher, "Bubble swarm characteristics in bubble columns," *The Canadian Journal of Chemical Engineering*, vol. 54, pp. 503-508, 1976.
- [380] I. Leibson, E. G. Holcomb, A. G. Cacos, and J. J. Jacmic, "Rate of flow and mechanics of bubble formation from single submerged orifices. I. Rate of flow studies," *AIChE Journal*, vol. 2, pp. 296-300, 1956.

- [381] I. Leibson, E. G. Holcomb, A. G. Cacosso, and J. J. Jacmic, "Rate of flow and mechanics of bubble formation from single submerged orifices. II. Mechanics of bubble formation," *AIChE Journal*, vol. 2, pp. 300-306, 1956.
- [382] S. H. Marshall, M. W. Chudacek, and D. F. Bagster, "A model for bubble formation from an orifice with liquid cross-flow," *Chemical Engineering Science*, vol. 48, pp. 2049-2059, 1993.
- [383] O. Pamperin and H.-J. Rath, "Influence of buoyancy on bubble formation at submerged orifices," *Chemical Engineering Science*, vol. 50, pp. 3009-3024, 1995.
- [384] Y. Park, A. Lamont Tyler, and N. de Nevers, "The chamber orifice interaction in the formation of bubbles," *Chemical Engineering Science*, vol. 32, pp. 907-916, 1977.
- [385] A. Satyanarayan, R. Kumar, and N. R. Kuloor, "Studies in bubble formation—II bubble formation under constant pressure conditions," *Chemical Engineering Science*, vol. 24, pp. 749-761, 1969.
- [386] H. Tsuge and S.-I. Hibino, "BUBBLE FORMATION FROM AN ORIFICE SUBMERGED IN LIQUIDS," *Chemical Engineering Communications*, vol. 22, pp. 63-79, 1983/07/01 1983.
- [387] H. Tsuge, Y. Nakajima, and K. Terasaka, "Behavior of bubbles formed from a submerged orifice under high system pressure," *Chemical Engineering Science*, vol. 47, pp. 3273-3280, 1992.
- [388] H. Tsuge, Y. Tanaka, K. Terasaka, and H. Matsue, "Bubble formation in flowing liquid under reduced gravity," *Chemical Engineering Science*, vol. 52, pp. 3671-3676, 1997.
- [389] H. Tsuge, Y. Tezuka, and M. Mitsudani, "Bubble formation mechanism from downward nozzle—Effect of nozzle shape and operating parameters," *Chemical Engineering Science*, vol. 61, pp. 3290-3298, 5// 2006.
- [390] P. M. Wilkinson and L. L. Van Dierendonck, "A theoretical model for the influence of gas properties and pressure on single-bubble formation at an orifice," *Chemical Engineering Science*, vol. 49, pp. 1429-1438, 1994.
- [391] A. E. Wraith, "Two stage bubble growth at a submerged plate orifice," *Chemical Engineering Science*, vol. 26, pp. 1659-1671, 1971.
- [392] A. V. Kulkarni and J. B. Joshi, "Design and selection of sparger for bubble column reactor. Part I: Performance of different spargers," *Chemical Engineering Research and Design*, vol. 89, pp. 1972-1985, 10// 2011.

- [393] B. A. Toseland, "Engineering Development of Slurry Bubble Column Reactor (SBCR) Technology," 2000., 2000.
- [394] P. Gupta, "Engineering Development of Slurry Bubble Column Reactor (SBCR) Technology," Air Products & Chemicals Incorporated 2002.
- [395] C. B. Millikan and A. L. Klein, "The Effect of Turbulence," *Aircraft Engineering and Aerospace Technology*, vol. 5, pp. 169-174, 1933.
- [396] H. Gupta, S. Sorooshian, and P. Yapo, "Status of Automatic Calibration for Hydrologic Models: Comparison with Multilevel Expert Calibration," *Journal of Hydrologic Engineering*, vol. 4, pp. 135-143, 1999.
- [397] N. Balasubramanian, C. Srinivasakannan, and C. Ahmed Basha, "Drying kinetics in the riser of circulating fluidized bed with internals," *Drying Technology*, vol. 25, pp. 1595-1599, 2007.
- [398] H. Tong and H. Li, "Floating internals in fast bed of cohesive particles," *Powder Technology*, vol. 190, pp. 401-409, 2009.
- [399] J. Makibar, A. R. Fernandez-Akarregi, L. Díaz, G. Lopez, and M. Olazar, "Pilot scale conical spouted bed pyrolysis reactor: Draft tube selection and hydrodynamic performance," *Powder Technology*, vol. 219, pp. 49-58, 2012.
- [400] M. Olazar, G. Lopez, H. Altzibar, M. Amutio, and J. Bilbao, "Drying of biomass in a conical spouted bed with different types of internal devices," *Drying Technology*, vol. 30, pp. 207-216, 2012.
- [401] H. Koppers, "Rheinpreussen-Koppers Liquid-Phase Process of Fischer-Tropsch Synthesis," *Chem. Age India*, vol. 12, p. 7, 1961.
- [402] H. P. Withers, K. F. Eliezer, and J. W. Mitchell, "Slurry-phase Fischer-Tropsch synthesis and kinetic studies over supported cobalt carbonyl derived catalysts," *Industrial & Engineering Chemistry Research*, vol. 29, pp. 1807-1814, 1990/09/01 1990.
- [403] J. Chang, L. Bai, B. Teng, R. Zhang, J. Yang, Y. Xu, H. Xiang, and Y. Li, "Kinetic modeling of Fischer-Tropsch synthesis over Fe-Cu-K-SiO₂ catalyst in slurry phase reactor," *Chemical Engineering Science*, vol. 62, pp. 4983-4991, 2007.
- [404] J. J. Marano and G. D. Holder, "General Equation for Correlating the Thermophysical Properties of n-Paraffins, n-Olefins, and Other Homologous Series. 1. Formalism for Developing Asymptotic Behavior Correlations," *Industrial & Engineering Chemistry Research*, vol. 36, pp. 1887-1894, 1997/05/01 1997.

- [405] H. F. Svendsen, H. A. Jakobsen, and R. Torvik, "Local flow structures in internal loop and bubble column reactors," *Chemical Engineering Science*, vol. 47, pp. 3297-3304, 1992.
- [406] W. Brötz, "Zur Systematik der Fischer-Tropsch-Katalyse," *Zeitschrift für Elektrochemie und angewandte physikalische Chemie*, vol. 53, pp. 301-306, 1949.
- [407] C. C. Hall, D. Gall, and S. L. Smith, "A comparison of the fixed-bed, liquid phase ('slurry'), and fluidized-bed techniques in the Fischer-Tropsch synthesis," *Journal of the Institute of Petroleum*, vol. 38, pp. 845-876, 1952.
- [408] J. R. Anderson and M. Boudart, *Catalysis: science and technology*: Springer-Verlag, 1983.
- [409] R. B. Anderson and F. S. Karn, "A rate equation for the Fischer-Tropsch synthesis on iron catalysts," *The Journal of Physical Chemistry*, vol. 64, pp. 805-808, 1960/06/01 1960.
- [410] H. Kölbl, "Kinetics and reaction mechanism of the hydrocarbon synthesis from carbon monoxide and water vapor on iron, cobalt, and nickel catalysts," presented at the Actes du 2ème Congrès International de Catalyse, Paris, 1960.
- [411] R. B. Anderson, F. S. Karn, and J. F. Shultz, "Kinetics of the Fischer-Tropsch synthesis on iron catalysts," *US Bureau of Mines Bulletin*, vol. 614, 1964.
- [412] M. E. Dry, T. Shingles, and L. J. Boshoff, "Rate of the Fischer-Tropsch reaction over iron catalysts," *Journal of Catalysis*, vol. 25, pp. 99-104, 1972.
- [413] M. E. Dry, "Advances in Fischer-Tropsch chemistry," *Industrial & Engineering Chemistry Process Design and Development*, vol. 15, pp. 282-286, 1976.
- [414] H. E. Atwood and C. O. Bennett, "Kinetics of the Fischer-Tropsch Reaction over Iron," *Industrial & Engineering Chemistry Process Design and Development*, vol. 18, pp. 163-170, 1979/01/01 1979.
- [415] W. J. Thomson, "Applied Fischer-Tropsch kinetics for a flame sprayed iron catalyst," *Preprint Papers - American Chemical Society. Division of Fuel Chemistry.*, vol. 25, pp. 101-118, 1979.
- [416] J. L. Feimer, P. L. Silveston, and R. R. Hudgins, "Steady-state study of the Fischer-Tropsch reaction," *Industrial & Engineering Chemistry Product Research and Development*, vol. 20, pp. 609-615, 1981/12/01 1981.
- [417] T. M. Leib and J. C. W. Kuo, "Modeling the Fischer-Tropsch Synthesis in Slurry Bubble-Column Reactors," in *AIChE Annual Meeting*, San Francisco, 1984.

- [418] H. Nettelhoff, "Studies on the kinetics of Fischer-Tropsch synthesis in slurry phase.," *German Chemical Engineering*, vol. 8, pp. 177-185, 1985.
- [419] W. D. Deckwer, R. Kokuun, E. Sanders, and S. Ledakowicz, "Kinetic studies of Fischer-Tropsch synthesis on suspended iron/potassium catalyst - rate inhibition by carbon dioxide and water," *Industrial & Engineering Chemistry Process Design and Development*, vol. 25, pp. 643-649, 1986/07/01 1986.
- [420] W. H. Zimmerman and D. B. Bukur, "Reaction kinetics over iron catalysts used for the fischer tropsch synthesis," *Canadian Journal of Chemical Engineering*, vol. 68, pp. 292-300, 1990.
- [421] H.-S. Liu, W.-C. Chiung, and Y.-C. Wang, "Effect of lard oil, olive oil and castor oil on oxygen transfer in an agitated fermentor," *Biotechnology Techniques*, vol. 8, pp. 17-20, 1994.
- [422] Z.-T. Liu, Y.-W. Li, J.-L. Zhou, and B.-J. Zhang, "Intrinsic kinetics of Fischer-Tropsch synthesis over an Fe-Cu-K catalyst," *Journal of the Chemical Society, Faraday Transactions*, vol. 91, pp. 3255-3261, 1995.
- [423] G. P. van der Laan and A. A. C. M. Beenackers, "Hydrocarbon Selectivity Model for the Gas-Solid Fischer-Tropsch Synthesis on Precipitated Iron Catalysts," *Industrial & Engineering Chemistry Research*, vol. 38, pp. 1277-1290, 1999/04/01 1999.
- [424] P. J. Van Berge, "Fischer-Tropsch studies in the slurry phase favouring wax production," North-West University, Potchefstroom Campus, 1994.
- [425] G. P. van der Laan and A. a. C. M. Beenackers, "Intrinsic kinetics of the gas-solid Fischer-Tropsch and water gas shift reactions over a precipitated iron catalyst," *Applied Catalysis A: General*, vol. 193, pp. 39-53, 2000.
- [426] A. Jess, R. Popp, and K. Hedden, "Fischer-Tropsch-synthesis with nitrogen-rich syngas: Fundamentals and reactor design aspects," *Applied Catalysis A: General*, vol. 186, pp. 321-342, 1999.
- [427] E. van Steen and H. Schulz, "Polymerisation kinetics of the Fischer-Tropsch CO hydrogenation using iron and cobalt based catalysts," *Applied Catalysis A: General*, vol. 186, pp. 309-320, 1999.
- [428] S. A. Eliason and C. H. Bartholomew, "Reaction and deactivation kinetics for Fischer-Tropsch synthesis on unpromoted and potassium-promoted iron catalysts," *Applied Catalysis A: General*, vol. 186, pp. 229-243, 1999.

- [429] Y. Wang, N., "Modelization and Simulation of Fixed-Bed Fischer-Tropsch Synthesis: Kinetics, Pellet and Reactor.," Ph.D. Dissertation, Institute of Coal Chemistry, Chinese Academy of Sciences, Taiyuan, China, 2001.
- [430] Y.-N. Wang, W.-P. Ma, Y.-J. Lu, J. Yang, Y.-Y. Xu, H.-W. Xiang, Y.-W. Li, Y.-L. Zhao, and B.-J. Zhang, "Kinetics modelling of Fischer–Tropsch synthesis over an industrial Fe–Cu–K catalyst," *Fuel*, vol. 82, pp. 195-213, 2003.
- [431] J. Yang, Y. Liu, J. Chang, Y.-N. Wang, L. Bai, Y.-Y. Xu, H.-W. Xiang, Y.-W. Li, and B. Zhong, "Detailed Kinetics of Fischer–Tropsch Synthesis on an Industrial Fe–Mn Catalyst," *Industrial & Engineering Chemistry Research*, vol. 42, pp. 5066-5090, 2003/10/01 2003.
- [432] B.-T. Teng, J. Chang, C.-H. Zhang, D.-B. Cao, J. Yang, Y. Liu, X.-H. Guo, H.-W. Xiang, and Y.-W. Li, "A comprehensive kinetics model of Fischer–Tropsch synthesis over an industrial Fe–Mn catalyst," *Applied Catalysis A: General*, vol. 301, pp. 39-50, 2006.
- [433] F. G. Botes and B. B. Breman, "Development of a new kinetic expression for the iron-based Fischer-Tropsch reaction," in *AIChE Annual Meeting, Conference Proceedings*, 2006.
- [434] J. Chang, L. Bai, B. Teng, R. Zhang, J. Yang, Y. Xu, H. Xiang, and Y. Li, "Kinetic modeling of Fischer-Tropsch synthesis over Fe-Cu-K-SiO₂ catalyst in slurry phase reactor," *Chemical Engineering Science*, vol. 62, pp. 4983-4991, 2007.
- [435] L.-P. Zhou, X. Hao, J.-H. Gao, Y. Yang, B.-S. Wu, J. Xu, Y.-Y. Xu, and Y.-W. Li, "Studies and Discriminations of the Kinetic Models for the Iron-Based Fischer–Tropsch Catalytic Reaction in a Recycle Slurry Reactor," *Energy & Fuels*, vol. 25, pp. 52-59, 2011/01/20 2011.
- [436] W. J. Shen, J. L. Zhou, and B. J. Zhang, "Kinetics of Fischer-Tropsch synthesis over precipitated iron catalyst," *Journal of Natural Gas Chemistry*, vol. 4, pp. 385-400, 1994.
- [437] M. J. Keyser, R. C. Everson, and R. L. Espinoza, "Fischer–Tropsch Kinetic Studies with Cobalt–Manganese Oxide Catalysts," *Industrial & Engineering Chemistry Research*, vol. 39, pp. 48-54, 2000.
- [438] F. G. Botes, "Water–gas-shift kinetics in the iron-based low-temperature Fischer–Tropsch synthesis," *Applied Catalysis A: General*, vol. 328, pp. 237-242, 2007.
- [439] G. P. van der Laan, A. A. C. M. Beenackers, and R. Krishna, *Chem. Eng. Sci.*, vol. 54, p. 5013, 1999.

- [440] C.-H. Yang, E. Massoth F, and G. Oblad A, "Kinetics of CO + H₂ Reaction over Co-Cu-Al₂O₃ Catalyst," in *Hydrocarbon Synthesis from Carbon Monoxide and Hydrogen*. vol. 178, ed: AMERICAN CHEMICAL SOCIETY, 1979, pp. 35-46.
- [441] R. B. Pannell, C. L. Kibby, and T. P. Kobylinski, "A Steady-State Study of Fischer-Tropsch Product Distributions Over Cobalt, Iron and Ruthenium," in *Studies in Surface Science and Catalysis*. vol. Volume 7, Part A, T. Seivama and K. Tanabe, Eds., ed: Elsevier, 1981, pp. 447-459.
- [442] C. G. Visconti, E. Tronconi, L. Lietti, R. Zennaro, and P. Forzatti, "Development of a complete kinetic model for the Fischer–Tropsch synthesis over Co/Al₂O₃ catalysts," *Chemical Engineering Science*, vol. 62, pp. 5338-5343, 2007.
- [443] J. Anfray, M. Bremaud, P. Fongarland, A. Khodakov, S. Jallais, and D. Schweich, "Kinetic study and modeling of Fischer–Tropsch reaction over a catalyst in a slurry reactor," *Chemical Engineering Science*, vol. 62, pp. 5353-5356, 2007.
- [444] P. Kaiser, F. Pöhlmann, and A. Jess, "Intrinsic and Effective Kinetics of Cobalt-Catalyzed Fischer-Tropsch Synthesis in View of a Power-to-Liquid Process Based on Renewable Energy," *Chemical Engineering & Technology*, vol. 37, pp. 964-972, 2014.
- [445] S. D. Kim, C. G. I. Baker, and M. A. Bergougnou, "Phase holdup characteristics of three phase fluidized beds," *The Canadian Journal of Chemical Engineering*, vol. 53, pp. 134-139, 1975.
- [446] M. Kito, K. Tabei, and K. Murata, "Gas and Liquid Holdups in Mobile Beds under the Countercurrent Flow of Air and Liquid," *Industrial & Engineering Chemistry Process Design and Development*, vol. 17, pp. 568-571, 1978/10/01 1978.
- [447] J. S. Oh and S. D. Kim, "Phase Holdup Characteristics of Three Phase Fluidized Beds of Mixed Particles," *Hwahak Konghak (Journal of the Korean Institute of Chemical Engineers)*, vol. 18, pp. 375-384, 1980.
- [448] J. M. Begovich and J. Watson, *Hydrodynamic characteristics of three-phase fluidized beds*: Cambridge University Press: Cambridge, 1978.
- [449] S. Khang, J. Schwartz, and R. Buttke, "A practical wake model for estimating bed expansion and holdup in three phase fluidized systems," in *AIChE Symposium Series*, 1983, pp. 47-54.
- [450] V. Sivakumar, K. Senthilkumar, and T. Kannadasan, "Prediction of gas holdup in the three-phase fluidized bed: air/Newtonian and non-Newtonian liquid systems," in *Polish Journal of Chemical Technology* vol. 12, ed, 2010, p. 64.

- [451] D. N. Smith, W. Fuchs, J. Lynn R, D. H. Smith, and M. Hess, "Bubble Behavior in a Slurry Bubble Column Reactor Model," in *Chemical and Catalytic Reactor Modeling*. vol. 237, ed: American Chemical Society, 1984, pp. 125-147.
- [452] I. G. Reilly, D. S. Scott, T. De Bruijn, A. Jain, and J. Piskorz, "A correlation for gas holdup in turbulent coalescing bubble columns," *The Canadian Journal of Chemical Engineering*, vol. 64, pp. 705-717, 1986.
- [453] A. Schumpe, A. K. Saxena, and L. K. Fang, "Gas/liquid mass transfer in a slurry bubble column," *Chemical Engineering Science*, vol. 42, pp. 1787-1796, 1987.
- [454] S. L. P. Lee and H. I. de Lasa, "Phase holdups in three-phase fluidized beds," *AIChE Journal*, vol. 33, pp. 1359-1370, 1987.
- [455] R. Krishna and S. T. Sie, "Design and Scale-up of the Fischer-Tropsch bubble Column Slurry Reactor," *Fuel Processing Technology*, vol. 64, pp. 73-105, 2000.
- [456] C.-M. Chen and L.-P. Leu, "Hydrodynamics and mass transfer in three-phase magnetic fluidized beds," *Powder Technology*, vol. 117, pp. 198-206, 2001.
- [457] K. Ramesh and T. Murugesan, "Minimum fluidization velocity and gas holdup in gas-liquid-solid fluidized bed reactors," *Journal of Chemical Technology & Biotechnology*, vol. 77, pp. 129-136, 2002.
- [458] H. M. Jena, G. K. Roy, and B. C. Meikap, "Prediction of gas holdup in a three-phase fluidized bed from bed pressure drop measurement," *Chemical Engineering Research and Design*, vol. 86, pp. 1301-1308, 11// 2008.
- [459] W. G. Eversole, G. H. Wagner, and E. Stackhouse, "Rapid Formation of Gas Bubbles in Liquids," *Industrial & Engineering Chemistry*, vol. 33, pp. 1459-1462, 1941/11/01 1941.
- [460] D. VanKrevelen and P. Hoftijzer, "Studies of Gas-Bubble Formation-Calculation of Interfacial Area in Bubble Contactors," *Chemical Engineering Progress*, vol. 46, pp. 29-35, 1950.
- [461] S. Nedeltchev and A. Schumpe, "New Approaches for Theoretical Estimation of Mass Transfer Parameters in Both Gas-Liquid and Slurry Bubble Columns," M. El-Amin, Ed., ed: InTech, 2011, pp. 780-780.
- [462] R. Kumar and N. Kuloor, "The formation of bubbles and drops," *Advances in Chemical Engineering*, vol. 8, pp. 255-368, 1970.

- [463] S. Ramakrishnan, R. Kumar, and N. R. Kuloor, "Studies in bubble formation—I bubble formation under constant flow conditions," *Chemical Engineering Science*, vol. 24, pp. 731-747, 1969.
- [464] A. Acharya and J. J. Ulbrecht, "Note on the influence of viscoelasticity on the coalescence rate of bubbles and drops," *AIChE Journal*, vol. 24, pp. 348-351, 1978.
- [465] N. Rabiger and A. Vogelpohl, "Bubble formation and its movement in Newtonian and Non-Newtonian liquids.," in *Encyclopaedia of Fluid Mechanics*, ed Houston: Gulf Publishing, 1986, p. 59.
- [466] R. G. Rice and N. B. Lakhani, "BUBBLE FORMATION AT A PUNCTURE IN A SUBMERGED RUBBER MEMBRANE," *Chemical Engineering Communications*, vol. 24, pp. 215-234, 1983/12/01 1983.
- [467] E. S. Gaddis and A. Vogelpohl, "Bubble formation in quiescent liquids under constant flow conditions," *Chemical Engineering Science*, vol. 41, pp. 97-105, 1986.
- [468] H. Tsuge, Uuml, P. Din, and R. Kammel, "BUBBLE FORMATION FROM A VERTICALLY DOWNWARD FACING NOZZLE IN LIQUIDS AND MOLTEN METALS," *Journal of Chemical Engineering of Japan*, vol. 19, pp. 326-330, 1986.
- [469] E. Sada, S. Katoh, H. Yoshii, and T. Tanaka, "Bubble formation in molten sodium nitrate," *INDUSTRIAL & ENGINEERING CHEMISTRY PROCESS DESIGN AND DEVELOPMENT*, vol. 25, pp. 838-839, 1986/07/01 1986.
- [470] J. O. Hinze, "Fundamentals of the hydrodynamic mechanism of splitting in dispersion processes," *AIChE Journal*, vol. 1, pp. 289-295, 1955.
- [471] V. G. Levich, *Physicochemical hydrodynamics: (by) veniamin G. Levich. Transl. by scripta technica, inc*: Prentice-Hall, 1962.
- [472] X. Luo, D. J. Lee, R. Lau, G. Yang, and L.-S. Fan, "Maximum stable bubble size and gas holdup in high-pressure slurry bubble columns," *AIChE Journal*, vol. 45, pp. 665-680, 1999.
- [473] G. G. Stokes, *On the effect of the internal friction of fluids on the motion of pendulums* vol. 9: Pitt Press, 1851.
- [474] D. T. Dumitrescu, "Strömung an einer Luftblase im senkrechten Rohr," *ZAMM - Journal of Applied Mathematics and Mechanics / Zeitschrift für Angewandte Mathematik und Mechanik*, vol. 23, pp. 139-149, 1943.

- [475] F. N. Peebles and H. J. Garber, "Studies on the motion of gas bubbles in liquids," *Chemical Engineering Progress*, vol. 49, p. 88, 1953.
- [476] W. L. Haberman and R. K. Morton, "An experimental study of bubbles moving in liquids," *Transactions of the American Society of Civil Engineers*, vol. 121, pp. 227-250, 1956.
- [477] T. Z. Harmathy, "Velocity of large drops and bubbles in media of infinite or restricted extent," *AIChE Journal*, vol. 6, pp. 281-288, 1960.
- [478] H. Angelino, "Hydrodynamique des grosses bulles dans les liquides visqueux," *Chemical Engineering Science*, vol. 21, pp. 541-550, 1966.
- [479] H. D. Mendelson, "The prediction of bubble terminal velocities from wave theory," *AIChE Journal*, vol. 13, pp. 250-253, 1967.
- [480] J. R. Grace, T. Wairegi, and T. H. Nguyen, "Shapes and velocities of single drops and bubbles moving freely through immiscible liquids," *Trans Inst Chem Eng*, vol. 54, pp. 167-173, 1976.
- [481] I. H. Lehrer, "A rational terminal velocity equation for bubbles and drops at intermediate and high Reynolds numbers," *Journal of Chemical Engineering of Japan*, vol. 9, pp. 237-240, 1976.
- [482] M. Fukuma, K. Muroyama, and A. Yasunishi, "Properties of Bubble Swarm in a Slurry Bubble Column," *Journal of Chemical Engineering of Japan*, vol. 20, pp. 28-33, 1987.
- [483] H. V. Nickens and D. W. Yannitell, "The effects of surface tension and viscosity on the rise velocity of a large gas bubble in a closed, vertical liquid-filled tube," *International Journal of Multiphase Flow*, vol. 13, pp. 57-69, 1987.
- [484] D. G. Karamanev, "Rise of gas bubbles in quiescent liquids," *AIChE Journal*, vol. 40, pp. 1418-1421, 1994.
- [485] C. C. Maneri, "New look at wave analogy for prediction of bubble terminal velocities," *AIChE Journal*, vol. 41, pp. 481-487, 1995.
- [486] A. V. Nguyen, "Prediction of bubble terminal velocities in contaminated water," *AIChE Journal*, vol. 44, pp. 226-230, 1998.
- [487] R. Krishna, M. I. Urseanu, J. M. van Baten, and J. Ellenberger, "Rise velocity of a swarm of large gas bubbles in liquids," *Chemical Engineering Science*, vol. 54, pp. 171-183, 1999.

- [488] G. Yang, X. Luo, R. Lau, and L. Fan, "Heat-transfer characteristics in slurry bubble columns at elevated pressures and temperatures," *Industrial & engineering ...*, vol. 39, pp. 2568-2577, 2000.
- [489] D. Rodrigue, "Generalized correlation for bubble motion," *AIChE Journal*, vol. 47, pp. 39-44, 2001.
- [490] W. Gestrich, H. Esenwein, and W. Krauss, "Der flüssigkeitsseitige Stoffübergangskoeffizient in Blasenschichten," *Chemie Ingenieur Technik*, vol. 48, pp. 399-407, 1976.
- [491] T. Sauer and D.-C. Hempel, "Fluid dynamics and mass transfer in a bubble column with suspended particles," *Chemical Engineering & Technology*, vol. 10, pp. 180-189, 1987.
- [492] M. Fukuma, K. Muroyama, and A. Yasunishi, "Specific Gas-Liquid Interfacial Area and Liquid-Phase Mass Transfer Coefficient in a Slurry Bubble Column," *Journal of Chemical Engineering of Japan*, vol. 20, pp. 321-324, 1987.
- [493] P. H. Calderbank and M. B. Moo-Young, "The continuous phase heat and mass transfer properties of dispersions," *Chemical Engineering Science*, vol. 50, pp. 3921-3934, 1995.
- [494] G. Vázquez, E. Alvarez, J. M. Navaza, R. Rendo, and E. Romero, "Surface Tension of Binary Mixtures of Water + Monoethanolamine and Water + 2-Amino-2-methyl-1-propanol and Tertiary Mixtures of These Amines with Water from 25 °C to 50 °C," *Journal of Chemical & Engineering Data*, vol. 42, pp. 57-59, 1997/01/01 1997.
- [495] Y. X. Guo, M. N. Rathor, and H. C. Ti, "Hydrodynamics and mass transfer studies in a novel external-loop airlift reactor," *Chemical Engineering Journal*, vol. 67, pp. 205-214, 1997.
- [496] W. Yang, J. Wang, and Y. Jin, "Mass Transfer Characteristics of Syngas Components in Slurry System at Industrial Conditions," *Chemical Engineering & Technology*, vol. 24, pp. 651-657, 2001.
- [497] H. Kölbl, W. Siemes, R. Maas, and K. Müller, "Wärmeübergang an Blasensäulen," *Chemie Ingenieur Technik*, vol. 30, pp. 400-404, 1958.
- [498] H. Kölbl, E. Borchers, and J. Martins, "Wärmeübergang in Blasensäulen III. Messungen an gasdurchströmten Suspensionen," *Chemie Ingenieur Technik*, vol. 32, pp. 84-88, 1960.
- [499] W. Kast, "Untersuchungen zum Wärmeübergang in Blasensäulen," *Chemie Ingenieur Technik*, vol. 35, pp. 785-788, 1963.

- [500] W. Burkel, "Auslegung von Gasverteilern und Gasgehalt in Blasensäulen," *Chemie Ingenieur Technik*, vol. 46, pp. 205-205, 1974.
- [501] A. Shaykhutdinov, N. Bakirov, and A. Usmanov, "Determination and mathematical correlation of heat transfer coefficient under conditions of bubble flow, cellular and turbulent foam," *Int Chem Eng J*, vol. 11, pp. 641-5, 1975.
- [502] M. Nishikawa, H. Kato, and K. Hashimoto, "Heat Transfer in Aerated Tower Filled with Non-Newtonian Liquid," *Industrial & Engineering Chemistry Process Design and Development*, vol. 16, pp. 133-137, 1977/01/01 1977.
- [503] C. G. J. Baker, E. R. Armstrong, and M. A. Bergougnou, "Heat transfer in three-phase fluidized beds," *Powder Technology*, vol. 21, pp. 195-204, 1978.
- [504] Y. Louisi, "Ermittlung von fluiddynamischen Kenngrößen für die Fischer-Tropsch-Synthese in Blasensäulenreaktoren," Technical University of Berlin, 1979.
- [505] W. D. Deckwer, "On the mechanism of heat transfer in bubble column reactors," *Chemical Engineering Science*, vol. 35, pp. 1341-1346, 1980.
- [506] J. B. Joshi, M. M. Sharma, Y. T. Shah, C. P. P. Singh, M. Ally, and G. E. Klinzing, "Heat transfer in multiphase contactors," *Chemical Engineering Communications*, vol. 6, pp. 257-271, 1980/01/01 1980.
- [507] Y. Kato, K. Uchida, T. Kago, and S. Morooka, "Liquid holdup and heat transfer coefficient between bed and wall in liquid solid and gas-liquid-solid fluidized beds," *Powder Technology*, vol. 28, pp. 173-179, 1981.
- [508] P. Zehner, "Momentum, Mass and Heat Transfer in Bubble Columns - 1. Flow Model of the Bubble Column and Flow Velocities," *Verfahrenstechnik*, vol. 16, pp. 347-351, 1982.
- [509] R. Wendt, *Untersuchungen zum Wärmeübergang an Einzelrohren und querangeströmten Rohrbündelwärmeaustauschern in Blasensäulenreaktoren*: na, 1983.
- [510] R. Michael and K. H. Reichert, "Polymerisation von Ethylen in Blasensäulenreaktoren—Untersuchungen zum Stoffübergang und Gasgehalt," *Chemie Ingenieur Technik*, vol. 55, pp. 564-565, 1983.
- [511] T.-M. Chiu and E. N. Ziegler, "Heat transfer in three-phase fluidized beds," *AIChE Journal*, vol. 29, pp. 677-685, 1983.
- [512] Y. Kang, I. S. Suh, and S. D. Kim, "Heat Transfer Characteristics of Three-Phase Fluidized Beds," in *Proc. PACH E III*, Seoul, Korea, 1983, p. 1.

- [513] K. Muroyama, M. Fukuma, and A. Yasunishi, "Wall-to-bed heat transfer coefficient in gas—liquid—solid fluidized beds," *The Canadian Journal of Chemical Engineering*, vol. 62, pp. 199-208, 1984.
- [514] T.-M. Chiu and E. N. Ziegler, "Liquid holdup and heat transfer coefficient in liquid-solid and three-phase fluidized beds," *AIChE Journal*, vol. 31, pp. 1504-1509, 1985.
- [515] Y. Kang, I. SUH, and S. Kim, "Heat transfer characteristics of three phase fluidized beds," *Chemical Engineering Communications*, vol. 34, pp. 1-13, 1985.
- [516] M. Saberian-Broudjenni, G. Wild, N. Midoux, and J. C. Charpentier, "Contribution à l'étude du transfert de chaleur à la paroi dans les récteurs à lit fluidisé gaz-liquide-solide à faible vitesse de liquide," *The Canadian Journal of Chemical Engineering*, vol. 63, pp. 553-564, 1985.
- [517] I. S. Suh, G. T. Jin, and S. D. Kim, "Heat transfer coefficients in three phase fluidized beds," *International Journal of Multiphase Flow*, vol. 11, pp. 255-259, 1985.
- [518] S. D. Kim, Y. Kang, and H. K. Kwon, "Heat transfer characteristics in two-and three-phase slurry-fluidized beds," *AIChE Journal*, vol. 32, pp. 1397-1400, 1986.
- [519] K. Muroyama, M. Fukuma, and A. Yasunishi, "Wall-to-bed heat transfer in liquid—solid and gas—liquid—solid fluidized beds part II: Gas—liquid—solid fluidized beds," *The Canadian Journal of Chemical Engineering*, vol. 64, pp. 409-418, 1986.
- [520] K. Muroyama, M. Fukuma, and A. Yasunishi, "Wall-to-bed heat transfer in liquid—solid and gas—liquid—solid fluidized beds part I: Liquid—solid fluidized beds," *The Canadian Journal of Chemical Engineering*, vol. 64, pp. 399-408, 1986.
- [521] Y. Hatate, S. Tajiri, T. Fujita, T. Fukumoto, A. Ikari, and T. Hano, "Heat transfer coefficient in three-phase vertical upflows of gas-liquid-fine solid particle systems," *Journal of Chemical Engineering of Japan*, vol. 20, pp. 568-574, 1987.
- [522] H. J. Korte, *Wärmeübergang in Blasensäulen mit und ohne Einbauten*: H.-J.Korte, 1987.
- [523] M. Magiliotou, Y.-M. Chen, and L.-S. Fan, "Bed-immersed object heat transfer in a three-phase fluidized bed," *AIChE Journal*, vol. 34, pp. 1043-1047, 1988.
- [524] J. O. Kim, D. H. Park, and S. D. Kim, "Heat transfer and wake characteristics in three-phase fluidized beds with floating bubble breakers," *Chemical Engineering and Processing: Process Intensification*, vol. 28, pp. 113-119, 1990.

- [525] A. Zaidi, W. D. Deckwer, A. Mrani, and B. Benchechou, "Hydrodynamics and heat transfer in three-phase fluidized beds with highly viscous pseudoplastic solutions," *Chemical Engineering Science*, vol. 45, pp. 2235-2238, 1990.
- [526] S. Saxena, N. Rao, and A. Saxena, "Estimation of heat transfer coefficient for immersed surfaces in bubble columns involving fine powders," *Powder Technology*, vol. 63, pp. 197-202, 1990.
- [527] S. Kumar and L.-S. Fan, "Heat-transfer characteristics in viscous gas-liquid and gas-liquid-solid systems," *AIChE Journal*, vol. 40, pp. 745-755, 1994.
- [528] N. Kantarci, K. O. Ulgen, and F. Borak, "A Study on Hydrodynamics and Heat Transfer in a Bubble Column Reactor with Yeast and Bacterial Cell Suspensions," *The Canadian Journal of Chemical Engineering*, vol. 83, pp. 764-773, 2005.
- [529] K. S. K. R. Patnail, "Heat Transfer Coefficients in Three-Phase Sparged Reactors: A Unified Correlation," presented at the Proceedings of the World Congress on Engineering and Computer Science, San Francisco, USA, 2007.
- [530] A. K. Jhawar and A. Prakash, "Influence of bubble column diameter on local heat transfer and related hydrodynamics," *Chemical Engineering Research and Design*, vol. 89, pp. 1996-2002, 2011.
- [531] Y. Ohki and H. Inoue, "Longitudinal mixing of the liquid phase in bubble columns," *Chemical Engineering Science*, vol. 25, pp. 1-16, 1970.
- [532] R. Badura, W.-D. Deckwer, H.-J. Warnecke, and H. Langemann, "Durchmischung in Blasensäulen," *Chemie Ingenieur Technik*, vol. 46, pp. 399-399, 1974.
- [533] H. Hikita and H. Kikukawa, "Liquid-phase mixing in bubble columns: Effect of liquid properties," *The Chemical Engineering Journal*, vol. 8, pp. 191-197, 1974.
- [534] J. B. Joshi and Y. T. Shah, "Kinetics of organic sulphur removal from coal by oxydesulphurization," *Fuel*, vol. 60, pp. 612-614, 1981.
- [535] H.-P. Riquarts, "Strömungsprofile, Impulsaustausch und Durchmischung der flüssigen Phase in Blasensäulen," *Chemie Ingenieur Technik*, vol. 53, pp. 60-61, 1981.
- [536] K. H. Mangartz and T. Pilhofer, "Interpretation of mass transfer measurements in bubble columns considering dispersion of both phases," *Chemical Engineering Science*, vol. 36, pp. 1069-1077, 1981.

- [537] Y. Kawase and M. Moo-Young, "Liquid phase mixing in bubble columns with Newtonian and non-Newtonian fluids," *Chemical Engineering Science*, vol. 41, pp. 1969-1977, 1986.
- [538] D. N. Smith and J. A. Ruether, "Dispersed solid dynamics in a slurry bubble column," *Chemical Engineering Science*, vol. 40, pp. 741-753, 1985.
- [539] P. Calderbank, F. Evans, R. Farley, G. Jepson, and A. Poll, "Catalysis in practice," in *Symposium of the Institution of Chemical Engineers, London*, 1963.
- [540] C. Satterfield and G. Huff, "25 Effects of mass transfer on Fischer-Tropsch synthesis in slurry reactors," *Chemical Engineering Science*, vol. 35, pp. 195-202, 1980.
- [541] W. D. Deckwer, Y. Serpemen, M. Ralek, and B. Schmidt, "On the relevance of mass transfer limitations in the Fischer-Tropsch slurry process," *Chemical Engineering Science*, vol. 36, pp. 773-774, 1981.
- [542] W. D. Deckwer, Y. Serpemen, M. Ralek, and B. Schmidt, "Modeling the Fischer-Tropsch synthesis in the slurry phase," *Industrial & Engineering Chemistry Process Design and Development*, vol. 21, pp. 231-241, 1982/04/01 1982.
- [543] J. Kuo, F. Sanzo, W. Garwood, K. Gupte, C. Lang, T. Leib, M. Malladi, T. Molina, D. Nace, and J. Smith, "Slurry Fischer-Tropsch/Mobil Two-Stage Process of Converting Syngas to High Octane Gasoline," *DOE Contract No., DE-AC22-80PC30022, Final Report, June*, 1983.
- [544] T. Leib, P. Mills, J. Lerou, and J. Turner, "Evaluation of Neural Networks for Simulation of 3-Phase Bubble-Column Reactors," *Chemical engineering research & design*, vol. 73, pp. 690-696, 1995.
- [545] H.-S. Song, D. Ramkrishna, S. Trinh, and H. Wright, "Operating strategies for Fischer-Tropsch reactors: A model-directed study," *Korean Journal of Chemical Engineering*, vol. 21, pp. 308-317, 2004/03/01 2004.
- [546] R. Guettel and T. Turek, "Comparison of different reactor types for low temperature Fischer-Tropsch synthesis: A simulation study," *Chemical Engineering Science*, vol. 64, pp. 955-964, 2009.
- [547] W. Freedman, "Hold-up and liquid circulation in bubble columns," *Trans. Inst. Chem. Engrs.*, vol. 47, pp. 251-262, 1969.
- [548] K. Rietema and S. P. P. Otengraf, "Laminar liquid circulation and bubble street formation in a gas-liquid system," *Trans. Inst. Chem. Engrs.*, vol. 48, pp. 54-62, 1970.

- [549] K. Rietema, "Science and technology of dispersed two-phase systems—I and II," *Chemical Engineering Science*, vol. 37, pp. 1125-1150, 1982.
- [550] P. Whalley and J. F. Davidson, "Liquid Circulation in Bubble Columns," presented at the Symposium on Multi-phase Flow Systems, Institute of Chemical Engineering Symposium Series, 1974.
- [551] J. Joshi, "Axial Mixing in Multiphase Contactors - A Unified Correlation," *Trans. Inst. Chem. Engrs.*, vol. 58, pp. 155-164, 1980.
- [552] N. N. Clark, J. W. Van Egmond, and E. P. Nebiolo, "The drift-flux model applied to bubble columns and low velocity flows," *International Journal of Multiphase Flow*, vol. 16, pp. 261-279, 1990.
- [553] H. E. Gasche, C. Edinger, H. Kömpel, and H. Hofmann, "Hydrodynamics in bubble columns," *Chemical Engineering and Processing: Process Intensification*, vol. 26, pp. 101-109, 1989.
- [554] N. W. Geary and R. G. Rice, "Circulation in bubble columns: Corrections for distorted bubble shape," *AIChE Journal*, vol. 37, pp. 1593-1594, 1991.
- [555] V. V. Ranade, "Flow in bubble columns: some numerical experiments," *Chemical Engineering Science*, vol. 47, pp. 1857-1869, 1992.
- [556] A. Sokolichin and G. Eigenberger, "Gas—liquid flow in bubble columns and loop reactors: Part I. Detailed modelling and numerical simulation," *Chemical Engineering Science*, vol. 49, pp. 5735-5746, 1994.
- [557] M. Millies, "Fluiddynamik, Vermischung und Stoffübertragung in Zirkulationszellen in Blasensäulen," Ph.D. thesis, University of Hannover, 1992.
- [558] M. Bahary, "Experimental and computational studies of hydrodynamics in three-phase and two-phase fluidized beds," Ph.D. Dissertation, Chemical Engineering, Illinois Institute of Technology, 1994.
- [559] B. A. Kashiwa and R. A. Gore, "A Four Equation Model for Multiphase Turbulent Flow," presented at the First Joint ASME/JSME Fluids Engineering Conference, 1991.
- [560] F. F. Pironti, V. R. Medina, R. Calvo, and A. E. Sáez, "Effect of draft tube position on the hydrodynamics of a draft tube slurry bubble column," *The Chemical Engineering Journal and the Biochemical Engineering Journal*, vol. 60, pp. 155-160, 1995.

- [561] N. T. Padiál, W. B. VanderHeyden, R. M. Rauenzahn, and S. L. Yarbrow, "Three-dimensional simulation of a three-phase draft-tube bubble column," *Chemical Engineering Science*, vol. 55, pp. 3261-3273, 2000.
- [562] T. J. Lin, J. Reese, T. Hong, and L. S. Fan, "Quantitative analysis and computation of two-dimensional bubble columns," *AIChE Journal*, vol. 42, pp. 301-318, 1996.
- [563] J. Zhang, Y. Li, and L.-S. Fan, "Discrete phase simulation of gas–liquid–solid fluidization systems: single bubble rising behavior," *Powder Technology*, vol. 113, pp. 310-326, 2000.
- [564] H. Dziállas, V. Michele, and D. C. Hempel, "Measurement of Local Phase Holdups in a Two- and Three-Phase Bubble Column," *Chemical Engineering & Technology*, vol. 23, pp. 877-884, 2000.
- [565] V. Michele and D. C. Hempel, "Liquid flow and phase holdup—measurement and CFD modeling for two-and three-phase bubble columns," *Chemical Engineering Science*, vol. 57, pp. 1899-1908, 2002.
- [566] M. R. Rampure, V. V. Buwa, and V. V. Ranade, "Modelling of Gas-Liquid/Gas-Liquid-Solid Flows in Bubble Columns: Experiments and CFD Simulations," *The Canadian Journal of Chemical Engineering*, vol. 81, pp. 692-706, 2003.
- [567] I. K. Gamwo, J. S. Halow, D. Gidaspow, and R. Mostofi, "CFD models for methanol synthesis three-phase reactors: reactor optimization," *Chemical Engineering Journal*, vol. 93, pp. 103-112, 2003.
- [568] G. M. Cartland Glover and S. C. Generalis, "Gas–liquid–solid flow modelling in a bubble column," *Chemical Engineering and Processing: Process Intensification*, vol. 43, pp. 117-126, 2004.
- [569] D. Wiemann and D. Mewes, "Calculation of flow fields in two and three-phase bubble columns considering mass transfer," *Chemical Engineering Science*, vol. 60, pp. 6085-6093, 2005.
- [570] M. van Sint Annaland, N. G. Deen, and J. A. M. Kuipers, "Numerical simulation of gas–liquid–solid flows using a combined front tracking and discrete particle method," *Chemical Engineering Science*, vol. 60, pp. 6188-6198, 2005.
- [571] K.-T. Nguyen and S.-C. Huang, "Simulation of Hydrodynamic Characteristics of Glass Beads in Gas-Liquid-Solid Three Phase Fluidized Beds by Computational Fluid Dynamics," *Journal of Engineering Technology and Education*, vol. 8, pp. 248-261, 2007.

- [572] F. Wang, Z.-S. Mao, Y. Wang, and C. Yang, "Measurement of phase holdups in liquid–liquid–solid three-phase stirred tanks and CFD simulation," *Chemical Engineering Science*, vol. 61, pp. 7535-7550, 2006.
- [573] K. Kiared, F. Larachi, J. Chaouki, and C. Guy, "Mean and Turbulent Particle Velocity in the Fully Developed Region of a Three-Phase Fluidized Bed," *Chemical Engineering & Technology*, vol. 22, pp. 683-689, 1999.
- [574] Y. H. Yu and S. D. Kim, "Bubble-Wake Model for Radial Velocity Profiles of Liquid and Solid Phases in Three-Phase Fluidized Beds," *Industrial & Engineering Chemistry Research*, vol. 40, pp. 4463-4469, 2001/10/01 2001.
- [575] C. Cao, M. Liu, J. Wen, and Q. Guo, "Experimental measurement and numerical simulation for liquid flow velocity and local phase hold-ups in the riser of a GLSCFB," *Chemical Engineering and Processing: Process Intensification*, vol. 48, pp. 288-295, 2009.
- [576] P. Muthiah, K. Ponnusamy, and T. K. Radhakrishnan, "CFD Modeling of Flow Pattern and Phase Holdup of Three Phase Fluidized Bed Contactor," *Chemical Product and Process Modeling*, vol. 4, p. Art. 36, 2009.
- [577] P. J. O'Rourke, P. Zhao, and D. Snider, "A model for collisional exchange in gas/liquid/solid fluidized beds," *Chemical Engineering Science*, vol. 64, pp. 1784-1797, 2009.
- [578] X. Jia, J. Wen, W. Feng, and Q. Yuan, "Local Hydrodynamics Modeling of a Gas–Liquid–Solid Three-Phase Airlift Loop Reactor," *Industrial & Engineering Chemistry Research*, vol. 46, pp. 5210-5220, 2007/07/01 2007.
- [579] J. M. D. Ville, *Micromeritics*. New York: Pitman Publishing Co., 1948.
- [580] S. Morsi and A. Alexander, "An investigation of particle trajectories in two-phase flow systems," *J. Fluid Mech*, vol. 55, pp. 193-208, 1972.
- [581] J. Garside and M. R. Al-Dibouni, "Velocity-voidage relationships for fluidization and sedimentation in solid-liquid systems," *Industrial & Engineering Chemistry Process Design And Development*, vol. 16, pp. 206-214, 1977.
- [582] E. Achenbach, "Experiments on the flow past spheres at very high Reynolds numbers," *Journal of fluid mechanics*, vol. 54, pp. 565-575, 1972.
- [583] H. D. Arnold, "LXXIV. Limitations imposed by slip and inertia terms upon Stoke's law for the motion of spheres through liquids," *Philosophical Magazine Series 6*, vol. 22, pp. 755-775, 1911/11/01 1911.

- [584] A. B. Bailey and J. Hiatt, "Sphere Drag Coefficients for a Broad Range of Mach and Reynolds Numbers," *AIAA Journal*, vol. 10, pp. 1436-1440, 1972/11/01 1972.
- [585] K. V. Beard and H. R. Pruppacher, "A Determination of the Terminal Velocity and Drag of Small Water Drops by Means of a Wind Tunnel," *Journal of the atmospheric sciences*, vol. 26, pp. 1066-1072, 1969/09/01 1969.
- [586] C. N. Davies, "Definitive equations for the fluid resistance of spheres," *Proceedings of the Physical Society*, vol. 57, p. 259, 1945.
- [587] S. C. R. Dennis and J. D. A. Walker, "Calculation of the steady flow past a sphere at low and moderate Reynolds numbers," *Journal of fluid mechanics*, vol. 48, pp. 771-789, 1971.
- [588] K. L. Goin and W. R. Lawrence, "Subsonic drag of spheres at Reynolds numbers from 200 to 10,000," *AIAA Journal*, vol. 6, pp. 961-962, 1968/05/01 1968.
- [589] A. Goldburg and B. H. Florsheim, "Transition and Strouhal Number for the Incompressible Wake of Various Bodies," *Physics of Fluids (1958-1988)*, vol. 9, pp. 45-50, 1966.
- [590] R. Gunn and G. D. Kinzer, "THE TERMINAL VELOCITY OF FALL FOR WATER DROPLETS IN STAGNANT AIR," *Journal of Meteorology*, vol. 6, pp. 243-248, 1949/08/01 1949.
- [591] S. Hoerner, *Tests of spheres with reference to Reynolds number, turbulence, and surface roughness*: National Advisory Committee for Aeronautics, 1935.
- [592] F. Ihme, H. Schmidt-Traub, and H. Brauer, "Theoretische Untersuchung über die Umströmung und den Stoffübergang an Kugeln," *CHEMIE INGENIEUR TECHNIK*, vol. 44, pp. 306-313, 1972.
- [593] B. P. LeClair, *Viscous flow in multiparticle systems at intermediate Reynolds numbers*: McMaster University, 1970.
- [594] H. Liebster, "Über den Widerstand von Kugeln," *Annalen der Physik*, vol. 387, pp. 541-562, 1927.
- [595] J. H. Masliyah, "Symmetric flow past orthotropic bodies: single and clusters," University of British Columbia, 1970.
- [596] T. Maxworthy, "Accurate measurements of sphere drag at low Reynolds numbers," *Journal of fluid mechanics*, vol. 23, pp. 369-372, 1965.
- [597] T. Maxworthy, "Experiments on the Flow Around a Sphere at High Reynolds Numbers," *Journal of Applied Mechanics*, vol. 36, pp. 598-607, 1969.

- [598] W. Möller, *Experimentelle Untersuchungen zur Hydrodynamik der Kugel*: Hirzel, 1937.
- [599] E. Pettyjohn and E. Christiansen, "Effect of particle shape on free-settling rates of isometric particles," *CHEMICAL ENGINEERING PROGRESS*, vol. 44, pp. 157-172, 1948.
- [600] H. R. Pruppacher and E. H. Steinberger, "An Experimental Determination of the Drag on a Sphere at Low Reynolds Numbers," *Journal of Applied Physics*, vol. 39, pp. 4129-4132, 1968.
- [601] Y. Rimon and S. I. Cheng, "Numerical Solution of a Uniform Flow over a Sphere at Intermediate Reynolds Numbers," *Physics of Fluids (1958-1988)*, vol. 12, pp. 949-959, 1969.
- [602] F. W. Roos and W. W. Willmarth, "Some experimental results on sphere and disk drag," *AIAA Journal*, vol. 9, pp. 285-291, 1971/02/01 1971.
- [603] S.-W. Woo, "Simultaneous Free and Forced Convection Around Submerged Cylinders and Spheres," 1971.
- [604] C. Wieselsberger, "Weitere Feststellungen über die Gesetze des Flüssigkeits- und Luftwiderstandes," *Physikalische Zeitschrift*, vol. 23, pp. 219-224, 1922.
- [605] O. Molerus, "A coherent representation of pressure drop in fixed beds and of bed expansion for particulate fluidized beds," *Chemical Engineering Science*, vol. 35, pp. 1331-1340, 1980.
- [606] H. Heywood, "Calculation of particle terminal velocities," *The Journal of the Imperial College Chemical Engineering Society*, vol. 4, 1948.
- [607] H. Heywood, "Uniform and non-uniform motion of particles in fluids," presented at the Interaction between Fluids and Particles, London, UK, 1962.
- [608] C. E. Lapple and C. B. Shepherd, "Calculation of particle trajectories," *Industrial & Engineering Chemistry*, vol. 32, pp. 605-617, 1940/05/01 1940.
- [609] R. L. C. Flemmer and C. L. Banks, "On the drag coefficient of a sphere," *Powder Technology*, vol. 48, pp. 217-221, 1986.
- [610] R. Turton and O. Levenspiel, "A short note on the drag correlation for spheres," *Powder Technology*, vol. 47, pp. 83-86, 1986.
- [611] M. Vlajinac and E. E. Covert, "Sting-free measurements of sphere drag in laminar flow," *Journal of fluid mechanics*, vol. 54, pp. 385-392, 1972.

- [612] H. H. Rosenbrock, "An Automatic Method for Finding the Greatest or Least Value of a Function," *The Computer Journal*, vol. 3, pp. 175-184, January 1, 1960 1960.
- [613] A. R. Khan and J. F. Richardson, "THE RESISTANCE TO MOTION OF A SOLID SPHERE IN A FLUID," *Chemical Engineering Communications*, vol. 62, pp. 135-150, 1987/12/01 1987.
- [614] S. Ergun, "Fluid flow through packed columns," *Chem. Eng. Prog.*, vol. 48, 1952.
- [615] J. F. Richardson and W. N. Zaki, "Sedimentation and fluidisation: Part I," *Chemical Engineering Research and Design*, vol. 75, Supplement, pp. S82-S100, 1997.
- [616] C. Boyer, A.-M. Duquenne, and G. Wild, "Measuring techniques in gas-liquid and gas-liquid-solid reactors," *Chemical Engineering Science*, vol. 57, pp. 3185-3215, 2002.
- [617] S. D. Gharat and J. B. Joshi, "Transport phenomena in bubble column reactors, II: pressure drop," *The Chemical Engineering Journal*, vol. 48, pp. 153-166, 1992.
- [618] A. Behkish, R. Lemoine, L. Sehabiague, R. Oukaci, and B. I. Morsi, "Gas holdup and bubble size behavior in a large-scale slurry bubble column reactor operating with an organic liquid under elevated pressures and temperatures," *Chemical Engineering Journal*, vol. 128, pp. 69-84, 1 April 2007 2007.
- [619] A. Behkish, Z. Men, J. R. Inga, and B. I. Morsi, "Mass transfer characteristics in a large-scale slurry bubble column reactor with organic liquid mixtures," *Chemical Engineering Science*, vol. 57, pp. 3307-3324., 2002.
- [620] R. Lemoine, A. Behkish, and B. I. Morsi, "Hydrodynamic and Mass-Transfer Characteristics in Organic Liquid Mixtures in a Large-Scale Bubble Column Reactor for the Toluene Oxidation Process," *Industrial & Engineering Chemistry Research*, vol. 43, pp. 6195-6212, 2004/09/01 2004.
- [621] K. Sriram and R. Mann, "Dynamic Gas Disengagement: A New Technique for Assessing the Behavior of Bubble Columns," *Chemical Engineering Science*, vol. 32, pp. 571-580, 1977.
- [622] M. Fukuma, K. Muroyama, and A. Yasunishi, "Properties of bubble swarn in a slurry bubble column," *Journal of Chemical Engineering of Japan*, vol. 20, pp. 28-33, 1987.
- [623] L. S. FAN, K. Tsuchiya, and H. Brenner, *Bubble Wake Dynamics in Liquids and Liquid-Solid Suspensions*: Elsevier Science, 2013.

- [624] D. Bukur, S. Patel, and J. Daly, "Gas holdup and solids dispersion in a three phase slurry bubble column," *AIChE journal*, vol. 36, pp. 1731-1735, 1990.
- [625] D. Bukur, J. Daly, and S. Patel, "Hydrodynamics of the three-phase slurry Fischer-Tropsch bubble column reactors: Final Report No. DOE/PC/90012-10," U.S Department of Energy 1990.
- [626] D. B. Bukur, J. G. Daly, S. A. Patel, M. L. Raphael, and G. B. Tatterson, "Hydrodynamics of Fischer-Tropsch synthesis in slurry bubble column reactors: Final report No. DOE/PC/70027-10," U.S. Department of Energy 1987.
- [627] D. B. Bukur and J. G. Daly, "Gas hold-up in bubble columns for Fischer-Tropsch synthesis," *Chemical Engineering Science*, vol. 42, pp. 2967-2969, 1987.
- [628] S. A. Patel, J. G. Daly, and D. B. Bukur, "Bubble-size distribution in Fischer-Tropsch-derived waxes in a bubble column," *AIChE Journal*, vol. 36, pp. 93-105, 1990.
- [629] D. B. Bukur, S. A. Patel, and R. Matheo, "Hydrodynamic studies in Fischer-Tropsch derived waxes in a bubble column," *Chemical Engineering Communications*, vol. 60, pp. 63-78, 1987/10/01 1987.
- [630] A. Kemoun, B. C. Ong, P. Gupta, H. Al-Dahhan, and M. P. Dudukovic, "Gas holdup in bubble columns at elevated pressure via computed tomography," *International Journal of Multiphase Flow*, vol. 27, pp. 929-946, 2001.
- [631] A. B. Gandhi, J. B. Joshi, V. K. Jayaraman, and B. D. Kulkarni, "Development of support vector regression (SVR)-based correlation for prediction of overall gas hold-up in bubble column reactors for various gas-liquid systems," *Chemical Engineering Science*, vol. 62, pp. 7078-7089, 2007.
- [632] M. I. Urseanu, R. P. M. Guit, A. Stankiewicz, G. van Kranenburg, and J. H. G. M. Lommen, "Influence of operating pressure on the gas hold-up in bubble columns for high viscous media," *Chemical Engineering Science*, vol. 58, pp. 697-704, 2003.
- [633] S. V. Dharwadkar, S. B. Sawant, and J. B. Joshi, "Gas hold-up in highly viscous pseudoplastic non-newtonian solutions in three phase sparged reactors," *The Canadian Journal of Chemical Engineering*, vol. 65, pp. 406-411, 1987.
- [634] I. G. Reilly, D. S. Scott, T. J. W. de Bruijn, A. Jain, and J. Piskorz, "A Correlation for Gas Holdup in Turbulent Coalescing Bubble Columns," *Canadian Journal of Chemical Engineering*, vol. 64, pp. 705-717, 1986.

- [635] P. M. Wilkinson, H. Haringa, and L. L. van Dierendonck, "Mass Transfer and Bubble Size in a Bubble Column under Pressure," *Chemical Engineering Science*, vol. 49, pp. 1417-1427, 1994.
- [636] R. Lemoine and B. I. Morsi, "An algorithm for predicting the hydrodynamic and mass transfer parameters in agitated reactors," *Chemical Engineering Journal*, vol. 114, pp. 9-31, 2005.
- [637] R. Lemoine, A. Behkish, L. Sehabiague, Y. Heintz, R. Oukaci, and B. I. Morsi, "An Algorithm for Predicting the Hydrodynamic and Mass Transfer Parameters in Slurry Bubble Column Reactors for Fischer-Tropsch Synthesis," *Proceedings of the Twenty Second Annual International Pittsburgh Coal Conference, Pittsburgh, PA, September 12-16, 2005*.
- [638] S. K. Majumder, *Hydrodynamics and Transport Processes of Inverse Bubbly Flow*: Elsevier Science, 2016.
- [639] S. Bordel, R. Mato, and S. Villaverde, "Modeling of the evolution with length of bubble size distributions in bubble columns," *Chemical Engineering Science*, vol. 61, pp. 3663-3673, 2006.
- [640] Y. Kang, Y. J. Cho, K. J. Woo, and S. D. Kim, "Diagnosis of bubble distribution and mass transfer in pressurized bubble columns with viscous liquid medium," *Chemical Engineering Science*, vol. 54, pp. 4887-4893, 1999.
- [641] G. M. Evans, G. J. Jameson, and B. W. Atkinson, "Prediction of the bubble size generated by a plunging liquid jet bubble column," *Chemical Engineering Science*, vol. 47, pp. 3265-3272, 9// 1992.
- [642] A. Matsuura and L.-S. Fan, "Distribution of bubble properties in a gas-liquid-solid fluidized bed," *AIChE Journal*, vol. 30, pp. 894-903, 1984.
- [643] M. R. Rahimpour, S. M. Jokar, and Z. Jamshidnejad, "A novel slurry bubble column membrane reactor concept for Fischer-Tropsch synthesis in {GTL} technology," *Chemical Engineering Research and Design*, vol. 90, pp. 383-396, 2012.
- [644] M. Millies and D. Mewes, "Interfacial area density in bubbly flow," *Chemical Engineering and Processing: Process Intensification*, vol. 38, pp. 307-319, 9// 1999.
- [645] R. Krishna, J. M. van Baten, and M. I. Urseanu, "Three-phase Eulerian simulations of bubble column reactors operating in the churn-turbulent regime: a scale up strategy," *Chemical Engineering Science*, vol. 55, pp. 3275-3286, 8// 2000.

- [646] B. G. Kelkar, S. P. Godbole, M. F. Honath, Y. T. Shah, N. L. Carr, and W. D. Deckwer, "Effect of addition of alcohols on gas holdup and backmixing in bubble columns," *AIChE Journal*, vol. 29, pp. 361-369, 1983.
- [647] M. Ishii, S. Kim, and J. Uhle, "Interfacial area transport equation: model development and benchmark experiments," *International Journal of Heat and Mass Transfer*, vol. 45, pp. 3111-3123, 7// 2002.
- [648] W. C. Yang, *Handbook of Fluidization and Fluid-Particle Systems*: Taylor & Francis, 2003.
- [649] A. Behkish, R. Lemoine, L. Sehabiague, R. Oukaci, and B. I. Morsi, "Prediction of the gas holdup in industrial-scale bubble columns and slurry bubble column reactors using back-propagation neural networks," *International Journal of Chemical Reactor Engineering*, vol. 3, p. A53, 2005.
- [650] S. Ghasemi, M. Sohrabi, and M. Rahmani, "A comparison between two kinds of hydrodynamic models in bubble column slurry reactor during Fischer–Tropsch synthesis: Single-bubble class and two-bubble class," *Chemical Engineering Research and Design*, vol. 87, pp. 1582-1588, 2009.
- [651] L. Sehabiague, O. M. Basha, S. Zhansheng, H. Jia, Y. Hong, L. Weng, Z. Men, Y. Cheng, K. Liu, and B. I. Morsi, "Assessing the Performance of an Industrial SBCR for Fischer-Tropsch Synthesis: Experimental and Modeling," *AIChE J.*, vol. In Press, 2015.